

Contract No:

This document was prepared in conjunction with work accomplished under Contract No. 89303321CEM000080 with the U.S. Department of Energy (DOE) Office of Environmental Management (EM).

Disclaimer:

This work was prepared under an agreement with and funded by the U.S. Government. Neither the U.S. Government or its employees, nor any of its contractors, subcontractors or their employees, makes any express or implied:

- 1) warranty or assumes any legal liability for the accuracy, completeness, or for the use or results of such use of any information, product, or process disclosed; or
- 2) representation that such use or results of such use would not infringe privately owned rights; or
- 3) endorsement or recommendation of any specifically identified commercial product, process, or service.

Any views and opinions of authors expressed in this work do not necessarily state or reflect those of the United States Government, or its contractors, or subcontractors.

4. IMPLEMENTATION OF GROUNDWATER MODELING

This chapter describes the GW flow and transport conceptual models in the VZ for both generic and special waste forms in STs, ETs, LAWV, ILV, and NRCDA. The development and implementation of the GoldSim[®] system model for trenches is also introduced. The Trench System Model is used for sensitivity analysis and uncertainty quantification as reported in Chapter 6.

- **Section 4.1** discusses VZ conceptual models for generic waste forms in STs and ETs.
- **Section 4.2** describes VZ conceptual models for simple SWFs in trenches, including CIG trench segments.
- **Section 4.3** introduces VZ conceptual models for complex SWFs in trenches.
- **Section 4.4** details the GoldSim[®] Trench System Model.
- **Sections 4.5 and 4.6** outline the VZ conceptual models for the LAWV and ILV, respectively.
- **Section 4.7** describes the VZ conceptual models implemented for NRCDA welded casks and bolted containers.

As in PA2008, mechanical dispersion is not included in the VZ transport models of all DU types for the following two reasons:

- VZ flow is generally perpendicular with respect to geological formations and, as such, the choice of dispersion parameter values becomes difficult to defend.
- In general, the choice of zero mechanical dispersion is assumed to provide more conservative estimates of contaminant fluxes to the underlining water table.

4.1. SLIT AND ENGINEERED TRENCHES

Disposal limits for STs and ETs through the 1,000-year period of performance are developed for the following exposure pathways: GW protection, all-pathways, IHI,

KEY TAKEAWAYS

- ✓ Conceptual models of the waste zone and VZ have been developed for five types of DUs: ST, ET, LAWV, ILV, and NRCDA.
- ✓ Generic waste and both simple and complex SWFs are modeled differently by DU and SWF type.
- ✓ Simple SWF conceptual models of the VZ include CIG trench segments, effective K_d , delayed release, solubility controlled, diffusion controlled, and tall box.
- ✓ Complex SWF conceptual models are for the Heavy Water Components Test Reactor, Reactor Process HXs, and 232-F concrete rubble.
- ✓ VZ conceptual models have been implemented in PORFLOW for GW flow and radionuclide transport modeling.
- ✓ PORFLOW models have been successfully benchmarked against flow and transport results from PA2008.
- ✓ A Trench System Model of the ELLWF VZ and aquifer has been developed in GoldSim[®] to perform sensitivity analysis and uncertainty quantification for STs and ETs.
- ✓ The Trench System Model has been successfully benchmarked against PORFLOW flow and transport results for key radionuclides.

air, and radon. This section describes the development and implementation of conceptual models for STs and ETs for the GW protection pathway. The ST and ET conceptual models for the IHI exposure pathway are described in Section 3.7.3 and Section 7.3. ST and ET conceptual models for the air and radon pathways are described in Section 3.6. STs and ETs are considered together in this section because the similarities in their facility design; waste characterization; and physical, hydraulic, and chemical properties result in the same (or nearly the same) GW conceptual model.

A GW transport analysis is conducted to determine maximum radionuclide concentrations as a function of time within the 100-meter POA buffer zone. PORFLOW (ACRi, 2018), which models both steady-state and transient flow and transport of radionuclide chains (parents and daughters) in porous media, is the primary analysis tool used. Two- and three-dimensional flow and transport analyses are performed to describe, in detail, the migration of species from the trench waste zones downward through the VZ to the underlying water table.

VZ simulations (treated as source terms) results are input into a 3-D aquifer transport model to compute maximum GW concentrations of radionuclides within the 100-meter POA. Preliminary GW protection and all-pathways disposal limits for STs and ETs over the 1,000-year period of performance are developed from the computed maximum GW concentrations using the *PA/CA Limits and Doses Tool* in the SRNL Dose Toolkit (Aleman, 2019).

The sections below present hydraulic and geochemical properties specific to STs and ETs as well as conceptual models and associated implementation approaches for the GW protection pathway.

4.1.1. Waste Zone Conceptual Model: Material and Hydraulic Properties

4.1.1.1. Slit Trenches

An analysis of historical data in CWTS (SRS, 2021c) for a 15-year period from 1995 to 2010 by Sink (2010) found that 66.7% of all waste disposed of in STs is bulk waste and 33.3% is stacked containerized waste (typically B-25 boxes). Based on the analysis by Sink (2010), a hybrid ST waste representation was developed by Phifer (2010) and refined by Nichols and Butcher (2020) to address uncertainties in porosity and bulk density of the actual disposed waste both before and after dynamic compaction. Dynamic compaction is employed to achieve waste layer stabilization at or near the end of the 100-year IC period when significant corrosion of the containers has occurred. Container degradation improves the effectiveness of dynamic compaction in eliminating potential future subsidence of the final closure cap. A representation of the ST waste zone before and after dynamic compaction is shown in Figure 4-1(a) and Figure 4-2(a), respectively.

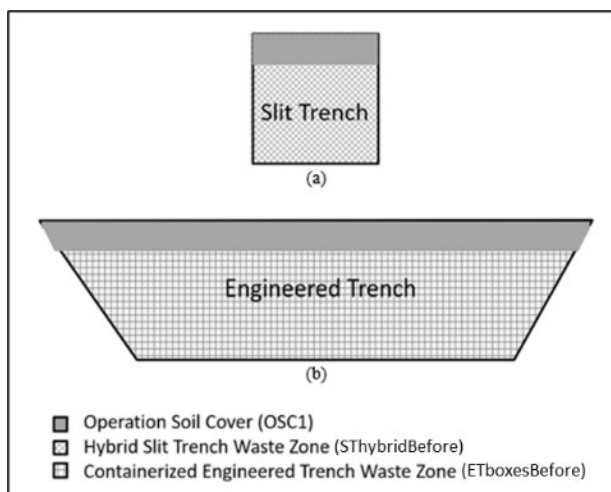


Figure 4-1. Conceptual Model Representing Hydraulic Properties of Slit and Engineered Trenches Before Dynamic Compaction (Nichols and Butcher, 2020)

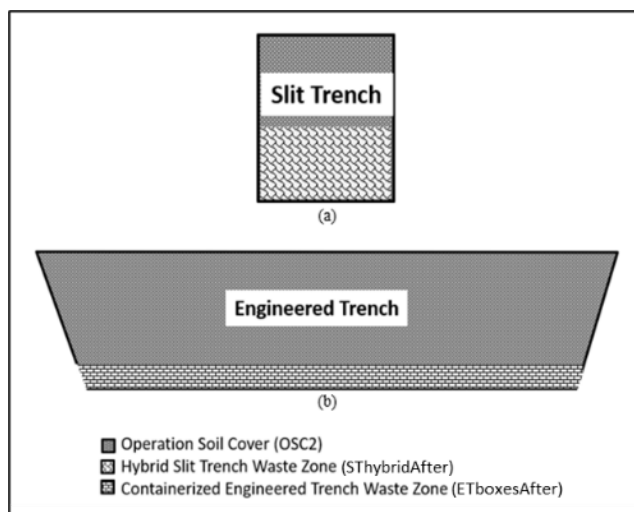


Figure 4-2. Conceptual Model Representing Hydraulic Properties of Slit and Engineered Trenches After Dynamic Compaction (Nichols and Butcher, 2020)

4.1.1.1. Bulk Waste Disposal in Slit Trenches

Bulk waste, typically consisting of rubble and debris, is frequently delivered by roll-off pans and bulldozed into one end of a ST segment (Figure 2-59 and Figure 2-60). Clean soil is then bulldozed over the emplaced bulk waste to prevent spreading contamination. As a result, the waste zone contains a significant quantity of clean backfill soil mixed with contaminated rubble and debris. Four feet of clean soil is placed over the waste layer to bring the trench up to grade and serve as the required OSC. More soil is added as needed to ensure positive drainage away from the trench. Based on the substantial mass of uncompacted soil mixed with rubble in the waste layer, Phifer (2010) determined that ST areas containing bulk waste can be adequately represented by OSCs both before and after dynamic compaction (referred to as OSC1 and OSC2, respectively). Table 4-1, in the two columns labeled “Bulk (ST only),” lists the recommended property values for ST bulk waste based on the properties of OSC1 and OSC2. The ST bulk waste form alone is

not included in ST or ET VZ models. Instead, bulk waste (and its associated properties) is included in property calculations for the ST hybrid waste form as described below in Section 4.1.1.1.3.

Table 4-1. Slit and Engineered Trench Waste Properties Before and After Dynamic Compaction (Nichols and Butcher, 2020; Table 7-1)

Property	Bulk (ST only)		Container (ST and ET)		Hybrid (ST only)	
	Before DC	After DC	Before DC	After DC	Before DC	After DC
Porosity, η (volume fraction)	0.456	0.275	0.889	0.303	0.600	0.277
Bulk Density, ρ_b (g cm ⁻³)	1.442	1.922	0.293	1.847	1.059	1.915
Particle Density, ρ_p (g cm ⁻³)	2.65	2.65	2.65	2.65	2.65	2.65
Saturated Hydraulic Conductivity, K_{sat} (cm s ⁻¹)	1.3E-04	1.6E-05	2.2E-05	8.7E-06	9.4E-05	1.5E-05
Saturated Effective Diffusion Coefficient, D_e (cm ² s ⁻¹)	5.3E-06	4.0E-06	5.3E-06	4.0E-06	5.3E-06	4.0E-06
Thickness (feet)	16.0	12.0	16.0 ¹	2.5	16.0	11.1
Fraction, f_i	N/A	N/A	0.0346/0.9654 (OSC1/B25)	0.0816/0.9184 (OSC2/B25)	0.667/0.333 (OSC1/B25)	0.9058/0.0942 (OSC2/B25)
θ_s	0.456000	0.275000	WRC and k_r are calculated using Eq. (4-8) and Eq. (4-11)			
θ	0.121330	0.073171				
α	0.040416	0.018263				
n	1.153656	1.153659				
m	0.133191	0.133193				
Blended Material ID	OscBefore (OSC1)	OscAfter (OSC2)	ETboxesBefore	ETboxesAfter	SThybridBefore	SThybridAfter

Notes:

¹ A stack of four B-25 boxes before OSC placement is 17.292 feet high. After OSC placement, the stack is assumed to be approximately 16 feet high (15.74 feet actual) due to the collapse of the 6-inch vertical spacers between the boxes (Phifer, 2010).

van Genuchten (VG) parameters = θ_s , θ , α , n , and m

B25: B-25 box before dynamic compaction

OSC1: OSC before dynamic compaction

OSC2: OSC after dynamic compaction

WRC: Water retention curve

4.1.1.1.2. Containerized Waste Disposal in Slit Trenches

Various types of disposal containers are crane-lifted into STs. Containers are frequently stacked during disposal to optimize use of the disposal space and to fill up the 16-foot-thick waste zone. To estimate hydraulic properties, Phifer (2010) and Nichols and Butcher (2020) assume that a four-high stack of B-25 boxes is representative of a containerized waste section of a trench. Once a section of the trench is filled with boxes, 4 feet of clean OSC is placed in a single lift over the

completed stack of boxes using a bulldozer. This step brings the trench up to grade and fills in voids between the individual boxes and between the stacks of boxes and the trench sidewalls. Based on this conceptual model, Phifer (2010) developed, and Nichols and Butcher (2020) later refined, a recommended set of blended material and hydraulic property values for containerized waste disposal in STs before and after dynamic compaction (see Table 4-1). This conceptual model also applies to containerized waste in ETs as discussed in Section 4.1.1.2.

Inputs and assumptions for the blending calculations are as follows (SRNL, 2020):

- The outside dimensions of a B-25 box are 6.0182-foot long, 3.8482-foot wide, and 3.9353-foot high, equating to an average exterior volume of 91.1380 ft³ (2,580,742 cm³).
- The inside dimensions of a B-25 box are 6.0000-foot long, 3.8300-foot wide, and 3.9170-foot high, equating to an average interior volume of 90.0127 ft³ (2,548,875 cm³).
- The volume of waste in a B-25 box is equal to the interior volume 90.0127 ft³ (2,548,875 cm³); the total waste volume in a stack of four B-25 boxes is 360.0506 ft³ (10,195,499 cm³).
- The average density of uncompacted waste within a B-25 box is 0.1785 g cm⁻³ (Phifer and Wilhite, 2001).
- The total waste mass in a four-high stack of B-25 boxes is 1,819,897 grams (10,195,499 cm³ × 0.1785 g cm⁻³).
- The volume of metal comprising a B-25 box is 31,867 cm³ (2,580,742 cm³ - 2,548,875 cm³), or 127,468 cm³ for four B-25 boxes before and after dynamic compaction.
- The average mass of an empty B-25 box is 262,520 grams (Phifer, 2010).
- Assuming a porosity of 0, the bulk and particle densities of the metal in a B-25 box are equal to 8.238 g cm⁻³ (262,520 g ÷ 31,867 cm³) before and after dynamic compaction.
- A stack of four B-25 boxes before OSC placement is 17.292-foot high (4 boxes × 3.9352 feet + 3 spacers × 0.517 feet). After OSC placement but before dynamic compaction, the stack is assumed to be 15.741-foot high (4 boxes × 3.9352 feet) due to spacer collapse (rounded to 16 feet in Table 4-1 per table footnote #1).
- The subsidence potential of a stack of four B-25 boxes is estimated to be approximately 13.5 feet within the 16-foot waste layer after OSC placement. Therefore, the compacted waste layer thickness is approximately 2.5 feet (Phifer and Wilhite, 2001).
- For STs, a 1-inch soil-filled gap is assumed to exist between the stacks of B-25 boxes (0.5 inches of soil allocated to each side of a B-25 box) and the soil is assumed to be loose with a bulk density equal to one-half that of OSC1 (1.442 g cm⁻³ ÷ 2 = 0.721 g cm⁻³) before dynamic compaction occurs. After dynamic compaction occurs, the bulk density of soil is assumed to equal that of OSC2 (1.922 g cm⁻³, Table 4-1).
- The total volume of a 0.5-inch-thick soil layer on four sides (not top and bottom) of a collapsed stack of four B-25 boxes before dynamic compaction is 369,579 cm³ (see SRNL, 2020 for detailed calculations) and after dynamic compaction is 138,592 cm³ [369,579 cm³ × (0.721 g cm⁻³ ÷ 1.922 g cm⁻³)].

- The total volume (soil + waste + metal) of a containerized waste stack after dynamic compaction is 1,698,209 cm³ [2.5 feet high × (6.0182 + 1/12) feet long × (3.8482 + 1/12) feet wide].
- The volume of waste after dynamic compaction is 1,432,148 cm³ (1,698,209 cm³ total volume after dynamic compaction 138,592 cm³ soil after dynamic compaction 127,468 cm³ metal after dynamic compaction).
- The bulk density of waste after dynamic compaction is 1.271 g cm⁻³ [1,819,897 g ÷ 1,432,148 cm³].

4.1.1.1.2.1. Before Dynamic Compaction

A containerized waste section in a ST initially comprises intact impermeable metal boxes containing waste, permeable soil, and void space. A conceptual representation of the hydraulic properties of these diverse components is a uniform blended waste zone material with equivalent hydraulic properties. To that end, each four-high stack of B-25 boxes with OSC1 is represented as a calculated material blend of 3.46 vol% OSC1 and 96.54 vol% B-25 boxes (1.19 vol% metal + 95.35 vol% waste) using the methodology originally proposed by Phifer (2010), implemented by Flach and Whiteside (2016; Appendix A), and later refined and implemented by Nichols and Butcher (2020) in SRNL (2020). The property blending schemes for bulk density and porosity are detailed below. Values for D_e and ρ_p in the uniform blended material are assumed to be the same as for ST bulk waste before dynamic compaction as shown in Table 4-1.

The equivalent bulk density of the stack of containerized waste before dynamic compaction ($\rho_{b \text{ ETboxesBefore}}$) is calculated from the individual bulk densities for gap soil (half OSC1), the metal boxes, and the waste inside the containers using the calculated volume fraction ($f_{i \text{ Before}}$) for each waste type as shown in Eq. (4-1).

$$\rho_{b \text{ ETboxesBefore}} = (\rho_{b1\text{Before}} \times f_{1\text{Before}}) + (\rho_{b2\text{Before}} \times f_{2\text{Before}}) + (\rho_{b3\text{Before}} \times f_{3\text{Before}}) \quad \text{Eq. (4-1)}$$

where subscript 1 refers to soil, subscript 2 refers to the metal, and subscript 3 refers to the waste. Substitution into Eq. (4-1) gives:

$$\rho_{b \text{ ETboxesBefore}} = (0.721 \times 0.0346) + (8.238 \times 0.0119) + (0.1785 \times 0.9535) = 0.293 \text{ g cm}^{-3} \quad \text{Eq. (4-2)}$$

where:

$$f_{1\text{Before}} = \frac{369,579 \text{ cm}^3 \text{ soil}}{(369,579 \text{ cm}^3 \text{ soil} + 127,469 \text{ cm}^3 \text{ metal} + 10,195,499 \text{ cm}^3 \text{ waste})} = 0.0346 \quad \text{Eq. (4-3)}$$

$$f_{2\text{Before}} = \frac{127,469 \text{ cm}^3 \text{ metal}}{(369,579 \text{ cm}^3 \text{ soil} + 127,469 \text{ cm}^3 \text{ metal} + 10,195,499 \text{ cm}^3 \text{ waste})} = 0.0119 \quad \text{Eq. (4-4)}$$

$$f_{3\text{Before}} = \frac{10,195,499 \text{ cm}^3 \text{ waste}}{(369,579 \text{ cm}^3 \text{ soil} + 127,469 \text{ cm}^3 \text{ metal} + 10,195,499 \text{ cm}^3 \text{ waste})} = 0.9535 \quad \text{Eq. (4-5)}$$

Containerized waste zone porosity is derived using Eq. (4-6).

$$\eta = 1 - \frac{\rho_b}{\rho_p} \quad \text{Eq. (4-6)}$$

where:

η	Porosity (cm ³ cm ⁻³)
ρ_b	Bulk density (g cm ⁻³)
ρ_p	Particle density (g cm ⁻³)

Substitution of the calculated containerized waste bulk density before dynamic compaction (0.293 g cm⁻³) and assumed particle density (2.65 g cm⁻³) gives:

$$\eta_{ETboxesBefore} = 1 - \frac{0.293}{2.65} = 0.889 \quad \text{Eq. (4-7)}$$

As developed by Nichols and Butcher (2020) and implemented in SRNL (2020), Eq. (4-8) is used to generate a composite WRC for the ST and ET containerized waste zones before dynamic compaction (e.g., ETboxesBefore) based on a blend of the individual WRCs for OSC1 and a four-high stack of intact B-25 boxes (metal + waste). The WRC for stacked B-25 boxes is a special case where S_2 is assumed to equal S_1 (OSC1) at all capillary pressures.

$$S_{CW} = \frac{f_1 S_1 \eta_1 + f_2 S_2 \eta_2}{\eta_{CW}} \quad \text{Eq. (4-8)}$$

where:

S_{CW}	Saturation of stacked containerized waste (cm ³ cm ⁻³)
S_1	Saturation of OSC1 (cm ³ cm ⁻³)
S_2	Saturation of B-25 boxes = S_1 (cm ³ cm ⁻³)
f_1	Volume fraction of OSC1 (unitless)
f_2	Volume fraction of B-25 boxes [metal + waste] (unitless)
η_1	Porosity of OSC1 (cm ³ cm ⁻³)
η_2	Porosity of B-25 boxes [metal + waste] (cm ³ cm ⁻³)
η_{CW}	Porosity of stacked containerized waste (cm ³ cm ⁻³)

Water saturation for OSC1 (S_l) in Eq. (4-8) is calculated using Eq. (4-9) and the VG parameters for OSC1 reported in SRNL (2020; OscBefore worksheet).

$$S_e = \left[1 + |\alpha \psi|^n \right]^{-m} \quad \text{Eq. (4-9)}$$

where:

S_e	Effective water saturation ($\text{m}^3 \text{m}^{-3}$)
ψ	Pressure head (m)
m	$1 - (1/n)$ (constraint to yield closed-form permeability expressions) [unitless]
α and n	Fitting parameters (i.e., shape factors) [unitless]

K_{sat} for the ST containerized waste zone is based on a blend of the properties of OSC1 and B-25 boxes as calculated by Eq. (4-10).

$$K_{sat} = f_1 K_{sat1} + f_2 K_{sat2} \quad \text{Eq. (4-10)}$$

where K_{sat2} is defined as K_{sat1} (OSC1) divided by a resistance factor (7.0 before dynamic compaction based on expert judgment) to account for the hydraulic impact of the metal walls of the boxes.

Similarly, blended relative permeability (k_r) is calculated using Eq. (4-11).

$$k_r = \frac{f_1 k_{r1} K_{sat1} + f_2 k_{r2} K_{sat2}}{K_{sat}} \quad \text{Eq. (4-11)}$$

where subscript 1 refers to OSC1 and subscript 2 refers to the B-25 boxes. For container waste zone hydraulic properties, k_{r2} is assumed equal to k_{r1} ; therefore, Eq. (4-11) simplifies to $k_r = k_{r1}$. The value for k_{r1} for OSC1 is derived using Eq. (3-50) in Section 3.8.3.1.1.

For ETboxesBefore via Eq. (4-10):

$$K_{sat} = (0.0346)(1.3\text{E} - 04 \text{ cm s}^{-1}) + (0.9654) \left(\frac{1.3\text{E} - 04 \text{ cm s}^{-1}}{7.0} \right) = 2.2\text{E} - 05 \text{ cm s}^{-1} \quad \text{Eq. (4-12)}$$

In addition, vertical and horizontal hydraulic conductivities (K_v and K_h) for the various container waste zones (ETboxesBefore, ETboxesAfter, SThybridBefore, SThybridAfter, NRcontainerLeak, and NRcontainerNoLeak) are assumed to be equal (isotropic).

$$K_h = K_v = k_r \times K_{sat} \quad \text{Eq. (4-13)}$$

Tabular and graphical hydraulic property results are reported in the *Hydraulic Properties Data Package, Rev. 3, dated December 1, 2020* (SRNL, 2020; Table 4 and ETboxesBefore worksheet). Graphical and tabular results for ETboxesBefore are also presented in Figure 4-3 (K_v versus suction head) and Figure 4-4 (K_h versus suction head). Figure 4-5 is a graph of the suction head versus water saturation.

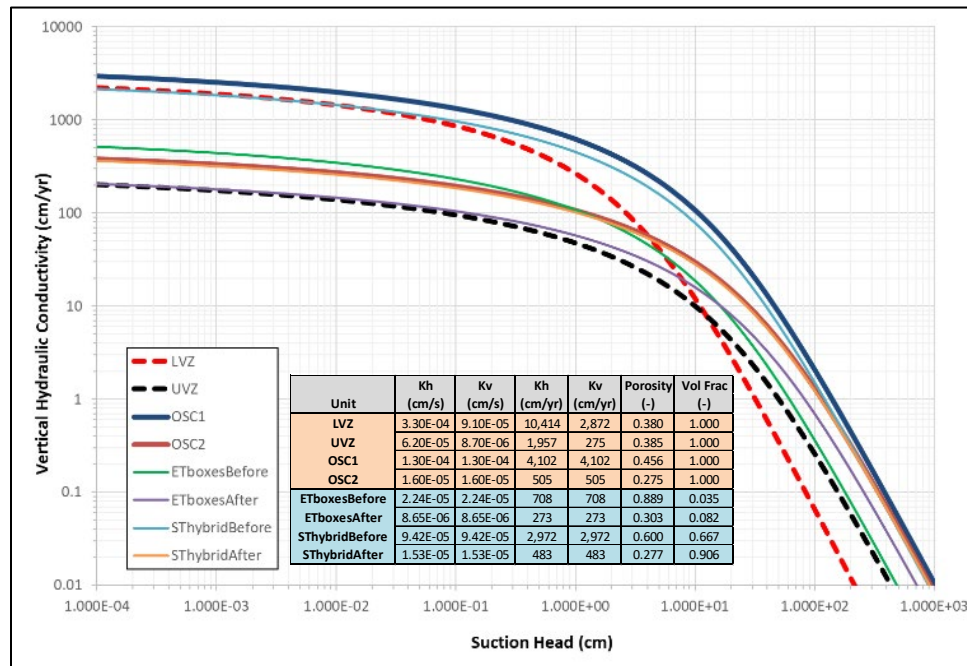


Figure 4-3. K_v versus Suction Head for Material Types Relevant to Slit and Engineered Trench Groundwater Simulations (SRNL, 2020)

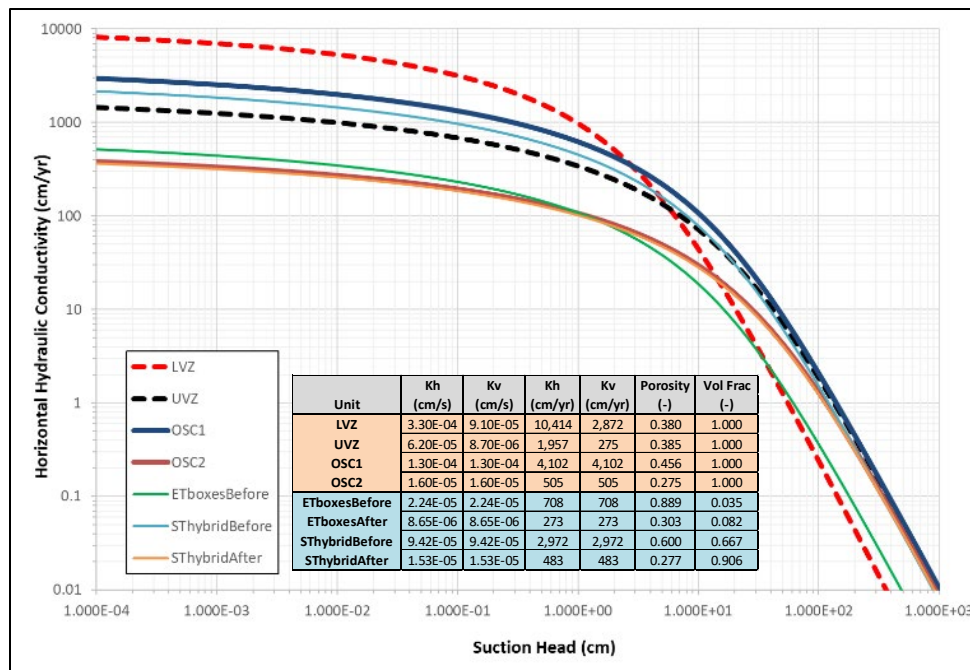


Figure 4-4. K_h versus Suction Head for Material Types Relevant to Slit and Engineered Trench Groundwater Simulations (SRNL, 2020)

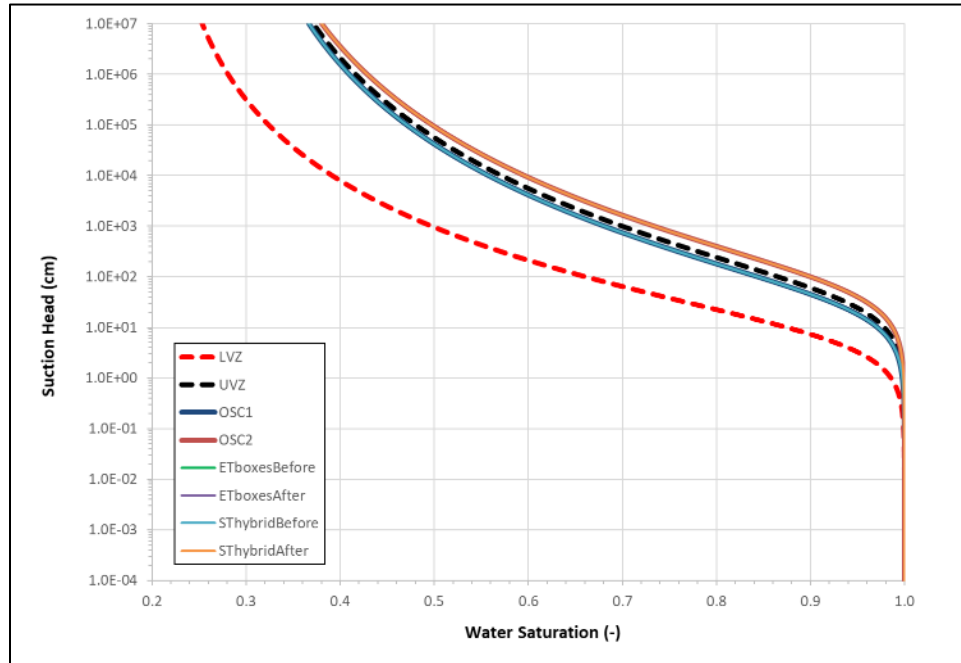


Figure 4-5. WRCs for Material Types Relevant to Slit and Engineered Trench Groundwater Simulations (SRNL, 2020)

4.1.1.1.2.2. After Dynamic Compaction

Each four-high stack of intact B-25 boxes with OSC1 is represented as a calculated material blend of 8.16 vol% OSC2 and 91.84 vol% B-25 boxes (7.51 vol% metal + 84.33 vol% waste) using the methodology originally proposed by Phiher (2010), implemented by Flach and Whiteside (2016; Appendix A), and later refined and implemented by Nichols and Butcher (2020) in SRNL (2020). The property blending schemes for bulk density and porosity for containerized waste before dynamic compaction (ETboxesBefore) are detailed above. Similar calculations are performed for containerized waste after dynamic compaction (ETboxesAfter) using Eq. (4-1) and Eq. (4-6).

$$\rho_{b \text{ ETboxesAfter}} = (1.922 * 0.0816) + (8.238 * 0.0751) + (1.271 * 0.8433) = 1.847 \text{ g cm}^{-3} \quad \text{Eq. (4-14)}$$

where:

$$f_{1\text{After}} = \frac{138,592 \text{ cm}^3 \text{ soil}}{(138,592 \text{ cm}^3 \text{ soil} + 127,469 \text{ cm}^3 \text{ metal} + 1,432,148 \text{ cm}^3 \text{ waste})} = 0.0816 \quad \text{Eq. (4-15)}$$

$$f_{2\text{After}} = \frac{127,469 \text{ cm}^3 \text{ soil}}{(138,592 \text{ cm}^3 \text{ soil} + 127,469 \text{ cm}^3 \text{ metal} + 1,432,148 \text{ cm}^3 \text{ waste})} = 0.0751 \quad \text{Eq. (4-16)}$$

$$f_{3\text{After}} = \frac{1,432,148 \text{ cm}^3 \text{ soil}}{(138,592 \text{ cm}^3 \text{ soil} + 127,469 \text{ cm}^3 \text{ metal} + 1,432,148 \text{ cm}^3 \text{ waste})} = 0.8433 \quad \text{Eq. (4-17)}$$

Substitution of the calculated containerized waste bulk density after dynamic compaction (1.847 g cm^{-3}) and assumed particle density (2.65 g cm^{-3}) into Eq. (4-6) gives:

$$\eta_{ETboxesAfter} = 1 - \frac{1.847}{2.65} = 0.303 \quad \text{Eq. (4-18)}$$

Values for D_e and ρ_p in the blended material after dynamic compaction are assumed to be the same as for ST bulk waste after dynamic compaction.

Eq. (4-8) is used again to generate a composite WRC for the ST and ET containerized waste zones after dynamic compaction (e.g., ETboxesAfter) based on a blend of the individual WRCs for OSC2 and a compacted stack of four B-25 boxes (metal + waste). The WRC for the compacted B-25 boxes again assumes S_2 is equal to S_1 (OSC2) at all capillary pressures. Water saturation for OSC2 (S_l) in Eq. (4-8) is calculated using Eq. (4-9) and the VG parameters for OSC2 reported in SRNL (2020; OscAfter worksheet). K_{sat} for the ST containerized waste zone after dynamic compaction is based on a blend of the properties of OSC2 and compacted B-25 boxes as calculated by Eq. (4-10).

$$K_{sat} = (0.0816)(1.6\text{E} - 05 \text{ cm s}^{-1}) + (0.9184)\left(\frac{1.6\text{E} - 05 \text{ cm s}^{-1}}{2.0}\right) = 8.65\text{E} - 06 \text{ cm s}^{-1} \quad \text{Eq. (4-19)}$$

where K_{sat2} is defined as K_{sat1} (OSC2) divided by a resistance factor (2.0 after dynamic compaction based on expert judgment) to account for the hydraulic impact of the metal walls of the compacted boxes.

K_v and K_h are similarly calculated via Eq. (4-13), where $k_r = k_{r1}$ as discussed for Eq. (4-11) above. Tabular and graphical hydraulic property results are reported in the *Hydraulic Properties Data Package, Rev. 3, dated December 1, 2020* (SRNL, 2020; Table 4 and ETboxesAfter worksheet). Graphical results for ETboxesAfter are also presented in Figure 4-3 (K_v versus suction head), Figure 4-4 (K_h versus suction head), and Figure 4-5 (suction head versus water saturation).

A summary of ST containerized waste zone properties before and after dynamic compaction is provided in Table 4-1. In addition, Table 3-64 summarizes waste zone material and hydraulic properties before and after dynamic compaction for all ELLWF DUs, including STs.

4.1.1.1.3. Hybrid Slit Trench

The exact location of bulk waste and containerized waste in individual STs is not known. To address uncertainties in the porosity and bulk density of disposed waste before and after dynamic compaction, Phiher (2010) developed and Nichols and Butcher (2020) updated a hybrid waste zone that represents each trench unit as a mix of bulk waste (66.7% by volume OSC1) and containerized waste (33.3% by volume ETboxesBefore) based on historical information in CWTS (SRS, 2021c) and analysis by Sink (2010). The method, outlined by Flach and Whiteside (2016; Appendix A) and implemented and refined by Nichols and Butcher (2020) in SRNL (2020), blends properties

for bulk and containerized wastes in STs based on the historical fraction of each waste disposed of in STs.

4.1.1.1.3.1. Before Dynamic Compaction

Equivalent bulk density of the hybrid ST waste zone before dynamic compaction ($\rho_{b\ STHybridBefore}$) is calculated from the individual bulk densities for bulk waste (OSC1) and containerized waste (ETboxesBefore) using the volume fraction ($f_{i\ Before}$) for each waste type as shown in Eq. (4-20).

$$\rho_{b\ STHybridBefore} = (\rho_{b1Before} \times f_{1Before}) + (\rho_{b2Before} \times f_{2Before}) \quad \text{Eq. (4-20)}$$

where subscript 1 refers to bulk waste and subscript 2 refers to containerized waste. Substitution into Eq. (4-20) gives:

$$\rho_{b\ STHybridBefore} = (1.442\ \text{g cm}^{-3} \times 0.667) + (0.293\ \text{g cm}^{-3} \times 0.333) = 1.059\ \text{g cm}^{-3} \quad \text{Eq. (4-21)}$$

Porosity of the hybrid ST waste zone before dynamic compaction is derived from Eq. (4-6) using the calculated hybrid bulk density ($1.059\ \text{g cm}^{-3}$) and assumed particle density ($2.65\ \text{g cm}^{-3}$):

$$\eta_{STHybridBefore} = 1 - \frac{1.059}{2.65} = 0.600 \quad \text{Eq. (4-22)}$$

D_e and ρ_p assume the same numerical values assigned to bulk waste and containerized waste before dynamic compaction.

4.1.1.1.3.2. After Dynamic Compaction

The volume fractions of bulk and containerized waste after dynamic compaction (f_{1After} and f_{2After} , respectively) are computed using the following equations:

$$f_{1After} = \frac{(b_{1After} \times f_{1Before})}{(b_{1After} \times f_{1Before}) + (b_{2After} \times f_{2Before})} = \frac{(12\ \text{ft} \times 0.667)}{(12\ \text{ft} \times 0.667) + (2.5\ \text{ft} \times 0.333)} = 0.9058 \quad \text{Eq. (4-23)}$$

$$f_{2After} = \frac{(b_{2After} \times f_{2Before})}{(b_{1After} \times f_{1Before}) + (b_{2After} \times f_{2Before})} = \frac{(2.5\ \text{ft} \times 0.333)}{(12\ \text{ft} \times 0.667) + (2.5\ \text{ft} \times 0.333)} = 0.0942 \quad \text{Eq. (4-24)}$$

where b_{1After} and b_{2After} are the bulk waste height after dynamic compaction and containerized waste height after dynamic compaction, respectively.

The equivalent thickness of the hybrid ST waste zone after dynamic compaction ($b_{STHybridAfter}$) is calculated using the equation:

$$b_{STHybridAfter} = (b_{1After} \times f_{1After}) + (b_{2After} \times f_{2After}) \quad \text{Eq. (4-25)}$$

Substitution into Eq. (4-25) yields:

$$b_{SThybridAfter} = (12 \text{ ft} \times 0.9058) + (2.5 \text{ ft} \times 0.0942) = 11.10 \text{ ft} \quad \text{Eq. (4-26)}$$

Equivalent bulk density of the hybrid ST waste zone after dynamic compaction ($\rho_{b \text{ SThybridAfter}}$) is calculated using Eq. (4-27), the volume fractions of bulk and containerized waste after dynamic compaction (f_{1After} and f_{2After} , respectively) from Eq. (4-23) and Eq. (4-24), and the individual bulk densities from Table 4-1 for bulk waste after dynamic compaction ($\rho_{b1After}$, OSC2) and containerized waste after dynamic compaction ($\rho_{b2After}$, ETboxesAfter).

$$\rho_{b \text{ SThybridAfter}} = (\rho_{b1After} \times f_{1After}) + (\rho_{b2After} \times f_{2After}) \quad \text{Eq. (4-27)}$$

where subscript 1 refers to bulk waste and subscript 2 refers to containerized waste. Substitution into Eq. (4-27) gives:

$$\rho_{b \text{ SThybridAfter}} = (1.922 \text{ g cm}^{-3} \times 0.9058) + (1.847 \text{ g cm}^{-3} \times 0.0942) = 1.915 \text{ g cm}^{-3} \quad \text{Eq. (4-28)}$$

Porosity of the hybrid ST waste zone after dynamic compaction is derived from Eq. (4-6) using the calculated hybrid bulk density (1.915 g cm^{-3}) and assumed particle density (2.65 g cm^{-3}):

$$\eta_{SThybridAfter} = 1 - \frac{1.915}{2.65} = 0.277 \quad \text{Eq. (4-29)}$$

D_e , and ρ_p for the hybrid waste zone use the same numerical values as assumed for bulk waste and containerized waste after dynamic compaction.

Eq. (4-8) is used to generate composite WRCs for the ST hybrid waste zone before (SThybridBefore) and after (SThybridAfter) dynamic compaction based on a blend of the individual WRCs for OSC (OSC1 and OSC2) and the containerized waste zone (ETboxesBefore for before dynamic compaction and ETboxesAfter for after dynamic compaction). Water saturation for OSC1 and OSC2 (S_1) in Eq. (4-8) is calculated using Eq. (4-9) and the VG parameters for OSC1 and OSC2 reported in SRNL (2020; OscBefore and OscAfter worksheets). Water saturation values for ETboxesBefore and ETboxesAfter (S_2) are assumed equal to S_1 at all capillary pressures as explained in Section 4.1.1.1.2. Blended K_{sat} values for the ST hybrid waste zone before and after dynamic compaction are calculated using Eq. (4-10).

$$K_{sat \text{ Before}} = (0.667)(1.3\text{E} - 04 \text{ cm s}^{-1}) + (0.333)(2.2\text{E} - 05 \text{ cm s}^{-1}) = 9.4\text{E} - 05 \text{ cm s}^{-1} \quad \text{Eq. (4-30)}$$

$$K_{sat \text{ After}} = (0.9058)(1.6\text{E} - 05 \text{ cm s}^{-1}) + (0.0942)(8.65\text{E} - 05 \text{ cm s}^{-1}) = 1.5\text{E} - 05 \text{ cm s}^{-1} \quad \text{Eq. (4-31)}$$

K_v and K_h are calculated using Eq. (4-13), where $k_r = k_{r1}$ as discussed for Eq. (4-11) above. Tabular and graphical hydraulic property results are reported in the *Hydraulic Properties Data Package, Rev. 3, dated December 1, 2020* (SRNL, 2020; Table 5, SThybridBefore, and SThybridAfter worksheets). Graphical results for SThybridBefore and SThybridAfter are also presented in Figure 4-3 (K_v versus suction head), Figure 4-4 (K_h versus suction head), and Figure 4-5 (suction head versus water saturation).

A summary of ST hybrid waste zone properties before and after dynamic compaction is provided in Table 4-1. In addition, Table 3-64 summarizes waste zone material and hydraulic properties before and after dynamic compaction for all ELLWF DUs, including STs.

4.1.1.2. Engineered Trenches

Dynamic compaction is employed to achieve waste layer stabilization at or near the end of the 100-year IC period when significant container corrosion has occurred. Container degradation improves dynamic compaction effectiveness in eliminating subsidence potential. Waste containers that can be effectively crushed and compacted at the time of dynamic compaction are termed crushable containers, while the remaining are considered non-crushable. A representation of the ST and ET waste zones before and after dynamic compaction are shown in Figure 4-1 and Figure 4-2, respectively. For B-25 boxes in ETs, an estimated subsidence/compaction potential of approximately 13.5 feet exists within the 16-foot waste layer, resulting in a post-compaction waste layer thickness of approximately 2.5 feet (Phifer and Wilhite, 2001).

The intact waste disposal configuration in ETs (i.e., four-high stack of B-25 boxes covered with a 4-foot-thick OSC) is equivalent to the conceptual model for ST containerized waste (ETboxesBefore) presented in Section 4.1.1.1.2. The same is true for containerized waste after dynamic compaction (ETboxesAfter). Material and hydraulic properties of the waste zone in ETs before and after dynamic compaction are therefore the same as those for containerized waste only in STs. Tabular and graphical hydraulic property results are reported in the *Hydraulic Properties Data Package, Rev. 3, dated December 1, 2020* (SRNL, 2020; Table 4, ETboxesBefore, and ETboxesAfter worksheets). Graphical results for ETboxesBefore and ETboxesAfter are also presented in Figure 4-3 (K_v versus suction head), Figure 4-4 (K_h versus suction head), and Figure 4-5 (suction head versus water saturation).

ET waste zone properties before and after dynamic compaction are summarized in Table 4-1. In addition, Table 3-64 summarizes waste zone material and hydraulic properties before and after dynamic compaction for all ELLWF DUs, including ETs.

4.1.1.3. Trench Segments with Components in Grout

Structural modeling of the CIG trench segments (Peregoy, 2006a) is conducted to evaluate a CIG trench segment design life of 300 years in terms of structural integrity. The structural modeling indicates that CIG trench segments can achieve a structural design life of 300 years provided the interior void spaces of the components are fully grouted, the waste form is otherwise structurally stable (i.e., no voids or robust container design), or the segments are covered with a 20-inch-thick reinforced-concrete mat. Components disposed of in these trench segments consist of large radioactively contaminated equipment along with other containerized waste. The components are mostly made of carbon steel; the type of component with the thinnest walls is most likely a B-25 box with a 12-gauge (0.1094 inch) wall thickness. Dunn (2002) estimated that the time to through-wall pitting of a 12-gauge carbon steel B-25 box buried in soil is a minimum of 40 years. Through-wall pitting of a B-25 box encapsulated within a cementitious grout takes longer than 40 years due to the elevated pH within such an environment. Furthermore, the encapsulating grout tends to seal minor openings or joints associated with the components. Therefore, components are assumed to

be hydraulically intact for 40 years. Based on this information, the following three CIG trench waste segment representations are provided: structurally and hydraulically intact conditions for 40 years; structurally intact with hydraulically degraded conditions from Year 40 to Year 371 [71 years operation (1994 to 2065) plus 300 years structural design life]; and structurally and hydraulically degraded conditions beyond Year 371.

4.1.1.3.1. Structurally and Hydraulically Intact Conditions

Under structurally and hydraulically intact conditions (Year 0 to Year 40), the CIG waste forms consist of components and containerized waste that are encapsulated in at least 12 inches of grout. CIGgrout1to8 (C1) [referred to as “old CIG grout” in PA2008] and CIGgrout9on (C2) [referred to as “future CIG grout” in PA2008] are described by Nichols and Butcher (2020). Before disposal, the bottom of the excavated trench segment is filled with grout to a minimum 1 foot and allowed to cure. The component(s) are then placed on the 12-inch-thick base grout layer and grout is poured around, between, and over the component(s) to completely encapsulate the component(s) with a minimum of 12 inches of grout on all sides. Additional layers of component(s) and grout may be placed on top of previous layers until approximately 16 feet of the trench is filled up with component(s) (i.e., an approximately 14-foot-thick waste segment plus approximately 24 inches of grout). The operation is conducted so that a minimum of 12 inches of grout is present (1) between the component(s) and the trench bottom and trench sides and (2) across the top of the upper-most component(s). The CIG waste form is assumed to consist of an intact carbon-steel container with a saturated hydraulic conductivity of $1.0\text{E-}12 \text{ cm s}^{-1}$ (i.e., a low, but nonzero, saturated hydraulic conductivity to avoid potential model instability issues) that is half-filled with air. Under these conditions, no flow and no advective release of contaminants occur before Year 40. Therefore, characteristic curves are not relevant until a leak occurs. The intact CIG trench waste segment (CIGint) is assumed to have the same material properties as OSC1 but with the hydraulic conductivity of concrete ($K_h = K_v = 1.0\text{E-}12 \text{ cm s}^{-1}$) as highlighted in Figure 4-6 for C1 and C2.

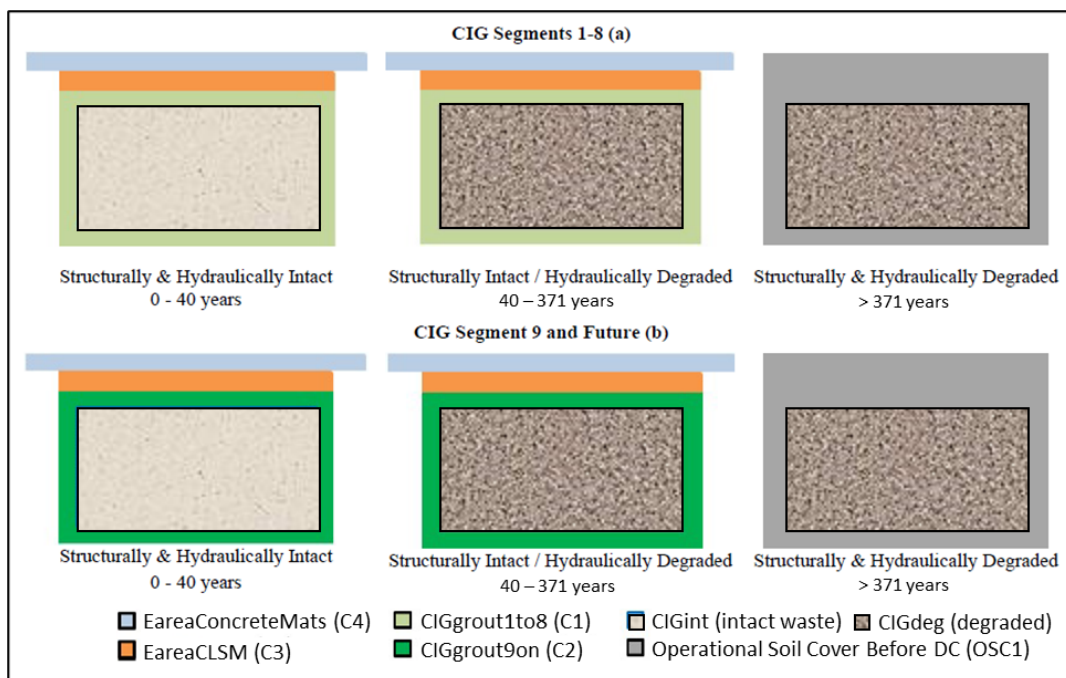


Figure 4-6. Conceptual Model Representing Hydraulic Properties of Components-in-Grout Trench Segment Waste Unit from Fully Intact to Degraded Condition for C1 and C2 (Nichols and Butcher, 2020; Figure 7-4)

4.1.1.3.2. Structurally Intact with Hydraulically Degraded Conditions

After Year 40, the CIG waste forms are assumed to have through-wall pitting and no longer be hydraulically intact. However, based on structural modeling (Peregoy, 2006a), these trenches are assumed to remain structurally intact (i.e., no subsidence) for 300 years after operational closure in relative Year 71 (calendar year 2065). Under these conditions, the degraded waste form (CIGdeg) is assumed to have the same material properties and a similar hydraulic conductivity ($K_h = K_v = 1.2\text{E-}04 \text{ cm s}^{-1}$) as OSC1 as shown in Figure 4-6 for both C1 and C2. The degraded hydraulic properties for the CIG waste forms are defined below in Section 4.2.1.3, Table 4-28 and Table 4-29.

4.1.1.3.3. Structurally and Hydraulically Degraded Conditions

The void space within and the integrity of CIG waste forms varies widely. The subsidence potential of the 14-foot CIG waste form has not been estimated. If the waste within a CIG trench segment is assumed to consist of three layers of B-25 boxes containing waste with the same density as the B-25 boxes disposed of within the ETs (Phifer and Wilhite, 2001), the subsidence potential of the CIG trench waste segment is approximately 10 feet and the subsided waste segment has a thickness of 4 feet. Although a significant subsidence potential may exist, the CIG trench waste segment does not solely consist of low-density waste in B-25 boxes. Therefore, the subsidence potential is assumed to be half of the waste segment thickness or 7 feet.

Under structurally and hydraulically degraded conditions (300 years after operational closure), the components and containerized waste as well as the overlying grout and concrete mat are assumed to break up and collapse and result in a 7-foot-thick waste segment. Subsidence of the overlying

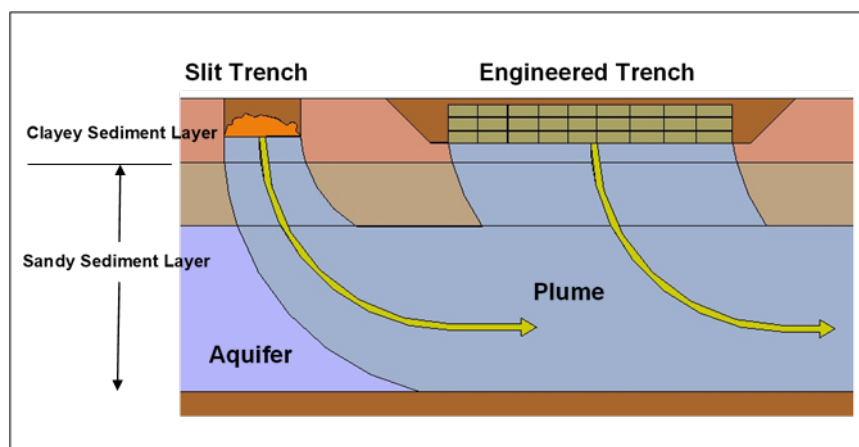
closure cap soil into the trench segment will simultaneously occur. Each degraded CIG trench segment contains a substantial amount of soil; upon collapse, the soil is disturbed and becomes unsettled or “fluffed.” Therefore, the post-subsidence CIG waste form for both C1 and C2 is also represented hydraulically by CIGdeg (see Figure 4-6). The degraded hydraulic properties for the CIG trench segments are defined below in Section 4.2.1.3, Table 4-28, and Table 4-29.

4.1.2. Waste Zone Conceptual Model: Geochemical Properties

4.1.2.1. Slit and Engineered Trenches

This section describes the key features of STs and ETs that will impact the geochemical environments within and beneath the DUs. More specifically, a geochemical conceptual model for STs and ETs is presented that identifies the aqueous chemistry and associated solid phases comprising the waste zone, upper vadose zone (UVZ), lower vadose zone (LVZ), and aquifer. The conceptual model developed by Kaplan (2016b) also assigns geochemical parameters to each material zone. Kaplan (2016b) provides a detailed description of the development of the geochemical conceptual model, the definitions of the different geochemical environments and materials, and the assignment of appropriate geochemical parameters for each radionuclide of interest.

Figure 4-7 (Kaplan, 2016b) is a schematic of the geochemical conceptual model for ST and ET units. The cross-section does not show dimensionality and facility-specific details, which are instead assigned in the numerical model (Section 4.1.3). The two relevant geochemical environments for a ST and ET are a clayey sediment and a sandy sediment. Section 3.8.2.5 provides a description of the two geochemical conceptual environments.



Not shown is the overlying final closure cap that will be installed at the end of the 100-year IC period.

Figure 4-7. Slit and Engineered Trench Geochemical Conceptual Model Schematic (Kaplan, 2016b)

Table 4-2 (Kaplan, 2016b) lists the relevant solid and aqueous phases for ST and ET units, together with the associated geochemical parameters (K_d and k_s values) necessary in the PA model to describe the chemical interactions of radionuclides with these geochemical materials (e.g., sandy sediment, clayey sediment, reducing cement). SRNL (2018) provides look-up tables containing

the recommended K_d and k_s values for each radionuclide (table rows) as a function of the different geochemical materials or solid phases (table columns).

Table 4-2. Conceptual Geochemical Model of Features and Parameters of Slit and Engineered Trenches [refer to Figure 4-7; after Kaplan (2016b)]

Feature		Geochemical Parameter
Solid Phases	Aqueous Phase	
Waste Zone: Active components are iron metal and corrosion products. Metal containers will rust to form Fe-oxides. Cellulosic materials are also present but do not degrade to form cellulose degradation products (CDPs) in sufficient quantity to affect sorption. ^{a, b}	Same as SRS GW: pH 5.5, ionic strength 0.01 molal, except for trace levels of radionuclides	Use Clayey Sediment K_d . Fe-oxide content will control the sorption chemistry of this zone. It is assumed that the geochemistry of the Clayey Sediment will approximate that of the rusted metal waste form. In reality, the rusted waste form will contain much greater Fe-oxide content than the typical clayey SRS sediment. Thus, use of a clayey sediment K_d is a bounding assumption. No cementitious materials are included as engineered barriers.
Clayey Sediment: Upper Vadose Zone	As above	Use Clayey Sediment K_d
Sandy Sediment: Lower Vadose Zone		Use Sandy Sediment K_d
Sandy Sediment: Aquifer Zone		As above

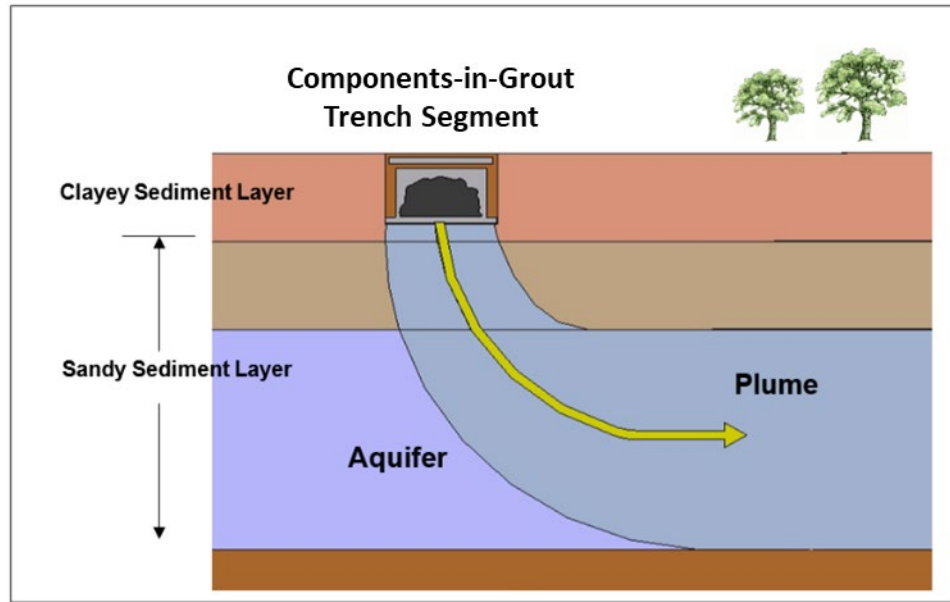
Notes:

- ^a A ST DU nominally consists of a series of five 20-foot-wide parallel trench segments not accessible by personnel or vehicles. An ET DU is a vehicle-accessible, open-trench design.
- ^b Kaplan (2012) determined that CDPs are not at a high enough concentration in GW beneath the ORWBG to warrant application of a CDP correction factor to K_d values for E-Area. Flach et al. (2014) evaluated eliminating CDP corrections for Clayey and Sandy Sediment K_d s and Oxidizing and Reducing Cement K_d s and incorporated the associated changes into the PA baseline. The current geochemical data package eliminates CDP effects on all categories of K_d s.

4.1.2.2. Trench Segments with Components in Grout

Key features of CIG trench segments that will influence the geochemical environments within and below the CIG segment waste zones are described below. More specifically, a geochemical conceptual model for the CIG trench segments is presented that identifies the aqueous chemistry and associated solid phases comprising the waste zone, UVZ, LVZ, and aquifer. The conceptual model developed by Kaplan (2016b) also assigns geochemical parameters to each material zone. Kaplan (2016b) provides a detailed description of the development of the geochemical conceptual model, the definitions of the different geochemical environments and materials, and the assignment of appropriate geochemical parameters for each radionuclide of interest.

Figure 4-8 (Kaplan, 2016b) is a schematic of the geochemical conceptual model for the CIG trench segments. The cross-section does not show dimensionality and facility-specific details, which are instead assigned in the numerical model (Section 4.2.1.1). The relevant geochemical conceptual environments for the CIG trench segments are fourfold: oxidizing cement, sandy sediment, cementitious-leachate-impacted clayey sediment, and cementitious-leachate-impacted sandy sediment. Section 3.8.2.5 provides a description of the four geochemical conceptual environments.



Not shown is the overlying final closure cap that will be installed at the end of the 100-year IC period.

Figure 4-8. Components-in-Grout Trench Segment Geochemical Conceptual Model Schematic (Kaplan, 2016b)

Table 4-3 (Kaplan, 2016b) lists the relevant solid and aqueous phases for CIG trench segments, together with the associated geochemical parameters (K_d and k_s values) necessary in the PA model to describe the chemical interactions of radionuclides with these geochemical materials (e.g., sandy sediment, clayey sediment, reducing cement). SRNL (2018) provides look-up tables containing the recommended K_d and k_s values for each radionuclide (table rows) as a function of the different geochemical materials or solid phases (table columns).

Table 4-3. Conceptual Geochemical Model of Features and Parameters of Components-in-Grout Trench Segments [refer to Figure 4-8; after Kaplan (2016b)]

Feature		Geochemical Parameter
Solid Phases	Aqueous Phase	
Waste Zone: Active components are grout, iron metal and corrosion products. Because of intimate contact between encapsulating grout and waste form, cement phases are considered to be controlling sorption chemistry. The impact of Fe-oxides is ignored. Cellulosic materials are also present but do not degrade to form CDPs in sufficient quantity to affect sorption. ^{a, b}	Cementitious Impacted Leachate: Three general types of oxidizing grout leachate chemistries controlled by different aged cement phases characterized by elevated pH and ionic strength relative to SRS GW.	Use Oxidizing Cement K_d or apparent solubility concentration limits for the three cement ages.
Grout / Concrete: Active components are cement phases. ^a		Use Oxidizing Cement K_d or apparent solubility concentration limits for the three cement ages.
Clayey Sediment: Upper Vadose Zone	Fe-Oxide-Impacted Cementitious Leachate: Cement leachate chemistry altered by passing through Fe-oxide-controlled environment. Still characterized by elevated pH and ionic strength relative to SRS GW.	Use cementitious-leachate-impacted Clayey Sediment K_d ; $K_{dCementLeach}$. ^c
Sandy Sediment: Lower Vadose Zone		Use cementitious-leachate-impacted Sandy Sediment K_d ; $K_{dCementLeach}$. ^c
Sandy Sediment: Aquifer Zone	Cementitious Leachate Porewater: Gets diluted with typical SRS GW and the aqueous phase takes on the properties of the latter: pH 5.8, ionic strength 0.01 molal, trace levels of radionuclides.	Use Sandy Sediment K_d .

Notes:

- ^a CIG trench segment waste consists of equipment (components) that was too bulky and too large to have placed in the LAWV or ILV, but which contains more radioactivity than allowed in STs and ETs. A section (segment) of an individual trench in ST23 was excavated to act as a form and a 12-inch-thick grout floor was poured and cured. The waste component was placed on the floor and grout was pumped into the trench segment to encapsulate the component with a minimum of 12 inches of grout. If needed, an 18-inch-thick reinforced concrete slab was installed directly on top of the grout layer above the newly installed waste component for long-term (300-year) structural support of the final closure cap. Soil backfill was added to bring the trench segment to grade and to promote positive drainage. It is expected that some cellulosic material is included in this waste.
- ^b Kaplan (2012) determined that CDPs are not at a high enough concentration in GW beneath the ORWBG to warrant application of a CDP correction factor to K_d values for E-Area. Flach et al. (2014) evaluated eliminating CDP corrections for Clayey and Sandy Sediment K_d s and Oxidizing and Reducing Cement K_d s and incorporated the associated changes into the PA baseline. The current geochemical data package eliminates CDP effects on all categories of K_d s.
- ^c The 2010 geochemical data package (Kaplan, 2010) introduced the concept of a cementitious-leachate-impacted zone beneath concrete/grout DUs. This change specifically affected the CIG trench segments, LAWV, and ILV models but was never formally evaluated through the UDQE process for inclusion in the PA baseline. Kaplan (2016b) maintains this concept.

4.1.3. PORFLOW Implementation of Vadose Zone Conceptual Model

The conceptual models of the VZ for STs and ETs in PORFLOW (ACRi, 2018) flow and transport simulations are described below. Key details include the model geometries, spatially dependent hydrostratigraphic representations, model dimensionality, and boundary conditions (i.e., infiltration rates, cover overhangs, and subsidence). Accounting for differences in the percentage of non-crushable materials, 17 unique models (as defined by seven hydrostratigraphic groupings)

are required to satisfactorily represent the entire collection of existing and future STs and ETs within the ELLWF.

The relevance of several hydrostratigraphic and design features specific to the ELLWF is evaluated by Danielson (2019c) using PORFLOW to assist in the development and implementation of the VZ conceptual models for the PA. A summary of these screening evaluations is presented below to highlight the actions taken and decisions made in the development and implementation of the proposed conceptual models.

4.1.3.1. Disposal Unit Length

The ELLWF trench unit with the longest footprint is ST01 at 675.3 feet. While the length of most STs and ETs is within 3% of ST01's, the length difference for ST10, ST11, ST21, ST22, and ET03 is greater than 10%, with a maximum of 33%. As a result, PORFLOW simulations are conducted to determine whether a generic model of any length can be used to represent any trench without impacting flux to the water table. A generic 2-D model with waste uniformly distributed across 600-, 500-, 400-, 300-, 200-, and 100-foot lengths is implemented to calculate steady-state flow and transient transport solutions to obtain fluxes to the water table for the nine radionuclide species investigated by Hamm et al. (2018). Because the specified quantity of each radionuclide species is the same regardless of footprint length, and no solubility limitations are imposed, all differences in peak-flux to the water table are negligible (i.e., less than ~3%) and are attributed to numerical dispersion. As a result, a single, generic, waste zone length can be assumed for all ST and ET DUs in the ELLWF.

4.1.3.2. Hydrostratigraphy

The elevations of the water table and various subsurface hydrostratigraphic features for the ELLWF have been reported on a trench-by-trench basis by Bagwell and Bennett (2017). Of interest during the development of the ST and ET conceptual models are those features that will impact the radionuclide travel time through the VZ, such as depth to the water table and the quantity of clayey material beneath the waste zone. A 3-D reconstruction (Figure 4-9) and contour mappings (Figure 4-10, Figure 4-11, Figure 4-12, and Figure 4-13) of the hydrostratigraphic surfaces are created to highlight the relevant features that should be represented in the ST and ET conceptual models.

Inspection of the depth to the water table (Figure 4-10) reveals a substantial difference moving from the western sector of the ELLWF (~80 feet from ground surface to water table) to the eastern sector (~45 feet from ground surface to water table); therefore, the travel time through the VZ will vary significantly based on location. Clayey material is present in the UVZ and/or the TCCZ beneath every waste zone. The lower hydraulic conductivity of the clayey material when compared to the sandy material comprising the LVZ and LAZ, coupled with higher K_d values for the radionuclides of interest in clay, increases travel times through the VZ.

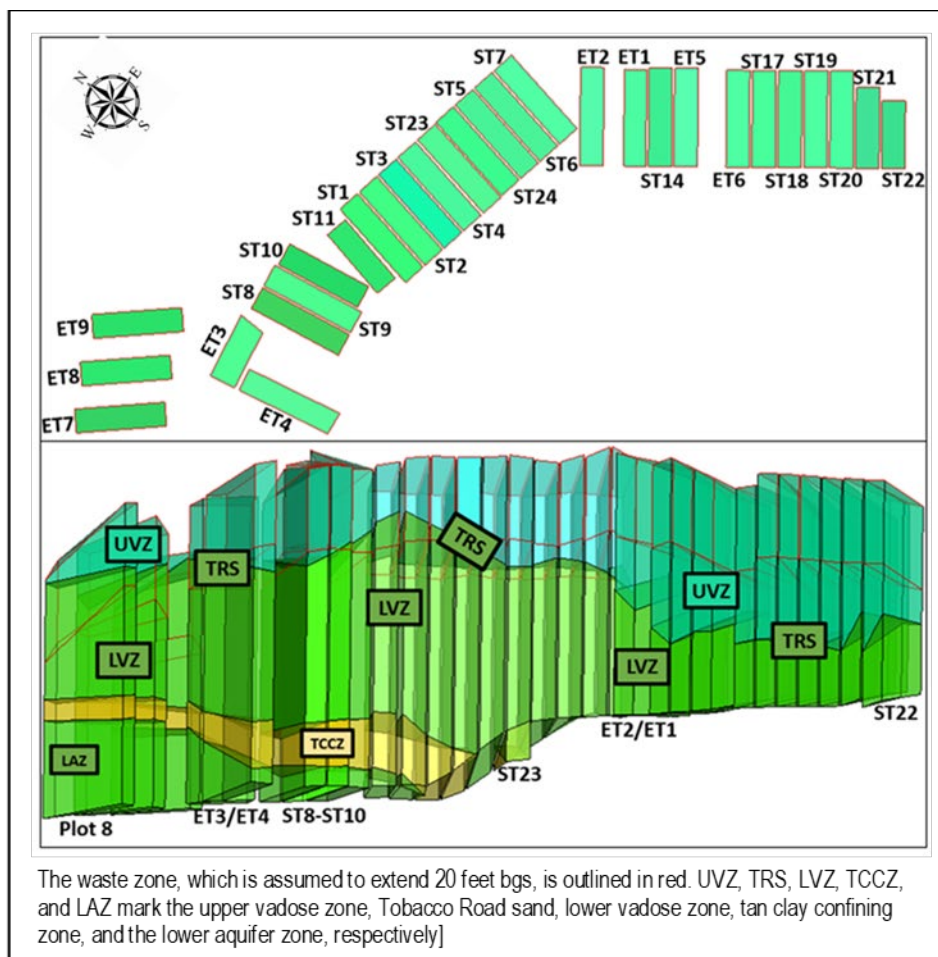


Figure 4-9. Three-Dimensional Reconstruction of Hydrostratigraphic Surfaces for Slit and Engineered Trenches as Reported by Bagwell and Bennett (2017) (Danielson, 2019c; Figure 1)

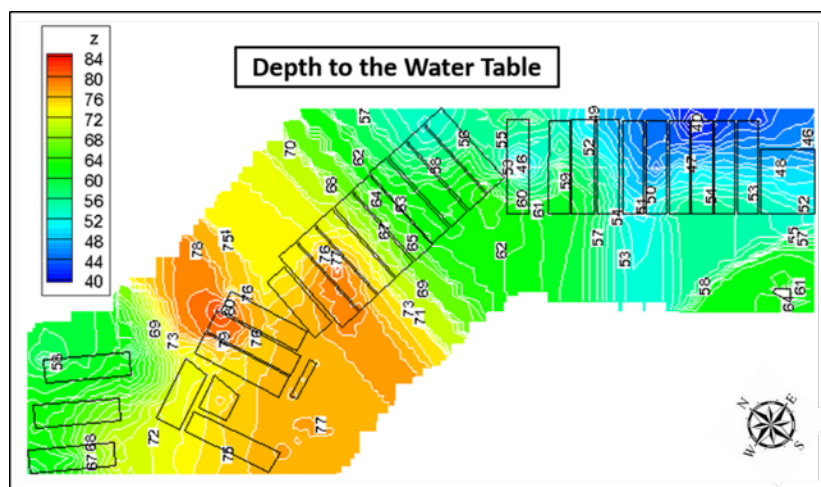


Figure 4-10. Depth (feet) to the Water Table from Ground Surface (Danielson, 2019c; Figure 2)

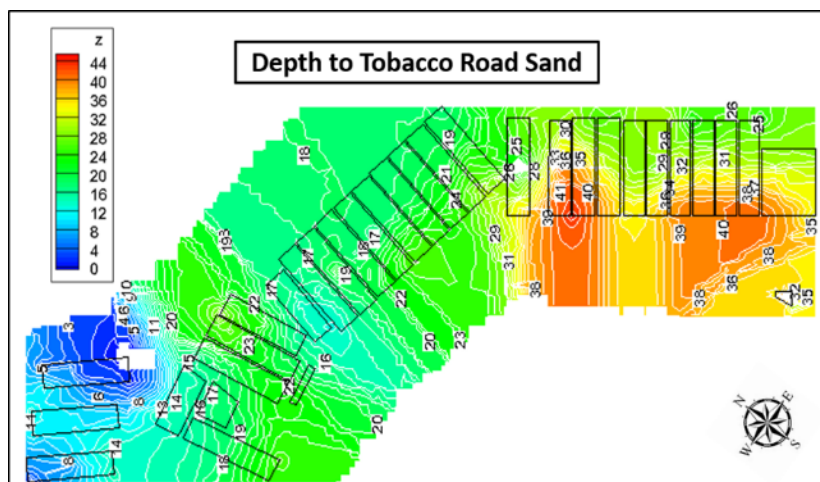


Figure 4-11. Depth (feet) to Tobacco Road Sand from Ground Surface (Danielson, 2019c; Figure 3)

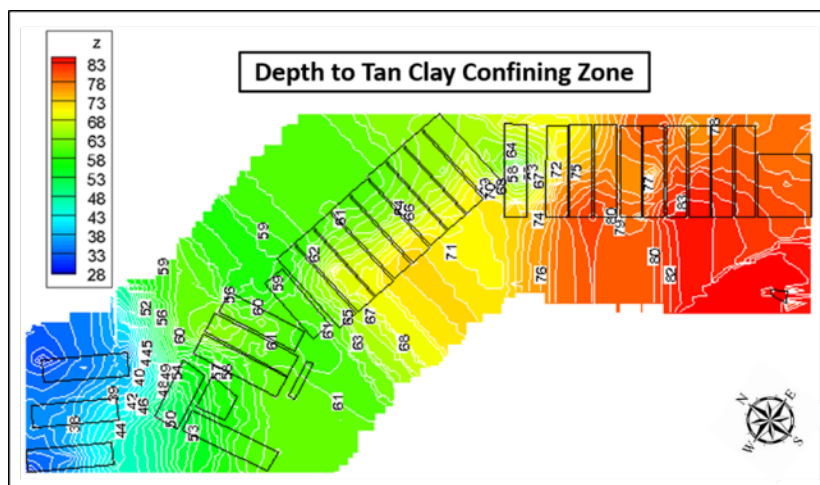


Figure 4-12. Depth (feet) to Tan Clay Confining Zone from Ground Surface (Danielson, 2019c; Figure 4)

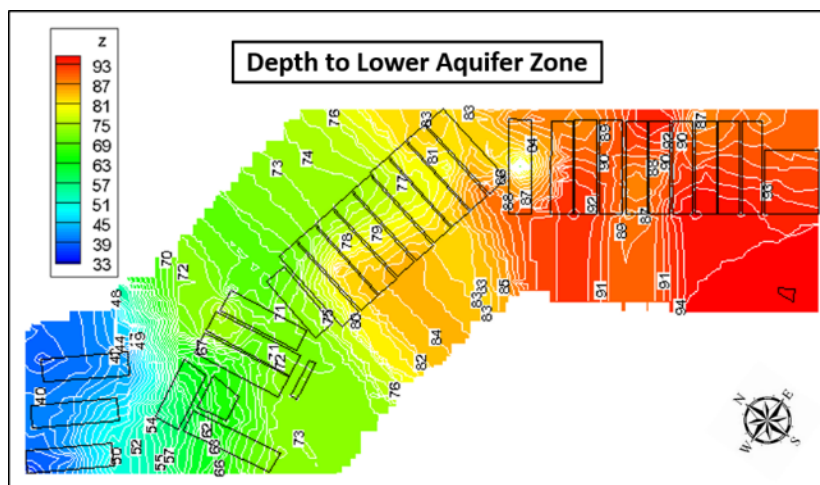


Figure 4-13. Depth (feet) to Lower Aquifer Zone from Ground Surface (Danielson, 2019c; Figure 5)

Figure 4-14 shows the range in thickness of clayey material beneath the ELLWF waste zones (i.e., the thickness of UVZ clayey material beneath the waste zone plus the thickness of TCCZ material beneath the waste zone). The minimum and maximum thicknesses of clayey material are approximately 2 feet and 17 feet, respectively. The clayey material thickness reaches a minimum in the central sector beneath ST24 and ST05.

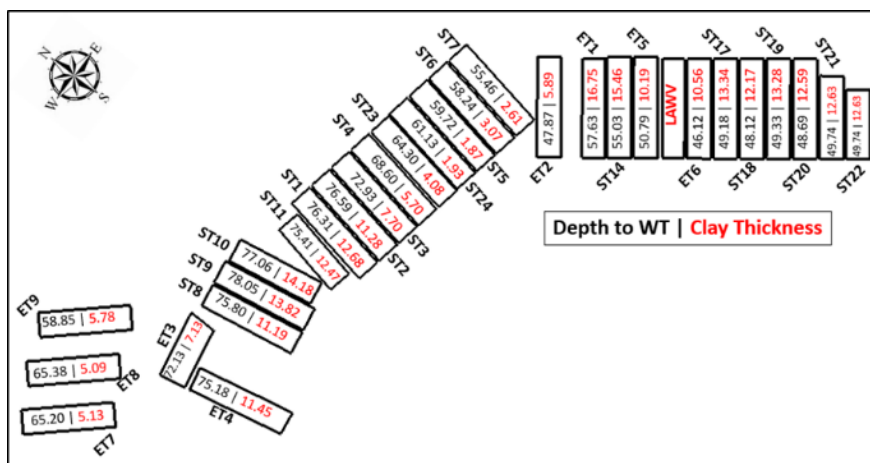


Figure 4-14. Depth (feet) to Water Table (WT) and Average Thickness (feet) of Clayey Material Beneath Waste Zone (Danielson, 2019c; Figure 6)

Additional spatially varying features of importance to radionuclide fate and transport in the VZ are evident in Figure 4-9. To the west (left) of ST23, the VZ material bordering the base of the waste zones is sandy (LVZ), and not clayey (UVZ), as it is to the east/southeast (right) of ST23. Also, to the west of ST23, the water table is located beneath the TCCZ in the sandy LAZ rather than above the TCCZ in the sandy LVZ, as it is to the east/southeast of ST23. As a result of the change in positioning of the water table relative to the TCCZ to the east/southeast of ST23, only clayey material (UVZ) borders the trench waste zones and only sandy material is present between the UVZ and the water table.

The minimum-maximum ranges for depth to the water table and clayey material thickness beneath the waste zone (Figure 4-14) require use of multiple models to adequately represent the relevant hydrostratigraphic features, while maintaining a reasonable level of conservatism. On the other hand, it is desirable to use the fewest number of models necessary to reduce overall complexity and cost associated with model development. Two approaches are taken to reduce the overall number of models: (1) eliminating irrelevant or favorable features to create generic model representations; (2) grouping trenches that share common hydrostratigraphy (the final groupings are shown in Figure 4-42).

For the first approach, two key features are investigated using PORFLOW: (1) vertical positioning of clayey material beneath the waste zone (Figure 4-15) and (2) sandy versus clayey material neighboring the waste zone (Figure 4-16). A series of steady-state flow solutions assuming different infiltration boundary conditions is obtained from PORFLOW and provided as input for the PORFLOW transient radionuclide contaminant transport simulations through the VZ. The calculated peak fluxes to the water table from the transport simulations for nine radionuclides are

then carefully examined to isolate relevant differences introduced by the various features (model geometries) and to ensure that conservative assumptions are not excluded when creating a generalized conceptual model. With the exception of changed model geometries, the PORFLOW simulations employ the same material properties, time discretization, boundary conditions, subsidence models, and radionuclides assumed by Hamm et al. (2018).

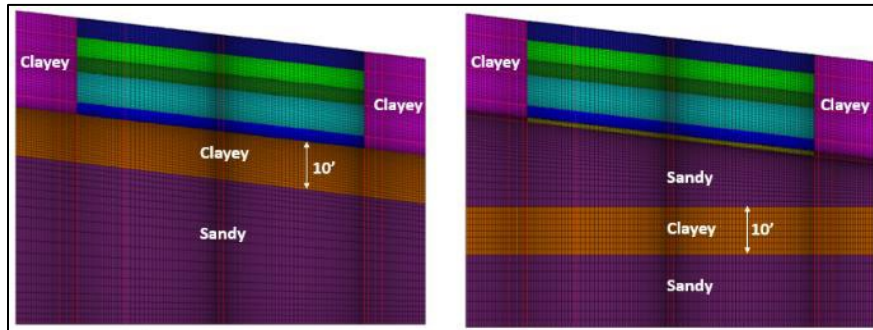


Figure 4-15. PORFLOW Model Geometries Used to Investigate Vertical Positioning of Clayey Material Beneath Waste Zone (Danielson, 2019c; Figure 7)

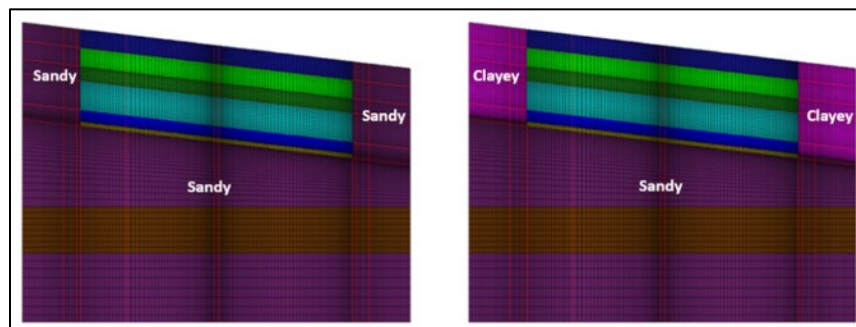


Figure 4-16. PORFLOW Model Geometries Used to Investigate Sandy versus Clayey Material Neighboring Waste Zone (Danielson, 2019c; Figure 8)

The vertical positioning of the clayey material beneath the waste zone is found to have no impact on the flux to the water table. This suggests that it is reasonable to use a generic clayey material beneath the waste zone with a thickness corresponding to the sum of the TCCZ and UVZ thicknesses and to assume that the material properties are the same. Comparing the results for sandy versus clayey material neighboring the waste zone, negligible difference is found in the overall peak-flux to the water table; however, slightly higher concentrations are observed through time when clayey material neighbors the waste zone as shown for three radionuclides in Figure 4-17. This result suggests clayey material neighboring the waste zone is bounding. Based on these investigations, the conclusion is reached that depth to the water table and thickness of the clayey material layer beneath the waste zone are the two primary considerations when creating conceptual models that represent groups of DUs in the ELLWF.

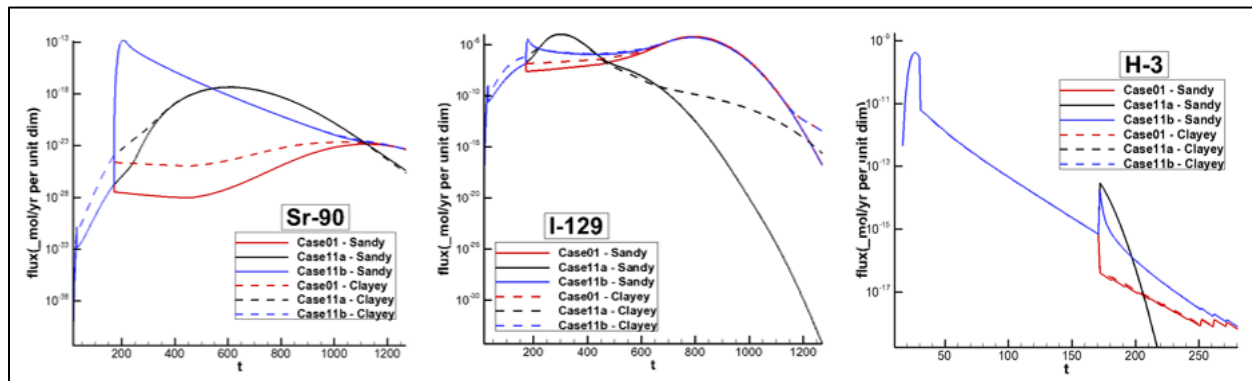
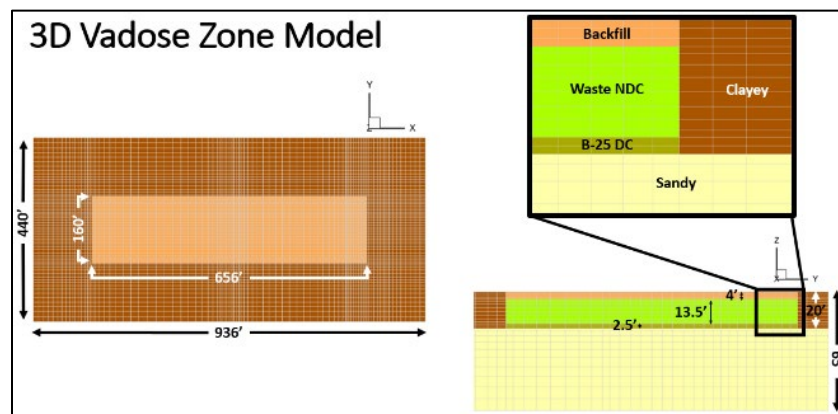


Figure 4-17. Sr-90, I-129, and H-3 Fluxes to Water Table for Sandy versus Clayey Material Neighboring Waste Zone (Danielson, 2019c; Figure 9)

4.1.3.3. Model Geometry

A preliminary analysis is performed to compare 2-D and 3-D model geometries (Figure 4-18) and to understand if a 2-D model sufficiently represents asymmetrical features such as discrete subsided areas (also referred to as holes) in the closure cap. In previous work by Hamm et al. (2018), a discrete hole is represented by a 12-foot-wide section in the center of the DU.

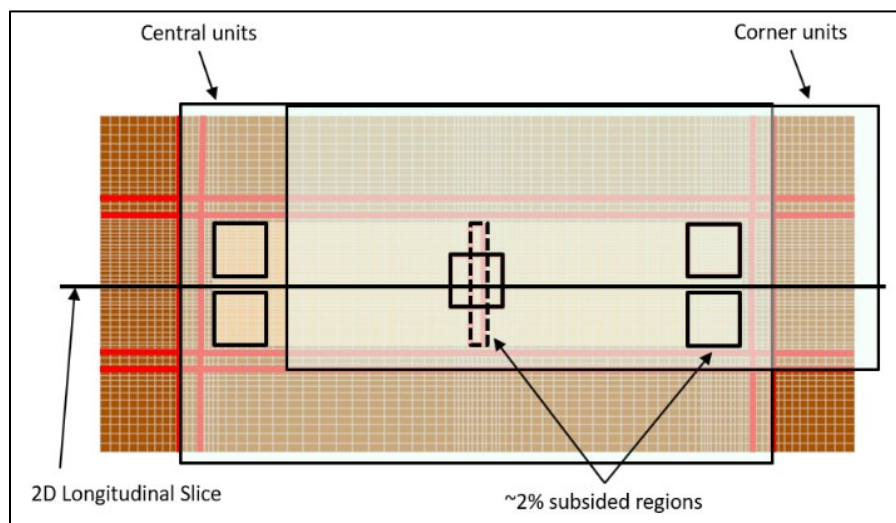


Note: The 2-D cross-section on the left matches the cross-section in the bottom right corner where the longitudinal axis is into the page.

Figure 4-18. Three-Dimensional Vadose Zone Model for Disposal Unit 65 feet Above Water Table (Danielson, 2019c; Figure 10)

Translating this 2-D representation to 3-D, the 12-foot-wide hole is shown as a dashed rectangle in the center of the DU in Figure 4-19. A discrete region that represents 2% subsidence can also be defined by a 46-foot x 46-foot square, as shown by the solid outlined squares in Figure 4-19. The generic 2-D trench models (Case01 and Case11a) as defined by Hamm et al. (2018) translate directly to 3-D for all trench units except the corner units (ET03, ET04, and ST22), where boundary conditions for solving the flow equations in PORFLOW are applied to different “surface” regions (covered versus uncovered; intact versus subsided; corner versus central location) across the top of the model domain as shown in Figure 4-19. In the 3-D model, the X and Y boundaries are considered no-flow, while the Z boundaries represent the water table at the bottom of the model domain, where the pressure is set to zero, and the water infiltration rate at the

top of the model domain, which depends on the different “surface” regions described above. For the generic 3-D models that are described in the current section below, only the model geometry has changed. Material properties, time discretization, radionuclide properties, and so on are the same as those used by Hamm et al. (2018).

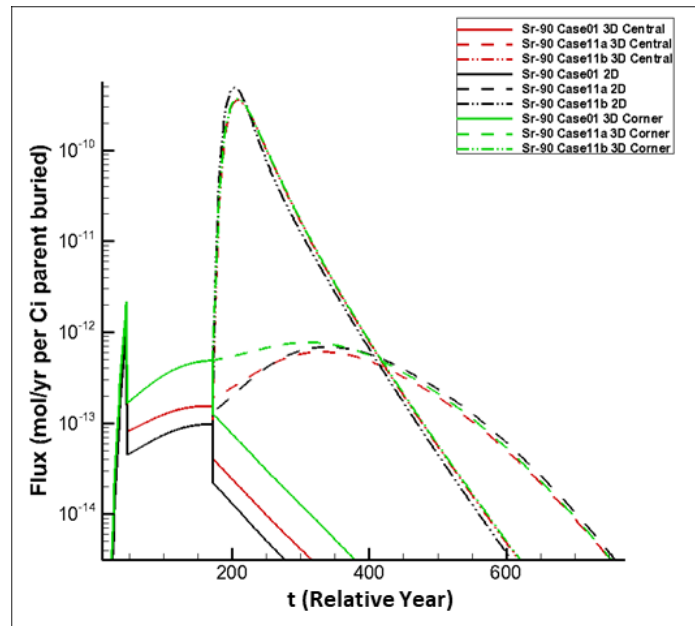


Note: Red lines mark 10- and 40-foot cover overhangs for interim and final covers, respectively.

Figure 4-19. Subsidence Hole Shapes and Locations for Three-Dimensional Trench Model (Danielson, 2019c; Figure 11)

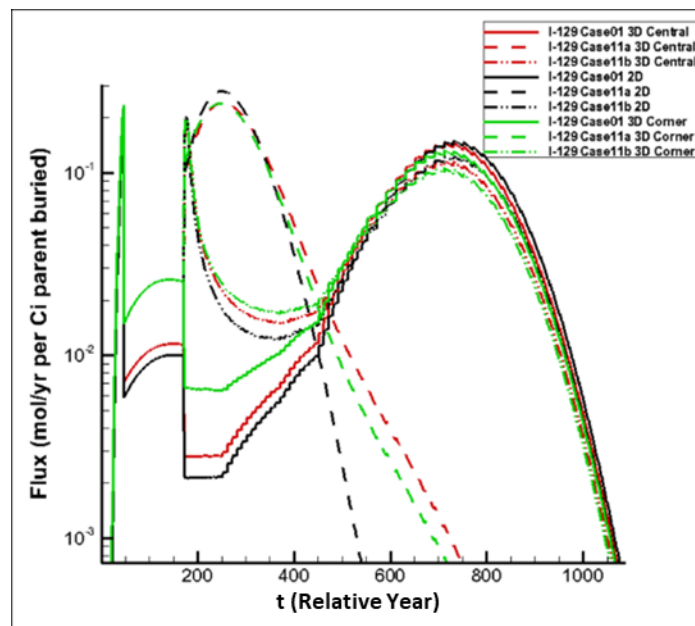
Figure 4-20, Figure 4-21, Figure 4-22, and Figure 4-23, respectively, compare the fluxes to the water table for Sr-90, I-129, Tc-99, and Ni-59 (select radionuclides with short/long half-lives and high/low K_d values) for the 2-D model and the 3-D analogues [i.e., center and corner trench unit cases with a 12-foot-wide hole representing Case11b in the report by Hamm et al. (2018)]. The comparisons indicate very little difference between the central and corner trench unit cases. In addition, the 2-D model is shown to be generally bounding because it yields the highest absolute peaks for all four radionuclides. Therefore, sources of asymmetry related to the DU’s location within the ELLWF can be simplified to 2-D.

Fluxes to the water table for a set of asymmetric subsidence cases (see Table 4-4) for discrete-hole Case11b are also analyzed against the 2-D and 3-D model results above. Figure 4-24 shows that peak fluxes to the water table for the asymmetric, discrete-hole, subsidence cases are substantially greater than peak fluxes for the 2-D case and the 3-D, central, 12-foot-hole case. This finding supports the choice of a 3-D model for the trench unit VZ simulations to properly account for the asymmetries in subsidence models, especially given that the overall increase in computational load is negligible.



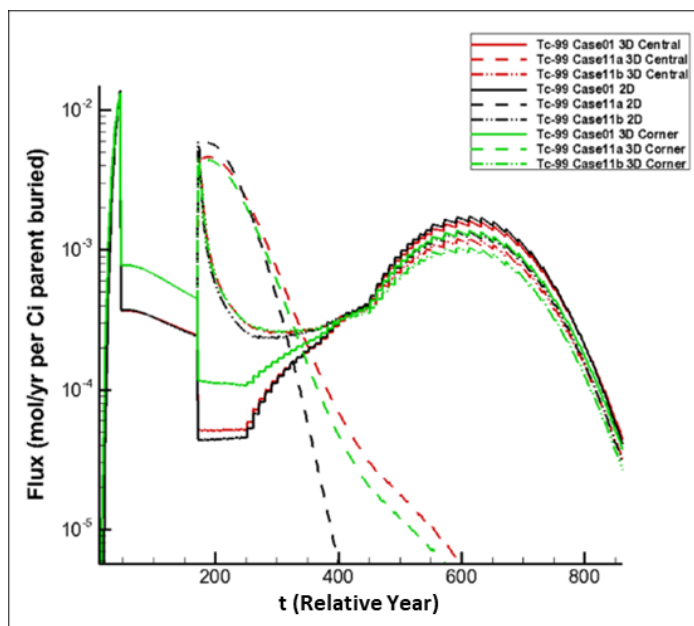
Note: The 2-D longitudinal peak is 33% higher than the peaks for the 3-D central and corner trench unit models, which are within 3% of each other.

Figure 4-20. Comparison of Sr-90 (half-life: 28.9 years; Sandy K_d : 5; Clayey K_d : 17) Fluxes to Water Table for Two-Dimensional Longitudinal Slice, Three-Dimensional Central Unit Model, and Three-Dimensional Corner Unit Model (Danielson, 2019c; Figure 12)



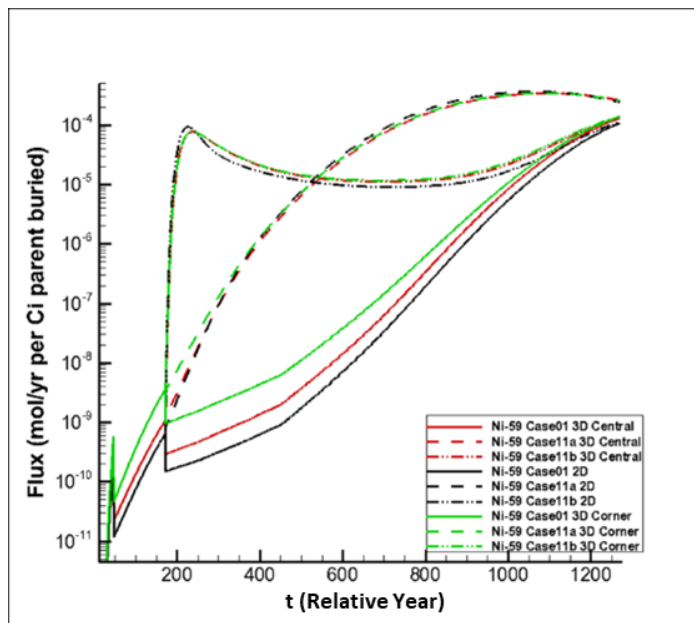
Note: The 2-D longitudinal peak is 15% higher than the peaks for the 3-D central and corner trench unit models.

Figure 4-21. Comparison of I-129 (half-life: 1.57E+07 years; Sandy K_d : 1; Clayey K_d : 3) Fluxes to Water Table for Two-Dimensional Longitudinal Slice, Three-Dimensional Central Unit Model, and Three-Dimensional Corner Unit Model (Danielson, 2019c; Figure 13)



Note: The absolute peaks of the three models are within 3% of each other, while the 2-D model has a secondary peak that is 25% higher than the secondary peaks for the 3-D central and corner trench unit models.

Figure 4-22. Comparison of Tc-99 (half-life: 2.111×10^5 years; Sandy K_d : 0.6; Clayey K_d : 1.8) Fluxes to the Water Table for Two-Dimensional Longitudinal Slice, Three-Dimensional Central Unit Model, and Three-Dimensional Corner Unit Model (Danielson, 2019c; Figure 14)

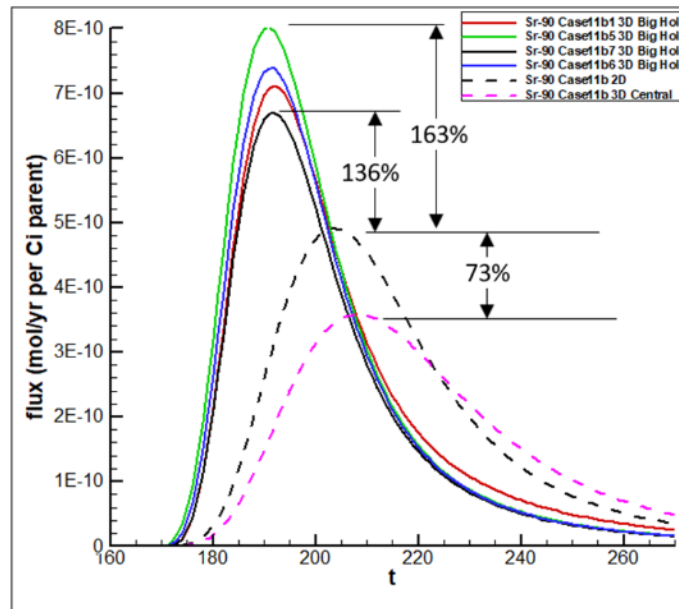


Note: The 2-D longitudinal peak is 20% higher than the peaks for the central and corner trench unit models.

Figure 4-23. Comparison of Ni-59 (half-life: 76,000 years; Sandy K_d : 7; Clayey K_d : 30) Fluxes to Water Table for Two-Dimensional Longitudinal Slice, Three-Dimensional Central Unit Model, and Three-Dimensional Corner Unit Model (Danielson, 2019c; Figure 15)

Table 4-4. Description of Asymmetric Cases Based on Case11b (Hamm et al., 2018)

Case	Description
Case11b1	46-foot x 46-foot hole in center of central DU
Case11b2	46-foot x 46-foot hole in center of corner DU
Case11b3	46-foot x 46-foot hole in top right corner of central DU
Case11b4	46-foot x 46-foot hole in bottom right corner of corner DU
Case11b5	46-foot x 46-foot hole in bottom left corner of corner DU
Case11b6	46-foot x 46-foot hole in top left corner of corner DU
Case11b7	46-foot x 46-foot hole in top right corner of corner DU

**Figure 4-24. Sr-90 Flux to Water Table for Various Discrete-Hole Cases with Substantially Different Peak Fluxes (Danielson, 2019c; Figure 16)**

4.1.3.4. Trench-Specific Features in Three-Dimensional Models

Along with accounting for the asymmetrical model features, 3-D trench models allow for a more detailed implementation of features specific to STs and ETs. For example, in previous 2-D model implementations (Hamm et al., 2018), a longitudinal cross-section is used because infiltration boundary conditions for the bounding infiltration model are most appropriately represented along the longitudinal axis. However, such a representation is not capable of accounting for differences in the ET and ST geometries (i.e., one 157-foot x 656-foot trench for ETs compared to five 20-foot x 656-foot trench segments for STs). While there are benefits to a generic model representation (e.g., using the ET geometry for both STs and ETs), the preference is to avoid introducing overly simplified, bounding assumptions when they can be readily avoided. Several screening simulations are conducted to compare trench models implemented using an ET geometry versus a ST geometry for both intact and subsidence closure-cap conditions. Danielson (2020a) and Danielson (2020b) both investigated differences in the peak flux to the water table brought forth by ST- and ET-specific geometric features; they ultimately concluded that trench-specific features should be included on a trench-by-trench basis rather than employing a generic waste form trench model. For example, Table 4-5 displays the ratio of the peak-flux to the water table for C-14, Tc-99, Sr-90,

Np-237, I-129, U-238, and H-3 at nine different subsidence hole locations in a centrally located ET versus ST unit. The hole locations are shown in Figure 4-25 for a centrally located ST or ET.

Table 4-5. Slit and Engineered Trench Ratio of Peak-Flux to Water Table Highlighting Geometric Impacts (Danielson, 2020a; Table 11)

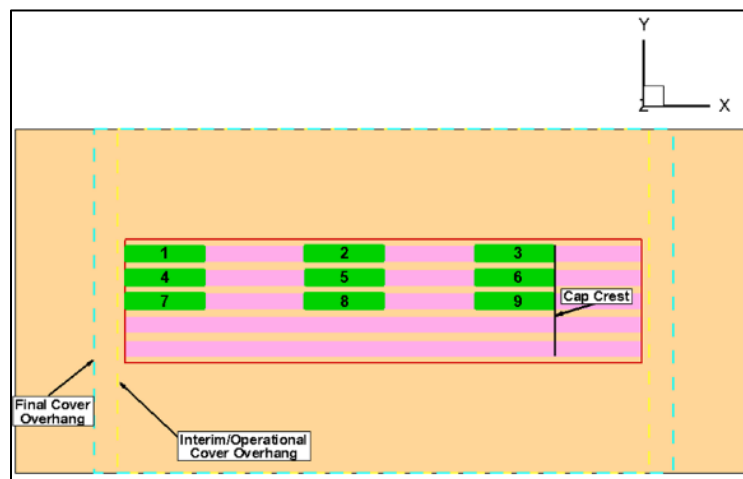
Radionuclide	Intact	Hole 1	Hole 2	Hole 3	Hole 4	Hole 5	Hole 6	Hole 7	Hole 8	Hole 9
C-14	0.71	0.71	0.71	0.71	0.72	0.72	0.72	0.72	0.72	0.72
Tc-99	1.72	1.72	1.72	1.72	1.72	1.72	1.72	1.72	1.72	1.72
Sr-90	1.08	0.57	0.50	0.37	0.57	0.51	0.38	0.57	0.51	0.38
Np-237	0.99	0.99	0.99	0.99	1.00	1.00	1.00	1.00	1.00	0.99
I-129	1.12	1.12	1.11	1.11	1.12	1.10	1.11	1.12	1.10	1.10
U-238	1.14	0.21	0.16	0.15	0.23	0.18	0.19	0.23	0.18	0.19
H-3	0.94	0.94	0.94	0.94	0.94	0.94	0.94	0.94	0.94	0.94

Notes:

Orange highlight: ST peak flux greater than ET peak flux

Green highlight: ET peak flux greater than ST peak flux

Bolded text: difference greater than 10%



Note: ST geometry shown, hole placements identical for ET geometry

Figure 4-25. Unique Subsidence Hole Locations for a Centrally Located Slit or Engineered Trench

Note that the ratio of the peaks across all simulation setups is consistent for C-14, Tc-99, Np-237, I-129, and H-3. Likewise, for Sr-90 and U-238, the ratio of the peak-flux to the water table for subsidence cases having the same infiltration rate (i.e., holes 1, 4, and 7; holes 2, 5, and 8; holes 3, 6, and 9) is consistent. However, because many of the peak ratios are substantially greater than 1.1 or less than 0.9 (>10% difference), the ET and ST geometries should be accounted for on a trench-by-trench basis.

To simplify mesh generation of models for ETs and STs, the spatial discretization of the mesh along the X and Y directions of the mesh is the same for all models. Figure 4-26 and Figure 4-27 show the common mesh used for ETs and STs for trench units centrally located and along the corners beneath the final closure cap, respectively. Variations along the Z direction occur only to account for differences in the depth to the water table and clayey material thickness; however, the

discretization of the trench is always the same. Therefore, the only difference between the ET and ST models for a specific hydrostratigraphic grouping is the assignment of material types within regions of the mesh corresponding to the DU. More specifically, ETs have uniformly specified waste across the entire DU footprint that corresponds to boxed waste (16-foot-tall before dynamic compaction and 2.5-foot-tall after dynamic compaction). STs, on the other hand, have a 10-foot-wide section of UVZ material separating each of the five trench segments and 8.5-foot-wide sections of UVZ material separating the edge trench segments (1 and 5) from the edge of the overall footprint. Additionally, the waste form for STs is assumed to be hybrid waste (16-foot-tall before dynamic compaction and 11.1-foot-tall after dynamic compaction). Because a ST receives both bulk and boxed waste throughout a trench, a “hybrid” waste zone is assumed by combining the two waste types into a set of equivalent properties based on an estimated fraction of each waste type. The ST and ET models are shown in Figure 4-28 and Figure 4-29, respectively.

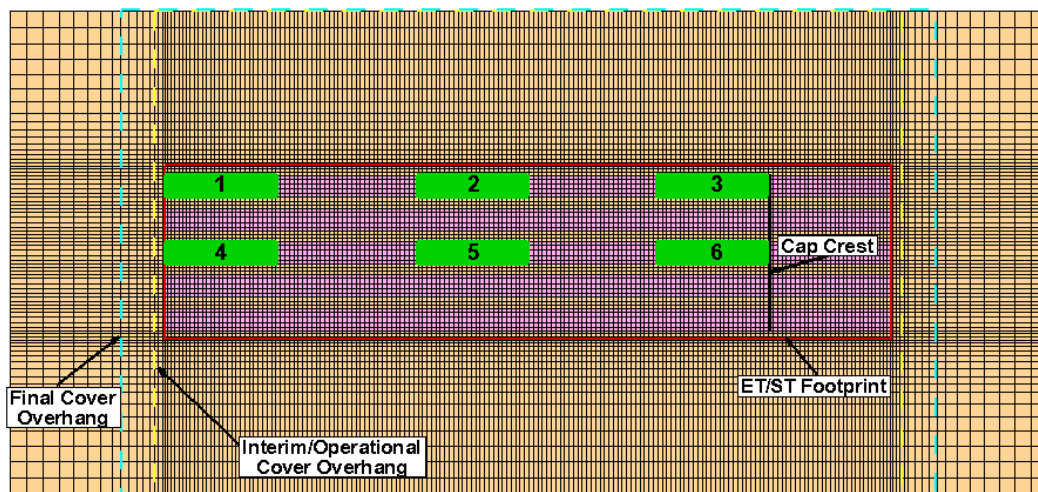


Figure 4-26. Common Mesh and Discrete Hole Locations for Centrally Located Slit and Engineered Trenches (Danielson, 2019c; Figure 19)

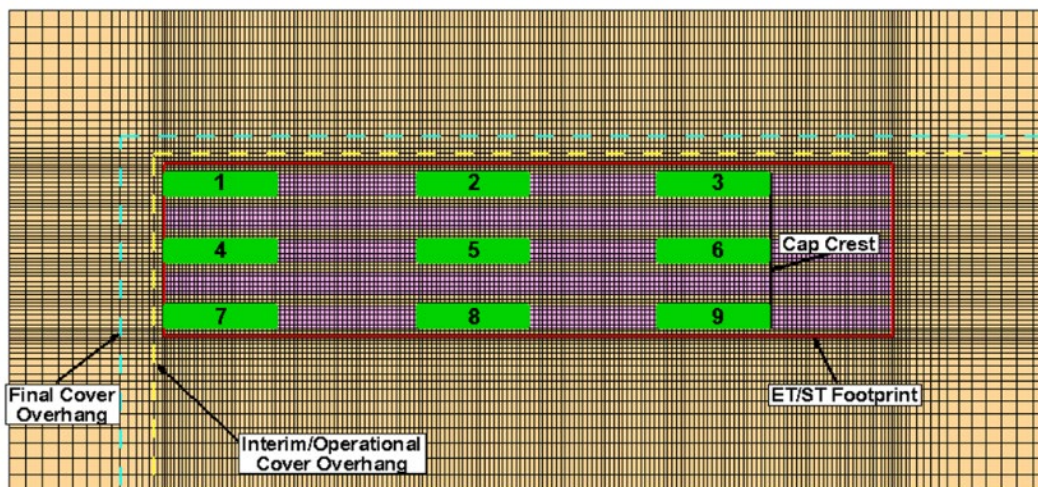


Figure 4-27. Common Mesh and Discrete Hole Locations for Slit and Engineered Trenches in Corner Positions under Final Closure Cap (Danielson, 2019c; Figure 20)

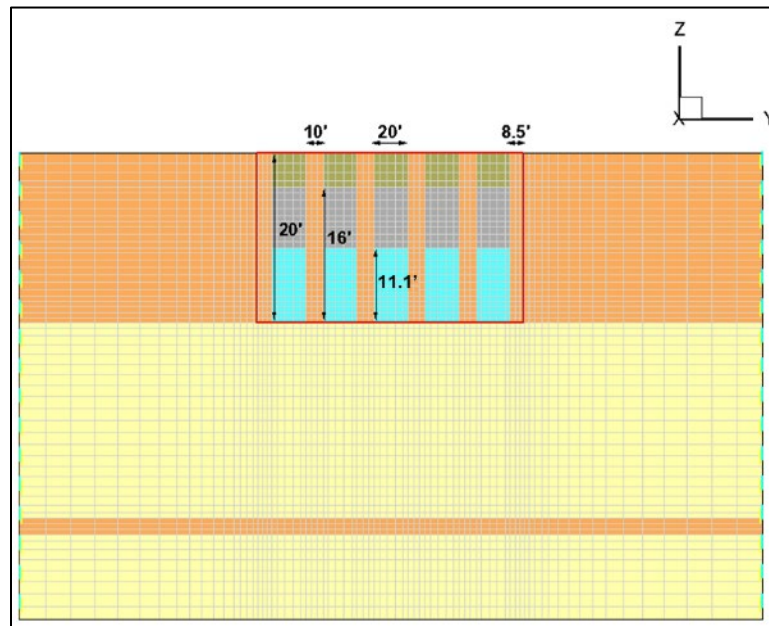


Figure 4-28. Cross-Section of Three-Dimensional Slit Trench Model (Danielson, 2019c; Figure 17)

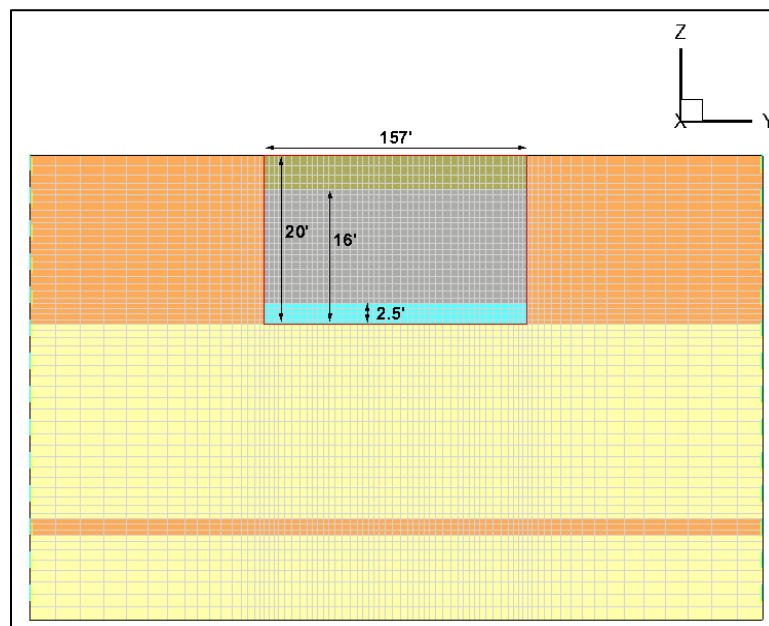


Figure 4-29. Cross-Section of Three-Dimensional Engineered Trench Model (Danielson, 2019c; Figure 18)

4.1.3.5. Timelines

Table 4-6 provides a summary of the DU-specific timeline assumed for each ST and ET in the PORFLOW VZ model. Included in the table are the dates for first and last waste placements, installation of the operational cover (HDPE stormwater runoff cover for STs or OSC for ETs), interim closure, and final closure.

Table 4-6. Assumed Model Timelines for Slit and Engineered Trenches

DU	Date of First Waste Placement	Date of Last Waste Placement	Date of Operational Cover Placement ^a	Interim Closure	Final Closure
ST01	12/21/1995	09/19/2003	12/21/2010	09/30/2065	09/30/2165
ST02	09/20/2001	08/31/2006	12/21/2010		
ST03	10/20/2003	01/06/2010	12/21/2010		
ST04	02/26/2004	08/19/2010	12/21/2010		
ST05	05/27/2004	10/16/2006	12/21/2010		
ST06	04/29/2006	11/07/2029	04/07/2036		
ST07	06/26/2006	04/07/2032	04/07/2036		
ST08	02/06/2007	10/27/2037	01/25/2042		
ST09	03/17/2011	07/01/2020	01/25/2042		
ST10	12/18/2020	11/18/2028	01/25/2042		
ST11	09/30/2021	05/06/2026	05/06/2030		
ST14	03/29/2011	09/14/2021	09/14/2025		
ST17	09/30/2021	07/29/2027	07/29/2031		
ST18	09/30/2021	07/29/2027	07/29/2031		
ST19	09/30/2021	07/29/2027	07/29/2031		
ST20	09/30/2021	07/29/2027	07/29/2031		
ST21	09/30/2021	08/09/2026	08/09/2030		
ST22	09/30/2021	10/17/2025	10/17/2029		
ST23	09/30/2021	10/15/2025	10/15/2029		
ST24	09/30/2021	08/25/2027	08/25/2031		
ET01	02/13/2001	03/30/2017	09/30/2040		
ET02	06/03/2004	01/24/2028	09/29/2040		
ET03	09/19/2013	09/02/2021	09/30/2040		
ET04	12/18/2020	11/10/2027	09/30/2040		
ET05	09/30/2021	08/15/2028	09/30/2065		
ET06	09/30/2021	07/14/2028	09/30/2065		
ET07-09	09/30/2021	12/21/2040	09/30/2065		

Notes:

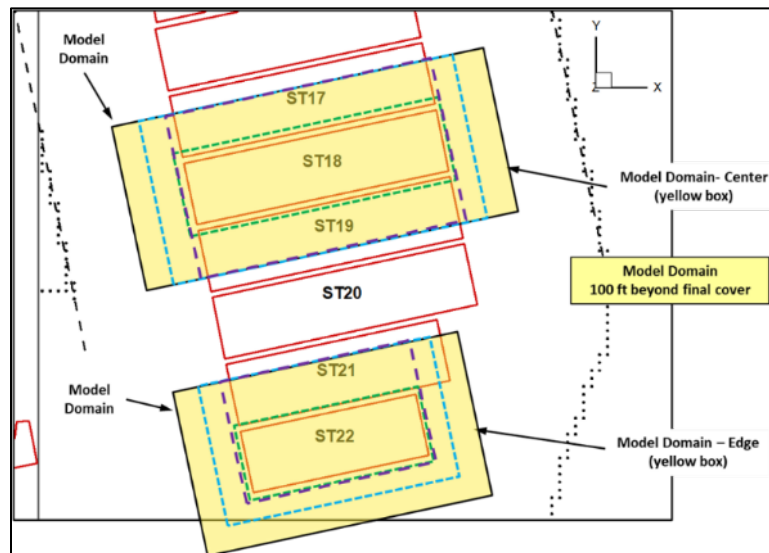
DU highlight color definition: Closed Open Future

^a Operational cover date reflects placement of HDPE stormwater runoff cover for STs and soil cover (OSC) for ETs.

4.1.3.6. Infiltration Rate Boundary Conditions

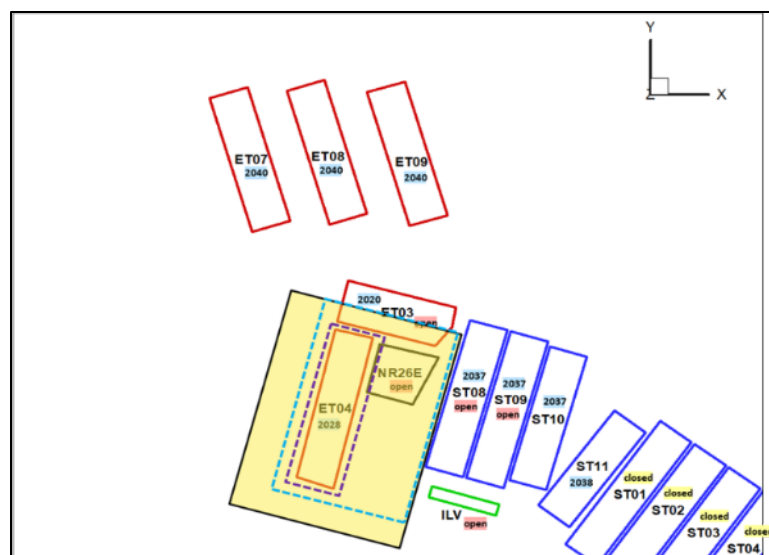
The upper boundary condition for the PORFLOW models is defined by time-dependent infiltration rates to account for the operational period (uncovered), the IC period (interim cover), and the post-IC period (final cover system installed followed by ongoing degradation of the closure cap). Several conceptual and numerical modeling studies (Dyer, 2017b; Dyer, 2017d; 2018a; 2018b; Dyer, 2019b; 2019c; Dyer and Flach, 2017; 2018) have been conducted to identify a set of bounding conceptual infiltration models for the final closure cap design and to provide sets of both intact and subsidence infiltration rates as a function of time and non-crushable container content (i.e., percent subsidence). This collective body of work is summarized by Dyer (2019b) in the Infiltration Data Package for the ELLWF. Each unique percent-subsidence infiltration case requires a separate model setup for upper boundary condition specification. Additionally, if a trench falls along an edge (e.g., ST22) or a corner (e.g., ET03 and ET04) of the final closure cap, a separate PORFLOW model is required so that the upper boundary conditions can be applied as

shown in Figure 4-30 for a centrally located (ST18) versus edge-located (ST22) DU and in Figure 4-31 for a corner-located (ET04) DU. The final multilayer soil-geomembrane cover overhangs the trench by 40 feet while the interim cover overhangs the trench by 10 feet. The operational stormwater runoff cover (HDPE only) that is installed over STs after emplacement of the last waste package (see Table 4-6 for DU-specific dates) has the same overhang and infiltration rate as the interim cover.



Note: Green, purple, and blue dashed lines represent operational, interim, and final covers, respectively.

Figure 4-30. Example of Centrally Located and Edge-Located Trenches



Note: Blue and purple dashed lines represent final and interim covers, respectively.

Figure 4-31. Example of a Corner-Located Trench

Except for trench units known to not (or never) contain non-crushable containers, all trench models will include both intact and subsidence cases. As noted by Dyer (2019b), two different approaches are considered for incorporating the effect of localized cap subsidence on infiltration rates in the PORFLOW flow and transport simulations of STs and ETs. In the first approach, a Monte Carlo (MC) probabilistic model is developed to calculate infiltration rates for 0.54%, 2%, 3.6%, and 4.9% subsidence scenarios, reflecting historical and future non-crushable content for the STs and ETs (Dyer and Flach, 2017; 2018). The resulting blended (spatially and slope-length averaged) infiltration rates become an upper boundary condition for the PORFLOW VZ model simulations as originally implemented by Danielson (2019a). In the second and ultimately preferred approach, an MC rectangle packing algorithm (Danielson, 2019b) and a simplified equation for the total mass flux of water draining into a subsided compartment [see Eq. (4-32) below] are employed to implement a weighted blending of radionuclide fluxes to the water table using the results of deterministic PORFLOW VZ simulations representative of specific subsidence cases.

In choosing to perform a weighted blending of radionuclide fluxes at the water table (rather than a weighted blending of infiltration rates for the upper boundary condition), subsidence cases will be investigated using discrete holes with a specific dimension and location. The dimensions of the holes have been selected according to the relevant geometric features so that it is possible to obtain one-to-one comparisons whether an ET or ST geometry is used. More specifically, the hole length is bounded at 20 feet (i.e., the width of a slit trench segment) in one direction, while its length in the longitudinal direction of the trench is equal to the percent non-crushable content rounded to the nearest whole number that can be accommodated by the spatial discretization of the mesh. The discrete hole sizes for each percent subsidence are provided in Table 4-7.

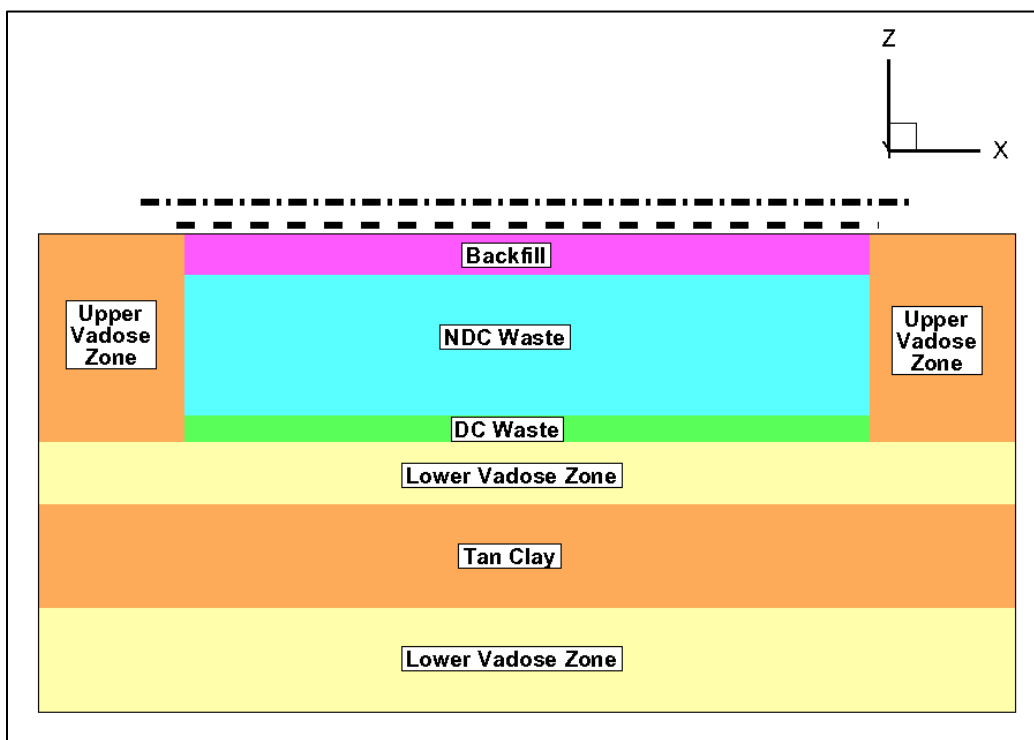
Table 4-7. Dimensions of Discrete Holes for Percent Subsidence Cases (Danielson, 2019c; Table 2)

Percent Subsidence	Subsided Area (square feet)	Length (feet)	Width (feet)	Model Length (feet)
0.54	556.16	27.81	20	29.87 and 28 ^a
2.0	2059.84	102.99	20	100
3.6	3707.71	185.39	20	184
4.9	5046.61	252.33	20	252

^a Two model lengths are required for the 0.54% subsidence case because non-uniform spatial discretization occurs along the edge of the trench.

The placement of subsidence “holes” is extensively investigated in studies by Danielson (2019a; 2019b; 2019c) and Danielson (2020a; 2020b) over several years. Their individual relevance to the current conceptual model of the VZ for STs and ETs varies because they reflect an evolution over time in whether to perform a weighted blending of infiltration rates at the upper model boundary or a weighted blending of radionuclide fluxes at the water table (lower model boundary). Still, they each contribute in some way to the conceptual model adopted for the PA.

Danielson (2019a) employs two separate PORFLOW simulation setups for a 3-D VZ model of a centrally located ET (Figure 4-32) to analyze the impact of different spatial distributions of subsidence boundary conditions. One model setup assumed that a rectangular subsided region formed in the center of the trench, while the other setup assumed that the subsided region formed at the end of the trench as shown in Figure 4-33.



Note: Spatial extent of interim and final covers indicated by dashed and dashed-dotted lines, respectively.

Figure 4-32. Schematic of Engineered Trench Model Geometry from Ground Surface to Water Table (Danielson, 2019a; Figure 3)

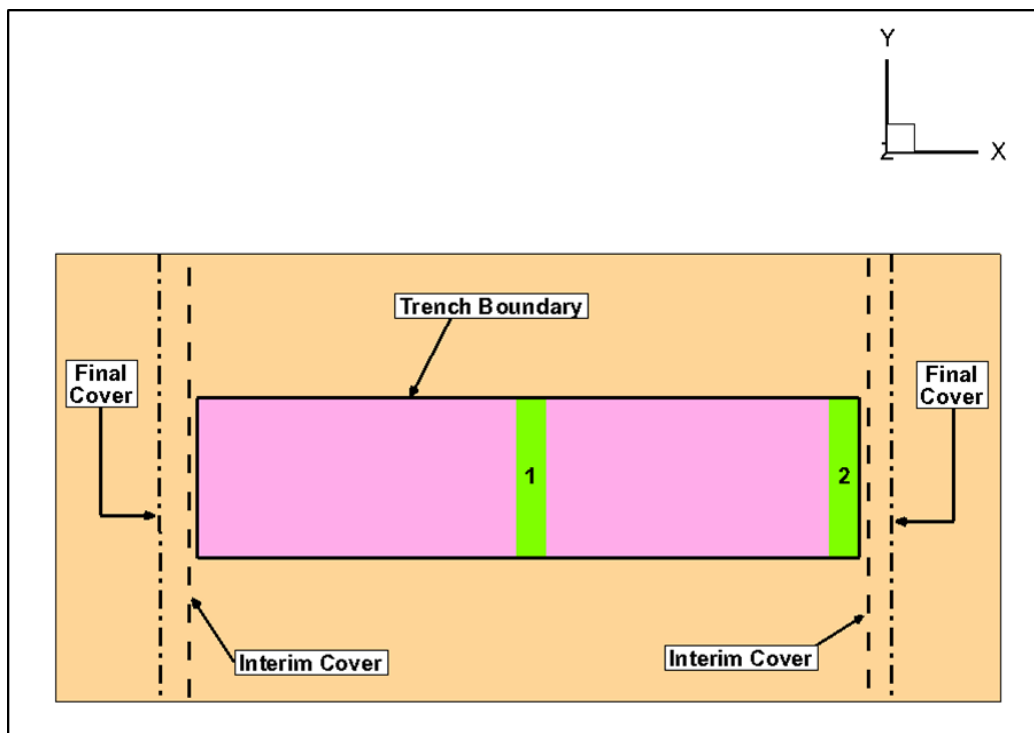


Figure 4-33. Schematic of Three-Dimensional PORFLOW Model Geometry Showing Boundaries for Final Cover, Interim Cover, and Center and End Subsided Regions [green] (Danielson, 2019a; Figure 2)

Both subsided regions had the same geometric specifications (i.e., length of 20 feet, width of 157 feet, and short dimension oriented longitudinally); however, they used water infiltration rate boundary conditions that appropriately accounted for surface runoff and lateral drainage from the adjacent upslope intact regions of the final closure cap. Because of the substantially higher water infiltration rate associated with the subsided region at the end of the trench (rectangle 2 in Figure 4-33), this geometry resulted in higher absolute peak fluxes to the water table for all six radionuclides simulated (Sr-90, H-3, Tc-99, U-235, I-129, and C-14). On the other hand, the slower release rate of the centrally located subsided hole geometry (rectangle 1 in Figure 4-33) generated a higher flux to the water table during the time period subsequent to the absolute peak. A third model is implemented as a control, where the water infiltration rate corresponding to the centrally located subsided region is applied at the end of the trench to highlight the purely geometric effects.

Danielson (2019a) concluded as highlighted in Figure 4-34 that a higher water infiltration rate (end hole) produces a sharper peak, while a lower infiltration rate (central hole) leads to a broader peak. A centrally located hole impacts a greater portion of the waste zone, leading to a higher peak when an equal infiltration rate is applied at both the end and central hole locations. The generalized insights from this study played an important role in the positioning of the discrete subsidence holes as described below.

Danielson (2019c) determined that there are nine unique subsidence hole locations out of 15 possible locations¹ for a centrally located trench unit as indicated in Figure 4-25. ST segments 4 and 5 (looking top to bottom) with no holes are equivalent by symmetry to the trench segments with hole locations 4-5-6 and 1-2-3, respectively. An additional assumption is made that hole locations 4-5-6 and 7-8-9 in Figure 4-25 will be essentially equivalent due to their proximity and similar surroundings (i.e., a waste zone bounded on both sides by undisturbed UVZ clayey soil plus another waste zone). In contrast, the waste zone for hole locations 1-2-3 (Figure 4-25) is bounded by undisturbed UVZ clayey soil plus another waste zone on the lower side and simply undisturbed UVZ clayey soil on the top side.

For corner units (Figure 4-35), Danielson (2019c) shows that the symmetry is broken (i.e., note the truncated cover overhangs at the top end of the schematic for corner units versus centrally located units). In particular, hole locations 1-2-3 for a corner unit will experience a greater “suction effect” beneath the cover (i.e., flow lines drawn inward toward center of waste zone) compared to a centrally located unit. Holes located along ST segments 2 and 4 (top to bottom) in Figure 4-35 are reasonably assumed to behave similarly to hole locations 7-8-9, where the suction effect is negligible and the waste zone is bordered on both sides by undisturbed UVZ clayey soil plus another waste zone. This is considered a reasonable assumption because the transport behavior for the different subsided hole locations in ST segments 2, 3, and 4 is more heavily dominated by differences in the infiltration rate that occur in the x-direction. Finally, hole locations 4-5-6 are bordered by undisturbed UVZ clayey soil plus another waste zone on the top side and UVZ clayey soil on the lower side.

¹ Five total trench segments by three holes per trench segment using the ST geometry as a basis for both STs and ETs.

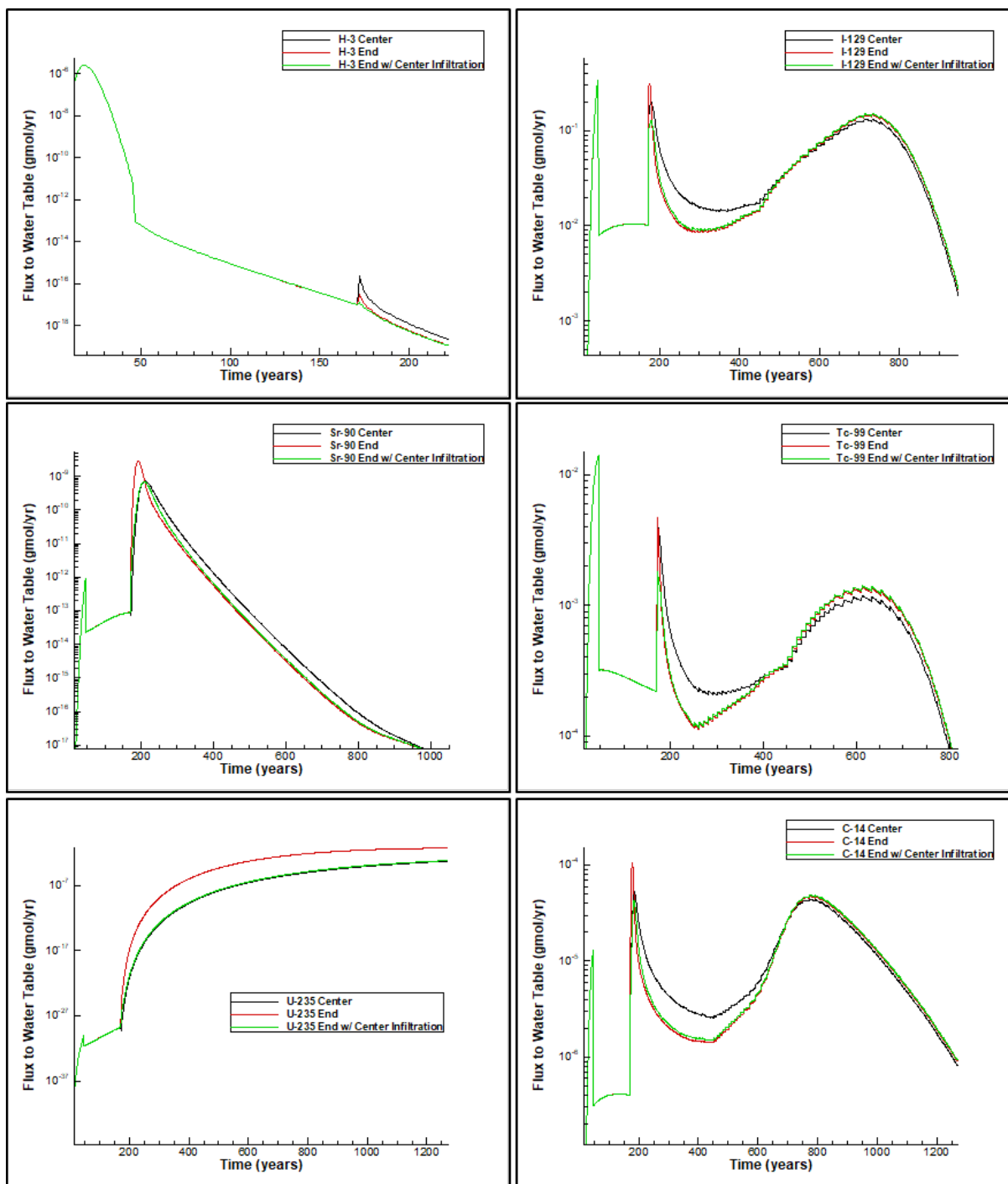
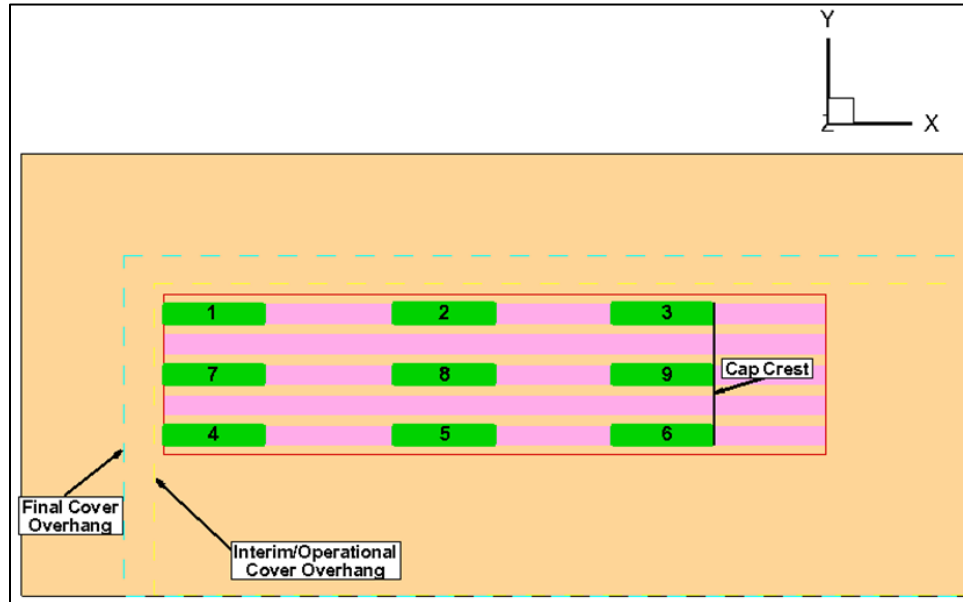


Figure 4-34. Flux to Water Table (gmol yr^{-1} per Ci parent buried) Comparison for a Subsided Region at Trench Center with a Center-Hole Infiltration Rate [black], Trench End with an End-Hole Infiltration Rate [red], and Trench End with a Center-Hole Infiltration Rate [green] (Danielson, 2019a; Figures 4 thru 9)



Note: ST geometry is shown; hole placements are identical for ET geometry.

Figure 4-35. Unique Subsidence Hole Locations for Corner Slit or Engineered Trench

Based on the reasoning above, Danielson (2019c) recommended implementation of six discrete hole locations for centrally located units and nine discrete hole locations for corner units as marked and labeled in Figure 4-26 and Figure 4-27, respectively.² The purple mesh areas represent the footprint of five ST segments. The length dimensions of each hole are adjusted on a percent-subsidence-case basis according to Table 4-7.

Holes 1, 4, and 7 are all placed with their left edge at the end of the trench. Holes 2, 5, and 8 are each placed with their right edge at the midpoint of the trench. Holes 3, 6, and 9 are all placed with their right edge at the cap crest, which corresponds to 544 feet from the left edge of the trench using the generalized spatial discretization. The infiltration rates for each percent subsidence case and each hole location are calculated using Eq. (4-32):

$$I_S = I_B + \frac{L_U}{L_H}(I_B - I_I) \quad \text{Eq. (4-32)}$$

² There is an incentive to employ even fewer subsidence holes (fewer PORFLOW models, less computational resources, and a simpler and more generalized model overall). Using the hydrostratigraphy of centrally located ST06 as a representative model of ST and ET geometries, Danielson (2020a) analyzed whether fewer discrete hole locations are sufficient to adequately predict peak radionuclide flux to the water table for centrally located and corner units. With only one exception (Sr-90 for subsidence holes 1-2-3 as shown in Figure 4-25 for a centrally located trench and in Figure 4-35 for a corner trench), Danielson (2020a) found that the ratio of the peak flux to the water table (central ET/corner ET) for C-14, Tc-99, Sr-90, Np-237, I-129, U-238, and H-3 fell within the range $0.9 \leq \text{ratio} \leq 1.0$. The author concluded that advective transport (the impact of subsidence infiltration rates on radionuclide transport) generally dominates over geometric differences between the hole locations (boundary condition specifications). As a result, three discrete hole locations are sufficient to model radionuclide transport for both centrally located and corner units and are adopted for PA production runs reported in Chapter 5. To ensure capturing the worst case, Holes 1, 2, and 3 in subsidence cases are assumed to be located along the trench segment where the greatest hydraulic suction occurs. For example, the holes for corner units neighbor the 40-foot overhang rather than infinite cover side. This makes less of a difference for a centrally located trench; however, the holes are still placed along the edge segment.

where:

- I_I Intact infiltration rate (in yr^{-1})
 L_U Length of the intact area upslope of the hole (ft)
 L_H Length of the subsided region [both lengths are measured in the direction parallel to surface runoff] (ft)
 I_B Closure-cap-specific subsidence scenario background infiltration rate [i.e., annual-average rainfall minus annual-average evapotranspiration], which is 16.5 in yr^{-1} for the ELLWF PA as determined by Dyer (2019b) [in yr^{-1}].

The infiltration rates are provided in Table 4-8, Table 4-9, Table 4-10, and Table 4-11.

Table 4-8. Trench Infiltration Rates for 0.54% Subsidence Cases (Danielson, 2019c; Table 3)

Time (year)	Intact (in yr^{-1})	Infiltration Rate for 0.54% Subsidence Cases (in yr^{-1})		
		Holes 1, 4, and 7 End Position	Holes 2, 5, and 8 Trench Midpoint	Holes 3, 6, and 9 Crest Position
100	0.0008	101.33	52.14	16.50
180	0.007	101.30	52.12	16.50
290	0.16	100.51	51.79	16.50
300	0.18	100.41	51.75	16.50
340	0.3	99.79	51.49	16.50
380	0.38	99.38	51.32	16.50
480	1.39	94.19	49.14	16.50
660	3.23	84.73	45.16	16.50
1,100	6.82	66.27	37.41	16.50
1,900	10.24	48.68	30.02	16.50
2,723	11.1	44.26	28.16	16.50
3,300	11.18	43.85	27.99	16.50
5,700	11.3	43.24	27.73	16.50
10,100	11.35	42.98	27.62	16.50

Notes:

Holes 1, 4, and 7 are each 29.87-foot long. Remaining holes are each 28-foot long.

Table 4-9. Trench Infiltration Rates for 2.0% Subsidence Cases (Danielson, 2019c; Table 4)

Time (year)	Intact (in yr ⁻¹)	Infiltration Rate for 2.0% Subsidence Cases (in yr ⁻¹)		
		Holes 1, 4, 7 End Position	Holes 2, 5, 8 Trench Midpoint	Holes 3, 6, 9 Crest Position
100	0.0008	89.76	52.14	16.50
180	0.007	89.73	52.12	16.50
290	0.16	89.05	51.79	16.50
300	0.18	88.96	51.75	16.50
340	0.3	88.43	51.49	16.50
380	0.38	88.07	51.32	16.50
480	1.39	83.59	49.14	16.50
660	3.23	75.42	45.16	16.50
1,100	6.82	59.48	37.41	16.50
1,900	10.24	44.29	30.02	16.50
2,723	11.1	40.48	28.16	16.50
3,300	11.18	40.12	27.99	16.50
5,700	11.3	39.59	27.73	16.50
10,100	11.35	39.37	27.62	16.50

Notes:

All holes are 100-foot long.

Table 4-10. Trench Infiltration Rates for 3.6% Subsidence Cases (Danielson, 2019c; Table 5)

Time (year)	Intact (in yr ⁻¹)	Infiltration Rate for 3.6% Subsidence Cases (in yr ⁻¹)		
		Holes 1, 4, 7 End Position	Holes 2, 5, 8 Trench Midpoint	Holes 3, 6, 9 Crest Position
100	0.0008	75.90	52.14	16.50
180	0.007	75.87	52.12	16.50
290	0.16	75.32	51.79	16.50
300	0.18	75.25	51.75	16.50
340	0.3	74.82	51.49	16.50
380	0.38	74.53	51.32	16.50
480	1.39	70.90	49.14	16.50
660	3.23	64.27	45.16	16.50
1,100	6.82	51.35	37.41	16.50
1,900	10.24	39.04	30.02	16.50
2,723	11.1	35.94	28.16	16.50
3,300	11.18	35.65	27.99	16.50
5,700	11.3	35.22	27.73	16.50
10,100	11.35	35.04	27.62	16.50

Notes:

All holes are 184-foot long.

Table 4-11. Trench Infiltration Rates for 4.9% Subsidence Cases (Danielson, 2019c; Table 5)

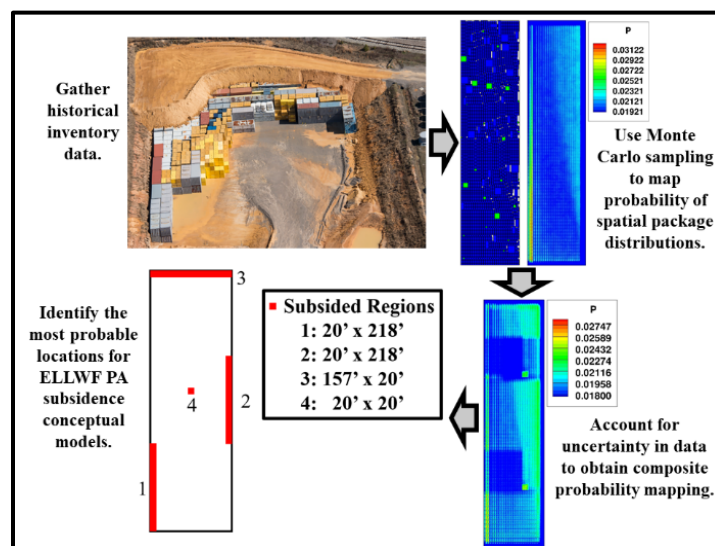
Time (year)	Intact (in yr ⁻¹)	Infiltration Rate for 4.9% Subsidence Cases (in yr ⁻¹)		
		Holes 1, 4, 7 End Position	Holes 2, 5, 8 Trench Midpoint	Holes 3, 6, 9 Crest Position
100	0.0008	64.68	52.14	16.50
180	0.007	64.66	52.12	16.50
290	0.16	64.21	51.79	16.50
300	0.18	64.15	51.75	16.50
340	0.3	63.80	51.49	16.50
380	0.38	63.57	51.32	16.50
480	1.39	60.62	49.14	16.50
660	3.23	55.25	45.16	16.50
1,100	6.82	44.77	37.41	16.50
1,900	10.24	34.78	30.02	16.50
2,723	11.1	32.27	28.16	16.50
3,300	11.18	32.03	27.99	16.50
5,700	11.3	31.68	27.73	16.50
10,100	11.35	31.54	27.62	16.50

Notes:

All holes are 252-foot long.

4.1.3.7. Blending Flux-to-the-Water Table Profiles

This section presents the approach used for each of the centrally located and corner trench units to blend the flux-to-the-water-table profiles at each time step for each radionuclide. A Monte Carlo (MC) rectangle packing algorithm, illustrated in Figure 4-36, has been developed by Danielson (2019b) to gain a better understanding of the likely spatial distribution of subsidence regions in the final closure cap resulting from the placement of non-crushable waste containers within STs and ETs. Details on the development of the algorithm and Python source code are presented by Danielson (2019b).

**Figure 4-36. Summary of the Monte Carlo Rectangle Packing Algorithm Workflow (Danielson, 2019b; Figure ES-1)**

4.1.3.7.1. Inventory Distribution of Non-Crushable and Crushable Packages

An inventory of all non-crushable packages (NCPs) placed (or to be placed) in ELLWF STs and ETs, along with the footprint area associated with each package, is provided by SWM at SRS. While the inventory listing provides the footprint area, the length and width dimensions of the NCPs are not readily available. Therefore, NCPs are initially assumed to be square and are binned based on package area only, yielding 14 unique package types with a total areal footprint of 13,446 square feet [see Danielson (2019b), Appendix B, for listing of NCPs]. The assumed distribution of all crushable ST and ET waste package types is listed in Table 4-12 and is based on data provided by Phifer (2010) and communications with SWM.

Table 4-12. Percentage Breakdown of Crushable Waste Types (Danielson, 2019b; Table 2-1)

DU Type	Percent Bulk Waste	Percent Boxed Waste	B-25 Percentage of Boxed Waste	SeaLand Percentage of Boxed Waste	Percentage of SeaLands 20 feet long	Percentage of SeaLands 40 feet long
ET	5%	95%	95%	5%	95%	5%
ST	67%	33%	95%	5%	95%	5%

Dyer (2019b) identified four relevant “percent subsidence” scenarios (0.54%, 2.0%, 3.6%, and 4.9%) based on the number and size of non-crushable containers placed in STs and ETs. Each scenario is investigated by the MC rectangle packing algorithm to identify how the spatial distribution of crushable and NCPs changed as a function of the percentage of NCPs. The areal footprint of the total distribution of crushable and non-crushable containers is reported in Table 4-13. The assumed dimensions in feet of each waste type (Table 4-14) are rounded to the nearest whole number for the benefit of the grid resolution.

Table 4-13. Total Areal Footprints of Non-Crushable and Crushable Packages Comprising Slit and Engineered Trench Waste Distribution (Danielson, 2019b; Table 2-2)

Percent Subsidence	Non-Crushable Waste Areal Footprint (ft ²)	Crushable Waste Areal Footprint (ft ²)
0.54%	13,446	2,476,554
2%	13,446	658,854
3.6%	13,446	360,054
4.9%	13,446	260,962
10%	13,446	121,014

Table 4-14. Assumed Dimensions of Crushable Waste Types in Waste Distribution (Danielson, 2019b; Table 2-3)

Dimension	Crushable Waste Type			
	Bulk Waste	B-25 Box	20-foot SeaLand	40-foot SeaLand
Length (feet)	20	4	9	9
Width (feet)	20	6	20	40

Based on the percentage of each waste type (Table 4-12) to be represented in the probability distributions, Eq. (4-33) is used to calculate the number of crushable waste packages for each waste type, trench type (ST and ET), and percent subsidence (0.54%, 2.0%, 3.6%, and 4.9%), resulting in the probability distribution of unique crushable waste containers shown in Table 4-15.

$$\frac{\sum_{i=1}^{N_C} n_i A_i}{A_T} \approx P_C \quad \text{Eq. (4-33)}$$

where:

- n_i Number of waste packages of type i in the inventory (unitless)
- A_i Area of the waste package of type i (ft²)
- A_T Summed total area of all rectangular objects in the inventory (ft²)
- N_C Total number of crushable waste types (unitless)
- P_C Probability of selecting a crushable package (unitless)

Similarly, the probability distribution of unique non-crushable waste containers is given by:

$$\frac{\sum_{j=1}^{N_{NC}} n_j A_j}{A_T} \approx P_{NC} \quad \text{Eq. (4-34)}$$

where:

- n_j Number of waste packages of type j in the inventory (unitless)
- A_j Area of the waste package of type j (ft²)
- N_{NC} Total number of non-crushable waste types (unitless)
- P_{NC} Probability of selecting an NCP [note that $P_C + P_{NC} = 1$] (unitless)

Along with the crushable and NCP distributions and dimensions, the dimensions of the rectangular trench (e.g., ET or ST) in which the packages are placed also influences the packing arrangement of the waste packages. For the ELLWF, ET footprint dimensions are 157-foot wide by 656-foot long while ST footprint dimensions are 20-foot wide by 656-foot long. (Note: The packing algorithm for a ST is based on a single trench segment only to reflect actual filling operations.)

Table 4-15. Total Area and Number of Crushable Package Types Represented in Package Inventory Distributions for Slit and Engineered Trench Percent Subsidence Cases (Danielson, 2019b; Table 2-4)

Percent Subsidence	Trench Type	Waste Type	Total Area (ft ²)	Number
0.54%	ET	Bulk	123,827.700	310
		B-25	2,235,089.985	93,129
		20-foot SeaLand	111,754.499	621
		40-foot SeaLand	5,881.816.000	16
	ST	Bulk	1,651,036.000	4,128
		B-25	784,242.100	32,677
		20-foot SeaLand	39,212.105	218
		40-foot SeaLand	2,063.795	6
2%	ET	Bulk	32,942.700	82
		B-25	594,615.735	24,776
		20-foot SeaLand	29,730.787	165
		40-foot SeaLand	1,564.778	4
	ST	Bulk	439,236	1,098
		B-25	208,637.100	8,693
		20-foot SeaLand	10,431.855	58
		40-foot SeaLand	549.045	2
3.6%	ET	Bulk	18,002.700	45
		B-25	324,948.735	13,540
		20-foot SeaLand	16,247.437	90
		40-foot SeaLand	855.128	4
	ST	Bulk	240,036.000	600
		B-25	114,017.100	4,751
		20-foot SeaLand	5,700.855	32
		40-foot SeaLand	300.045	1
4.9%	ET	Bulk	13,048.108	33
		B-25	235,518.352	9,813
		20-foot SeaLand	11,775.918	65
		40-foot SeaLand	619.785	2
	ST	Bulk	173,974.776	435
		B-25	82,638.018	3,443
		20-foot SeaLand	4,131.901	23
		40-foot SeaLand	217.468	1

4.1.3.7.2. Composite Probability Map

For a particular case, the MC sampling algorithm introduced above is employed to sequentially select waste containers for placement in a rectangular region bounded by the trench unit footprint. In this MC approach, the probability of a container type being selected is weighted by the fractional abundance relative to all other container types. During each MC realization, the frequency of non-crushable waste containers appearing at each location is updated on a spatially discretized rectangular mesh. After many tens of thousands of realizations, a probability contour map is generated that identifies the location(s) with the highest frequencies of non-crushable waste containers (i.e., the most likely locations where a subsidence hole will form). A few probability contour maps are shown on the right half of Figure 4-36.

Danielson (2019b) repeated this process for numerous varied test cases, investigating the impact of trench geometry (ET or ST), percentage of NCPs, NCP shape (rectangular and square),

orientation, and aspect ratio, as well as the presence and location of drainage sumps. Modifying the shape (i.e., aspect ratio and default orientation) of NCPs led to the most substantial differences in the most probable spatial distribution when compared to altering the percentage of NCPs. Because uncertainty is embedded in the shape of past and future NCPs, the probability contour maps for several cases are combined to produce a composite probable spatial distribution of NCPs as shown in Figure 4-37.

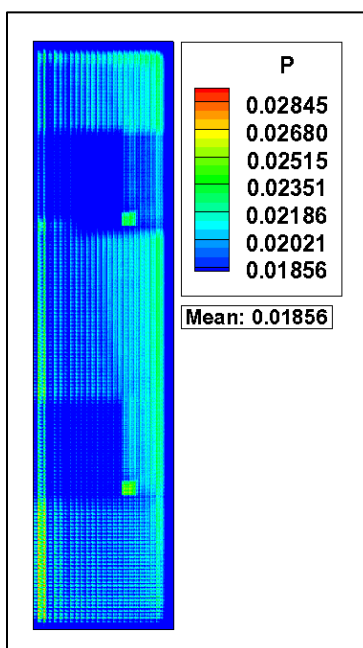


Figure 4-37. Composite Contour Map of Probability of a Non-Crushable Package Being Present at a Given Location in Engineered Trench Geometry (Danielson, 2019b; Figure 3-19)

The composite contour map includes the following test cases, all of which are derived from the 2% NCP base case:

- Base case (2% subsidence, square NCPs)
- NCPs elongated with 1.778:1 aspect ratio
- NCPs elongated with 4:1 aspect ratio
- NCPs elongated with 1.778:1 aspect ratio and default orientation rotated
- NCPs elongated with 4:1 aspect ratio and default orientation rotated
- ET geometry filled with ST inventory distribution³ and square NCPs
- B-25 boxed waste default orientation rotated
- All sump pump cases

Generally, the most probable locations are along the edges and corners of the ET geometry. In addition, sump pump test cases show an increased probability of finding NCPs in central regions of the trench.

³ The bulk waste form dominates in a ST; boxed waste is the dominant waste form in an ET.

4.1.3.7.3. Application of Monte Carlo Algorithm to Blending Flux-to-the-Water Table Profiles

GW radionuclide transport simulations performed with PORFLOW for each DU produce the flux-to-the-water-table profiles for the relevant discrete hole geometry (i.e., centrally located or corner ST or ET). Meanwhile, the composite probability contour map (Figure 4-37) provides the weighting factors needed to appropriately blend the flux-to-the-water-table data for each radionuclide. Such an approach accounts for all relevant subsidence scenarios, while giving the most weight to the most probable of the selected scenarios.

By way of example, consider the subsidence cases displayed in Figure 4-38 for a hypothetical DU, together with the composite probability contour map shown in Figure 4-37. Assume that the means of the MC probability values for the four subsided regions in Figure 4-38 correspond to the mean probability values listed in Table 4-16.

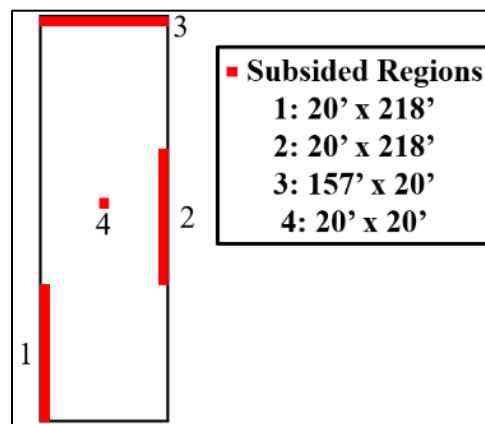


Figure 4-38. Hypothetical Subsidence Regions for Engineered Trench Based on Historical E-Area Low-Level Waste Facility Non-Crushable Package Data and Figure 4-37 (Danielson, 2019b; Figure 5-1)

Table 4-16. Average Probabilities and Flux Weighting Factors for Subsided Regions Shown in Figure 4-38 (Danielson, 2019b; Table 5-1)

Subsided Region from Figure 4-38	Average Probability	Flux Weighting Factor
1	0.027	0.290323
2	0.022	0.236559
3	0.020	0.215054
4	0.024	0.258065

The flux weighting factors in the table are computed by:

$$W_i = \frac{P_i}{\sum_{i=1}^N P_i} \quad \text{Eq. (4-35)}$$

where:

W_i Weighting factor for subsided region i (unitless)

P_i Mean probability of subsided region i [obtained from Figure 4-37] (unitless)

The denominator is the summation taken across the mean probabilities of the N subsided regions. Using this method, the radionuclide flux to the water table resulting at each time step from each subsided region will be blended to obtain a blended flux-to-the-water-table profile by:

$$F(t) = \sum_{i=1}^N W_i f_i(t) \quad \text{Eq. (4-36)}$$

where:

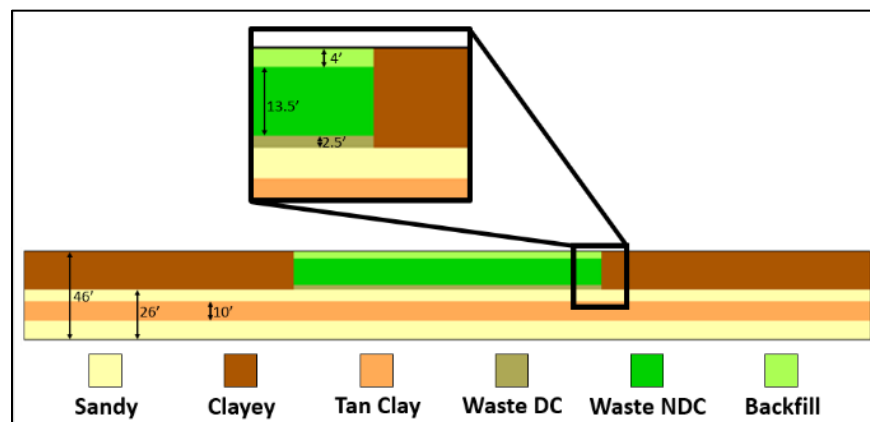
W_i Weighting factor for the subsided region i (unitless)

$f_i(t)$ Flux to the water table at time t resulting from a simulation that considers the subsided region i (gmol yr^{-1})

The summation is taken across all N subsided regions.

4.1.3.8. Automated Implementation of Three-Dimensional Models

An updated automation scheme has been developed and deployed to more rapidly implement the various models discussed in the previous sections, while also reducing the likelihood of errors in creating PORFLOW flow and transport input files. An example case based on the hydrostratigraphic grouping that includes ET05 has been implemented using the updated automated scheme. As noted in Figure 4-9, the ET05 waste zone lies within the clayey UVZ, while the TCCZ is absent from the VZ in this sector of E-Area. Figure 4-39 highlights the material zones for a YZ-plane located at the center of the 3-D model. Importantly, the model represents clayey UVZ material beneath the waste zone generically as tan clay. Because material properties for tan clay are assumed to be represented by those for the clayey UVZ, the implementation of a separate generic 10-foot clay layer below the waste zone is inconsequential as detailed in Section 4.1.3.2.



Note: Waste zone lies within clayey UVZ.

Figure 4-39. Material Zones for Hydrostratigraphic Grouping Corresponding to ET05 (Danielson, 2019c; Figure 22)

Figure 4-40 displays the XY-plane for the UVZ (i.e., the clayey top layer in the vertical cross-section shown in Figure 4-39). Overlapping material zones are avoided in PORFLOW because if the user is not careful in material type definitions for each material zone, and the *order* in which

the properties are specified does not coincide with the ordering of the material type definitions for each zone, PORFLOW will overwrite one region with the properties of another. For example, the clayey UVZ spans the X and Y coordinates of the mesh from Z=26 to Z=46 feet with a volume corresponding to the 20-foot thickness of the trench unit in the center of the mesh. Rather than initially defining all nodes within the UVZ as clayey and then overwriting with the trench material zones, a better practice is to form the UVZ from the union of four separate clayey regions (i.e., UVZ Regions 1, 2, 3, and 4 in Figure 4-40) without ever specifying the material zones corresponding to the trench region (i.e., cross-hatched region in Figure 4-40). PORFLOW material zones (e.g., CLAYEY1, CLAYEY2, CLAYEY3, and CLAYEY4) are explicitly defined by specifying the grid coordinates that bound a particular material region (e.g., UVZ Regions 1, 2, 3, and 4).

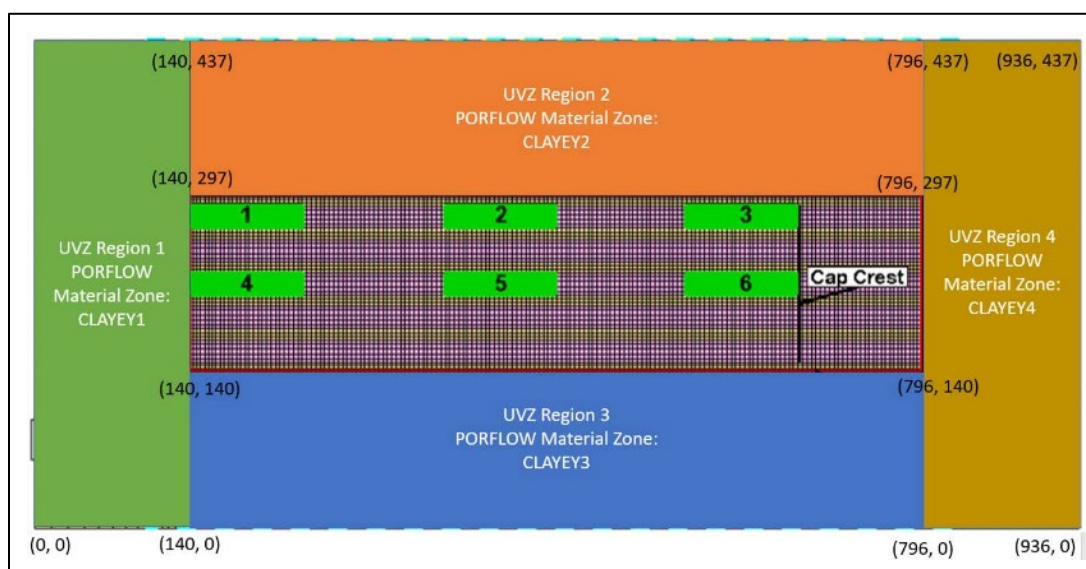


Figure 4-40. XY Plan View of Upper Vadose Zone Implementation in PORFLOW Three-Dimensional Model

Using this union approach, the mesh can be easily transitioned from ST to ET, as necessary. The properties for the different trench zones (Waste NDC, Waste DC, Backfill) are extracted by the automation scheme from the files ‘MaterialZones.xlsx’ (specifies the material type for the zone), ‘MaterialPalette.xlsx’ (specifies the hydraulic properties for the material type), and ‘Chemistry.xlsx’ (specifies the chemical properties of the zone for each radionuclide). Every single region of the mesh that has a different material type is specified in this way and then the union is taken to avoid overlapping different material zones. This union approach is unnecessary for material zones such as the Tan Clay and Sandy (LVZ) because they consist of a homogeneous material type (TAN_CLAY, SANDY) across all nodes in the mesh.

Timing for trench units is specified in the Microsoft Excel⁴ file “Actual-Projected_STET-OperTimeline_Updated_16-Dec.xlsx” and is based on a modification of the “Case1” timeline originally defined by Hamm et al. (2018). In general, time is discretized into 98 time-periods with

⁴ Microsoft, Excel, and Word are trademarks of the Microsoft group of companies.

each period having a unique flow field that is representative of the materials present and the state of cap degradation (i.e., as reflected in the water infiltration rate). All DUs that are “future units” (i.e., no waste packages placed at the start of the PA) have the same timeline. Temporal discretization may be refined if it is necessary for capturing a given radionuclide peak. If a trench unit has a different timeline than other trench units in its grouping, this difference is accounted for only during a separate transport run where steady-state flow fields are used for solving the transport equations for the appropriate time-periods.

Like the material properties, infiltration zones across the top boundary of the model are explicitly specified in PORFLOW by capturing the grid coordinates that bound each region. Therefore, if one wishes to explore alternative subsidence cases, the specified grid coordinates can be changed. The infiltration rates for each infiltration zone in the intact and subsidence cases are specified in the file ‘BoundaryConditions.xlsx,’ where each infiltration rate is sourced from Table 4-8 through Table 4-11. The operational stormwater runoff cover and interim cover are assumed to be maintained in their intact condition, while the final cover is subject to long-term degradation and catastrophic subsidence due to the failure of underlying non-crushable containers. Because the operational and interim covers do not degrade through time, the change in infiltration rate during these two periods appears as a step change as illustrated in Figure 4-41. To account for the degradation profile of the final closure cap, the PORFLOW automation scheme interpolates the infiltration rate at the midpoint of each time period.

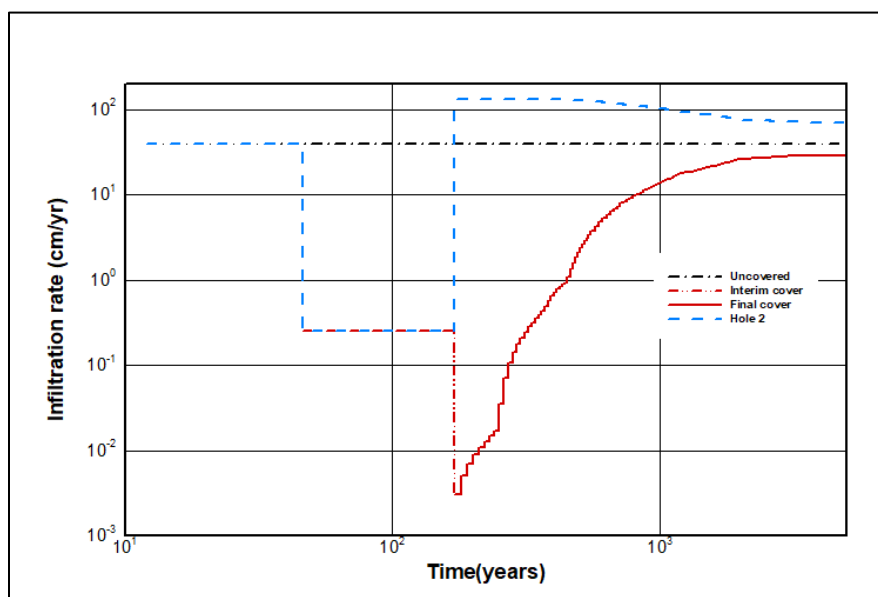


Figure 4-41. Slit and Engineered Trench Infiltration Rates through Top of PORFLOW Modeling Domain (Wohlwend and Aleman, 2020; Figure 3-4)

Infiltration zones for a centrally located trench are listed in Table 4-17 for illustrative purposes only (the infiltration zones for a corner or edge trench will differ and are not shown). A series of PORFLOW LOCAtE and BOUNDary FLUX commands are executed for each infiltration zone in the order listed in Table 4-17. The Domain infiltration zone contains all top boundary nodes that remain uncovered throughout the simulation period (i.e., background areas adjacent to the closure

cap). For PORFLOW VZ simulations, the intact Case01 includes only the top three infiltration zones (Domain, Final cover, and Interim cover), while the subsidence Case11b includes the additional subsidence infiltration for the relevant hole (e.g., Hole 2).

Table 4-17. Infiltration Zones for PORFLOW Vadose Zone Flow Simulations for Centrally Located Trench (Wohlwend and Aleman, 2020; Table 3-1)

Infiltration Zone	Coordinates (lower-left, feet)		Coordinates (upper-right, feet)		Lengths (feet)					
	x ₁	y ₁	x ₂	y ₂	dx	dy				
Domain	0.0	0.0	936.0	437.0	936	437				
Final cover	100.0		836.0		736					
Interim cover	130.0		806.0		676					
Hole 1	140.0	268.5	240.0	288.5	100	20				
Hole 2	368.0		468.0							
Hole 3	584.0		684.0							
Hole 4	140.0	238.5	240.0	258.5			100	20		
Hole 5	368.0		468.0							
Hole 6	584.0		684.0							
Hole 7	140.0	208.5	240.0	228.5					100	20
Hole 8	368.0		468.0							
Hole 9	584.0		684.0							

Notes:

$$dx = (x_2 - x_1); dy = (y_2 - y_1)$$

Notably, all geometries and material zones for the ST and ET models will be similar to the example shown in Figure 4-39, with only the depth to the water table and the tan clay thickness updated. As summarized in Figure 4-42, the ELLWF PA will require 17 unique VZ models in total from seven unique hydrostratigraphic groupings to cover all existing and future STs and ETs. For each trench, Bagwell and Bennett (2017) reported five values for depth to the various hydrostratigraphic surfaces, representing the four corners as well as the centroid. Average depth to the water table for a trench is taken as the arithmetic mean of these five values. The average clay thickness is calculated as the sum of the tan clay thickness and the UVZ clayey material thickness that extends beyond the bottom of the DU (i.e., beyond 20 feet bgs). The minimum depth to the water table and the minimum clay thickness are selected as representative of each hydrostratigraphic grouping to maintain a reasonable degree of conservatism. The depths and thicknesses are input to PORFLOW models as rounded whole integer values.

The PORFLOW VZ analysis involves a two-step simulation workflow that proceeds as follows:

- Steady-state VZ flow fields are obtained in a sequence of time periods each having a unique set of material properties that represent changes following dynamic compaction. The flow fields include changes in infiltration due to subsidence at the end of IC and placement of operational, interim, and final covers (with subsequent degradation).
- VZ contaminant transport models are supplied steady-state flow fields as input to solve the time-dependent transport equations and obtain the total flux from the waste zone and the total flux to the water table for each species.

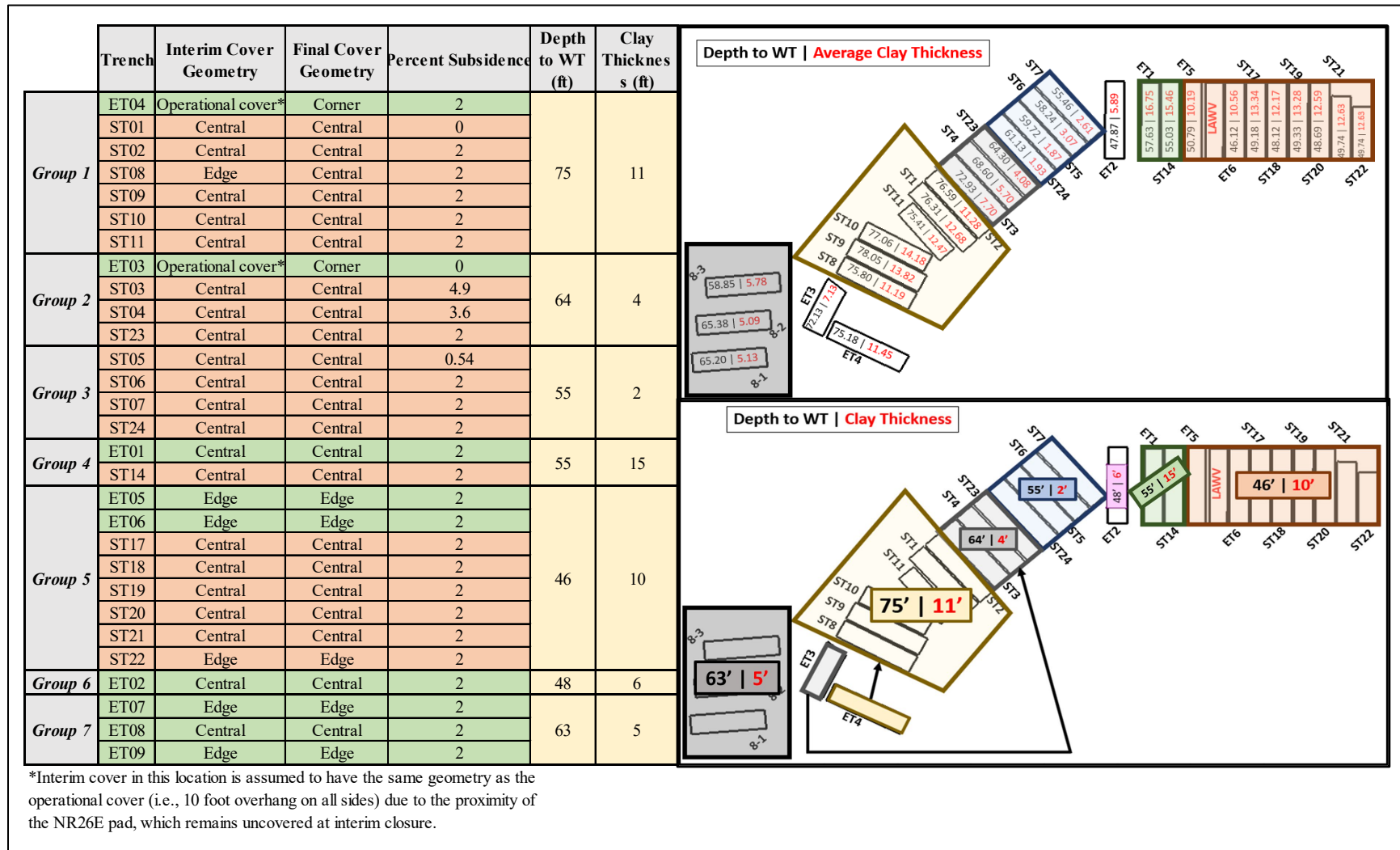


Figure 4-42. Summary of Slit and Engineered Trench Hydrostratigraphic Groupings and Number of Unique PORFLOW Vadose Zone Models

To demonstrate the implementation of the VZ conceptual models for STs and ETs in PORFLOW, the next two sections present 3-D VZ models developed by Wohlwend and Aleman (2020) for a centrally located ET and ST, respectively, using the depth to water table and hydrostratigraphic surfaces for ST06.⁵ ST06 is a centrally located unit in Group 3 of the seven hydrostratigraphic groups shown in Figure 4-42 with a minimum depth to water table of 55 feet and a minimum clay thickness of 2 feet.

4.1.3.9. Example PORFLOW Vadose Zone Model Implementation for Centrally Located Engineered Trench

Transient infiltration rates through the top boundary nodes (Table 4-17) of the PORFLOW VZ flow model are separated by Wohlwend and Aleman (2020) into a series of 98 steady-state flow simulations that span the simulation period from zero to 5,000 years. Figure 4-41 displays the transient infiltration rates used for the following ET and ST implementations.

The extent of the PORFLOW ET mesh is 201 vertices in the x-direction, 76 vertices in the y-direction, and 47 vertices in the z-direction. The length of the mesh in the x, y, and z directions is 936 feet, 437 feet, and 55 feet, respectively. The ET resides within a 656-foot by 157-foot region in the interior of the mesh. Figure 4-43 displays a chair cutout of the 3-D mesh with material zones.

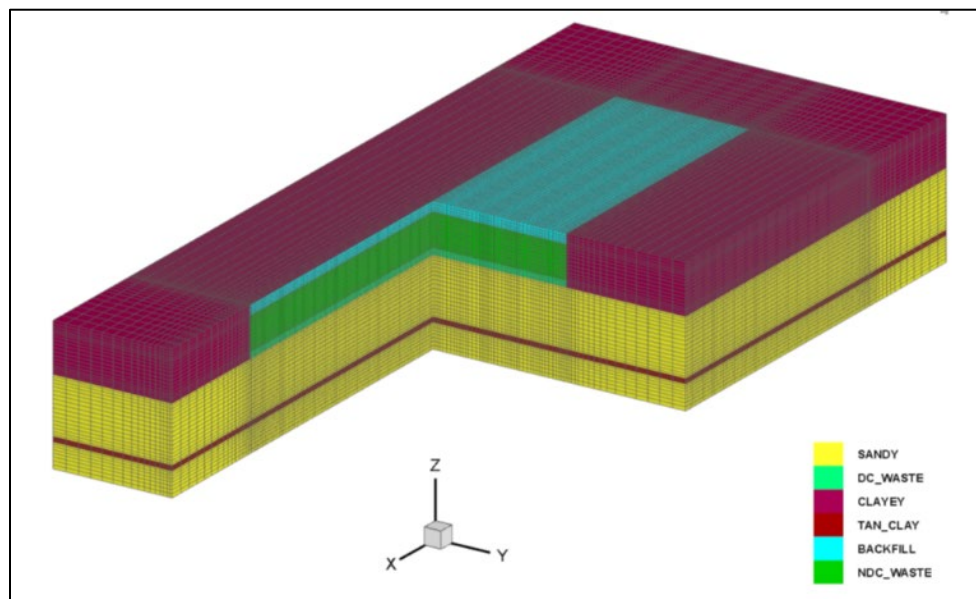


Figure 4-43. Chair Cutout of PORFLOW Engineered Trench Three-Dimensional Mesh with Material Zones (Wohlwend and Aleman, 2020; Figure 3-5)

An x-slice of the PORFLOW ET 3-D VZ model through the center of the trench is shown in Figure 4-44.

⁵ At the time of the PORFLOW benchmarking simulations by Wohlwend and Aleman (2020), the thickness of the ST hybrid waste zone after DC had not yet been finalized. Wohlwend and Aleman (2020) used a thickness of 8.87 feet for the ST hybrid waste zone after DC per PA2008. As noted, the thickness was subsequently revised to 11.1 feet for the final PORFLOW ST and ET VZ model production runs (Nichols and Butcher, 2020).

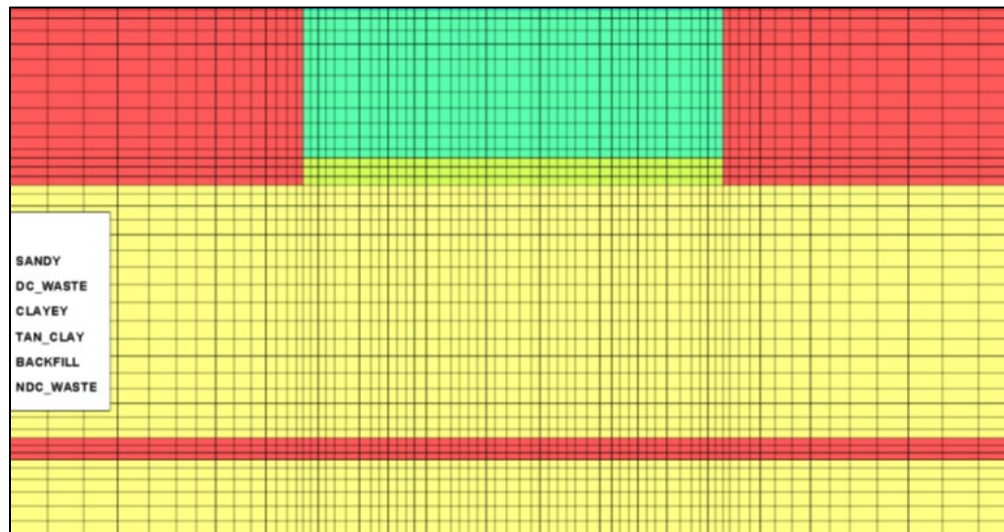


Figure 4-44. YZ Cross-Section of PORFLOW Engineered Trench Three-Dimensional Mesh with Material Zones (Wohlwend and Aleman, 2020; Figure 3-6)

Table 4-18 lists the coordinates and lengths of the material zones within the footprint of the ET. The SANDY soil layer is broken into two layers: SANDY2 is the region above the TAN_CLAY and SANDY1 is the region below the TAN_CLAY.

Table 4-18. Material Zones within Engineered Trench Footprint (Wohlwend and Aleman, 2020; Table 3-2)

Material Zone	Coordinates (lower-left, feet)			Coordinates (upper-right, feet)			Lengths (feet)		
	x ₁	y ₁	z ₁	x ₂	y ₂	z ₂	dx	dy	dz
BACKFILL	140.0	140.0	51.0	796.0	297.0	55.0	656	157	4
NDC_WASTE			37.5			51.0			13.5
DC_WASTE			35.0			37.5			2.5
SANDY2			12.0			35.0			23
TAN_CLAY			10.0			12.0			2
SANDY1			0.0			10.0			10

Notes:

$$dx = (x_2 - x_1); dy = (y_2 - y_1); dz = (z_2 - z_1)$$

Hydraulic and transport properties of the porous media in an ET are specified before and after dynamic compaction for each material type. Table 4-19 provides nominal parameter values for saturated effective diffusivity (D_e), porosity, dry bulk density (rhob) and particle density (rhop) for each material type.

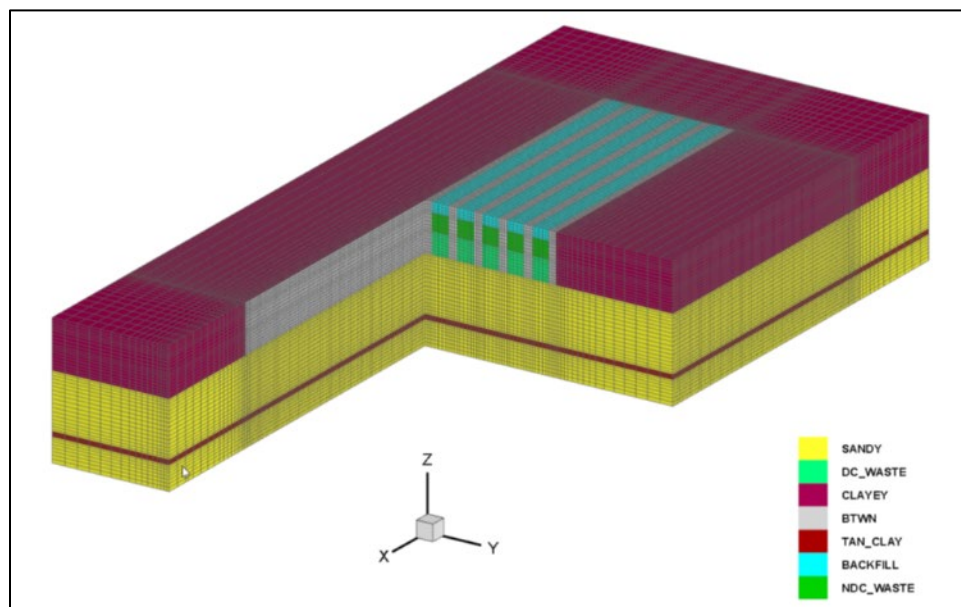
PORFLOW results for the centrally located ET in this example are presented in Section 4.4.10 as part of the benchmarking discussion for the GoldSim[®] trench system model.

Table 4-19. Hydraulic and Transport Properties of Porous Media in an Engineered Trench (Wohlwend and Aleman, 2020; Table 3-3)

Material ID	Material Name	D_e (cm ² yr ⁻¹)	Porosity	Rhob (g cm ⁻³)	Rhop (g cm ⁻³)	Time Period	
						Year 0 to Year 171	Year 171 to Year 5,000
UpperVadoseZone	UVZ	167.25528	0.385	1.6544	2.69	CLAYEY TAN_CLAY	CLAYEY TAN_CLAY
LowerVadoseZone	LVZ		0.380	1.6554	2.67	SANDY2 SANDY1	SANDY2 SANDY1
OscBefore (OSC1)	OSC1		0.456	1.4417	2.65	BACKFILL	N/A
OscAfter (OSC2)	OSC2	126.2304	0.275	1.9222		N/A	BACKFILL NDC_WASTE
STETboxesBC	ET boxed waste before dynamic compaction	167.25528	0.894	0.2821		DC_WASTE NDC_WASTE	N/A
STETboxesAC	ET boxed waste after dynamic compaction	126.2304	0.275	1.9222		N/A	DC_WASTE

4.1.3.10. Example PORFLOW Vadose Zone Model Implementation for a Centrally Located Slit Trench

The extent of the PORFLOW ST mesh is 201 vertices in the x direction, 76 vertices in the y direction, and 47 vertices in the z direction. The length of the mesh in the x, y, and z directions is 936 feet, 437 feet, and 55 feet, respectively. The ST resides within a 656-foot by 157-foot region in the interior of the mesh. Figure 4-45 displays a chair cutout of the 3-D mesh with material zones, while Figure 4-46 presents an x-slice of the PORFLOW ST 3-D VZ model through the center of the trench.

**Figure 4-45. Chair Cutout of PORFLOW Slit Trench Three-Dimensional Mesh with Material Zones (Wohlwend and Aleman, 2020; Figure 3-7)**

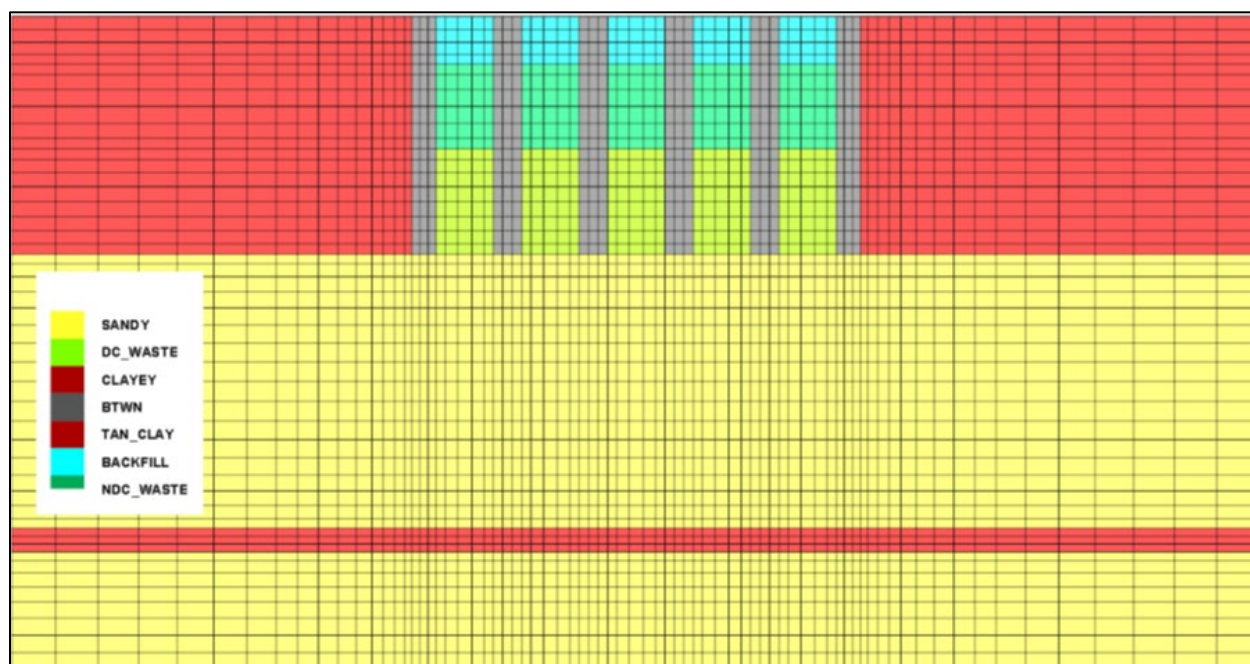


Figure 4-46. YZ Cross-Section of PORFLOW Slit Trench Three-Dimensional Mesh with Material Zones (Wohlwend and Aleman, 2020; Figure 3-8)

Table 4-20 lists the coordinates and lengths of the material zones within the footprint of ST and non-waste segments. The ST segments are numbered 1 through 5 with the material zones listed in the ascending y-direction. BTWN_STx_STy is the 10-foot-wide non-waste segment between STx and STy adjacent waste segments. ST_EDGE1 is the 8.5-foot-wide non-waste segment below ST1. ST_EDGE2 is the 8.5-foot-wide non-waste segment above ST5. The SANDY soil layer is broken into two layers: SANDY2 is the region above the TAN_CLAY and SANDY1 is the region below the TAN_CLAY.

Hydraulic and transport properties of the porous media in a ST are specified before and after dynamic compaction for each material type. Table 4-21 provides nominal parameter values for saturated effective diffusivity (D_e), porosity, dry bulk density (rhob) and particle density (rhop) for each material type.

PORFLOW results for the centrally located ST in this example are presented in Section 4.4.10 as part of the benchmarking discussion for the GoldSim[®] ST and ET VZ models.

Table 4-20. Material Zones in Footprint of Slit Trench and Non-Waste Segments (Wohlwend and Aleman, 2020; Table 3-4)

Segment	Material Zone	Coordinates (lower-left, feet)			Coordinates (upper-right, feet)			Lengths (feet)		
		x ₁	y ₁	z ₁	x ₂	y ₂	z ₂	dx	dy	dz
ST1	BACKFILL	140.00	148.50	51.00	796.00	168.50	55.00	656.00	20.00	4.00
	NDC_WASTE			43.87			51.00			7.13
	DC_WASTE			35.00			43.87			8.87
	SANDY2			12.00			35.00			23.00
	TAN_CLAY			10.00			12.00			2.00
	SANDY1			0.00			10.00			10.00
ST2	BACKFILL	140.00	178.50	51.00	796.00	198.50	55.00	656.00	20.00	4.00
	NDC_WASTE			43.87			51.00			7.13
	DC_WASTE			35.00			43.87			8.87
	SANDY2			12.00			35.00			23.00
	TAN_CLAY			10.00			12.00			2.00
	SANDY1			0.00			10.00			10.00
ST3	BACKFILL	140.00	208.50	51.00	796.00	228.50	55.00	656.00	20.00	4.00
	NDC_WASTE			43.87			51.00			7.13
	DC_WASTE			35.00			43.87			8.87
	SANDY2			12.00			35.00			23.00
	TAN_CLAY			10.00			12.00			2.00
	SANDY1			0.00			10.00			10.00
ST4	BACKFILL	140.00	238.50	51.00	796.00	258.50	55.00	656.00	20.00	4.00
	NDC_WASTE			43.87			51.00			7.13
	DC_WASTE			35.00			43.87			8.87
	SANDY2			12.00			35.00			23.00
	TAN_CLAY			10.00			12.00			2.00
	SANDY1			0.00			10.00			10.00
ST5	BACKFILL	140.00	268.50	51.00	796.00	288.50	55.00	656.00	20.00	4.00
	NDC_WASTE			43.87			51.00			7.13
	DC_WASTE			35.00			43.87			8.87
	SANDY2			12.00			35.00			23.00
	TAN_CLAY			10.00			12.00			2.00
	SANDY1			0.00			10.00			10.00
ST_EDGE1	BACKFILL	140.00	140.00	51.00	796.00	148.50	55.00	656.00	8.50	4.00
	NDC_WASTE			43.87			51.00			7.13
	DC_WASTE			35.00			43.87			8.87
	SANDY2			12.00			35.00			23.00
	TAN_CLAY			10.00			12.00			2.00
	SANDY1			0.00			10.00			10.00
ST_EDGE2	CLAYEY	140.00	288.50	51.00	796.00	297.00	55.00	656.00	8.50	4.00
	CLAYEY			43.87			51.00			7.13
	CLAYEY			35.00			43.87			8.87
	SANDY2			12.00			35.00			23.00
	TAN_CLAY			10.00			12.00			2.00
	SANDY1			0.00			10.00			10.00

Notes:

$$dx = (x_2 - x_1); dy = (y_2 - y_1); dz = (z_2 - z_1)$$

Table 4-20 (cont'd). Material Zones in Footprint of Slit Trench and Non-Waste Segments (Wohlwend and Aleman, 2020; Table 3-4)

Segment	Material Zone	Coordinates (lower-left, feet)			Coordinates (upper-right, feet)			Lengths (feet)		
		x ₁	y ₁	z ₁	x ₂	y ₂	z ₂	dx	dy	dz
BTWN_ST1_ST2	CLAYEY	140.00	168.50	51.00	796.00	178.50	55.00	656.00	10.00	4.00
	CLAYEY			43.87			51.00			7.13
	CLAYEY			35.00			43.87			8.87
	SANDY2			12.00			35.00			23.00
	TAN_CLAY			10.00			12.00			2.00
	SANDY1			0.00			10.00			10.00
BTWN_ST2_ST3	CLAYEY	140.00	198.50	51.00	796.00	208.50	55.00	656.00	10.00	4.00
	CLAYEY			43.87			51.00			7.13
	CLAYEY			35.00			43.87			8.87
	SANDY2			12.00			35.00			23.00
	TAN_CLAY			10.00			12.00			2.00
	SANDY1			0.00			10.00			10.00
BTWN_ST3_ST4	CLAYEY	140.00	228.50	51.00	796.00	238.50	55.00	656.00	10.00	4.00
	CLAYEY			43.87			51.00			7.13
	CLAYEY			35.00			43.87			8.87
	SANDY2			12.00			35.00			23.00
	TAN_CLAY			10.00			12.00			2.00
	SANDY1			0.00			10.00			10.00
BTWN_ST4_ST5	CLAYEY	140.00	258.50	51.00	796.00	268.50	55.00	656.00	10.00	4.00
	CLAYEY			43.87			51.00			7.13
	CLAYEY			35.00			43.87			8.87
	SANDY2			12.00			35.00			23.00
	TAN_CLAY			10.00			12.00			2.00
	SANDY1			0.00			10.00			10.00

Notes:

$$dx = (x_2 - x_1); dy = (y_2 - y_1); dz = (z_2 - z_1)$$

Table 4-21. Hydraulic and Transport Properties of Porous Media in a Slit Trench (Wohlwend and Aleman, 2020; Table 3-5)

Material ID	Material Name	D_e (cm ² yr ⁻¹)	Porosity	R _{hob}	R _{hop}	Time Period	
				(g cm ⁻³)		Years 0 to 171	Years 171 to 5,000
UpperVadoseZone	UVZ	167.25528	0.385	1.6544	2.69	CLAYEY TAN_CLAY	CLAYEY TAN_CLAY
LowerVadoseZone	LVZ		0.380	1.6554	2.67	SANDY2 SANDY1	SANDY2 SANDY1
OscBefore	OSC1		0.456	1.4417	2.65	BACKFILL	N/A
OscAfter	OSC2	126.2304	0.275	1.9222		N/A	BACKFILL NDC_WASTE
SThybridBC	ST hybrid waste before dynamic compaction	167.25528	0.600	1.0590		DC_WASTE NDC_WASTE	N/A
SThybridAC	ST hybrid waste after dynamic compaction	126.2304	0.275	1.9222		N/A	DC_WASTE

4.2. SIMPLE SPECIAL WASTE FORM MODELS FOR TRENCHES

Multiple SWF models developed by Danielson (2021) are used in this PA: effective K_d ; delayed release; solubility-controlled release; diffusion-controlled release; and complex SWF models. CIG trench segments within ST23 (Section 4.1.2.2) and tall used-equipment storage boxes disposed in ST08-ST10 are also treated in this PA as SWFs with unique SWF VZ models. This section introduces methods for implementing “simple” SWFs in the PORFLOW deterministic models for STs and ETs. As defined in this PA, simple SWF models include CIG trench segments; effective K_d ; delayed release; solubility-controlled release; and tall boxes. Three complex SWFs and their associated models are addressed separately in Section 4.3. These include the HWCTR, HXs, and 232-F concrete rubble.

SWFs are a category of trench waste that exceeds or consumes a large fraction of the allowable inventory for specific radionuclides without taking credit for the waste form or disposal container. Additional characterization and modeling, generally performed as part of an SA, are needed to produce acceptable trench disposal limits. SWF modeling incorporates chemistry, corrosion rates, hydraulics, radionuclide decay, and administrative controls, as needed, to produce acceptable disposal limits through hold up or controlled release of contaminants into the backfill soil within the waste zone. Radionuclide limits treated in this manner are given a unique designation in CWTS to distinguish them from the equivalent “generic” radionuclide limit (i.e., limits established assuming instantaneous release of radionuclides to the surrounding backfill soil); they contribute independently to the SOF calculation to ensure the distribution of radionuclides in a trench is always at or below a SOF of one. SWFs are typically obtained from limited waste campaigns (e.g., deactivation and decommissioning, disposition of legacy LLW items) or are generated from site processes. Most SWFs are disposed in ETs and STs (which now include formerly designated CIG Trenches 1 and 2 that are repurposed as STs for this PA due to the lack of CIG waste projections from site generators). CIG SWF segments are addressed in Section 4.2.1. SWFs in other DUs, specifically the ILV and NRCDA, are addressed in Section 4.6.3.6 (TPBAR Tritium and Argon Releases) and Section 4.7.8.5 (PORFLOW Modeling Approach), respectively. Table 4-22 provides a complete listing of ST and ET SWFs and associated historical characterization and modeling references.

In all SWF models, placement of SWF inventory is assumed to occur on the date when each trench unit is first opened to waste (Table 4-23 for all simple and complex SWFs; Table 4-24 for CIG trench segments), which is consistent with the modeling assumption for generic waste (i.e., instantaneous disposal of all inventory at the start of operations for each trench unit). Placement of future SWF inventory that is targeted for disposal in future trenches is assumed to be placed on September 30, 2021 (Table 4-6). Timing of closure activities is based on the current facility lifecycle assumptions (i.e., dates for operational stormwater cover, interim cover, and final closure cap) summarized in Table 4-6.

Table 4-22. Summary of Important References for Slit and Engineered Trench Special Waste Forms (Danielson, 2021; Appendix A)

Special Waste Form	CWTS ID	Waste Characterization References	SA and/or UDQE References
Reactor Heat Exchangers	C14X, H3X	Kaplan (2010)	Hamm et al. (2012)
ETF GT-73	I129I	Powell et al. (2002) Kaplan et al. (1999)	Collard (2001)
F-WTU CG-8	I129G	Kaplan and Serkiz (2000)	
F-WTU Dowex 21K	I129D	Powell et al. (2002) Kaplan et al. (1999)	
F-WTU Filtercake	I129J	Kaplan and Iversen (2001)	
H-WTU CG-8	I129H	Powell et al. (2002) Kaplan and Serkiz (2000)	
H-WTU Dowex 21K	I129E	Powell et al. (2002) Kaplan and Serkiz (2000)	
H-WTU Filtercake	I129F	Kaplan and Iversen (2001)	
Naval Reactors Pump	C14N	Kaplan (2010)	WSRC (2008)
Effluent Treatment Facility Carbon Column	H3C		Collard (2003) Cook et al. (1999)
Effluent Treatment Facilities Carbon Columns	I129C	Kaplan et al. (1999)	Collard (2003) Cook et al. (1999) Collard (2000)
M-Area Glass	U234G, U235G, U236G, U238G	Kaplan (2010)	Cook and Yu (2002)
Paducah Cask	U235P		Hiergesell (2004)
232-F Concrete	H3F		Flach et al. (2005)
HWCTR	Ag108MH, C14H, Co60H, Fe55H, Mo93H, Nb93MH, Nb94H, Ni59H, Ni63H, Tc99H		Hamm and Smith (2010)

Table 4-23. Date Special Waste Form Inventories Placed in PORFLOW Models for Existing Slit and Engineered Trench Special Waste Forms (Danielson, 2021; Table 1)

Trench	Open Date
ET01	2/13/2001
ST01	12/21/1995
ST02	9/20/2001
ST03	10/20/2003
ST04	2/26/2004
ST05	5/27/2004
ST07	6/26/2006
ST08	2/6/2007
ST09	3/17/2011
ST14	3/29/2011

Table 4-24. Date of First Waste Placement in Each Components-in-Grout Trench Segment (Danielson, 2020c)

CIG Trench Segment	Start Date	Relative Time ¹
CIG-1	8/29/2000	6
CIG-2	7/17/2001	7
CIG-3	7/17/2001	7
CIG-4	8/7/2002	8
CIG-5	9/10/2002	8
CIG-6	8/21/2003	9
CIG-7	8/21/2003	9
CIG-8	8/18/2004	10
CIG-9	6/4/2007	13

Notes:

¹ Relative time is rounded to the next integer year.

4.2.1. Components-in-Grout Trench Segment Conceptual Model

The CIG DUs are below-grade earthen trenches that contain grout-encapsulated waste components. Historically, there were two CIG-designated trench DUs in the ELLWF (i.e., CIG01 and CIG02). Over time, the CIG disposal method has become less favorable due to the high cost of disposition and the nature of contemporary waste streams (i.e., grout encapsulation is generally unnecessary). Therefore, existing trench CIG01 and future trench CIG02 have been repurposed as slit trenches ST23 and ST24, respectively (Hamm, 2019). The location of ST23 and ST24 relative to other trenches in the ELLWF is highlighted in magenta in Figure 4-47. To date, only nine CIG trench segments exist; they are placed within two of the nominally 20-foot-wide by 656-foot-long trench segments within the ST23 footprint between 08/29/2000 and 06/26/2007. Since that time, the remaining volume of the ST23 footprint has been reallocated for standard ST waste. Future CIG disposals will therefore require a SA before placement.

**Figure 4-47. Location of ST23 and ST24 (formerly CIG01 and CIG02, respectively)**

The components that have been disposed within the existing nine CIG trench segments include large radioactively contaminated components such as tankers, radioactive sources from a concrete culvert, flatbed trailers, SeaLand containers, and various high-integrity containers. In addition, other waste forms such as B-25 boxes and B-12 boxes are placed around and above larger equipment to maximize use of the disposal volume and to eliminate void space. CIG trench segments have been excavated as needed, and the unit numbers are designated sequentially in order of placement [e.g., CIG Trench Segment 1 (CIG-1) was created first and CIG Trench Segment 9 (CIG-9) last]. CIG trench segments are nominally 20-foot deep, although in practice, are excavated only to the necessary depth and length for the component(s) to reduce the cost associated with grouting. Excavated soil from the unit is set aside for later use as backfill material. Before waste placement, the base of the CIG trench segment is filled with a high-flow grout to a minimum 12-inch thickness (Figure 4-48). After the grout base solidifies, components are placed and additional grout is poured around, between, and over the components to encapsulate them (Figure 4-48). Waste is placed such that a 12-inch-thick grout encapsulation layer (i.e., the same as the base) separates the grouted components from the soil along the sides of the trench segments. Additional components or other waste forms can be placed on top of previously grouted components up to a maximum height of 15 feet such that a 12-inch-thick grout encapsulation layer can be placed over top to separate waste from the backfill material (Figure 4-48).



Figure 4-48. CIG-6 Placement Sequence (Nichols and Butcher, 2020; Figure 4-13)

The lifecycle of the CIG trench segments is carried out in accordance with the rest of the ELLWF, starting with the operational period when waste is placed. Once a CIG component is encapsulated, a minimum 4 feet of backfill material is placed in the remaining volume of trench space above the composite grouted waste form (Figure 4-48). The subsidence potential of CIG trench segments is highly variable. Two segments (CIG-8 and CIG-9) have had a reinforced-concrete mat placed over top of the composite grouted waste form to decrease the subsidence potential over time and, therefore, have less backfill material. Finally, an initial plastic cover is required to be installed over each newly completed CIG trench segment within three months of the component(s) being disposed to reduce infiltration. As previously mentioned, CIG Trench, CIG01, is being repurposed as ST23 with the remaining space to be filled with ST waste. Upon operational closure of ST23 in its entirety, soil will be built up and grading will be performed over the trench to promote positive drainage; an operational stormwater runoff cover will be placed and maintained over the trench.

The first modeling step involves deterministic simulations of radionuclide transport from the DU of interest through the VZ such that a time-dependent aquifer source term can be obtained for each radionuclide from the flux-to-the-water-table profile. The following subsections detail the development of a conceptual model by Danielson (2020c) for the original nine CIG SWF segments by employing the nominal CIG trench segment geometry (Section 4.2.1.1), operational timeline/closure sequence and boundary conditions (Section 4.2.1.2), and properties of the CIG disposal system materials (Section 4.2.1.3) in a PORFLOW-based flow and transport model. The radionuclide flux to the water table from the nine existing CIG trench segments will be inserted into the appropriate aquifer source cells beneath ST23 and combined with flux from generic ST waste sections in the trench for a representative flux to the water table for each radionuclide. In Section 4.2.1.4, preliminary VZ flow and transport results for the existing CIG trench segments are presented based on the conceptual model's implementation in PORFLOW (ACRi, 2018).

4.2.1.1. Model Geometry

To reduce the overall number of conceptual models, a generalized conceptual model geometry is developed based on a 2-D cross-section of a CIG trench segment. The foundation for this model geometry is based on the nominal dimensions of a CIG trench segment (Figure 4-49). The CIG trench segments are nominally 20-foot wide and 20-foot deep with a 12-inch-thick grout encapsulation layer on all sides. CIG trench segments located alongside adjacent ST segments are separated by a minimum of 10 feet of UVZ clayey material. The impact of a neighboring trench unit on the flow of water around a CIG trench segment is considered negligible; therefore, only one segment is represented within the simulation geometry.

The cross-sectional material layout for the CIG trench segment model is shown in Figure 4-50. The hydrostratigraphic surfaces present around and beneath the CIG trench segments are taken directly from the ST and ET conceptual model report by Danielson (2019c), which are based on the hydrostratigraphic surfaces data package (Bagwell et al., 2017; SRNL, 2017). The grout thickness surrounding the waste zone is 1 foot on all sides, and the waste zone is 18-foot wide by 14-foot tall (excluding the grout encapsulating layer). The thickness of the CLSM and reinforced mat is 16 inches and 24 inches, respectively, and both span the width of the 20-foot trench segment. Notably, these two materials are present only if a reinforced-concrete mat is placed over the

composite grout waste form (i.e., CIG-8 and CIG-9). Otherwise, these material regions consist of a soil backfill (chemical and physical properties of the material regions are discussed in Section 4.2.1.3). Figure 4-50 shows the extents of the operational, interim, and final covers; however, they are not modeled explicitly. Only boundary condition specifications (Section 4.2.1.2) are applied across these regions. The operational cover extends only 10 feet past the edge of the trench segment, whereas the interim and final covers extend across the entire model domain.

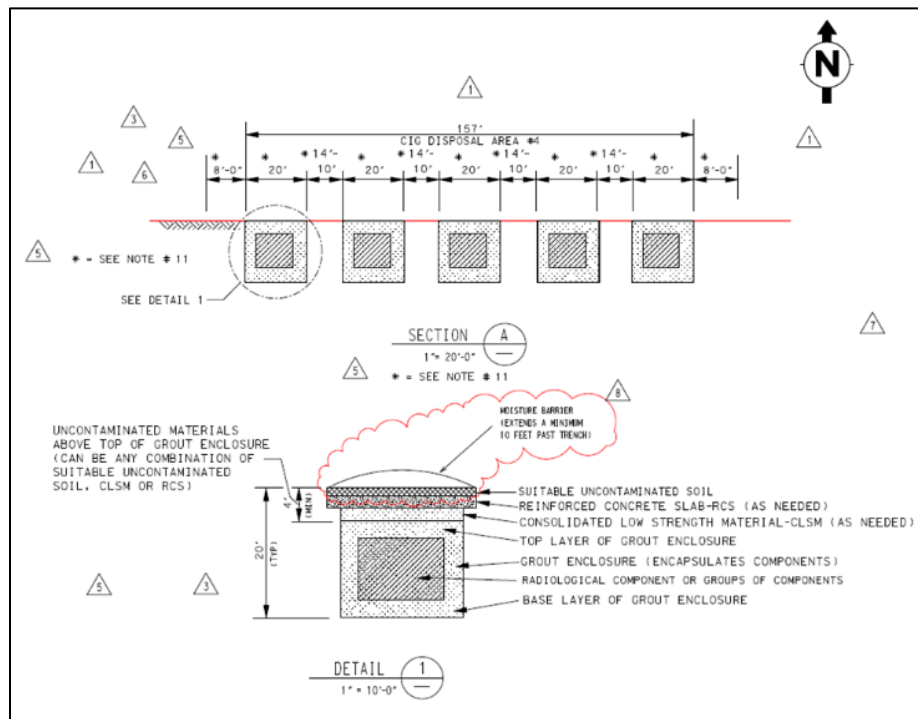


Figure 4-49. Nominal Cross-Sectional Layout and Design of Components-in-Grout Trench Segments within Slit Trench Footprint (Danielson, 2020c)

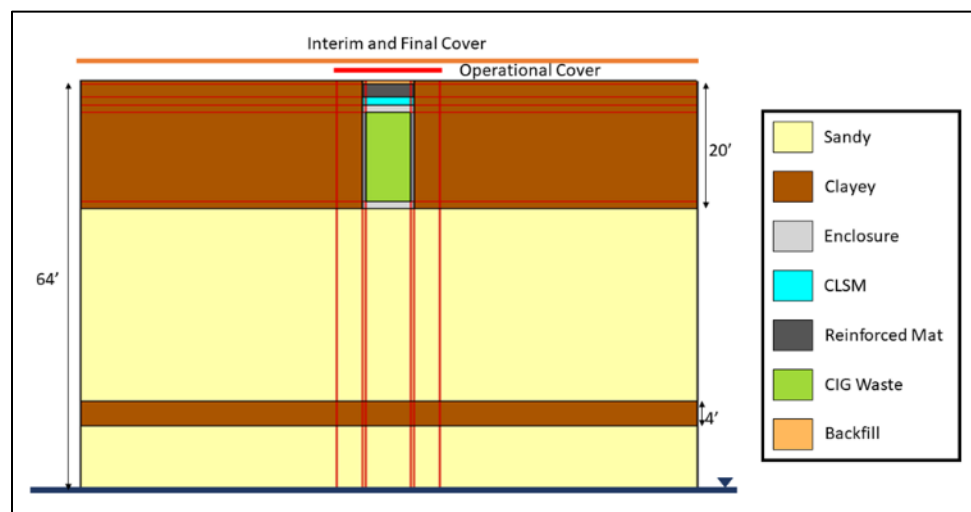


Figure 4-50. Material Layout of Cross-Sectional Model of Components-in-Grout Trench Segment (Danielson, 2020c)

4.2.1.2. Timeline and Boundary Conditions

The operations and closure timeline serves as the basis for waste placement and closure sequencing during radionuclide transport simulation and for specification of water infiltration boundary conditions. As a conservative assumption, all waste is assumed to be placed at the start date of operations for each CIG trench segment as listed in Table 4-24. The reference date is taken as the start of ELLWF operations (September 28, 1994), which is the start date for the LAWV.

Flow fields are computed for predetermined water infiltration rate boundary conditions out to 10,000 years. For each CIG trench segment, the 10,000-year period is discretized into 98 time periods such that steady-state flow fields are computed based on the infiltration transients for conditions representing the operational, operational closure, interim closure, and final closure time periods. Bounding water infiltration rates (Table 4-25) for the intact final closure cap are reported by Dyer (2019b) and are linearly interpolated across the midpoints of the 98 time intervals. The requirement for an operational stormwater runoff cover is documented in the current ELLWF closure plan (Phifer et al. 2009) and states that an operational stormwater runoff cover should be placed over the CIG segment no later than three months after placement of the last waste component. Given that this conclusion was reached approximately two years after the operational closure of CIG-1 through CIG-8, each of the eight segments is given the same date for the application of the operational stormwater runoff cover: relative Year 12 (i.e., April 1, 2006). CIG-9 began operation after this date; therefore, its operational cover is placed at relative Year 13. The interim and final covers are placed at relative Years 46 and 171, respectively.

Table 4-25. Time-Dependent Water Infiltration Rate through Intact Final Closure Cap [Dyer (2019b)]

Relative Year	Intact Infiltration Rate (in yr ⁻¹)
No Cover	15.78
Operational Cover	0.1
46 (Interim Cover)	0.1
171 (Final Cover)	0.0008
251	0.0070
361	0.16
371	0.18
411	0.30
451	0.38
551	1.39
731	3.23
1,171	6.82
1,971	10.24
2,794	11.10
3,371	11.18
5,771	11.30
10,171	11.35

In addition to the intact infiltration conditions, four CIG trench segments, CIG-4 to CIG-7, contain components or low-density waste that are not filled with grout and are estimated to have a maximum of 7 feet of subsidence potential (Nichols and Butcher, 2020). Reinforced-concrete mats

were not placed over CIG-4 to CIG-7 after final waste placement. CIG-8 and CIG-9 also have subsidence potential; however, a reinforced-concrete mat has been placed over these two segments.

In the conceptual model implementation, subsidence is assumed to occur only over the waste zone (i.e., excludes grout encapsulation along walls of the trench segment) where settling and degradation of the composite cementitious waste form occurs. For CIG-4 to CIG-7, a bounding subsidence base case assumes that subsidence occurs immediately at the end of IC. For CIG-8 and CIG-9, the best estimate subsidence case assumes subsidence occurs 200 years after the end of IC. As a sensitivity case, the best estimate subsidence scenario is explored for CIG-4 through CIG-7 as well, where a reinforced-concrete mat is introduced in the models even though no mat has been placed at the present time. The best estimate case is based on studies by Peregoy (2006a), Jones et al. (2004), and Phifer (2004b) who explored the subsidence potential of the waste in each segment. Subsidence infiltration rates are based on the formulation presented by Dyer (2019b) to account for background rainfall minus evapotranspiration and the upslope intact area expressed as:

$$I_S = I_B + \frac{L_U}{L_H}(I_B - I_I) \quad \text{Eq. (4-37)}$$

where:

I_I	Intact infiltration rate at a given time (in yr^{-1})
L_U	Length of the intact area upslope of the hole (ft)
L_H	Length of the subsided region [i.e., the length of the grouted component] (ft)
I_B	Closure-cap-specific subsidence scenario background infiltration rate [i.e., annual-average rainfall minus annual-average evapotranspiration], which is 16.5 in yr^{-1} for the ELLWF PA as determined by Dyer (2019b) [in yr^{-1}].

Table 4-26 provides the bounding and best estimate infiltration cases for CIG-4 through CIG-9.

The as-built layout of the CIG trench segments is shown in Figure 4-51. The dimensions of each CIG trench segment have been used to compute the length of the subsided region and the upslope intact distance between the crest of the final closure cap (located approximately 110 feet from the edge of the ST nearest CIG-1 and CIG-7) and the edge of the unit closest to the crest. The upslope intact length and subsided region lengths used for calculating subsided infiltration rates for CIG-4 through CIG-9 are given in Table 4-27.

Table 4-26. Infiltration Rates for Bounding and Best Estimate Subsidence Cases for CIG-4 to CIG-7 (Danielson, 2020c)

Relative Year	Intact Rate	Bounding Subsidence Case (in yr ⁻¹)					Best Estimate Subsidence Case (in yr ⁻¹)					
		CIG-4	CIG-5	CIG-6	CIG-7		CIG-4	CIG-5	CIG-6	CIG-7	CIG-8	CIG-9
No Cover	15.78	15.78	15.78	15.78	15.78		15.78	15.78	15.78	15.78	15.78	15.78
OSC	0.1	0.10	0.10	0.10	0.10		0.10	0.10	0.10	0.10	0.10	0.10
461	0.1	0.10	0.10	0.10	0.10		0.10	0.10	0.10	0.10	0.10	0.10
171	0.0008	33.43	55.57	62.86	16.82		0.0008	0.0008	0.0008	0.0008	0.0008	0.0008
251	0.0070	33.43	55.56	62.84	16.82		0.01	0.01	0.01	0.01	0.007	0.007
361	0.16	33.27	55.20	62.41	16.82		0.16	0.16	0.16	0.16	0.16	0.16
371	0.18	33.25	55.15	62.35	16.82		33.25	55.15	62.35	16.82	18.03	24.87
411	0.30	33.13	54.86	62.02	16.82		33.13	54.86	62.02	16.82	18.02	24.81
451	0.38	33.04	54.68	61.79	16.82		33.04	54.68	61.79	16.82	18.01	24.77
551	1.39	32.01	52.28	58.95	16.80		32.01	52.28	58.95	16.80	17.91	24.25
731	3.23	30.12	47.93	53.78	16.76		30.12	47.93	53.78	16.76	17.74	23.31
1,171	6.82	26.44	39.42	43.70	16.69		26.44	39.42	43.70	16.69	17.41	21.46
1,971	10.24	22.92	31.32	34.09	16.62		22.92	31.32	34.09	16.62	17.09	19.71
2,794	11.10	22.04	29.29	31.67	16.61		22.04	29.29	31.67	16.61	17.01	19.27
3,371	11.18	21.96	29.10	31.45	16.60		21.96	29.10	31.45	16.60	17.00	19.23
5,771	11.30	21.84	28.81	31.11	16.60		21.84	28.81	31.11	16.60	16.99	19.17
10,171	11.35	21.79	28.70	30.97	16.60		21.79	28.70	30.97	16.60	16.99	19.14

¹ Interim cover placed at relative Year 46 and final cover at relative Year 171.

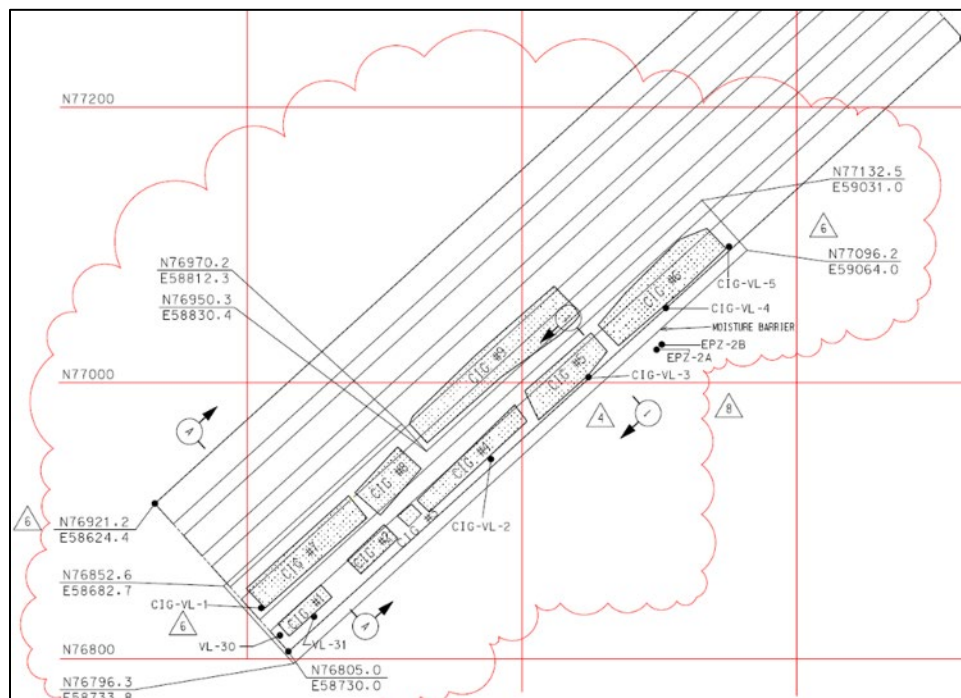
**Figure 4-51. Layout of As-Built CIG-1 through CIG-9 within ST23 Footprint (Danielson, 2020c)**

Table 4-27. Upslope Intact Length and Subsided Region Lengths to Calculate Subsidence Infiltration Rates (Danielson, 2020c)

CIG Trench Segment	Upslope Distances (feet)	Subsided Segment Lengths (feet)
CIG-4	33.1	32.25
CIG-5	144.46	61
CIG-6	216.34	77
CIG-7	1.67	85
CIG-8	3.35	35.8
CIG-9	66.36	129.4

4.2.1.3. Physical and Chemical Properties

Specific values for the physical and chemical properties of the composite cementitious waste form and the surrounding native soils of the UVZ and LVZ are discussed in the Hydraulic Properties Data Package (Nichols and Butcher, 2020) and the Geochemical Data Package (Kaplan, 2016b). As water passes through the CIG waste form, chemical constituents are leached from the cementitious materials, which leads to a gradual physical degradation and a decrease in the hydraulic integrity (i.e., increased porosity and hydraulic conductivity). Physical degradation of the cementitious materials is represented by step-changes at predetermined times corresponding to the operational, interim closure, and final closure time periods. Most notably, the CIG degrades from an intact CIG waste form (CIGint) to the degraded waste form (CIGdeg) at Year 40 when the hydraulic conductivity increases by nine orders of magnitude. At Year 371 (200 years after the end of IC), the CIG waste form is considered fully degraded. The material types and the values of the physical properties assigned to each material zone (Figure 4-50) are listed in Table 4-28 and Table 4-29. Note that dynamic compaction is not performed over CIG waste.

Table 4-28. Material Types Applied to Each Base Case Material Zone through Time (Danielson, 2020c)

Material Type	Time Interval	CIG-1 through CIG-7	CIG-8	CIG-9
Backfill	0 - 40	OSC Before	OSC Before	OSC Before
	40 - 171			
	171 - 371			
	371+			
Reinforced Mat	0 - 40	OSC Before	EareaConcreteMats	EareaConcreteMats
	40 - 171		OSC Before	OSC Before
	171 - 371			
	371+			
CLSM	0 - 40	OSC Before	CLSM	CLSM
	40 - 171		OscBefore	OscBefore
	171 - 371			
	371+			
Enclosure	0 - 40	CIGgrout1to8	CIGgrout1to8	CIGgrout9on
	40 - 171			
	171 - 371			
	371+	OscBefore	OscBefore	OscBefore
CIG Waste	0 - 40	CIGint	CIGint	CIGint
	40 - 171			
	171 - 371			
	371+			
Sandy	All	LowerVadoseZone	LowerVadoseZone	LowerVadoseZone
Clayey	All	UpperVadoseZone	UpperVadoseZone	UpperVadoseZone

Table 4-29. Physical Properties for Each Material Type (Danielson, 2020c)

Material Type	K_h (cm yr ⁻¹)	K_v (cm ² yr ⁻¹)	D_e (cm ² yr ⁻¹)	Porosity	Bulk Density (g cm ⁻³)
OSC Before	4.10E+03	4.10E+03	1.67E+02	0.456	1.44
CIGgrout1to8	1.42E+03	1.42E+03	6.00E+01	0.224	1.79
CIGgrout9on	2.84E-01	2.84E-01	2.52E+01	0.233	1.90
CLSM	6.94E+01	6.94E+01	1.26E+02	0.328	1.78
CIGint	3.16E-05	3.16E-05	1.67E+02	0.456	1.44
CIGdeg	3.79E+03	3.79E+03	1.67E+02	0.456	1.44
EareaConcreteMats	2.84E-01	2.84E-01	2.52E+01	0.233	1.90
UpperVadoseZone	1.96E+03	2.75E+02	1.67E+02	0.385	1.65
LowerVadoseZone	1.04E+04	2.87E+03	1.67E+02	0.380	1.66

In addition to degradation of physical properties, chemical degradation occurs as chemical constituents are leached from cementitious material zones, leading to a reduction in the partition coefficients (K_d values) for the radionuclide contaminants. The degradation of cementitious materials proceeds through four stages from young (Stage I) to old (Stage III) and is tracked through time using the number of pore volumes (PVs) of water that have passed through the material. Beyond Stage III, the enhanced chemical attenuation of the cementitious materials is assumed to dissipate, and K_d values revert to those for the surrounding soils. The four stages of cementitious aging are:

- Stage I (“Young”) – 0 to 50 PVs
- Stage II (“Middle”) – 50 to 500 PVs
- Stage III (“Old”) – 500 to 7,000 PVs
- Beyond (“Gone”) – greater than 7,000 PVs

The reduction in K_d at each stage occurs in a stepwise fashion, whereby a post-processing algorithm computes the number of PVs through each cementitious material zone for the CIG trench segment of interest during each of the 98 time-intervals. Because flow occurs in both the x and y directions during the 2-D simulations and steady-state flow fields are supplied for transport such that a fixed saturation profile exists across the entire mesh at time zero, all cementitious materials are considered to be chemically aged simultaneously rather than sequentially. The sequential approach will delay the chemical aging process and slow the release of radionuclide contaminants; therefore, the simultaneous approach is considered bounding. For each cementitious zone, the number of PVs per unit time is computed using the expression:

$$\Phi_i(t) = \frac{Q_i(t)}{V_i(t)} \quad \text{Eq. (4-38)}$$

where:

Φ_i Number of PV flushes per time (PV yr^{-1}) passing through the i^{th} material zone
 Q_i Volumetric flowrate (mL yr^{-1}) passing through the i^{th} material zone volume
 V_i Total PV (mL) of the i^{th} material zone (void space available for water)

The transition time between stages for each cementitious material zone can be computed over the course of the CIG timeline by dividing the number of PVs to each transition by Φ_i .

As chemical constituents are leached from the cementitious materials above the LVZ, the K_d within the neighboring soils is multiplied by a cementitious leachate factor until all cementitious regions have been fully chemically depleted. During the implementation of the conceptual model, an abbreviated suite of seven parent radionuclides is tested. The K_d values and half-lives for each are listed in Table 4-30.

Table 4-30. Half-Lives and K_d Values for the Suite of Radionuclides Tested During Implementation (Danielson, 2020c)

Radionuclide	Half-Life (years)	K_d Value				Cementitious Leachate Factor	K_d Value	
		Stage I (mL g ⁻¹)	Stage II (mL g ⁻¹)	Stage III (mL g ⁻¹)	Gone (mL g ⁻¹)		Sandy (mL g ⁻¹)	Clayey (mL g ⁻¹)
C-14	5.70E+03	2,000	5,000	50	30	5	1	30
H-3	1.23E+01	0	0	0	0	1	0	0
I-129	1.57E+07	8	10	4	3	0.1	1	3
Np-237	2.14E+06	10,000	10,000	5,000	9	1.5	3	9
U-233	1.59E+05	1,000	5,000	5,000	400	3	300	400
Th-229	7.34E+03	10,000	10,000	2,000	2,000	2	900	2,000
Sr-90	2.88E+01	90	15	90	17	3	5	17
Tc-99	2.11E+05	0.8	0.8	0.5	1.8	0.1	0.6	1.8
U-238	4.47E+09	1,000	5,000	5,000	400	3	300	400
U-234	2.46E+05	1,000	5,000	5,000	400	3	300	400
Th-230	7.54E+04	10,000	10,000	2,000	2,000	2	900	2,000
Ra-226	1.60E+03	200	100	200	180	3	25	180
Pb-210	2.22E+01	300	300	100	5,000	3.2	2,000	5,000

Notes:

¹ Parent radionuclides in bold text; progeny in plain text.

4.2.1.4. Results and Discussion

Preliminary results are presented below to demonstrate that the pre- and post-processing automation schemes and the conceptual model approach have been implemented correctly. The temporal discretization into 98 time periods is listed in Table 4-31 where a steady-state flow field that serves as input to radionuclide transport simulations is computed for each time interval.

4.2.1.4.1. Preliminary Flow Results

Figure 4-52 displays the saturation profiles for CIG-4, which is representative of CIG-1 through CIG-7, for intact infiltration conditions through 371 simulation years. Notably, most of the rainfall that infiltrates from the top boundary is redirected laterally around the cementitious waste form and its outer enclosure in the first 40 simulation years before hydraulic degradation commences. After hydraulic degradation of the low-permeability CIG waste, the water volume passing through the cementitious mass increases, although the velocity is low due to the high-integrity closure cap systems. As the cap degrades, however, the water velocity through the CIG waste increases.

Figure 4-53 and Figure 4-54, respectively, present the saturation profiles for CIG-8 and CIG-9 for a period of 371 years to highlight the impacts of both the reinforced-concrete mat on the flow field and of the improved grout formulation employed for disposal in CIG-9. In a similar manner to CIG-1 through CIG-7, most of the water is redirected laterally around the CIG mass; however, the water velocity is substantially lower in the regions above the waste zone because of the reinforced-concrete mats that lead to a higher water saturation above the waste zone. After hydraulic degradation of the CIG waste zone, the hydraulic properties of the reinforced-concrete mat do not provide increased redirection of water around the CIG mass, demonstrating that they are primarily present for structural integrity.

Table 4-31. Temporal Discretization of the Performance Assessment Time Period for Components-in-Grout Trench Segments (Danielson, 2020c)

Time Period	Start Year	End Year	Time Period	Start Year	End Year	Time Period	Start Year	End Year
TI01	0	First Waste ¹	TI34	461	471	TI67	1,041	1,061
TI02	First Waste ¹	Op. Cover ¹	TI35	471	481	TI68	1,061	1,081
TI03	Op. Cover ¹	46	TI36	481	491	TI69	1,081	1,101
TI04	46	171	TI37	491	501	TI70	1,101	1,121
TI05	171	181	TI38	501	511	TI71	1,121	1,141
TI06	181	191	TI39	511	521	TI72	1,141	1,161
TI07	191	201	TI40	521	531	TI73	1,161	1,211
TI08	201	211	TI41	531	541	TI74	1,211	1,261
TI09	211	221	TI42	541	561	TI75	1,261	1,361
TI10	221	231	TI43	561	581	TI76	1,361	1,461
TI11	231	241	TI44	581	601	TI77	1,461	1,561
TI12	241	251	TI45	601	621	TI78	1,561	1,661
TI13	251	261	TI46	621	641	TI79	1,661	1,761
TI14	261	271	TI47	641	661	TI80	1,761	1,861
TI15	271	281	TI48	661	681	TI81	1,861	1,961
TI16	281	291	TI49	681	701	TI82	1,961	2,461
TI17	291	301	TI50	701	721	TI83	2,461	2,961
TI18	301	311	TI51	721	741	TI84	2,961	3,461
TI19	311	321	TI52	741	761	TI85	3,461	3,961
TI20	321	331	TI53	761	781	TI86	3,961	4,461
TI21	331	341	TI54	781	801	TI87	4,461	4,961
TI22	341	351	TI55	801	821	TI88	4,961	5,461
TI23	351	361	TI56	821	841	TI89	5,461	5,961
TI24	361	371	TI57	841	861	TI90	5,961	6,461
TI25	371	381	TI58	861	881	TI91	6,461	6,961
TI26	381	391	TI59	881	901	TI92	6,961	7,461
TI27	391	401	TI60	901	921	TI93	7,461	7,961
TI28	401	411	TI61	921	941	TI94	7,961	8,461
TI29	411	421	TI62	941	961	TI95	8,461	8,961
TI30	421	431	TI63	961	981	TI96	8,961	9,461
TI31	431	441	TI64	981	1,001	TI97	9,461	9,961
TI32	441	451	TI65	1,001	1,021	TI98	9,961	10,471
TI33	451	461	TI66	1,021	1,041	--	--	--

Notes:

¹ First waste and time to operational stormwater runoff cover are CIG-unit dependent (see Section 4.2.1.2).

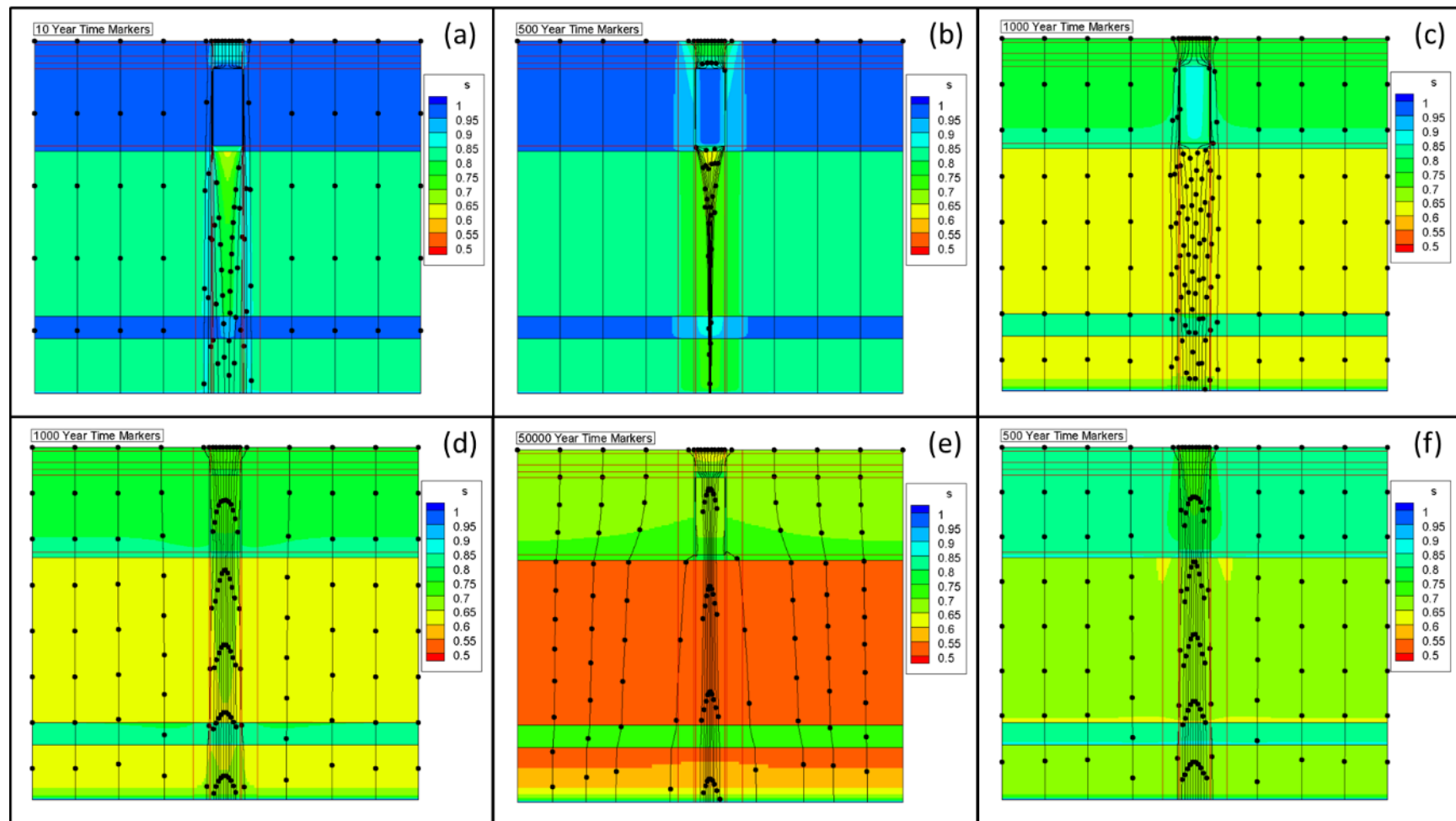


Figure 4-52. Saturation Profile for CIG-4 (a) during Operational Period; (b) during Operational Closure Period; (c) during Interim Closure Period *before* Hydraulic Degradation; (d) during Interim Closure Period *after* Hydraulic Degradation; (e) at End of Institutional Control; (f) at Year 371 (extracted from Danielson, 2020c)

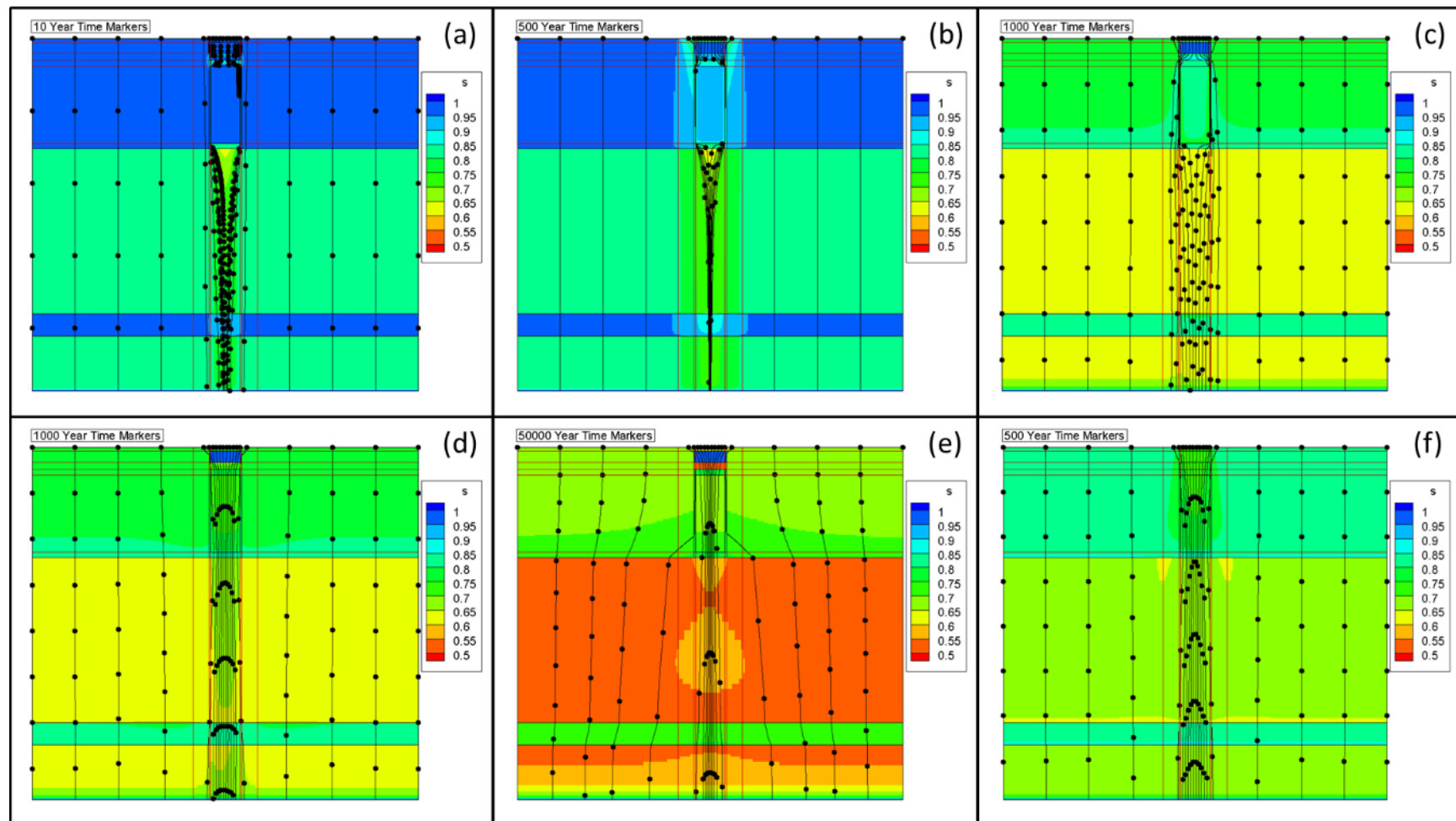


Figure 4-53. Saturation Profile for CIG-8 (a) during Operational Period; (b) during Operational Closure Period; (c) during Interim Closure Period *before* Hydraulic Degradation; (d) during Interim Closure Period *after* Hydraulic Degradation; (e) at End of Institutional Control; (f) at Year 371 (extracted from Danielson, 2020c)

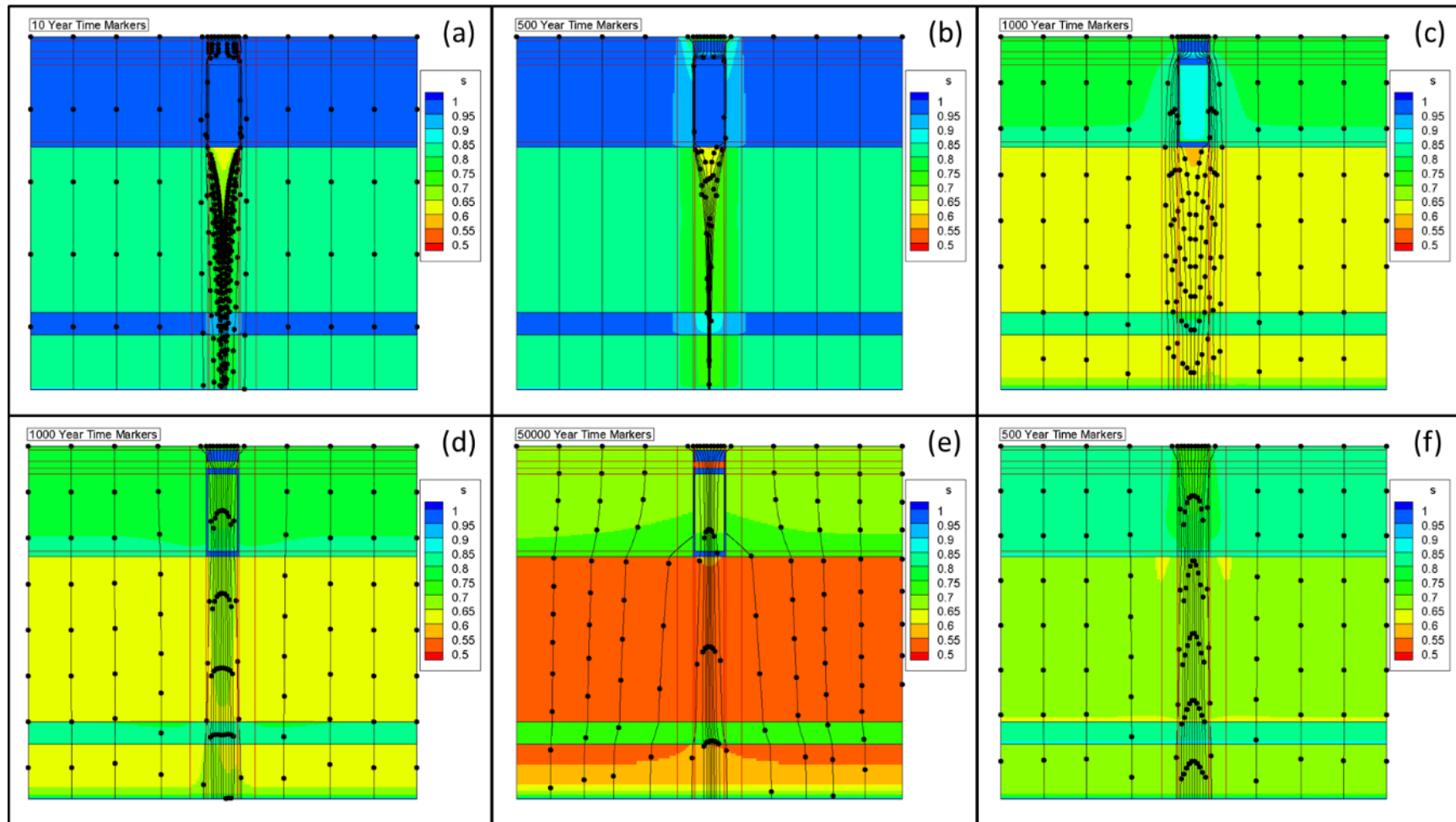


Figure 4-54. Saturation Profile for CIG-9 (a) during Operational Period; (b) during Operational Closure Period; (c) during Interim Closure Period *before* Hydraulic Degradation; (d) during Interim Closure Period *after* Hydraulic Degradation; (e) at End of Institutional Control; (f) at Year 371 (extracted from Danielson, 2020c)

Figure 4-55 displays the saturation profile for the CIG-4 bounding subsidence case. Notably, subsidence in the bounding case occurs immediately upon final closure when the final closure cap is installed. Meanwhile, the lateral extent of the final closure cap is essentially undegraded outside the subsided region, which allows for lateral spreading as water infiltrates through the subsided region. The water velocity through the subsided region is listed in Table 4-26.

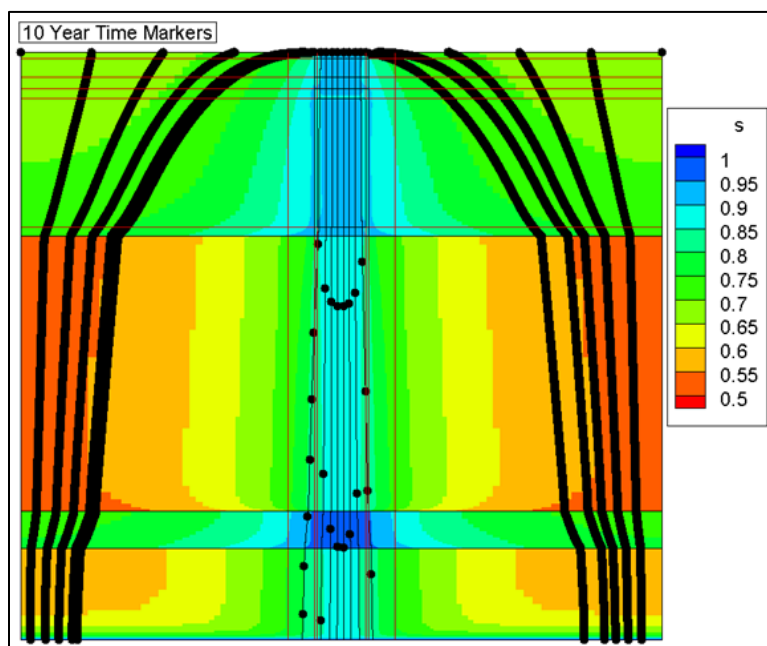


Figure 4-55. Saturation Profile for CIG-4 with Subsidence at Year 171 (Danielson, 2020c)

4.2.1.4.2. Preliminary Transport Results

The aging times for each cementitious material region, shown in Table 4-32 for CIG trench segments 4, 8, and 9, are computed using the steady-state flow fields for each time interval and each CIG trench segment. These aging times serve as triggers for making stepwise changes to K_d for each radionuclide species during PORFLOW transport simulations. The bounding subsidence case for CIG-4 has the shortest cementitious aging times because of the elevated water infiltration during the subsidence time periods that first occur at the end of IC. The best estimate subsidence case for CIG-4 has the second shortest aging times. Neither the presence of the reinforced-concrete mats for CIG-8 and -9 nor the improved grout formulation (i.e., lower hydraulic conductivity) used with CIG-9 substantially increase aging times as the early transition from Stage I to Stage II occurs after the degradation of these features. Notably, none of the CIG trench segments ever reach full chemical aging during the 1,100-year compliance period.

Radionuclide transport from the CIG trench segments through the VZ is simulated for a suite of seven parent radionuclides (bolded species in Table 4-30) to produce a flux-to-the-water-table profile. At the start of a CIG trench segment's operations, 1.0 gmole of inventory is distributed uniformly throughout the 'CIG Waste' material zone (refer to Figure 4-50). For those segments where subsidence occurs (i.e., CIG-4 through CIG-7), all radionuclide inventory that has not migrated from the waste zone is transferred to the lower half (i.e., the lower 7 feet) of the 'CIG Waste' material zone at the time of subsidence.

Table 4-32. Cementitious Material Aging Times for Components-in-Grout Trench Segments Computed from Steady-State Flow Fields (Danielson, 2020c)

Unit	Infiltration Case	Transition	Model Simulation Year ¹			
			Outer Enclosure	CIG	Reinforced Mat	CLSM
CIG-4	Intact	Stage I to Stage II	622	1,157	-	-
		Stage II to Stage III	1,286	3,698	-	-
		Stage III to Stage IV	5,887	36,735	-	-
CIG-4	Bounding Subsidence	Stage I to Stage II	177	297	-	-
		Stage II to Stage III	251	1,555	-	-
		Stage III to Stage IV	2,550	22,150	-	-
CIG-8	Intact	Stage I to Stage II	636	1,157	678	612
		Stage II to Stage III	1,291	3,698	1,412	1,189
		Stage III to Stage IV	5,890	36,735	6,980	4,916
CIG-8	Best Estimate Subsidence	Stage I to Stage II	394	608	399	388
		Stage II to Stage III	666	2,445	700	592
		Stage III to Stage IV	4,023	27,420	4,653	3,210
CIG-9	Intact	Stage I to Stage II	646	1,158	680	621
		Stage II to Stage III	1,294	3,697	1,413	1,191
		Stage III to Stage IV	5,892	36,734	6,980	4,917
CIG-9	Best Estimate Subsidence	Stage I to Stage II	389	545	391	384
		Stage II to Stage III	591	2,118	615	534
		Stage III to Stage IV	3,537	24,930	4,070	2,781

Notes:

¹ Model simulation year referenced from the start of operations in the ELLWF on September 28, 1994.

Figure 4-56 presents a comparison of the flux-to-the-water-table profiles for CIG-4, CIG-8, and CIG-9 for all parent radionuclides except for U-238 (due to the low concentration reaching the water table). Radionuclide flux in the early time periods is lower for CIG-8 and CIG-9 than for CIG-4. This is primarily attributed to the presence of the reinforced-concrete mats and the lower hydraulic conductivity of the grout formulation used in CIG-9. Notably, the peak fluxes for the three CIG trench segments are comparable for all radionuclides except H-3, whose peak occurs before complete hydraulic degradation Year 371.

In summary, conceptual models of the VZ for ST DUs containing CIG waste have been developed by Danielson (2020c) for both intact and subsidence infiltration scenarios for application in PA2022. The conceptual models for trench segments CIG-1 through CIG-9 are implemented in PORFLOW and preliminary results are presented for an abbreviated suite of seven parent radionuclides and their progeny.

4.2.2. Effective- K_d Conceptual Model

The effective- K_d implementation is applied to seven specific waste forms that have been disposed and/or are approved for future disposal in STs and ETs in the ELLWF. Table 4-33 lists the waste forms; K_d values are taken directly from the 2016 Geochemical Data Package (Kaplan, 2016b). The seven SWFs are strictly for I-129-containing waste generated by water treatment processes, including the F-Area GW treatment unit (F-WTU), the H-Area GW treatment unit (H-WTU), and the Effluent Treatment Facility (ETF). Figure 4-57 provides two examples of I-129-containing

spent resin waste. The effective- K_d implementation assumes that the SWF is distributed uniformly throughout the waste zone except where a unique or sporadic disposal pattern requires a bounding type analysis (e.g., SWF placed at the downgradient end of a trench closest to the GW POA).

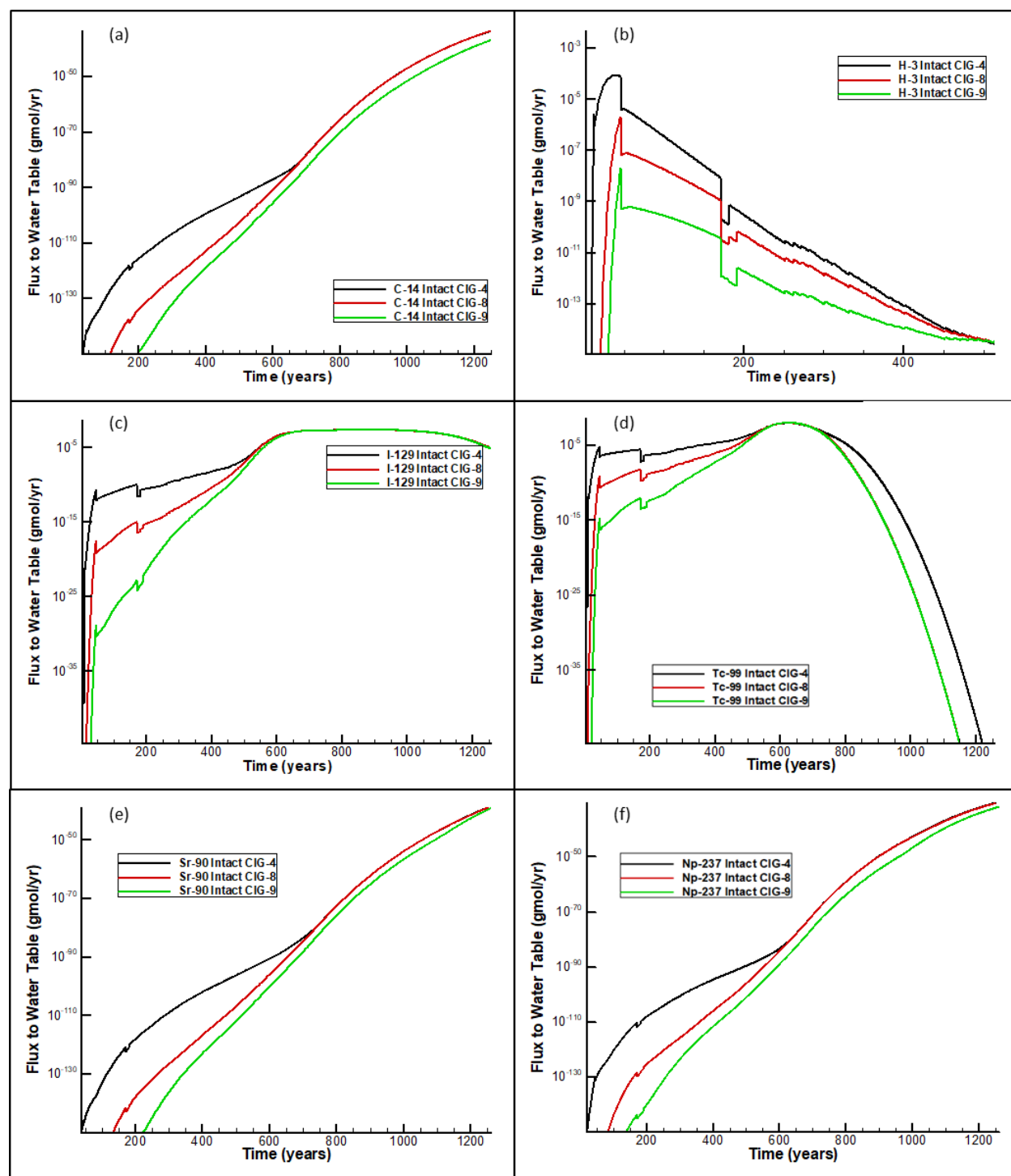


Figure 4-56. Flux to Water Table (gmol yr^{-1} per gmole parent buried) from CIG-4, CIG-8, and CIG-9 for (a) C-14; (b) H-3; (c) I-129; (d) Tc-99; (e) Sr-90; (f) Np-237 (extracted from Danielson, 2020c)

Table 4-33. Special Waste Forms Modeled Using Effective- K_d Implementation (Danielson, 2021; Table 2)

Waste Form	CWTS Designation	Existing Trench Locations	Potential Future Locations	Still Being Generated?	K_d (mL g ⁻¹)
ETF GT-73	I129I	ST02-ST04, ET01	N/A	No	10,000
F-WTU CG-8	I129G	ST02, ET01	N/A	No	50
F-WTU Dowex 21K	I129D	ST02, ET01	N/A	No	6,800
F-WTU Filtercake	I129J	ST01-ST05, ST07, ET01	N/A	No	56.9
H-WTU CG-8	I129H	ST02, ST04, ET01	N/A	No	380
H-WTU Dowex 21K	I129E	ET01	N/A	No	15,600
H-WTU Filtercake	I129F	ST01	N/A	No	650

Notes:

F-WTU: F-Area GW treatment unit

H-WTU: H-Area GW treatment unit

ETF: Effluent Treatment Facility

**Figure 4-57. GT-73 Spent Resin in a B-12 Box from the ETF (left) and Spent Resins from the F-Area and H-Area Groundwater Treatment Units (right)**

Each trench type (i.e., ST and ET) has been assigned a unique set of waste zone chemical and hydraulic properties into which the SWF is placed. The waste zone K_d is specified based on the values given in the 2016 Geochemical Data Package (Kaplan, 2016b) for clayey material. The set of hydraulic properties is selected to represent the types of waste forms and waste zone conditions over the ST or ET lifecycle. Effective or “hybrid” hydraulic properties are estimated for the ST waste zone based on a proportional blending of containerized waste and bulk waste that have historically been received. Alternatively, ETs are assigned a set of hydraulic properties reflecting containerized waste disposals surrounded by backfill soil. Hydraulic properties before and after dynamic compaction are estimated for both STs and ETs. Descriptions and values of ST and ET hydraulic waste zone properties are provided by Nichols and Butcher (2020).

ELLWF hydrostratigraphy, as updated by Bagwell and Bennett (2017), is used as the basis for the development of the ST and ET conceptual models (Danielson, 2019c). STs and ETs containing

these SWFs will be modeled using data provided by Danielson (2019c) for depth to the water table and clayey thickness beneath the waste zone.

4.2.3. Delayed-Release Conceptual Model

The delayed-release SWF implementation is similar to the effective- K_d implementation except that the specific radionuclides are kept immobile until dynamic compaction occurs at the beginning of the post-closure period (i.e., calendar year 2165). For this SWF category, credit is taken for the integrity of the disposal container in radionuclide holdup. Two waste forms are included this category: NR pumps (Figure 4-58) and ETF carbon vessels (Figure 4-59).



Figure 4-58. Naval Reactor Pumps on NR26E Pad (darker gray tubes in foreground)



Figure 4-59. ETF Activated Carbon Columns Being Prepared for Shipment to E-Area (left) and Disposed in ST03 (right)

These two waste forms as well as their locations and K_d values are listed in Table 4-34. Again, the waste is assumed to be uniformly distributed throughout the waste zone except where a unique or sporadic disposal pattern requires a bounding-type analysis (e.g., SWF placed at the downgradient end of a trench closest to the GW POA). In PORFLOW, during the operational and IC periods, the waste zone K_d values are set equal to $1.0E20 \text{ mL g}^{-1}$ to effectively render the radionuclides immobile (i.e., to reflect an intact-container condition). Following dynamic compaction, the

radionuclides are assigned their respective K_d values listed in Table 4-34, which are obtained from the 2016 Geochemical Data Package (Kaplan, 2016b).

Table 4-34. Special Waste Forms Modeled using the Delayed-Release Implementation

Waste Form	CWTS Designation	Existing Inventory	Existing + Future Inventory	Potential Future Inventory	Still Being Generated?	K_d (mL g ⁻¹)
NR Pump	C14N	ST01-ST05, ST08	ST07, ST09, ST14	ST10, ST11, ST17-ST22	Yes	30
ETF Carbon Column	H3C	ST03, ST07	N/A	N/A	No	0
ETF Carbon Columns	I129C	ST03, ST07	N/A	N/A	No	7,400

STs and ETs containing these two SWFs are assigned the waste zone chemical and hydraulic properties obtained from the property data packages prepared by Kaplan (2016b) and Nichols and Butcher (2020). The hydrostratigraphy is based on the ST and ET conceptual model developed and documented by Danielson (2019c).

4.2.4. Solubility-Controlled Release Conceptual Model

Solubility-controlled release models require a specially defined source term in PORFLOW simulations. M-Area glass (Figure 4-60), one of the two solubility-controlled SWFs, was generated by the vitrification of waste sludge from the production of depleted uranium targets.



Figure 4-60. Disposal of Containers of Vitrified M-Area Glass in ST02 in 2003

The second SWF in this category is the Paducah Demonstration Cask (Figure 4-61), which is a depleted uranium, shielded cask containing various radioactive sources from SRS reactors. For both SWFs, the same source term from PA2008 is used for each of the radionuclides of interest. The source-term files specify the radionuclide release concentration through time. The waste zone K_d values are based on the values reported by Kaplan (2016b) for clayey material as listed in Table 4-35. Both SWFs have already been emplaced, and no future disposals of this SWF category

type are expected. For this reason, the waste form is placed at the location in the generic ST model setup that is most representative of the known location within the trench.



Figure 4-61. Paducah Demonstration Cask Loaded in L-Area at Savannah River Site (left); Sealed Cask Placed in ST05 on May 27, 2004 (right)

Table 4-35. Special Waste Forms Assuming Solubility-Controlled and Diffusion-Controlled Release

Waste Form	CWTS Designation	Existing Trench Locations	Potential Future Locations	Still Being Generated?	K_d (mL g ⁻¹)
Solubility-Controlled					
M-Area Glass	U234G	ST02	N/A	No	400
M-Area Glass	U235G				
M-Area Glass	U236G				
M-Area Glass	U238G				
Paducah Cask	U235P	ST05			

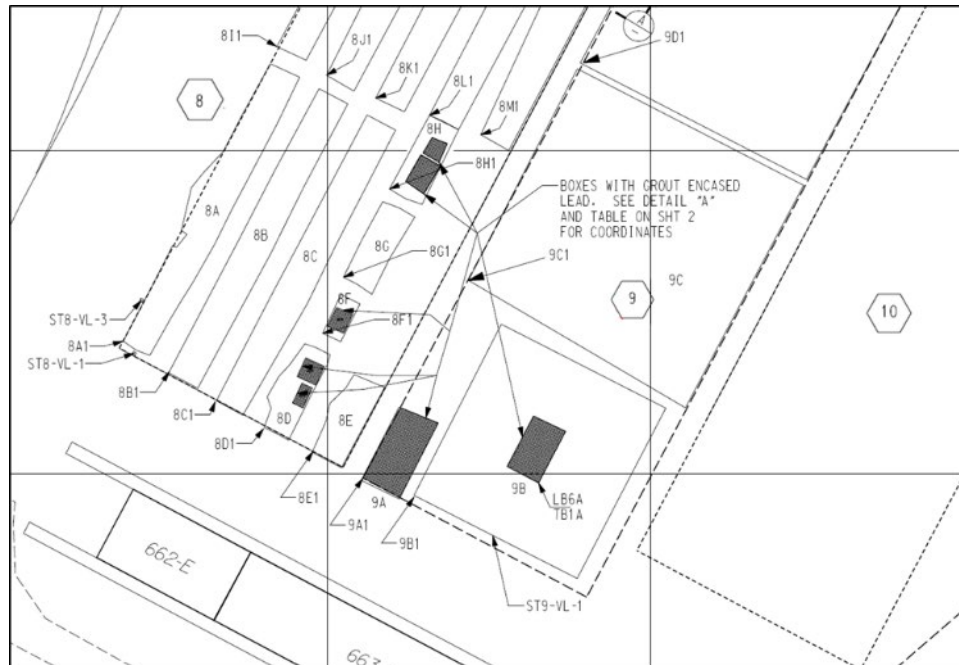
ST02 and ST05 are modeled using chemical and hydraulic property data for the waste zone provided by Kaplan (2016b) and Nichols and Butcher (2020). The depth to the water table and the clayey thickness beneath the waste zone for each trench unit is modeled as specified by Danielson (2019c).

4.2.5. Tall Box Conceptual Models

Tall used-equipment storage boxes (“tall boxes”) disposed (or approved for disposal) in ST08, ST09, and ST10 are treated as a SWF in the VZ modeling. Tall box burial is limited to the southern 220 feet of ST08 and ST09 and the southern 180 feet of ST10 as highlighted in Figure 4-62 (C-CV-E-00207, 2016). ST08, ST09, and ST10 are in a hydrostratigraphic grouping (Figure 4-42) with an assumed depth to the water table of 75 feet and a clay thickness beneath the waste zone of 11 feet (Danielson, 2019c) as shown in Figure 4-63. Tall box models are 3-D and incorporate a portion of a ST segment that is 35 feet deep (i.e., maximum depth of the tall boxes). The 35-foot depth comprises a 31-foot waste zone and a 4-foot backfill layer placed above. Both intact and subsidence cases will be modeled using a procedure similar to that employed by Flach and Jones (2010).

Some of the tall boxes contain lead (Pb) which requires a 12-inch encapsulation layer of grout surrounding the waste component. While the grout encapsulation layer is intact, it provides a barrier to infiltration and changes the chemistry of the waste zone. Both grouted and non-grouted tall-box waste forms will be compacted at the end of IC from 31 feet down to 4.8 feet

(Figure 4-63), which is consistent with the analysis by Flach and Jones (2010) as well as the 6.4:1 compaction ratio assumed for the standard, 16-foot-high, B-25-boxed waste form that is compacted to 2.5 feet. The grout encasement is degraded to ILV Backfill soil properties at the time of compaction.



Notes: Zoomed screen capture from Savannah River Site drawing (C-CV-E-00207, Rev. 7); tall boxes are shaded in dark gray

Figure 4-62. Slit Trench 8, 9, and 10 Burial Area for Tall Boxes Circa 2016

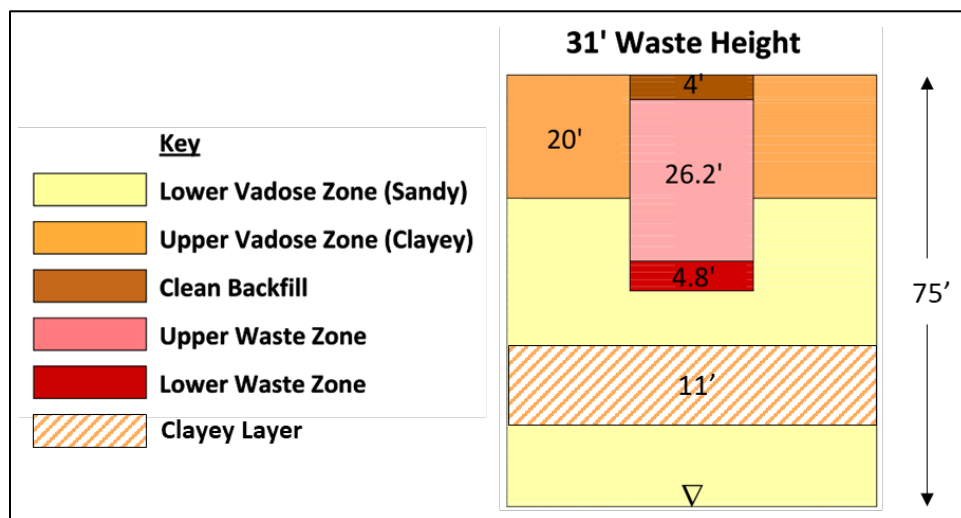


Figure 4-63. Geometric Configuration for Tall Box Special Waste Form Model

A single tall-box VZ model is used to represent both grouted and non-grouted waste forms. The hydraulic properties of the intact grout layer are not explicitly modeled, but the geochemistry of the waste zone is modeled during the operational and IC periods using the lesser of the concrete

and clay K_d values. During the post-closure period, following dynamic compaction, radionuclide partitioning in the waste zone is based on the clay K_d values, reflecting the breakup of the grout encapsulation layer.

4.2.6. Automation of Special Waste Form Conceptual Model Implementation

To ensure proper linking of datasets and error-free construction of PORFLOW input files, the automation scheme developed for generic waste forms is updated to accommodate the SWF models. The implementation of SWF models into the scheme for generic waste forms required updates to the PORFLOW Transport input file pre-processor only. For SWFs in the effective- K_d , delayed-release, and solubility-controlled-release classifications, the CWTS designation for the radionuclide [e.g., H3C (SWF) versus H-3 (generic)] is used to trigger the algorithm to appropriately select either the SWF K_d and/or the appropriate source-term file and to write the proper syntax of the PORFLOW “SOURce” command.

The tall-box models in PORFLOW required a new grid mesh which took advantage of the same automation scheme developed for the generic waste forms.

4.3. COMPLEX SPECIAL WASTE FORM CONCEPTUAL MODELS FOR TRENCHES

Three complex SWFs are included in the VZ models for STs and ETs in PA2022: HWCTR shown in Figure 4-64, HXs displayed in Figure 4-65, and 232-F concrete rubble in Figure 4-66. Table 4-36 identifies the specific radionuclides of interest for these three SWFs.

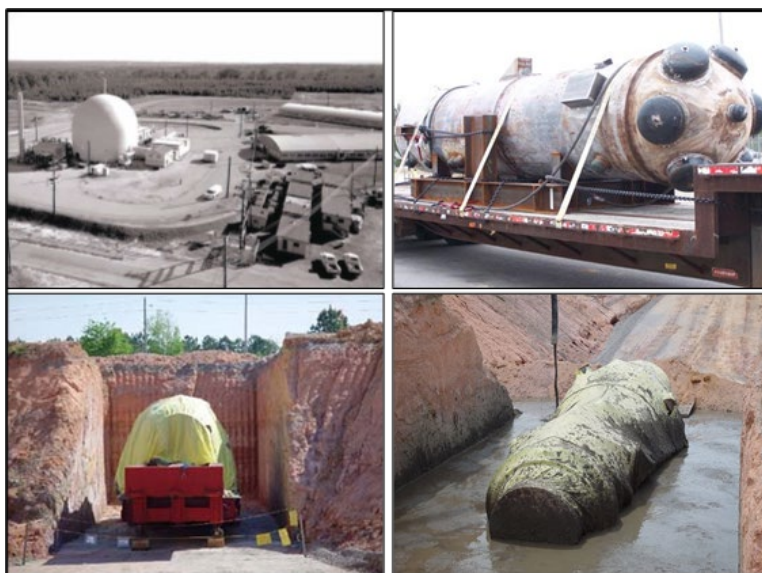


Figure 4-64. 770-U Heavy Water Components Test Reactor Reactor Building at Savannah River Site in 1962 (upper left); Heavy Water Components Test Reactor Reactor Core for Transport to E-Area Low-Level Waste Facility on 2/9/2011 (upper right); Heavy Water Components Test Reactor and Sacrificed Trailer Bed in ST14 on 4/14/2011 (lower left); Heavy Water Components Test Reactor in “Cradle” of CLSM to Eliminate Voids Beneath Trailer Bed on 4/20/2011 (lower right)



Figure 4-65. Reactor Process Heat Exchangers in Long-Term Storage on 10/1/1998 (left) and Emplaced in ST09 on 8/16/2012 (right)



Figure 4-66. Concrete Rubble from 232-F Demolition Activities: Dropping of the 232-F Concrete Stack (left) and Resulting Concrete Rubble (right)

Table 4-36. Complex Special Waste Form Radionuclides Released from Heavy Water Components Test Reactor and Reactor Process Heat Exchangers (Danielson, 2021; Table 5)

Special Waste Form	Radionuclide	Existing Trench Location	K_d (mL g ⁻¹)
HWCTR	Ag-108m	ST14	Table 4-37
	C-14		
	Co-60		
	Fe-55		
	Mo-93		
	Nb-93m		
	Nb-94		
	Ni-59		
	Ni-63		
	Tc-99		
HX	C-14	ST09	30
	H-3		0
232-F Concrete Rubble	H-3	ST01	0

Table 4-37. Reproduction (Danielson, 2021; Table 6) of Table 4-8 by Hamm and Smith (2010) for Heavy Water Components Test Reactor Special Waste Form with Updated Chemical Properties Reported by Kaplan (2016b)

Material	Porewater pH	K_d (mL g ⁻¹)									
		Ag-108m	C-14	Co-60	Fe-55	Mo-93	Nb-93m	Nb-94	Ni-59	Ni-63	Tc-99
K _d Sand	High	32	5	128	300	1,400	1,400	1,400	22.4	22.4	0.06
K _d Clay	High	96	150	320	600	1,400	1,400	1,400	96	96	0.18
K _d Sand	Low	10	1	40	200	1,000	1,000	1,000	7	7	0.6
K _d Clay	Low	30	30	100	400	1,000	1,000	1,000	30	30	1.8
K _d ConYng	--	4,000	2,000	4,000	6,000	3	1,000	1,000	65	65	0.8
K _d ConMid	--	4,000	5,000	4,000	6,000	3	1,000	1,000	400	400	0.8
K _d ConOld	--	400	50	400	600	3	500	500	400	400	0.5
K _d ConGone ^a	--	30	30	100	400	3	500	500	30	30	0.5
K _d Met	--	0	0	0	0	0	0	0	0	0	0
K _d Grv	--	0	0	0	0	0	0	0	0	0	0
K _d Cks	--	0	0	0	0	0	0	0	0	0	0

Notes:

^a K_dConGone is set equal to the lesser of the Stage III concrete and clay K_d values as a bounding estimate (increased mobility), which is consistent with the SA methodology.

SWF model implementation in the current ELLWF PA makes use of earlier models deployed for each waste form in SAs performed by Hamm and Smith (2010), Hamm et al. (2012), and Flach et al. (2005) for the HWCTR, HXs, and 232-F concrete rubble, respectively (i.e., new VZ models were not developed for PA2022). HWCTR and HXs utilize the existing flux-to-the-water-table profiles provided by Hamm and Smith (2010) and Hamm et al. (2012), respectively, as a source term at the water table to simulate transport through the updated GSA flow model. Tritium-containing concrete rubble (Figure 4-66) disposed in ST01 from the demolition of building 232-F (the old tritium facility) is the only SWF that falls in the diffusion-controlled release category. The presence of concrete rubble changes the hydraulic properties of the waste zone, effectively lowering the saturated hydraulic conductivity and the porosity. The rate of leaching of H-3 from chunks of rubble is diffusion-dominated and depends upon the size distribution of the concrete chunks (i.e., small chunks with a higher specific surface area release tritium at a faster rate than large chunks). Flach et al. (2005) employed a methodology that accounts for the size distribution and diffusion of H-3 from the concrete rubble; however, later placement of an operational stormwater runoff cover over ST01, which substantially lowers infiltration rates compared to an OSC-only scenario, was not accounted for in the model. Because of this substantial difference, the source term from the original SA cannot be used. Rather than redeveloping this complex VZ model, generic-waste-form limits for H-3, which are pessimistically bounding, are employed for SWF radionuclide H-3F instead.

4.4. GOLDSIM® TRENCH SYSTEM MODEL

The high-level conceptual model for the GoldSim® Trench System Model is illustrated in Figure 3-73. Trench units representing three of the seven unique hydrostratigraphic zones defined by Danielson (2019c) are selected for the Trench System Model: ST06, ST09, and ET06. Contaminant transport in the porous medium aqueous phase includes the following advective processes: infiltration of precipitation from the ground surface, downward migration through the VZ, recharge of the aquifer at the water table (from the base of the LVZ), and lateral transport in the aquifer saturated zone to the 100-meter POA.

The discussion that follows is generally applicable to all GoldSim® trench submodels but is focused on the development of the first trench submodel within the ST06 footprint. To simplify the initial model calibration, the ST06 submodel utilizes the PORFLOW ET geometry and waste properties. All three trench units (ST06, ST09, and ET06) are ultimately modeled and calibrated against PORFLOW output within the GoldSim® Trench System Model.

4.4.1. Inventory

The inventory is uniformly distributed within the waste zone at the time operations begin in the trench. The inventory placed into the waste zone is controlled by dashboard buttons. For the Trench System Model, there are six radionuclides of interest: I-129, H-3, C-14, Tc-99, Sr-90, and Np-237. The short-chain progeny (one-year half-life cutoff value) of Np-237 are also included in the inventory: Np-237 → U-233 → Th-229.

The species list contains eight radionuclides including the six parents and two daughters. All of the radionuclide inventory is treated as “generic,” meaning it is immediately available for release at the time of emplacement (i.e., no credit for the container or waste form in radionuclide holdup). Through the dashboard, the user can choose to run the model with either a 1.0 gmole inventory or the projected inventory at closure.

4.4.2. Radionuclide and Material Properties

The “Material” container (Figure 4-67) includes definitions of radionuclide contaminant species and their decay rates, and the bulk physical and hydraulic properties of the materials making up the solid porous media. The radionuclide data for the modeled species are obtained from the SRNL configuration-controlled Radionuclide-Dose Data Package (SRNL, 2019b) by Smith et al. (2019) and are given in Table 3-41. Radionuclide properties are well known and, therefore, are not assigned uncertainty distributions.

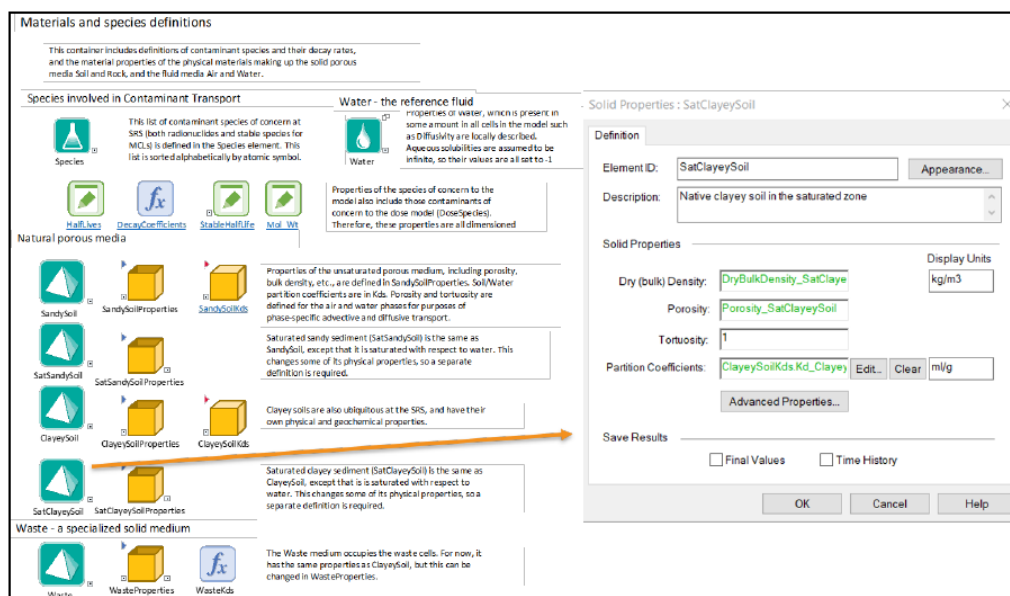


Figure 4-67. Contents of Materials Container and SatClayeySoil Material Definition (Wohlwend and Hamm, 2020; Figure 2-14)

Four porous media zones comprising the disposal system are represented in the GoldSim[®] Trench System Model: waste zone (WZ), UVZ, LVZ and saturated (SAT) zone. The hydraulic properties within these zones employ the following six material types (Nichols and Butcher, 2020): ET Waste before dynamic compaction, ET waste after dynamic compaction, ClayeySoil (UVZ), SandySoil (LVZ), SatSandySoil, and SatClayeySoil.

Differences in bulk material properties between the saturated and unsaturated zone soils are based on recommendations for using effective material properties in the SAT zone from the configuration-controlled Hydraulic Properties Data Package (SRNL, 2020) by Nichols and Butcher (2020). Effective SAT zone material properties are assigned based on the knowledge that total porosity overestimates the effective porosity that participates in contaminant transport because of the presence of dead-end pore spaces and intermittent clay lenses.

The ST waste zone properties are based on those for the “hybrid” ST defined by Phifer (2010). The “hybrid” ST waste zone representation combines bulk waste and containerized waste properties in a manner that conserves mass so that radionuclide retardation is neither overly optimistic nor overly pessimistic. Because a ST receives both bulk and containerized waste throughout a trench, a “hybrid” waste zone is assumed by combining the two waste types into a set of equivalent properties based on an estimated fraction of each waste type.

Properties of the porous media are defined in separate GoldSim[®] containers for each material type. Nominal parameter values for dry bulk density, porosity, and saturated effective diffusion coefficient for each of the six material types are listed in Table 4-38. Water content is the product of porosity and saturation.

Table 4-38. Material Property Assumptions for the GoldSim[®] Trench System Model (Wohlwend, 2020; Table 2-2)

Material Type	Dry Bulk Density (g cm ⁻³)	Porosity	Effective Diffusion Coefficient (cm ² yr ⁻¹)
ET Waste Before Compaction	0.293 ¹	0.889	1.67E+02
ET Waste After Compaction	1.847 ¹	0.303	1.26E+02
ST Waste Before Compaction	1.059	0.600	1.67E+02
ST Waste After Compaction	1.915	0.277	1.26E+02
ClayeySoil (UVZ)	1.650	0.385	1.67E+02
SandySoil (LVZ)	1.660	0.380	
SatSandySoil	1.040	0.250	
SatClayeySoil			

Notes:

¹ Dry bulk density of waste is dependent on particle density (2.65 g cm⁻³) and porosity: Dry Bulk Density = (Particle Density) × (1 - Porosity)

Uncertainties in the hydraulic property values reported in Table 4-38 for the two VZ soils and waste zone are based on statistical evaluation of site-specific field and laboratory data or literature data as described by Nichols and Butcher (2020). Explicit representation of uncertainty for the saturated zones is not included in the model due to a lack of data on which to perform statistics.

Geochemical data used in the System Model are imported from the configuration-controlled Geochemical Data Package (SRNL, 2018) by Kaplan (2016b). Figure 4-68 displays the contents of the GoldSim[®] Geochemical container where radionuclide partition coefficients (K_d values) for the soil materials are defined.

Best estimate soil/water partition coefficients (K_d values) for the solid material types listed in Table 4-38 are defined for each chemical element in the model (i.e., not for each radionuclide species because a single K_d value is assigned to all isotopes of an element). K_d values for ClayeySoil and SandySoil as defined by Kaplan (2016b) are assigned to radionuclides in the four different material zones in the model (i.e., WZ, UVZ, LVZ, and SAT zone) based on the chemical characteristics of the material types as indicated below.

- ClayeySoil K_d – WZ, ClayeySoil, SatClayeySoil
- SandySoil K_d – SandySoil, SatSandySoil


Soil/water partition coefficients - Clayey Sediment

A soil/water partition coefficient (K_d) for clayey sediments is defined for each chemical element in the model (not each radionuclide Species).

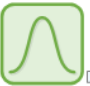
reference:
Kaplan, D., 2016, Geochemical Data Package for Performance Assessment Calculations Related to the Savannah River Site, SRNL-STI-2009-00473, Rev. 1. Savannah River National Laboratory, Aiken, South Carolina, July 2016

Non-zero-valued K_d s

The following scheme was introduced to the model by Glenn Taylor for version 1.0, with a revision in implementation by Neptune and Co in version 1.008 (though is still expected to be updated):



[ClayeyMedian](#)




[Kd_Dist](#)

A collection of median K_d values for clayey soil is provided for each chemical element. Those elements with zero or undefined K_d s are given a temporary median value of small mL/g in this definition


K_d values are based upon stochastic evaluation of a normal distribution based on the central limit theorem as discussed in SRNL-STI-2009-00473 Rev. 1, Section 4.8.1.

The standard deviation is based on the 95th Confidence Interval as discussed in SRNL-STI-2009-00473 Rev.1.


Kd Distributions Summary



[Value_Species](#)



[Zero_Kds](#)



[Kd](#)

The K_d values collected here, with zero values restored. Definitions are made dimensioned by Species for use in the contaminant transport modeling, and by DoseSpecies for the dose modeling.

An alternative definition is all $K_d = 0$, which is provided in this data element.

All references to K_d s should point to this selector element. The actual K_d values used in the modeling are determined here, and are equal to the values determined above, to zero if the user has chosen to disable chemical partitioning (retardation), or to the PA K_d s if in benchmarking mode.

Figure 4-68. Contents of Clayey Soil Geochemical Container with Trench System Model Chemical Properties Defined (Wohlwend and Hamm, 2020; Figure 2-15)

Note that the saturated sandy and clayey soils use the same partition coefficients as their unsaturated counterparts. ClayeySoil K_d values are assigned to radionuclides in the WZ (i.e., waste cells in the model) because the geochemistry of ClayeySoil is assumed to approximate that of the rusted metal waste containers. Nominal soil/water partition coefficients used in the GoldSim[®] Trench System Model are presented in Table 3-42; uncertainty distributions for these best estimate K_d values are derived from recommendations by Kaplan (2016b). All K_d values are normally distributed with a standard deviation of $0.75 \times K_d \div 2$ in sandy soils and $0.5 \times K_d \div 2$ in clayey soils. Additionally, the range in K_d is from a minimum of $0.25 \times K_d$ to a maximum of $1.75 \times K_d$ for sandy soils and $0.5 \times K_d$ to $1.5 \times K_d$ for clayey soils.

4.4.3. Infiltration and Saturation

The interim and final cover systems are not explicitly modeled within the GoldSim® Trench System Model. Instead, the covers are implicitly accounted for by utilizing modified flow rates and saturation values from the PORFLOW 3-D VZ flow model. In the GoldSim® Trench System Model, infiltration refers to the rate of water flowing downward (only the vertical component) into the waste zone. Before the surface interim runoff cover is applied, infiltration through the OSC is assumed to equal 15.78 inches per year, which is essentially equivalent to the annual-average rainfall minus the sum of the annual-average evapotranspiration and surface runoff (Dyer, 2019b). While the interim HDPE geomembrane cover is in place but before the final cover system is installed, the annual-average infiltration rate is assumed to equal 0.1 inches per year. Infiltration through the final closure cap varies through time due to cap degradation as predicted by the HELP model and reported by Dyer (2019b). In addition to the infiltration rate through the cap, the hydraulic conductivities of the unsaturated media (waste and clayey/sandy layers that make up the VZ) are incorporated into the PORFLOW VZ flow model to yield flow rates and saturation values for each section of the unsaturated zone through time. The flow rates and saturation values are incorporated into the GoldSim® Trench System Model in the form of time-series elements. Two relevant closure-cap cases (intact and subsidence) are discussed below, including their impact on infiltration and flow fields.

4.4.3.1. Intact Case

Water infiltration into the waste zone is impacted by the physical condition of the intact closure cap over time and has a graded impact on radionuclide transport. The intact case represents the condition where uniform subsidence of the waste zone and slow deterioration of closure cap barriers (e.g., the HDPE geomembrane layer) over decades gradually degrade the safety feature provided by the final closure cap. HELP model sensitivity studies by Dyer (2019b) generated infiltration degradation profiles for the intact case over a 10,000-year period. PORFLOW-generated flow fields using bounding infiltration rates provided spatially averaged velocities and saturation values that are used as input in the form of time-series elements to the GoldSim® Trench System Model. To address uncertainty and sensitivity, the GoldSim® Trench System Model utilizes stochastic elements that behave as multipliers: one for water saturation and another for velocity. These multipliers (with a normal distribution; mean = 1.0; minimum = 0.7; maximum = 1.3; standard deviation = 0.1) are then applied to the PORFLOW-generated velocity and water saturation time series elements.

4.4.3.2. Subsidence Cases

Subsidence infiltration cases are distinct from the intact case and result from localized waste zone failures that create subsided areas (or holes) in the overlying closure cap surface. The localized failures are caused by non-crushable containers and equipment that do not collapse during previous waste stabilization measures, such as dynamic compaction, but instead are assumed to fail catastrophically immediately upon installation of the final multilayer closure cap. The area under the subsidence region (hole) is modeled in parallel with the intact region in GoldSim®. While infiltration through the intact portion of the cap is obtained directly from the HELP model (Dyer,

2019b), infiltration through a hole depends on the hole size and location with respect to the crest of the closure cap as described in Section 4.1.3.6.

Similar to the intact infiltration case methodology (Section 4.4.3.1), using the bounding subsidence case for hole location “2”, PORFLOW-generated coupled flow rates and saturation values are utilized as input to the GoldSim[®] Trench System Model in the form of flow velocity and soil saturation time-series elements for each layer in the unsaturated zone (WZ, UVZ, LVZ).

4.4.4. Chronology

During the operational period, LLW is typically disposed within the trenches beginning at one end of the trench unit and proceeding toward the other end. In the GoldSim[®] Trench System Model, however, an entire ST is assumed to be filled immediately upon receipt of the first waste package in a particular DU. Trench closure is then conducted in stages. Operational closure consists of a minimum 4-foot-thick, clean soil layer placed over the waste zone (i.e., an OSC) sloped for positive drainage away from the trench. For STs, this is followed by the installation of a HDPE geomembrane cover (i.e., operational stormwater runoff cover) no later than four years after the trench is filled with waste. The stormwater runoff covers are assumed to be maintained (i.e., no change in intact infiltration rate) until the end of the operational period for the ELLWF, at which time the runoff covers are either replaced or, if still serviceable, incorporated into an area-wide geomembrane cover over all closed trench units as part of interim closure. For ETs, a geomembrane cover is not installed until calendar year 2040 or the start of IC in 2065 depending on when the ET is operational. The interim cover is assumed to be maintained throughout the 100-year IC period. Final closure using a multilayer, soil-geomembrane closure cap over all DUs (i.e., STs, ETs, ILV, LAWV, NRCDAs) will take place at the end of the assumed 100-year IC period. Performance is assessed throughout the operational, IC, and 1,000-year post-closure periods.

Within the GoldSim[®] Trench System Model, the “Chronology” container defines all model events. The condition and status of the site during any period are controlled by data elements based on actual and projected DU lifecycles. The data elements are then utilized to create milestones and status elements based on when (in model time) the events occur. Waste emplacement occurs when the “Open_ST” status element is triggered by the “OpsOpened_ST” milestone. Similarly, the estimated infiltration rate into the waste zone is modified by the status elements “Cap_None,” “Cap_Operational,” and “Cap_Final” which are functions of “OpsOpened_ST,” “OpsClosed_ST,” and “ClosureCap_Constructed” milestones, respectively. Subsidence is triggered by the “ClosureCap_Constructed” milestone. This is graphically shown in Figure 4-69 where the dates are specific to ST06.

Infiltration begins when the entire inventory is placed within the waste zone on the date each trench becomes operational (“OpsOpened_ST”). Initial infiltration following waste emplacement is through the OSC until the operational stormwater runoff (HDPE geomembrane) cover is installed (“OpsClosed_ST”). Infiltration then changes to the Interim infiltration rate (i.e., a greatly reduced infiltration rate through the relatively impermeable HDPE geomembrane). The Interim infiltration rate is maintained until the end of the 100-year IC period when the final closure cap is installed.

Subsidence is assumed to occur immediately after the final cap is installed in 2165 (100 years after the assumed ELLWF closure date of 2065) as described in Section 4.4.3.2, followed by gradual closure cap degradation resulting in changes to infiltration throughout the post-closure period as described in Section 4.4.3.1. Peak impacts for strongly sorbed radionuclides may occur after the 1,000-year post-closure period for near-surface disposal facilities. To address potential peaks far in the future, SUA calculations can be extended for several thousand more years.

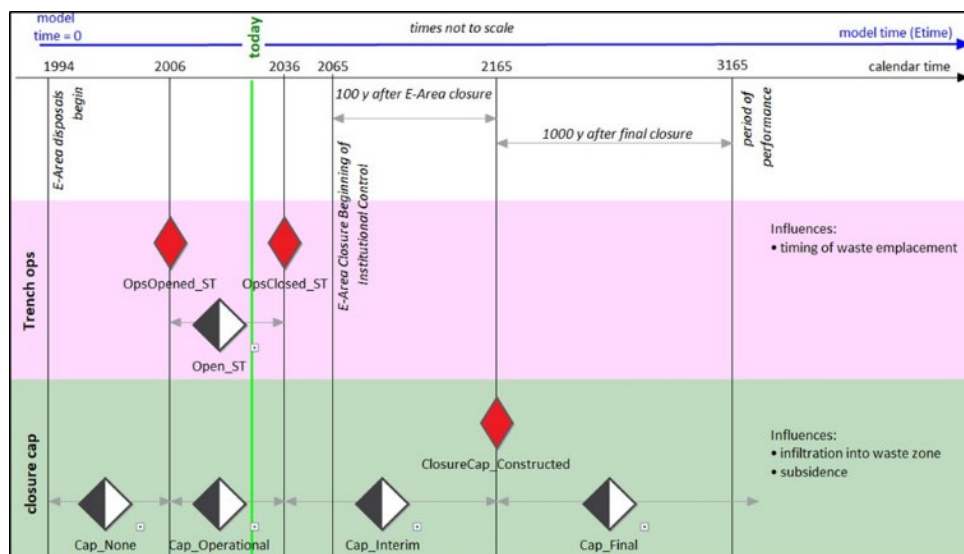


Figure 4-69. GoldSim® Trench System Model Chronology for ST06 (Wohlwend, 2020; Figure 2-4)

4.4.5. Stochastic Parameters

Uncertainty analysis is concerned with how uncertainty in the stochastic model input parameters propagates through the model to the selected model results. Sensitivity analysis, on the other hand, focuses on determining which input parameters exert the most influence on the overall uncertainty in the model. Stochastic elements in GoldSim® are designed to capture the overall *parameter* uncertainty in the model; they do not capture *conceptual model* uncertainty or uncertainty induced by *model structure*, such as discretization.

It is important to establish and to understand potential sources of uncertainty and biases in the System Model so that (1) conclusions drawn from the PA studies account for the stochastic behavior of the system and (2) predictions of long-term performance are reasonably accurate. Uncertainty in models can arise from multiple sources including parametric uncertainty, which originates from a lack of knowledge of the exact values that model parameters should take in the simulations. In addition, there is a need to examine the sensitivity of model predictions to uncertainties in the input parameters. A comprehensive SUA should help to identify important physical processes affecting outcome and determine which model components explain the majority of the System Model uncertainty. Parameters that are not known well or are poorly characterized are selected for stochastic input if judged to have a significant effect on the calculated GW concentrations and dose, as determined by previous sensitivity analyses or professional judgment. Propagating the uncertainty in the selected input parameters through the model, the GoldSim® Monte Carlo analysis generates a statistical distribution of GW concentrations. The GW

concentrations are then input to the SRNL Dose Toolkit to generate a statistical distribution of dose impacts.

SUA is limited by the uncertainty assigned to input parameters. For some parameters, uncertainty is well defined based on statistics calculated for a set of sample results (e.g., E-Area soil physical properties). For other input parameters, a stochastic distribution of values is less well known and is assigned based on a data review (e.g., chemical sorption or K_d values). In cases where little or no data are available, a predetermined range of uncertainty behavior (e.g., triangular, uniform, or discrete distribution of uncertainty) is assigned based on different levels of optimism and pessimism. Incorporating the predetermined uncertainty distributions in the model provides the PA team insight on the importance of these parameters to overall system performance. The remaining input parameters in the model are not defined by stochastic elements for a variety of reasons. Some deterministic inputs are well characterized (e.g., radionuclide half-lives), others are assigned reasonably bounding values, and, lastly, some are to be treated outside of the SUA framework (e.g., inventory uncertainty to be examined as part of the closure analysis through scaling of the deterministic results). The stochastic elements within the GoldSim® Trench System Model are listed in Table 4-39.

Table 4-39. Stochastic Elements in GoldSim® Trench System Model (Wohlwend, 2020; Table 2-5)

Stochastic Element Name	Description
DryBulkDensity_ClayeySoil	Samples clayey soil dry bulk density
DryBulkDensity_SandySoil	Samples sandy soil dry bulk density
Porosity_ClayeySoil	Samples clayey soil porosity
Porosity_SandySoil	Samples sandy soil porosity
ParticleDensity_Waste	Samples particle density (and therefore dry bulk density) of waste
Porosity_Waste_PostC_ET	Samples waste porosity after compaction for ETs
Porosity_Waste_Prec_ET	Samples waste porosity prior to compaction for ETs
Porosity_Waste_PostC_ST	Samples waste porosity after compaction for STs
Porosity_Waste_Prec_ST	Samples waste porosity prior to compaction for STs
Velocity_Distribution	Multiplier used to sample uncertainty of PORFLOW-generated velocity in the VZ
SatZoneDarcyVelDist	Multiplier used to sample uncertainty of PORFLOW-derived saturated zone Darcy velocity
Kd_Dist (Clayey Soil)	Samples uncertainty in K_d for transport through clayey soil; waste assumes this distribution also
Kd_Dist (Sandy Soil)	Samples uncertainty in K_d for transport through sandy soil
Clay_thickness_stoch	Samples uncertainty in clayey thickness within VZ
Upper_Sandy_Stoch	Samples uncertainty in sandy thickness within VZ
FinalWasteThickness_ST	Samples uncertainty of waste layer thickness after compaction for STs
FinalWasteThickness_ET	Samples uncertainty of waste layer thickness after compaction for ETs

4.4.6. Dashboard User Interface

The home screen of the GoldSim® ELLWF Trench System Model is shown in Figure 4-70. The model at this level contains ten containers and two hyperlinks. Choosing the “Home Dashboard” hyperlink (upper right) accesses the “Home Dashboard for the Trench Model” (Figure 4-71) where the user can move to the Model Switches and Trenches dashboards (Figure 4-72 and Figure 4-73, respectively). The “Home Dashboard for the Trench Model” also contains the Simulation Settings and Run Model buttons.

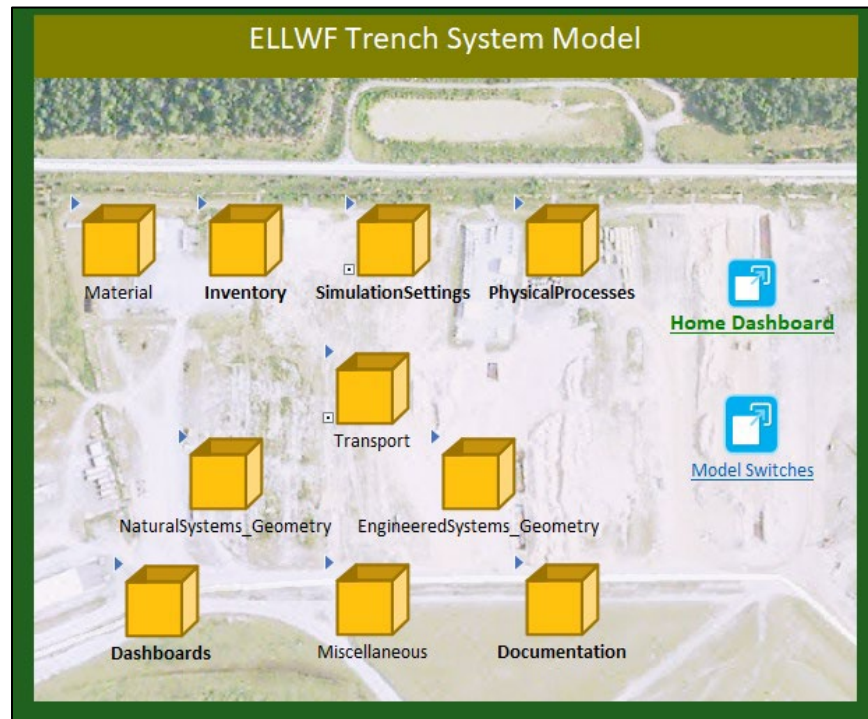


Figure 4-70. Top-Level Container of GoldSim® Trench System Model (Wohlwend, 2020; Figure 2-10)

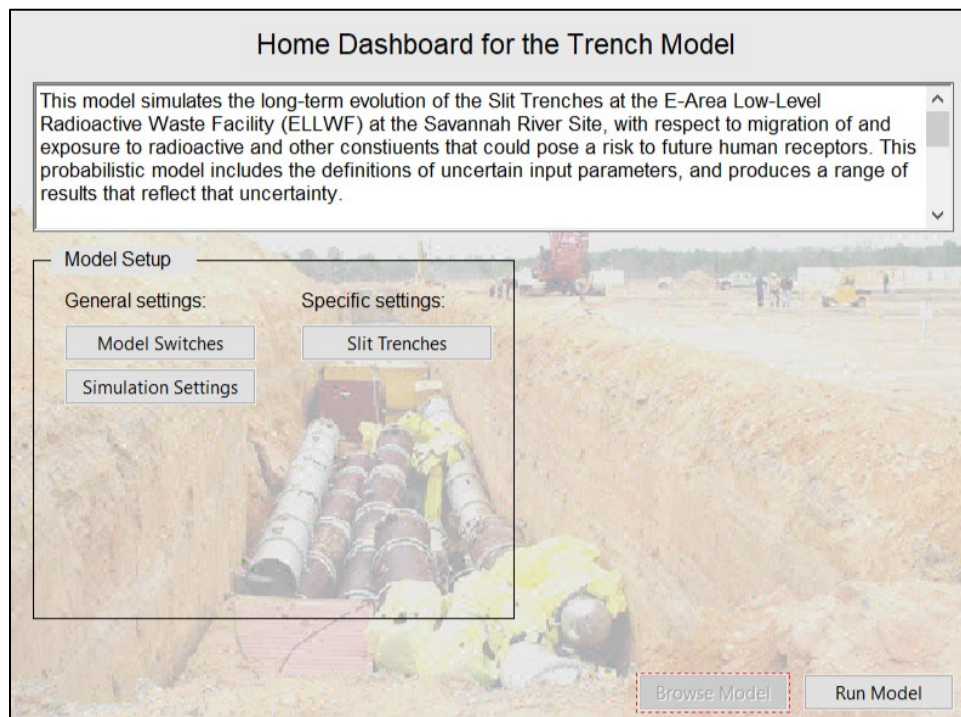
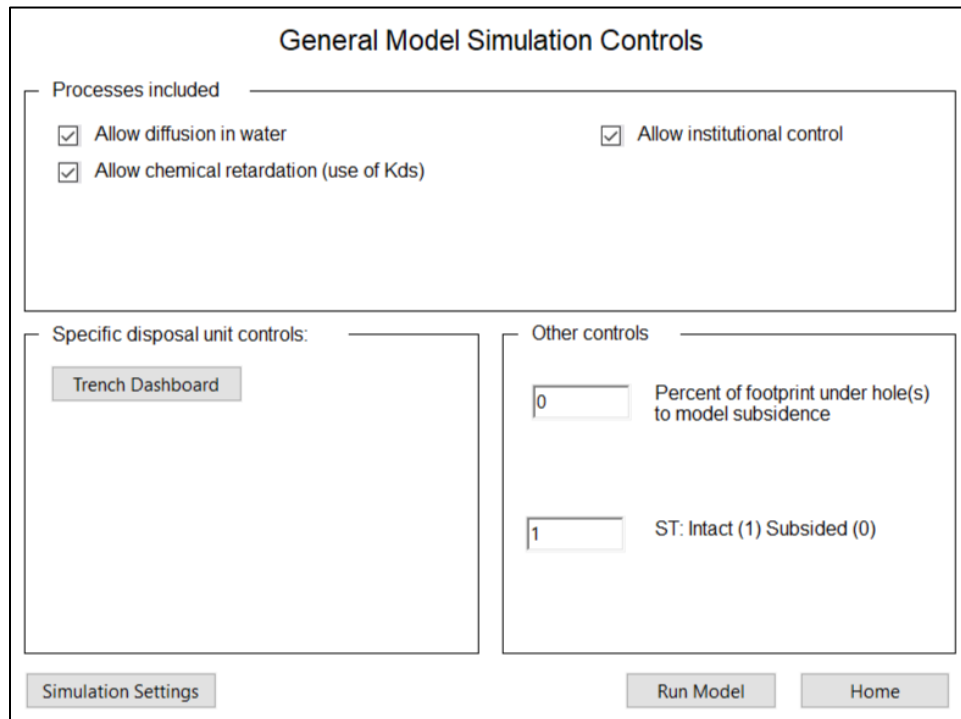


Figure 4-71. Home Dashboard for Trench System Model (Wohlwend and Aleman, 2020; Figure 4-2)



General Model Simulation Controls

Processes included

- ☒ Allow diffusion in water
- ☒ Allow institutional control
- ☒ Allow chemical retardation (use of Kds)

Specific disposal unit controls:

Trench Dashboard

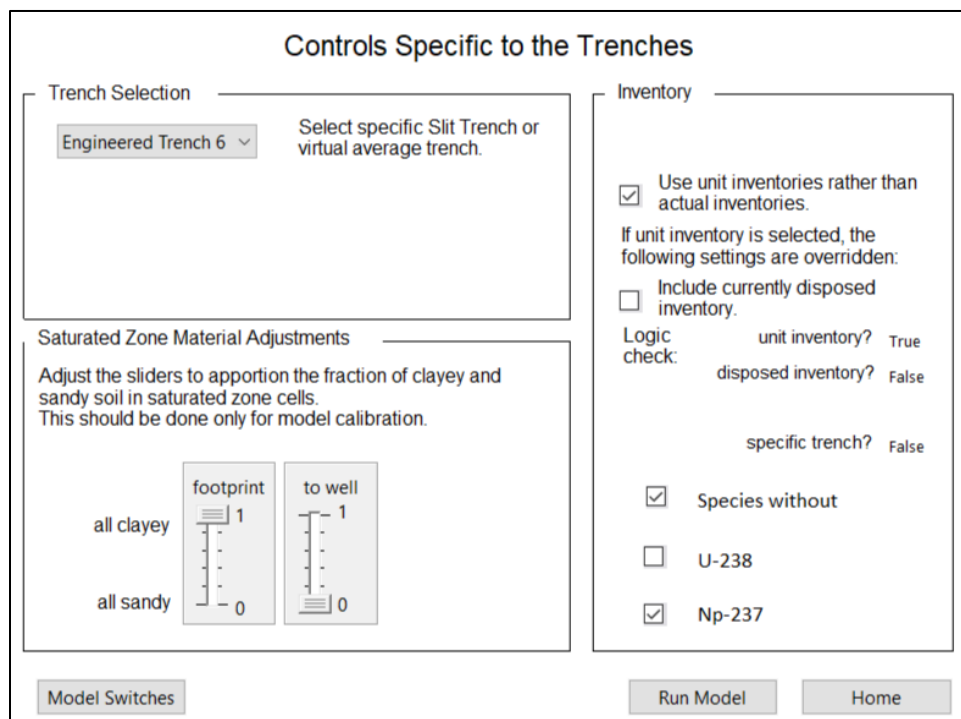
Other controls

0 Percent of footprint under hole(s) to model subsidence

1 ST: Intact (1) Subsided (0)

Simulation Settings Run Model Home

Figure 4-72. General Model Simulation Controls Dashboard (Wohlwend and Hamm, 2020; Figure 2-12)



Controls Specific to the Trenches

Trench Selection

Engineered Trench 6 Select specific Slit Trench or virtual average trench.

Saturated Zone Material Adjustments

Adjust the sliders to apportion the fraction of clayey and sandy soil in saturated zone cells. This should be done only for model calibration.

all clayey footprint 1 to well 1

all sandy 0 0

Inventory

- ☒ Use unit inventories rather than actual inventories.

If unit inventory is selected, the following settings are overridden:

- ☐ Include currently disposed inventory.

Logic check: unit inventory? True

disposed inventory? False

specific trench? False

- ☒ Species without
- ☐ U-238
- ☒ Np-237

Model Switches Run Model Home

Figure 4-73. Controls Specific to Trenches (Wohlwend and Hamm, 2020; Figure 2-13)

By clicking the Model Switches hyperlink in Figure 4-71, the user accesses the “General Model Simulation Controls” dashboard shown in Figure 4-72. Here, the user can choose to allow diffusion in water, chemical retardation, and institutional control. This dashboard also controls the subsidence parameters that are used in the VZ portion of the model. Specific DU controls can be selected via the Trenches dashboard button (Figure 4-73). The Trenches dashboard enables the user to select which trench to model, inventory parent(s) to run, and inventory options. Lastly, the “General Model Simulation Controls” dashboard includes the Simulation Settings, Run Model, and Home buttons.

The Transport container in the GoldSim® System Model contains the VZ models for ETs and STs as shown in Figure 4-74. The WasteZone_ET06 and VadoseZone_ET06 containers encapsulate the ET VZ models. The WasteZoneST and VadoseZoneST localized containers encapsulate the ST VZ models.

The GoldSim® ET and ST VZ models are described in detail in Sections 4.4.8 and 4.4.9, respectively.

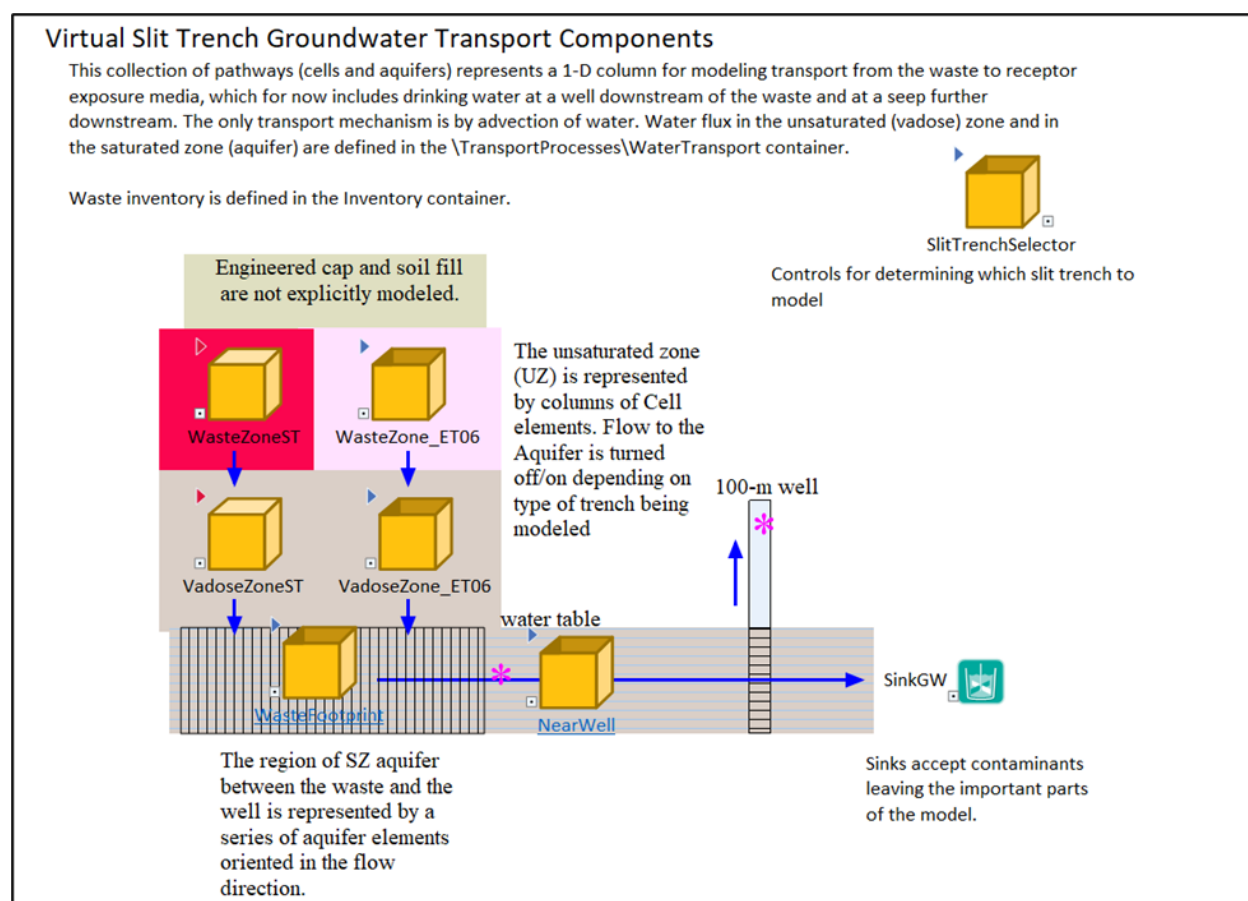


Figure 4-74. GoldSim® Vadose Zone Models for Slit and Engineered Trenches in Transport Container (Wohlwend and Aleman, 2020; Figure 4-5)

4.4.7. Layout and Structure

An overview of the layout and structure of the ELLWF Trench System Model, as represented on the home screen (Figure 4-70), is provided below. Container names are italicized and enclosed in quotation marks.

- “*Material*” contains definitions of the contaminant species and their associated decay rates as well as material properties of the physical materials that comprise the porous media and the fluid medium (water).
- “*Inventory*” includes definitions of the radionuclide inventory for each DU.
- “*Simulation Settings*” defines the simulation controls and has two sub-containers.
 - “*Chronology*” defines the conditions and status of the site.
 - “*Trench_Events*” includes the timing of operational start/end, interim closure, and final closure.
 - “*Switches*” includes multiple switches that can be used to control the behavior of the model and to investigate the effects of model assumptions; most switches are controlled through dashboard controls.
- “*PhysicalProcesses*” defines processes influencing contaminant transport.
 - “*WaterTransport_Vadose*” includes data elements that describe water advection in the unsaturated (vadose) zone for the ET; ST advection is handled within the ST transport containers.
 - “*Subsidence*” describes dynamic compaction.
- “*Documentation*” provides useful illustrations of the saturated zone and plume function.
- “*Miscellaneous*” provides numerical data values used throughout the model that represent small/large values and sets up arrays for the modeled species.
- “*Dashboards*” stores the dashboards in the model. Generally, all dashboards are navigable from the others with the principal connection point located in the Home dashboard.
- “*EngineeredSystems_Geometry*” includes parameters for the dimensions of the DUs including area, length, and width as well as the thickness of the waste zone before and after dynamic compaction.
- “*NaturalSystems_Geometry*” defines parameters for dimensions, rates, and so on for the natural materials surrounding the waste DUs including:
 - Clayey layer thickness
 - Sandy layer thickness
- “*Transport*” includes containers that hold the trench GW transport components. Figure 4-74 is a screen capture of the “*Transport*” container in GoldSim[®].
 - “*WasteZoneST*” consists of two containers that hold the elements that model transport through the waste zone within a ST: one associated with the fraction of waste that is crushable at the end of IC and the other associated with the fraction of waste that is non-crushable at the end of IC.

- “WasteZone_Intact” includes elements that define the geometry of the waste cells as well as cell pathway elements that simulate flow and transport of crushable waste inventory through the waste zone of a ST (Section 4.4.9).
 - “WasteZone_Subsidied” includes elements that define the geometry of the waste cells as well as cell pathway elements that simulate flow and transport of non-crushable waste inventory through the waste zone of a ST (Section 4.4.9).
- “WasteZone_ET06” consists of two containers that hold the elements that model transport through the waste zone within an ET: one associated with the fraction of waste that is crushable at the end of IC and the other associated with the fraction of waste that is non-crushable at the end of IC.
 - “WasteZone_Crushed” includes elements that define the geometry of the waste cells as well as cell pathway elements that simulate flow and transport of crushable waste inventory through the waste zone of an ET (Section 4.4.8).
 - “WasteZone_Noncrushed” includes elements that define the geometry of the waste cells as well as cell pathway elements that simulate flow and transport of non-crushable waste inventory through the waste zone of an ET (Section 4.4.8).
- “VadoseZoneST” includes two containers that hold elements which model transport through the VZ of the STs: one associated with the crushable waste fraction at the end of IC and the other associated with the non-crushable waste fraction at the end of IC.
 - “VadoseZone_Intact” includes elements that define the geometry of the VZ cells as well as cell pathway elements that simulate flow and transport of crushable waste inventory through the VZ (Section 4.4.9).
 - “VadoseZone_Subsidied” includes elements that define the geometry of the VZ cells as well as cell pathway elements that simulate flow and transport of non-crushable waste inventory through the VZ (Section 4.4.9).
- “VadoseZone_ET06” includes two containers that hold elements which model transport through the VZ of the ETs: one associated with the crushable waste fraction at the end of IC and the other associated with the non-crushable waste fraction at the end of IC.
 - “VadoseZone_Crushed” includes elements that define the geometry of the VZ cells as well as cell pathway elements that simulate flow and transport of crushable waste inventory through the VZ (Section 4.4.8).
 - “VadoseZone_Noncrushed” includes elements that define the geometry of the VZ cells as well as cell pathway elements that simulate flow and transport of non-crushable waste inventory through the VZ (Section 4.4.8).

- “*WasteFootprint*” includes elements that define the geometry of the footprint cells as well as cell pathway elements that simulate flow from the unsaturated zone into each cell positioned under the waste footprint (Section 4.4.11).
- “*NearWell*” includes elements that simulate flow and transport from the edge of the building to the 100-meter well (Section 4.4.11).

4.4.8. Vadose Zone Model for Engineered Trenches

GoldSim® VZ models of the ELLWF trenches are built using the Contaminant Transport Module in GoldSim® Ver. 12.1.4 #235 (October 22, 2019). A GoldSim® cell pathway element is used to build a column and network of cells for modeling the advective and diffusive transport of radionuclides below the OSC to the water table in the ST and ET, respectively. The cell pathway allows inventory transfer within the WZ during dynamic compaction. The cell pathway accommodates back diffusion which can occur after dynamic compaction of the waste zone. The GoldSim® ET Trench Model includes intact and subsidence cell pathway elements. The GoldSim® ST Trench Model, which is described in Section 4.4.9, includes intact, between-segment, and subsidence cell pathway elements. Dynamic compaction of the waste zone and subsidence are assumed to occur at the end of IC.

The conceptual model of the ET VZ is shown schematically in Figure 4-75.

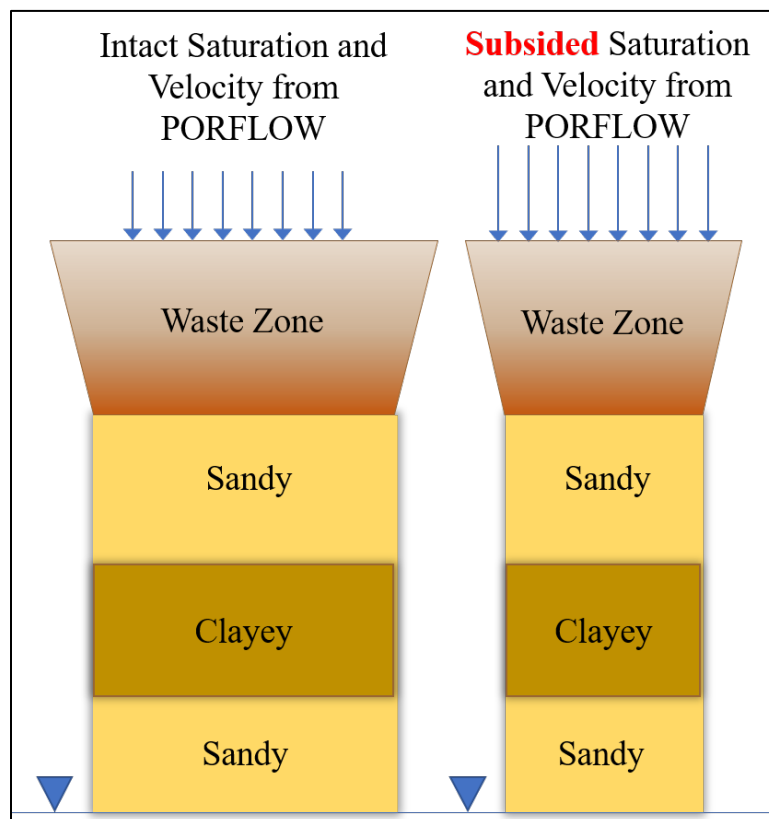


Figure 4-75. Schematic of GoldSim® Vadose Zone Conceptual Model for Engineered Trenches (Wohlwend and Aleman, 2020; Figure 4-6)

The closure cap is not explicitly modeled but accounted for by utilizing volume-averaged vertical velocities and water saturations extracted from the PORFLOW ET VZ flow models. The VZ is modeled by a series of 1-D WZ (spanning the entire thickness of the UVZ) and LVZ (comprised of Sandy and Clayey layers) cell pathways. The cell pathways are connected via advective and diffusive fluxes. Lateral advective and diffusive fluxes to and from the overall ET footprint are not modeled in the GoldSim® ET VZ model. The two series represent areas within the trench that contain either crushable containers (intact cap case) or non-crushable containers (subsided cap case) as described in Section 4.4.3.

The WasteZone_ET06 container includes the WasteZone_Crushed and WasteZone_Noncrushed containers as shown in Figure 4-76. These containers encapsulate the GoldSim® ET WZ models.

The VadoseZone_ET06 container includes the VadoseZone_Crushed and VadoseZone_Noncrushed containers as shown in Figure 4-77. These containers encapsulate the GoldSim® ET VZ models.

The WasteZone_Crushed and WasteZone_Noncrushed containers have advective and diffusive flux links to the VadoseZone_Crushed and VadoseZone_Noncrushed containers, respectively.

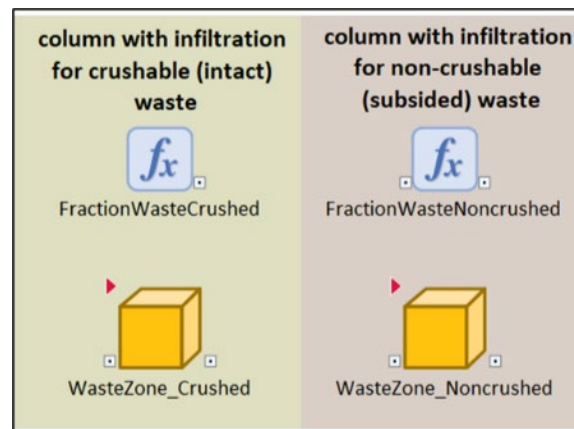


Figure 4-76. GoldSim® Engineered Trench Waste Zone Containers (Wohlwend and Aleman, 2020; Figure 4-7)

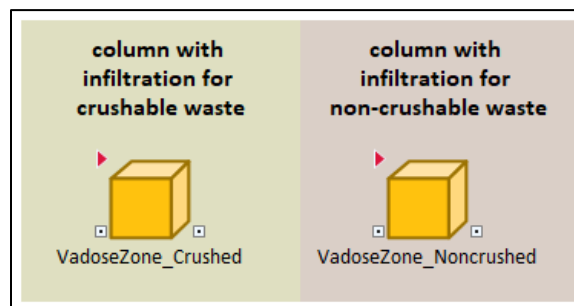


Figure 4-77. GoldSim® Engineered Trench Lower Vadose Zone Containers (Wohlwend and Aleman, 2020; Figure 4-8)

Vertical Darcy velocities and water saturations from the PORFLOW ET VZ flow simulations are extracted for each steady-state simulation (time period) and averaged within user-specified material zones for the GoldSim® ET VZ model. Volume-averaged vertical Darcy velocities are computed for each intact and subsided cell pathway column (WZ and LVZ) within the GoldSim® ET VZ model.

Figure 4-78 shows ET06 Case01 vertical velocities through the WZ and LVZ. The AVERAGE NDC (non-dynamic compacted) and DC (dynamic compacted) velocities are input data into the Vel_Intact_Case01_ET06_Waste time series element (WaterTransport_Vadose). The AVERAGE of the Sandy1, Sandy2, and TanClay velocities are input data into the Velocity_intact_Case01_ET06_VZ. These velocities are used to compute volumetric flowrates in the Flowrate_Intact_Case01 expression elements in WasteZone_Crushed and VadoseZone_Crushed.

Figure 4-79 displays ET Case11b vertical velocities through the WZ and LVZ in Hole 2. The AVERAGE NDC and DC velocities are input data into the Velocity_ET06_Hole2_Waste time series element (WaterTransport_Vadose). The AVERAGE of the Sandy1, Sandy2, and TanClay velocities are input data into the Velocity_ET06_Hole2_VZ time series element. These velocities are used to compute volumetric flowrates in the Flowrate_H2 expression elements (WasteZone_Noncrushed and VadoseZone_Noncrushed).

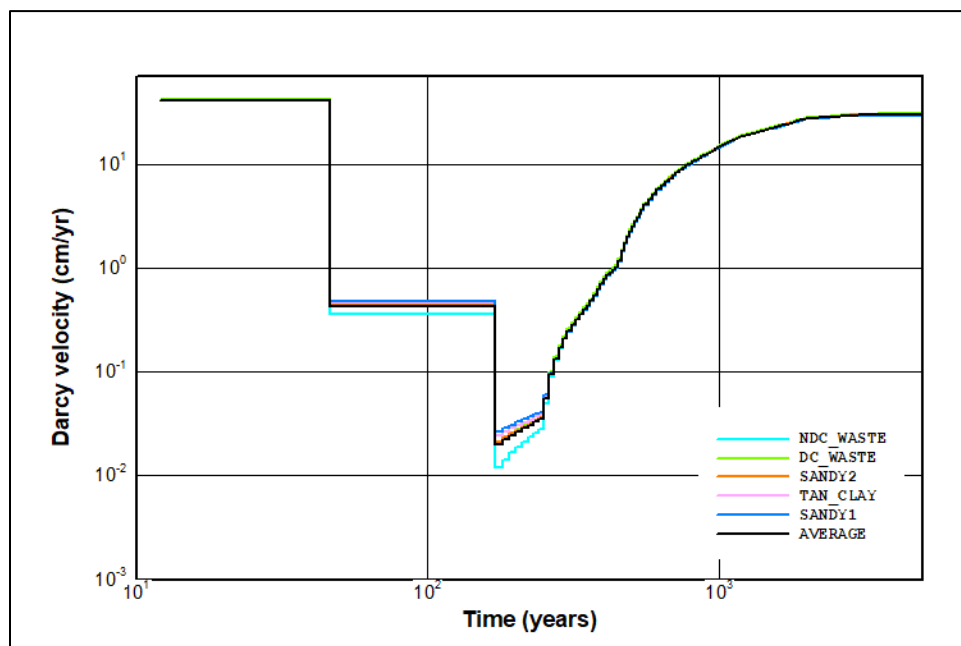


Figure 4-78. Engineered Trench Case01 Vertical Velocities in Waste Zone and Lower Vadose Zone (Wohlwend and Aleman, 2020; Figure 4-9)

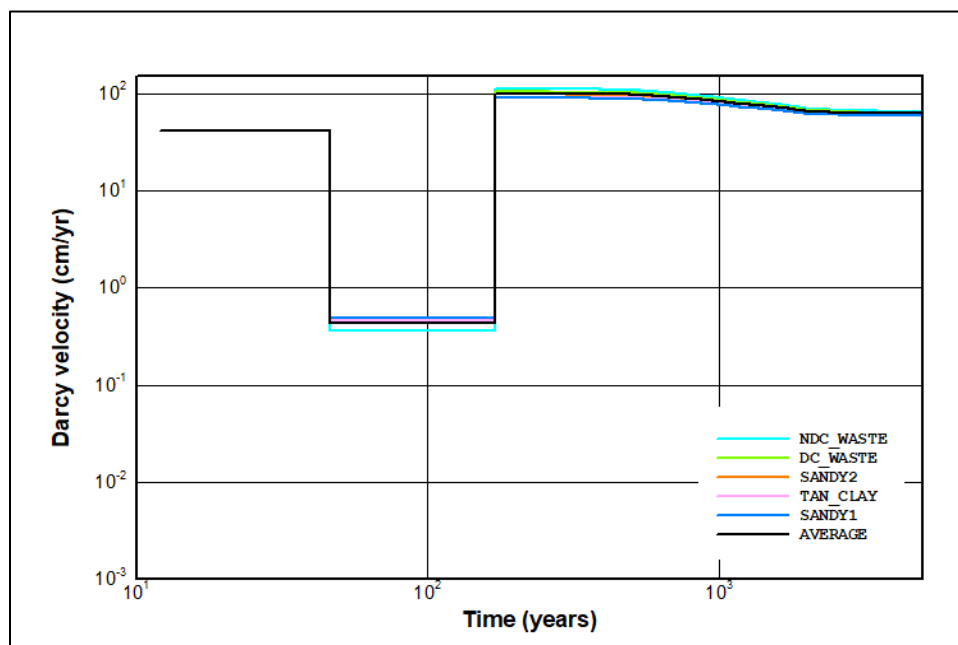


Figure 4-79. Engineered Trench Case11b Vertical Velocities in Waste Zone and Lower Vadose Zone in Hole 2 (Wohlwend and Aleman, 2020; Figure 4-10)

4.4.8.1. Intact and Subsided Waste Zone Models

The WZ is represented by a series of cell pathways. The flow area is the product of the trench width (157 feet) and the length (656 feet). The area is also multiplied by the fraction of the waste that is either crushable or non-crushable depending on which series the cells represent. The fraction of non-crushable waste (Hole 2 area) is initially set to 2% of ET waste area but is modified during calibration to match the PORFLOW subsided flux to the water table. To model dynamic compaction at the end of IC, the WZ is separated into two sections: 22 cells in the upper WZ (NDC_WASTE) and six cells in the lower WZ (DC_WASTE) as shown in Figure 4-80. The height of the NDC_WASTE and DC_WASTE cells are $13.5 \text{ feet} \div 22 \text{ cells}$ (0.6136 feet) and $2.5 \text{ feet} \div 6 \text{ cells}$ (0.4167 feet), respectively, for ET and $4.9 \text{ feet} \div 12 \text{ cells}$ (0.41 feet) and $11.1 \text{ feet} \div 16 \text{ cells}$ (0.2115 feet), respectively, for ST.

Figure 4-81 and Figure 4-82 show the cell pathway properties for WasteZone_02_1. An initial inventory of 1.0 gmole is assigned to each parent radionuclide. The parent radionuclide inventories are converted to grams internally for use throughout the WZ and VZ models. The initial inventory is distributed between crushable and non-crushable WZs on the date the trench begins operations. Within each crushable and non-crushable WZ, species inventories are further distributed between upper and lower WZs.

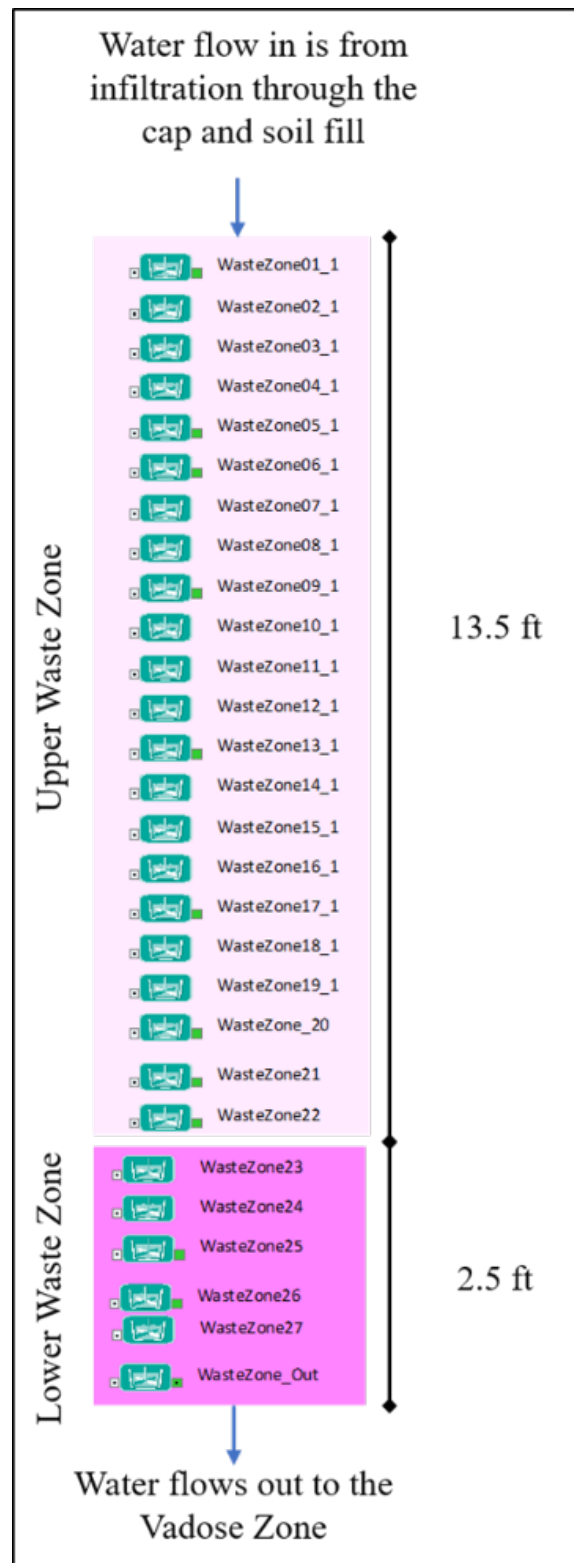


Figure 4-80. GoldSim® Waste Zone Cell Pathways for Engineered Trenches (Wohlwend, 2020; Figure 2-6)

Cell Pathway Properties : WasteZone02_1

Definition Inflows Outflows Diffusive Fluxes

Element ID: WasteZone02_1 Appearance...

Description:

Media in Cell

Medium	Amount	F	H	S
Water	UpperWasteCellVolume * WaterContent_NDC			
Waste	UpperWasteCellVolume * WasteDensity			

Add Medium Delete Medium

Cell Inventory

Cumulative Input

Discrete Changes: DisposalEvent_Upper_ZeroMassInNDC

Save Masses in Pathway

☐ Output Precipitated Mass

☐ Final Values ☐ Time History

OK Cancel Help

Cell Pathway Properties : WasteZone02_1

Definition Inflows Outflows Diffusive Fluxes

List of Inflows

From Pathway	To Pathway	Medium
WasteZone01_1	WasteZone02_1	Water

Add Inflow Delete Inflow

Properties of Selected Inflow

Inflow: WasteZone02_1.Water_from_WasteZone01_1

Link Type: Coupled

Flow Rate: Flowrate_Intact

Species flux rates: ☐ Save Final Values ☐ Save Time History

OK Cancel Help

Figure 4-81. WasteZone_02_1 Cell Pathway Properties: Definition and Inflows (Wohlwend and Aleman, 2020; Figure 4-12)

Cell Pathway Properties : WasteZone02_1

Definition Inflows Outflows Diffusive Fluxes

List of Outflows

From Pathway	To Pathway	Medium
WasteZone02_1	WasteZone03_1	Water

Add Outflow Delete Outflow

Properties of Selected Outflow

Outflow: WasteZone02_1.Water_to_WasteZone03_1

Link Type: Coupled

Flow Rate: Flowrate_Intact

Species flux rates: ☐ Save Final Values ☐ Save Time History

Total outflow rate of Water = 2859 m³/yr

OK Cancel Help

Cell Pathway Properties : WasteZone02_1

Definition Inflows Outflows Diffusive Fluxes

List of Diffusive Fluxes

From Pathway	Fluid	To Pathway	Fluid
WasteZone02_1	Water	WasteZone03_1	Water
WasteZone01_1	Water	WasteZone02_1	Water

Add Flux Delete Flux

Properties of Selected Diffusive Flux

Diffusive Flux: WasteZone02_1.Water_to_Water_in_WasteZone03_1

Link Type: Coupled

Length: UpperWasteCellThickness / UpperWasteCellThickness /

Porous Medium: Waste Waste

Diffusive Area: DisposalUnitArea_5Tonushed * WaterDiffusion_Switch

Species flux rates: ☐ Save Final Values ☐ Save Time History

OK Cancel Help

Figure 4-82. WasteZone_02_1 Cell Pathway Properties: Outflows and Diffusive Fluxes (Wohlwend and Aleman, 2020; Figure 4-13)

Discrete change elements DisposalEvent_Upper and DisposalEvent_Lower trigger the placement of species inventories in upper and lower WZ cells, respectively. The species inventories distributed to each crushable upper and lower WZ cell are computed in Eq. (4-39) and Eq. (4-40), respectively.

$$I_{NDC_cell,crushed} = I_P f_{crushed} \frac{H_{NDC_cell}}{H_{WZ}} \quad \text{Eq. (4-39)}$$

$$I_{DC_cell,crushed} = I_P f_{crushed} \frac{H_{DC_cell}}{H_{WZ}} \quad \text{Eq. (4-40)}$$

where:

$I_{NDC_cell,crushed}$	Species inventory of NDC cell crushed (g)
$I_{DC_cell,crushed}$	Species inventory of DC cell crushed (g)
I_P	Inventory of parent radionuclide (g)
$f_{crushed}$	Fraction of crushable waste, 0.98 (unitless)
H_{NDC_cell}	Height of NDC waste cell, 13.5 ft ÷ 22 cells (ft)
H_{DC_cell}	Height of DC waste cell, 2.5 ft ÷ 6 cells (ft)
H_{WZ}	Height of the WZ (16 ft)

The species inventories distributed to each non-crushable upper and lower WZ cell are computed in Eq. (4-41) and Eq. (4-42), respectively.

$$I_{NDC_cell,noncrushed} = I_P f_{noncrushed} \frac{H_{NDC_cell}}{H_{WZ}} \quad \text{Eq. (4-41)}$$

$$I_{DC_cell,noncrushed} = I_P f_{noncrushed} \frac{H_{DC_cell}}{H_{WZ}} \quad \text{Eq. (4-42)}$$

where:

$I_{NDC_cell,noncrushed}$	Species inventory of NDC cell noncrushed (g)
$I_{DC_cell,noncrushed}$	Species inventory of DC cell noncrushed (g)
$f_{noncrushed}$	Fraction of non-crushable waste, 0.02 (unitless)

When the final cap is emplaced at end of IC, the species inventories (Mass_In_Pathway) within the upper WZ are transferred to the lower WZ using a series of discrete change elements (AddMassFromNDC, ZeroMassinNDC and AddMasstoDC) as well as a mass collector cell pathway (MassCollector). The AddMassFromNDC element sums the Mass_In_Pathway from WasteZone01_1 to WasteZone22 cell pathways and makes them available in the MassCollector.

The ZeroMassinNDC element replaces the species inventories in the upper WZ with zero values. The AddMassToDC element adds and distributes the species inventories from the upper WZ evenly among the lower WZ cell pathways. Figure 4-83 shows the ET water saturations in the WZ for intact and subsided cases. These saturations are time-series inputs and are used to compute water contents in the Water Content expression elements.

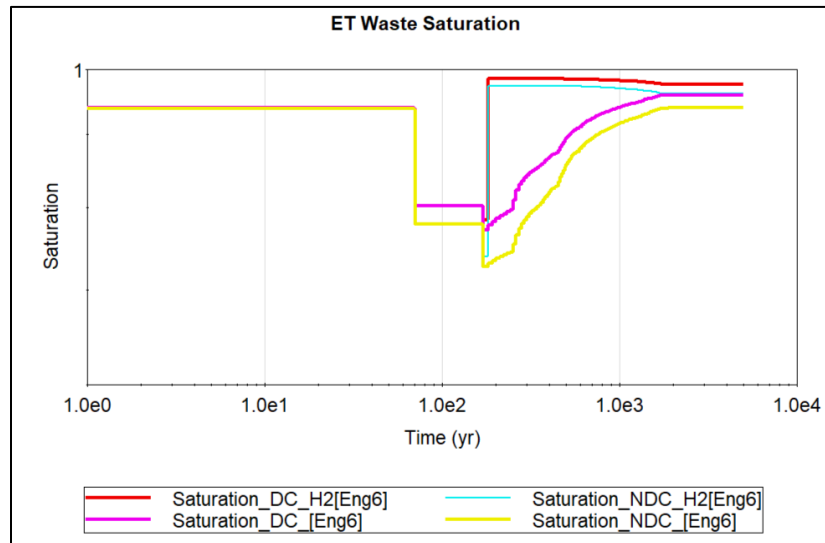


Figure 4-83. Engineered Trench Water Saturations in Waste Zone (Wohlwend and Aleman, 2020; Figure 4-14)

4.4.8.2. Vadose Zone Models

Advective and diffusive species mass flow rates leave the WZ and enter the upper sandy layer (SANDY2) of each intact and subsided LVZ. Each section is modeled by a series of cell pathways. After leaving the upper sandy layer, species mass flow rates go through cell pathways in the clayey layer (TAN_CLAY) and then cell pathways in the lower sandy layer (SANDY1). Although many DUs have two layers of clayey soil separated by sandy layers, the clayey layers are combined in the System Model. This is consistent with the PORFLOW VZ Model and produces only a ~1% difference in flux to the water table (Danielson, 2019c). Figure 4-84 displays the representation of the LVZ. The height of the SANDY2, TAN_CLAY and SANDY1 cells are listed in Table 4-40.

Table 4-40. Upper and Lower Vadose Zone Sandy and Clayey Thicknesses (Wohlwend and Aleman, 2020; Table 6-7)

Disposal Unit	Zone Thickness (feet)		
	Sandy Above ¹	Clayey ¹	Sandy Below ¹
ST06	23	2	10
ST09	34	11	10
ET06	6	10	10

Notes:

¹ Refer to Figure 4-75.

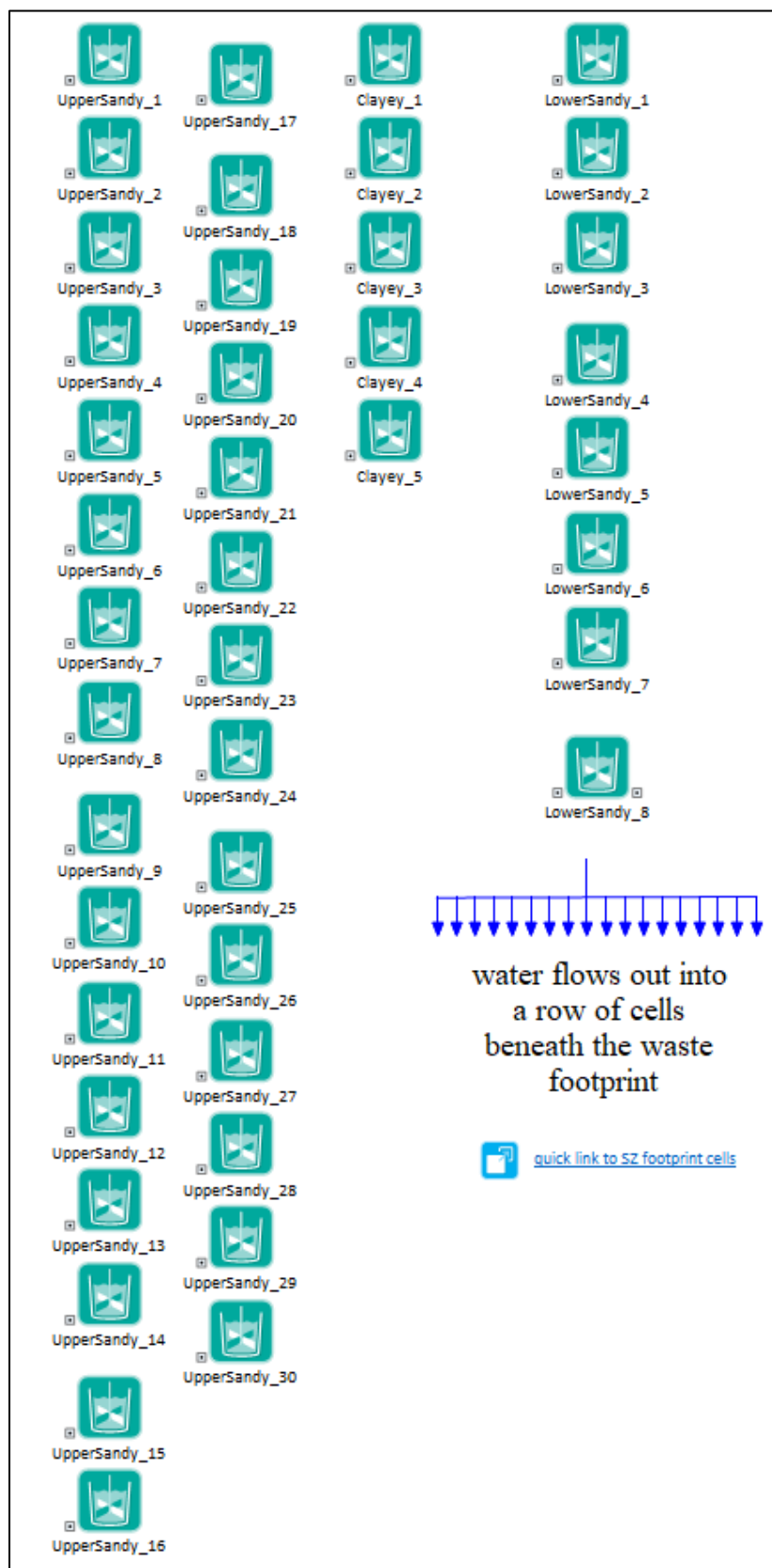


Figure 4-84. GoldSim® Engineered Trench Lower Vadose Zone Cell Pathways (Wohlwend and Aleman, 2020; Figure 4-16)

Figure 4-85 and Figure 4-86 show the cell pathway properties for Clayey_1.

Figure 4-85: Clayey_1 Cell Pathway Properties: Definition and Inflows

Definition Tab:

- Parent ID: Clayey_1
- Description:
- Media in Cell:

Medium	Amount	F	H	S
Water	DisposalUnitArea_STCrushed*ClayeyCell_Thi	<input checked="" type="checkbox"/>	<input checked="" type="checkbox"/>	<input checked="" type="checkbox"/>
ClayeySoil	DisposalUnitArea_STCrushed*ClayeyCell_Thi	<input type="checkbox"/>	<input type="checkbox"/>	<input type="checkbox"/>
- Cell Inventory: Initial Inventory
- Discrete Changes:
- Save Masses in Pathway:
 - ☐ Output Precipitated Mass
 - ☐ Final Values
 - ☒ Time History

Inflows Tab:

List of Inflows:

From Pathway	To Pathway	Medium
UpperSandy_30	Clayey_1	Water

Properties of Selected Inflow:

- Inflow: Clayey_1.Water_from_UpperSandy_30
- Link Type: Coupled
- Flow Rate: Flowrate_intact
- Species flux rates: ☐ Save Final Values ☐ Save Time History

Figure 4-85. Clayey_1 Cell Pathway Properties: Definition and Inflows (Wohlwend and Aleman, 2020; Figure 4-17)

Figure 4-86: Clayey_1 Cell Pathway Properties: Outflows and Diffusive Fluxes

Outflows Tab:

List of Outflows:

From Pathway	To Pathway	Medium
Clayey_1	Clayey_2	Water

Properties of Selected Outflow:

- Outflow: Clayey_1.Water_to_Clayey_2
- Link Type: Coupled
- Flow Rate: Flowrate_intact
- Species flux rates: ☐ Save Final Values ☒ Save Time History

Total outflow rate of Water = 2859 m³/yr

Diffusive Fluxes Tab:

List of Diffusive Fluxes:

From Pathway	Fluid	To Pathway	Fluid
Clayey_1	Water	Clayey_2	Water
UpperSandy_30	Water	Clayey_1	Water

Properties of Selected Diffusive Flux:

- Diffusive Flux: Clayey_1.Water_to_Water_in_Clayey_2
- Link Type: Coupled
- Length: Clayey_1: ClayeyCell_Thickness/2, Clayey_2: ClayeyCell_Thickness/2
- Porous Medium: ClayeySoil
- Diffusive Area: DisposalUnitArea_STCrushed * WaterDiffusion_Switch
- Species flux rates: ☐ Save Final Values ☒ Save Time History

Figure 4-86. Clayey_1 Cell Pathway Properties: Outflows and Diffusive Fluxes (Wohlwend and Aleman, 2020; Figure 4-18)

Figure 4-87 presents ST06 water saturations in the VZ for the LS (lower sandy), TC (Tan Clay), and US (upper sandy) layers for the intact and subsided (H2) cases. These time-series are used to compute the water content for the VZ cells.

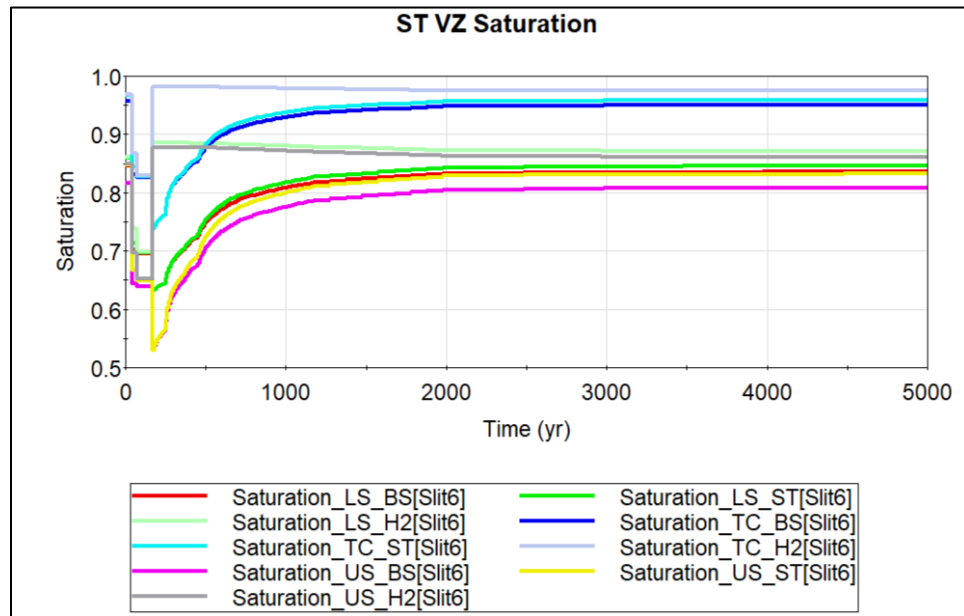


Figure 4-87. Slit Trench Water Saturations in the Vadose Zone

Figure 4-88 displays ET water saturations in the VZ. The LS (lower sandy), TC (Tan Clay), and US (upper sandy) layers for the intact and subsided (H2) cases. These time-series are again used to compute the water content for the VZ cells

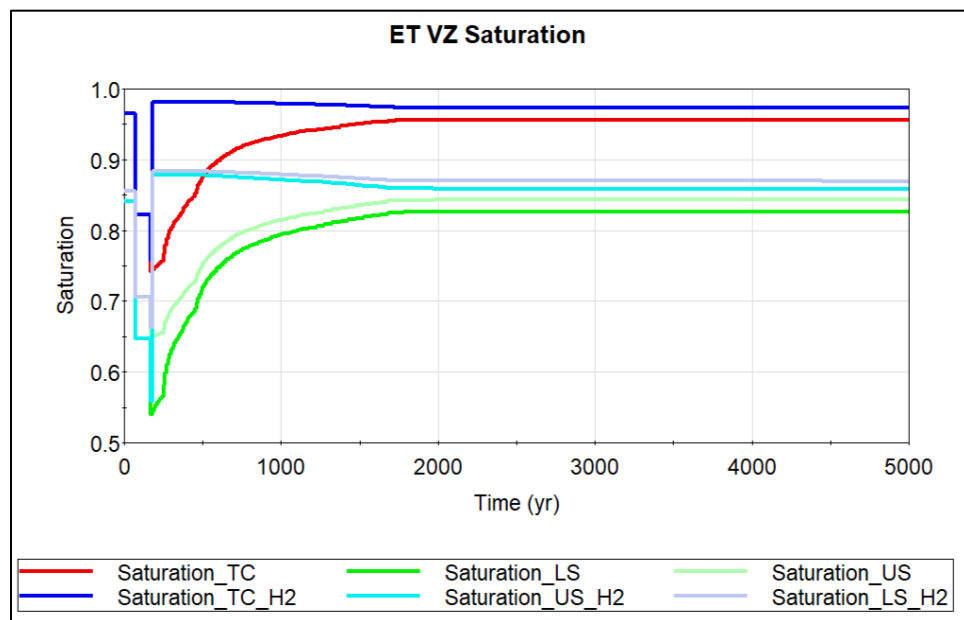


Figure 4-88. Engineered Trench Water Saturations in the Vadose Zone

4.4.9. Vadose Zone Model for Slit Trenches

The initial conceptual model of the GoldSim® ST VZ is shown schematically in Figure 4-89. The ST VZ model includes the five individual ST *segments* (ST1 thru ST5; not to be confused with Slit Trenches ST01 though ST05) separated by 10-foot-wide non-waste segments and

20-foot-wide non-waste segments located to the outside of segments ST1 and ST5. A single, intact ST segment advects and diffuses into non-waste segments on either side of the segment. The subsided ST segment advects and diffuses from the hole to the intact portion of the ST segment and into non-waste segments on either side of the subsided segment. The advective fluxes from the ST segment to the non-waste segment are not modelled due to the lack of detailed water budget information within the ST layout. Advective and diffusive fluxes to and from the overall ST footprint are not modeled in the GoldSim ST VZ model.

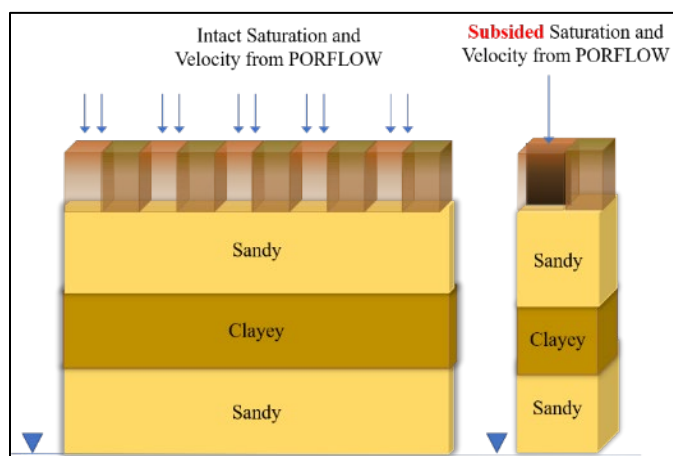


Figure 4-89. Schematic of the GoldSim® Five-Segment Slit Trench Vadose Zone Model (Wohlwend and Aleman, 2020; Figure 4-21)

To reduce the computational cost for the GoldSim® ST VZ Model, symmetry of the ST layout is utilized to separately model a single intact and subsided ST segment as shown in Figure 4-90 and Figure 4-91, respectively. The intact and subsided ST segments are further simplified as shown on the righthand side of the figures. The subsidence case evaluated is Hole 2 located within trench segment ST5 as shown in Figure 4-26. In Figure 4-91, the black downward arrows represent the change in infiltration due to subsidence.

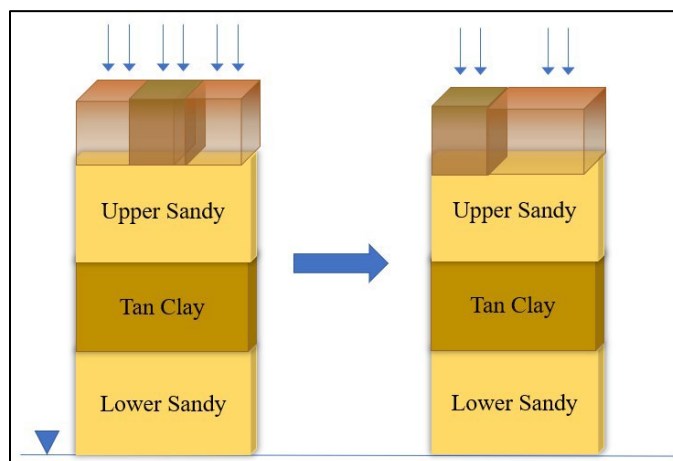


Figure 4-90. Schematic of GoldSim® Slit Trench Intact Segment (S1 to S4) Vadose Zone Model (Wohlwend and Aleman, 2020; Figure 4-22)

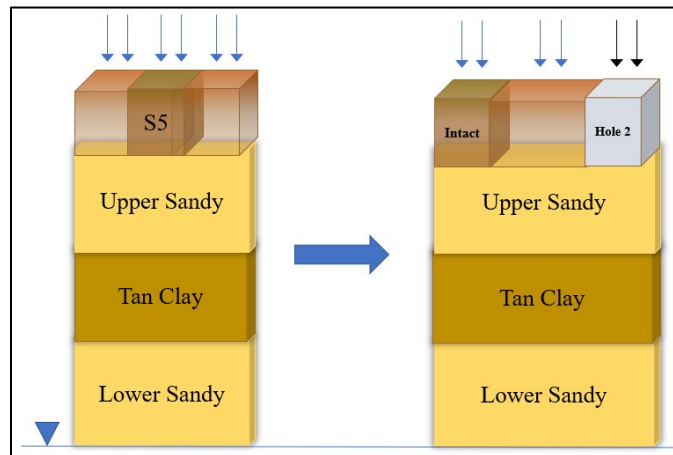


Figure 4-91. Schematic of GoldSim® Slit Trench Subsided Segment (S5) Vadose Zone Model (Wohlwend and Aleman, 2020; Figure 4-23)

The final ELLWF closure cap is not explicitly modeled but is accounted for by utilizing volume-averaged vertical Darcy velocities and water saturations extracted from the PORFLOW ST VZ flow models. The VZ is modeled by a series of WZ and non-waste zone (spanning the entire thickness of the UVZ) plus LVZ (comprised of Sandy and Clayey layers) cell networks. The cell networks are connected via advective and diffusive fluxes. The intact and subsided series represent areas within the trench that contain either crushable containers (intact cap case), non-waste, or non-crushable containers (subsided cap case) as described in Section 3.4.

The WasteZoneST container in Figure 4-74 includes the WasteZone_Intact and WasteZone_Subsided containers as shown in Figure 4-92. These localized containers encapsulate the GoldSim® ST WZ models.

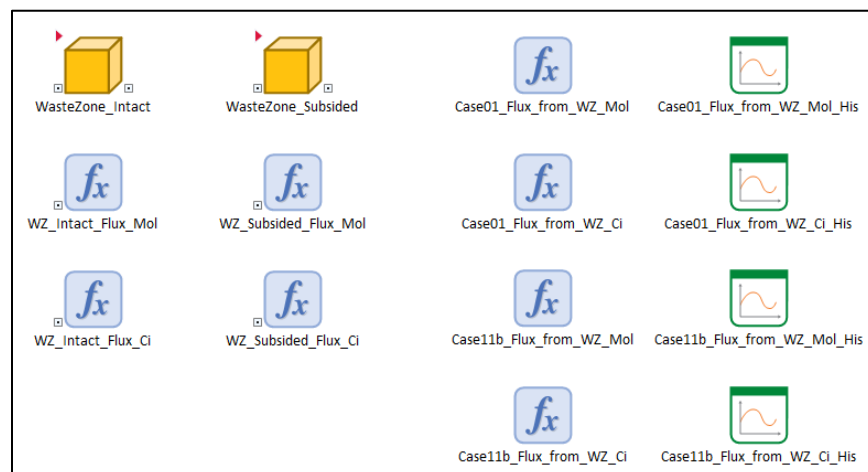


Figure 4-92. GoldSim® Slit Trench Waste Zone Containers (Wohlwend and Aleman, 2020; Figure 4-24)

The VadoseZoneST container in Figure 4-74 includes the VadoseZone_Intact and VadoseZone_Subsided containers as shown in Figure 4-93. These localized containers encapsulate the GoldSim® ST LVZ models. The WasteZone_Intact and WasteZone_Subsided containers have

advective and diffusive flux links to the VadoseZone_Intact and VadoseZone_Subsidied containers, respectively.

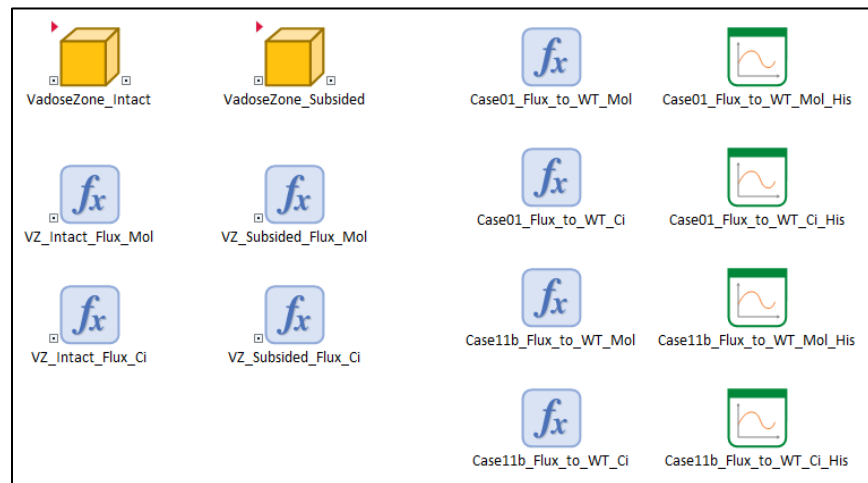


Figure 4-93. GoldSim® Slit Trench Lower Vadose Zone Containers (Wohlwend and Aleman, 2020; Figure 4-25)

Vertical Darcy velocities and water saturations from the PORFLOW ST VZ flow simulations are extracted for each steady-state simulation (time period) and averaged within user-specified material zones for the GoldSim® ST VZ model. Volume-averaged vertical Darcy velocities are computed for each intact and subsided cell network (WZ, UVZ, and LVZ) within the GoldSim® ST VZ model.

Figure 4-94 shows the ST06/ST Case01 average vertical velocities in segments ST1 through ST5 (WZ and LVZ). The AVERAGE velocities are input data into the Velocity_NDC_ST and Velocity_DC_ST time series elements (within /Transport/WasteZoneST/WasteZone_Intact container). These velocities are used to compute volumetric flowrates in the Flowrate_NDC_ST and Flowrate_DC_ST expression elements. The AVERAGE velocities are input data into the Velocity_US_ST, Velocity_TC_ST, and Velocity_LS_ST time series elements (within /Transport/VadoseZoneST/VadoseZone_Intact container). These velocities are used to compute volumetric flowrates in the Flowrate_US_ST, Flowrate_TC_ST and Flowrate_LS_ST expression elements.

Figure 4-95 presents the ST06/ST Case01 average vertical velocities between ST segments (BS) in the UVZ and LVZ. The AVERAGE velocities are input data into the Velocity_NDC_BS and Velocity_DC_BS time series elements (within /Transport/WasteZoneST/WasteZone_Intact container). These velocities are used to compute volumetric flowrates in the Flowrate_NDC_BS and Flowrate_DC_BS expression elements. The AVERAGE velocities are input data into the Velocity_US_BS, Velocity_TC_BS, and Velocity_LS_BS time series elements (within /Transport/VadoseZoneST/VadoseZone_Intact container). These velocities are used to compute volumetric flowrates in the Flowrate_US_BS, Flowrate_TC_BS and Flowrate_LS_BS expression elements.

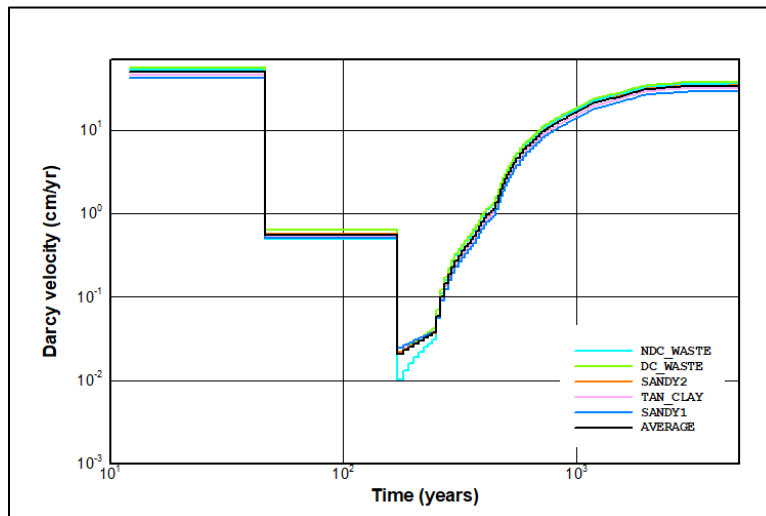


Figure 4-94. ST06/Slit Trench Case01 Average Vertical Velocities in Segments ST1 through ST5 [Waste Zone and Lower Vadose Zone] (Wohlwend and Aleman, 2020; Figure 4-26)

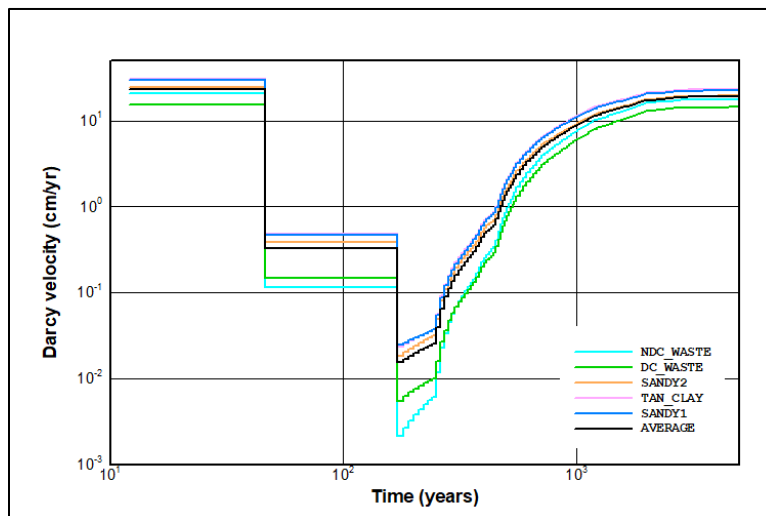


Figure 4-95. ST06/Slit Trench Case01 Average Vertical Velocities between Slit Trench Segments (Wohlwend and Aleman, 2020; Figure 4-27)

Figure 4-96 displays the ST06/ET Case11b vertical velocities through segment ST5 (WZ and LVZ). The AVERAGE velocities are input data into the Velocity_NDC_ST and Velocity_DC_ST time series elements (within /Transport/WasteZoneST/WasteZone_Subsided container). These velocities are used to compute volumetric flowrates in the Flowrate_NDC_ST and Flowrate_DC_ST expression elements. The AVERAGE velocities are also input data into the Velocity_US_ST, Velocity_TC_ST, and Velocity_LS_ST time series elements (within /Transport/VadoseZoneST /VadoseZone_Subsided container). These velocities are used to compute volumetric flowrates in the Flowrate_US_ST, Flowrate_TC_ST, and Flowrate_LS_ST expression elements.

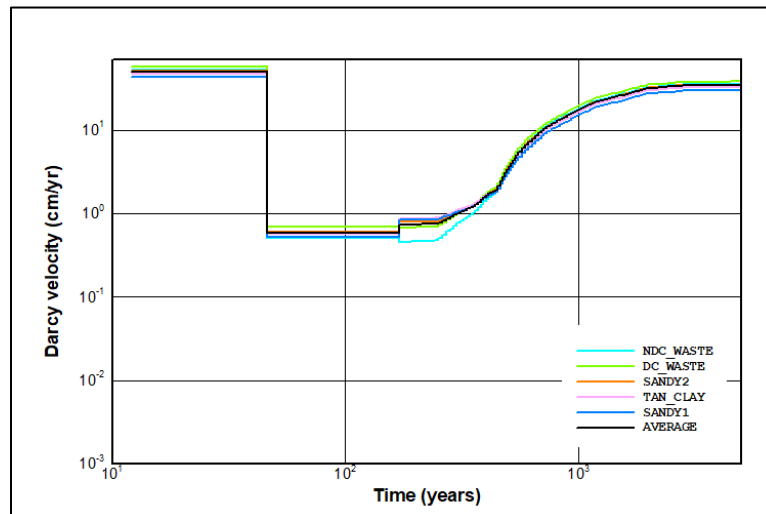


Figure 4-96. ST06/Slit Trench Case11b Vertical Velocities through Segment ST5 [Waste Zone and Lower Vadoso Zone] (Wohlwend and Aleman, 2020; Figure 4-28)

Figure 4-97 shows the ST06/ST Case11b vertical velocities between segments ST4 and ST5 (UVZ and LVZ). The AVERAGE velocities are input data into the Velocity_NDC_BS and Velocity_DC_BS time series elements (within /Transport/WasteZoneST/WasteZone_Subsided container). These velocities are used to compute volumetric flowrates in the Flowrate_NDC_BS and Flowrate_DC_BS expression elements. The AVERAGE velocities are input data into the Velocity_US_BS, Velocity_TC_BS, and Velocity_LS_BS time series elements (within /Transport/VadosoZoneST /VadosoZone_Subsided container). These velocities are used to compute volumetric flowrates in the Flowrate_US_BS, Flowrate_TC_BS and Flowrate_LS_BS expression elements.

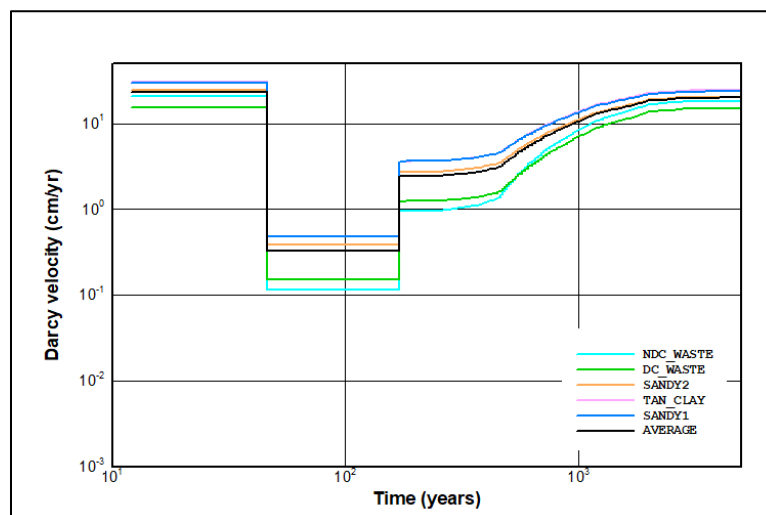


Figure 4-97. ST06/Slit Trench Case11b Average Vertical Velocities between Segments ST4 and ST5 [Upper and Lower Vadoso Zone] (Wohlwend and Aleman, 2020; Figure 4-29)

Figure 4-98 shows the ST06/ET Case11b vertical velocities through Hole 2 (H2) in segment ST5 (WZ and LVZ). The AVERAGE velocities are input data into the Velocity_NDC_H2 and

Velocity_DC_H2 time series elements (within /Transport/WasteZoneST/WasteZone_Subsidied container). These velocities are used to compute volumetric flowrates in the Flowrate_NDC_H2 and Flowrate_DC_H2 expression elements. The AVERAGE velocities are also input data into the Velocity_US_H2, Velocity_TC_H2 and Velocity_LS_H2 time series elements (within /Transport/VadoseZoneST /VadoseZone_Subsidied container). These velocities are used to compute volumetric flowrates in the Flowrate_US_H2, Flowrate_TC_H2 and Flowrate_LS_H2 expression elements.

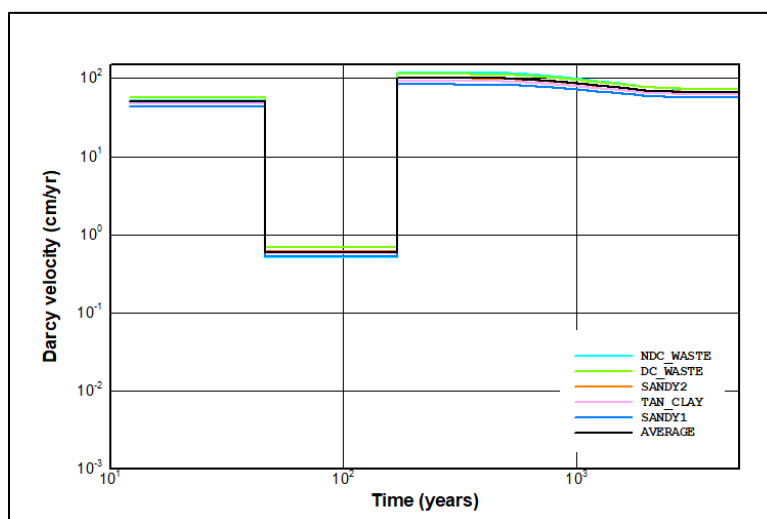


Figure 4-98. ST06/Slit Trench Case11b Vertical Velocities through H2 in Segment ST5 [Waste Zone and Lower Vadose Zone] (Wohlwend and Aleman, 2020; Figure 4-30)

4.4.9.1. Intact Waste Zone Model

The intact WZ model is represented by a cell network consisting of a ST segment (ST) and clayey between segment (BS). Each column of ST and BS cell pathways are connected through advective and diffusive flux links. There are only diffusive flux links between the ST and BS as explained in an earlier section. The widths of the ST and BS are 20 feet and 10 feet, respectively. The length of the ST and BS is 656 feet. To model dynamic compaction at the end of IC, the waste zone is separated into two sections: 12 cell pathways in NDC_WASTE (NDC_ST) and 16 cell pathways in DC_WASTE (DC_ST). The adjacent cell pathways are designated NDC_BS and DC_BS, respectively. The GoldSim[®] intact ST segment WZ cell network is shown in Figure 4-99. The height of the NDC_(ST/BS) and DC_(ST/BS) cell pathways is 4.9 feet ÷ 12 cells (0.408 feet) and 11.1 feet ÷ 16 cells (0.694 feet), respectively.

Figure 4-100 and Figure 4-101 present the cell pathway properties for NDC_ST_X1Y1. An initial inventory of 1/5 mole is assigned to each parent radionuclide and tracer. The parent radionuclide inventories are converted to grams internally for use throughout the WZ and VZ models. For ST, the species inventories are distributed between NDC and DC waste zones 12 years after the start of ELLWF operations. Discrete change elements DisposalEvent_NDC and DisposalEvent_DC trigger the placement of species inventories in NDC_ST and DC_ST cell pathways, respectively.

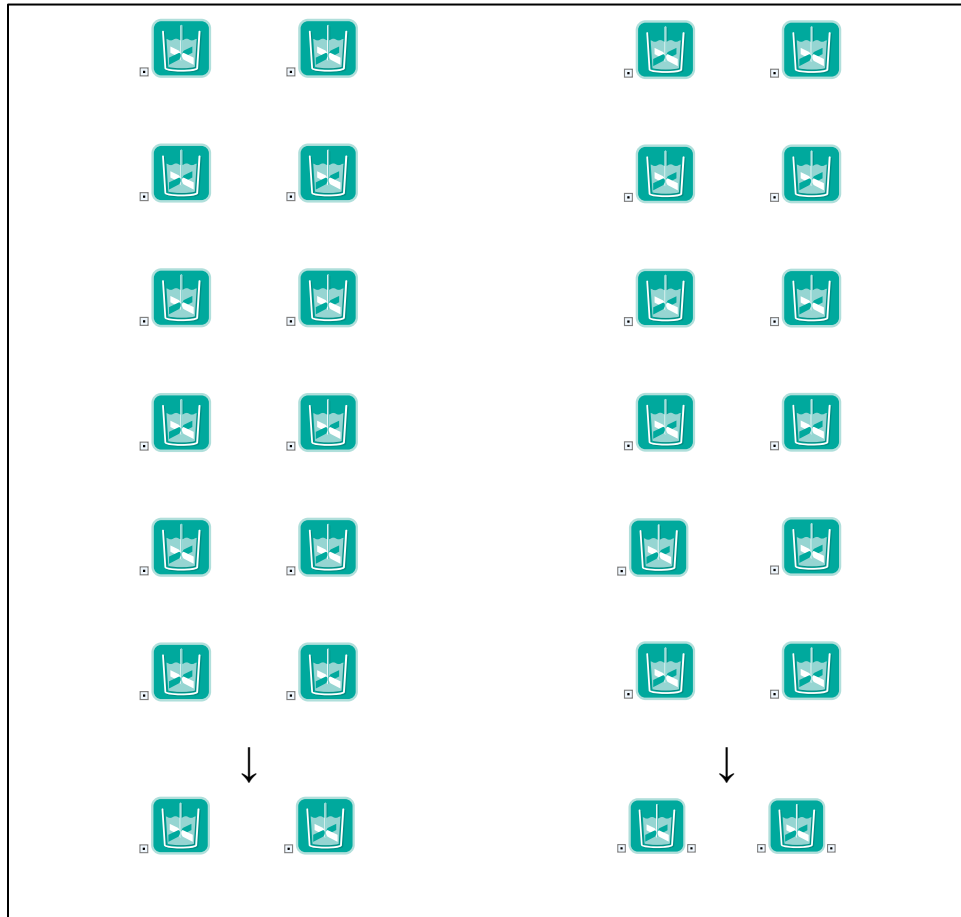


Figure 4-99. GoldSim® Intact Slit Trench Segment Waste Zone Cell Network (Wohlwend and Aleman, 2020; Figure 4-31)

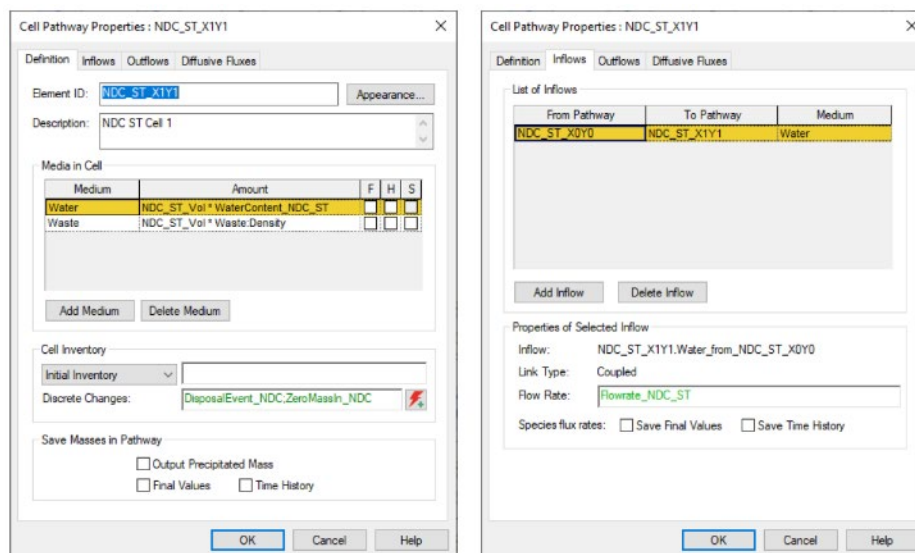


Figure 4-100. NDC_ST_X1Y1 Cell Pathway Properties: Definition and Inflows (Wohlwend and Aleman, 2020; Figure 4-32)

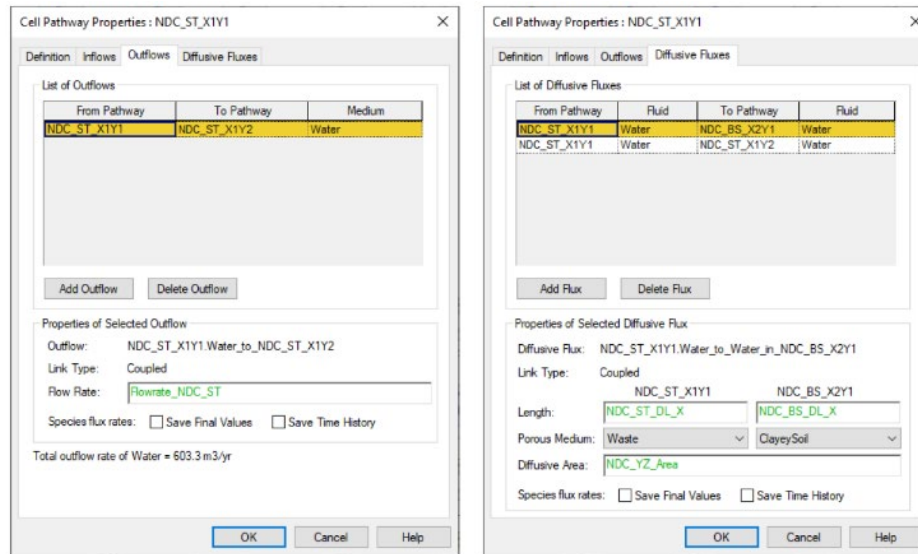


Figure 4-101. NDC_ST_X1Y1 Cell Pathway Properties: Outflows and Diffusive Fluxes (Wohlwend and Aleman, 2020; Figure 4-33)

The species inventories distributed to each NDC_ST and DC_ST cell pathways are computed in Eq. (4-43) and Eq. (4-44), respectively.

$$I_{NDC_ST} = I_p \frac{H_{NDC_ST}}{H_{WZ}} \quad \text{Eq. (4-43)}$$

$$I_{DC_ST} = I_p \frac{H_{DC_ST}}{H_{WZ}} \quad \text{Eq. (4-44)}$$

where:

I_{NDC_ST}	Species inventory of NDC_ST cell (g)
I_{DC_ST}	Species inventory of DC_ST cell (g)
I_p	Inventory of parent radionuclide (g)
H_{NDC_ST}	Height of NDC_ST cell, 7.13 ft ÷ 12 cells (ft)
H_{DC_ST}	Height of DC_ST cell, 8.87 ft ÷ 16 cells (ft)
H_{WZ}	Height of the WZ (16 ft)

When the final cap is emplaced at the end of IC, the species inventories (Mass_In_Pathway) within NDC_ST cell pathways are transferred to the DC_ST cell pathways. A series of discrete change elements (AddMassFrom_NDC, ZeroMassin_NDC, and AddMassto_DC) and a cell pathway (MassCollector_NDC) are used to transfer the species inventories. The AddMassFrom_NDC element sums the Mass_In_Pathway from NDC_ST cell pathways and makes them available in the MassCollector. The ZeroMassin_NDC element replaces the species inventories in the

NDC_ST cell pathways with zero values. The AddMassTo_DC element adds and distributes the species inventories from the NDC_ST cell pathways evenly among the DC_ST cell pathways.

4.4.9.2. Subsided Waste Zone Model

The subsidized WZ model is represented by a cell network consisting of a ST segment (ST), clayey between segment (BS) and subsided hole (H2). Each column of ST, BS, and H2 cell pathways are connected through advective and diffusive flux links. There are only diffusive flux links between the ST to BS and H2 to BS pairs as explained in an earlier section. The width of the ST/H2 and BS are 20 feet and 10 feet, respectively. The length of the ST, BS, and H2 are 556 feet, 656 feet and 100 feet, respectively. To model dynamic compaction at the end of IC, the WZ is separated into two sections: 12 cell pathways in NDC_WASTE (NDC_ST and NDC_H2) and 16 cell pathways in DC_WASTE (DC_ST and DC_H2). The adjacent cell pathways are designated NDC_BS and DC_BS, respectively. The GoldSim® subsidized ST segment WZ cell network is shown in Figure 4-102. The height of the NDC_(ST/BS/H2) and DC_(ST/BS/H2) cell pathways are 4.90 feet ÷ 12 cells (0.408 feet) and 11.1 feet ÷ 16 cells (0.694 feet), respectively. Figure 4-103 and Figure 4-104 present the cell pathway properties for NDC_H2_X3Y1.

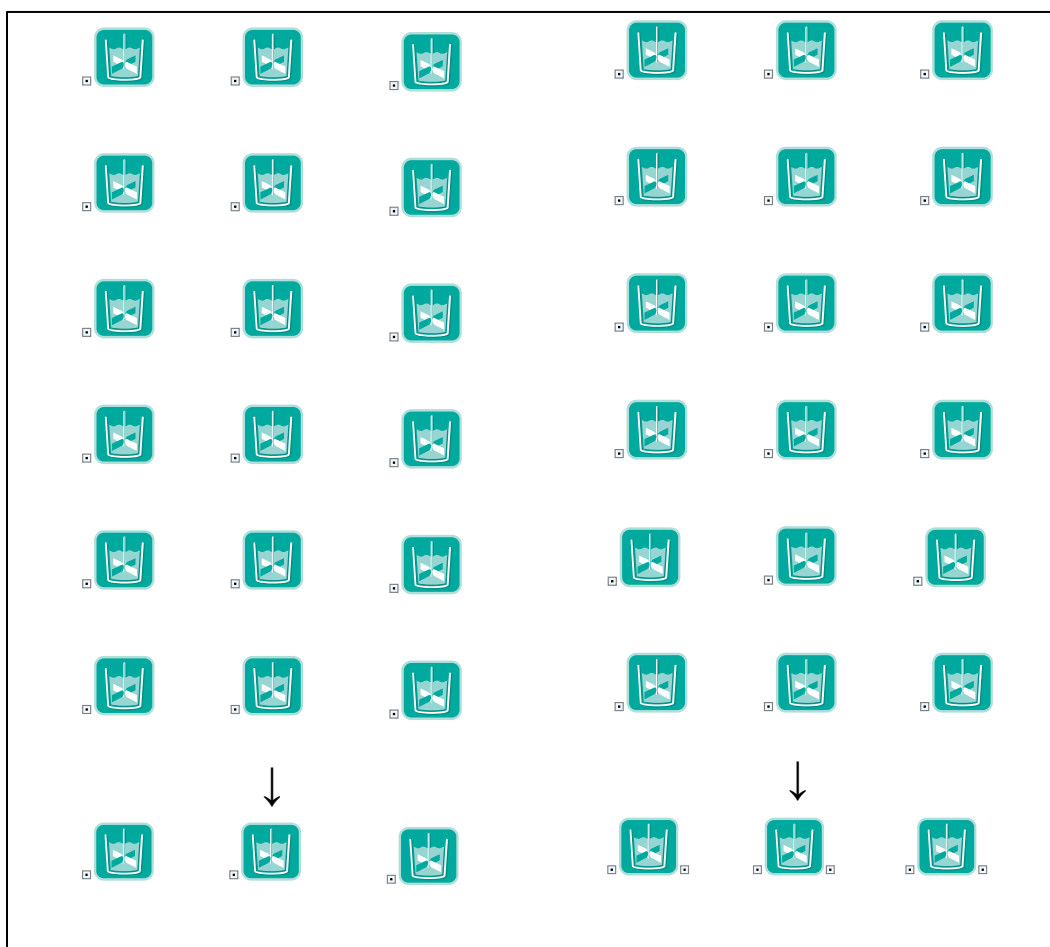


Figure 4-102. GoldSim® Subsided Slit Trench Segment Waste Zone Cell Network (Wohlwend and Aleman, 2020; Figure 4-36)

Cell Pathway Properties : NDC_H2_X3Y1

Definition Inflows Outflows Diffusive Fluxes

Element ID: **NDC_H2_X3Y1** Appearance...

Description: **NDC H2 Cell 1**

Media in Cell

Medium	Amount	F	H	S
Water	$NDC_H2_Vol * WaterContent_NDC_H2$	<input type="checkbox"/>	<input type="checkbox"/>	<input type="checkbox"/>
Waste	$NDC_H2_Vol * WasteDensity$	<input type="checkbox"/>	<input type="checkbox"/>	<input type="checkbox"/>

Add Medium Delete Medium

Cell Inventory

Initial Inventory

Discrete Changes: **DisposalEvent_NDC_H2.ZeroMassIn_NDC_I**

Save Masses in Pathway

☐ Output Precipitated Mass

☐ Final Values ☐ Time History

OK Cancel Help

Cell Pathway Properties : NDC_H2_X3Y1

Definition Inflows Outflows Diffusive Fluxes

List of Inflows

From Pathway	To Pathway	Medium
NDC_H2_X3Y0	NDC_H2_X3Y1	Water

Add Inflow Delete Inflow

Properties of Selected Inflow

Inflow: **NDC_H2_X3Y1.Water_from_NDC_H2_X3Y0**

Link Type: **Coupled**

Flow Rate: **Flowrate_NDC_H2**

Species flux rates: ☐ Save Final Values ☐ Save Time History

OK Cancel Help

Figure 4-103. NDC_H2_X3Y1 Cell Pathway Properties: Definition and Inflows (Wohlwend and Aleman, 2020; Figure 4-37)

Cell Pathway Properties : NDC_H2_X3Y1

Definition Inflows Outflows Diffusive Fluxes

List of Outflows

From Pathway	To Pathway	Medium
NDC_H2_X3Y1	NDC_H2_X3Y2	Water

Add Outflow Delete Outflow

Properties of Selected Outflow

Outflow: **NDC_H2_X3Y1.Water_to_NDC_H2_X3Y2**

Link Type: **Coupled**

Flow Rate: **Flowrate_NDC_H2**

Species flux rates: ☐ Save Final Values ☐ Save Time History

Total outflow rate of Water = 122.9 m3/yr

OK Cancel Help

Cell Pathway Properties : NDC_H2_X3Y1

Definition Inflows Outflows Diffusive Fluxes

List of Diffusive Fluxes

From Pathway	Fluid	To Pathway	Fluid
NDC_H2_X3Y1	Water	NDC_BS_X2Y1	Water
NDC_H2_X3Y1	Water	NDC_H2_X3Y2	Water

Add Flux Delete Flux

Properties of Selected Diffusive Flux

Diffusive Flux: **NDC_H2_X3Y1.Water_to_Water_in_NDC_BS_X2Y1**

Link Type: **Coupled**

Length: **NDC_ST_DL_X** **NDC_BS_DL_X**

Porous Medium: **Waste** **ClayeySoil**

Diffusive Area: **NDC_H2_YZ_Area**

Species flux rates: ☐ Save Final Values ☐ Save Time History

OK Cancel Help

Figure 4-104. NDC_H2_X3Y1 Cell Pathway Properties: Outflows and Diffusive Fluxes (Wohlwend and Aleman, 2020; Figure 4-38)

An initial inventory of 1/5 mole is assigned to each parent radionuclide. The parent radionuclide inventories are converted to grams internally for use throughout the WZ and VZ models. For ST06/ST, the species inventories are distributed between NDC and DC waste zones 12 years after the start of ELLWF operations. Discrete change elements DisposalEvent_NDC_ST, DisposalEvent_NDC_H2, DisposalEvent_DC_ST, and DisposalEvent_DC_H2 trigger the placement of species inventories in NDC_ST, NDC_H2, DC_ST, and DC_H2 cell pathways,

respectively. The species inventories distributed to each NDC_ST and DC_ST cell pathways are computed in Eq. (4-45) and Eq. (4-46), respectively.

$$I_{NDC_ST} = I_p f_{ST} \frac{H_{NDC_ST}}{H_{WZ}} \quad \text{Eq. (4-45)}$$

$$I_{DC_ST} = I_p f_{ST} \frac{H_{DC_ST}}{H_{WZ}} \quad \text{Eq. (4-46)}$$

where:

I_{NDC_ST}	Species inventory of NDC_ST cell (g)
I_{DC_ST}	Species inventory of DC_ST cell (g)
I_p	Inventory of parent radionuclide (g)
f_{ST}	Area fraction of intact segment, 0.8476 (unitless)
H_{NDC_ST}	Height of NDC_ST cell, 7.13 ft ÷ 12 cells (ft)
H_{DC_ST}	Height of DC_ST cell, 8.87 ft ÷ 16 cells (ft)
H_{WZ}	Height of the WZ (16 ft)

The species inventories distributed to each NDC_H2 and DC_H2 cell pathways are computed in Eq. (4-47) and Eq. (4-48), respectively.

$$I_{NDC_H2} = I_p f_{H2} \frac{H_{NDC_H2}}{H_{WZ}} \quad \text{Eq. (4-47)}$$

$$I_{DC_H2} = I_p f_{H2} \frac{H_{DC_H2}}{H_{WZ}} \quad \text{Eq. (4-48)}$$

where:

I_{NDC_H2}	Species inventory of NDC_H2 cell (g)
I_{DC_H2}	Species inventory of DC_H2 cell (g)
f_{H2}	Area fraction of H2 segment, 0.1524
H_{NDC_ST}	Height of NDC_H2 cell, 7.13 ft ÷ 12 cells (ft)
H_{DC_ST}	Height of DC_H2 cell, 8.87 ft ÷ 16 cells (ft)

When the final cap is emplaced at end of IC, the species inventories (Mass_In_Pathway) within NDC_ST and NDC_H2 cell pathways are transferred to the DC_ST and DC_H2 cell pathways, respectively. A series of discrete change elements (AddMassFrom_NDC_ST, AddMassFrom_NDC_H2, ZeroMassin_NDC_ST, ZeroMassin_NDC_H2, AddMassto_DC_ST,

and AddMassto_DC_H2) and cell pathways (MassCollector_NDC_ST and MassCollector_NDC_H2) are used to transfer the species inventories. The AddMassFrom_NDC_ST and AddMassFrom_NDC_H2 elements sum the Mass_In_Pathway from the NDC_ST and NDC_H2 cell pathways, respectively, and make them available in the MassCollectors. The ZeroMassin_NDC_ST and ZeroMassin_NDC_H2 elements replace the species inventories in the NDC_ST and NDC_H2 cell pathways, respectively, with zero values. The AddMassTo_DC_ST and AddMassTo_DC_H2 elements add and distribute the species inventories from the NDC_ST and NDC_H2 cell pathways evenly among the DC_ST and DC_H2 cell pathways, respectively.

Figure 4-105 shows the ST water saturations in the WZ for both the intact and subsided case. The saturations are time-series inputs used to compute water contents for the ST waste.

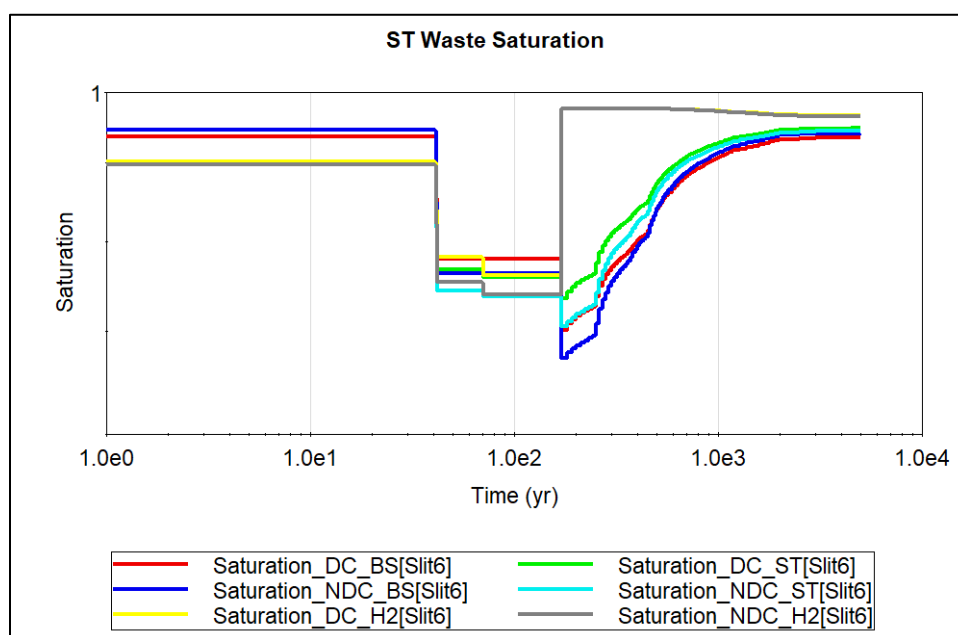


Figure 4-105. Slit Trench Water Saturations in the Waste Zone

4.4.9.3. Lower Vadose Zone Model

4.4.9.3.1. Intact Waste Zone

Advective and diffusive species fluxes leave the DC_ST and DC_BS cell pathways from WasteZone_Intact and enter the upper sandy (US) layer (SANDY2) of the LVZ. The SANDY2 soil layer is represented by a cell network consisting of a column of 40 US_ST and US_BS cell pathways. The advective and diffusive species fluxes leave the SANDY2 cell network and enter the TAN_CLAY (TC) soil layer. The TAN_CLAY soil layer is represented by a cell network consisting of a column of 6 TC_ST and TC_BS cell pathways. The advective and diffusive species fluxes leave the TAN_CLAY cell network and enter the lower sandy (LS) layer (SANDY1). The SANDY1 soil layer is represented by a cell network consisting of a column of 16 LS_ST and LS_BS cell pathways. The GoldSim® ST LVZ (Intact WZ) cell network is shown in Figure 4-106.

Each column of LVZ cell pathways is connected through advective and diffusive flux links. There are only diffusive flux links between the ST and BS cell pathways as explained in an earlier section.



Figure 4-106. GoldSim® Slit Trench Lower Vadose Zone Cell Network [Intact Waste Zone] (Wohlwend and Aleman, 2020; Figure 4-42)

Figure 4-107 and Figure 4-108 present the cell pathway properties for US_ST_X1Y1. Figure 4-109 show the ST06/ST Case01 average water saturations in segments ST1 through ST5 (LVZ). The SANDY2, TAN_CLAY, and SANDY1 water saturations are data inputs to the Saturation_US_ST, Saturation_TC_ST, and Saturation_LS_ST expression elements, respectively (within the /Transport/VadoseZoneST/VadoseZone_Intact container). Figure 4-110 display the ST06/ST Case01 average water saturations between ST segments (LVZ). The SANDY2, TAN_CLAY, and SANDY1 water saturations are data inputs to the Saturation_US_BS, Saturation_TC_BS, and Saturation_LS_BS expression elements, respectively within the /Transport/VadoseZoneST/VadoseZone_Intact container).

Cell Pathway Properties: US_ST_X1Y1

Definition Inflows Outflows Diffusive Fluxes

Element ID: **US_ST_X1Y1** Appearance...

Description: x-length = 20ft, y-length = 0.575ft, thickness = 656ft.

Media in Cell

Medium	Amount	F	H	S
Water	7544 ft ³ * SandySoil.Porosity*WaterSat_US	<input type="checkbox"/>	<input type="checkbox"/>	<input type="checkbox"/>
SandySoil	7544 ft ³ * SandySoil.Density	<input type="checkbox"/>	<input type="checkbox"/>	<input type="checkbox"/>

Add Medium Delete Medium

Cell Inventory

Initial Inventory

Discrete Changes:

Save Masses in Pathway

☐ Output Precipitated Mass

☐ Final Values ☐ Time History

OK Cancel Help

Cell Pathway Properties: US_ST_X1Y1

Definition Inflows Outflows Diffusive Fluxes

List of Inflows

From Pathway	To Pathway	Medium
DC_ST_X1Y16	US_ST_X1Y1	Water

Add Inflow Delete Inflow

Properties of Selected Inflow

Inflow: US_ST_X1Y1.Water_from_DC_ST_X1Y16

Link Type: Coupled

Flow Rate: **Flowrate_DC_ST**

Species flux rates: ☐ Save Final Values ☒ Save Time History

OK Cancel Help

Figure 4-107. US_ST_X1Y1 Cell Pathway Properties: Definition and Inflows (Wohlwend and Aleman, 2020; Figure 4-43)

Cell Pathway Properties: US_ST_X1Y1

Definition Inflows Outflows Diffusive Fluxes

List of Outflows

From Pathway	To Pathway	Medium
US_ST_X1Y1	US_ST_X1Y2	Water

Add Outflow Delete Outflow

Properties of Selected Outflow

Outflow: US_ST_X1Y1.Water_to_US_ST_X1Y2

Link Type: Coupled

Flow Rate: **Flowrate_US_ST**

Species flux rates: ☐ Save Final Values ☐ Save Time History

Total outflow rate of Water = 412.3 m³/yr

OK Cancel Help

Cell Pathway Properties: US_ST_X1Y1

Definition Inflows Outflows Diffusive Fluxes

List of Diffusive Fluxes

From Pathway	Fluid	To Pathway	Fluid
US_ST_X1Y1	Water	US_BS_X2Y1	Water
US_ST_X1Y1	Water	US_ST_X1Y2	Water
DC_ST_X1Y16	Water	US_ST_X1Y1	Water

Add Flux Delete Flux

Properties of Selected Diffusive Flux

Diffusive Flux: US_ST_X1Y1.Water_to_Water_in_US_BS_X2Y1

Link Type: Coupled

Length: **10 ft** **5 ft**

Porous Medium: **SandySoil** **SandySoil**

Diffusive Area: **377.2 ft²**

Species flux rates: ☐ Save Final Values ☐ Save Time History

OK Cancel Help

Figure 4-108. US_ST_X1Y1 Cell Pathway Properties: Outflows and Diffusive Fluxes (Wohlwend and Aleman, 2020; Figure 4-44)

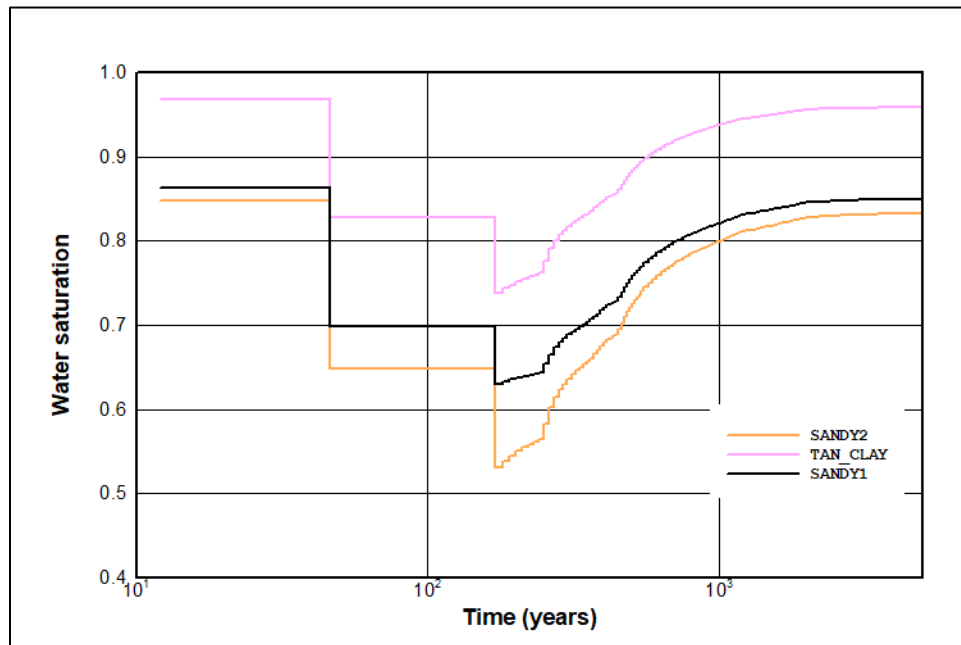


Figure 4-109. ST06/Slit Trench Case01 Average Water Saturations in Segments ST1 through ST5 [Lower Vadose Zone] (Wohlwend and Aleman, 2020; Figure 4-45)

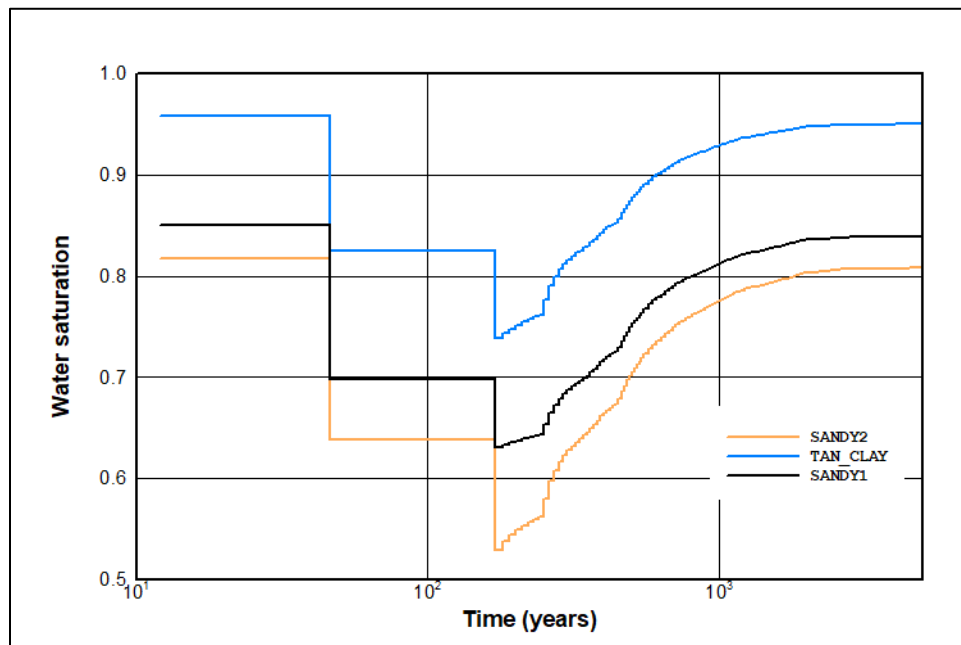


Figure 4-110. ST06/Slit Trench Case01 Average Water Saturations between Slit Trench Segments [Lower Vadose Zone] (Wohlwend and Aleman, 2020; Figure 4-46)

4.4.9.3.2. Subsided Waste Zone

The VadoseZone_Subside container is split into three localized containers for the UpperSandyLayer, TanClayLayer, and LowerSandyLayer models as shown in Figure 4-111. With

the additional subsided columns, US/TC/LS_H2, there is a need to split the models for ease of development. The remainder of this section describes the models within these containers.

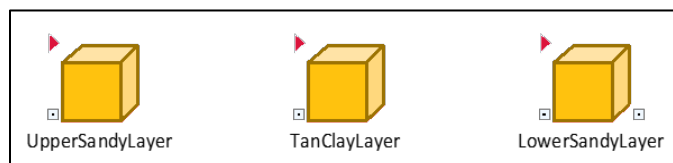


Figure 4-111. GoldSim® Slit Trench Lower Vadose Zone Containers [Subsided Waste Zone] (Wohlwend and Aleman, 2020; Figure 4-47)

Advective and diffusive species fluxes leave the DC_ST, DC_BS, and DC_H2 cell pathways from WasteZone_Subside and enter the upper sandy layer (SANDY2) of the LVZ. The SANDY2 soil layer is represented by a cell network consisting of a column of 40 US_ST, US_BS, and US_H2 cell pathways. Each column of upper sandy layer cell pathways is connected through advective and diffusive flux links. There are only diffusive flux links between the US_ST to US_BS and US_H2 to US_BS pairs as explained in an earlier section. The widths of the US_ST/H2 and US_BS cell pathways are 20 feet and 10 feet, respectively. The length of the US_ST, US_BS, and US_H2 are 556 feet, 656 feet, and 100 feet, respectively. The GoldSim® ST upper sandy layer cell network (Subsided WZ) is shown in Figure 4-112.

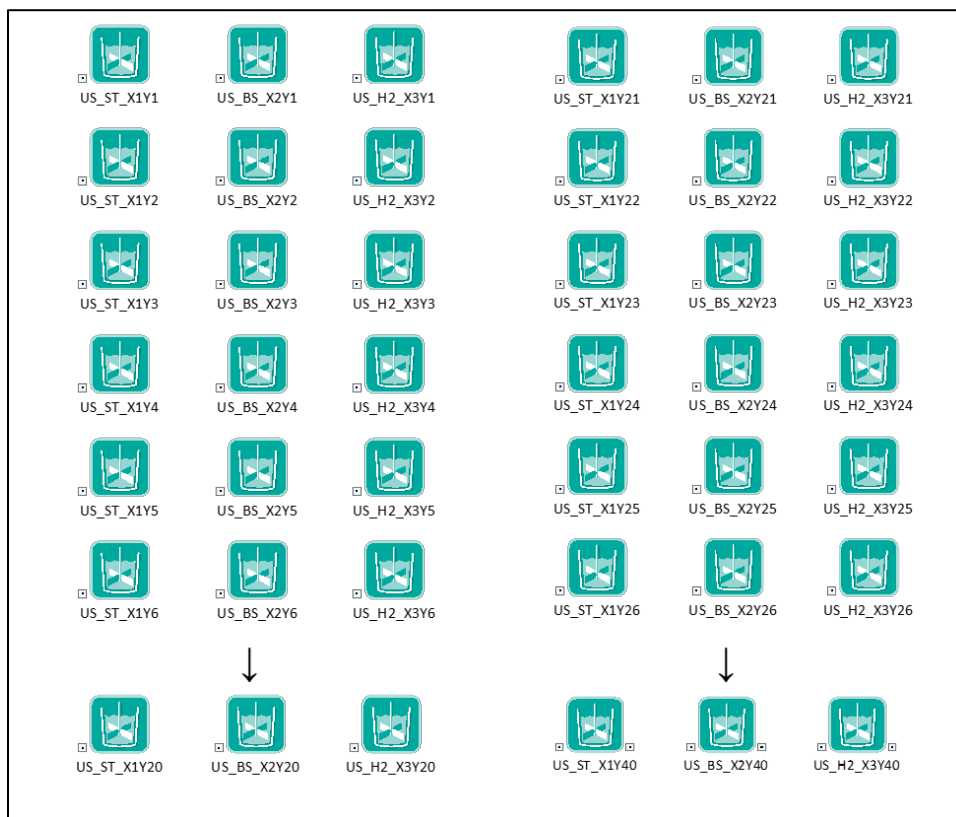


Figure 4-112. GoldSim® Slit Trench Upper Sandy Layer Cell Network [Subsided Waste Zone] (Wohlwend and Aleman, 2020; Figure 4-48)

The advective and diffusive species fluxes leave the SANDY2 cell network and enter the TAN_CLAY soil layer. The TAN_CLAY soil layer is represented by a cell network consisting of a column of six TC_ST, TC_BS, and TC_H2 cell pathways. Each column of the TAN_CLAY layer cell pathways is connected through advective and diffusive flux links. There are only diffusive flux links between the TC_ST to TC_BS and TC_H2 to TC_BS pairs as explained in an earlier section. The widths of the TC_ST/H2 and TC_BS cell pathways are 20 feet and 10 feet, respectively. The length of the US_ST, US_BS and US_H2 are 556 feet, 656 feet, and 100 feet, respectively. The GoldSim[®] ST tan clay layer cell network (Subsided WZ) is shown in Figure 4-113.

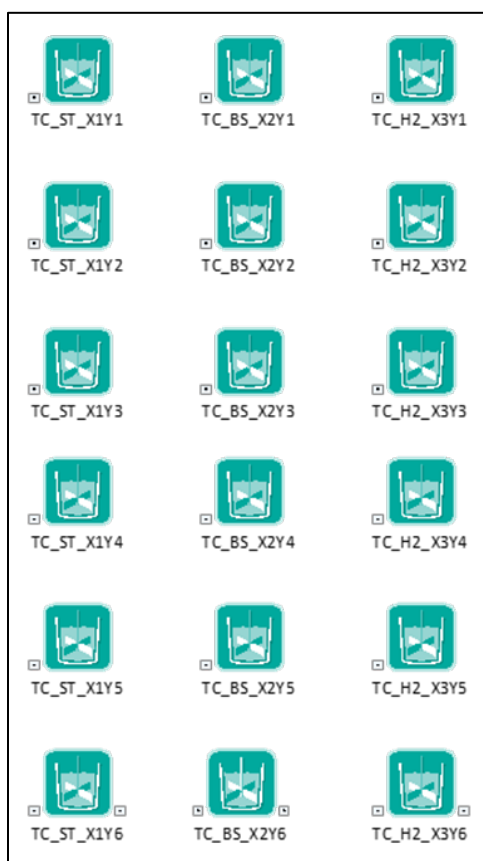


Figure 4-113. GoldSim[®] Slit Trench Tan Clay Layer Cell Network [Subsided Waste Zone] (Wohlwend and Aleman, 2020; Figure 4-49)

The advective and diffusive species fluxes leave the TAN_CLAY cell network and enter the lower sandy layer (SANDY1). The SANDY1 soil layer is represented by a cell network consisting of a column of 16 LS_ST, LS_BS, and LS_H2 cell pathways. Each column of the SANDY1 soil layer cell pathways is connected through advective and diffusive flux links. There are only diffusive flux links between the LS_ST to LS_BS and LS_H2 to LS_BS pairs as explained in an earlier section. The widths of the LS_ST/H2 and LS_BS cell pathways are 20 feet and 10 feet, respectively. The length of the LS_ST, LS_BS, and LS_H2 are 556 feet, 656 feet, and 100 feet, respectively. The GoldSim[®] ST lower sandy layer cell network (Subsided WZ) is shown in

Figure 4-114. Figure 4-115 and Figure 4-116 present the cell pathway properties for US_H2_X3Y1.

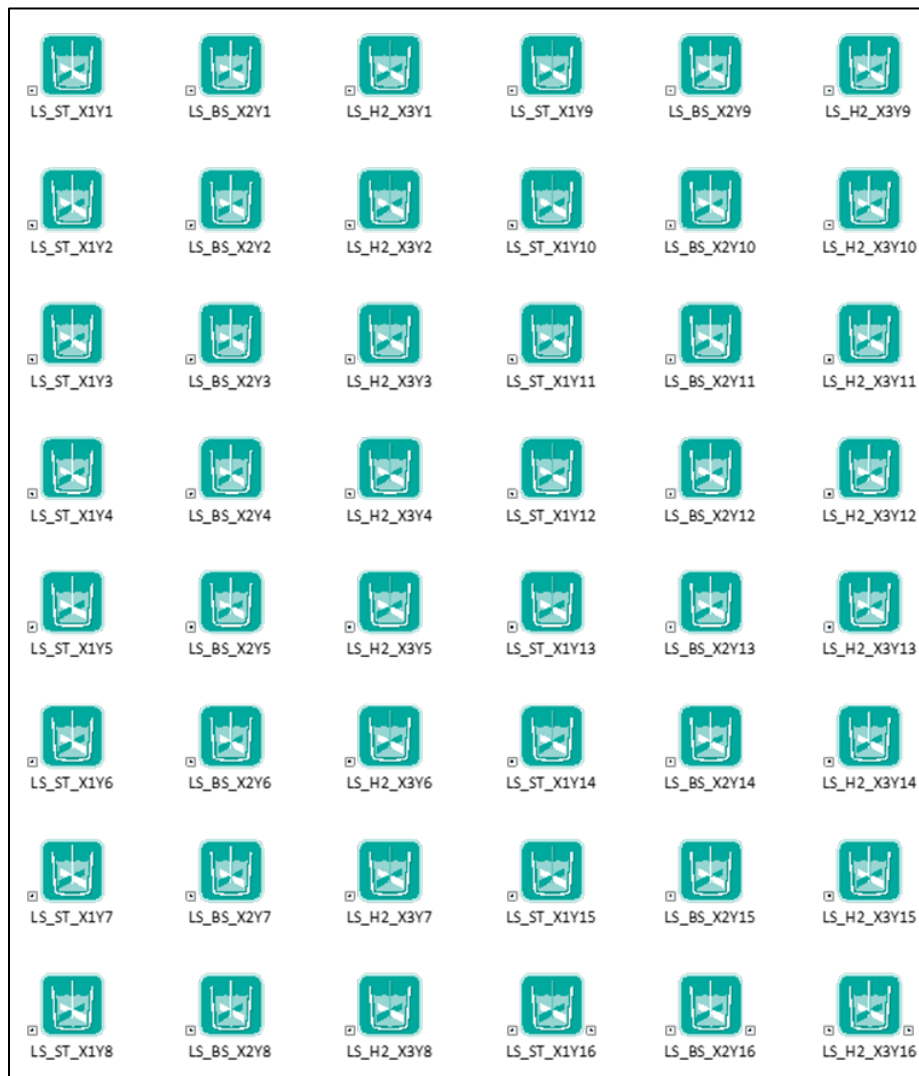


Figure 4-114. GoldSim® Slit Trench Lower Sandy Layer Cell Network [Subsided Waste Zone]
(Wohlwend and Aleman, 2020; Figure 4-50)

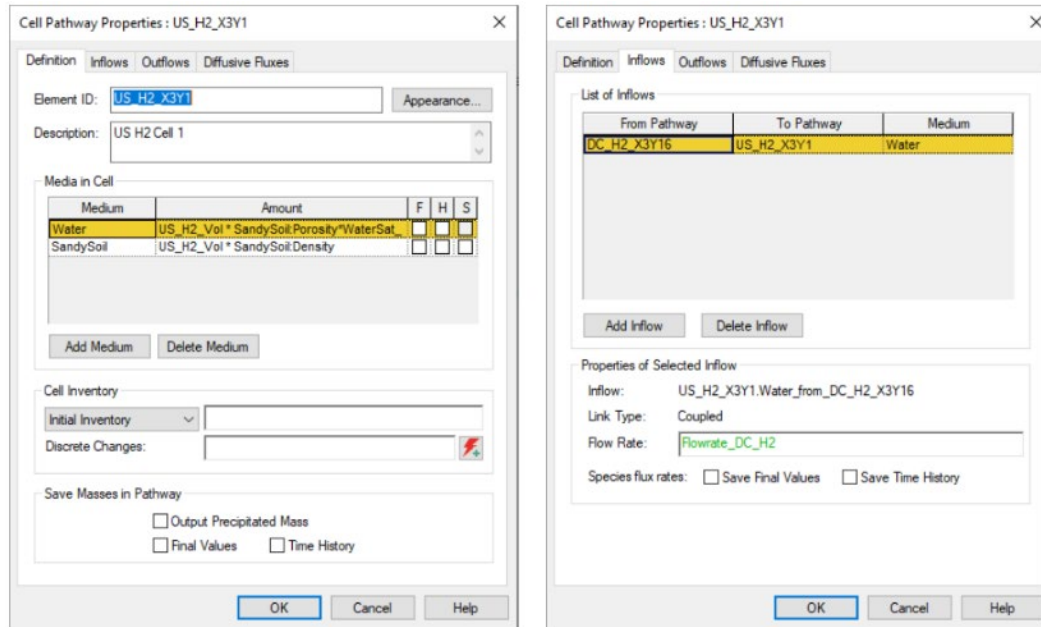


Figure 4-115. US_H2_X3Y1 Cell Pathway Properties: Definition and Inflows (Wohlwend and Aleman, 2020; Figure 4-51)

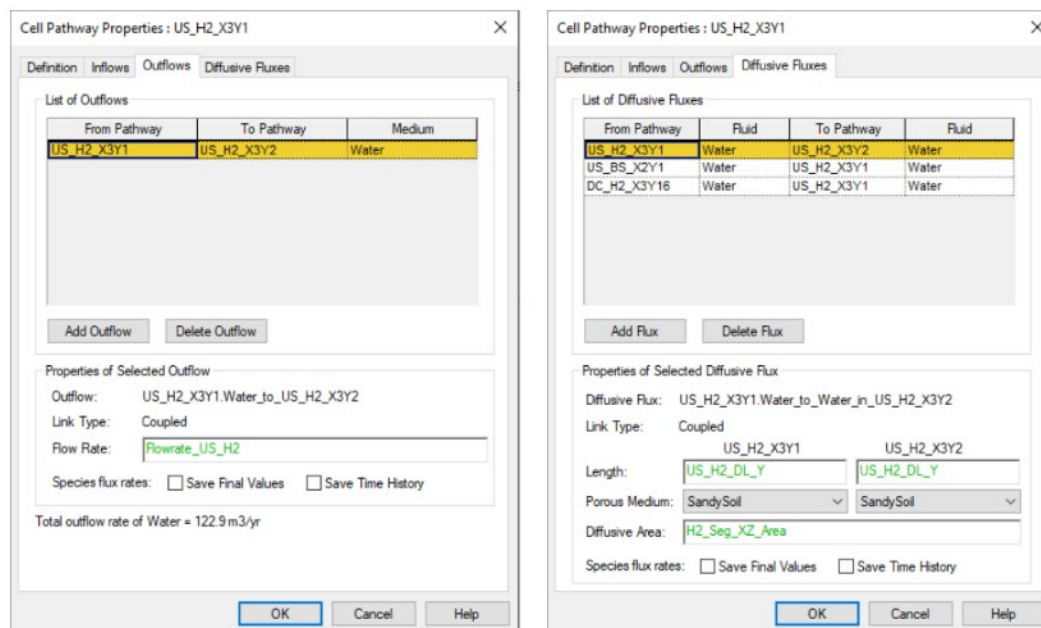


Figure 4-116. US_H2_X3Y1 Cell Pathway Properties: Outflows and Diffusive Fluxes (Wohlwend and Aleman, 2020; Figure 4-52)

Figure 4-117 shows the ST06/ST Case11b water saturations in segment ST5 (LVZ). The SANDY2, TAN_CLAY, and SANDY1 water saturations are data inputs to the Saturation_US_ST (UpperSandyLayer), Saturation_TC_ST (TanClayLayer) and Saturation_LS_ST (LowerSandyLayer) expression elements, respectively, in the /Transport/VadoseZoneST/VadoseZone_Subsid container.

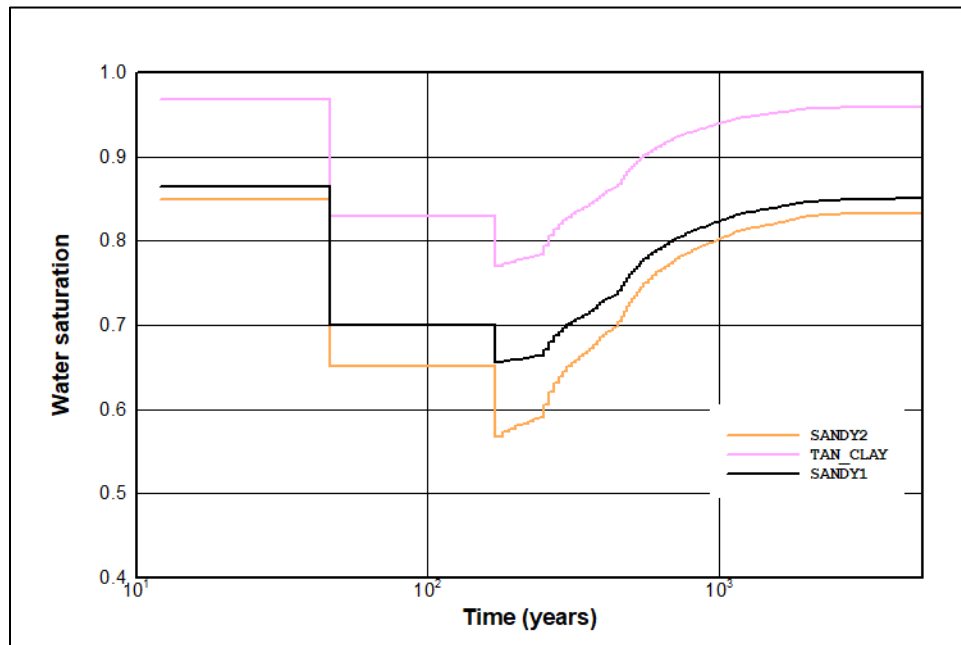


Figure 4-117. ST06/Slit Trench Case11b Water Saturations in Segment ST5 [Lower Vadose Zone] (Wohlwend and Aleman, 2020; Figure 4-53)

Figure 4-118 displays the ST06/ST Case11b (subsided) water saturations between segments ST4 and ST5 (LVZ). The SANDY2, TAN_CLAY, and SANDY1 water saturations are data inputs to the Saturation_US_BS (UpperSandyLayer), Saturation_TC_BS (TanClayLayer), and Saturation_LS_BS (LowerSandyLayer) expression elements, respectively, in the /Transport/VadoseZoneST/VadoseZone_Subside container.

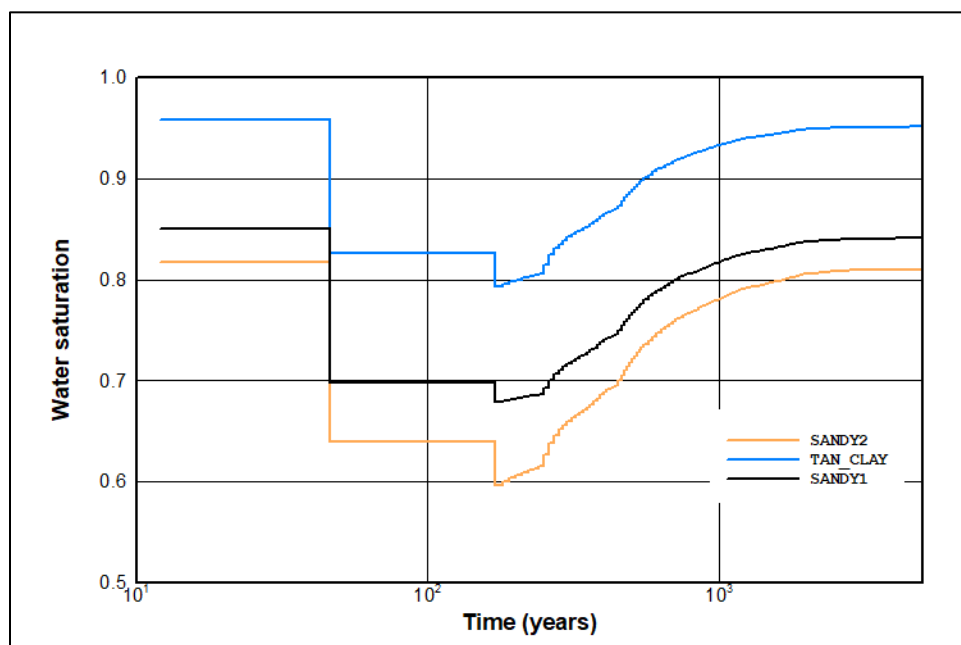


Figure 4-118. ST06/Slit Trench Case11b Water Saturations between Segments ST4 and ST5 [Lower Vadose Zone] (Wohlwend and Aleman, 2020; Figure 4-54)

Figure 4-119 shows the ST06/ST Case11b (subsided) water saturations in H2 of segment ST5 (LVZ). The SANDY2, TAN_CLAY, and SANDY1 water saturations are data inputs to the Saturation_US_H2 (UpperSandyLayer), Saturation_TC_H2 (TanClayLayer), and Saturation_LS_H2 (LowerSandyLayer) expression elements, respectively, in the /Transport/VadoseZoneST /VadoseZone_Subsidied container.

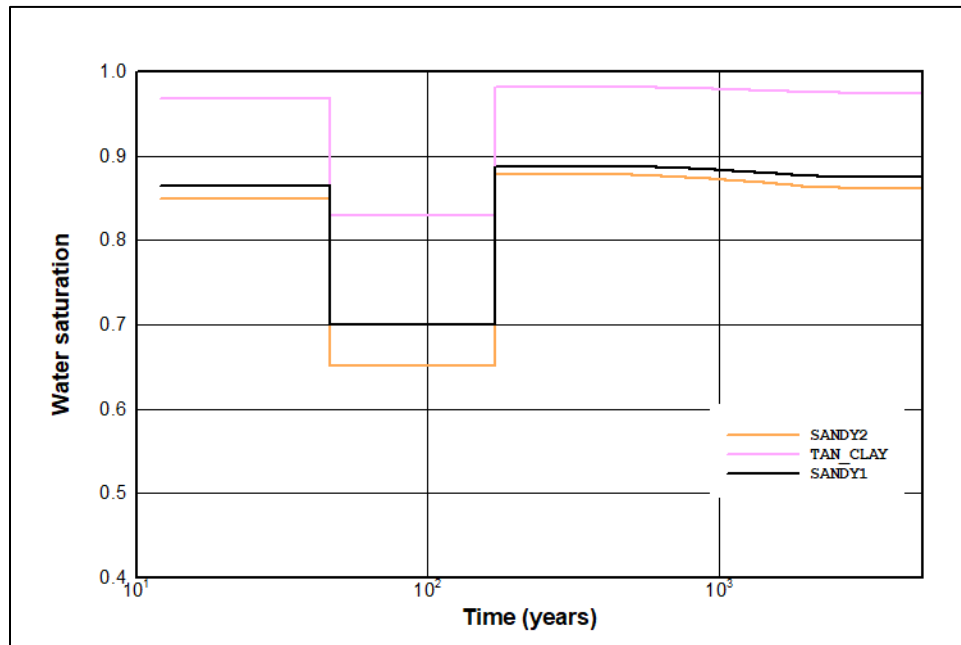


Figure 4-119. ST06/Slit Trench Case11b Water Saturations in H2 of Segment ST5 [Lower Vadose Zone] (Wohlwend and Aleman, 2020; Figure 4-55)

4.4.10. Vadose Zone Model Benchmarking to PORFLOW

Total species fluxes (advective and diffusive) from the waste zone and to the water table are computed for comparison between the 3-D PORFLOW and simplified 1-D GoldSim[®] VZ transport models. The GoldSim[®] ET WZ and VZ models span the entire footprint of the active DU. The GoldSim[®] ST WZ and VZ models include intact and subsided single ST and non-waste segment models with 1/5 of the parent species inventories. If not stated otherwise, comparisons between the GoldSim[®] and PORFLOW model flux profiles, expressed as percent difference, are based on comparisons of the peak flux values.

4.4.10.1. Flux from the Waste Zone to Vadose Zone

The total species fluxes from the GoldSim[®] ET WZ for Case01 are the sum of the advective and diffusive fluxes from the WasteZone_Crushed container. The total species fluxes from the GoldSim[®] ET WZ for Case11b are the sum of the advective and diffusive fluxes from the WasteZone_Crushed and WasteZone_Noncrushed containers.

The total species fluxes from the GoldSim[®] ST WZ for Case01 are five times the total fluxes from the WasteZone_Intact container. The total species fluxes from the GoldSim[®] ST WZ for Case11b

(subsided) are the sum of the total fluxes from the WasteZone_Intact and four times the total fluxes from the WasteZone_Subsided containers.

4.4.10.1.1. ET06

Figure 4-120 and Figure 4-121 show the ET06 Case01 (intact) and Case11b (subsided) fluxes at the bottom of the waste zone, respectively. The GoldSim[®] model accurately simulates the flux from the waste zone over the entire time period with the largest difference in peak flux being 8%. The only calibration performed on the ET WZ model was to modify the percent subsidence. The PORFLOW model simulation is performed assuming 2% subsidence; however, because of the 3-D nature of the PORFLOW model, the increase in infiltration rate beneath the subsidence region hole affects a larger area than simply below the hole. Because GoldSim[®] is a 1-D model, the region beneath the hole is a single series of cell pathways. By increasing the size of the hole (percent subsidence), the affected region is calibrated to that of the PORFLOW model. The calibrated subsidence for the GoldSim[®] model is 5%.

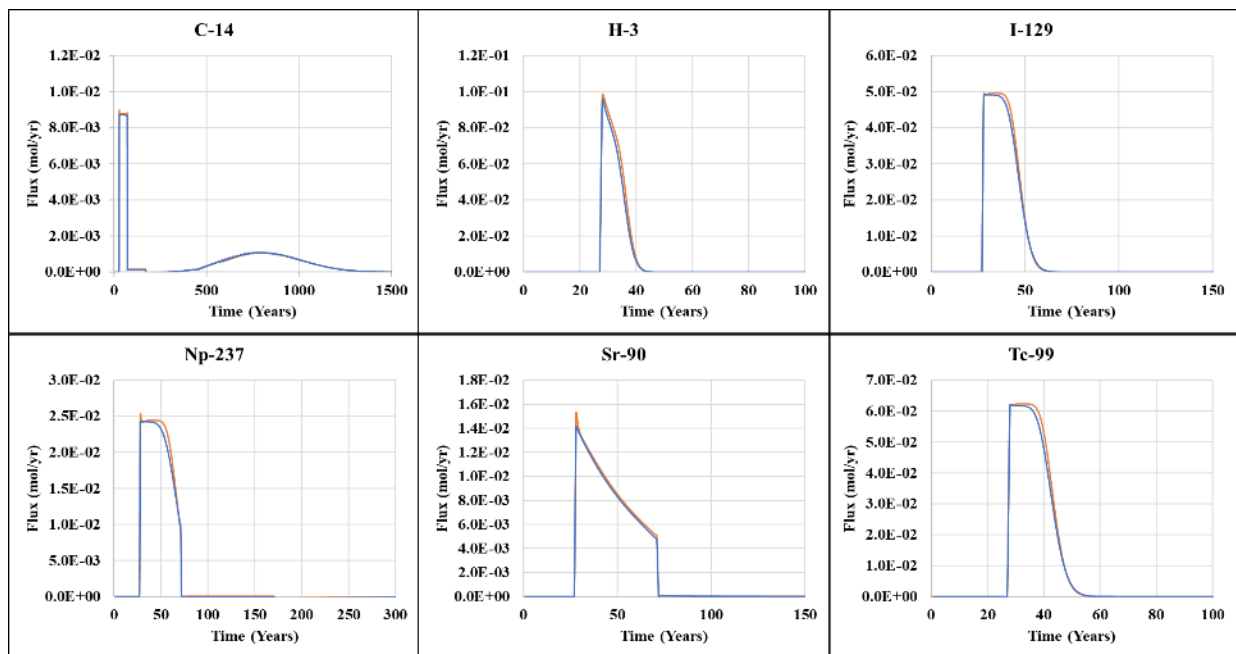


Figure 4-120. ET06 Case01 (Intact) Flux of C-14, H-3, I-129, Np-237, Sr-90, and Tc-99 from Waste Zone for the PORFLOW (blue) and GoldSim[®] (gold) Models

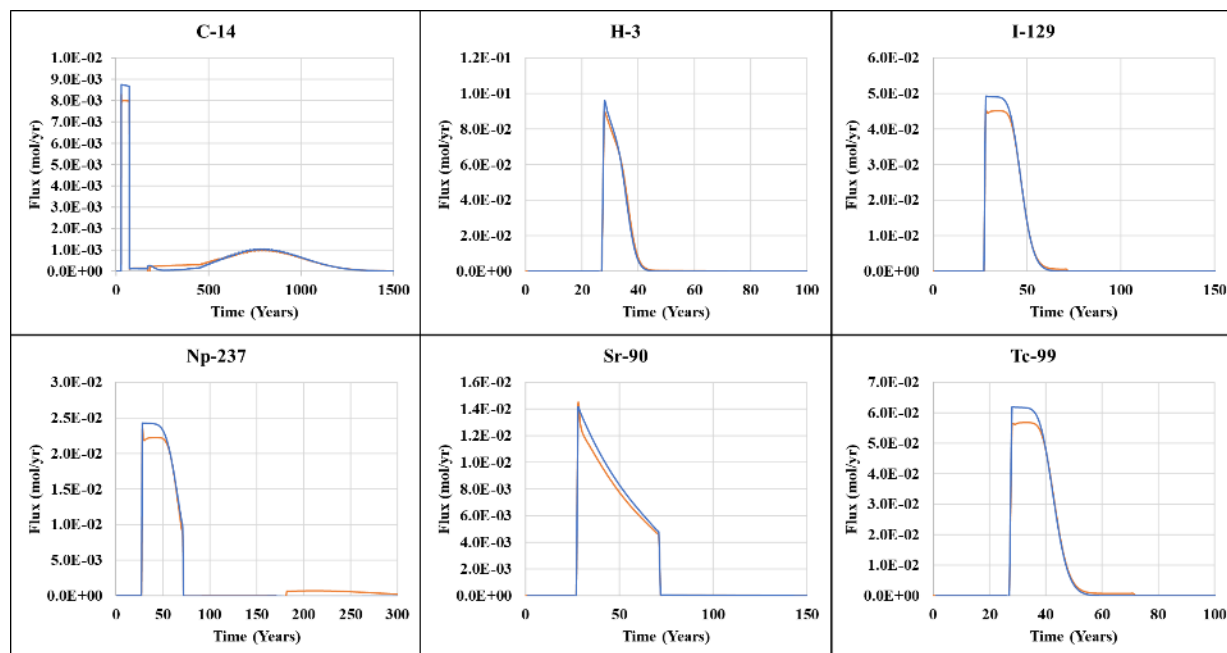


Figure 4-121. ET06 Case11b (Subsided) Flux of C-14, H-3, I-129, Np-237, Sr-90, and Tc-99 from Waste Zone for the PORFLOW (blue) and GoldSim® (gold) Models

4.4.10.1.2. ST06

Figure 4-122 and Figure 4-123 display the ST06 Case01 (intact) and Case11b (subsided) fluxes at the bottom of the waste zone, respectively. The flux from the waste zone between the PORFLOW and GoldSim® models is in good agreement for all radionuclides investigated with a maximum difference in peak flux of 5%. No calibration was performed for the ST06 waste zone model.

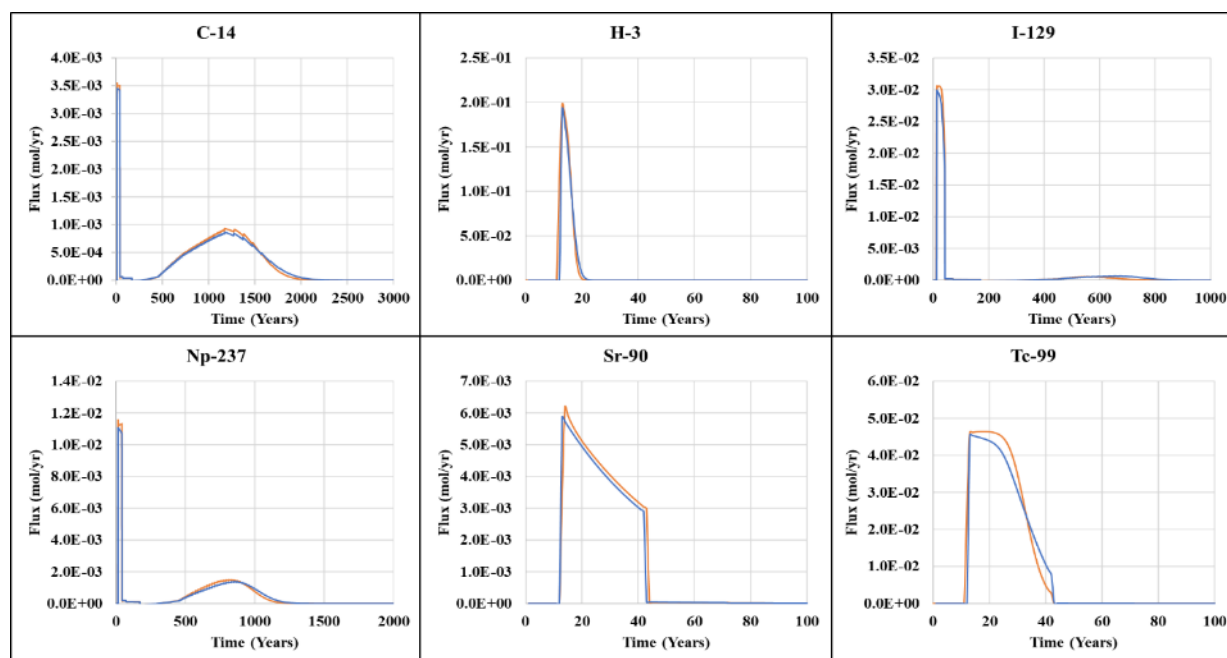


Figure 4-122. ST06 Case01 (Intact) Flux of C-14, H-3, I-129, Np-237, Sr-90, and Tc-99 from Waste Zone for the PORFLOW (blue) and GoldSim® (gold) Models

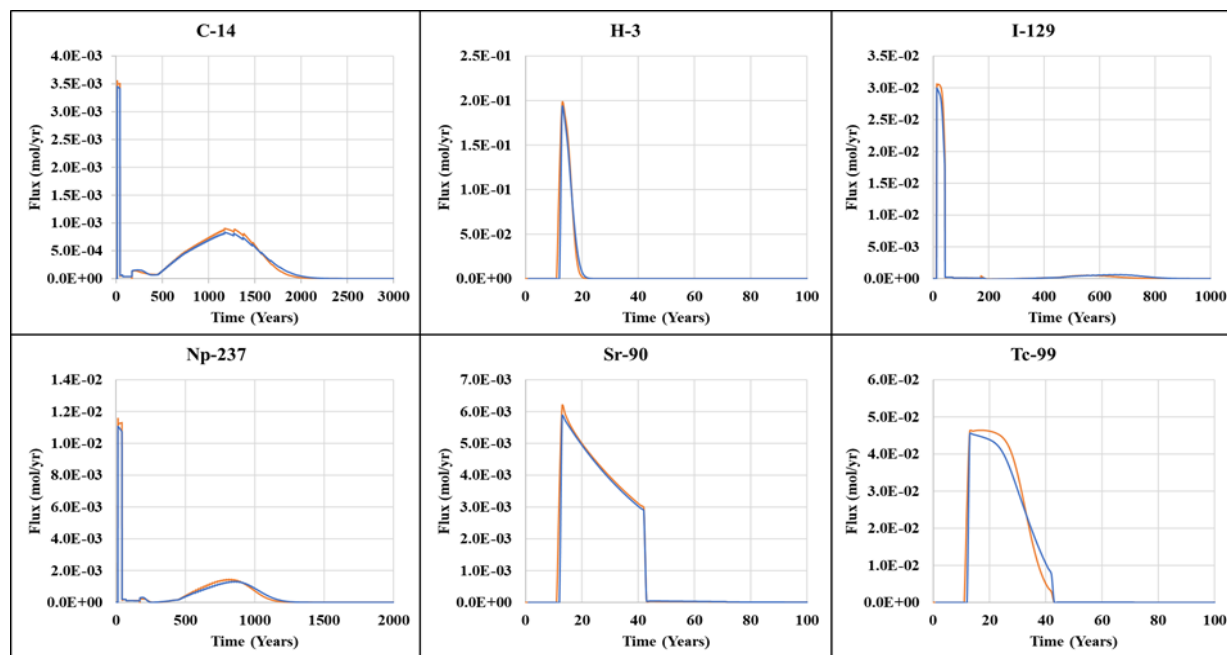


Figure 4-123. ST06 Case11b (Subsided) Flux of C-14, H-3, I-129, Np-237, Sr-90, and Tc-99 from Waste Zone for the PORFLOW (blue) and GoldSim® (gold) Models

4.4.10.1.3. ST09

Figure 4-124 and Figure 4-125 display the ST09 Case01 (intact) and Case11b (subsided) fluxes at the bottom of the waste zone. The flux from the waste zone between the PORFLOW and GoldSim® models is in good agreement for all radionuclides investigated with a maximum difference in peak flux of 8%. No calibration was performed for the ST09 waste zone model.

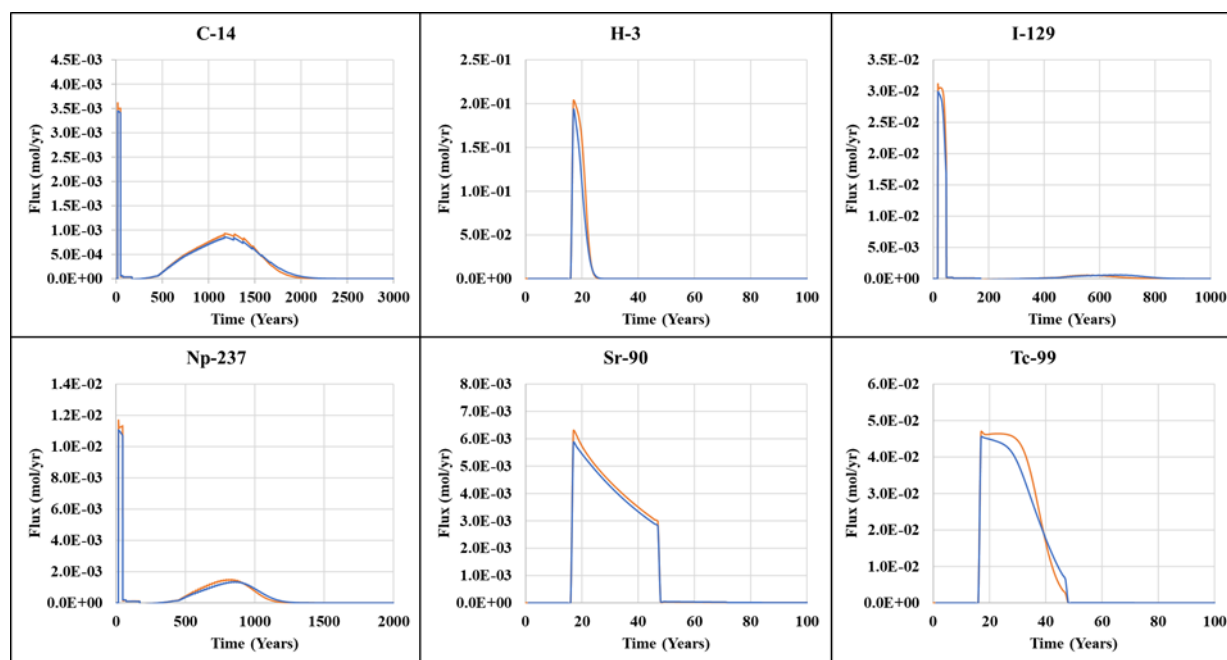


Figure 4-124. ST09 Case01 (Intact) Flux of C-14, H-3, I-129, Np-237, Sr-90, and Tc-99 from Waste Zone for the PORFLOW (blue) and GoldSim® (gold) Models

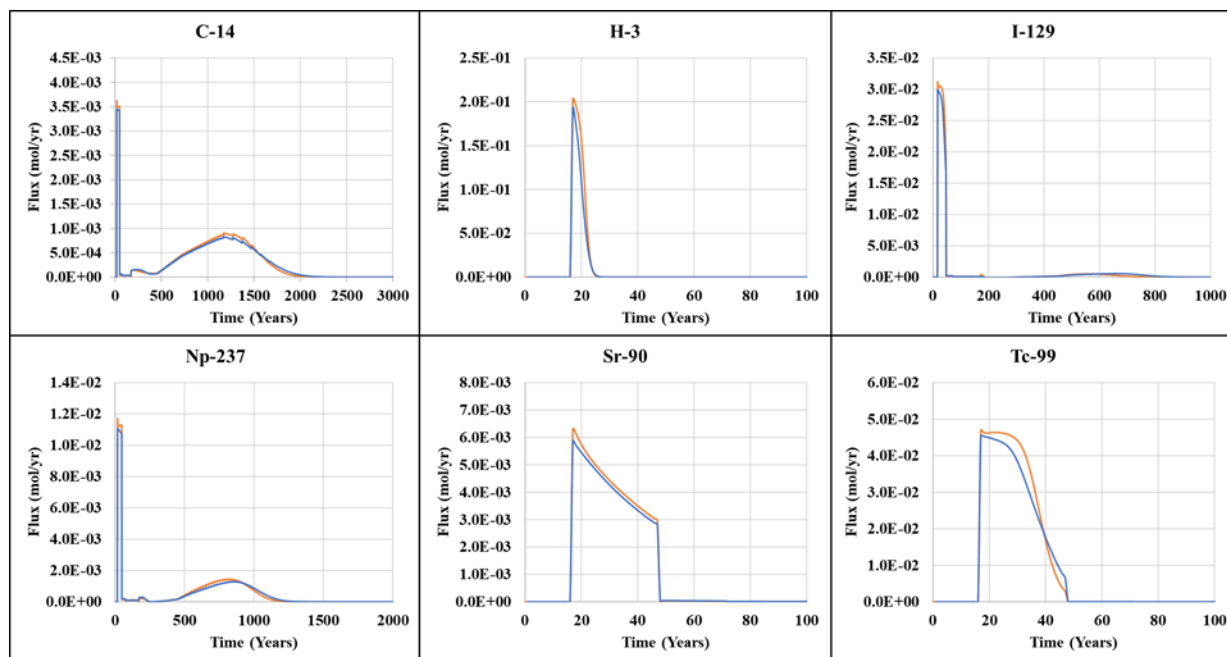


Figure 4-125. ST09 Case11b (Subsided) Flux of C-14, H-3, I-129, Np-237, Sr-90, and Tc-99 from Waste Zone for the PORFLOW (blue) and GoldSim® (gold) Models

4.4.10.2. Flux to the Water Table from Vadose Zone

The total species fluxes from the GoldSim® ET VZ for Case01 are the total fluxes from VadoseZone_Crushed container. The total species fluxes from the GoldSim® ET VZ for Case11b are the sum of the total fluxes from the VadoseZone_Crushed and VadoseZone_Noncrushed containers.

The total species fluxes from the GoldSim® ST VZ for Case01 are five times the total fluxes from VadoseZone_Intact container. The total species fluxes from the GoldSim® ST VZ for Case11b are the sum of the total fluxes from the VadoseZone_Intact and four times the total fluxes from the VadoseZone_Subside containers.

4.4.10.2.1. ET06

Figure 4-126 shows the ET06 Case01 fluxes to the water table. The fluxes to the water table for C-14, H-3, Np-237, and Tc-99 show excellent agreement (8%, 2%, 13%, and 10% lower than the PORFLOW model peak fluxes, respectively). Peak flux to the water table for I-129 is 45% higher than predicted by the PORFLOW model before placement of the interim and final covers. As the final closure cap degrades, fluxes from both models converge. The differences in peak flux to the water table for H-3 between the two models are probably due to mesh and time-step refinement and numerical dispersion. Peak flux to the water table for Sr-90 is several orders of magnitude higher than predicted by PORFLOW before the final cover is applied. This is due to the significant amount of back-diffusion and lateral diffusion predicted by PORFLOW which cannot be modeled in GoldSim®.

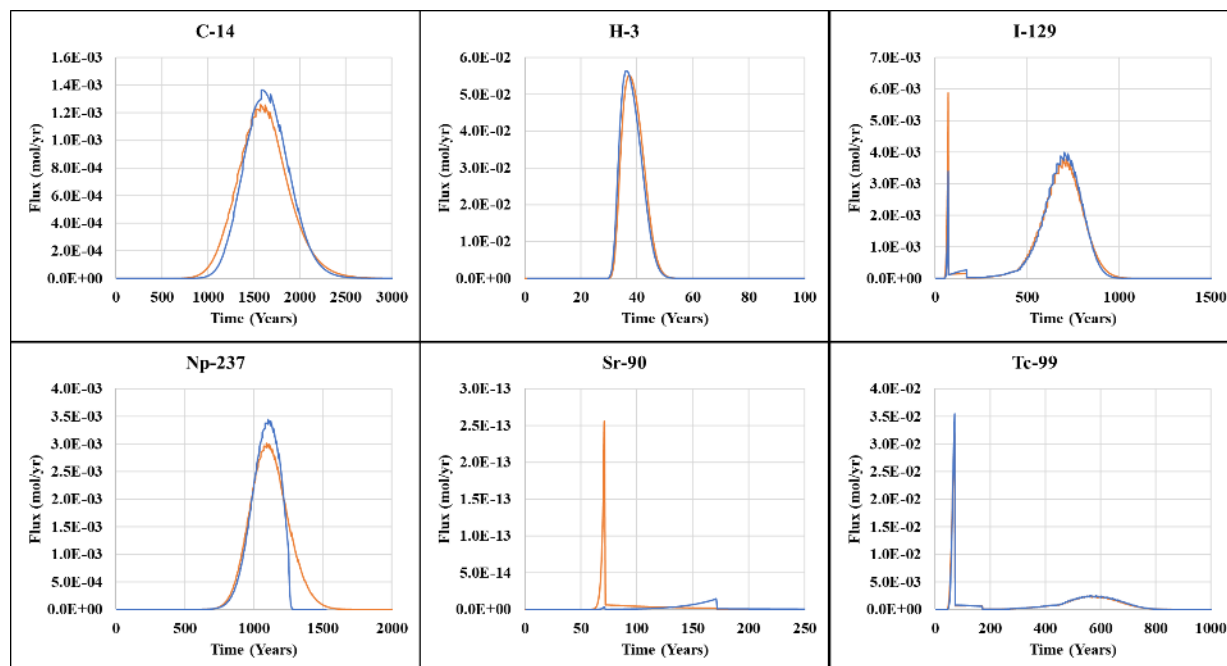


Figure 4-126. ET06 Case01 (Intact) Flux to the Water Table of C-14, H-3, I-129, Np-237, Sr-90, and Tc-99 for the PORFLOW (blue) and GoldSim® (gold) Models

Figure 4-127 displays the ET06 Case11b (subsided) fluxes to the water table for C-14, H-3, I-129, Np-237, Sr-90, and Tc-99. C-14 flux to the water table tracks the response in the PORFLOW model except for the period immediately following dynamic compaction and installation of the final cover. The GoldSim® model peak fluxes for C-14 and Tc-99 are 12% and 16%, respectively, lower than the peak fluxes predicted by PORFLOW. Peak flux to the water table for I-129 is predicted by GoldSim® to be 43% higher during the time directly following interim cover placement. Np-237 peak flux to the water table is 16% lower for the GoldSim® model compared to PORFLOW. Sr-90 peak flux is 53% lower for the GoldSim® model compared to PORFLOW, which is opposite of what is seen in Case01 (intact). This different behavior is believed to be caused by a reduction in diffusion-dominated flow (the infiltration rate for Case11b (subsided) is higher than for Case01 (intact) and, therefore, advection dominates). As the final closure cap degrades, the fluxes predicted by both models converge. The small differences in peak flux to the water table for H-3 (9%) between the two models are probably due to mesh and time-step refinement and numerical dispersion.

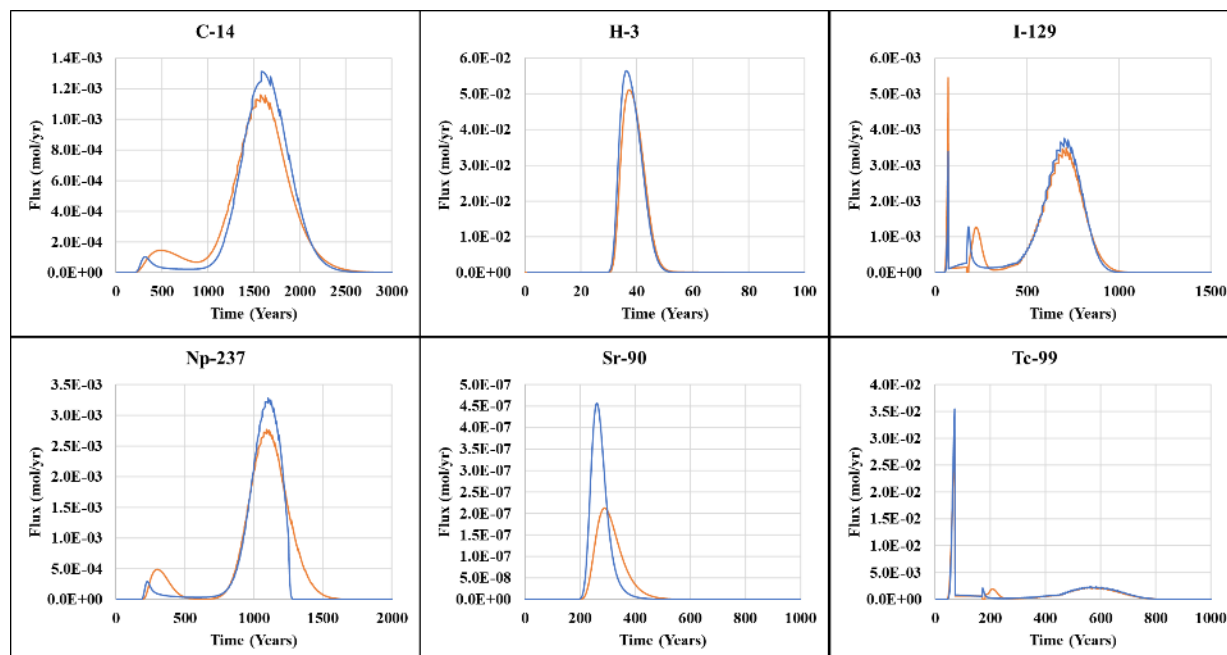


Figure 4-127. ET06 Case11b (Subsided) Flux to the Water Table of C-14, H-3, I-129, Np-237, Sr-90, and Tc-99 for the PORFLOW (blue) and GoldSim® (gold) Models

4.4.10.2.2. ST06

Figure 4-128 shows the ST06 Case01 (intact) fluxes to the water table. The GoldSim® model fluxes to the water table for C-14, H-3, I-129, Np-237, and Tc-99 show good agreement with PORFLOW (GoldSim® model peak fluxes are 5%, 23%, 20%, 17%, and 3% higher, respectively, than PORFLOW). For Sr-90, the GoldSim® model does not capture the spike in flux between Years 46 and 171. The Sr-90 peak fluxes beyond Year 1,000 are different in magnitude (46% lower in the GoldSim® model than PORFLOW) and lag each other (peak time difference of 8%). Examination of PORFLOW slices through the center of the domain and at the water table reveals spikes in concentrations at the east and west edges of the ST footprint. These edges are near the 40-foot overhang of the final closure cap where intact infiltration can enter the edges of the waste footprint and advective fluxes to the water table are faster than in the interior core of the footprint. As the final cover degrades, fluxes predicted by both models converge.

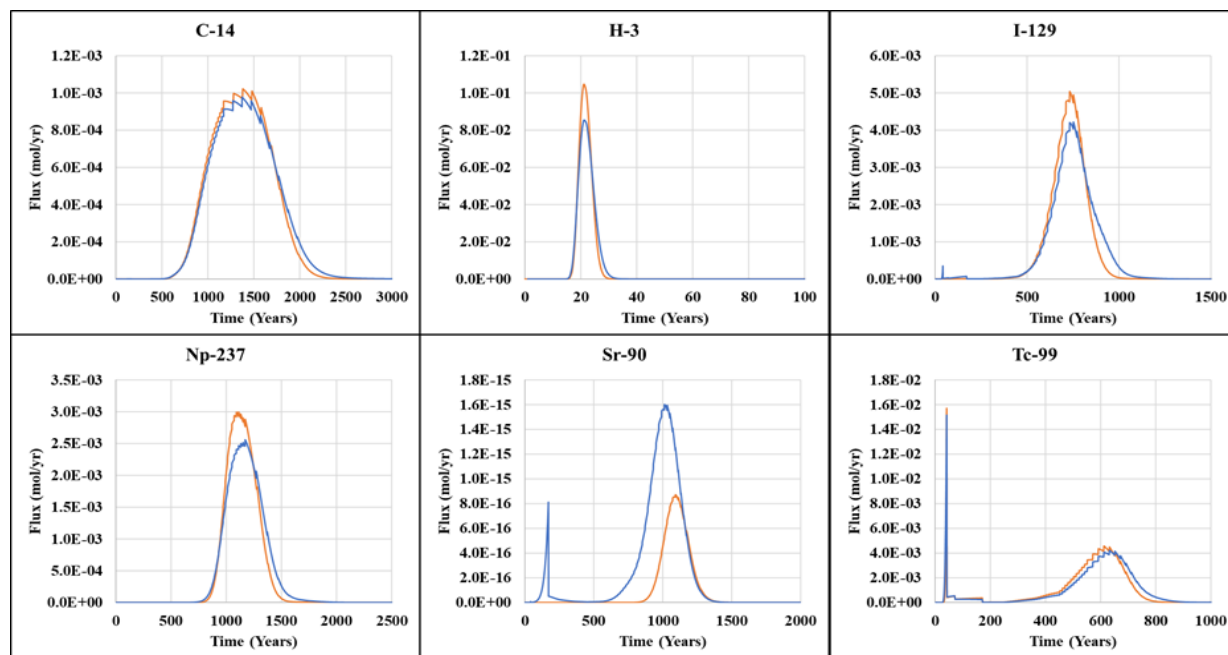


Figure 4-128. ST06 Case01 (Intact) Flux to the Water Table of C-14, H-3, I-129, Np-237, Sr-90, and Tc-99 for the PORFLOW (blue) and GoldSim® (gold) Models

Figure 4-129 displays the ST06 Case11b (subsided) fluxes to the water table. The fluxes to the water table for C-14, H-3, I-129, Np-237, and Tc-99 show good agreement (11%, 1%, 4%, 0%, and 16% difference in peak flux, respectively). Like ST06 Case01 (intact) above, Sr-90 flux to the water table in the GoldSim® model poorly tracks the PORFLOW flux curve; peak Sr-90 flux in the GoldSim® model is 89% lower than the peak flux in PORFLOW.

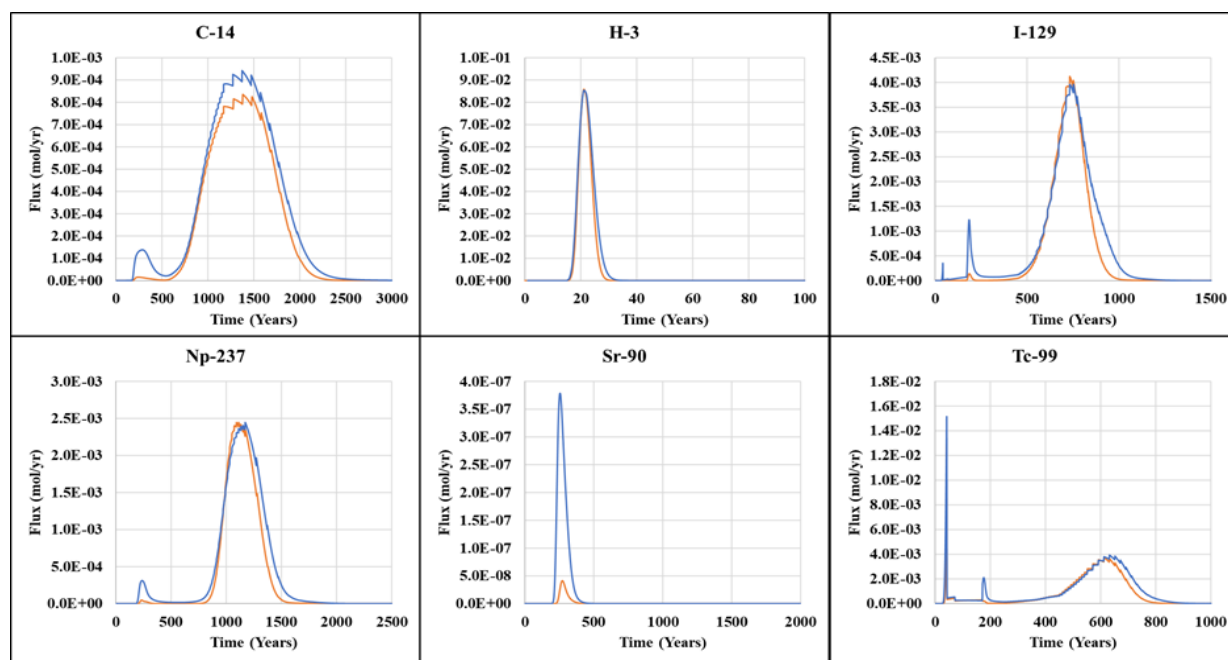


Figure 4-129. ST06 Case11b (Subsided) Flux to the Water Table of C-14, H-3, I-129, Np-237, Sr-90, and Tc-99 for the PORFLOW (blue) and GoldSim® (gold) Models

4.4.10.2.3. ST09

Figure 4-130 shows the ST09 Case01 (intact) fluxes to the water table. Fluxes to the water table for C-14, H-3, I-129, Np-237, and Tc-99 show good agreement (9%, 14%, 0%, 2%, and 4% difference in peak flux, respectively). Peak flux to the water table for Sr-90 is 212% higher in GoldSim[®] than predicted by PORFLOW before the final closure cap is placed. This is due to the significant amount of back-diffusion and lateral diffusion predicted by PORFLOW which cannot be reproduced in GoldSim[®].

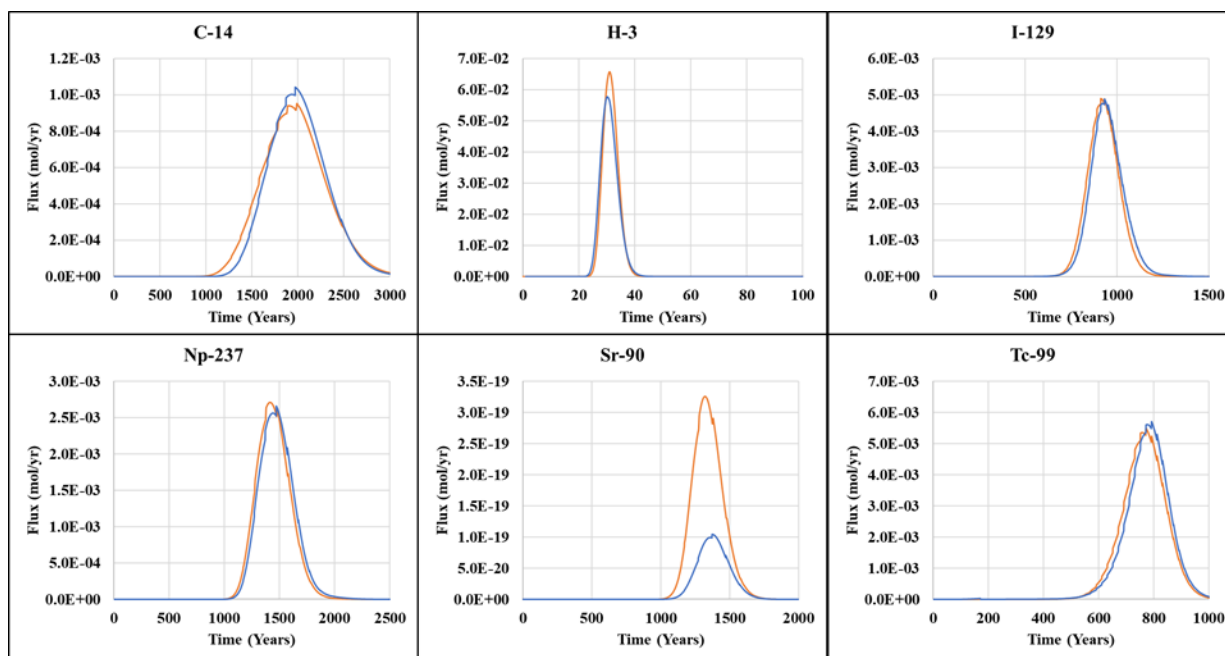


Figure 4-130. ST09 Case01 (Intact) Flux to the Water Table of C-14, H-3, I-129, Np-237, Sr-90, and Tc-99 for the PORFLOW (blue) and GoldSim[®] (gold) Models

Figure 4-131 displays the ST09 Case11b (subsided) fluxes to the water table. Fluxes to the water table for C-14, H-3, I-129, Np-237, and Tc-99 show good agreement (23%, 6%, 13%, 13%, and 16% difference in peak flux, respectively). Like ST06 Case01 (intact and subsided) above, Sr-90 flux to the water table poorly tracks the PORFLOW flux curve; peak Sr-90 flux in the GoldSim[®] model is 92% higher than the peak flux in PORFLOW.

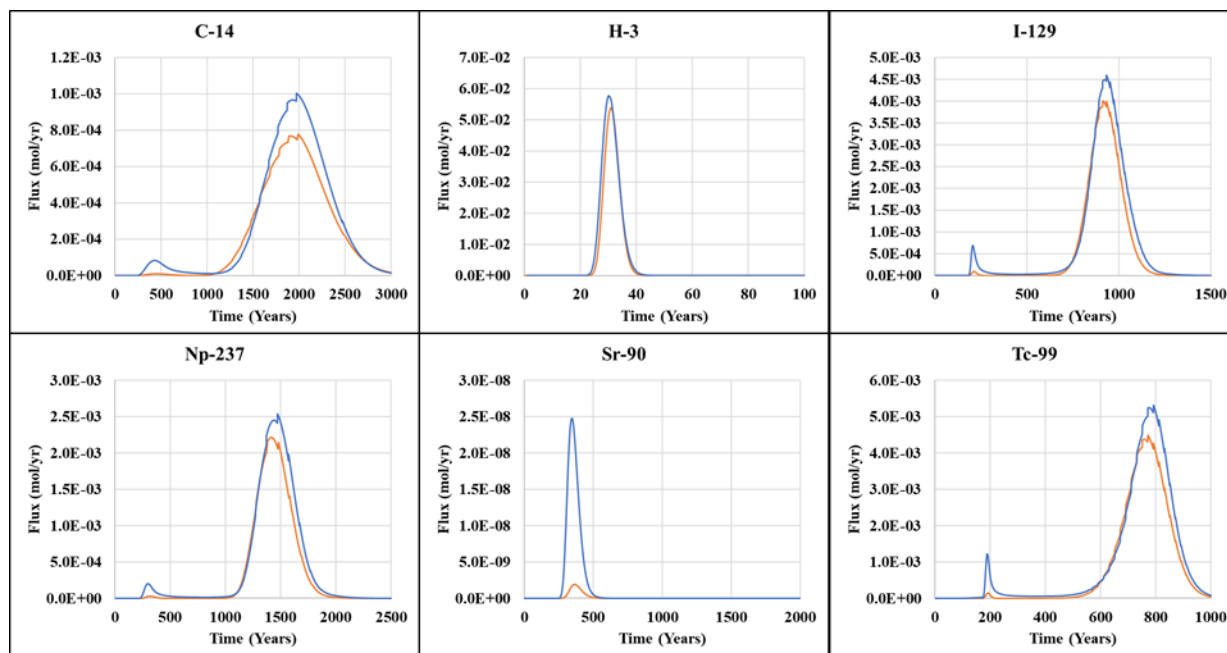


Figure 4-131. ST09 Case11b (Subsided) Flux to the Water Table of C-14, H-3, I-129, Np-237, Sr-90, and Tc-99 for the PORFLOW (blue) and GoldSim® (gold) Models

4.4.10.3. Summary and Conclusions

GoldSim® cell and cell network models are developed to simulate the transport of radionuclides from the WZ within the ET and ST footprint through the VZ to the water table using the hydrostratigraphy for ET06, ST06, and ST09. The GoldSim® model calculates advective and diffusive fluxes for parent radionuclides. During the development of the GoldSim® VZ model, results from the PORFLOW 3-D ET and ST VZ models have been postprocessed to generate soil layer Darcy velocities and water saturations as input to the GoldSim® models.

Results from PORFLOW transport simulations are used to benchmark the GoldSim® model as described above in Section 4.4.10. GoldSim® model results are found to be comparable to those obtained via the 3-D PORFLOW models considering the limitations of the 1-D GoldSim® transport models. The results presented in Section 4.4.10 are for benchmarking only; the only calibration is for ET06 percent subsidence. A reassessment is made when the GoldSim® ET and ST VZ models are coupled to the GoldSim® aquifer zone model introduced in Section 4.4.11.

A comparison of PORFLOW and GoldSim® peak fluxes to the water table and peak times for ET06 Case01 and ET Case11b are shown in Table 4-41. Similarly, Table 4-42 and Table 4-43 present a comparison of PORFLOW and GoldSim® model peak fluxes to the water table and peak times for ST06 Case01 (intact) plus Case11b (subsided) and ST06 Case01 (intact) and Case11b (subsided), respectively.

Table 4-41. Comparison of PORFLOW and GoldSim® Peak Fluxes to Water Table and Peak Times for ET06 Case01 (Intact) and Case 11b (Subsided)

Radionuclide	PORFLOW		GoldSim®		% Difference (GoldSim® - PORFLOW)	
	Peak Flux (gmol yr ⁻¹)	Peak Time (Year)	Peak Flux (gmol yr ⁻¹)	Peak Time (Year)	Peak Flux	Peak Time
ET06 Intact						
C-14	1.36E-03	1,589	1.26E-03	1,572	-8	-1
H-3	5.63E-02	36	5.50E-02	37	-2	3
I-129	3.99E-03	702	5.79E-03	71	45	-90
Np-237	3.44E-03	1,102	3.01E-03	1,092	-13	-1
Sr-90	1.44E-14	171	2.52E-13	71	>200	-58
Tc-99	3.53E-02	71	3.19E-02	71	-10	0
ET06 Subsided						
C-14	1.31E-03	1,587	1.16E-03	1,572	-12	-1
H-3	5.63E-02	36	5.10E-02	37	-9	3
I-129	3.76E-03	702	5.37E-03	71	43	-90
Np-237	3.28E-03	1,102	2.77E-03	1,092	-16	-1
Sr-90	4.57E-07	261	2.13E-07	289	-53	11
Tc-99	3.53E-02	71	2.96E-02	71	-16	0

Table 4-42. Comparison of PORFLOW and GoldSim® Peak Fluxes to Water Table and Peak Times for ST06 Case01 (Intact) and Case 11b (Subsided)

Radionuclide	PORFLOW		GoldSim®		% Difference (GoldSim® - PORFLOW)	
	Peak Flux (gmol yr ⁻¹)	Peak Time (Year)	Peak Flux (gmol yr ⁻¹)	Peak Time (Year)	Peak Flux	Peak Time
ST06 Intact						
C-14	9.78E-04	1,372	1.02E-03	1,372	5	0
H-3	8.52E-02	21	1.05E-01	21	23	0
I-129	4.22E-03	752	5.04E-03	732	20	-3
Np-237	2.56E-03	1,172	3.00E-03	1,092	17	-7
Sr-90	1.60E-15	1,012	8.67E-16	1,092	-46	8
Tc-99	1.49E-02	42	1.53E-02	42	3	0
ST06 Subsided						
C-14	9.42E-04	1,372	8.35E-04	1,372	-11	0
H-3	8.52E-02	21	8.57E-02	21	1	0
I-129	3.96E-03	752	4.12E-03	732	4	-3
Np-237	2.45E-03	1,172	2.45E-03	1,092	0	-7
Sr-90	3.79E-07	255	4.13E-08	271	-89	6
Tc-99	1.49E-02	42	1.25E-02	42	-16	0

Table 4-43. Comparison of PORFLOW and GoldSim® Peak Fluxes to Water Table and Peak Times for ST09 Case01 (Intact) and Case 11b (Subsided)

Radionuclide	PORFLOW		GoldSim®		% Difference (GoldSim® - PORFLOW)	
	Peak Flux (gmol yr ⁻¹)	Peak Time (Year)	Peak Flux (gmol yr ⁻¹)	Peak Time (Year)	Peak Flux	Peak Time
ST09 Intact						
C-14	1.04E-03	1,972	9.52E-04	1,972	-9	0
H-3	5.76E-02	30	6.58E-02	31	14	3
I-129	4.89E-03	932	4.90E-03	912	0	-2
Np-237	2.66E-03	1,472	2.71E-03	1,407	2	-4
Sr-90	1.04E-19	1,373	3.26E-19	1,316	>200	-4
Tc-99	5.71E-03	792	5.50E-03	772	-4	-3
ST09 Subsided						
C-14	1.00E-03	1,972	7.77E-04	1,972	-23	0
H-3	5.76E-02	30	5.39E-02	31	-6	3
I-129	4.60E-03	932	4.01E-03	912	-13	-2
Np-237	2.54E-03	1,472	2.22E-03	1,408	-13	-4
Sr-90	2.48E-08	345	1.92E-09	362	-92	5
Tc-99	5.31E-03	792	4.49E-03	772	-16	-3

4.4.11. Aquifer Zone Model

The conceptual model of the aquifer zone is shown schematically in Figure 3-73. After transport through the VZ, the radionuclides enter the aquifer zone at the top surface of the water table. Contaminant flux from the VZ is transferred to an aquifer pathway that represents the footprint below the VZ DU. Multiple aquifer pathways are then utilized to model radionuclide transport through the aquifer, ending at the 100-meter POA, as described in Section 3.5.4.5.

The PORFLOW 3-D Aquifer Flow and Transport Model is utilized to estimate initial aquifer geometric parameters and Darcy velocity as well as to provide target concentration profiles for calibration. To calibrate the GoldSim® aquifer model against the PORFLOW aquifer model, 1.0 gmole of the parent radionuclides (C-14, H-3, I-129, Np-237, Sr-90, and Tc-99) are included in the source term at the waste zone to evaluate model calibration.

4.4.11.1. ET06

Figure 4-132 and Figure 4-133 display the concentration at the 100-meter POA for the six parent radionuclides for aquifer model calibration of the ET06 intact (Case01) and ET06 subsided (Case11b) cases, respectively. Initial benchmarking (prior to any modifications to the geometric parameters or Darcy velocity) predicts peak concentrations that are orders of magnitude higher than predicted by PORFLOW. To better match PORFLOW model results, multipliers are utilized to modify the Darcy velocity, flow area, and dispersivity. The Darcy velocity of each layer of the aquifer model (upper sandy, clayey, and lower sandy) is multiplied by 0.4; flow area is multiplied by 0.2; and dispersivity is multiplied by 0.5. It is found that Sr-90 and Tc-99 cannot be calibrated to match the predicted PORFLOW model concentrations. For this reason, only C-14, H-3, I-129,

and Np-237 are included in the uncertainty and sensitivity analysis of radionuclide transport in trenches.

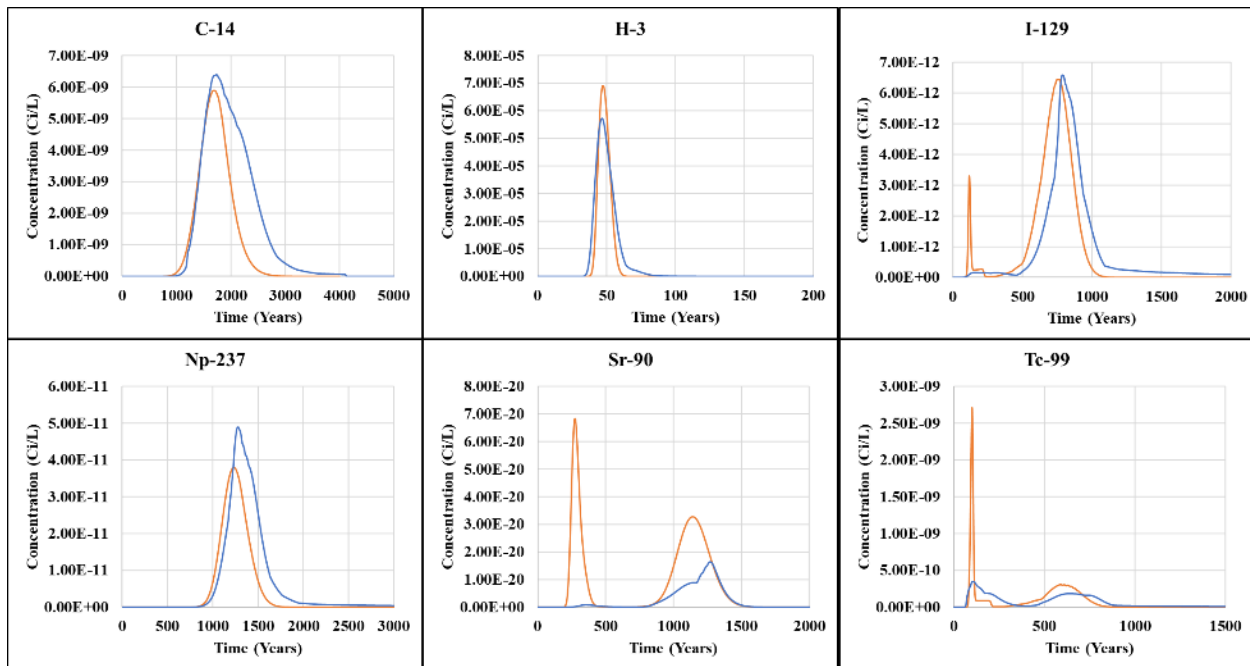


Figure 4-132. Concentrations of C-14, H-3, I-129, Np-237, Sr-90, and Tc-99 at the 100-meter POA for ET06 Case01 (Intact) for the PORFLOW (blue) and GoldSim® (gold) Models

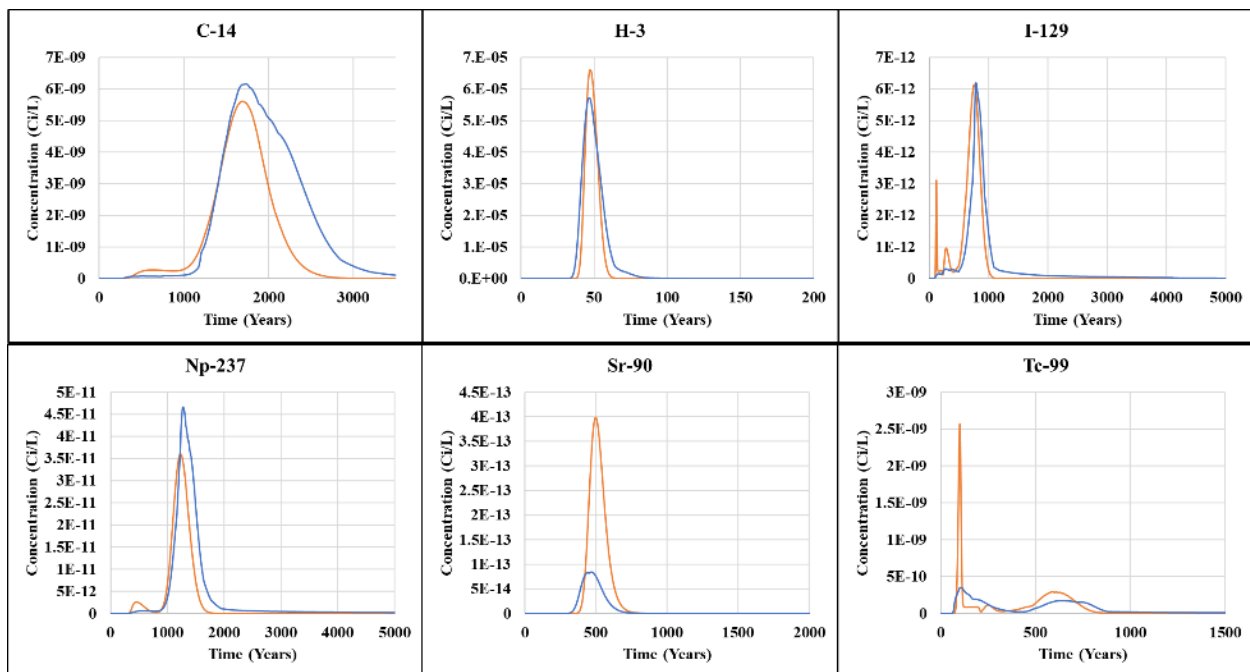


Figure 4-133. Concentrations of C-14, H-3, I-129, Np-237, Sr-90, and Tc-99 at the 100-meter POA for ET06 Case11b (Subsided) for the PORFLOW (blue) and GoldSim® (gold) Models

The maximum concentration values and the time of the highest peak predicted for ET06 are listed in Table 4-44. The percent differences in the maximum concentrations of Sr-90 and Tc-99 are greater than 200%. This is believed to be caused by the complex hydrostratigraphy below the ET06 footprint, which further complicates the 3-D to 1-D abstraction. The limited set of radionuclides selected for the uncertainty analysis (C-14, H-3, I-129, and Np-237) reflects a wide range in K_d values (Table 3-42) and half-lives (Table 3-41).

Table 4-44. Comparison of GoldSim® and PORFLOW Model Peak Concentrations and Times at 100-meter POA for ET06

Radionuclide	PORFLOW		GoldSim®		% Difference (GoldSim® - PORFLOW)	
	Max. Conc. (gmol L^{-1})	Time of Max. Conc. (Year)	Max. Conc. (gmol L^{-1})	Time of Max. Conc. (Year)	Max. Conc.	Time of Max. Conc.
ET06 Intact						
C-14	6.39E-09	1,733.31	5.89E-09	1,690	-8	-2
H-3	5.71E-05	47	6.90E-05	47	21	0
I-129	6.58E-12	787	6.45E-12	764	-2	-3
Np-237	4.89E-11	1,279.82	3.80E-11	1,235	-22	-4
Sr-90	1.65E-20	1,271.68	6.83E-20	275	>200	-78
Tc-99	3.50E-10	107	2.71E-09	100	>200	-7
ET06 Subsided						
C-14	6.16E-09	1,733.31	5.61E-09	1,690	-9	-2
H-3	5.71E-05	47	6.59E-05	47	15	0
I-129	6.19E-12	787	6.14E-12	764	-1	-3
Np-237	4.66E-11	1,279.82	3.60E-11	1,235	-23	-4
Sr-90	8.42E-14	1,271.68	3.99E-13	499	>200	-61
Tc-99	3.50E-10	107	2.57E-09	100	>200	-7

4.4.11.2. ST06

Figure 4-134 and Figure 4-135 display the concentration at the 100-meter POA for the six parent radionuclides for aquifer model calibration of the ST06 intact (Case01) and ST06 subsided (Case11b) cases, respectively. As for ET06, multipliers are utilized to modify the Darcy velocity, flow area, and dispersivity to better match PORFLOW model results. The Darcy velocity of each layer of the aquifer model (upper sandy, clayey, and lower sandy) is multiplied by 0.3 and dispersivity is multiplied by 0.5. The flow area of the upper sandy layer, clayey layer, and lower sandy layer is multiplied by 0.15, 0.15, and 0.13, respectively. Sr-90 cannot be calibrated to match the predicted PORFLOW model concentrations for the intact case. Both timing and peak concentration match well with the PORFLOW target concentrations for the other five radionuclides.

The maximum concentration values and the time of the highest peak predicted for ST06 are listed in Table 4-45. The percent difference in the maximum concentration of Sr-90 predicted by the PORFLOW and GoldSim® models for the intact case is less than the difference for ET06, but it is still significant at -88%. This is thought to be caused by the complex hydrostratigraphy below the ST06 footprint, which further complicates the 3-D to 1-D abstraction. It is noted that the maximum

concentration of Sr-90 in the subsidence case shows excellent agreement with the PORFLOW model in contrast to the intact case.

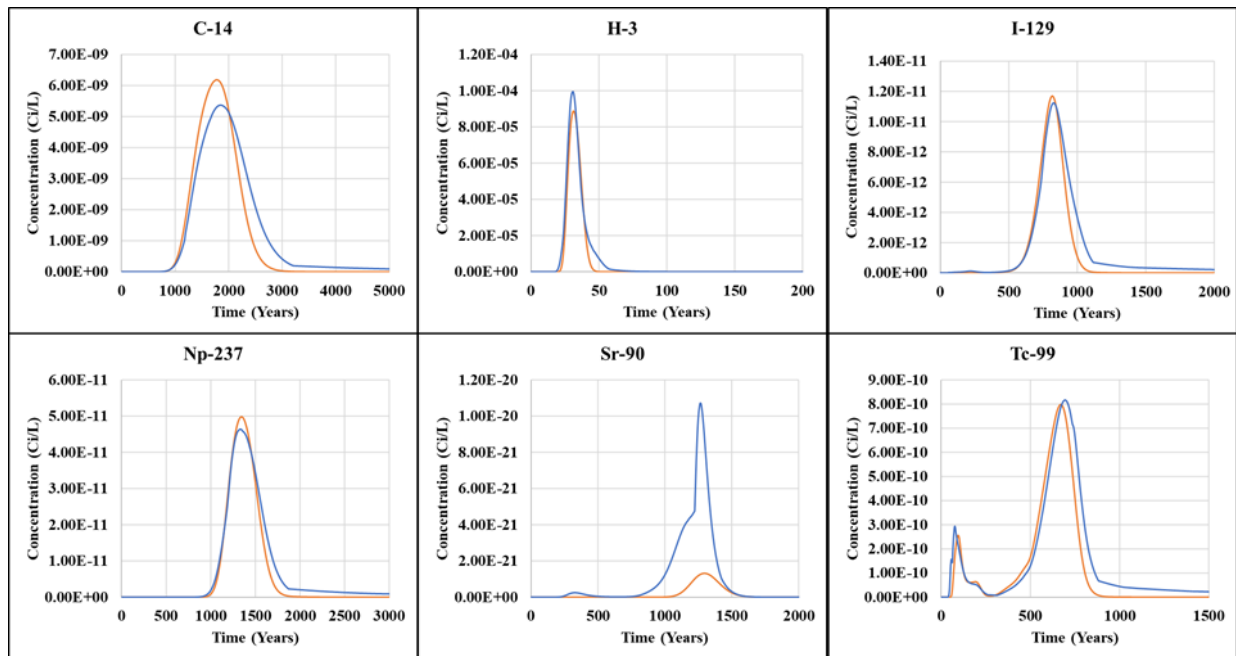


Figure 4-134. Concentrations of C-14, H-3, I-129, Np-237, Sr-90, and Tc-99 at the 100-meter POA for ST06 Case01 (Intact) for the PORFLOW (blue) and GoldSim® (gold) Models

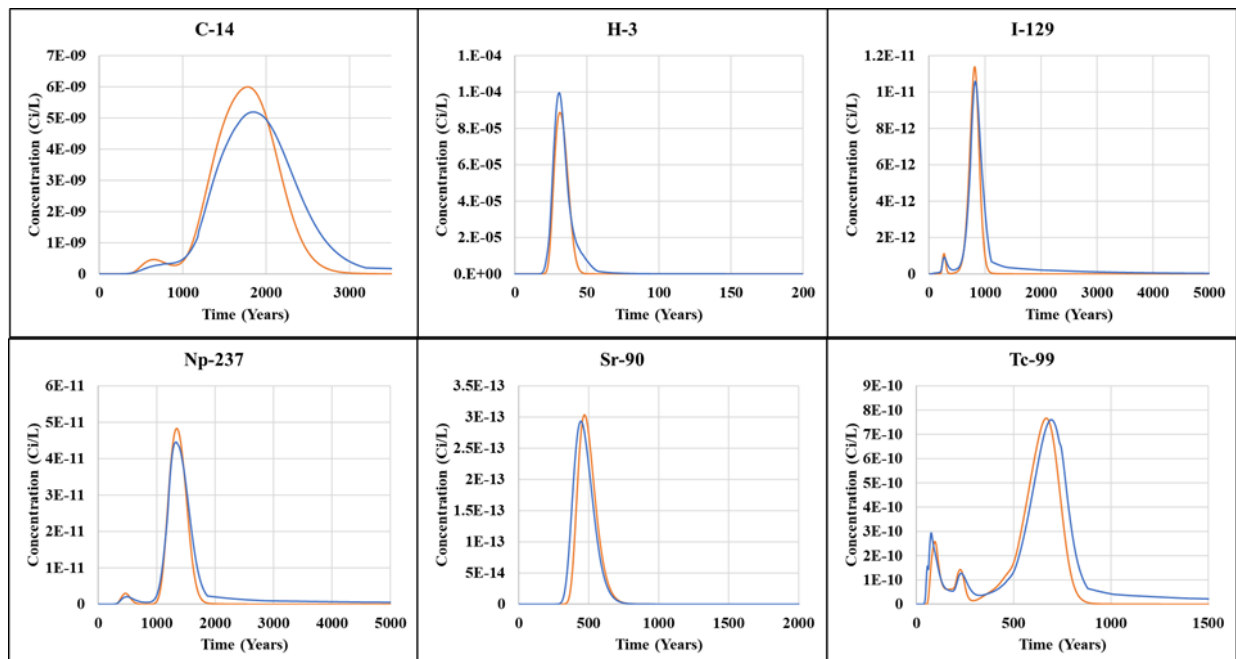


Figure 4-135. Concentrations of C-14, H-3, I-129, Np-237, Sr-90, and Tc-99 at the 100-meter POA for ST06 Case11b (Subsided) for the PORFLOW (blue) and GoldSim® (gold) Models

Table 4-45. Comparison of GoldSim® and PORFLOW Model Peak Concentrations and Times at 100-meter POA for ST06

Radionuclide	PORFLOW		GoldSim®		% Difference (GoldSim® - PORFLOW)	
	Max. Conc. (gmol L ⁻¹)	Time of Max. Conc. (Year)	Max. Conc. (gmol L ⁻¹)	Time of Max. Conc. (Year)	Max. Conc.	Time of Max. Conc.
ST06 Intact						
C-14	5.37E-09	1,855	6.19E-09	1,780	15	-4
H-3	9.95E-05	31	8.87E-05	31	-11	0
I-129	1.12E-11	827	1.17E-11	818	4	-1
Np-237	4.64E-11	1,331	4.98E-11	1,345	7	1
Sr-90	1.07E-20	1,266	1.32E-21	1,295	-88	2
Tc-99	8.17E-10	694	7.98E-10	670	-2	-3
ST06 Subsided						
C-14	5.19E-09	1,840	6.00E-09	1,780	16	-3
H-3	9.95E-05	31	8.87E-05	31	-11	0
I-129	1.06E-11	826	1.14E-11	815	8	-1
Np-237	4.45E-11	1,328	4.83E-11	1,340	8	1
Sr-90	2.93E-13	444	3.04E-13	471	3	6
Tc-99	7.61E-10	693	7.67E-10	667	1	-4

4.4.11.3. ST09

Figure 4-136 and Figure 4-137 display the concentration at the 100-meter POA for the six parent radionuclides for aquifer model calibration of the ST09 intact (Case01) and ST09 subsided (Case11b) cases, respectively. As for ET06 and ST06, multipliers are utilized to modify the Darcy velocity, flow area, and dispersivity to better match PORFLOW model results. The Darcy velocity of each layer of the aquifer model (upper sandy, clayey, and lower sandy) is multiplied by 0.8 and dispersivity is multiplied by 0.4. The flow area of the upper sandy layer, clayey layer, and lower sandy layer is multiplied by 0.16. Both timing and peak concentration match well with the PORFLOW target concentrations for all radionuclides but Sr-90.

The maximum concentration values and the time of the highest peak predicted for ST09 are listed in Table 4-46. The percent difference in the maximum concentration of Sr-90 for the subsidence case is quite high at 68%. This is believed to be caused by the complex hydrostratigraphy below the ST09 footprint, which further complicates the 3-D to 1-D abstraction. The limited set of radionuclides selected for the uncertainty analysis (C-14, H-3, I-129, and Np-237) display percent differences of less than 20%.

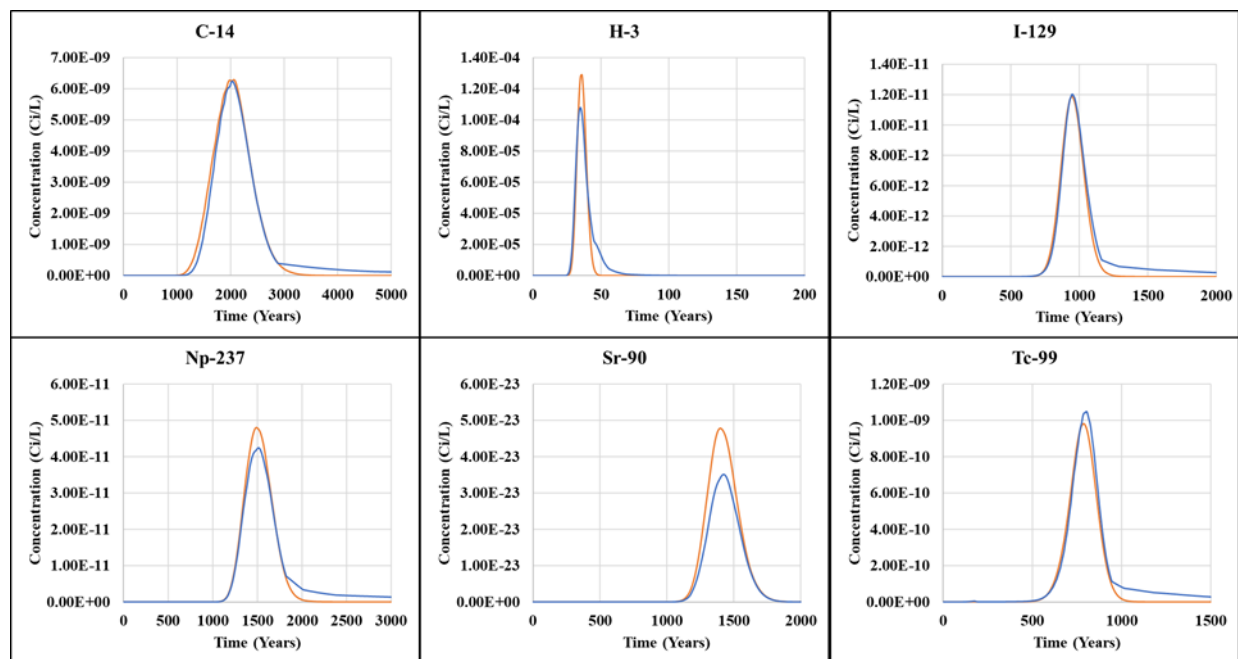


Figure 4-136. Concentrations of C-14, H-3, I-129, Np-237, Sr-90, and Tc-99 at the 100-meter POA for ST09 Case01 (Intact) for the PORFLOW (blue) and GoldSim® (gold) Models

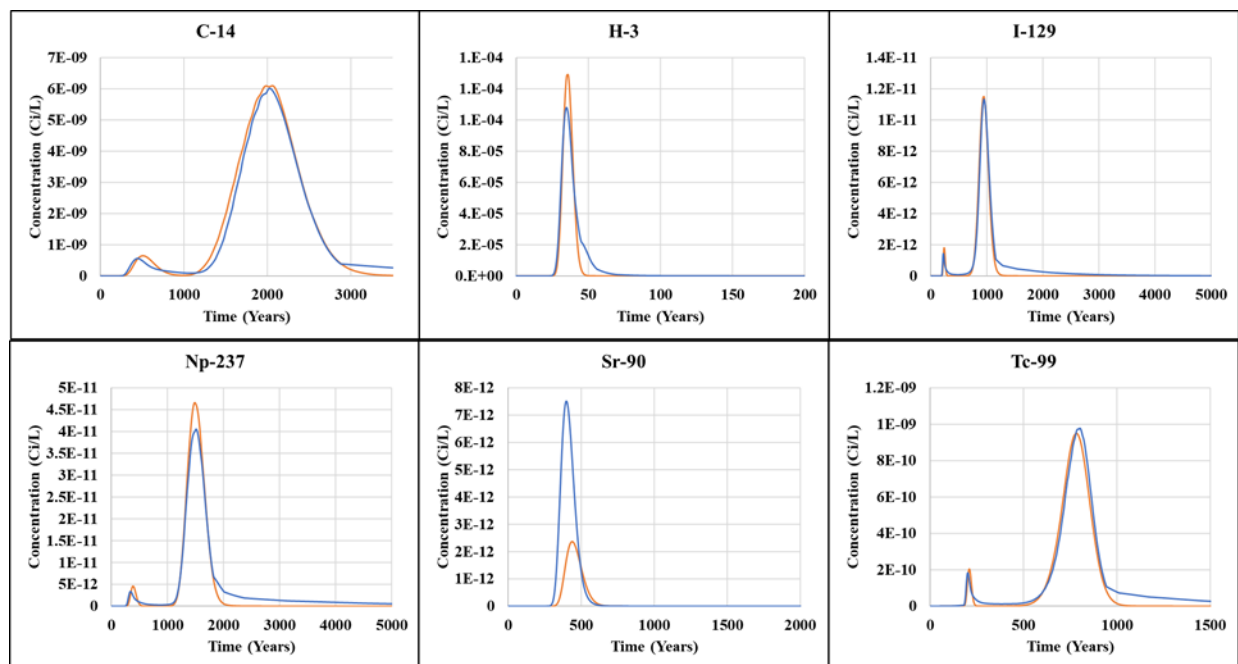


Figure 4-137. Concentrations of C-14, H-3, I-129, Np-237, Sr-90, and Tc-99 at the 100-meter POA for ST09 Case11b (Subsided) for the PORFLOW (blue) and GoldSim® (gold) Models

Table 4-46. Comparison of GoldSim® and PORFLOW Model Peak Concentrations and Times at 100-meter POA for ST09

Radionuclide	PORFLOW		GoldSim®		% Difference (GoldSim® - PORFLOW)	
	Max. Conc. (gmol L ⁻¹)	Time of Max. Conc. (Year)	Max. Conc. (gmol L ⁻¹)	Time of Max. Conc. (Year)	Max. Conc.	Time of Max. Conc.
ST09 Intact						
C-14	6.24E-09	2,028	6.29E-09	2,060	1	2
H-3	1.08E-04	35	1.29E-04	36	20	3
I-129	1.20E-11	949	1.19E-11	948	-1	0
Np-237	4.24E-11	1,511	4.80E-11	1,490	13	-1
Sr-90	3.51E-23	1,425	4.78E-23	1,400	36	-2
Tc-99	1.05E-09	802	9.82E-10	787	-6	-2
ST09 Subsided						
C-14	6.01E-09	2,028	6.10E-09	2,060	1	2
H-3	1.08E-04	35	1.29E-04	36	20	3
I-129	1.13E-11	949	1.15E-11	946	2	0
Np-237	4.05E-11	1,511	4.66E-11	1,485	15	-2
Sr-90	7.51E-12	398	2.37E-12	439	-68	10
Tc-99	9.78E-10	949	9.50E-10	784	-3	-17

4.5. LOW-ACTIVITY WASTE VAULT

LAWV disposal limits for the ELLWF through the 1,000-year period of performance are developed for the following exposure pathways: GW protection, air, all-pathways, IHI, and radon. This section describes in detail the development and implementation of conceptual models for the LAWV for the GW pathway. Conceptual models for the IHI exposure pathway are described in Section 3.7.3 and Section 7.3. Conceptual models for the air and radon pathways are described in Section 3.6.

4.5.1. Waste Zone Conceptual Model: Material and Hydraulic Properties

Based on structural modeling that considers vault loadings (both static and seismic) and rebar corrosion, Carey (2005) estimated that the mean time to LAWV collapse is 2,805 years with a standard deviation of 920 years. Two LAWV waste zone representations are considered: before vault collapse and after vault collapse.

4.5.1.1. Before Collapse

Before vault collapse, the LAWV waste zone will consist of low-activity waste contained within stacked B-25 boxes, B-12 boxes, drums, other metal containers and/or concrete containers. B-25 boxes are stacked four high for a waste thickness of 17.3 feet. The waste within the containers typically has a very low density and significant internal void space. No soil, grout, or any other material will exist between the stacked containers, and a significant void space will exist between the top of the container stack and the LAWV bridge beams and roof. The bridge beams are a minimum of 20 feet above the floor, while the roof is a minimum of 24 feet, 6 inches above the floor (Figure 2-68). Additionally, before vault collapse, significant corrosion of the metal waste

containers is also anticipated to occur, resulting in limited self-compaction of the waste zone under its own weight (the waste within the containers typically has a very low density) before the time of vault collapse. The PORFLOW code models flow and transport through porous media and cannot represent a significant empty space. Additionally, adjacent materials within a PORFLOW model that have significantly different saturated hydraulic conductivities can create flow convergence problems. Phifer et al. (2006) recommended that the LAWV waste zone and vault interior before vault collapse be represented hydraulically by E-Area CLSM, Figure 4-138(a), which has a saturated hydraulic conductivity six orders of magnitude greater than the vault concrete enclosing it. This is deemed appropriate because the vault concrete, not the waste zone represented by CLSM, will control the flow of water through the waste zone.

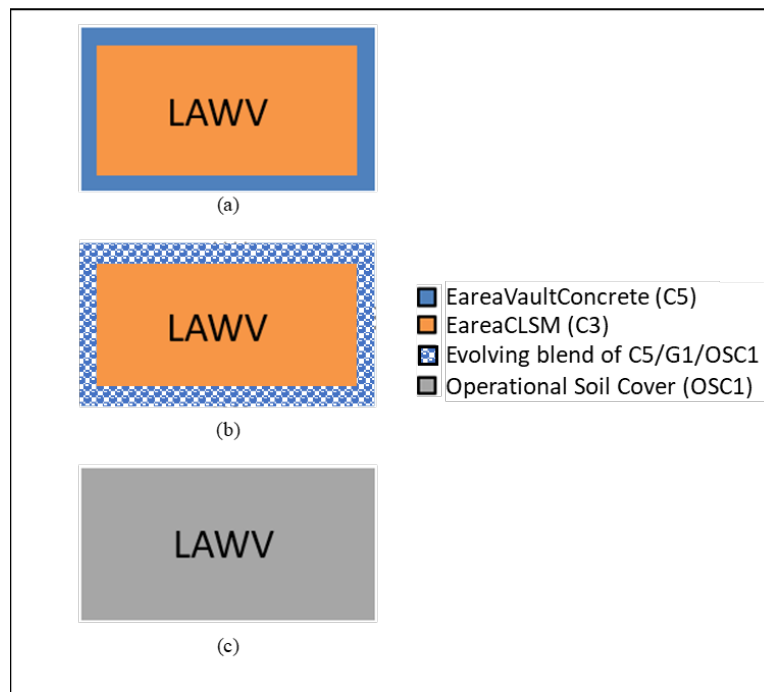


Figure 4-138. Low-Activity Waste Vault Waste Zone Conceptual Model of Hydraulic Properties in (a) Intact, (b) Cracked, and (c) Collapsed States

In past ELLWF PAs, the hydraulic properties of concrete have abruptly changed from those of intact concrete to soil to represent vault structural collapse or complete deterioration of the concrete matrix. In PA2022, concrete degradation is modeled as a gradual process where, starting at the time of site closure, concrete hydraulic properties are transformed into those of soil over a period of 500 years. A detailed conceptual model of LAWV concrete degradation and the associated impact on material and hydraulic properties are described in detail in Sections 4.5.3.1 and 4.5.3.6, respectively. In Figure 4-138(b), the concrete degradation is represented as an evolving blend over 500 years of EareaVaultConcrete (C5), Gravel (G1), and OSC1.

4.5.1.2. After Collapse

Jones and Phifer (2007) estimated that the interior of the LAWV has a subsidence potential of approximately 21 feet. Upon vault collapse, it is anticipated that the broken bridge beams and roof,

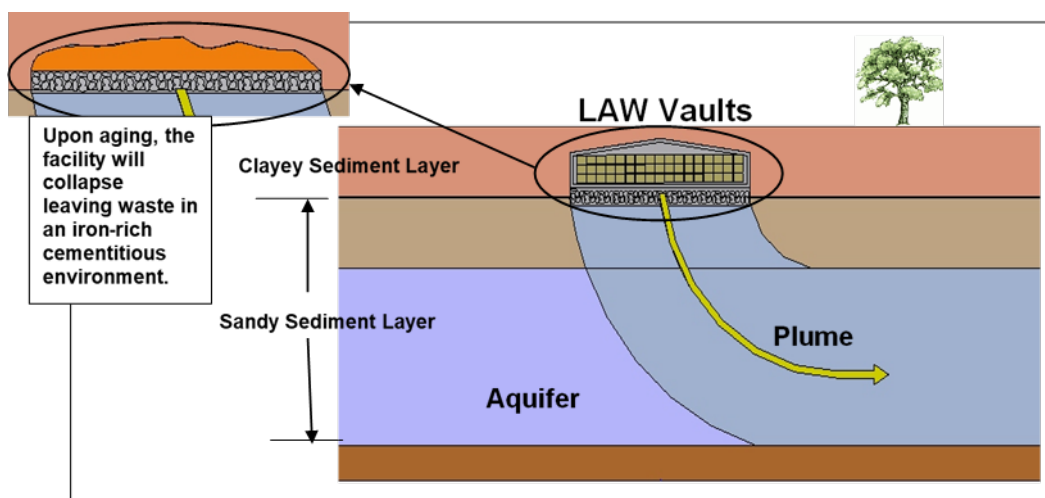
along with the overlying closure cap soils, will fall into the vault interior crushing the corroded containers and waste to a nominal 4.5-foot thickness (averaged over the entire waste zone footprint). Due to the significant soil presence within a collapsed LAWV and the fluffing of the soil as it collapses into the vault, the LAWV waste zone and vault interior after vault collapse will be represented hydraulically by OSC1 as shown in Figure 4-138(c). Because the OSC will be derived from UVZ soils, UVZ soil properties are used to estimate the properties of OSC1 as discussed in detail in Section 3.8.3.1.2.

Table 3-64 summarizes LAWV waste zone material properties both before and after vault collapse.

4.5.2. Waste Zone Conceptual Model: Geochemical Properties

Key features of the LAWV that impact the geochemical environments within and beneath the vault are described below. More specifically, a geochemical conceptual model for the LAWV is presented that identifies the aqueous chemistry and associated solid phases comprising the waste zone, UVZ, LVZ, and aquifer. The conceptual model also assigns geochemical parameters to each material zone. Kaplan (2016b) provides a detailed description of the development of the geochemical conceptual model, definitions of the different geochemical environments and materials, and assignment of appropriate geochemical parameters for each radionuclide of interest.

Figure 4-139 (Kaplan, 2016b) is a schematic of the geochemical conceptual model for the LAWV.



Note: Overlying final closure cap not shown.

Figure 4-139. Low-Activity Waste Vault Geochemical Conceptual Model Schematic

The cross-section does not show dimensionality and facility-specific details, which are instead assigned in the numerical model (Section 4.5.3 and Section 4.5.3.4). The relevant geochemical environments for the LAWV are fivefold: reducing cement, clayey sediment, sandy sediment, cementitious-leachate-impacted clayey sediment, and cementitious-leachate-impacted sandy sediment. Section 3.8.2.5 provides a description of the four geochemical conceptual environments.

Table 4-47 (Kaplan, 2016b) lists the relevant solid and aqueous phases for the LAWV, along with the associated geochemical parameters (K_d and k_s values) necessary in the PA model to describe

the chemical interactions of radionuclides with these geochemical materials (e.g., sandy sediment, clayey sediment, reducing cement). SRNL (2018) provides look-up tables containing the recommended K_d and k_s values for each radionuclide (table rows) as a function of the different geochemical materials or solid phases (table columns).

4.5.3. PORFLOW Implementation of Vadose Zone Conceptual Model

The LAWV DU is an above-grade reinforced concrete structure containing multiple layers of low-activity waste containers. The LAWV is used to dispose of waste containers exceeding radiological dose and radionuclide concentration limits of other LLW disposal facilities, such as STs and ETs, but not requiring confinement in the ILV. The LAWV is in the eastern sector of the ELLWF and is highlighted in magenta in Figure 4-140.

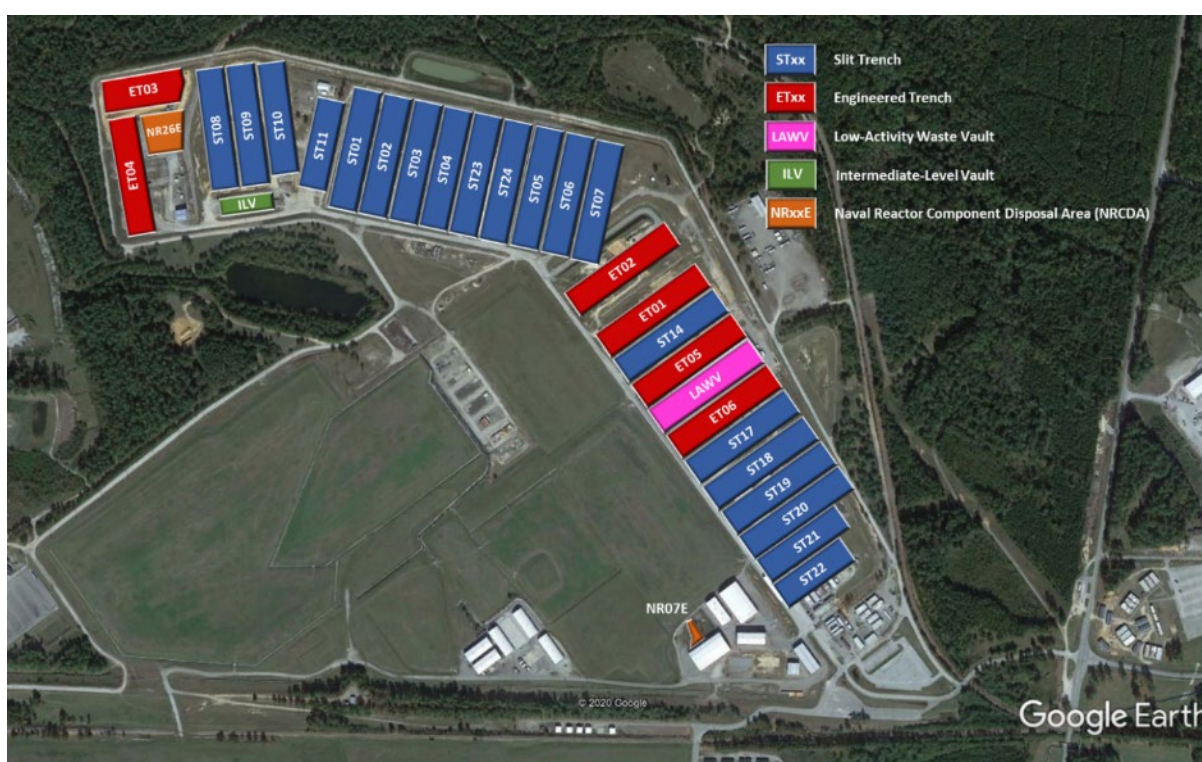


Figure 4-140. Low-Activity Waste Vault Location within the E-Area Low-Level Waste Facility

Section 2.2.5 and Smith (2021b) describe in detail the structural design features, waste types and characteristics, and waste placement procedures for the LAWV that are relevant to the development and implementation within PORFLOW of the LAWV VZ conceptual model. Figure 2-68 (bottom inset) provides an aerial view of the LAWV exterior. The roof peak and slope are just discernable in this view. Figure 2-69 displays an interior view of one cell with four sets of B-25 waste containers stacked four high. Figure 2-68 (middle-left inset) provides a simple plan view of the vault giving the overall dimensions, while Figure 2-68 (upper inset) shows a cross-sectional view (A-A') of a LAWV cell.

Table 4-47. Low-Activity Waste Vault: Conceptual Geochemical Model of Features and Parameters (see Figure 4-139)

Feature		Geochemical Parameter
Solid Phase	Aqueous Phase	
Waste Zone: Active components are iron metal, corrosion products, and surrounding concrete barrier. Metal containers will rust to form Fe-oxides. Eventually the concrete vault structure and B-25 boxes collapse leaving waste in an iron-rich cementitious environment. Cellulosic materials are also present but do not degrade to form CDPs in sufficient quantity to affect sorption. ^{a, b}	Cementitious Leachate: Contacts metal boxes or collapsed, rusted, iron rubble, entering through joints, cracks, and ultimately the collapse of the concrete vault. This is a cementitious-leachate-impacted aqueous phase (elevated pH and ionic strength).	Use cementitious-leachate-impacted Clayey Sediment K_d , $K_{dCementLeach}$. ^c Fe-oxide content will control the sorption chemistry of this zone. It is assumed that the geochemistry of the Clayey Sediment will approximate that of the rusted metal waste form. In reality, the rusted waste form will contain much greater Fe-oxide content than the typical clayey SRS sediment. Also, applying Clayey Sediment K_d values (which have an assumed pH of 5.5) to a system with a higher pH (concrete pH is typically >10) will be bounding because metal sorption (K_d values) will be greater in high-pH than in low-pH systems.
Reducing Concrete Vault: Active components are cement and slag added to concrete in roof, walls and floor. ^d	Cementitious-Impacted Leachate: Three general types of reducing concrete leachate chemistries are controlled by different aged cement phases characterized by elevated pH and ionic strength relative to SRS GW. Leachate will contain sulfides released from slag.	Use Reducing Cement K_d or apparent solubility concentration limits for the three cement ages.
Crushed Stone: Layer beneath LAWV facility. ^e	Fe-Oxide-Impacted Cementitious Leachate: Cement leachate chemistry altered by passing through Fe-oxide controlled environment. Still characterized by elevated pH and ionic strength relative to SRS GW.	Use cementitious-leachate-impacted Clayey Sediment K_d . ^c See footnote (e).
Clayey Sediment: Upper Vadose Zone		Use cementitious-leachate-impacted Clayey Sediment K_d , $K_{dCementLeach}$. ^c
Sandy Sediment: Lower Vadose Zone		Use cementitious-leachate-impacted Sandy Sediment K_d , $K_{dCementLeach}$. ^c
Sandy Sediment: Aquifer Zone	Cementitious Leachate Porewater: Gets diluted with typical SRS GW and the aqueous phase takes on the properties of the latter: pH 5.8 and ionic strength 0.01, except for trace levels of radionuclides.	Use Sandy Sediment K_d .

Notes:

- ^a Waste designated for LAWV contains greater radioactivity than waste disposed of in STs and ETs. Waste is packaged in standard metal boxes (B-25 and B-12 boxes) that are stacked within 12 individual disposal cells in the LAWV. Some cellulosic materials will be disposed of in the LAWV.
- ^b Kaplan (2012) determined that CDPs are not present in sufficient concentrations in the GW beneath the ORWBG to warrant application of a CDP correction factor to K_d values for E-Area. The 2015 update of the New PA Information UDQE (Flach et al., 2014) evaluated elimination of CDP corrections to Clay and Sand Sediment K_d s and Oxidizing and Reducing Cement K_d s and incorporated these changes into the PA baseline.
- ^c The 2010 geochemical data package (Kaplan, 2010) introduced the concept of a cementitious-leachate-impacted zone beneath concrete/grout DUs. This change specifically affected the CIG Trench, LAWV, and ILV models, but has never been formally evaluated through the UDQE process for inclusion in the PA baseline. The current geochemical data package maintains this concept which will be evaluated in the PA2022 revision.
- ^d Reducing cementitious materials are those that contain slag and change the porewater chemistry sufficiently to require unique geochemical parameters (Section 4.3; Kaplan, 2010). The LAWV is constructed with a 16-inch-thick concrete roof, 24-inch-thick interior and exterior concrete walls, and 12-inch-thick concrete floor.
- ^e A 45-inch-thick layer of crushed stone exists immediately beneath the concrete floor of the LAWV. It has not been included in previous PA models because it is believed that this layer will become "silted in" within a relatively short period of time. For this same reason, it is not included in the conceptual geochemical model of this DU and will be modeled as behaving like the cementitious-leachate-impacted Clayey Sediment: Upper Vadose Zone.

Figure 4-141 provides a schematic diagram depicting the 2-D PORFLOW model of the LAWV. The diagram is not to scale. The complete PORFLOW VZ model for the LAWV includes the VZ below the vault, soil backfill around and over the vault, and the final closure cap above the foundation layer. The model represents a slice through the vault cross-section. LAWV dimensions used to build the PORFLOW model are taken from Figure 2-68 (upper inset). Figure 4-141 and Figure 2-68 (upper inset) can be compared to discern modeling approximations. For example, the floor footing that extends beyond the vault walls is not included in the PORFLOW model because it will have little effect on flow and transport. Note that the height of the south wall (24'-9") is very close to that of the north wall (24'-6") but is not identical. The dimensions given in Figure 2-68 (upper inset) and specified slopes of the floor and roof are used to calculate model dimensions that resulted in the south wall being 3 inches taller than the north wall.

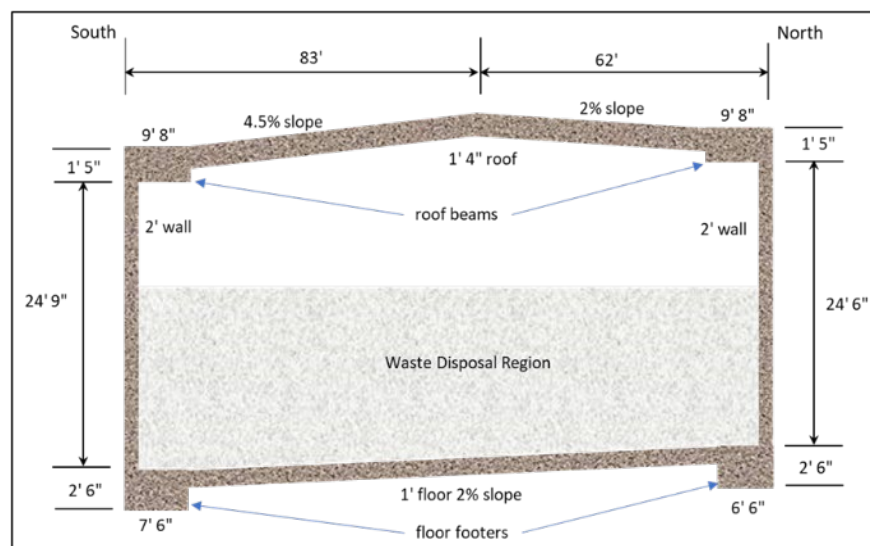


Figure 4-141. Low-Activity Waste Vault PORFLOW Vadose Zone Model Schematic (Smith, 2021b; Figure 2-5)

LAWV operation and closure are described in Section 2.2.5. Key differences from the conceptual model assumptions adopted in PA2008 for the LAWV are summarized below. Smith (2021b) provides more detail:

- The operational period in PA2022 is assumed to be 71 years versus 25 years in PA2008.
- In practice, cells have not been closed as they are filled as assumed in PA2008. Additionally, some waste stored in the LAWV has been recharacterized and transferred to trenches for final disposal. At present, only metal containers, primarily B-25 boxes, are disposed in the LAWV.
- The current conceptual design for the area-wide final closure cap now slopes away from the LAWV roof peak in both directions along the long and short axes of the vault. PA2008 assumed an individual closure cap for the LAWV that sloped in both directions along the short axis only (i.e., the apex of the cap ran parallel to the long axis of the vault).

- A HDPE geomembrane/GCL composite barrier is the primary barrier to water infiltration in the current final closure cap design. The PA2008 closure cap design included only the GCL barrier.

Table 4-48 provides a summary of significant features of the LAWV construction along with a brief description of the modeling approach used.

Table 4-48. Low-Activity Waste Vault Construction Features and Modeling Approach (Smith, 2021b; Table 2-1)

As-Built LAWV Features	As Modeled
Controlled compacted backfill soil base	LAWV soil base modeled as UVZ soil. Thickness of compacted backfill was not provided.
Crusher run stone base over a geotextile filter fabric beneath the vault.	Area beneath the vault modeled as UVZ soil. Crusher run stone base will silt-up following closure.
15-inch graded stone subdrainage system to collect and drain water under the vault to manhole drains during operations. Sealed with grout at end of operations.	Water under the vault conservatively drains to the water table. Subdrainage system is sealed, grouted, and is not functional after the end of operations.
30-inch-thick, reinforced concrete, wall supports that extend 4.5 feet beyond the exterior walls.	Concrete wall supports are modeled without the 4.5-foot extensions beyond the exterior walls.
12-inch-thick, cast-in-place, reinforced concrete floor slab sloped to an interior collection trench that drains to an external sump.	Sloped concrete floor modeled without drainage to external sump to conserve water and maintain material balances around the model. Sump will be grouted at end of operations.
Exterior and interior personnel openings with doors, exterior fan openings, and exterior forklift access openings during operations. Sealed with reinforced concrete at the end of operations	Cell walls modeled as continuous ELLWF vault concrete structures.
AASHTO Type IV bridge beams to support the concrete roof.	Vault interior construction is not modeled. Vault space above the waste region is modeled with waste material properties to allow good water drainage into the waste zone. No radionuclides are deposited in this region.
3-½-inch-thick precast deck panels overlain by 12-½-inch-thick, cast-in-place, reinforced concrete slab for a total 16-inch-thick concrete roof.	Roof modeled as continuous 16-inch-thick ELLWF vault concrete.
A bonded-in-place layer of fiberboard insulation and a layer of waterproof membrane roofing on top of the roof slab.	Sloped concrete roof is assumed to be in place from the start of LAWV operations until roof collapse occurs. The presence of fiberboard insulation and waterproofing on the roof top is simulated by using a very low infiltration rate (0.001 in yr ⁻¹) over the vault during operation and IC.
A gutter/downspout system to drain the roof.	Water draining off the roof is not included in lateral flow to the water table during operations and IC. Gutters and downspouts will be removed when final closure cap is installed.

4.5.3.1. Structural Stability and Cover Integrity

The LAWV is designed to withstand Design Basis Accident loads that ensure continued structural stability during its anticipated life. Carey (2005) conducted a structural degradation prediction analysis and documented the significant degradation points in the life of the LAWV. These are

listed below along with the modeling approach employed to simulate the event. Years given are time from the placement of the final closure cap.

- Upon placement of the closure cap overburden, non-through-slab static cracking of the LAWV roof slab will occur and remain relatively constant over time.
 - Model: When the closure cap is placed, roof and roof beam concrete hydraulic properties change from 100% E-Area Concrete to a blend of 90% E-Area Concrete and 10% gravel.
- Upon placement of the closure cap overburden, non-through-wall static cracking of the LAWV exterior side walls will occur and increase slightly over time.
 - Model: When the closure cap is placed, wall concrete hydraulic properties change from 100% E-Area Concrete to a blend of 90% E-Area Concrete and 10% gravel.
- The LAWV roof slab will collapse due to closure cap loading, seismic loading, and rebar corrosion at a mean time of 2,805 years with a standard deviation of 920 years.
 - Model: The LAWV roof acquires the hydraulic properties of soil 500 years after the closure cap is placed and transport properties of soil 2,805 years after the cap is placed. Infiltration over the vault is increased at 2,805 years to simulate both the absence of a closure cap and collection of roof runoff in the collapsed region.
- The LAWV exterior side walls will collapse due to closure cap loading, seismic loading, and rebar corrosion at a mean time of 9,415 years with a standard deviation of 2,290 years.
 - Model: Conservatively, all LAWV concrete acquires the hydraulic properties of soil 500 years after cap placement and the transport properties of soil when the roof collapses.
- Differential settlement due to seismic loading could result in through-wall cracking of the side walls that opens into the roof slab with a probability of 0.8% over a 1,000-year period.
 - Model: Low-probability event is not included in the modeling. However, concrete properties degrade to those of soil within 500 years.
- Differential settlement due to seismic loading could result in through-wall cracking of the side walls that opens into the footer with a probability of 1.2% over a 1,000-year period.
 - Model: Low-probability event is not included in the modeling. However, concrete properties degrade to those of soil within 500 years.
- Within 50 to 100 years after placement of the closure cap overburden, differential settlement between the wall footers and floor slab will occur due to differences in static loading between the two, resulting in a separation between the footers and floor slab.
 - Model: When the closure cap is placed, wall footer concrete hydraulic properties change from 100% E-Area Concrete to a blend of 90% E-Area Concrete with 10% gravel. As explained in Section 4.5.3.6, hydraulic performance of the footer concrete, like the roof and walls, degrades over a 500-year period by blending with the hydraulic properties of soil, increasing the soil content in 10% increments every 50 years. The floor degrades in a similar fashion but does not include 10% gravel. This means that the wall footers provide a preferential flow path during the period

of concrete degradation, thereby simulating separation between the footer and the floor.

- Differential settlement beneath the floor slab due to seismic loading could result in flexural cracking of the floor slab. The probability of such an event occurring over a 1,000-year period has been estimated to be 50%.
 - Model: Hydraulic properties of floor concrete degrade from concrete to soil properties over a 500-year period following closure cap placement.

The waste subsidence potential of 21 feet does not impact the structural stability of the LAWV until the anticipated time of roof structural failure at 2,805 years. At the time of roof failure, it is assumed that the LAWV roof will collapse into the vault itself and that subsidence of the waste will occur. After roof collapse, the GCL, blended soil-bentonite layer, and foundation layer below (Section 4.5.3.4) are assigned the properties of backfill soil.

4.5.3.2. Timeline

Table 4-49 provides an overview of the LAWV timeline used to develop the PORFLOW model. Model timing (time = 0) starts with the receipt of the first disposal container in the LAWV in late 1994. As a bounding approach, flow and transport modeling assume the entire waste inventory is placed at the start of operations. This allows daughter ingrowth to occur for decay chains and does not significantly reduce the concentration of long-lived radionuclides such as C-14, Tc-99, and I-129, which are typically strong contributors to dose. Radionuclides with very short half-lives, such as H-3, will largely decay away before the 1,000-year post-closure period, during which the performance of the LAWV is assessed for regulatory compliance and the assumption of early disposal is acceptable.

As described in Section 4.5.3.6, hydraulic properties of the vault concrete are assumed to degrade over a 500-year period starting at the end of IC when moisture buildup in the overlying cap, vault cracking, and the lack of access to the subdrain system lead to water infiltration through the vault. Based upon the structural analysis performed for the LAWV (Carey, 2005), installation of the final closure cap results in cracking that partially penetrates the vault walls and roof causing some immediate degradation in concrete hydraulic properties. The structural analysis also concluded that the vault roof will collapse from a combination of degradation and seismic events at a mean time of 2,805 years after installation of the closure cap.

4.5.3.3. Hydrostratigraphic Layers

Figure 4-142 shows a generalized (not to scale) 1-D schematic diagram of the LAWV disposal site and the underlying VZ hydrostratigraphic layers. The diagram intends to show only the VZ layers and omits many details of the actual PORFLOW model (see Figure 4-141). Table 4-50 lists the dimensions of the VZ segments for the LAWV disposal site (Bagwell and Bennett, 2017) as well as the soil material type assumed in the model. At the LAWV site, the water table sits above the TCCZ.

Table 4-49. Low-Activity Waste Vault Timeline (Smith, 2021b; Table 3-1)

Calendar Date	Numerical Calendar Date	Time from Start of LAWV Operation	Operational Events
9/28/1994	1,994.74	0.0	Start of ELLWF operations. Start of LAWV operations. ¹ Start of radionuclide decay and daughter ingrowth in waste material. Start of 10,000-year modeling period.
9/28/2065	2,065.74	71.0	End of ELLWF operations. End of LAWV operations. Start of IC.
9/28/2165	2,165.74	171.0	End of IC. Installation of final closure cap. Non-through cracking of vault roof, roof beams, walls, and wall footers. ² Start of 500-year concrete degradation. Start of 1,000-year period of performance.
9/28/2215	2,215.74	221.0	Separation between wall footers and floor slab occurs from differential settlement. ³
9/28/2665	2,665.74	671.0	Vault concrete fully degraded assuming hydraulic properties of uncompacted OSC1.
9/28/3165	3,165.74	1,171.0	End of 1,000-year period of performance. Additional floor cracking occurs from differential settlement.
9/28/4970	4,970.74	2,976.0	Vault roof collapses. Waste material subsides from initial 21.8-foot layer into 4.5-foot layer at bottom of vault. ⁴ Waste and vault concrete assume transport properties of clayey soil.
9/28/5156	5,165.74	3,171.0	Side-wall through-cracking occurs and opens into roof and wall footers. ⁵
9/28/11580	11,580.74	9,586.0	Side walls collapse. ⁵
9/28/12165	12,165.74	10,171.0	End of 10,000-year post-IC modeling period. ⁶

Notes:

- ¹ As a bounding assumption, all waste in the LAWV is placed at the start of operations.
- ² The structural analysis predicts that roof cracking remains constant and wall cracking increases slightly over time.
- ³ Separation predicted to occur between 50 and 100 years after closure cap is placed.
- ⁴ Waste depths are measured under the roof peak.
- ⁵ These events occur well beyond the period of compliance and are not included in the model. All vault concrete is assumed to have the flow properties of soil at 671 years and the transport properties of soil at 2,976 years.
- ⁶ For some radionuclides, modeling will be extended to 50,000 years to capture peak radionuclide concentrations.

Table 4-50. Nominal Thickness and Composition of Low-Activity Waste Vault Vadose Zone Segments (Smith, 2021b; Table 4-1)

Vadose Zone Segment	Segment Length (feet)
Average Depth to Water Table	46.8 feet
UVZ	30.1 feet clay
LVZ	16.7 feet sand

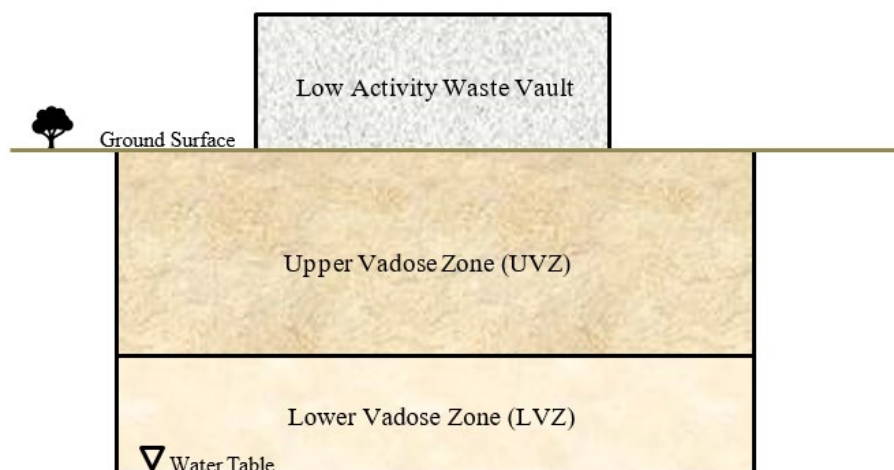


Figure 4-142. Schematic of Low-Activity Waste Vault Waste Disposal Site and Vadose Zone Hydrostratigraphic Layers (Smith, 2021b; Figure 4-1)

4.5.3.4. Model Geometry

Figure 4-143 (C-CT-E-00084, 2016) provides a north-south cross-sectional view of the LAWV with the final closure cap in place. As shown in Figure 4-140, the LAWV is located between ET05 and ET06 within the ELLWF. Because the LAWV creates a high point in elevation in the area, the final closure cap slopes away from the LAWV roof peak in both directions. As discussed in Section 4.5.3.5 below, HELP-model-predicted infiltration rates through the HDPE geomembrane are used as the upper boundary condition in the PORFLOW VZ model. The HDPE geomembrane/GCL composite layer is the limiting barrier to infiltration in the final closure cap design. The HELP infiltration model treats a 12-inch-thick section of the soil foundation layer above the concrete vault roof as a lateral drainage layer as detailed in Section 3.8.4.4.2. Including a drainage layer with the hydraulic properties of backfill soil in the HELP model allows water to drain away from the vault and avoids the buildup of hydraulic head on the concrete roof. The PORFLOW VZ model similarly includes a 12-inch-thick drainage layer of higher conductivity and a soil layer placed over the vault (referred to as the “foundation layer” in Figure 4-143). The drainage layer has a higher hydraulic conductivity than the foundation layer and functions to channel some of the infiltration water that passes through the geomembrane/GCL composite barrier layer away from the LAWV.

Figure 4-144 shows the PORFLOW model geometry. The figure is oriented south to the left and north to the right (which is opposite to Figure 4-143) and is consistent with Figure 4-141. The different material types comprising the LAWV model are color coded where mtyp in the figure legend is the material type number in PORFLOW. Key material types are labelled in Figure 4-144 and Figure 4-145.

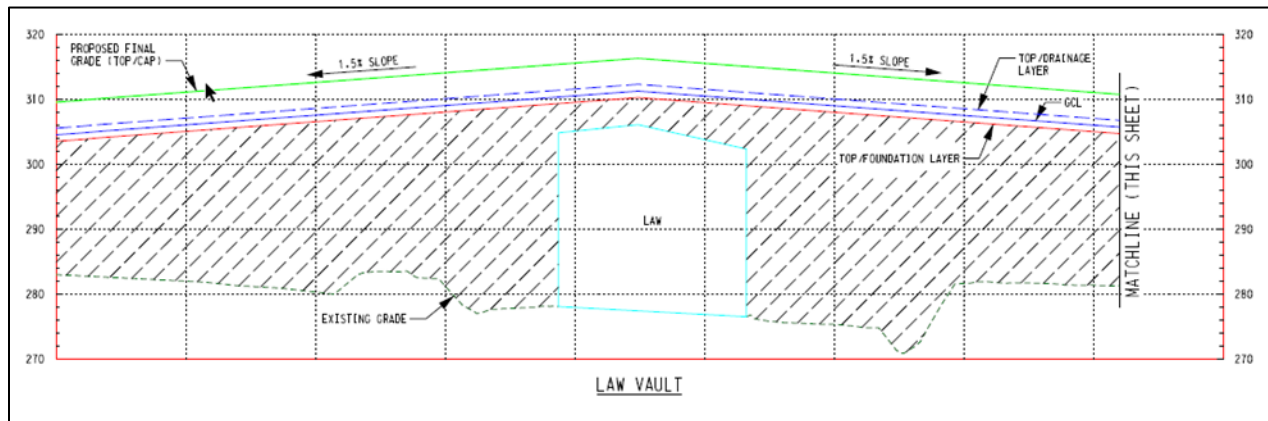


Figure 4-143. Low-Activity Waste Vault Final Closure Cap Configuration Looking East (C-CT-E-00084, 2016)

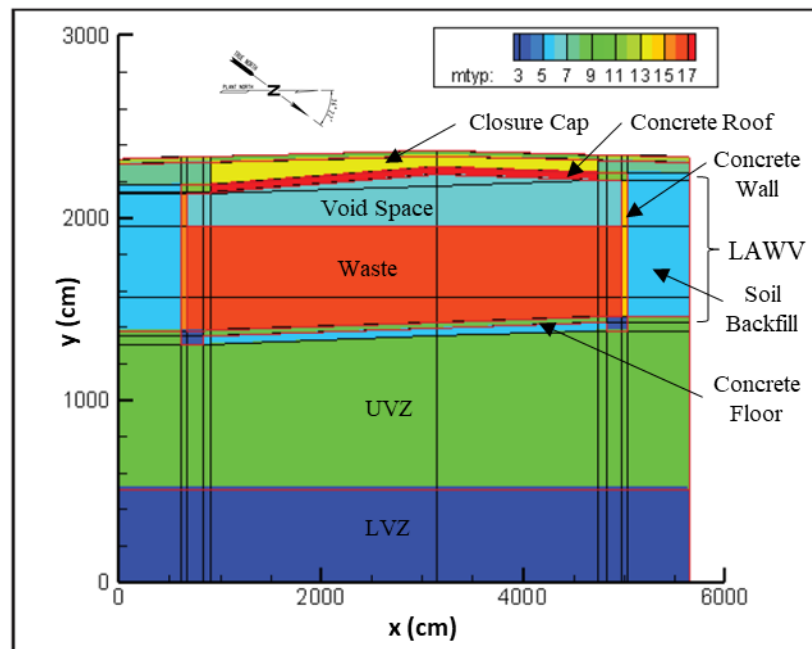


Figure 4-144. PORFLOW Model of Low-Activity Waste Vault Cell and Vadose Zone (Smith, 2021b; Figure 5-2)

In Figure 4-144, horizontal and vertical dimensions are in centimeters. Therefore, the 5,638.8 cm horizontal model dimension represents a model domain 185-foot long. The LAWV cross-section is 145 feet (4,419.6 cm) wide with the computational grid extending 20 feet (609.6 cm) to the north and south of the vault. The additional 20 feet includes an area under the closure cap to account for drainage away from the vault and possible flow into the VZ beneath the LAWV from background infiltration and roof runoff. As shown in Figure 4-140, the LAWV is located between two ETs. This restricted the side soil widths to 20 feet to avoid VZ regions that might be affected by the presence of the trenches. From its peak, the LAWV roof slopes 2% to the north and 4.5% to the south. The closure cap slopes 1.5% away from the LAWV roof peak in both directions.

Figure 4-145 shows a close-in view of the computational mesh immediately around the upper north corner of the LAWV. This figure gives an indication of the mesh detail and provides a better view of the vault concrete, closure cap, and the surrounding soil. Because parts of the vault concrete are modeled with different properties, they are identified as different materials. Material properties are obtained from the hydraulic properties database (Nichols and Butcher, 2020).

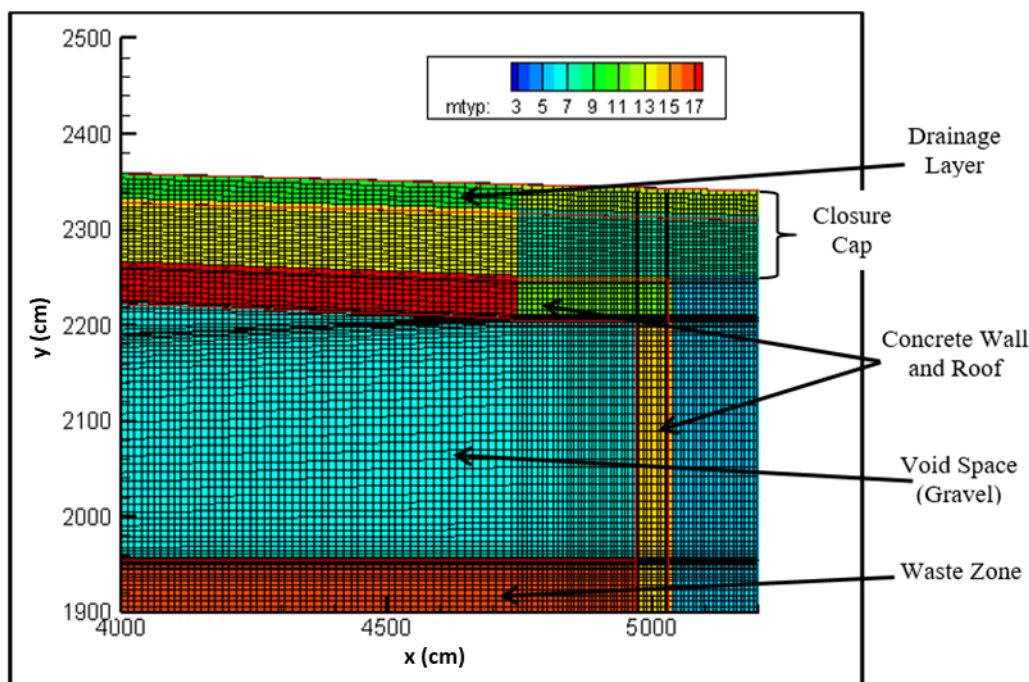


Figure 4-145. Portion of Computational Mesh in Low-Activity Waste Vault Model (Smith, 2021b; Figure 5-3)

4.5.3.5. Infiltration Boundary Conditions

Infiltration rates through the LAWV and surrounding area applied in the PORFLOW model are listed in Table 4-51. On-Vault represents infiltration directly over the vault, while Off-Vault refers to infiltration over the 20-foot side regions. The concrete vault roof in place during operation is shown in Figure 2-68 (bottom inset). As shown in Figure 2-68 (upper inset) and Figure 4-141, the roof slopes 2% on the north side of the vault and 4.5% on the south side of the vault. The roof has an overlying bonded-in-place fiberboard insulation and a waterproof membrane that effectively prevents rainwater from entering the cells. The sloped roof with overlying waterproof membrane will remain uncovered during the 71-year ELLWF operational period (calendar years 1994 to 2065) and subsequent 100-year IC period (calendar years 2065 to 2165). There will be essentially no water infiltration into the LAWV during this time for the following reasons:

- A roof slope of 2% to the north and 4.5% to the south along with the overlying waterproof membrane will shed rainwater from the top of the vault to gutters and downspouts that collect the water.
- The initial intact condition of the LAWV roof and guttering will be maintained during ELLWF operations and the 100-year period of IC.

- Absence of a soil cover during operations and IC prevents buildup of soil moisture above the roof. The PORFLOW model always includes the soil cover. However, for modeling purposes, a small infiltration rate of 0.001 in yr^{-1} is assumed to apply over the vault for the first 171 years of the simulation.

Table 4-51. Low-Activity Waste Vault Infiltration Rates (Smith, 2021b; Table 5-1)

Time Step No.	Numerical Calendar Date	HELP Times ¹ (year)	Start Time (year)	Event	Infiltration (cm yr ⁻¹)	
					On-Vault	Off-Vault
1	1994.74		0	Start of ELLWF and LAWV Operations	0.0012	40.081
	2065.74	0	71	Start of IC		
2	2165.74	100	171	End of IC, Placement of Closure Cap, Start of Period of Performance	0.007	
3	500 Year Period of Concrete Degradation (Year 171 to Year 671)	100 - 180	221	--	0.050	
4		180 - 290	271	--	0.177	
5			321	--	0.361	
6		300	371	--	0.635	
7		340 - 380	421	--	1.146	
8		380 - 480	471	--	2.120	
9			521	--	3.405	
10		480 - 660	571	--	4.699	
11			621	--	5.997	
12			671	Vault Hydraulic Failure	7.295	
13	2715.74	480 - 660	721	--	8.489	
14	2765.74	660 - 1,100	771	--	9.551	
15	2815.74		821	--	10.587	
16	2865.74		871	--	11.624	
17	2915.74		921	--	12.660	
18	2965.74		971	--	13.696	
19	3015.74		1,021	--	14.732	
20	3065.74		1,071	--	15.768	
21	3115.74		1,121	--	16.805	
22	3165.74	1,100	1,171	End of Period of Performance	18.137	
23	3315.74	1,100 - 1,900	1,321	--	19.766	
24	3465.74		1,471	--	21.395	
25	3615.74		1,621	--	23.024	
26	3765.74		1,771	--	24.652	
27	3915.74		1,921	--	25.871	
28	4065.74	1,900 - 2,723	2,071	--	26.474	
29	4215.74		2,221	--	26.872	
30	4365.74		2,371	--	27.270	
31	4515.74		2,521	--	27.668	
32	4665.74		2,671	--	28.036	
33	4815.74	2,723 - 2,905	2,821	--	28.238	
34	4970.74	2,905	2,976	Roof Collapses	47.981	28.219
	>4970.74	> 2,905	10,170	End of Simulation	47.981	28.219

Notes:

- ¹ Times used for interpolation. For example, HELP infiltration rates calculated at Year 660 and Year 1,100 are used to interpolate infiltration rates for Time Steps 14 – 21. Green-shaded area from Years 171 to 671 covers the 500-year period when concrete degradation occurs.

At the end of IC, a final closure cap is placed over the entire ELLWF. Infiltration rates above the LAWV and the surrounding soil cover are calculated using the HELP model (Dyer, 2019b) from the time of final closure cap placement until the time of roof collapse after 2,805 years (Year 2,905 in HELP model) as predicted by Carey (2005). Beyond HELP model Year 2,905, infiltration rates are assumed to remain constant. A structural analysis of the LAWV (Carey, 2005) determined the mean time to roof collapse from a combination of load stresses from the closure cap, seismic events, and rebar corrosion.

During the first 500 years following the end of IC, the model degrades concrete hydraulic properties and, at 500 years, assumes that the concrete behaves hydraulically like soil (concrete transport properties are retained until roof collapse). The model adjusts concrete properties in 50-year time steps by blending the hydraulic properties of concrete with those of the OSC. A description of the process for blending the hydraulic properties of concrete with soil is provided in Section 4.5.3.6. Because these time steps do not coincide with the HELP model infiltration calculations, the HELP results are linearly interpolated to follow the 50-year incremental changes in material properties.

Subsequently, it has been decided to smooth HELP infiltration predictions over 34 time periods using linear interpolation. The additional flow solutions serve to smooth out results from the radionuclide transport calculations. Results of this interpolation are shown in Table 4-51 where the green-shaded area from Years 171 to 671 covers the 500-year period when concrete degradation occurs. The column “HELP Times” gives the HELP model infiltration times employed to make the interpolation. PORFLOW preprocessing also averages infiltration rates over the time steps. For example, if the HELP infiltration rate at time $T(i)$ is $I(i)$ and at time $T(i+1)$ is $I(i+1)$, PORFLOW will use an infiltration rate equal to $0.5 \times [I(i) + I(i+1)]$ for flow time period $T(i)$ to $T(i+1)$. Infiltration rates listed in Table 4-51 are the averaged values used in the PORFLOW model. PORFLOW calculates 34 steady-state flow solutions over the entire computational domain using these averaged infiltration rates as a boundary condition at the top surface. The 34 flow solutions are then utilized to make the radionuclide transport calculations.

The 34 infiltration rates are shown in Figure 4-146, highlighting the associated time intervals. Table 4-51 also shows that, once the final closure cap is in place, infiltration over the vault (“On-Vault” infiltration) and the 20-foot capped regions on either side of the vault (“Off-Vault” infiltration), are identical until the vault roof collapses at PORFLOW model Year 2,976. Following roof collapse, flow through the vault is higher than background because it is collecting runoff from the upslope portion of the intact closure cap. Off-Vault infiltration to the areas beside the vault are only different before the closure cap is placed and after roof collapse.

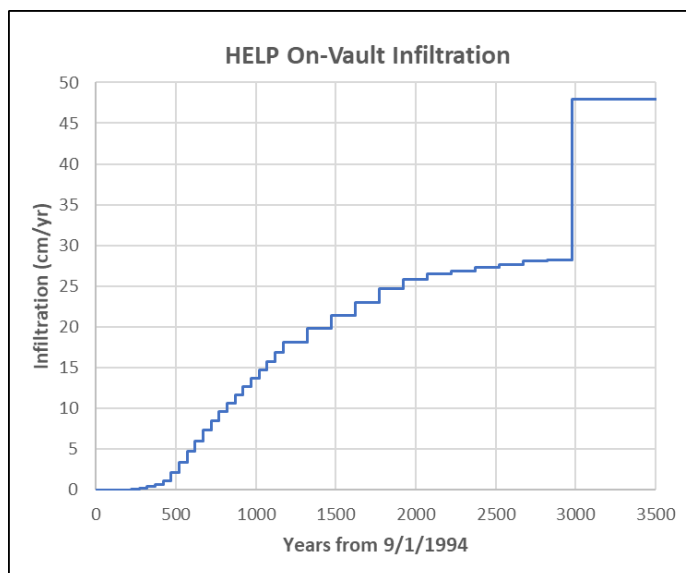


Figure 4-146. Interpolation of HELP Model On-Vault Infiltration to PORFLOW Time Zones (Smith, 2021b; Figure 5-4)

4.5.3.6. Modeling Concrete Degradation

In past ELLWF PAs, the hydraulic properties of concrete have been abruptly changed from those of intact concrete to soil to represent vault structural collapse or complete deterioration of the concrete matrix. In PA2022, concrete degradation is modeled as a gradual process where, starting at the time of site closure, concrete hydraulic properties are transformed into those of soil over a period of 500 years. The 500-year post-closure endpoint is adopted from the PA Working Group (PAWG) recommendation in NUREG-1573 (U.S. NRC, 2000). An excerpt from NUREG-1573 (§2, Section 3.2, “Performance of Engineered Barriers”) is reproduced below:

However, to limit unnecessary speculation as to their performance, the PAWG believes that materials typically used in engineered barriers can alternatively be assumed to have physically degraded after 500 years following site closure.

Thus, at 500 years and beyond, the engineered barriers can be assumed to function at levels of performance that are considerably less than their optimum level, but credit for structural stability and chemical buffering effects may be taken for longer periods of time...For timeframes longer than 500 years, it is unreasonable to assume that any physical engineered barrier such as a cover or a reinforced concrete vault can be designed to function long enough to influence the eventual release of long-lived radionuclides such as carbon-14 (half-life: 5,300 years); technetium-99 (half-life: 213,000 years); and iodine-129 (half-life: 15,700,000 years), if they are present. However, credit for structural stability and chemical buffering effects may be taken for the long-term provided that the applicant provides suitable information and justification. But again, this would have to be evaluated on a case-by-case basis.

Based on this recommendation, the LAWV and ILV models use a blend of concrete and soil to determine hydraulic properties in 50-year increments over the assumed 500-year lifetime of E-Area Vault concrete. At site closure, structural analysis of the LAWV (Carey, 2005) predicts that the LAWV roof and walls will experience limited non-through static cracking when the final closure cap is placed over the vault. Upon final closure, initial hydraulic properties for concrete in the vault roof, roof beams, walls, and wall footers are calculated as a blend of 90% E-Area Vault Concrete and 10% Gravel to represent the impact of early stress cracking in the concrete. Soil being blended with the concrete is represented by the hydraulic properties of OSC1. Table 4-52 provides a list of the material blends used to represent concrete degradation following site closure and the saturated hydraulic conductivity of each blend. The model further assumes that concrete sorption properties, adjusted for aging effects, are maintained until roof collapse.

Table 4-52. Low-Activity Waste Vault Material Blends for Degraded Concrete (Smith, 2021b; Table 5-2)

Years Post Closure	Roof, Roof Beams, Walls, and Wall Footers			Floor		
	90% Concrete 10% Gravel ¹	Soil (OSC1)	K_{sat} (cm s ⁻¹)	E-Area Concrete	Soil (OSC1)	K_{sat} (cm s ⁻¹)
0	100%	0%	1.80E-11	100%	0%	1.00E-12
50	90%	10%	9.84E-11	90%	10%	7.64E-12
100	80%	20%	5.21E-10	80%	20%	5.61E-11
150	70%	30%	2.69E-09	70%	30%	3.96E-10
200	60%	40%	1.35E-08	60%	40%	2.69E-09
250	50%	50%	6.61E-08	50%	50%	1.76E-08
300	40%	60%	3.16E-07	40%	60%	1.12E-07
350	30%	70%	1.47E-06	30%	70%	6.84E-07
400	20%	80%	6.70E-06	20%	80%	4.05E-06
450	10%	90%	2.98E-05	10%	90%	2.33E-05
500	0%	100%	1.30E-04	0%	100%	1.30E-04

Notes:

¹ Gravel K_{sat} = 1.50E-01 cm s⁻¹

Hydraulic properties for a mixture of concrete and another material (in this case, soil) are typically calculated as described by Flach (2017c). Composite porosity (ε_b) and saturated hydraulic conductivity (K_b) are calculated by:

$$\varepsilon_b^p = f_c \varepsilon_c^p + f_s \varepsilon_s^p \quad \text{Eq. (4-49)}$$

$$K_b^p = f_c K_c^p + f_s K_s^p \quad \text{Eq. (4-50)}$$

where:

ε Porosity (cm³ cm⁻³)

K Saturated hydraulic conductivity (cm s⁻¹)

f_c Volume fraction concrete (unitless)

f_s Volume fraction soil = $(1 - f_c)$ (unitless)

p Factor for arithmetic ($p = 1$), geometric ($p \rightarrow 0$), or harmonic ($p = -1$) blending (unitless)

b Blend
 c Concrete
 s Soil

Saturation and hydraulic conductivity for a composite material as functions of suction pressure (ψ) are calculated from:

$$[\varepsilon_b S(\psi)_b]^p = f_c [\varepsilon_c S(\psi)_c]^p + f_s [\varepsilon_s S(\psi)_s]^p \quad \text{Eq. (4-51)}$$

$$[K_b k_h(\psi)_b]^p = f_c [K_c k_h(\psi)_c]^p + f_s [K_s k_h(\psi)_s]^p \quad \text{Eq. (4-52)}$$

where:

$k_h(\psi)$ Hydraulic conductivity as a function of suction pressure (cm s^{-1})

$S(\psi)$ Saturation as a function of suction pressure ($\text{cm}^3 \text{cm}^{-3}$)

ψ Suction pressure (cm)

Example results for hydraulic conductivity obtained by blending E-Area Vault Concrete with OSC1 using arithmetic averaging are shown in Figure 4-147. Using this blending method, a small amount of soil homogeneously blended with the concrete significantly alters the hydraulic conductivity of the mixed material, leading to a large increase in water flow. With arithmetic blending, the material with the highest conductivity is weighted the most. Figure 4-148 displays the results of the harmonic blending method where the concrete properties are more heavily weighted. In harmonic blending, the material with the smallest conductivity is weighted the most. The legends in Figure 4-147 and Figure 4-148 correspond to the concrete-soil blends listed in Table 4-52.

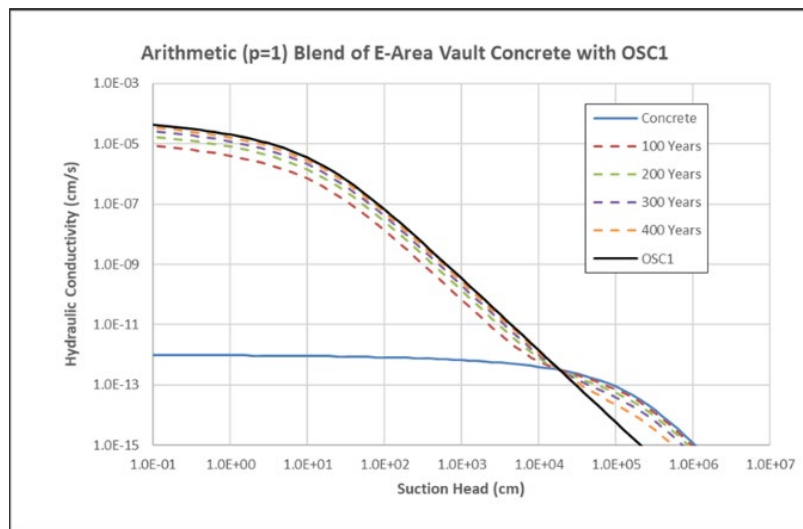


Figure 4-147. Hydraulic Conductivity for Blends of E-Area Vault Concrete with OSC1 Calculated Using Arithmetic Averaging (Smith, 2021b; Figure 5-5)

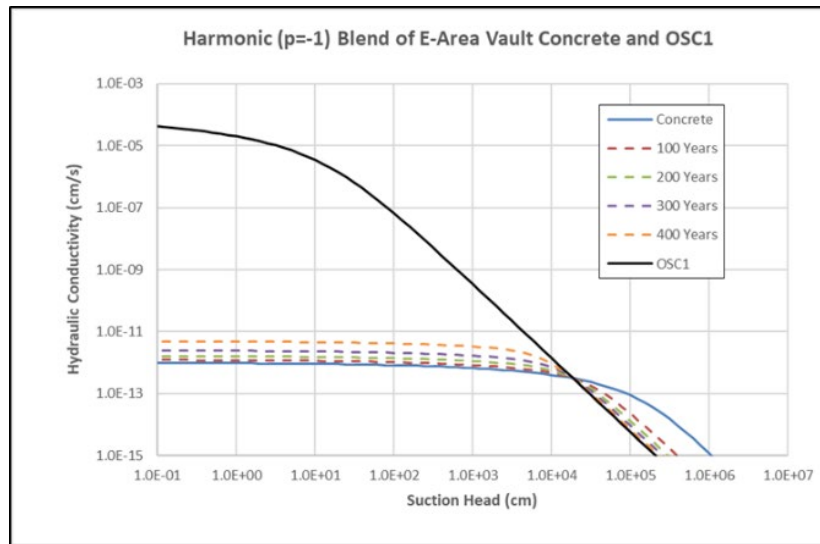


Figure 4-148. Hydraulic Conductivity for Blends of E-Area Vault Concrete with OSC1 Calculated Using Harmonic Averaging (Smith, 2021b; Figure 5-6)

Because neither of the blending methods demonstrated in Figure 4-147 and Figure 4-148 appear to represent concrete degradation satisfactorily, geometric averaging is employed using Eq. (4-51) and Eq. (4-52) with a small value of the factor p ($p = 0.01$). Results obtained using this blending method are shown in Figure 4-149 and Figure 4-150.

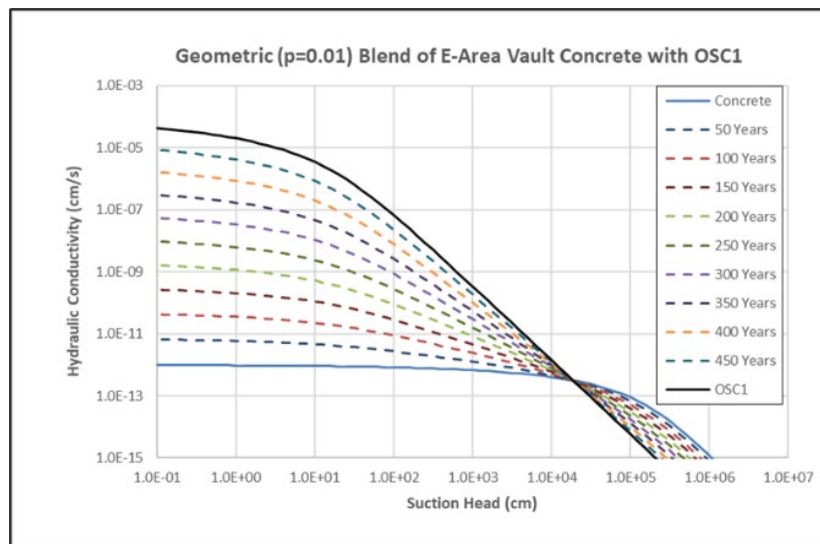


Figure 4-149. Hydraulic Conductivity for Blends of E-Area Vault Concrete with OSC1 Calculated Using Geometric Averaging (Smith, 2021b; Figure 5-7)

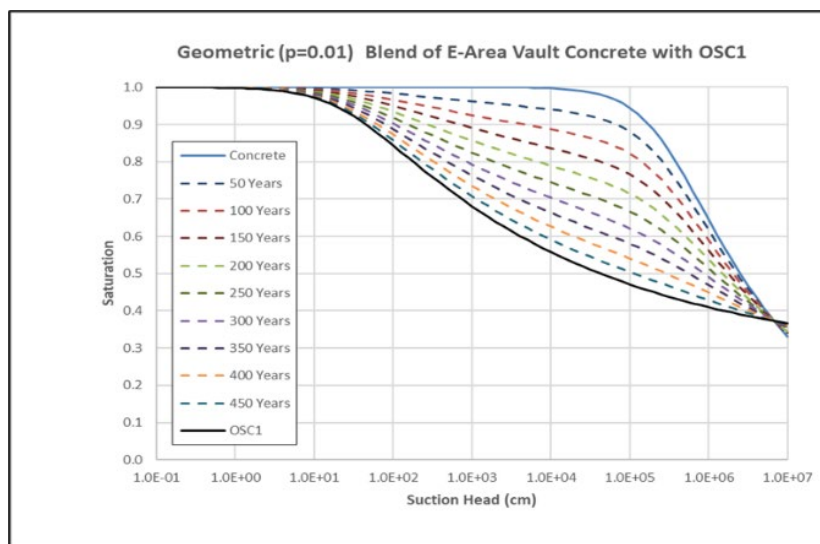


Figure 4-150. Water Saturation for Blends of E-Area Vault Concrete with OSC1 Calculated Using Geometric Averaging (Smith, 2021b; Figure 5-8)

These results appear to show a reasonable blending to represent the change in concrete properties over time and are adopted for use in the LAWV and ILV models. Figure 4-151 and Figure 4-152 display the hydraulic conductivity and water saturation curves obtained by blending a mixture of 90% E-Area Vault Concrete and 10% Gravel with OSC1, respectively. The mixture of 90% concrete with 10% gravel is used to model cracked concrete. Blending this mixture with soil is then used to model degradation of the cracked concrete.

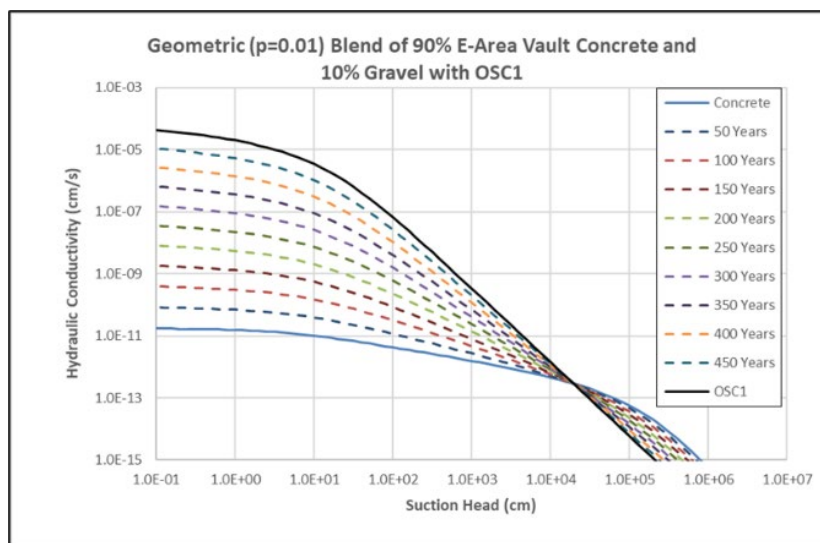


Figure 4-151. Hydraulic Conductivity for Blends of 90% E-Area Vault Concrete and 10% Gravel with OSC1 Calculated using Geometric Averaging (Smith, 2021b; Figure 5-9)

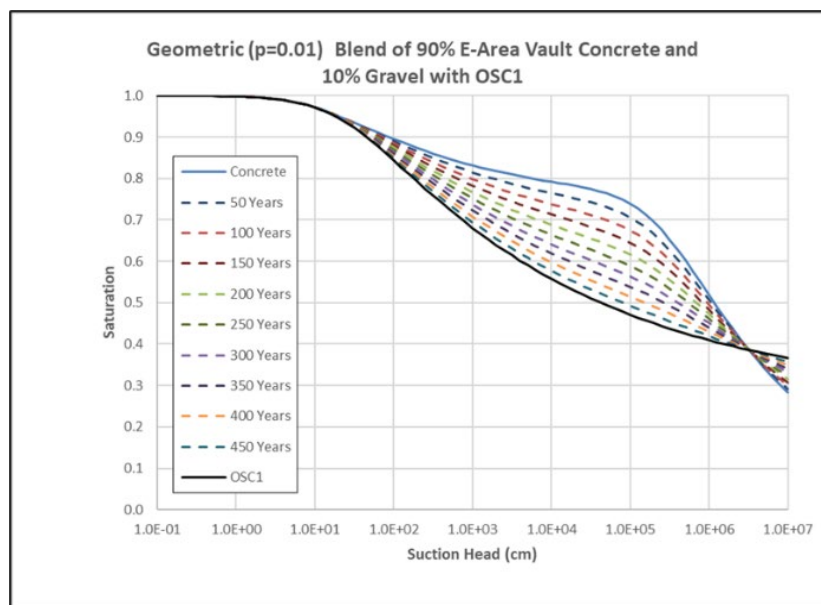


Figure 4-152. Water Saturation for Blends of 90% E-Area Vault Concrete and 10% Gravel with OSC1 Calculated Using Geometric Averaging (Smith, 2021b; Figure 5-10)

4.5.3.7. Preliminary Model Results for Vadose Zone Flow

PORFLOW modeling is used to calculate a steady-state flow field for each of the 34 time-intervals listed in the first column of Table 4-51. Starting times for each interval are listed in the fourth column of Table 4-51. For example, the first flow time is from 0 to 171 years, the second time is from 171 to 221 years, and so on down the table. “Years” as shown in the figure captions and used in this section are time from the start of LAWV operations in 1994.

Results obtained from the modeling include suction pressure, water saturation of the materials, and flow field throughout the computational domain. In addition, information on the deviation of saturation from the water retention curves and convergence of the flow calculations can be obtained to verify model accuracy. Preliminary steady-state flow fields based on Darcy velocity for 20 simulation periods are shown in Figure 4-153 through Figure 4-162, where x and y are the horizontal and vertical dimensions, respectively, of the 2-D PORFLOW model domain in centimeters. The 20 simulation periods include time intervals 1 through 14, 18, 22, 26, 30, 33, and 34 (refer to first column of Table 4-51). Each figure displays the flow field for two time-intervals. The corresponding infiltration flow rates calculated by the HELP model are also listed in Table 4-51.

The progressive deterioration in the hydraulic performance of both the final closure cap and the vault concrete over the simulation period are evident in Figure 4-153 through Figure 4-162. The 500-year period from Year 171 through Year 671 is the time during which degradation of the vault concrete is modeled as described in Section 4.5.3.6. The 1,000-year period of performance runs from Year 171 through Year 1,171. Results for water saturation and pressure are reported by Smith (2021b; Appendices A and B, respectively).

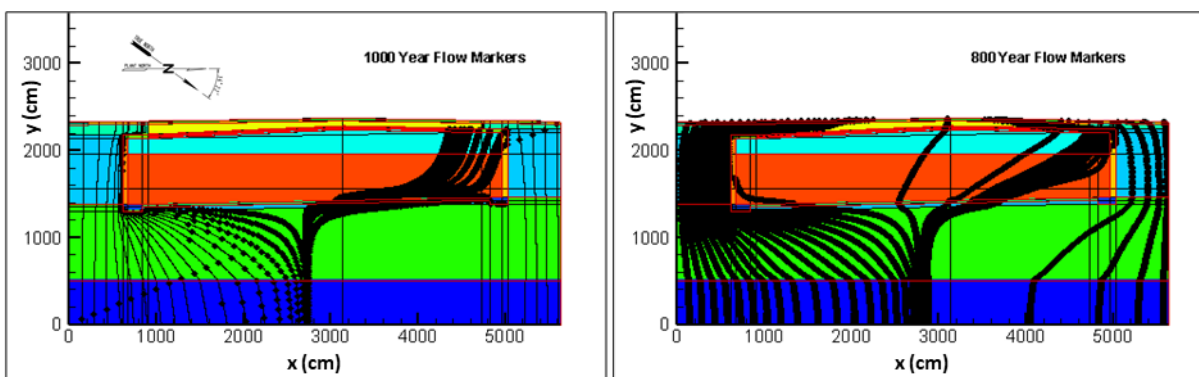


Figure 4-153. Low-Activity Waste Vault Flow Fields for Years 0 – 171 (left) and 171 – 221 (right) (Smith, 2021b; Figure 6-1)

Figure 4-153 displays flow fields from the start of LAWV operations (Time 0) until the end of IC and for the first 50 years following installation of the final closure cap. The final closure cap is placed over the vault in Year 171, marking the beginning of the 1,000-year period of performance. For the first 50 years, the vault concrete is modeled as intact E-Area Vault Concrete. As described in Section 4.5.3.4, the PORFLOW 2-D model domain extends 20 feet on both sides of the vault. For the first 171 years, the model is run with the soil cover in place, which is not physically correct. The infiltration is set to the low value of 0.001 in yr^{-1} over the vault and the nominal GSA background infiltration rate of 15.78 in yr^{-1} over the 20-foot side areas. The intent is to model the presence of the rain cover on the roof as well as the gutter/downspouts that collect runoff from the roof and send it to the sump. The drainage system prevents runoff from the roof adding to infiltration water on the sides of the vault. Figure 4-153 (left-hand plot) shows background flow beside the vault with only a very low flow rate through the vault (markers in the streamlines are spaced every 1,000 years) for the first 171 years. Water creep into the vault is more prevalent on the north (right) side where the roof slope is shallower. The plot shows that while the model for this time period is not entirely accurate, it still gives reasonable results. Following final closure cap placement at Year 171, Figure 4-153 (right-hand plot) displays very low flow throughout the entire computational domain.

Predicted flow fields for the first 100 years of degraded performance of the vault concrete and final closure cap are shown in Figure 4-154. During this time, the final closure cap is still performing as designed, the concrete is relatively intact [10% soil (left image) and 20% soil (right image)], and the infiltration rate through the vault is low. Time markers in Figure 4-154 are placed at 300-year (left) and 200-year (right) intervals. Therefore, while the figures show channeling of water to the sides and below the vault, the actual flow rate through the vault is still very low. The right-hand plot in Figure 4-154 begins to display water flow through the side walls. Figure 4-153 and Figure 4-154 both indicate that flow on the south side is being drawn underneath the vault because the concrete is blocking water flow directly into this region, creating suction beneath the vault floor.

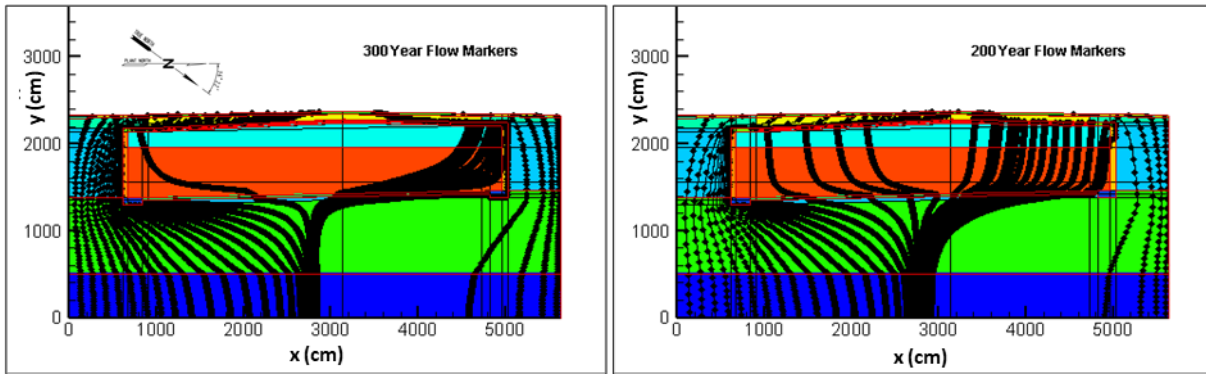


Figure 4-154. Low-Activity Waste Vault Flow Fields for Years 221 – 271 (left) and 271 – 321 (right) (Smith, 2021b; Figure 6-2)

Figure 4-155 shows water flow fields from Year 321 through Year 421. During this time, the concrete, mixed with 30% (left) and 40% (right) soil, and final closure cap continue to degrade. More water is flowing through the vault and its flow rate is higher as noted by the 100-year and 80-year time markers. The right-hand plot in Figure 4-155 (200 to 250 years after the final closure cap is installed) shows that the stream traces are beginning to straighten out, which indicates more uniform water flow through the entire region.

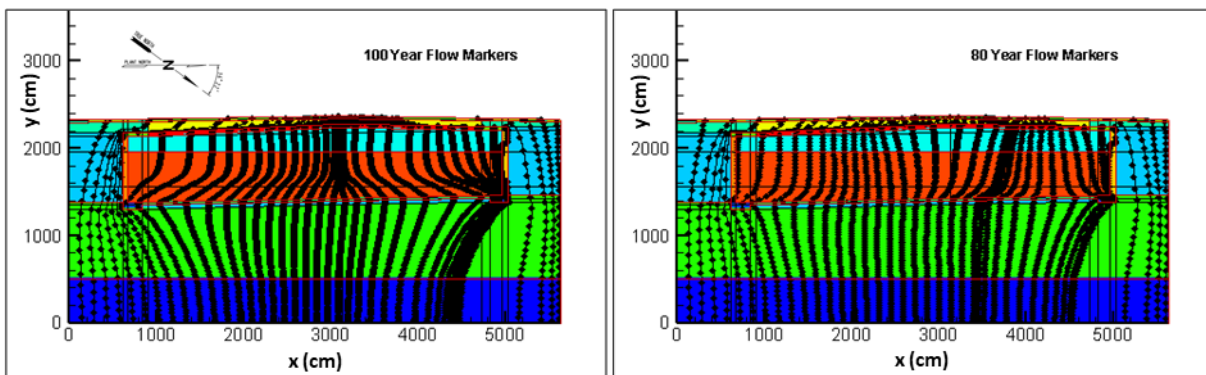


Figure 4-155. Low-Activity Waste Vault Flow Fields for Years 321– 371 (left) and 371 – 421 (right) (Smith, 2021b; Figure 6-3)

The increase in flow rate and the trend toward more uniform flow continues in Figure 4-156, which shows the flow fields from Year 421 through Year 521. In these two plots, the concrete is now mixed with 50% (left) and 60% (right) soil. Flow through the final closure cap is still only approximately 0.5 to 1.5 in yr^{-1} ; therefore, the trend toward more uniform flow is primarily due to concrete degradation.

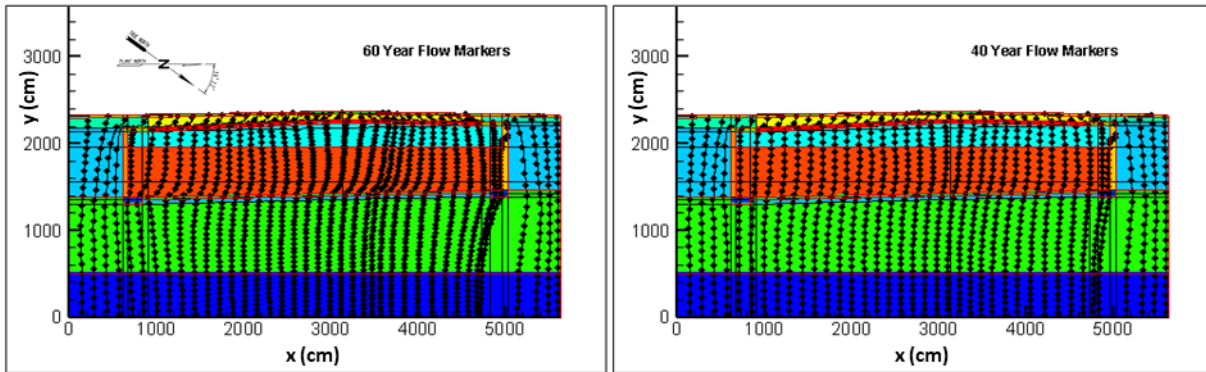


Figure 4-156. Low-Activity Waste Vault Flow Fields for Years 421 – 471 (left) and 471 – 521 (right) (Smith, 2021b; Figure 6-4)

Figure 4-157 through the left-hand plot in Figure 4-162 display a steady increase in flow through the vault as the final closure cap fails. By Year 671, hydraulic properties of the LAWV concrete in the roof, floor, and walls have degraded to those of OSC1. The vault concrete is fully degraded by the right-hand plot in Figure 4-158. Thereafter, flow increases as the final closure cap performance degrades (see infiltration rates listed in Table 4-51).

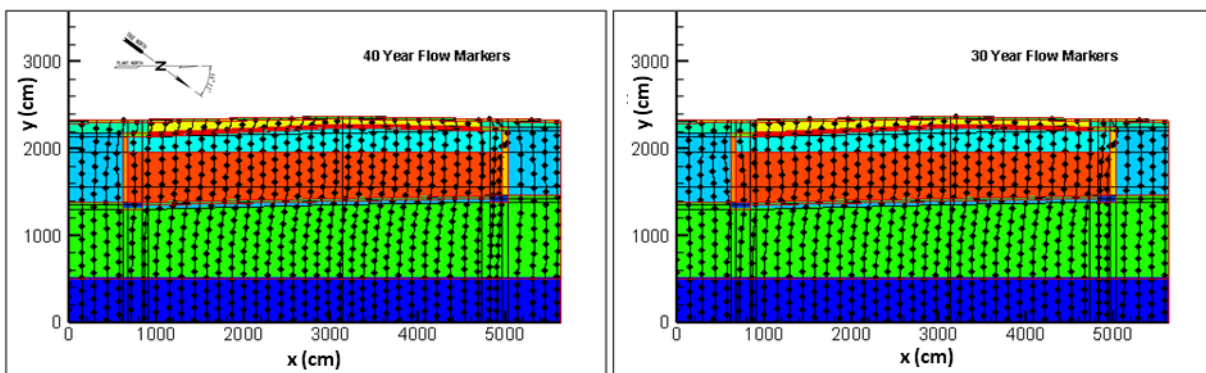


Figure 4-157. Low-Activity Waste Vault Flow Fields for Years 521 – 571 (left) and 571 – 621 (right) (Smith, 2021b; Figure 6-5)

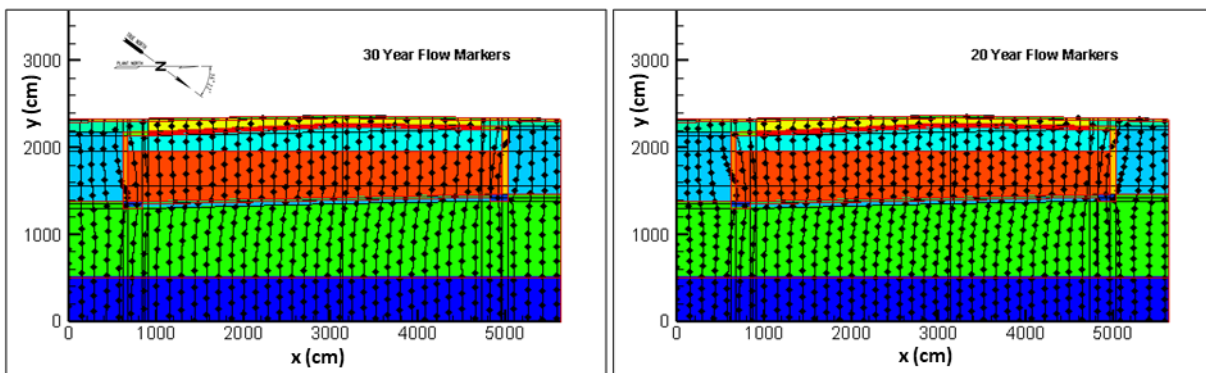


Figure 4-158. Low-Activity Waste Vault Flow Fields for Years 611 – 671 (left) and 671 – 721 (right) (Smith, 2021b; Figure 6-6)

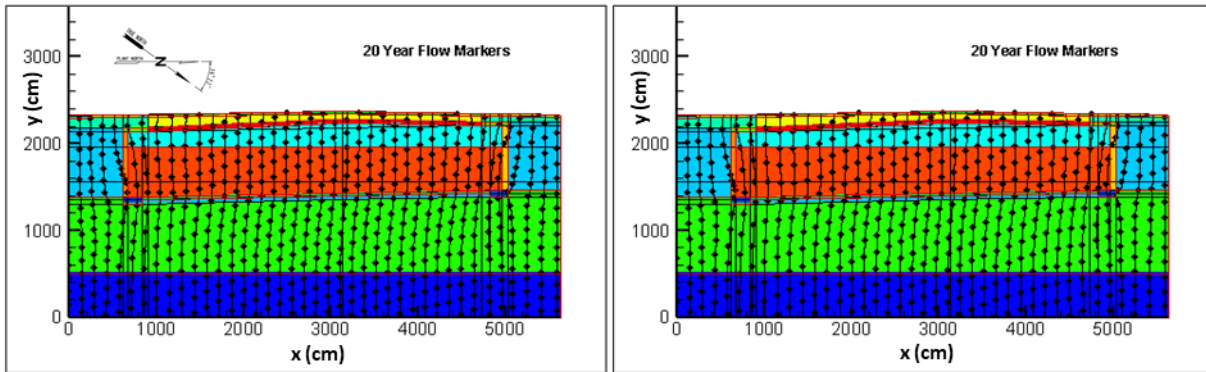


Figure 4-159. Low-Activity Waste Vault Flow Fields for Years 721 – 771 (left) and 771 – 821 (right) (Smith, 2021b; Figure 6-7)

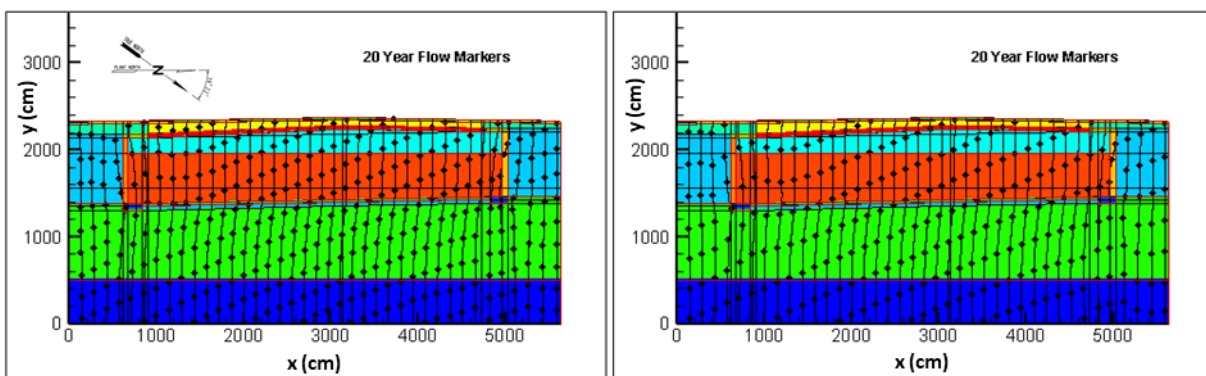


Figure 4-160. Low-Activity Waste Vault Flow Fields for Years 971 – 1,021 (left) and 1,171 – 1,321 (right) (Smith, 2021b; Figure 6-8)

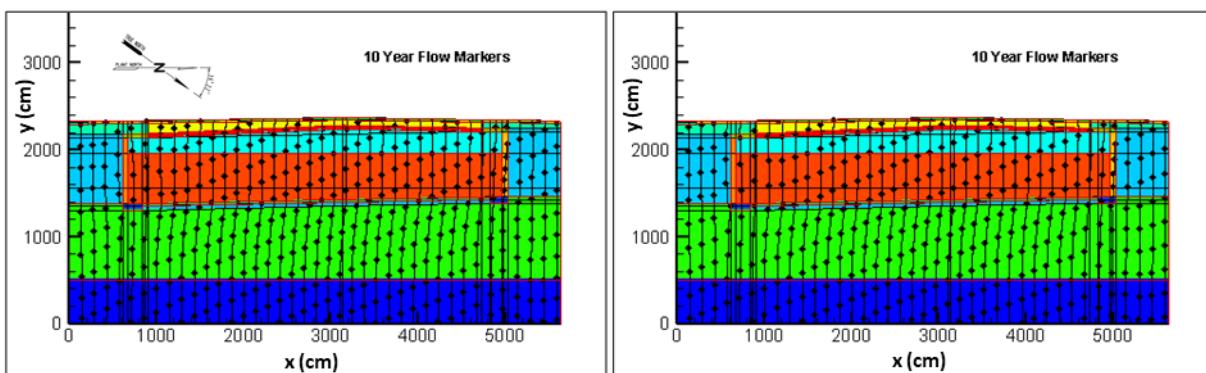


Figure 4-161. Low-Activity Waste Vault Flow Fields for Years 1,771 – 1,921 (left) and 2,371– 2,521 (right) (Smith, 2021b; Figure 6-9)

The LAWV roof is assumed to collapse at Year 2,976, thereby increasing flow through the vault region as runoff from the intact closure cap enters the space created by the roof collapse. This impact is evident in Figure 4-162 where the left-hand plot is before roof collapse and the right-hand plot is after roof collapse. The greater distance between flow markers within the vault in the right-hand plot indicates the increased flow rate. Beyond 2,976 years, the flow pattern is assumed to remain unchanged.

Graphs showing suction pressure and water saturation in the LAWV VZ at the same time intervals are documented by Smith (2021b; Appendices A and B, respectively).

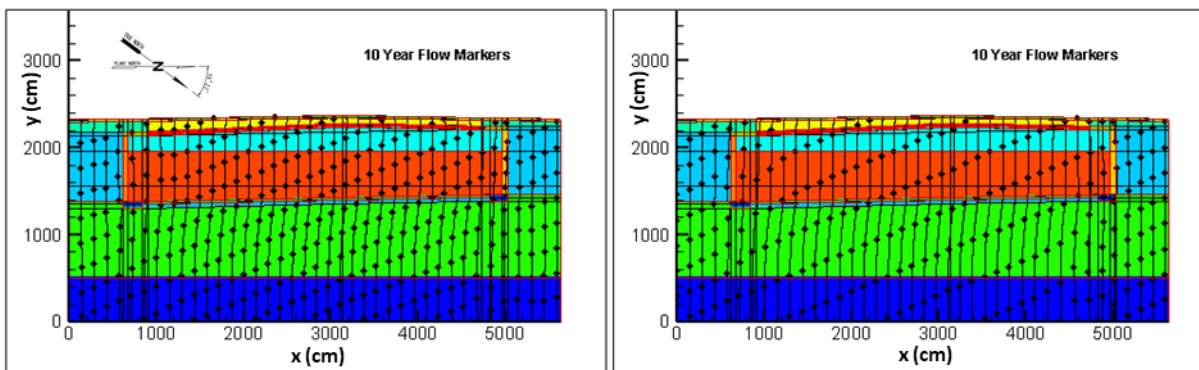


Figure 4-162. Low-Activity Waste Vault Flow Fields for Years 2,821 – 2,976 (left) and >2,976 (right) (Smith, 2021b; Figure 6-10)

4.5.3.8. Preliminary Model Results for Radionuclide Transport

LAWV transport calculations are made for the following nine parent radionuclides and five daughters: C-14, Cl-36, H-3, I-129, Nb-94, Np-237 (U-233, Th-229), Tc-99, U-235 (Pa-231, Ac-227), and Zr-93 (Nb-93m). These 14 radionuclides contribute a significant dose from LAWV disposal and, therefore, had relatively low disposal limits in PA2008. I-129 is a useful radionuclide to include for testing transport calculations because of its long half-life and small K_d , which ensures that the I-129 peak will be quickly observed and the area under the peak should equal the mass of I-129 initially deposited.

One g-mole (gmol) of each parent radionuclide is distributed uniformly in the waste zone and the resulting flux to the water table (gmol yr^{-1}) is calculated over a 50,000-year period. The parent radionuclides are introduced at the start of LAWV operations. At 2,976 years following the start of LAWV operations, when structural analysis predicts the vault roof will collapse, the existing waste inventory is relocated to the lower 4.5 feet of the waste zone. This is intended to mimic the consolidation of waste containers within the collapsed vault.

4.5.3.8.1. K_d Properties

K_d values are obtained from the *GeoChem Data Package* (SRNL, 2018) developed by Kaplan (2016b). As specified in Table 4-47, reducing-cement K_d values are used to represent LAWV concrete. The model uses clayey-sediment K_d values for the waste zone and UVZ and sandy-sediment K_d values for the LVZ. Table 4-47 recommends using K_d values impacted by cementitious leachate for the waste zone and upper and lower VZ soils. However, Table 4-47 (Footnote c) states that the use of cementitious-leachate-impacted K_d values in the waste and VZ regions below the vault has not been formally evaluated for use in the PA baseline. The PA2008 model did not use cementitious-leachate-impacted K_d values in VZ soil or the waste region. Therefore, the preliminary LAWV model results summarized in this section also do not use soil and waste K_d values with cementitious leachate factors applied.

4.5.3.8.2. Concrete Aging

K_d values for concrete change as concrete ages (Kaplan, 2016b). Concrete aging is related to the number of PV exchanges made as water flows through the material. Kaplan (2016b) assumes the following for concrete aging:

- Stage I (young) concrete lasts for 50 exchange cycles
- Stage II (middle) concrete lasts for 500 exchange cycles
- Stage III (aged) concrete lasts 4,000 exchange cycles

After 4,000 PV exchanges, concrete K_d values are assumed to become those for clayey sediment. For the LAWV PORFLOW model assessment, a relatively simple method is employed to estimate the number of PV exchanges. For the LAWV roof and floor and the waste zone, average vertical velocities from the PORFLOW calculations during each flow period (Table 4-51) are used to determine the number of PV exchanges. For the LAWV walls, the average horizontal velocity is utilized. The cumulative number of PV exchanges is tracked through each flow step and the times are calculated when the exchange volumes reached the end of each stage. Table 4-53 provides the resulting times when concrete stage changes occur. The concrete is aged to the next stage at the beginning of the time step when the number of exchange cycles is reached.

Table 4-53. Low-Activity Waste Vault Concrete Aging Times from Start of Operations (Smith, 2021b; Table 6-1)

Stage Transition	Roof and Roof Beams	Floor and Wall Footers	North Wall	South Wall	Waste
Stage I to II	771	771	1,171	1,171	2,071
Stage II to III	1,121	1,121	> 2,976	> 2,976	> 2,976
Stage III - Soil	> 2,976	> 2,976	> 2,976	> 2,976	> 2,976

The results in Table 4-53 are in reasonably good agreement with concrete aging times used in PA2008. PA2008 differentiated between cracked and uncracked concrete. For cracked concrete, which is comparable to the current model, all LAWV concrete is aged from Stage I to Stage II at 640 years, from Stage II to Stage III at 1,264.5 years, and from Stage III to soil at 4,689.5 years. A conceptual difference between the two models is that PA2008 assumed concrete K_d values remained active until 4,000 pore volume exchanges had been made, while the PA2022 model changes concrete K_d values to those of soil when the vault roof collapses.

4.5.3.8.3. Radionuclide Flux to Water Table

Figure 4-163 through Figure 4-168 summarize fluxes to the water table (gmol yr^{-1} per gmole of parent radionuclide) for the nine parent radionuclides and five daughters with half-lives greater than one year used for the LAWV VZ model evaluation. Figure 4-166 through Figure 4-168 display the parent and daughter radionuclides on both linear and semi-log scales to highlight progeny at low concentrations. Table 4-54 compares the maximum flux and the time when the maximum flux occurs for all radionuclides. Time values shown on the figures and reported in Table 4-54 are measured relative to the time LAWV operations started in 1994. The sharp peaks in flux for C-14, Tc-99, Np-237, Pa-231, and Ac-227 all occur at approximately 3,000 years, which is soon after LAWV roof collapse when there is a significant increase in infiltration rate through

the vault area. Concentration profiles highlighting C-14 transport through the LAWV VZ at simulation times from 50 to 12,000 years are reported by Smith (2021b; Appendix C).

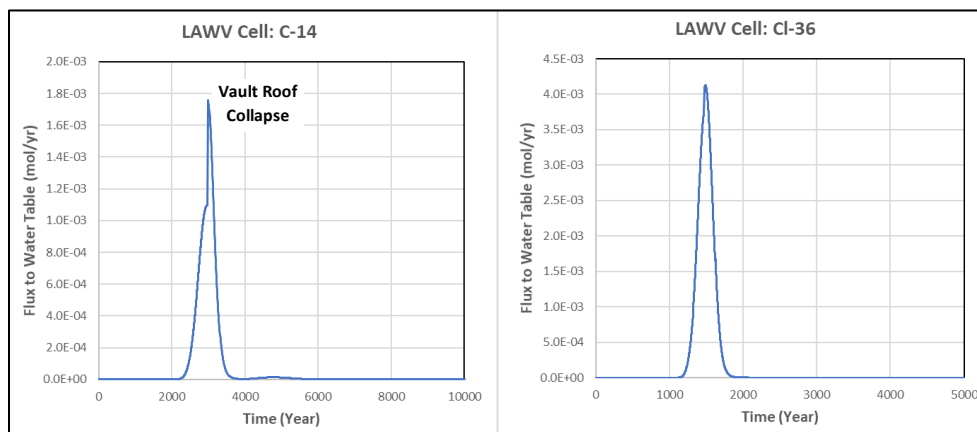


Figure 4-163. Linear Plot of Flux to Water Table (gmol yr^{-1} per gmole of parent) for C-14 and Cl-36 (Smith, 2021b; Figure 6-11)

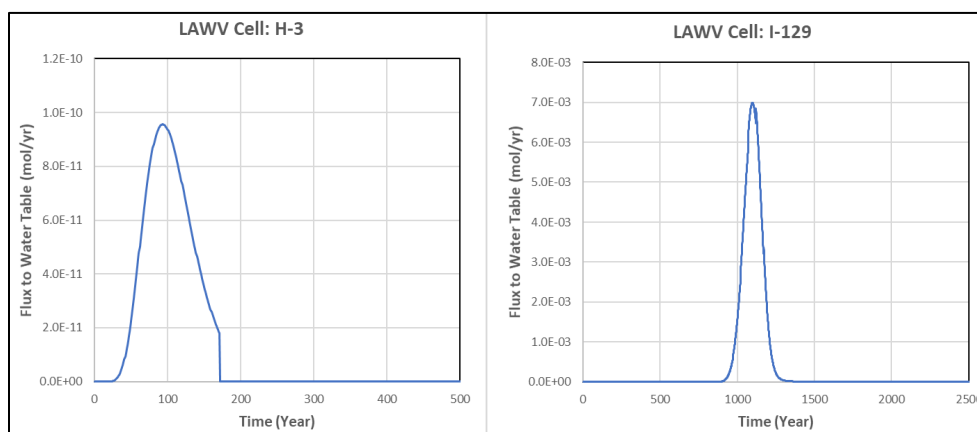


Figure 4-164. Linear Plot of Flux to Water Table (gmol yr^{-1} per gmole of parent) for H-3 and I-129 (Smith, 2021b; Figure 6-12)

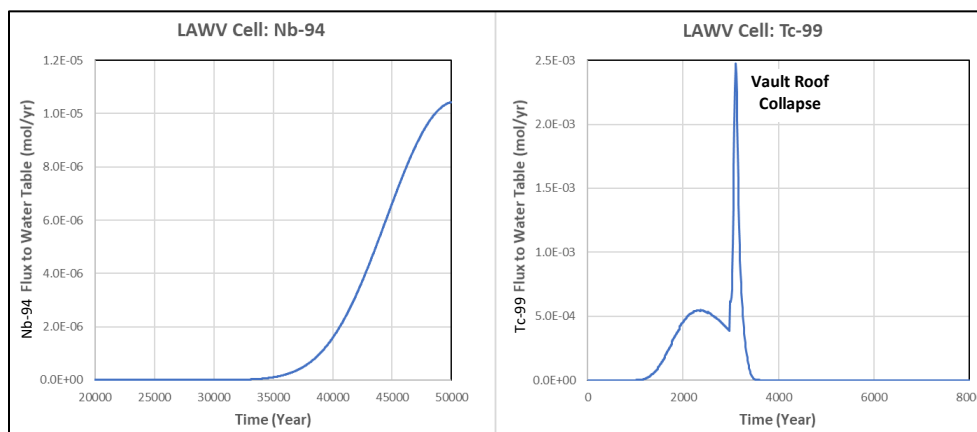


Figure 4-165. Linear Plot of Flux to Water Table (gmol yr^{-1} per gmole of parent) for Nb-94 and Tc-99 (Smith, 2021b; Figure 6-13)

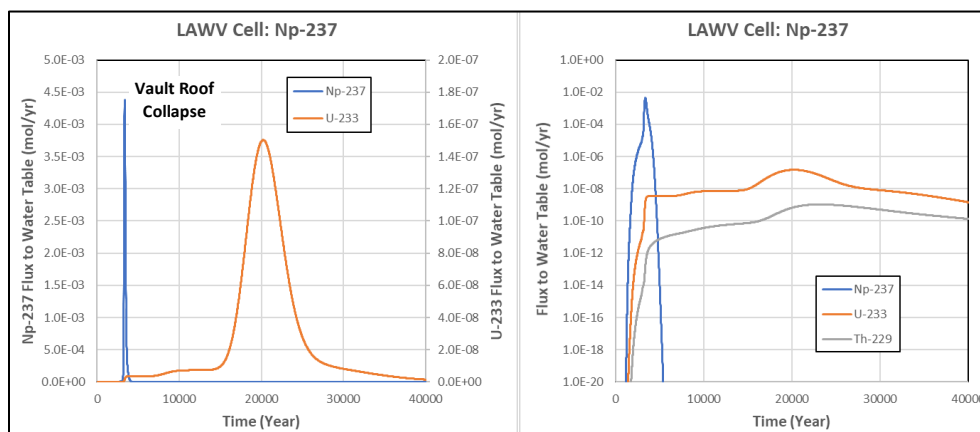


Figure 4-166. Linear and Semi-Log Plots of Flux to Water Table (gmol yr^{-1} per gmole of parent) for Np-237 and Daughters (Smith, 2021b; Figure 6-14)

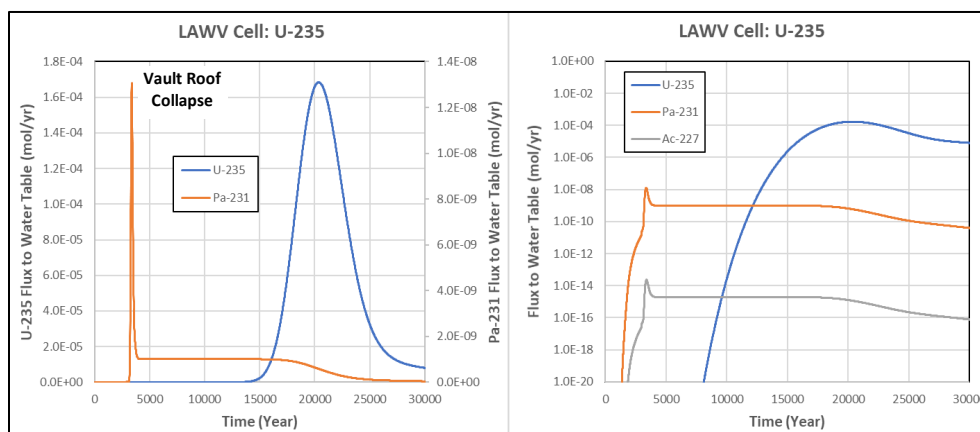


Figure 4-167. Linear and Semi-Log Plots of Flux to Water Table (gmol yr^{-1} per gmole of parent) for U-235 and Daughters (Smith, 2021b; Figure 6-15)

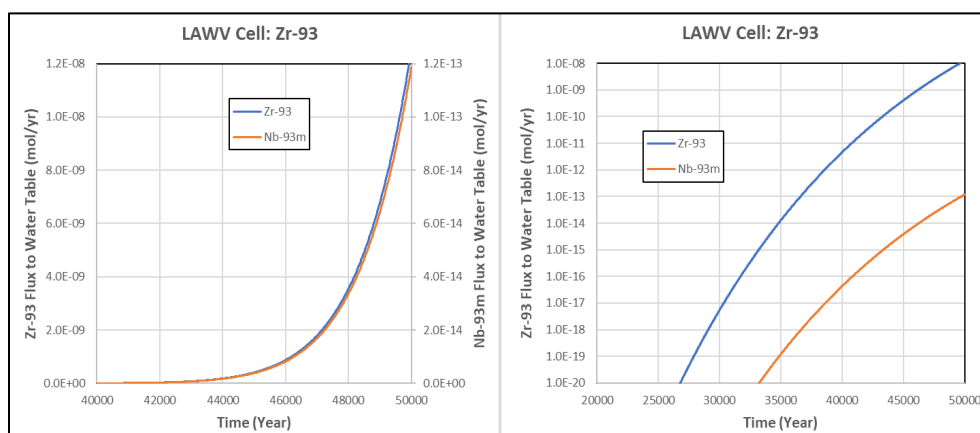


Figure 4-168. Linear and Semi-Log Plots of Flux to Water Table (gmol yr^{-1} per gmole of parent) for Zr-93 and Nb-93m (Smith, 2021b; Figure 6-16)

Table 4-54. Maximum Flux to Water Table and Time of Maximum Flux (Smith, 2021b; Table 6-2)

Radionuclide	Maximum Flux (gmol yr ⁻¹ per gmole of parent radionuclide)	Year
C-14	1.76E-03	2,986
Cl-36	4.13E-03	1,488
H-3	9.56E-11	93
I-129	6.99E-03	1,099
Nb-94	1.04E-05	≥50,000
Tc-99	2.48E-03	3,106
Np-237	4.38E-03	3,366
U-233	1.50E-07	20,236
Th-229	1.06E-09	23,136
U-235	1.68E-04	20,356
Pa-231	1.31E-08	3,366
Ac-227	2.36E-14	3,396
Zr-93	1.25E-08	≥50,000
Nb-93m	1.19E-13	≥50,000

Notes: Parent radionuclides in bold text; progeny in unbolded text

4.5.3.9. Differences in Methods Employed and Parameter Assumptions: 2022 versus 2008 E-Area Low-Level Waste Facility Performance Assessment

4.5.3.9.1. Timeline

In the PA2022 (or current) LAWV model, time zero is the start of operations in 1994; the end of ELLWF operations is expected to be in 2065 when the 100-year IC period will begin. This represents an operational period of 71 years. Conversely, PA2008 assumed an operational period of 25 years beginning in 1995 and ending in 2020 when the 100-year IC period began. Calendar year 2020 was defined as time zero in the PA2008 flow model. The PA2008 model also placed waste in the LAWV 12.5 years before closure, which was defined as the midpoint of operations. However, PA2008 radionuclide transport calculations appear to have shifted time zero to when the waste was placed, which places time zero in calendar year 2007.5 in the PA2008 transport model compared to 1994.74 in the PA2022 model. To be on the same calendar year scale, 12.5 years is added to the relative PA2008 transport times. This small correction makes little difference except for tritium where it represents exactly one half-life. The difference of 45 years in the length of the LAWV operational period between the two PA models (i.e., the final closure cap is installed 45 years earlier in the PA2008 calculation) makes a direct comparison of results difficult.

4.5.3.9.2. Vadose Zone Thickness

The PA2008 model assumed a VZ thickness of 40.5 feet compared to a thickness of 46.8 feet in the current model of the LAWV.

4.5.3.9.3. Infiltration

Figure 4-169 compares the LAWV on-vault infiltration rates used in PA2008 to the interpolated values employed in the current model which are based on the 2019 HELP model calculations reported by Dyer (2019b). Both calculations are made using the same version of the HELP model. The 2019 infiltration rates are lower than the PA2008 values during the first 600 years because of the addition of an HDPE geomembrane above the GCL layer in the current final closure cap design.

The HDPE geomembrane in the current closure cap design provides the primary barrier to water infiltration in the current HELP model simulations. A lower infiltration rate will slow the transport of radionuclides through the LAWV VZ. LAWV roof collapse at 2,976 years results in a large increase in flow through the vault area as runoff from the intact closure cap enters the cavity created by vault failure and waste subsidence. PA2008 chose to model roof collapse at 1,900 years to capture peak radionuclide concentrations more easily in the out years.

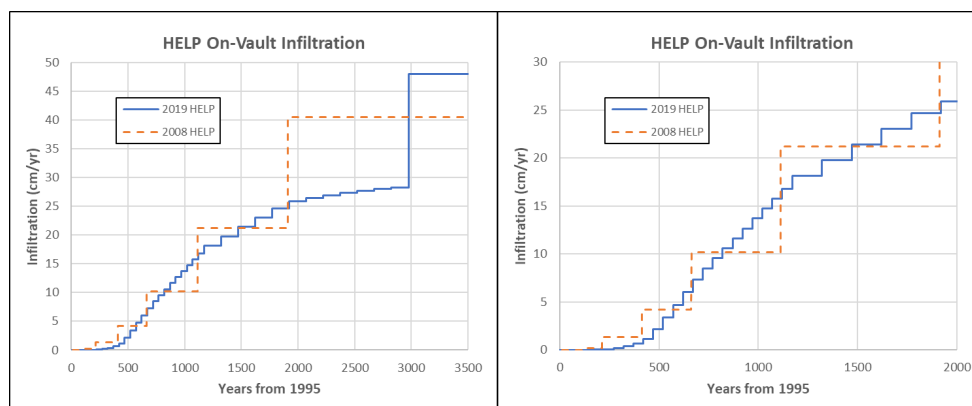


Figure 4-169. HELP Model Infiltration Rates Used in 2008 and 2022 E-Area Low-Level Waste Facility Performance Assessment Vadose Zone Models of Low-Activity Waste Vault (Smith, 2021b; Figure 6-17, same data but different scales)

4.5.3.9.4. Concrete Degradation

The method used to model concrete degradation and cracking in the current LAWV model is described in Sections 4.5.3.1 and 4.5.3.6. A different approach was used in PA2008 which is summarized below:

1. The structural analysis was used to determine the extent of concrete cracking.
2. Hydraulic conductivity of the cracks was calculated using standard methods.
3. Like the blending process used in the current model, saturated hydraulic conductivities for cracked concrete were calculated to include enhanced conductivity from the presence of the cracks.
4. Concrete assumed soil hydraulic properties when the vault roof collapsed.

The LAWV structural analysis predicts that static load cracks that do not penetrate the concrete occur over a limited area of the roof slab and walls when the final closure cap is placed over the vault. The analysis also predicts separation of the vault walls from the footers within 50 to 100 years after closure and estimates the probability of further concrete cracking from differential settlement. To address the structural findings, the LAWV model in PA2008 used two concrete degradation models. One model was termed the “Uncracked Model” and the other the “Cracked Model.” While both models included concrete cracking that the structural analysis predicted with high certainty, the “Cracked Model” also included cracking in the vault roof and walls over time. It was assumed that cracking only impacted concrete saturated hydraulic conductivity. Both concrete degradation models were used to predict flux to the water table, and composite results

were weighted 96.9% “Uncracked” and 3.1% “Cracked.” Full details of the concrete degradation models and methods used to calculate saturated hydraulic conductivity in the 2008 LAWV VZ model are reported by WSRC (2008; Chapter 3).

Table 4-55 lists saturated hydraulic conductivities used for concrete regions in PA2008 (WSRC, 2008; Tables 3-9 and 3-10). Cracking was confined to regions of the roof near the walls (80 inches total) and wall regions at the top, bottom, and center of the wall (2 feet each). The current LAWV VZ model assumes that all roof, floor, and wall concrete is cracked, including the roof beams and wall footers. PA2008 also included a region of high conductivity near the floor to simulate a leak (0.5-inch gap) caused by the separation between the wall and footer. This is not included in the current LAWV VZ model. The “Drain” in Table 4-55 is a 12-inch drainage layer above the roof analogous to the lower drainage layer in the current LAWV VZ model but having a lower hydraulic conductivity. The lower drainage layer hydraulic conductivity in the current model ($K_h = 1.40\text{E-}03 \text{ cm s}^{-1}$) is chosen to be close to the conductivity used in the HELP model infiltration calculations. Figure 4-170 compares PA2008 saturated hydraulic conductivities with values used in the current LAWV VZ model.

Table 4-55. 2008 E-Area Low-Level Waste Facility Performance Assessment Concrete K_{sat} Values (Smith, 2021b; Table 6-3)

Concrete Degrad. Model	Cement Region	K_{sat} Values							
		Years 0–125	Years 125–135	Years 135–225	Years 225–425	Years 425–675	Years 675–1,125	Years 1,125–1,925	After Year 1,925
Uncracked Model	Cracked Roof	1.00E-12	3.11E-09	3.11E-09	3.11E-09	3.11E-09	3.11E-09	3.11E-09	1.20E-04
	Wall	1.00E-12	3.20E-11	3.20E-11	3.20E-11	3.20E-11	3.20E-11	3.20E-11	1.20E-04
Cracked Model	Cracked Roof	1.00E-12	3.11E-09	2.43E-06	1.03E-05	2.24E-05	4.12E-05	4.37E-04	1.20E-04
	Wall	1.00E-12	3.20E-11	3.17E-06	1.33E-05	2.91E-05	5.36E-05	5.93E-04	1.20E-04
Both Models	Roof Center	1.00E-12	3.11E-09	3.11E-09	3.11E-09	3.11E-09	3.11E-09	3.11E-09	1.20E-04
	Floor Center	1.00E-12	1.00E-12	1.00E-12	1.00E-12	1.00E-12	1.00E-12	1.00E-12	1.20E-04
	Floor Leak	1.00E-12	1.90E-06	1.90E-06	1.90E-06	1.90E-06	1.90E-06	1.90E-06	1.20E-04
	Drain	4.09E-05	4.09E-05	4.09E-05	4.09E-05	4.09E-05	4.09E-05	4.09E-05	1.20E-04

Notes:

Time periods are years from the start of LAWV operation on September 28, 1994.

4.5.3.9.5. Sorption

Sorption properties (K_d values) for the radionuclides and significant materials used in this study (Kaplan, 2016b) are summarized in Table 4-56 and compared to values from the 2006 Geochemical Database (Kaplan, 2006) used for PA2008. Tritium is not included in Table 4-56 because it has a K_d of zero for all materials in both databases. K_d values are unchanged for actinium, thorium, and zirconium in sandy soil (LVZ) and clayey soil (UVZ, waste, and backfill). The trend for other elements is an increase in soil K_d , although for protactinium and neptunium, the K_d in clayey soil decreases. For reducing cement, iodine, chlorine, and technetium are the only elements that saw a decrease in K_d from 2006 to 2016. In general, there are significant differences in sorption

properties between the 2006 and 2016 versions of the geochemical database that will have a direct impact on radionuclide transport.

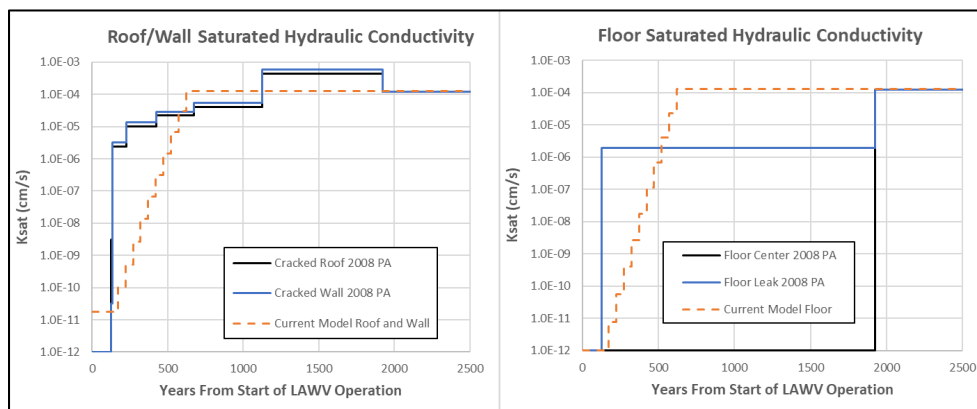


Figure 4-170. Concrete Saturated Hydraulic Conductivities used in the 2008 E-Area Low-Level Waste Facility Performance Assessment and Current Low-Activity Waste Vault Vadose Zone Models (Smith, 2021b; Figure 6-18)

Table 4-56. K_d Values from 2016 and 2006 Geochemical Databases (Smith, 2021b; Table 6-4)

Element	Geochemical Database ¹	Sand	Clay	Reducing Cement		
				Phase I	Phase II	Phase III
Ac	2016	1,100	8,500	7,000	7,000	1,000
	2006	1,100	8,500	5,000	5,000	500
C	2016	1	30	2,000	5,000	50
	2006	0	0	20	10	0
Cl	2016	1	8	0	10	1
	2006	0	0	0.8	2	0
I	2016	1	3	0	2	0
	2006	0	0.6	8	20	0
Nb	2016	1,000	1,000	1,000	1,000	500
	2006	0	0	1,000	1,000	500
Np	2016	3	9	10,000	10,000	5,000
	2006	0.6	35	2,000	2,000	200
Pa	2016	3	9	10,000	10,000	5,000
	2006	0.6	35	2,000	2,000	200
Tc	2016	0.6	1.8	1,000	1,000	1,000
	2006	0.1	0.2	5,000	5,000	5,000
Th	2016	900	2,000	10,000	10,000	2,000
	2006	900	2,000	5,000	5,000	500
U	2016	300	400	5,000	5,000	5,000
	2006	200	300	5,000	5,000	5,000
Zr	2016	900	2,000	10,000	10,000	2,000
	2006	900	2,000	5,000	5,000	500

Notes:

¹ Kaplan (2016b); 2006: Kaplan (2006)

In addition to differences in K_d values, the PA2008 model assumed that the vault concrete retained concrete transport properties after hydraulic failure. K_d values in the concrete regions were

changed according to the 50, 500, 4,000 pore-volume exchange aging mechanism assuming soil properties only after 4,000 pore-volumes passed through each region. In the current model, all vault concrete takes on the K_d values for clayey soil following vault roof collapse at 2,976 years.

4.5.3.10. Comparison of Model Results: 2022 versus 2008 E-Area Low-Level Waste Facility Performance Assessment

Comparisons of flux to the water table are shown in Figure 4-171 through Figure 4-177 for the nine parent and five daughter radionuclides as calculated using the PA2008 and the PA2022 VZ models for the LAWV. In Figure 4-171 through Figure 4-177, PA2008 results are shown as a dashed-orange curve with the designation “PA” in the legend; PA2022 results are shown as a blue-dashed curve. Both Cracked and Uncracked PA2008 results are examined, and there is surprisingly little difference between the two. Comparison plots in this section use the PA2008 Cracked analysis.⁶

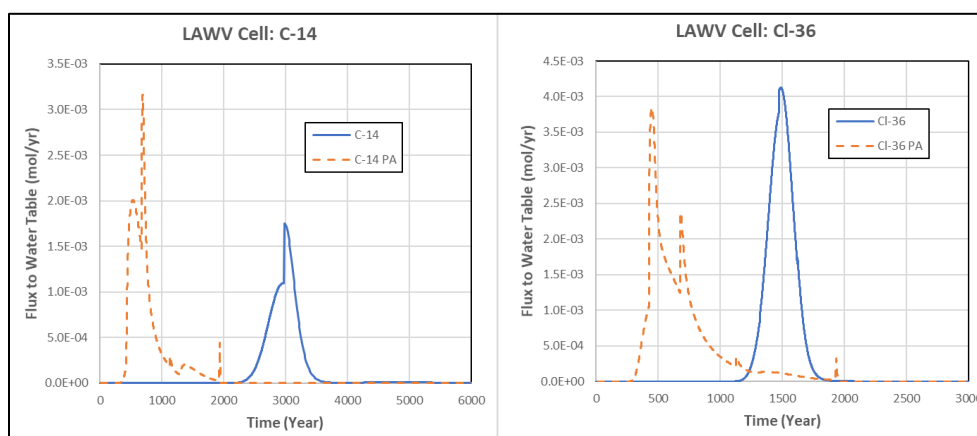


Figure 4-171. Flux to Water Table (gmol yr⁻¹ per gmole of parent) for C-14 and Cl-36 in Current and 2008 E-Area Low-Level Waste Facility Performance Assessment Models (Smith, 2021b; Figure 6-19)

PA2008 results for C-14, Cl-36, and I-129 (Figure 4-171 and Figure 4-172) all display the same general characteristics: three peaks in flux that extend from a more gradual flux curve, followed by a fourth sharp peak around 2,000 years. The peaks occur at the same time for each radionuclide and, as annotated on the I-129 plot, occur when there is an increase in flow and when the LAWV roof collapses. Only eight infiltration rates were used in PA2008 modeling for the LAWV, which likely caused the irregular flux shapes. The increases in K_d shown in Table 4-56 also affect the results with all of the PA2022 model flux peaks occurring later than in the PA2008 calculations. The peak fluxes for C-14 and Cl-36 in the current model occur beyond the period of performance (171 to 1,171 years), while I-129 flux peaks near the end of the period of performance. However, allowing for transport time to the POA, the peak I-129 flux will produce a maximum dose beyond the period of performance. C-14 peak flux is approximately 50% of the PA2008 peak value, Cl-36 peak flux is about the same as the PA2008 peak flux, and I-129 peak flux is more than twice

⁶ The cracked concrete analysis without CDP factors for carbonaceous material in the waste appears to be most like the current calculation. CDP factors were adjustments applied to K_d values in PA2008 for waste in a carbonaceous environment. They are not used in this PA.

the PA2008 peak value. The C-14 peak flux in the current model increased due to the timing of the vault roof collapse.

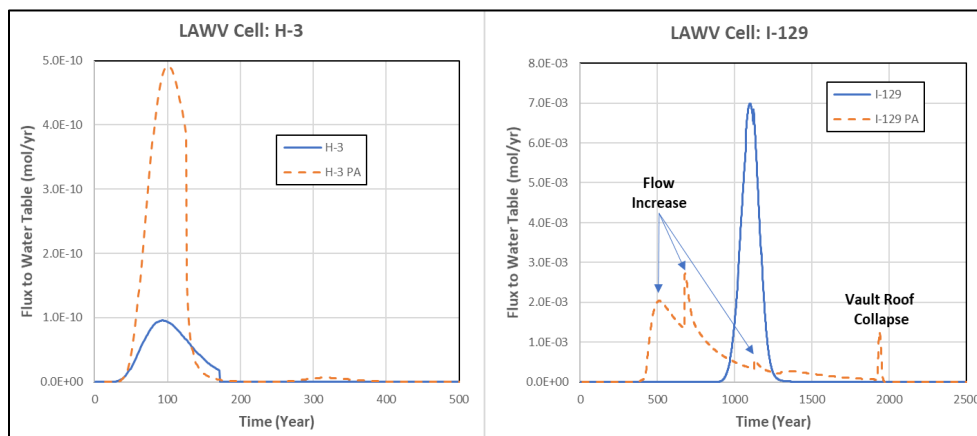


Figure 4-172. Flux to Water Table (gmol yr⁻¹ per gmole of parent) for H-3 and I-129 in Current and 2008 E-Area Low-Level Waste Facility Performance Assessment Models (Smith, 2021b; Figure 6-20)

The peak H-3 flux in the current model (Figure 4-172), which appears well before concrete degradation starts and before there is significant infiltration through the vault, is about 20% of the PA2008 peak flux. The timing of the peak flux is in close agreement between the two models. Both peaks show a flux decrease when the final closure cap is applied (Year 171 in the current model and Year 125 in the PA2008 model). Because there is little flow through the LAWV before and immediately after closure cap placement, H-3 flux must be caused by diffusion out of the vault. PA2008 placed the waste at the midpoint of operations while the PA2022 model simulation places the waste at the start of operations. Earlier placement adds about one half-life to the H-3 decay which will lower the peak flux by a factor of two. In either case, fluxes to the water table from 1.0 gmole of H-3 are relatively small.

The large increase in K_d for Nb-94 between 2008 ($K_d = 0$) and the present ($K_d = 1,000$) precludes a direct comparison of fluxes for this radionuclide (Figure 4-173). However, the overall trend is correct with a much later flux peak in the current model using the higher K_d . The later elution time will likely remove Nb-94 from consideration for GW protection limits.

In both models, the peak Tc-99 fluxes shown in Figure 4-173 occur shortly after concrete K_d values are replaced with soil K_d values. This transition occurs at about 4,700 years in the PA2008 model and at 3,000 years in the PA2022 model. In addition to increased flow through the vault, the PA2022 model assumes K_d values change from concrete to soil when the LAWV roof collapses, while the PA2008 model transition is based on 4,000 pore-volume exchanges in the concrete.

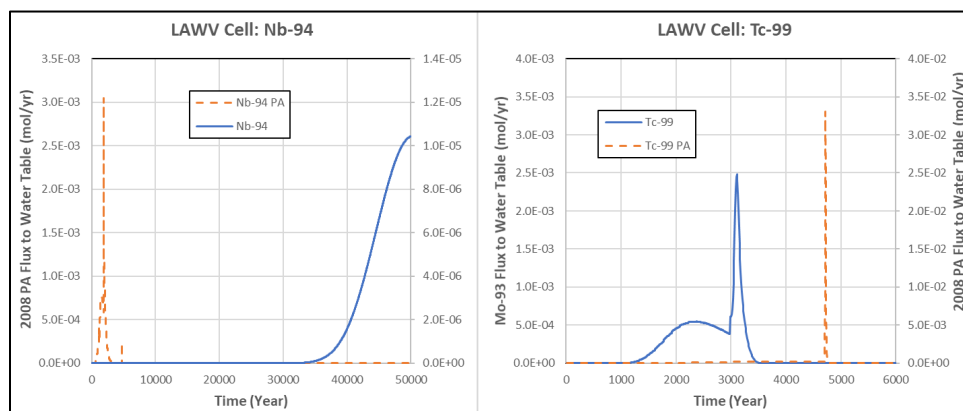


Figure 4-173. Flux to Water Table (gmol yr^{-1} per gmole of parent) for Nb-94 and Tc-99 in Current and 2008 E-Area Low-Level Waste Facility Performance Assessment Models (Smith, 2021b; Figure 6-21)

In Figure 4-174, Figure 4-175, and Figure 4-176, results are plotted on both linear (left) and semi-log (right) scales to include the daughter radionuclides which are at present at much lower concentrations than the parents. The Np-237 and U-235 series in Figure 4-174 and Figure 4-175, respectively, show similar behavior. As shown in Table 4-56, K_d values for Np-237 in the latest geochemical data package increased for sandy soil, decreased for clayey soil, and increased for cement. K_d values for Pa-231 are identical to those for Np-237. The net effect is that Np-237 and Pa-231 fluxes to the water table in the PA2022 model peak later than in the PA2008 model. Additionally, the peaks are sharper in the PA2022 model because they occur near the time of roof collapse. Uranium transport in both figures is very similar even though it is the parent radionuclide in one case and a decay product in the other. Uranium K_d values for soil increased in the 2016 geochemical database (Table 4-56), causing peak fluxes to occur later in the current LAWV PA model. Examining the semi-log plots (right side) in Figure 4-174 and Figure 4-175, there is a definite tendency in the current model for the fluxes to continue at a low level over an extended time. The daughter radionuclides are decay products that follow the parent's behavior. This effect is also noticeable in the concentration profiles for C-14 (Smith, 2021b; Appendix C) where a small residual concentration of contaminant appears to remain in the vicinity of the vault walls after most of the material has eluted.

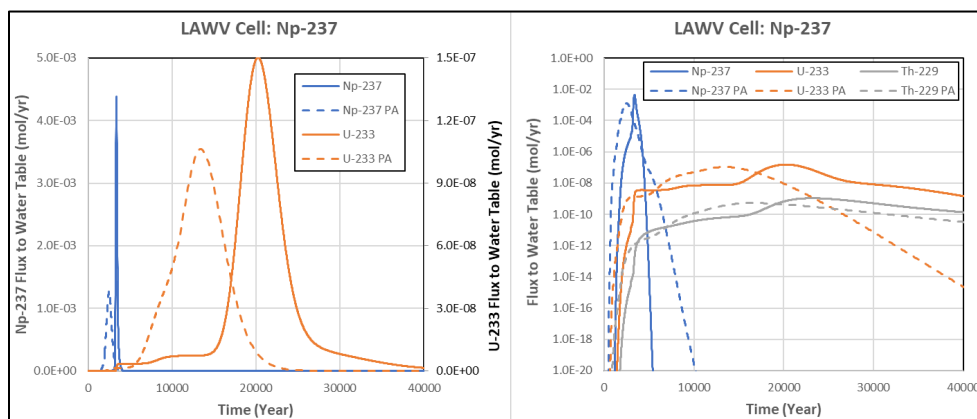


Figure 4-174. Flux to Water Table (gmol yr^{-1} per gmole of parent) for Np-237 and Daughters in Current and 2008 E-Area Low-Level Waste Facility Performance Assessment Models (Smith, 2021b; Figure 6-22)

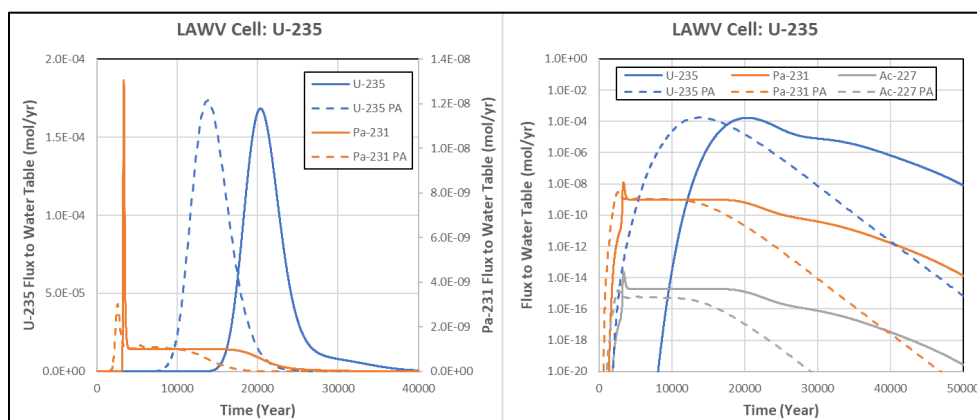


Figure 4-175. Flux to Water Table (gmol yr^{-1} per gmole of parent) for U-235 and Daughters in Current and 2008 E-Area Low-Level Waste Facility Performance Assessment Models (Smith, 2021b; Figure 6-23)

Figure 4-176 shows flux to the water table for Zr-93 and its daughter, Nb-93m. The linear plot of Zr-93 flux (left) is distorted by the extreme difference in scale with the PA2008 flux magnified by a factor of 5,000 relative to the flux from the current model. As before, a direct comparison of Nb fluxes cannot be made because of the large difference in K_d values between the two models. The semi-log plot (right) appears to show that Zr-93 is behaving differently in the PA2022 model than in the PA2008 version even though K_d values have not changed. However, not capturing the peak flux for Zr-93 makes it difficult to compare the two PA models because Figure 4-176 is only showing the leading edge of the peak.

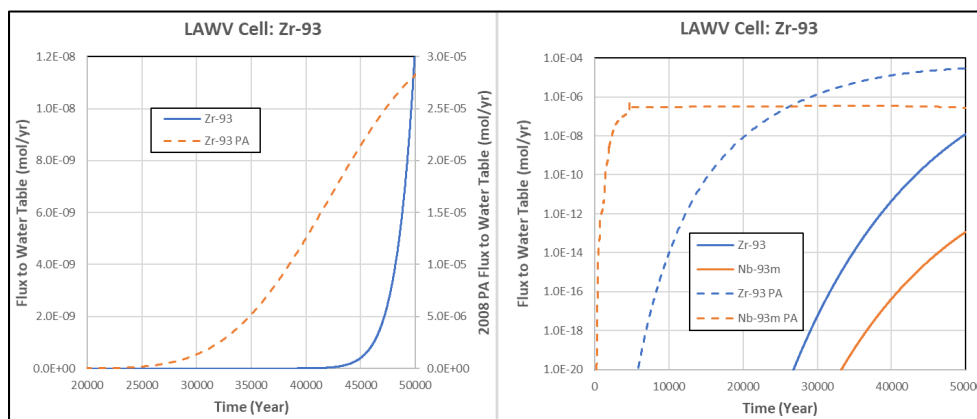


Figure 4-176. Flux to Water Table (gmol yr^{-1} per gmole of parent) for Zr-93 and Nb-93m in Current and 2008 E-Area Low-Level Waste Facility Performance Assessment Models (Smith, 2021b; Figure 6-24)

Finally, Tc-99 and Np-237, which appear to be potentially problematic, are replotted as shown in Figure 4-177 to examine the flux peaks more closely. The Tc-99 flux curve for the PA2022 model crosses the PA2008 model flux curve at the end of the period of compliance (Year 1,171), while the Np-237 flux curve for the PA2022 model falls below the flux curve for the PA2008 model except between approximately 3,300 and 4,300 years.

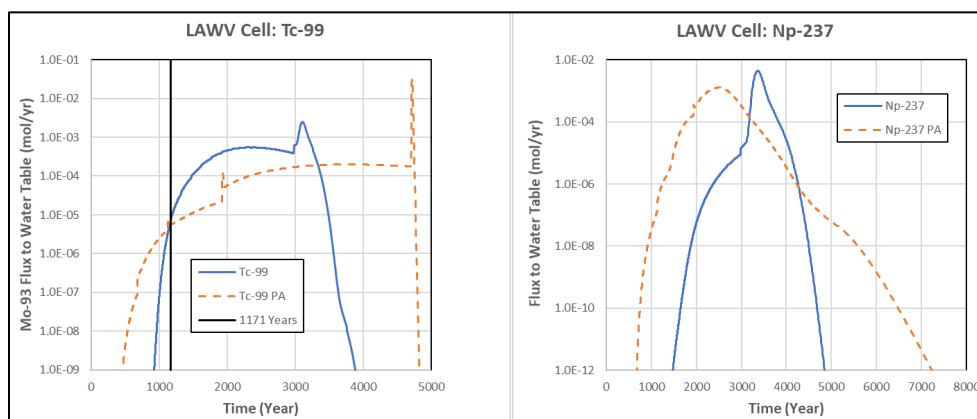


Figure 4-177. Flux to Water Table (gmol yr^{-1} per gmole of parent) for Tc-99 and Np-237 in Current and 2008 E-Area Low-Level Waste Facility Performance Assessment Models (Smith, 2021b; Figure 6-25)

In summary, preliminary PORFLOW transport simulations for nine parent radionuclides and five daughters designed to test the performance of the current, revised conceptual model for the LAWV VZ indicate that the current, revised model predicts flux to the water table curves that are significantly different than those obtained with the 2008 ELLWF PA model. The reasons for the differences can be attributed primarily to four factors:

1. Revised infiltration calculations
2. Revised K_d values for radionuclides
3. The inclusion of more time steps in the current model
4. Revised approach for simulating concrete cracking and degradation

All radionuclide transport model predictions using the revised VZ model appear reasonable, and peaks in flux to the water table generally occur later in time than in PA2008. Nevertheless, not all radionuclides with LA WV limits are tested in the preliminary PORFLOW simulations. Transport results for all radionuclides included in this PA are presented in Sections 5.2.1.2 and 5.2.2.1. In some instances, peak flux to the water table may exceed the PA2008 values during the period of compliance, which will lead to a decrease in disposal limits.

4.6. INTERMEDIATE-LEVEL VAULT

ILV disposal limits for the ELLWF through the 1,000-year period of performance are developed in PA2022 for the following exposure pathways: GW protection, all-pathways, IHI, air, and radon. This section describes in detail the development and implementation of conceptual models for the ILV for the GW pathway. Conceptual models for the IHI exposure pathway are described in Section 3.7.3 and Section 7.3. Conceptual models for the air and radon pathways are described in Section 3.6.

4.6.1. Waste Zone Conceptual Model: Material and Hydraulic Properties

Based upon structural modeling which considers vault loadings (both static and seismic) and rebar corrosion, Peregoy (2006b) estimated via Monte Carlo analysis that the mean and median times to ILV collapse are 6,703 years⁷ and 6,250 years, respectively, with a standard deviation of 1,976 years. Two ILV waste zone representations will be considered: before vault collapse and after vault collapse.

4.6.1.1. Before Collapse

Before vault collapse, the ILV waste zone will include vessels and waste contained within drums, B-12 boxes, B-25 boxes, other metal containers, and concrete containers. The first layer of containers is placed within a cell directly on top of the graded stone leachate collection system. This first layer of waste is encapsulated with the old E-Area CIG grout (see Table 2-20) and the overlying grout forms the surface for the placement of the next layer of waste. Subsequent layers of containers within a cell are encapsulated with E-Area CLSM (see Table 2-20). This process will continue until the waste/CLSM zone thickness is 25 feet, 10 inches in the ILNT cells and 21 feet, 9 inches in the ILT cells. A nominal 17-inch-thick final top layer of new E-Area CIG grout will be used to provide the surface upon which the final reinforced concrete roof will be placed for the ILNT cells and a nominal 37-inch-thick top layer of grout for the ILT cells (see Figure 2-74 and Figure 2-75). Before vault collapse after 7,000 years, it is anticipated that significant corrosion of the metal waste containers will occur, resulting in collapse of individual containers and overlying CSLM and/or grout before the time of vault collapse. Over time, this will result in a crumbling, fractured waste zone. Nichols and Butcher (2020) recommend that because of the anticipated crumbling, fractured waste zone, the ILV waste zone and vault interior before vault collapse will be represented hydraulically by Gravel (G1) as shown in Figure 4-178(a). This material property is deemed appropriate for representing the waste zone.

⁷ Rounded to 7,000 years by Peregoy (2006b) on Sheet 10.

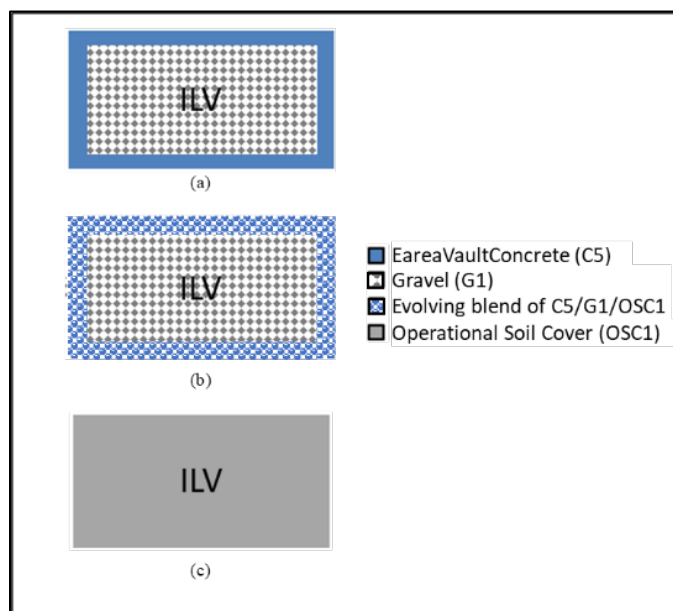


Figure 4-178. Intermediate-Level Vault Waste Zone Conceptual Model of Hydraulic Properties in (a) Intact, (b) Cracked, and (c) Collapsed States

In past ELLWF PAs, the hydraulic properties of concrete have abruptly changed from those of intact concrete to soil to represent vault structural collapse or complete deterioration of the concrete matrix. In PA2022, concrete degradation is modeled as a gradual process where, starting at the time of site closure, concrete hydraulic properties are transformed into those of soil over a period of 500 years. A detailed conceptual model of ILV concrete degradation and the associated impact on material and hydraulic properties are described in detail in Section 4.6.3.5. In Figure 4-178(b), the concrete degradation is represented as an evolving blend over 500 years of EareaVaultConcrete (C5), Gravel (G1), and OSC1.

4.6.1.2. After Collapse

Significant void space is assumed to exist in most of the containers within the ILV; however, the interior subsidence potential of the ILV has not been estimated. Assuming the waste zone within a cell consists of six layers of B-25 boxes and each box contains waste with the same density as B-25 boxes disposed in ETs, then the ILV would have an interior subsidence potential of approximately 20 feet and a corresponding subsided waste zone thickness of approximately 5 feet to 6 feet. This suggests that the subsidence potential of the ILV waste zone may be significant. However, because the waste zone does not contain low-density waste in B-25 boxes solely, the assumed subsided waste zone thickness will be 10 feet (Nichols and Butcher, 2020) or approximately twice the subsided waste zone thickness based on low-density waste in B-25 boxes alone. Given a 10-foot subsided waste zone thickness yields a subsidence potential of 17 feet.

Upon vault collapse, the roof and overlying closure cap soils are expected to fall into the vault interior, crushing the crumbling and fractured CLSM and grout; corroded containers; and waste to a nominal 10-foot thickness. Due to the significant soil mass within a collapsed ILV and the fluffing of the soil as it collapses into the vault, the ILV waste zone and vault interior after collapse

will be represented hydraulically by OSC1 as shown in Figure 4-178(c). Because the OSC will be derived from UVZ soils, UVZ soil properties are used to estimate the properties of OSC1 as discussed in detail in Section 3.8.3.1.2.

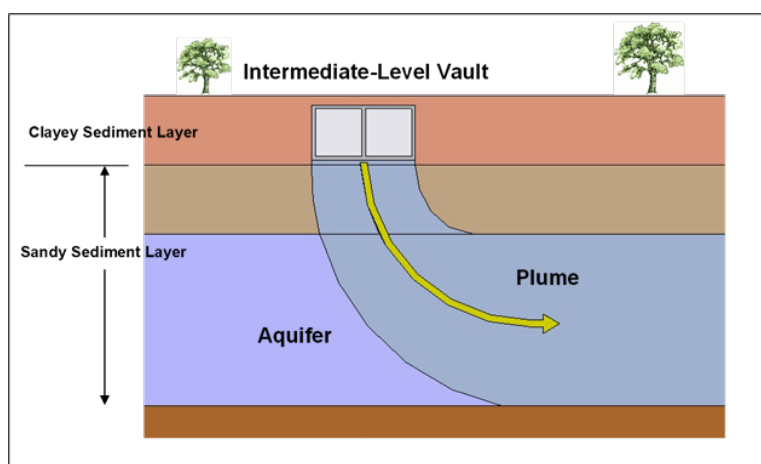
Table 3-64 summarizes waste zone material properties for the ILV before and after vault collapse.

4.6.2. Waste and Vadose Zone Conceptual Model: Geochemical Properties

Key features of the ILV that will impact the geochemical environments within and beneath the vault are described below. More specifically, a geochemical conceptual model for the ILV is presented that identifies the aqueous chemistry and associated solid phases comprising the waste zone, UVZ, LVZ, and aquifer. The conceptual model developed by Kaplan (2016b) also assigns geochemical parameters to each material zone. Kaplan (2016b) provides a detailed description of the development of the geochemical conceptual model, the definitions of the different geochemical environments and materials, and the assignment of appropriate geochemical parameters for each radionuclide of interest.

Figure 4-179 (Kaplan, 2016b) is a schematic of the geochemical conceptual model for the ILV. The cross-section does not show dimensionality and facility-specific details, which are instead assigned in the numerical model (see Section 4.6.3.3). The relevant geochemical environments for the ILV are fivefold: oxidizing cement, reducing cement, sandy sediment, cementitious-leachate-impacted clayey sediment, and cementitious-leachate-impacted sandy sediment. Section 3.8.2.5 provides a description of the four geochemical conceptual environments.

Table 4-57 (Kaplan, 2016b) lists the relevant solid and aqueous phases for the ILV, along with the associated geochemical parameters (K_d and k_s values) necessary in the PA model to describe the chemical interactions of radionuclides with these geochemical materials (e.g., sandy sediment, oxidizing cement, reducing cement). SRNL (2018) provides look-up tables containing the recommended K_d and k_s values for each radionuclide (table rows) as a function of the different geochemical materials or solid phases (table columns).



Note: Overlying final closure cap not shown.

Figure 4-179. Intermediate-Level Vault Geochemical Conceptual Model Schematic

Table 4-57. Conceptual Geochemical Model of Features and Parameters for Intermediate-Level Vault (see Figure 4-179)

Feature		Geochemical Parameter
Solid Phases	Aqueous Phase	
Waste Zone: Active components are grout, iron metal, and corrosion products. Because of intimate contact between encapsulating grout and waste form, cement phases are considered to be controlling sorption chemistry. The impact of Fe-oxides is ignored. ^a	Cementitious-Impacted Leachate: Three general types of oxidizing grout leachate chemistries controlled by different aged cement phases characterized by elevated pH and ionic strength relative to SRS GW.	Use Oxidizing Cement K_d or apparent solubility concentrations for the three cement ages. ^b
Reducing Concrete Vault: Active components are cement and slag added to concrete in roof, walls, and floor. ^c	Cementitious-Impacted Leachate: Three general types of reducing concrete leachate chemistries are controlled by different aged cement phases characterized by elevated pH and ionic strength relative to SRS GW. Leachate will contain sulfides released from slag.	Use Reducing Cement K_d or apparent solubility concentrations for the three cement ages. ^c
Clayey Sediment: Upper Vadose Zone	Fe-Oxide-Impacted Cementitious Leachate: Cement leachate chemistry altered by passing through Fe-oxide controlled environment. Still characterized by elevated pH and ionic strength relative to SRS GW.	Use cementitious-leachate-impacted Clayey Sediment K_d values; $K_{dCementLeach}$. ^d
Sandy Sediment: Lower Vadose Zone		Use cementitious-leachate-impacted Sandy Sediment K_d , $K_{dCementLeach}$. ^d
Sandy Sediment: Aquifer Zone	Cementitious Leachate Porewater: Gets diluted with typical SRS GW and the aqueous phase takes on the properties of the latter: pH 5.8 and ionic strength 0.01, except for trace levels of radionuclides.	Use Sandy Sediment K_d .

Notes:

- ^a Waste designated for the ILV contains greater radioactivity than the waste disposed in the LAWV. The ILV consists of two modules containing eight bulk waste cells and one cell constructed with 144 silos. Waste is packaged in a variety of metal or concrete containers. Within each bulk waste cell, the first layer of waste is placed directly on top of the graded stone drainage layer. The first layer of waste is encapsulated in grout which forms the surface for the placement of the next layer. Subsequent layers of waste are placed directly on top of the previously encapsulated waste. Subsequent layers may be encapsulated with CLSM rather than grout. The cell with silos is used for disposal and storage of tritium-bearing waste packed in 10-gallon drums, spent tritium extraction crucibles, and tritium job control waste.
- ^b Oxidizing grout or CLSM used to encapsulate waste containers is assumed to control the chemistry of the waste layer rather than the surrounding reducing concrete vault.
- ^c Reducing cementitious materials are those that contain slag and change the pore water chemistry sufficiently to require unique geochemical parameters. The ILV is constructed with a 17-inch to 54-inch-thick concrete roof, 18-inch to 30-inch-thick interior and exterior concrete walls, and 30-inch thick base slab. Reducing concrete roof will be added at the time of operational closure.
- ^d The 2010 geochemical data package (Kaplan, 2010) introduced the concept of a cementitious-leachate-impacted zone beneath concrete/grout DUs. This change specifically affected the CIG trench segments, LAWV, and ILV models, but has never been formally evaluated through the UDQE process for inclusion in the PA baseline. The current geochemical data package maintains this concept which will be evaluated in the PA2022 revision.

4.6.3. PORFLOW Implementation of Vadose Zone Conceptual Model

The ILV DU is a below-grade reinforced concrete structure containing multiple layers of high-activity waste containers encapsulated by grout or CLSM. The ILV is used to dispose of waste containers that exceed the radiological dose and radionuclide concentration limits of other LLW disposal facilities such as STs, ETs, and the LAWV. The ILV is in the western sector of the ELLWF and is highlighted in magenta in Figure 4-180.

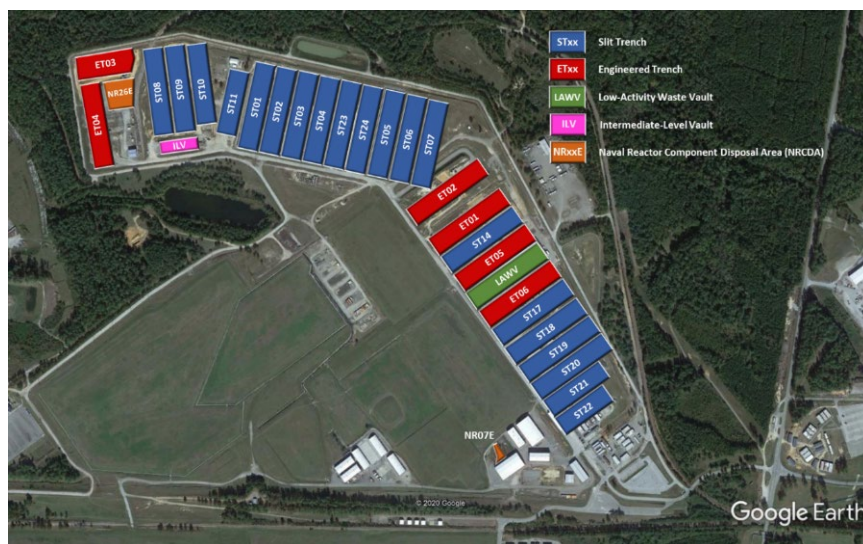


Figure 4-180. Intermediate-Level Vault Location within E-Area Low-Level Waste Facility

Section 2.2.6 and Smith (2021a) describe in detail the structural design features, waste types and characteristics, and waste placement procedures for the ILV that are relevant to the development and implementation within PORFLOW of the ILV VZ conceptual model. Because of its complicated structure as displayed in Figure 2-72 through Figure 2-75, the ILV will be modeled in PORFLOW as 2-D cross-sections depicting unique features along the short axis of the vault (see Figure 2-75). This is the same approach that was taken for PA2008 (WSRC, 2008) and is justified by considerations such as:

- Uniformity of the ILNT cells, except for the middle cell which has a construction joint not found in other cells. This makes Cell 4 structurally weaker than other vault cells and subject to greater cracking during seismic events, which require a separate model representation.
- The vault and closure cap are symmetric along the centerline of the short axis.
- 3-D modeling is used for STs and ETs to capture variations in location relative to the closure cap (e.g., center versus corner trench units) and hydrostratigraphy (i.e., depth to water table and clay thickness) not seen with the single ILV.

ILV dimensions used to create the PORFLOW model are taken from Figure 2-75. Table 4-58 lists significant features of the ILV's construction with the modeling approach noted.

Table 4-58. Intermediate-Level Vault Construction Features and Modeling Approach (Smith, 2021a; Table 2-1)

As-Built ILV Features	As Modeled
Controlled compacted backfill soil base.	Soil base modeled as ILV backfill.
A graded stone drainage layer with a minimum thickness of 14 inches overlays the floor.	14-inch stone drainage layer above floor modeled as gravel.
Graded stone sub-floor drainage system to collect and drain water under the vault to a dry well.	Water under the vault conservatively drains to the water table.
30-inch-thick, reinforced concrete, base slab, which extends 2 feet beyond the exterior walls.	30-inch-thick concrete base is modeled without the 2-foot extensions beyond wall.
30-inch-thick reinforced concrete, exterior end walls, 24-inch-thick reinforced concrete exterior side walls, and 18-inch-thick, reinforced concrete interior walls. All walls are structurally mated to the base slab and have no horizontal joints.	2-D model includes 2-foot-thick side walls.
Sloped rain covers, consisting of a roofing membrane on metal deck on steel framing installed over each cell to direct rainwater onto the ground for runoff. This is used during operations only and will be replaced with a permanent concrete roof after operations end.	Sloped concrete roof is assumed to be in place throughout the simulation, the metal roof and rain cover will prevent water entering the vault during operations and the model simulates this behavior by using a very low infiltration rate of 0.001 in yr ⁻¹ during ILV operations.
A 3-inch-thick layer of CLSM is used to close filled vault and provide a level surface for roof seating. CLSM or grout is also used to fill and cover waste layers as the vault is filled.	CLSM and grout are modeled indirectly by using radionuclide K_d values for a cementitious environment.

4.6.3.1. Timeline

Table 4-59 provides an overview of the ILV timeline assumed in developing the PORFLOW model. The model timing (i.e., time = 0) starts in 1994 with the receipt of the first disposal container in the LAWV, which was the first waste package placed in E-Area. As a conservative approach, the flow and transport model assumes that the entire waste inventory is placed at the start of operations except as discussed for the TPBAR SWF in Section 4.6.3.6. This allows daughter ingrowth to occur for decay chains and does not significantly reduce the concentration of long-lived radionuclides such as C-14, Tc-99, and I-129, which are typically strong contributors to dose. Radionuclides with very short half-lives, such as H-3, will largely decay away before the 1,000-year post-closure period during which the performance of the ILV is assessed for regulatory compliance. For this reason, the assumption of early disposal is acceptable.

As described in Section 4.6.3.5, hydraulic properties of the vault concrete are assumed to degrade over a 500-year period beginning at the end of IC when moisture buildup in the overlying cap, vault cracking, and lack of access to the subdrain system lead to water infiltration through the vault. Based on a structural analysis performed for the ILV (Peregoy, 2006b), installation of the final closure cap results in cracking that partially penetrates the vault walls and roof causing some immediate degradation in concrete hydraulic properties. The structural analysis also concluded that the vault roof will collapse from a seismic event having a 5% probability of occurrence at a mean time of 6,250 years. As explained in the discussion of infiltration rates in Section 4.6.3.4, the time of roof collapse is assumed to be at relative Year 5,770 in the model to coincide with an existing infiltration rate calculation.

Table 4-59. Intermediate-Level Vault Timeline (Smith, 2021a; Table 3-1)

Calendar Date	Numerical Calendar Date	Time from Start of ELLWF Operation	Operational Events
9/28/1994	1994.74	-1.0	Start of ELLWF operations.
9/28/1995	1995.74	0.0	Start of ILV operations. ^{1,2} Start of radionuclide decay and daughter ingrowth. Start of 10,000-year modeling period.
9/28/2040	2040.74	45.0	ILV filled, operations end. Metal roof replaced with final concrete roof covered by a waterproof membrane.
9/28/2065	2065.74	70.0	End of ELLWF operations. Start of IC.
9/28/2165	2165.74	170.0	End of IC. Installation of final closure cap. Non-through cracking of vault roof and walls. End of water removal from vault sump. Start of 500-year concrete degradation. Start of 1,000-year period of performance.
9/28/2665	2665.74	670.0	Vault concrete fails hydraulically.
9/28/3165	3165.74	1,170.0	End of 1,000-year period of performance.
9/28/7765	7765.74	5,770.0	Vault roof collapses. ⁴ Waste material subsides into 10-foot layer at bottom of vault.
9/28/12165	12165.74	10,170.0	End of 10,000-year modeling period. ³

Notes:

- ¹ Conservatively, it is assumed that all ILV waste (exclusive of TPBAR waste containers) is placed at the start of operation. TPBAR waste container disposal in the model follows the waste management disposal schedule.
- ² The earliest recorded date for disposal in the ILV is 5/12/1995. This information was found after the model was developed; the difference in using 9/28/1995 is deemed to be within modeling uncertainty.
- ³ For some radionuclides, modeling will be extended to 50,000 years to capture peak radionuclide concentrations.
- ⁴ For the PORFLOW model of the ILV, a decision was initially made to use the median time to roof collapse from a seismic event (6,250 years) instead of the mean time to roof collapse (6,703 years; rounded to 7,000 years). The selection of the median value is pessimistically bounding from an infiltration rate perspective. However, to align with the timing of the HELP model simulation cases out of convenience and to remain pessimistically bounding, the PORFLOW model assumes that ILV roof collapse will actually occur in Year 5,770 rather than Year 6,420 (Year 170 when closure cap installed + 6,250 years median collapse time = Year 6,420).

4.6.3.2. Hydrostratigraphic Layers

Figure 4-181 shows a generalized (not to scale) 1-D schematic diagram of the ILV disposal site and the underlying VZ hydrostratigraphic layers. The diagram intends to show only the VZ layers and omits many details of the actual PORFLOW model. Dimensions (Bagwell and Bennett, 2017) and soil specifications for the VZ segments comprising the ILV waste disposal site in the PORFLOW model are listed in Table 4-60. The PORFLOW model used in PA2008 did not include the TCCZ or the LAZ.

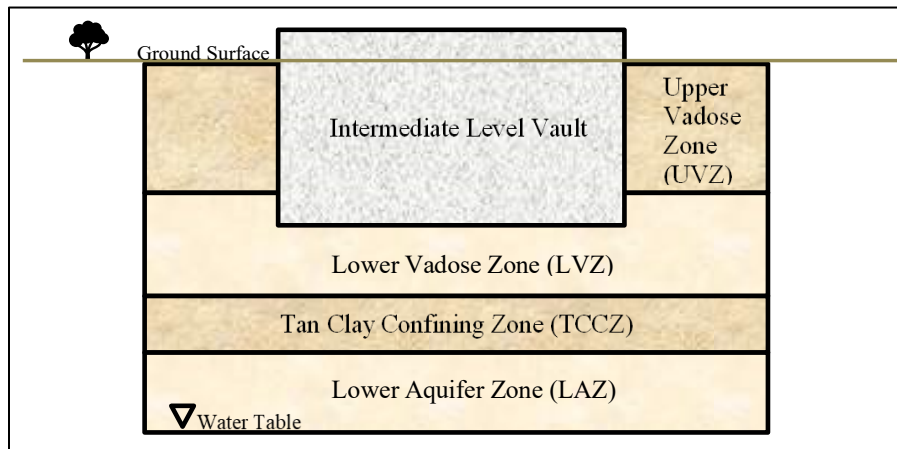


Figure 4-181. Schematic of Intermediate-Level Vault Waste Disposal Site and Vadose Zone Hydrostratigraphic Layers (Smith, 2021a; Figure 4-1)

Table 4-60. Nominal Thickness and Composition of Intermediate-Level Vault Vadose Zone Segments (Smith, 2021a; Table 4-1)

Vadose Zone Segment	Segment Length (feet)
Average Depth to Water Table	76.5 feet
UVZ	19.9 feet clay
LVZ	40.8 feet sand
TCCZ	11.7 feet clay
LAZ	4.1 feet sand

4.6.3.3. Model Geometry

Figure 4-182 provides a cross-sectional view of the ILV with the final closure cap in place. The ILV is located along the southern perimeter of the ELLWF area. Therefore, as shown in Figure 4-182, the side slope of the final closure cap will intersect the ground surface 40 feet south of the ILV. As discussed below in Section 4.6.3.4, calculated infiltration rates through the HDPE geomembrane layer (which sits on top of the GCL labeled in Figure 4-182) are used as an upper boundary condition in the PORFLOW model. The geomembrane is the limiting barrier to infiltration in the closure cap design. The PORFLOW model includes a structural soil layer placed over the vault (referred to as the “foundation layer” in Figure 4-182) forming the slope and supporting the overlying closure cap. Infiltration through the geomembrane reaches the top surface of this soil layer which then forms the upper boundary of the model.

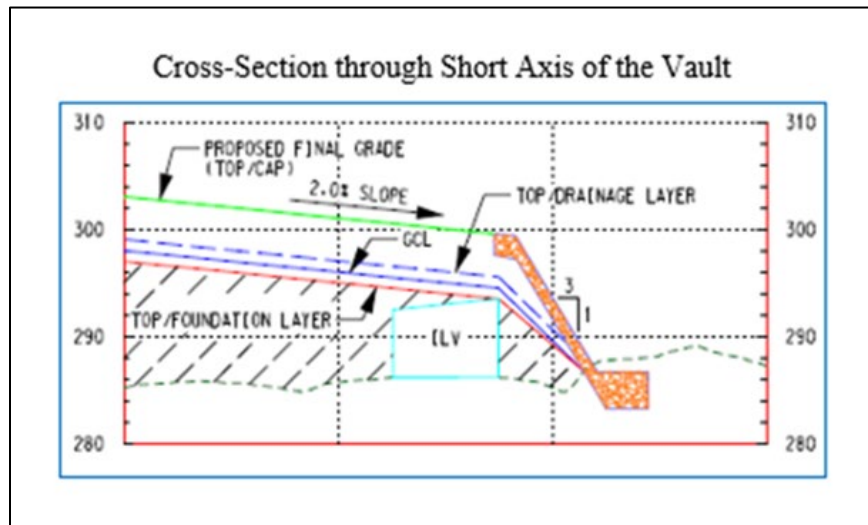


Figure 4-182. Detail of Intermediate-Level Vault Final Closure Cap Configuration (C-CT-E-00084, 2016)

Three 2-D models perpendicular to the long axis of the ILV facility are developed:

1. A model of the center ILNT cell (Cell #4) containing no TPBAR waste containers (Figure 4-183). The red region in the center of the vault is the region where waste material is disposed.
2. A model of a typical ILNT cell containing four TPBAR waste containers (Figure 4-184). The four TPBAR waste containers are in two stacks, with two waste containers in each stack, located 1 foot from the vault walls. Each stack is assumed to be 10 feet high.
3. A model of a typical ILNT cell containing eight TPBAR waste containers (Figure 4-185). The eight TPBAR waste containers are in four stacks, with two waste containers in each stack, located 1 foot from the vault walls.

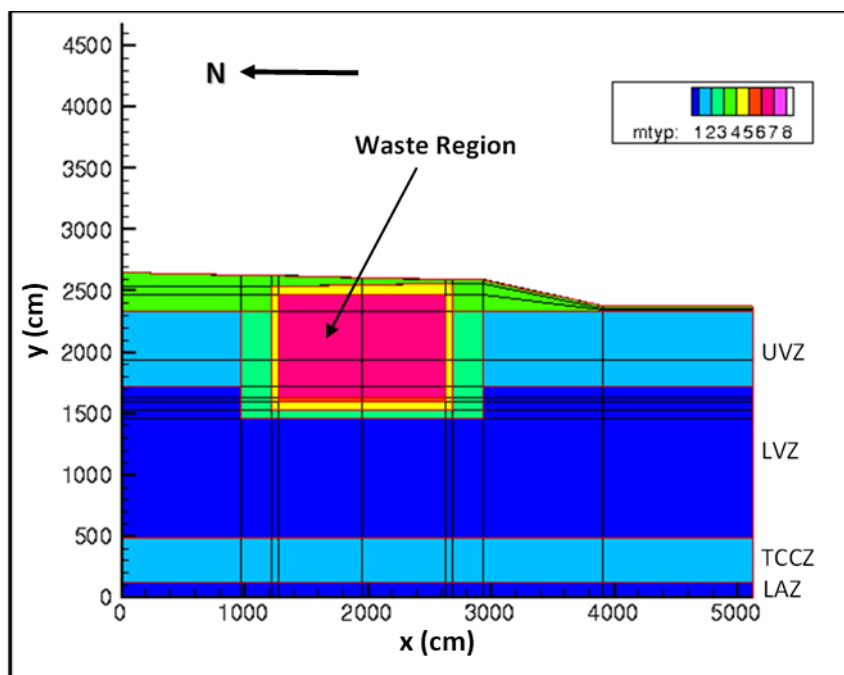


Figure 4-183. Center ILNT Cell Model with No TPBAR Waste Containers (Smith, 2021a; Figure 5-2)

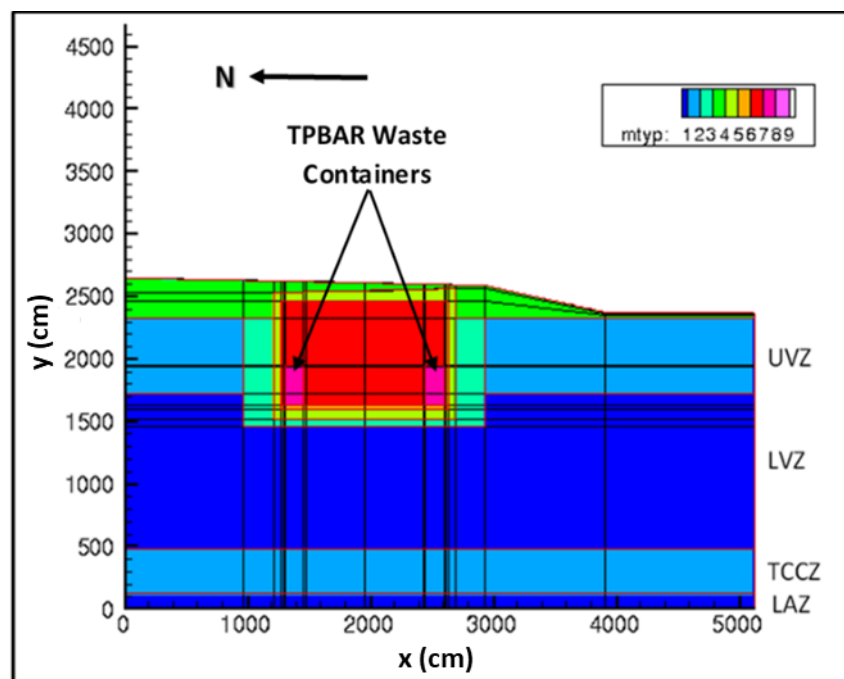


Figure 4-184. Typical ILNT Cell Model with Four TPBAR Waste Containers in Two Stacks of Two (Smith, 2021a; Figure 5-3)

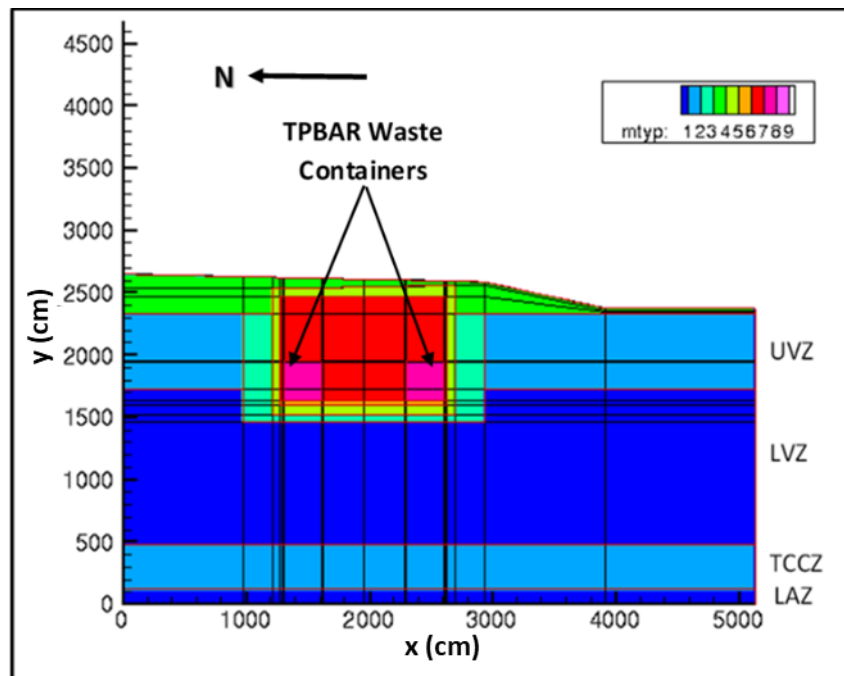


Figure 4-185. Typical ILNT Cell Model with Eight TPBAR Waste Containers in Four Stacks of Two (Smith, 2021a; Figure 5-4)

In Figure 4-183 through Figure 4-185, horizontal and vertical dimensions are given in centimeters; mtyp in legend is the material type number in PORFLOW. Therefore, the 5,136 cm horizontal dimension represents a model domain that is 168.5 feet in length. The vault is 48.5 feet (1,478 cm) wide with the computational grid extending 40 feet (1,219 cm) to the left of the vault (upslope – northern side of the closure cap) and 80 feet (2,438 cm) to the right (downslope - southern side). The additional 40 feet further south includes an area not under the closure cap to account for possible lateral flow into the VZ beneath the ILV from background infiltration. The ILV roof slopes about 2% from south to north while the closure cap slopes about 2% in the opposite direction. The model includes these sloped surfaces and, as can be seen by comparison with Figure 4-182, the model captures the closure cap 3:1 slope to ground level south of the ILV.

Figure 4-186 presents an enlarged view of the computational mesh immediately surrounding the ILV, highlighting the mesh detail and providing a better view of the vault concrete and surrounding soil. The same basic computational mesh is used for the three modeling cases with different mesh structure around TPBAR disposal containers and tritium release zones for each case.

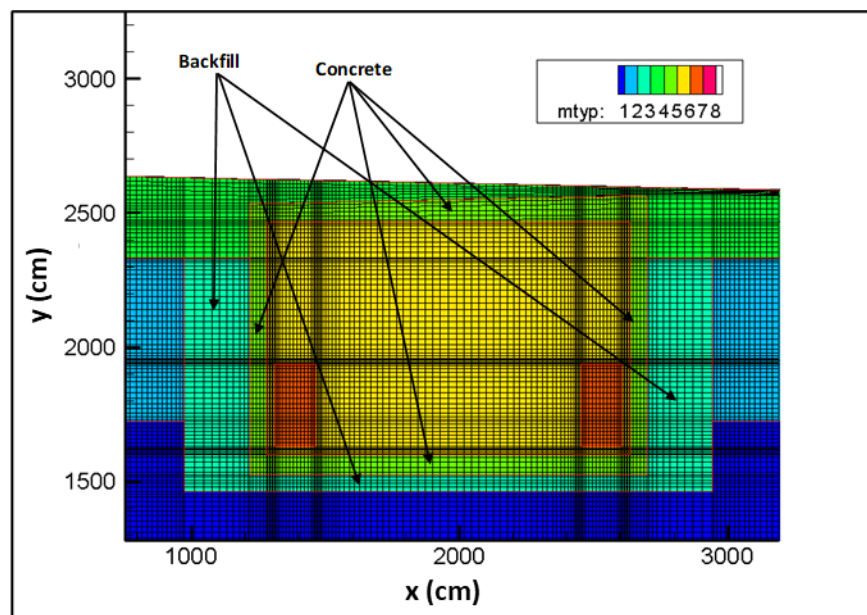


Figure 4-186. Computational Mesh around Intermediate-Level Vault in Typical ILNT Cell Model (Smith, 2021a; Figure 5-5)

The ILV was constructed on a controlled compacted soil base in an excavated region of the VZ to provide a foundation for the vault floor and sub-floor drainage system. Controlled compacted soil was then added as fill around the vault walls to ground surface for support of the vault walls and gantry crane runway along the sides of the vault. (Use of a gantry crane for waste disposal operations was ultimately abandoned in favor of a stick crane – see Figure 2-75). At final closure, controlled compacted soil will be built up across the entire ELLWF footprint as a foundation layer for the closure cap. As stated earlier, this foundation layer of the closure cap above and adjacent to the ILV serves as the top boundary of the PORFLOW model where infiltration is applied. The model assumes that the crane runway will be removed at site closure.

4.6.3.4. Infiltration Boundary Conditions

Infiltration rates through the ILV and surrounding area used in the PORFLOW model are listed in Table 4-61. During operations, the vault has a removable metal roof allowing access to the cells for waste disposal as can be seen in Figure 2-75. The metal roof prevents rainwater from entering the waste cells. It is assumed that the ILV will be filled by calendar year 2040 at which time the metal roof will be replaced with a permanent, sloped, reinforced-concrete roof slab with overlying bonded-in-place fiberboard insulation and a waterproof membrane (Dyer, 2019b). For modeling purposes, the permanent concrete roof is assumed to be in place throughout the ILV operating period and the function of the metal roof and rain cover are modeled by applying a very low infiltration rate (0.001 in yr^{-1}) during this time.

Table 4-61. Intermediate-Level Vault Infiltration Rates: HELP Model Infiltration with Closure Cap Intact until Year 5,770 (Smith, 2021a; Table 5-1)

Time Step	Numerical Calendar Date	Time from Start of ILV Operation	ILV Event	On-Vault Infiltration (in yr ⁻¹)	Off-Vault ¹ Infiltration (in yr ⁻¹)
1	1995.74	0.0	Start of ILV Operations	0.00010	15.78
	2040.74	45.0	ILV Closed		
	2065.74	70.0	Start of IC		
	2165.74	170.0	End of IC, Closure Cap Installed, Start of Compliance Period	0.00015	0.00015
2	500-Year Period of Concrete Degradation	220.0		0.00062	0.00062
3		270.0		0.00437	0.00437
4		320.0		0.01305	0.01305
5		370.0		0.022	0.022
6		420.0		0.085	0.085
7		470.0		0.162	0.162
8		520.0		0.317	0.317
9		570.0		0.496	0.496
10		620.0		0.709	0.709
11		670.0	Vault Hydraulic Failure ²	0.923	0.923
12	2725.74	720.0		1.137	1.137
13		770.0		1.424	1.424
14		820.0		1.728	1.728
15		870.0		2.033	2.033
16		920.0		2.337	2.337
17		970.0		2.642	2.642
18		1,020.0		2.946	2.946
19		1,070.0		3.251	3.251
20		1,120.0		3.555	3.555
21	3165.74	1,170.0	End of Compliance Period	3.860	3.860
22		1,320.0		4.764	4.764
23		1,470.0		5.668	5.668
24		1,620.0		6.571	6.571
25		1,770.0		7.475	7.475
26		1,920.0		8.379	8.379
27		2,070.0		8.913	8.913
28		2,220.0		9.263	9.263
29		2,370.0		9.613	9.613
30		2,520.0		9.963	9.963
31		2,670.0		10.313	10.313
32		2,820.0		10.606	10.606
33		3,370.0		10.710	10.710
34		5,770.0		10.890	10.890
35		5,770.1	Vault Roof Collapses, Closure Cap Over ILV Fails	36.85 ³	10.94
	12,165.74	50,000	End of Simulation	36.85	10.94

Notes:

¹ Infiltration on either side of vault.² Vault concrete fails hydraulically; closure cap remains intact.³ Following vault roof collapse, flow through the ILV increases due to closure cap runoff.

This sloped, permanent, reinforced-concrete roof with overlying waterproof membrane will remain uncovered during the remaining ELLWF operational period (calendar years 2040 to 2065) and the following 100 years of IC (calendar years 2065 to 2165). There will essentially be no water infiltration into the vault during this time for the following reasons:

- A 2% roof slope and overlying waterproof membrane shed rainwater over the vault.
- The initial intact condition of the ILV roof will be maintained during the remaining operations period after the ILV is closed as well as during the subsequent 100-year IC period.
- Absence of a soil cover during this period prevents buildup of soil moisture above the roof.

Thus, for modeling purposes, a small infiltration rate equal to 0.001 in yr^{-1} is assumed to apply for the first 170 years of the simulation.

At the end of IC, a final soil-geomembrane closure cap will be placed over the entire ELLWF. Infiltration rates above the ILV and the surrounding area beneath the cover were calculated using the HELP model (Dyer, 2019b) starting at the time of final closure cap placement (Year 100 in infiltration model) for a period of 7,000 years, when Dyer (2019b) assumed the vault roof would collapse (Year 7,100 in infiltration model). Beyond Year 7,100, infiltration rates are assumed to remain constant. For the PORFLOW model of the ILV, a decision was initially made to use the median time to roof collapse from a seismic event (6,250 years) instead of the mean time to roof collapse (6,703 years; rounded to 7,000 years). The selection of the median value is pessimistically bounding from an infiltration rate perspective. However, to align with the timing of the HELP model simulation cases and to remain pessimistically bounding, the PORFLOW model assumes that ILV roof collapse will actually occur in Year 5,770. That is, infiltration rates through the final closure cap calculated using the HELP model are used for the first 5,770 years of the PORFLOW ILV model simulation. Beyond Year 5,770, a constant infiltration rate following roof collapse is applied as calculated by the HELP model (Dyer, 2019b).

For 500 years following the end of IC, the PORFLOW ILV model degrades the concrete hydraulic properties. Then at 500 years, the model assumes that the concrete behaves hydraulically like soil. The model adjusts concrete properties in 50-year time steps by blending the hydraulic properties for concrete with those of OSC1. Because these steps do not directly coincide with the HELP model time steps, the infiltration cases reported by Dyer (2019b) are linearly interpolated to follow the 50-year incremental changes in material properties. Subsequently, it was decided to further refine the flow solution by adding more time steps interpolated from the HELP calculations. The results of this interpolation are shown in Table 4-61. The green-shaded area from Years 170 to 670 is the time when concrete degradation occurs. Flows in Table 4-61 are shown as follows:

- The infiltration rate from Years 0 to 170 is $0.00010 \text{ in yr}^{-1}$
- At Year 170, the infiltration rate changes to $0.00015 \text{ in yr}^{-1}$
- Thereafter, infiltration rates at the beginning of the indicated time period are shown. For example, infiltration changes from $0.00015 \text{ in yr}^{-1}$ to $0.00062 \text{ in yr}^{-1}$ at Year 220.

- PORFLOW input processing takes the average of the starting and ending infiltration rates as the steady-state flow for the time period.

Table 4-61 also highlights that, after the final closure cap is in place, infiltration over the vault (“on-vault” infiltration) and the 40-foot capped regions on either side of the vault (“off-vault” infiltration), are identical until the vault roof collapses at Year 5,770. Following roof collapse, infiltration through the ILV is greater than the background value because the gap (collapsed portion) in the closure cap collects runoff and drainage from the upslope intact portion of the closure cap. Infiltration through areas not under the closure cap is assumed to equal the background rate of 15.78 in yr⁻¹ (40 cm yr⁻¹).

4.6.3.5. Concrete Degradation

The property blending method used to calculate hydraulic properties for concrete mixed with soil for the ILV is identical to the method detailed for the LAWV in Section 4.5.3.6. As for the LAWV, the ILV model uses a blend of concrete and soil to determine hydraulic properties in 50-year increments over the assumed 500-year lifetime of the ILV concrete. At site closure, structural analysis of the ILV (Peregoy, 2006b) predicts that the ILV roof and walls will experience limited non-through static cracking upon application of the final closure cap over the vault. Upon final closure, initial hydraulic properties for vault roof and wall concrete are taken to be a blend of 90% E-Area Vault Concrete and 10% Gravel to represent the impact of early stress cracking in the concrete. Soil blended with the concrete is represented by the hydraulic properties of OSC1 as recommended by Nichols and Butcher (2020). Table 4-62 provides a list of the material blends used to represent concrete degradation following site closure.

Table 4-62. Material Blends for Degraded Concrete (Smith, 2021a; Table 5-2)

Years Post Closure	ILV Roof and Walls		ILV Floor	
	90% Concrete 10% Gravel	Soil	E-Area Concrete	Soil
0	100%	0%	100%	0%
50	90%	10%	90%	10%
100	80%	20%	80%	20%
150	70%	30%	70%	30%
200	60%	40%	60%	40%
250	50%	50%	50%	50%
300	40%	60%	40%	60%
350	30%	70%	30%	70%
400	20%	80%	20%	80%
450	10%	90%	10%	90%
500	0%	100%	0%	100%

Figure 4-151 and Figure 4-152 display the hydraulic conductivity and water saturation curves obtained by blending a mixture of 90% E-Area Vault Concrete and 10% Gravel with OSC1, respectively. The mixture of 90% concrete with 10% gravel is used to model cracked concrete. Blending this mixture with soil is then used to model degradation of the cracked concrete.

4.6.3.6. TPBAR Tritium and Argon Releases

Tritium and Ar-39 are the only radionuclides released from the SWF TPBAR disposal containers within the ILV VZ model (Gorensek, 2021). All other radionuclides are considered to be contained within the disposal containers.

For tritium in PA2008, the 17 TPBAR disposal containers expected to be sent to the ILV were assumed to be buried simultaneously at the end of operations (expected to occur in 2025 at that time). Further, the containers were assumed to be placed within ILV cells in two stacks of two containers each, near the outer walls, as shown in Figure 4-184. PA2008 and a related SA (Hiergesell, 2005) used an unclassified tritium release rate calculated by Pacific Northwest National Laboratory (Lanning and Gilbert, 2005). The release rate for a single disposal container is provided by Hiergesell (2005). The single container release rate is multiplied by the number of containers that will be disposed in the ILV, and the total calculated release rate is used as a source term in the PORFLOW model. The release is modeled as occurring directly into a “halo” region surrounding the disposal containers.

For PA2022, Gorensek (2021) recalculated the expected release of tritium from TPBAR disposal containers. The approach taken by Gorensek (2021)⁸ is based on the one developed by Lanning and Gilbert (2005). Lanning and Gilbert (2005) posited that the rate of tritium release from the TPBARs to the ILV environment is controlled by (1) the rate at which hydrogen is generated from corrosion of steel surfaces by moisture trapped inside the disposal containers and (2) the rate at which the hydrogen thus generated permeates the container walls. Gorensek (2021) adds one additional release path: a hypothetical leak at a rate equivalent to the maximum allowable leak rate ($1.0\text{E-}04 \text{ std. cm}^3 \text{ s}^{-1}$) between the interior and exterior of the disposal containers as set by the containers’ procurement specification (Snider, 2007). As a result, the computed tritium release rates are pessimistically bounding (permeation plus maximum allowable leak rate).

SWM currently expects to place 28 TPBAR disposal containers in the ILV. The current TPBAR modeling follows the PA2008 approach of releasing the tritium into a 6-inch region around each stack of disposal containers. The release region is above and on either side of the stacks. The stacks are placed 1 foot from the wall and the region surrounding the stacks, including the tritium release zone, are located within the cell waste zone. The updated calculation revised the PA2008 approach by timing tritium release to follow the expected TPBAR disposal schedule shown in Table 4-63

⁸ The analysis by Gorensek (2021) is based on an earlier source term analysis (Lanning and Gilbert, 2005), which treated the bulk of the tritium residual as tightly bound by the TPBAR getter material and only a small fraction existing as tritiated moisture in the lithium aluminate ceramic pellets. Together with atmospheric moisture trapped in the free volume, the tritiated water vapor is assumed to corrode steel surfaces inside the disposal container, covering them with a magnetite film while generating hydrogen. The carbon steel walls of the disposal container are permeable to hydrogen, providing a pathway for tritium to escape containment. The rate of hydrogen generation is assumed to be limited by the rate of corrosion, which is assumed to be governed by parabolic reaction kinetics obtained from the literature. This relies on the further assumption that the water vapor consumed by the corrosion reaction is continually replaced by moisture from the lithium aluminate pellets until all of that moisture is gone. In addition to tritium permeation, the analysis also includes a slow leak through the disposal container walls at the maximum allowable leak rate, 1×10^{-4} standard $\text{cm}^3 \text{ s}^{-1}$.

and using the SRNL release rate. The new ILV VZ model for PA2022 further assumes that the first 12 TPBAR disposal containers will be placed in three ILV cells with four containers per cell, while the last 16 TPBAR disposal containers will be placed in two ILV cells with eight containers per cell. The latter disposal configuration is shown in Figure 4-185.

Table 4-63. Schedule for Dispositioning TPBAR Disposal Containers (Smith, 2021a; Table 6-4)

Calendar Year	Number of TPBAR Disposal Containers	Calendar Year	Number of TPBAR Disposal Containers	Calendar Year	Number of TPBAR Disposal Containers
2009	1	2023	2	2029	2
2015	1	2024	1	2030	1
2017	1	2025	1	2031	2
2020	2	2026	2	2032	2
2021	1	2027	2	2033	2
2022	1	2028	2	2034	2

To assist in eliminating the potential need for a new ILV, the projected loading schedule provided in Table 4-63 can be increased from a total of 28 to a total of 36 TPBAR disposal containers as mentioned in Section 8.3.4.3. The eight additional containers are accommodated by replacing two sets of four containers per ILV cell with eight containers per ILV cell.

The SRNL analysis (Gorensek, 2021) considered four cases:

1. One-year-old TPBAR disposal containers, eight per ILV cell
2. Five-year-old TPBAR disposal containers, eight per ILV cell
3. One-year-old TPBAR disposal containers, four per ILV cell
4. Five-year-old TPBAR disposal containers, four per ILV cell

SRNL Case 1 and SRNL Case 3, which released the most total tritium (6,507 Ci and 3,279 Ci, respectively), are modeled in PA2022. Figure 4-187 compares tritium flux to the water table from PA2008 (H-3_TPBAR_PA) to the new ILV VZ model predictions (SRNL Case 1: H-3_TPBAR_8; SRNL Case 3: H-3_TPBAR_4; Sum of Cases 1 and 3: H-3_TPBAR_Sum). Time zero in Figure 4-187 is calendar year 1995, which is the approximate start date for ILV operations. The total peak flux to the water table in the new ILV VZ model (H-3_TPBAR_Sum) is approximately 82% of the PA2008 value (H-3_TPBAR_PA). Even though PA2022 modeling assumes 28 disposal containers instead of 17, the combination of a more realistic disposal schedule, which spreads the release over time, and a revised estimate of tritium release generated a slightly lower peak flux. As a result, TPBAR disposal limits are expected to remain approximately the same in PA2022.

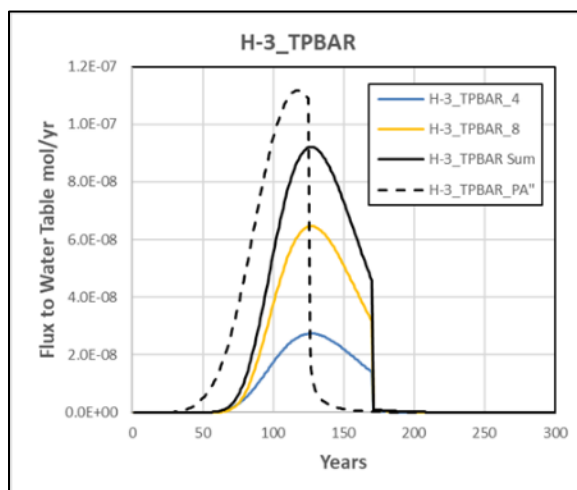


Figure 4-187. Tritium Flux to the Water Table from TPBAR Disposal Containers [2008 E-Area Low-Level Waste Facility Performance Assessment: H-3_TPBAR_PA; SRNL Case 1: H-3_TPBAR_8; SRNL Case 3: H-3_TPBAR_4; Sum of Cases 1 and 3: H-3_TPBAR_Sum] (Smith, 2021a; Figure 6-18)

Release of Ar-39 from the TPBAR containers was not considered in PA2008 but is included in PA2022. As a pessimistically bounding approach, Gorensek (2021) calculates a release rate assuming that 1 Ci of Ar-39 instantaneously enters the void volume of a TPBAR cask at the time of disposal. The Ar-39 is subsequently released from the cask into the ILV waste zone at the maximum allowed container leak rate of $1.0\text{E-}04 \text{ std. cm}^3 \text{ s}^{-1}$ (Gorensek, 2021). As will be shown in Section 5.3.1.5, scoping analyses indicate that the generic waste form inventory limits for Ar-39 are even more pessimistically bounding with respect to its release from the SWF TPBAR disposal containers (Smith, 2021a).

4.6.3.7. Preliminary Model Results for Vadose Zone Flow

The PORFLOW model is used to calculate a steady-state flow field for each of the 35 time-intervals listed in Table 4-61. Results obtained include infiltration water flow, water saturation in materials, and suction pressure throughout the three computational domains shown in Figure 4-183 through Figure 4-185. In addition, PORFLOW provides information on the deviation of saturation from the water retention curves as well as convergence of the flow calculations. To simplify data presentation, the ILV model assuming four TPBAR waste containers (Figure 4-184) is chosen as the nominal case. To simplify figure captions, the terminology “waste containers” is omitted and “4 TPBAR ILV Model” is used to identify the case. Flow patterns obtained with the other two PORFLOW models (Figure 4-183 and Figure 4-185) are very similar to those shown for the 4 TPBAR ILV Model below. Results reported by Smith (2021a) for the steady-state flow fields based on the Darcy velocity during each simulation time period are shown in Figure 4-188 through Figure 4-196. Corresponding infiltration flows are listed in Table 4-61. Including results for all 35 time-intervals is considered excessive; therefore, only the 18 results at odd number time intervals are shown. Results for water saturation and pressure are reported by Smith (2021a; Appendices A and B, respectively).

Figure 4-188 displays the flow field from the start of ILV operations until the end of IC and 50 to 100 years following closure cap installation. As seen in Figure 2-72, during ILV operations, a temporary metal roof with a rain cover is in place over each cell to allow access for waste disposal. At the end of operations, the metal covers will be removed and replaced with a permanent concrete roof covered by a waterproof membrane. During these early periods, it is assumed that the metal rain covers over each cell and the waterproof membrane covering the concrete roof are actively maintained and infiltration into the vault is nearly zero (0.001 in yr^{-1}). As described in Section 4.6.3.3, the PORFLOW 2-D model domain extends 40 feet north (upslope) of the vault and 80 feet south of the vault (the south side includes 40 feet from the ILV wall to the edge of the cap, plus an additional 40 feet of uncovered soil beyond the edge). Figure 4-188 shows that before the final closure cap is placed (Figure 4-188 left), flow through the vault is essentially zero and some of the water infiltration beside the vault is diverted underneath the ILV. After the final closure cap is placed in Year 170, Figure 4-188 (right) shows that the infiltration rate through the newly installed cap is very low but some infiltration flow from the uncovered region to the right of the ILV encroaches below the vault.

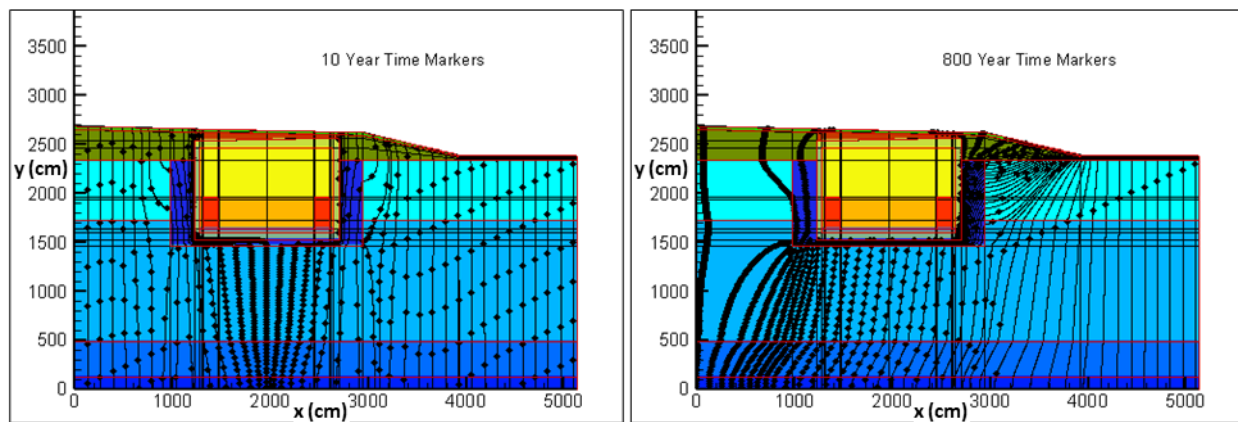


Figure 4-188. Flow Field in 4 TPBAR Intermediate-Level Vault Model: (left) Years (0 – 170) and (right) Years (220 – 270) (Smith, 2021a; Figure 6-1)

The hydraulic performance of both the closure cap and the vault concrete begins to deteriorate starting at Year 170. The predicted flow fields from 150 to 200 years following site closure (Years 320 to 370) and 250 to 300 years following site closure (Years 420 to 470) are shown in Figure 4-189. During this time, the closure cap performs well, the concrete remains relatively intact, and infiltration through the vault itself remains low. Time markers in Figure 4-189 are placed at 300-year (left) and 100-year (right) intervals; therefore, while the two flow fields indicate channeling of water to the sides and below the ILV, the actual flow near the vault is low.

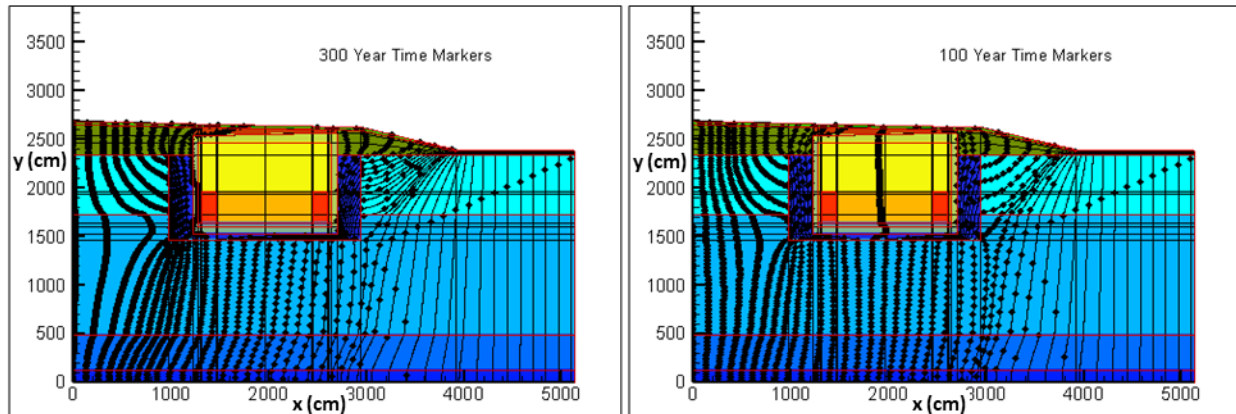


Figure 4-189. Flow Field in 4 TPBAR Intermediate-Level Vault Model: (left) Years (320 – 370) and (right) Years (420 – 470) (Smith, 2021a; Figure 6-2)

Figure 4-190 shows water infiltration from 350 to 400 years after closure cap installation (Years 520 to 570) and from 450 to 500 years after closure cap installation (Years 620 to 670). The 500-year period from Years 170 to 670 is when degradation of the vault concrete is modeled (Section 4.6.3.5). Progressive deterioration in hydraulic performance of the closure cap and vault concrete during this period is evident. In fact, comparison with Figure 4-188 shows a significant change with noticeable flow through the ILV. However, as the 100-year (left) and 50-year (right) time markers indicate, the flow rate is still relatively low. The vault concrete is assumed to completely fail hydraulically at Year 670 when it takes on the hydraulic properties of OSC1 (clayey soil). Further increases in infiltration through the vault are caused by deterioration of the HDPE geomembrane/GCL composite barrier in the final closure cap.

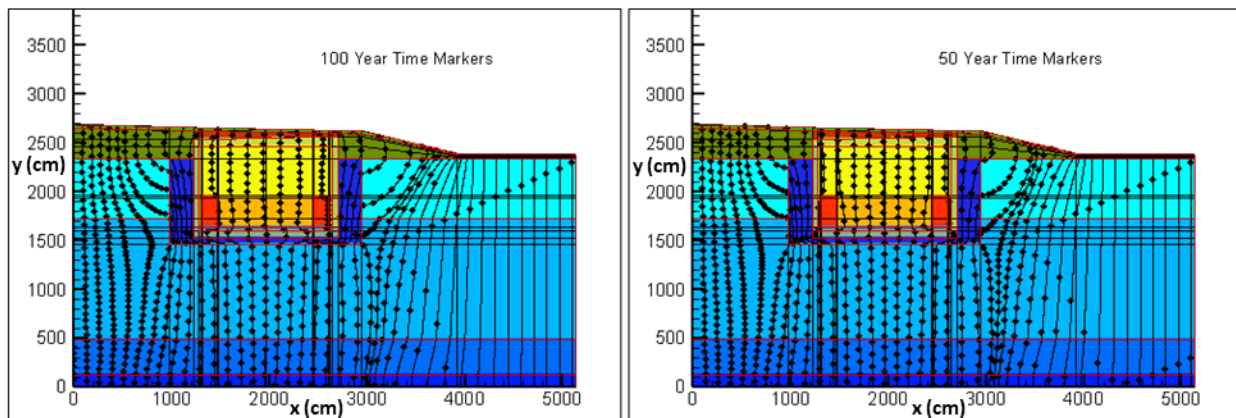


Figure 4-190. Flow Field in 4 TPBAR Intermediate-Level Vault Model: (left) Years (520 – 570) and (right) Years (620 – 670) (Smith, 2021a; Figure 6-3)

Figure 4-191, Figure 4-192, and Figure 4-193 display infiltration flow fields from Years 720 to 1,470. Progressive deterioration in the hydraulic performance of the closure cap is evident in all three figures. Note that spacing between the time markers decreases from 40 years to 20 years in this sequence, which indicates increased flow. It is notable that flow through the ILV becomes quite uniform following concrete degradation. As intended, there is zero flow through the TPBAR

disposal containers at all time intervals. The 1,000-year period of performance ends at Year 1,170; therefore, results beyond Figure 4-193 will have no impact on disposal limits.

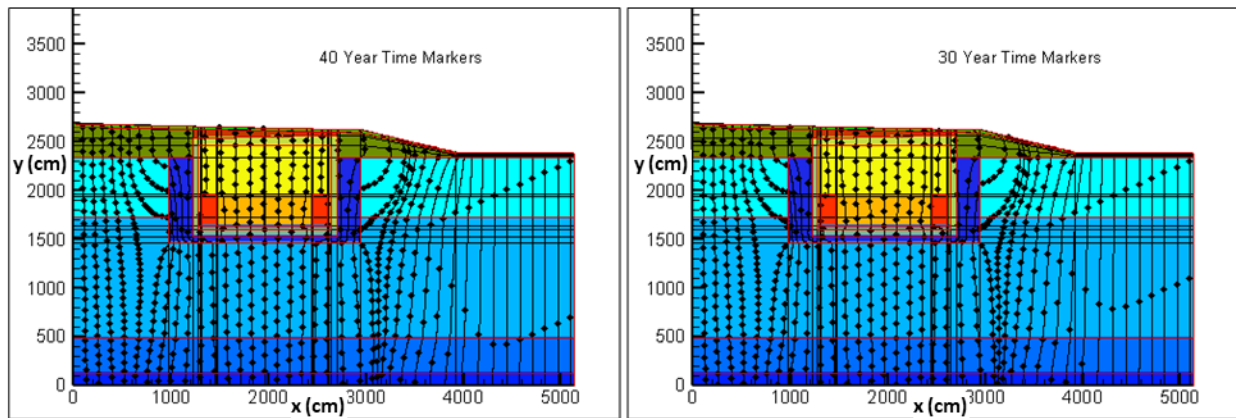


Figure 4-191. Flow Field in 4 TPBAR Intermediate-Level Vault Model: (left) Years (720 – 770) and (right) Years (820 – 870) (Smith, 2021a; Figure 6-4)

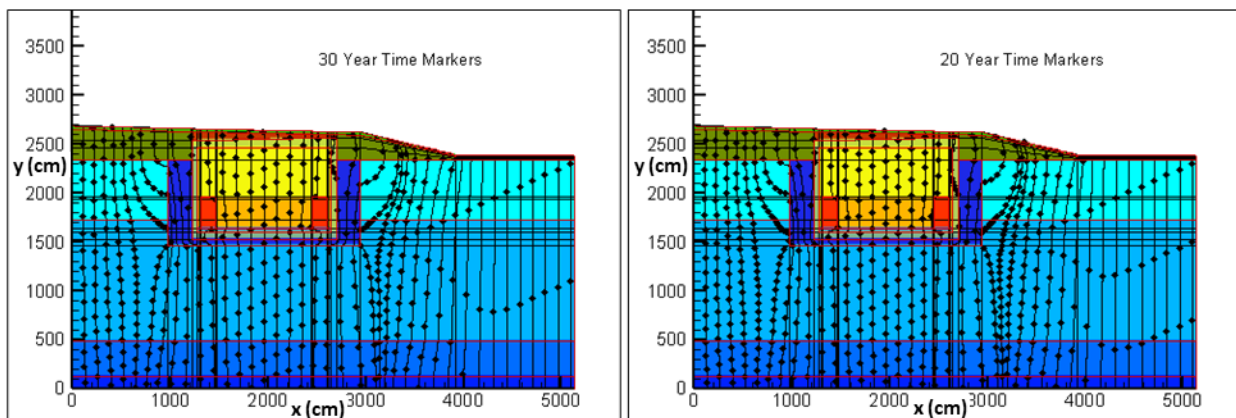


Figure 4-192. Flow Field in 4 TPBAR Intermediate-Level Vault Model: (left) Years (920 – 970) and (right) Years (1,020 – 1,070) (Smith, 2021a; Figure 6-5)

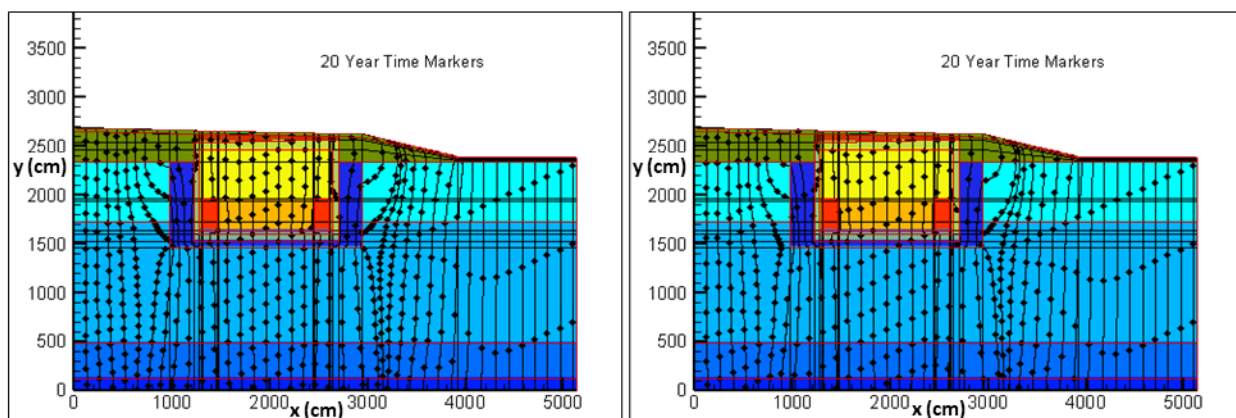


Figure 4-193. Flow Field in 4 TPBAR Intermediate-Level Vault Model: (left) Years (1,120 – 1,170) and (right) Years (1,320 – 1,470) (Smith, 2021a; Figure 6-6)

Figure 4-194, Figure 4-195, and Figure 4-196 highlight the flow fields for the years following the period of performance. Infiltration increases as degradation of the HDPE geomembrane/GCL composite barrier continues. After Year 1,770, infiltration increases enough that 10-year markers are used to better illustrate the flow pattern. As shown in Table 4-61, between Years 1,970 and 5,770, the infiltration rate does not change significantly. At Year 5,770, the ILV roof is assumed to collapse, increasing flow through the vault region as runoff from the upslope intact closure cap enters the subsided area created by the roof collapse. Beyond Year 5,770, this flow pattern is assumed to remain unchanged. The final ILV VZ flow field is displayed on the right-hand side of Figure 4-196 where high flow through the vault area is evident.

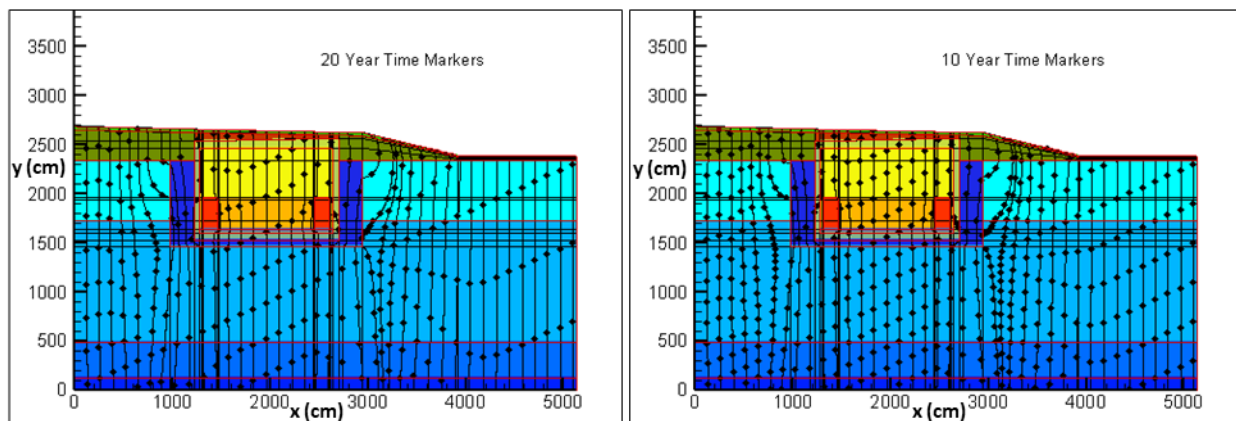


Figure 4-194. Flow Field in 4 TPBAR Intermediate-Level Vault Model: (left) Years (1,620 – 1,770) and (right) Years (1,920 – 2,070) (Smith, 2021a; Figure 6-7)

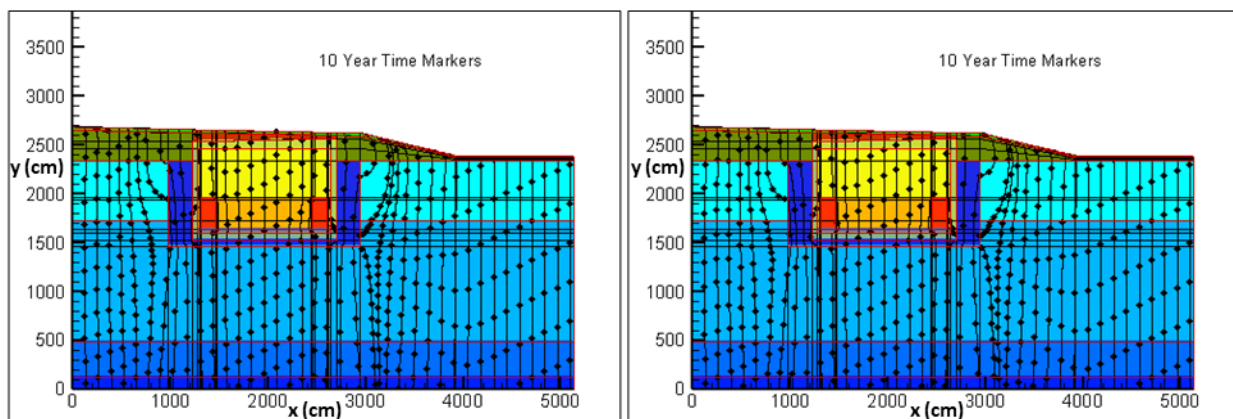


Figure 4-195. Flow Field in 4 TPBAR Intermediate-Level Vault Model: (left) Years (2,220 – 2,370) and (right) Years (2,520 – 2,670) (Smith, 2021a; Figure 6-8)

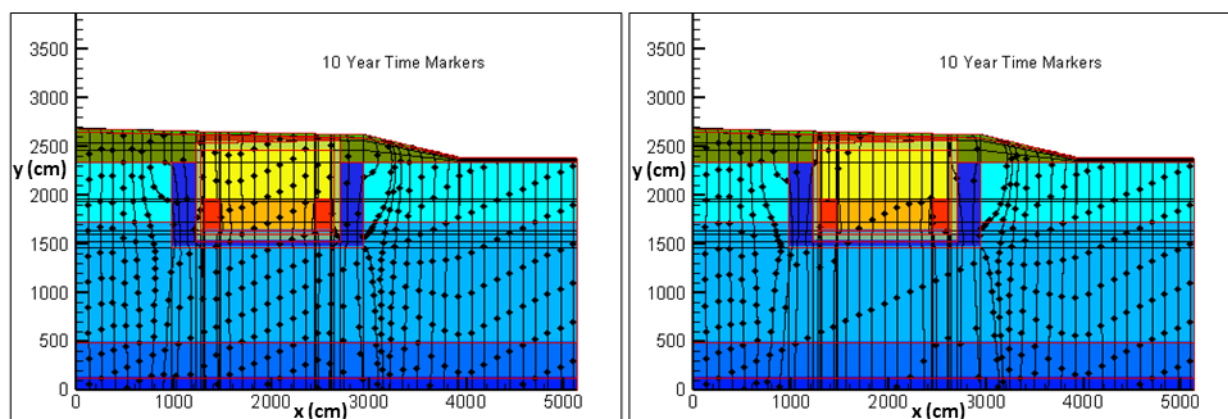


Figure 4-196. Flow Field in 4 TPBAR Intermediate-Level Vault Model: (left) Years (2,820 – 3,370) and (right) Year 5,770 (Smith, 2021a; Figure 6-9)

4.6.3.8. Preliminary Model Results for Radionuclide Vadose Zone Transport

Transport calculations are made using the PORFLOW ILV model for the following parent radionuclides (and daughters): H-3, C-14, Cl-36, I-129, Ra-226 (Pb-210), and U-234 (Th-230, Ra-226, Pb-210). These ten radionuclides are selected because they provide a significant dose and have relatively small disposal limits in PA2008. I-129 is a quite useful radionuclide to include to test transport behavior because it has both a long half-life and small K_d . This combination of properties ensures that the I-129 peak will be observed and that the area under the peak should equal the amount initially deposited.

One mole (mol) of each parent radionuclide is distributed uniformly in the waste zone, and the resulting flux to the water table (gmol yr^{-1} per gmole of parent radionuclide) is calculated over a 50,000-year period. The parent radionuclide is introduced at the start of ILV operations. Fluxes calculated with all three ILV models are quite similar; therefore, the conceptual model assuming four TPBAR disposal containers is again chosen as the nominal case to illustrate the transport calculations. Because of the impermeable nature of TPBAR containers, they are represented in the model as no-flow zones with flow moving around the computational mesh assigned to the containers (about 8.3% of the ILV interior space). At Year 5,770 when the ILV roof is assumed to collapse, the existing waste inventory is relocated to the lower 10 feet of the waste zone. This is intended to mimic the consolidation of waste containers within the collapsed vault.

4.6.3.8.1. K_d Values

K_d values are obtained from the *GeoChem Data Package* (SRNL, 2018) by Kaplan (2016b). As specified in Table 4-57, reducing cement K_d values are assigned to ILV slag-based concrete vault and oxidizing cement K_d values are assigned to the waste zone due to the intimate contact between encapsulating grout or CLSM and the waste containers. Table 4-57 also recommends using K_d values impacted by cementitious leachate in the upper and lower VZ soils. However, it has been decided that a more realistic application of cementitious leachate K_d values is in the ILV controlled compacted soil backfill region which is in immediate contact with vault concrete (see Figure 4-186). The PA2008 model did not use cementitious-leachate-impacted K_d values for the

VZ soil; therefore, the approach taken for the current PORFLOW ILV model is a compromise between the two approaches.

4.6.3.8.2. Concrete Aging

The conceptual model for concrete aging and its associated impact on K_d values for the ILV VZ transport model are identical to the methodology presented in Section 4.5.3.8.2 for the LA WV. For the ILV roof and floor and the waste zone, the average vertical velocity during each flow period (Table 4-61) is used to calculate the number of PV exchanges, while for the ILV walls, the average horizontal velocity is employed. Table 4-64 provides the resulting times when concrete stage changes occur for the nominal case. The concrete is aged to the next stage at the beginning of the time step when the number of exchange cycles is reached. Note that the vault concrete and waste zone remained in Stage I throughout the 1,000-year post-closure period of performance (Years 170 to 1,170) except for the vault roof and floor concrete which moved to Stage II 970 years after final closure (Year 1,140).

Table 4-64. Estimated Intermediate-Level Vault Concrete Aging Times in Years after Final Closure (Smith, 2021a; Table 6-1)

Stage Transition	Concrete Aging Times (years after final closure)				
	Roof	Floor	North Wall	South Wall	Waste
Stage I to II	970	970	2,070	2,070	2,220
Stage II to III	1,920	2,070	5,770	5,770	5,770
Stage III - Soil	5,770	5,770	5,770	5,770	5,770

The aging times listed in Table 4-64 are in reasonably good agreement with the aging times used in PA2008. PA2008 aged all ILV concrete from Stage I to Stage II after 1,600 years and from Stage II to Stage III after 3,800 years. PA2008 aged the cementitious waste zone from Stage I to Stage II after 1,900 years and from Stage II to Stage III after 3,800 years.

4.6.3.8.3. Radionuclide Flux to Water Table

Graphs of flux to the water table (gmol yr^{-1} per gmole of parent radionuclide) for the radionuclides included in this preliminary ILV VZ model evaluation are shown in Figure 4-197, Figure 4-198, Figure 4-199, and Figure 4-200.

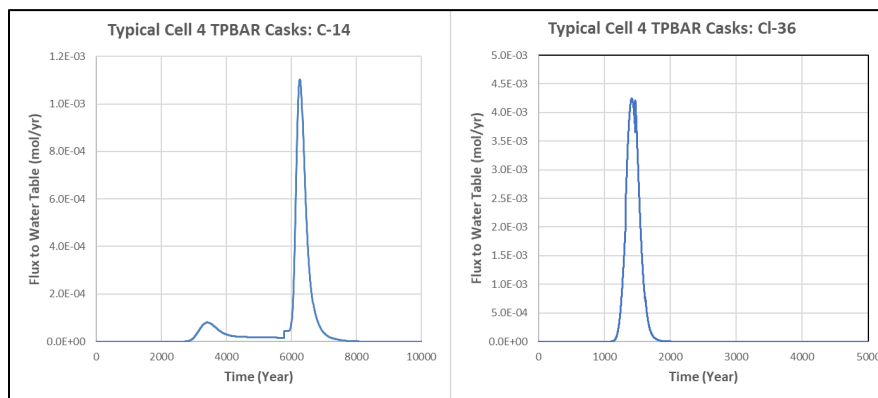


Figure 4-197. C-14 and Cl-36 Fluxes to the Water Table (gmol yr^{-1} per gmole of parent) for Intermediate-Level Vault Cell with Four TPBAR Casks (Smith, 2021a; Figure 6-10)

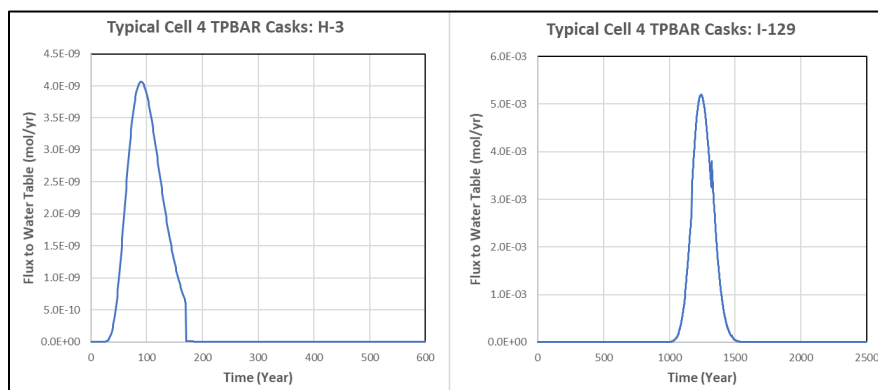


Figure 4-198. H-3 and I-129 Fluxes to the Water Table (gmol yr^{-1} per gmole of parent) for Intermediate-Level Vault Cell with Four TPBAR Casks (Smith, 2021a; Figure 6-11)

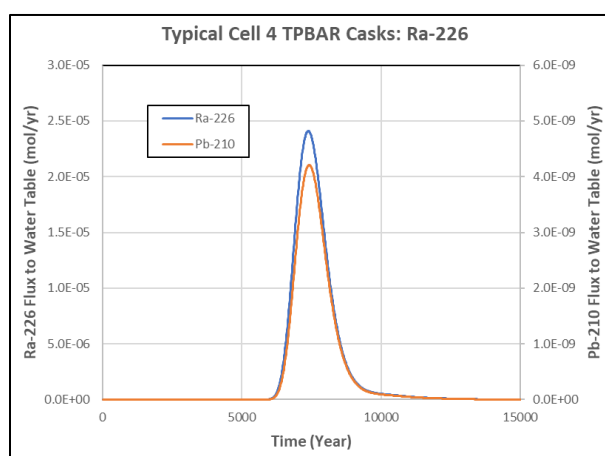


Figure 4-199. Ra-226 and Daughter Pb-210 Fluxes to the Water Table (gmol yr^{-1} per gmole of parent) for Intermediate-Level Vault Cell with Four TPBAR Casks (Smith, 2021a; Figure 6-12)

Figure 4-200 shows U-234 and its daughters on both a linear and a semi-log scale to include Pb-210. The flux results in Figure 4-197 through Figure 4-200 are for transport from an ILV cell with four TPBAR disposal containers. Table 4-65 reports the maximum flux to the water table and the time to maximum for all radionuclides in the three ILV cell configurations. In general, the maximum flux and timing of the maximum are very close for the three different configurations. Concentration profiles showing C-14 transport through the ILV VZ at 12 simulation times between 100 and 9,900 years are presented by Smith (2021a; Appendix C).

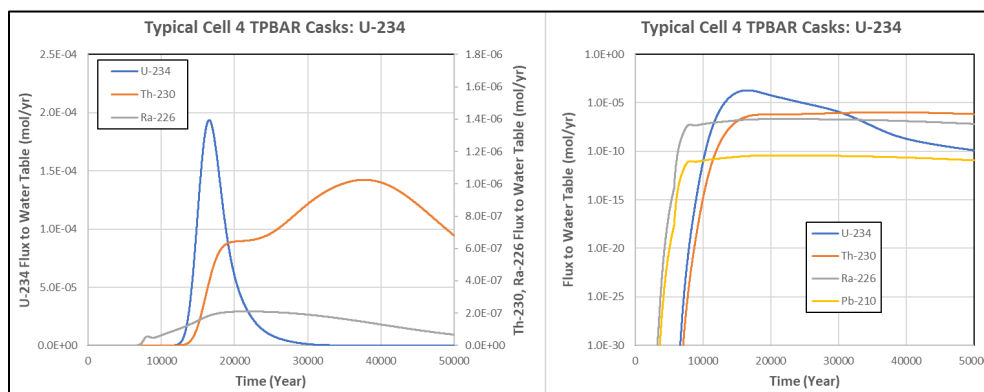


Figure 4-200. U-234 and Daughters Th-230, Ra-226, and Pb-210 Fluxes to the Water Table (gmol yr^{-1} per gmole of parent) for Intermediate-Level Vault Cell with Four TPBAR Casks (Smith, 2021a; Figure 6-13)

Table 4-65. Maximum Flux to Water Table and Time of Maximum Flux for Three Intermediate-Level Vault Configurations (Smith, 2021a; Table 6-2)

Radionuclide	Center Cell		4 TPBAR		8 TPBAR	
	Maximum Flux (gmol yr^{-1} per gmole parent)	Year	Maximum Flux (gmol yr^{-1} per gmole parent)	Year	Maximum Flux (gmol yr^{-1} per gmole parent)	Year
C-14	1.02E-03	6,260	1.11E-03	6,260	1.20E-03	6,240
Cl-36	4.15E-03	1,407	4.25E-03	1,415	4.30E-03	1,471
H-3	4.79E-09	88	4.06E-09	90	4.53E-09	90
I-129	5.07E-03	1,237	5.19E-03	1,241	5.31E-03	1,243
Ra-226	2.48E-05	7,410	2.41E-05	7,390	2.22E-05	7,210
Pb-210	4.32E-09	7,440	4.21E-09	7,420	3.88E-09	7,240
U-234	1.83E-04	16,680	1.94E-04	16,530	2.01E-04	15,890
Th-230	1.03E-06	38,500	1.02E-06	37,690	9.96E-07	35,680
Ra-226	2.10E-07	21,920	2.10E-07	21,620	2.05E-07	22,410
Pb-210	3.67E-11	21,950	3.68E-11	21,660	3.59E-11	22,450

Notes:

Parent radionuclides in bold text; progeny in unbolded text

4.6.3.9. Differences in Methods Employed and Parameter Assumptions: 2022 versus 2008 E-Area Low-Level Waste Facility Performance Assessment

The PORFLOW model of the ILV VZ developed and tested for this PA is geometrically similar to the model used in PA2008. Improvements to the PA2008 model include:

- Refined computational mesh encompassing a larger area
- Novel method to estimate degradation of concrete hydraulic properties
- Addition of the soil backfill cover over the ILV
- Revised VZ structure
- Revised infiltration rates
- Updated material properties
- Updated partition coefficients for radionuclides
- Updated schedule for disposition of TPBAR disposal containers and tritium release

For TPBAR transport, tritium release is based on the proposed disposal schedule instead of assuming simultaneous disposal of all TPBAR inventory. While all preliminary radionuclide transport calculations using the revised model are reasonable, hydraulic degradation of the vault concrete, coupled with lower infiltration rates, resulted in some radionuclide fluxes to the water table peaking close to the 1,000-year period of performance, which could lead to a decrease in some PA disposal limits.

The improvements are described in more detail below.

4.6.3.9.1. Timeline

In the current ILV VZ model, time zero is defined as the start of ELLWF operations, which is the date of the first waste package placed in the LAWV on 09/28/1994, while the end of ELLWF operations is expected 71 years later in calendar year 2065. Thus, the start of ILV operations is year one relative to the start of the LAWV. After 70 years of ILV operation, the 100-year IC period begins. The PA2008 calculations, on the other hand, assumed that ELLWF operations would end, and IC would begin, in calendar year 2020, which was chosen as time zero in the model. An initial period of -25 years was used in the PA2008 model to account for radionuclide decay and daughter ingrowth following waste disposal at the start of operations in 1995. The additional 45 years of operation in the PA2022 calculation provide more time for radionuclide decay and daughter ingrowth. However, except for H-3 with a half-life of 12.32 years, the additional time should not make a significant difference in the results. In the comparison presented in this section, results from PA2008 and the current models are both plotted taking time zero as the start of ILV operations.

4.6.3.9.2. Vadose Zone Thickness

A depth of 76.5 feet is assumed in the current model versus 60.5 feet in the PA2008 model. As noted in Section 4.6.3.2, the PORFLOW model used for PA2008 did not include the Tan Clay or Lower Aquifer zones.

4.6.3.9.3. Infiltration

Figure 4-201 compares the infiltration rates over the ILV vault used in PA2008 to those employed in the PA2022 model which are based on 2019 calculations by Dyer (2019b). Both calculations are made with the HELP model; however, the 2019 infiltration rates are significantly lower than the PA2008 values during the first 2,000 years and remain lower until vault roof collapse. Lower infiltration slows the transport of radionuclides through the ILV VZ. The biggest difference between the PA2008 and PA2022 final closure cap designs is that an HDPE geomembrane liner has been added above the GCL (composite barrier), whereas only a GCL was assumed in the PA2008 closure cap design. The geomembrane provides the primary barrier to water infiltration in the current HELP model results. ILV roof collapse at 5,770 years results in a large increase in flow through the vault area assuming runoff from the intact closure cap will enter the cavity created by vault failure and waste subsidence.

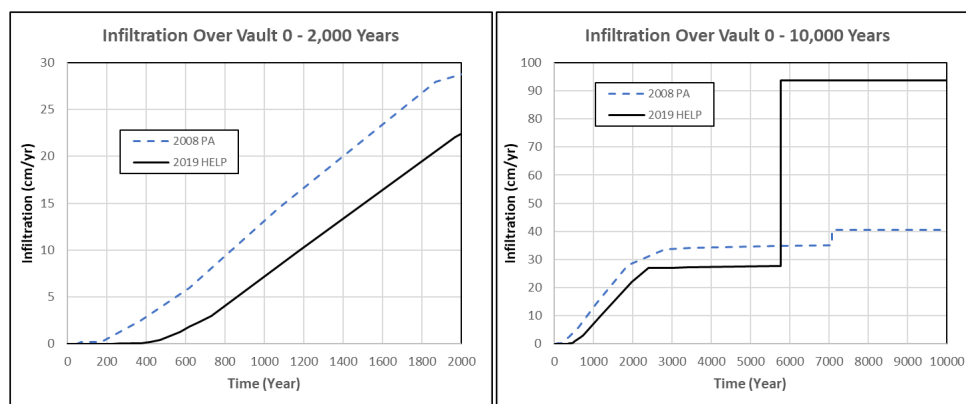


Figure 4-201. Comparison of HELP-Model-Predicted Infiltration Rates for the Intermediate-Level Vault in the 2008 (WSRC, 2008) versus Current (Dyer, 2019b) E-Area Low-Level Waste Facility Performance Assessments

4.6.3.9.4. Concrete Degradation

Static load cracks that do not penetrate the concrete are realized within the roof slab and walls as soon as the closure cap is emplaced as documented in the ILV structural analysis (Peregoy, 2006b). In PA2008, the cracks estimated to exist at 5,000 years were utilized to produce an equivalent saturated hydraulic conductivity for the roof slab and side and end walls at the time of closure cap emplacement. A separate simulation of Cell 4 (i.e., center cell) was conducted assuming a fully penetrating crack occurs due to a PC-4 seismic event at 400 years. The wall and floor concrete were assigned gravel properties at that time. The structural analysis estimated the probability of a P-4 seismic event to be 39.3% over 5,000 years and recommended linear extrapolation to time zero. This implies less than a 4% probability at 400 years.

In the current analysis, surface cracking at the time of closure cap placement is modeled by blending the roof and wall concrete with gravel (90% concrete and 10% gravel). The concrete/gravel mixture is then blended with ILV soil at 50-year increments over the next 500 years. At 400 years, the concrete will have the hydraulic properties of 80% soil, 2% gravel, and 18% E-Area concrete. Because the choice by Peregoy (2006b) of 400 years for through-cracking is somewhat arbitrary (choosing an approximate 5% probability of occurrence at 500 years would have also been acceptable), the current analysis does not include the change of wall and roof hydraulic properties to gravel at 400 years but simply continues the concrete degradation between 400 and 500 years. Both models transitioned to soil properties for the entire vault concrete at 500 years.

4.6.3.9.5. Sorption

Significant differences in radionuclide sorption properties exist between PA2008 and PA2022 models as shown in Table 4-66. These improvements in sorption properties are based on more than 70 new studies since PA2008 that are captured in the latest update of the *Geochemical Data Package* prepared by Kaplan (2016b). While there are significant differences in K_d values for Ra-226 and Pb-210, a comparison of these radionuclides is still included in the results presented below.

Table 4-66. Comparison of Sorption Properties in 2022 E-Area Low-Level Waste Facility Performance Assessment Intermediate-Level Vault Vadose Zone Model and 2008 E-Area Low-Level Waste Facility Performance Assessment Version (Smith, 2021a; Table 6-3)

PA2022 Model		PA2008 Model		Impact on Transport
C-14 K_d sand = 5, K_d clay = 150 Solubility: RC-I and OC-I = 10^{-5} gmol L ⁻¹ RC-II and OC-II = 10^{-6} gmol L ⁻¹		C-14 K_d sand = 0, K_d clay = 0 Solubility: RC-I and OC-I = 10^{-6} gmol L ⁻¹ RD-II and OC-II = 10^{-4} gmol L ⁻¹		C-14 released earlier in PA2008 model.
Ra-226 K_ds: Sand 25 Clay 180 ¹ RC-I 6,000 ² RC-II 600 ³ OC-I 200 ⁴ OC-II 200	Pb-210 K_ds: Sand 2,000 Clay 5,000 ¹ RC-I 5,000 ² RC-II 1,000 ³ OC-I 300 ⁴ OC-II 100	Ra-226 K_ds: Sand 5 Clay 17 ¹ RC-I 100 ² RC-II 70 ³ OC-I 100 ⁴ OC-II 70	Pb-210 K_ds: Sand 5 Clay 5,000 ¹ RC-I 500 ² RC-II 250 ³ OC-I 500 ⁴ OC-II 250	Transport of Ra-226 and Pb-210 reduced in current model except for Pb within the waste zone where K_d s are reduced.

Notes:

- ¹ Reducing concrete, Stage I: ILV concrete
- ² Reducing concrete, Stage II: ILV concrete
- ³ Oxidizing concrete, Stage I: waste
- ⁴ Oxidizing concrete, Stage II: waste

4.6.3.10. Comparison of Model Results: 2022 versus 2008 E-Area Low-Level Waste Facility Performance Assessment

Comparison of fluxes to the water table for six parent radionuclides and daughters are shown in Figure 4-202, Figure 4-203, and Figure 4-204. All radionuclide releases are all K_d controlled.

The peak flux for C-14 in Figure 4-202 occurs shortly after ILV roof collapse in both models (1,900 years and 5,770 years). The C-14 peak in the current model is only about 24% of the PA2008 peak both because of peak spreading and the longer retention time of approximately one half-life in the current model. As shown in Table 4-66, there are significant differences in both the K_d values and solubilities for C-14 between the two models.

The peak flux for Cl-36 in Figure 4-202, which occurs after concrete degradation is complete, appears sooner in the current ILV model than in the PA2008 version. This is likely a result of faster transport through the degraded ILV concrete. The peak flux in the current model is only 13% of the PA2008 value. As with C-14, the PA2008 flux is very high and narrow occurring almost immediately after roof collapse. This sudden flushing of the radionuclide from the VZ following roof collapse tends to cause these higher and narrower flux peaks. Although the Cl-36 peak flux in the current model is much lower than in the PA2008 version, it occurs closer to the period of performance and consequently may be more conservative.

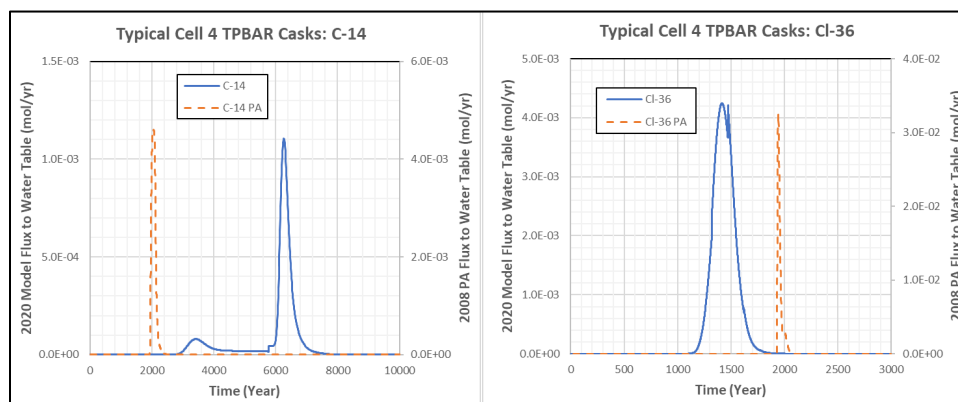


Figure 4-202. Flux to the Water Table (gmol yr^{-1} per gmole of parent) for C-14 and Cl-36 in the Current and 2008 E-Area Low-Level Waste Facility Performance Assessment Intermediate-Level Vault Vadose Zone Models (Smith, 2021a; Figure 6-15)

The peak H-3 flux shown in Figure 4-203, which appears well before concrete degradation begins, is 84% higher in the current model. The I-129 flux in Figure 4-203 is 16% higher than the PA2008 value which is the closest agreement seen among the two models. The fact that the I-129 peak flux also occurs earlier in the PA2022 model may adversely impact limits during the period of performance.

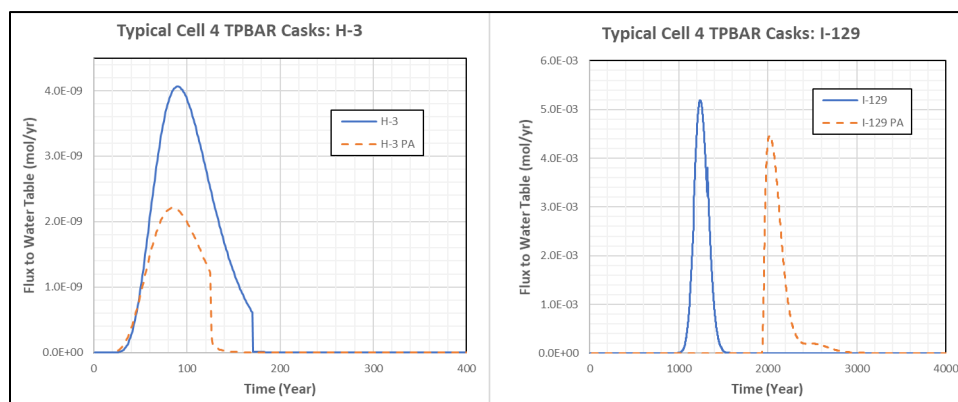


Figure 4-203. Flux to the Water Table (gmol yr^{-1} per gmole of parent) for H-3 and I-129 in the Current and 2008 E-Area Low Level Waste Facility Performance Assessment Intermediate-Level Vault Vadose Zone Models (Smith, 2021a; Figure 6-16)

Fluxes to the water table for Ra-226, U-234, and the U-234 daughters are presented in Figure 4-204. As shown in Table 4-66, K_d values for Ra-226 and Pb-210 are much different in the latest *Geochemical Data Package* (Kaplan, 2016b); therefore, the flux curve for Ra-226 has shifted to later times in the current model and the peak flux is much lower. Qualitatively, U-234 and daughter fluxes compare relatively well with all peak fluxes occurring after about 20,000 years, which is well beyond the compliance period. Ra-226 release from U-234 decay in PA2008 extends back to about 1,000 years and is likely the cause of GW pathway U-234 disposal limits.

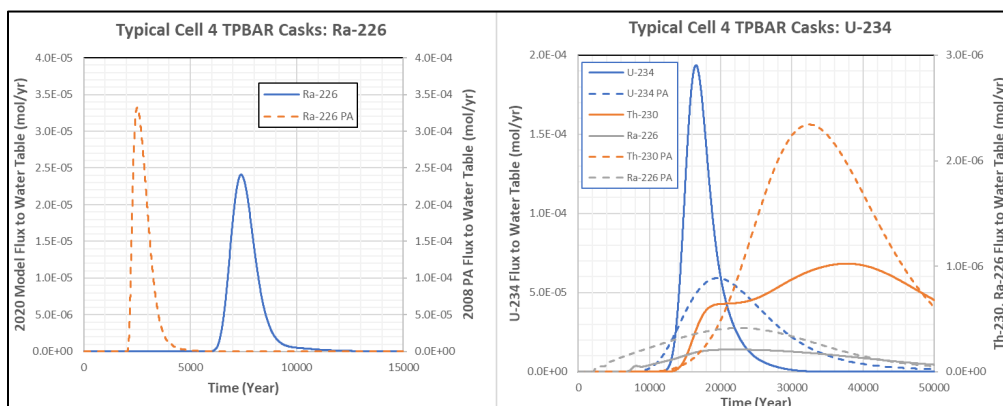


Figure 4-204. Flux to the Water Table (gmol yr^{-1} per gmole of parent) for Ra-226 and U-234 in the Current and 2008 E-Area Low-Level Waste Facility Performance Assessment Intermediate-Level Vault Vadose Zone Models (Smith, 2021a; Figure 6-17)

The PA2008 peak fluxes for C-14, Cl-36, I-129, and Ra-226 all appear at 1,900 years when the infiltration rate increases because of ILV roof collapse. The selection of 1,900 years for roof collapse was somewhat arbitrary and creates abnormally sharp peaks for these radionuclides. In the PA2022 model, the increase in K_d for C-14, Ra-226, and Pb-210 observed in Table 4-66 causes fluxes to the water table for these radionuclides to peak later, which should significantly increase their GW pathway disposal limits.

4.7. NAVAL REACTOR COMPONENT DISPOSAL AREAS

Above-grade storage of NR waste forms on the NR07E pad began in 1987. Waste was received from the Bettis Atomic Power Laboratory, Knolls Atomic Power Laboratory (KAPL), and various Naval shipyards. In 1997, U.S. DOE approved disposal of NR waste forms on the new NR26E pad. In 2004, the existing casks and containers stored on the NR07E pad were evaluated for in-place disposal and the storage pad reclassified as a disposal area (Wilhite and Flach, 2004). NR07E and NR26E locations in/adjacent to the ELLWF are shown in Figure 2-78.

Historically, welded shipping casks and bolted containers of components and auxiliary equipment have been shipped by NR programs to SRS by rail and placed on the NRCDA pads. The containers/casks are to remain on these pads for a period of years until covered by soil or, possibly, CLSM (a flowable soil-cement material used as backfill). For the closed NR07E pad, a soil cover was applied in 2005 to provide shielding due to the proximity of adjacent ELLWF operations. For the currently operating pad, NR26E, this cover is assumed to be applied at the time of interim closure of the ELLWF, which is estimated to be 2065. Following a minimum 100-year interim closure period where the closed facility will be monitored and maintained, the final multilayer soil-geomembrane cover will be installed over the ELLWF, including the two pads. Installation of the final cover is the start of the DOE M 435.1-1, Chg. 3 (U.S. DOE, 2021b) prescribed 1,000-year post-closure period. Implementation of a modeling timeline corresponding with this operational/closure sequence is described in Section 4.7.8.

NR components have consisted of core barrels, adapter flanges, closure heads, pumps, shear blocks and other similar equipment from the Navy. Due to the variety of NR waste components and levels

of contamination, there is no standard NR waste container. Detailed configurational descriptions of the NR waste components are not available because of the classified nature of this information. According to unclassified information supplied by the NR program, a representative type of activated metal component is the KAPL core barrel/thermal shield (CB/TS) in a heavily shielded, welded cask (Yu et al., 2002). The KAPL CB/TS has been used in PA modeling as a conceptual type of waste form representing the various types of activated metal components (McDowell-Boyer et al., 2000; WSRC, 1997; 2008; Yu et al., 2002) as the majority of the inventory projected for NR26E will be contained in this type of component. The key safety feature of this cask is its 1.25-inch continuous weld, representative of the minimum weld thickness for all welded casks received from NR Programs. A representative type of an activated corrosion products (ACP) contaminated component is the shear block contained in a thinner-walled box with a bolted-in-place gasket seal. No hydraulic credit is taken for radionuclide holdup from this type of container as described in Sections 4.7.2.1 and 4.7.2.2 below.

Corrosion of the outer container and inner waste forms is a key consideration in the release of contaminants from buried NR waste. Corrosion considerations for the two NR waste types are discussed below.

4.7.1. Key Safety Features and Corrosion Considerations

4.7.1.1. Welded Cask Waste Form

Highly radioactive components consisting of activated corrosion-resistant metal alloy are stored within thick carbon-steel welded casks. As described above, a representative type of activated metal component is the KAPL core barrel/thermal shield. The KAPL CB/TS welded cask is illustrated in Figure 2-51 and Figure 2-52. As seen in Figure 2-52, the robust design and construction of NR welded casks ensures they will remain structurally intact and support the overlying closure cap well past the end of the 1,000-year post-closure period.

In PA2008, corrosion of NR components within a heavily shielded cask was assumed to start 750 years after disposal. The conceptual model assumption was that after 750 years, water will enter the disposal casks via small holes due to corrosion in the welds. This estimate was based on communication from the Pittsburgh Naval Reactors Office (Datovech, 1994). Datovech performed a literature review to determine the time it will take to corrode through the cask welds (having a minimum 1.25-inch thickness) resulting in hydraulic failure of the cask and subsequent inventory release. The main reference used by Datovech (1994) in determining the puncture time is a condensed summary of the National Bureau of Standards (NBS) seminal investigation on the corrosion of metals in soils by Romanoff (1957).

In reviewing the NBS data, Romanoff (1957) noted that the physical and chemical nature of the soil controlled whether general or localized (i.e., pitting) corrosion is dominant regardless of the nature of the material sample. Of the soil types included in the NBS investigation, a Cecil clay loam from Atlanta is most representative of the soil at SRS. Although Datovech (1994) does not provide specifics on the calculation employed to arrive at a time-to-puncture of 750 years, he does

cite computations by Logan (1939), one of the NBS investigators involved in generating the data reported by Romanoff (1957).

Logan (1939) utilized a combined pit-depth-time and pit-depth-area equation, $P = kT^n (C \log A + 1)$, where P is the pit depth on an area, A , at any time, T , and C , k , and n are constants derived from an analysis of the data on pit depths. Using the above equation, the estimated time to first penetrate a metal thickness of 0.322 inches (Logan's study averaged data from pure open-hearth iron, wrought iron, Bessemer steel, open-hearth steel, and open-hearth steel containing 0.2% copper because they all produced similar results) was 190 years (Table 41; Romanoff, 1957). The metal thickness (0.322 inches) divided by the elapsed time to first puncture (190 years) yields a corrosion rate equal to 0.00169 inches per year (in yr^{-1}) which is equivalent to 42.9 micrometers per year ($\mu\text{m yr}^{-1}$). Assuming this corrosion rate is constant beyond 190 years (i.e., the pit-depth-time/pit-depth-area equation is not used), the time to first puncture for the NR casks will be 741 years for an assumed minimum weld thickness of 1.25 inches.

Alternatively, the pit-depth-time/pit-depth-area equation above can be used to calculate the minimum corrosion rate. For the Cecil clay loam from Atlanta, Logan (1939) lists in Table 4 of his paper a value of 68.8 for k (standard deviation of 2.3), 0.17 for n (standard deviation of 0.05), and 0.413 for C (standard deviation of 0.082). Using these parameter values to calculate the minimum corrosion rate, a time-to-puncture of 15,600 years is obtained for an NR cask with an assumed weld thickness of 1.25 inches.

Using a different approach, SRNL's Materials Technology Section (Chandler, 1998) calculated corrosion rates for carbon-steel pipe in Cecil clay loam from NBS data on weight loss versus time (Table 15; Romanoff, 1957). Calculated corrosion rates ranged from 52.8 $\mu\text{m yr}^{-1}$ (0.00208 in yr^{-1}) at two years to 12 $\mu\text{m yr}^{-1}$ (0.000472 in yr^{-1}) at 14.3 years. Based on these corrosion rates, penetrating a 1.25-inch weld was estimated to take between 600 and 2,650 years. The much lower corrosion rate after 14.3 years of burial is more representative of long-term corrosion; therefore, the time to penetration and hydraulic failure will be closer to 2,650 years than 600 years. At this lower corrosion rate, a time-to-puncture of 750 years as utilized in PA2008 is bounding for NR casks constructed from carbon steel.

Most of the welded casks on the NRCDA pads are constructed from carbon steel; however, a small number are fabricated (cask and welds) from HY-80 steel, a low-carbon, low-alloy steel with nickel, molybdenum, and chromium. A review by SRNL's Materials Technology Section determined that the corrosion performance of low-alloy steels tested by the NBS at the Cecil clay loam site in Atlanta (Romanoff, 1957) is representative of corrosion rates for HY-80 steel casks in SRS soils (Dunn, 2002). Soil characteristics pertinent to corrosion of low-alloy steels are similar for the two sites (i.e., pH, resistivity, aeration). The chemical compositions of NR HY-80 steel and the steel alloys tested by the NBS are also comparable. Based on these similarities, Dunn (2002) expected corrosion rates for HY-80 steel buried at SRS to be in the range of those calculated for the low-alloy steels at the Cecil clay loam site. Using weight loss measurements by the NBS (Table 21; Romanoff, 1957), Dunn (2002) calculated the corrosion rate of the HY-80 alloy in SRS soils to be in the range of 16.7 $\mu\text{m yr}^{-1}$ (0.000657 in yr^{-1}) to 42.9 $\mu\text{m yr}^{-1}$.

($0.00169 \text{ in yr}^{-1}$) for a two-year period and $8.9 \mu\text{m yr}^{-1}$ ($0.00035 \text{ in yr}^{-1}$) to $10.9 \mu\text{m yr}^{-1}$ ($0.00043 \text{ in yr}^{-1}$) for a 12-year period. Taking the highest corrosion rate from Dunn (2002)'s study ($42.9 \mu\text{m yr}^{-1}$ over a two-year period), the time to puncture is estimated to be 740 years. Dunn (2002) noted that the corrosion rate of steels with chromium, nickel, and molybdenum tend to decrease over time because the oxide layer that forms provides a protective layer on the steel. Assuming the longer duration period is more representative of long-term corrosion, the time to penetration and hydraulic failure will range from 2,900 to 3,600 years. Considering this rate, a time-to-puncture of 750 years as utilized in PA2008 is bounding for NR casks constructed from HY-80 steel.

Carbon steel in soil or air requires the presence of moisture to initiate corrosion. NR has indicated that there may be up to 3.5 gallons of water inside a typical welded KAPL CB/TS cask (Hsu and Roddy, 1997). This amount of moisture represents less than 1% by volume inside the cask. In theory, a pit could be forming on each side simultaneously, reducing the time to hydraulic failure. Chandler (1998) concluded, however, that this small amount of water inside a sealed carbon steel container will be readily absorbed/converted into metal oxide or hydroxide corrosion products on the inner walls and metal component surfaces. Dunn (2002) also noted that an adsorbent material is added to the cask that minimizes the free water. Therefore, corrosion from inside the cask to the outside is expected to be negligible.

SRS subsurface conditions are slightly acidic with soil moisture in the range of pH 5.5. An interim cover constructed of CLSM, rather than native SRS backfill soil, will beneficially reduce the rate of corrosion of carbon steel due to the presence of a small amount of cement in the standard SRS CLSM mix. The cement creates a higher-pH environment surrounding the casks. The pH will remain elevated until enough PVs of slightly acidic infiltrating water consume the neutralization capacity of the dominant calcium phases, changing the buffering capacity and, ultimately, lowering the pH to background conditions. Therefore, assuming a soil (versus CLSM) cover at interim closure is bounding.

The PA2008 modeling timeline for the NRCDA assumed corrosion in soil beginning immediately upon placement of casks on the pad, ignoring the open-air period during operations. A review for weathering of steel open to the atmosphere shows a range of corrosion rates based on atmospheric corrosivity conditions. In a 2013 study (Morcillo et al., 2013), investigators designated four primary corrosivity environments: rural, urban, industrial, and marine, in order of increasing corrosivity. Considering only rural and urban locations in the U.S., their study gives a corrosion rate in air ranging from $3.40 \mu\text{m yr}^{-1}$ ($0.00013 \text{ in yr}^{-1}$) to $12.2 \mu\text{m yr}^{-1}$ ($0.00048 \text{ in yr}^{-1}$). Thus, carbon steel corrosion rates in air are generally at or below the low end of corrosion rates in soil for atmospheric conditions representative of SRS. Assuming immediate burial under a soil cover at the beginning of operations is therefore bounding.

In summary, carbon steel corrosion rates in air are generally at or below the low end of corrosion rates in soil for atmospheric conditions representative of SRS (Wohlwend and Butcher, 2018). Therefore, assuming immediate NR waste burial under a soil cover (i.e., ignoring the open-air period) and initiating corrosion of the welded cask at the beginning of operations is bounding. In

addition, considering soil instead of CLSM as the interim cover material is bounding due to the impact of slightly acidic soil moisture on corrosion of carbon steel. Finally, corrosion from inside the cask to the outside is expected to be insignificant due to the negligible amount of water present in the casks before being welded closed. Taking these disposal conditions into consideration, corrosion is estimated to penetrate the welds after 750 years of disposal allowing water to enter the disposal casks via small holes in the welds (i.e., hydraulic failure).

4.7.1.2. Activated Metal Waste Components

As previously discussed, there is no standard NR waste container due to the variety of NR waste components. The KAPL CB/TS was used to represent the various types of activated metal components in the 2002 SA (Yu et al., 2002) and PA2008 (WSRC, 2008) because most of the activity projected for NR26E will be contained in this type of component. PA2008 employed a simplifying assumption that activated metal components are constructed of 304 stainless steel in calculating a corrosion-controlled release for each radionuclide. The 2002 SA (Yu et al., 2002) developed corrosion rates based on the Navy's description of component parts and recommended corrosion model.

The KAPL unit comprises component parts made of either Inconel or Zircaloy, both corrosion-resistant alloys. The distribution of activation products and corrosion rates are unequal between Inconel and Zircaloy because of the different constituents in each alloy. In addition, each component part has a different geometry and position within the reactor flux field resulting in a different fraction of the total inventory accumulating in each part. The corrosion rates for Inconel and Zircaloy metal are estimated to be $2.5 \times 10^{-5} \text{ cm yr}^{-1}$ ($0.25 \text{ } \mu\text{m yr}^{-1}$) and $2.5 \times 10^{-6} \text{ cm yr}^{-1}$ ($0.025 \text{ } \mu\text{m yr}^{-1}$), respectively, based on data from the Hanford site (Jenkins, 1993). Assuming corrosion occurs on both sides of a metal plate, effective corrosion rates for Inconel and Zircaloy metal are estimated at $5 \times 10^{-5} \text{ cm yr}^{-1}$ ($0.50 \text{ } \mu\text{m yr}^{-1}$) and $5 \times 10^{-6} \text{ cm yr}^{-1}$ ($0.05 \text{ } \mu\text{m yr}^{-1}$), respectively. An effective release rate (curies per year) is calculated for each radionuclide in each component part by combining the information on activity distribution between the two types of alloys and the different component parts (Yu et al., 2002; Table 3.1-1). Thus, the rate of release of each radionuclide from a representative KAPL cask is the sum of releases from the individual component parts accounting for radioactive decay.

Because of uncertainty in the composition of components and impacts of daughter ingrowth, a worst-case rate of release from the waste form is derived from the following two cases for the PA: (1) all radionuclides residing within Inconel have a corrosion rate of $5 \times 10^{-5} \text{ cm yr}^{-1}$ ($0.50 \text{ } \mu\text{m yr}^{-1}$); (2) all radionuclides residing within Zircaloy have a corrosion rate of $5 \times 10^{-6} \text{ cm yr}^{-1}$ ($0.05 \text{ } \mu\text{m yr}^{-1}$). Minimum disposal limits (or maximum dose impacts of closure inventory) selected from these two cases will make up a worst-case set of inventory limits.

As derived by Yu et al. (2002), the total rate of release (combining Inconel and Zircaloy) of a given radionuclide from activated metal at time t (years) is calculated by:

$$R_i(t) = I_{Ai}(t)(f_I \lambda_I + f_Z \lambda_Z) \quad \text{Eq. (4-53)}$$

where:

$I_{Ai}(t)$:	Total activated metal inventory at time t for the i^{th} radionuclide (Ci)
f_I :	Fraction of I_{Ai} in Inconel (unitless)
f_Z :	Fraction of I_{Ai} in Zircaloy ($1 - f_I$) (unitless)
λ_I :	Fractional corrosion rate for Inconel metal alloy (yr^{-1})
λ_Z :	Fractional corrosion rate for Zircaloy metal alloy (yr^{-1})
$R_i(t)$:	Total release rate of the i^{th} radionuclide at time t (Ci yr^{-1})

In applying Eq. (4-53) for the NRCDA release rate, the two endpoints are employed (i.e., $f_I = 1$ or 0 and, conversely, $f_Z = 0$ or 1). The fractional corrosion rates are given in Table 4-67. Note that λ_I and λ_Z are weighted, fractional-average corrosion rates calculated according to the footnote to Table 4-67.

Table 4-67. Corrosion Rates of Nuclear Reactor Waste Components

Metal Alloy	Fractional Corrosion Rate ^a , λ (yr^{-1})
Inconel	6.2194E-05
Zircaloy	9.5832E-06

Notes:

- ^a Fractional corrosion rates listed in the table are a weighted fractional average based on the different corrosion rates of the metal alloys ($5 \times 10^{-5} \text{ cm yr}^{-1}$ and $5 \times 10^{-6} \text{ cm yr}^{-1}$ for Inconel and Zircaloy, respectively), the fraction of the radionuclide inventory (I_i) residing in each of the different component parts for each alloy [four component parts for Inconel ($i = 1$ to 4) and two component parts for Zircaloy ($j = 1$ to 2)], and the different effective thickness (T_{eff}) of each component part in each alloy. Values for I_i and T_{eff} are given by Yu et al. (2002; Table 3.1-1).

$$\text{For Inconel: } \lambda_I = 5.0\text{E-}05 \text{ cm/yr} \sum_{i=1}^4 \left[I_{iI} (\text{unitless}) / T_{eff i} (\text{cm}) \right]$$

$$\text{For Zircaloy: } \lambda_Z = 5.0\text{E-}06 \text{ cm/yr} \sum_{j=1}^2 \left[I_{jZ} (\text{unitless}) / T_{eff j} (\text{cm}) \right]$$

Eq. (4-53) does not directly account for the impact of daughter ingrowth for radionuclides within a decay chain. For parent radionuclides with progeny, the time-dependent metal inventories are computed externally, and the metal release rates associated with all short-chain progeny are then provided as source terms to subsequent PORFLOW VZ transport runs. See Section 4.7.8.5.3 for further discussion of the rate of release from activated metal components.

NR programs has indicated that only negligible amounts of water are present inside the typical KAPL CB/TS cask (Hsu and Roddy, 1997). Due to the construction of the thick carbon-steel casks with full-penetration weld closures, the PORFLOW model assumes no corrosion of the metal alloys occurs while the cask remains sealed. The alloy corrosion begins with hydraulic failure of welds on KAPL CB/TS cask, allowing water entry into the casks. Therefore, radionuclides are released from the activated metal only after 750 years. Metal alloy corrosion will be complete in 16,079 years for Inconel and 104,349 years for Zircaloy.

4.7.1.3. Bolted Container Waste Form

Auxiliary equipment contaminated with ACP at low levels is stored within thinner-walled bolted containers. Because of the variety of bolted containers received from NR Programs, the large Shear

Block disposal container (SBDC) is selected as the representative type of bolted container for the PORFLOW model (BMPC-KAPL, 2009a; 2009b). Both large and small versions of SBDCs (8 ft³ and 4 ft³ internal volume, respectively) are being shipped to E-Area by the Navy with approximate external dimensions shown in Figure 2-83. The SBDC is selected because it represents the largest category of bolted containers currently disposed or projected to be shipped to the ELLWF. In addition, this waste configuration concentrates the inventory from larger bolted containers into the smaller SBDC volume located closer to the water table.

Because of their robust design and generally dense payload (e.g., shear blocks, hold-down barrels, closure heads, recirculating pumps) bolted containers are considered non-crushable during the 1,000-year period of performance. Dynamic compaction for waste-layer stabilization is prohibited over the two NRCDAAs at final closure.

Lids for bolted containers are sealed by a gasket and bolted in place. Because of uncertainty in the long-term durability of gaskets in a disposal environment, two cases are assumed to capture the range in potential behavior as described in the next section.

4.7.1.4. Surface-Contaminated Activated Corrosion Products Waste Components

The bolted, gasket-sealed containers containing surface-contaminated ACP components are expected to deter water infiltration for a period of years. However, time to hydraulic failure of the bolted seal is uncertain. To account for this uncertainty, Hang and Hamm (2022) proposed that the release model be based on two extreme cases for bounding:

- Case 1: Assume all bolted containers hydraulically fail immediately when soil is initially mounded (or CLSM backfilled) around and over the containers on the pad at operational closure (early failure). At that time, ACP contamination is assumed to be instantaneously released into the surrounding soil.
- Case 2: Assume bolted containers are not breached for 750 years, roughly coinciding with the hydraulic failure of the more robust welded casks (late failure). Thus, SBDC inventories are retained and released at the start of KAPL CB/TS corrosion and radionuclide release allowing for some plume overlap to occur. Additionally, waiting 750 years allows time for daughter ingrowth before release.

Cases 1 and 2 represent the bounding scenarios for evaluation of the impact of ACP contaminant release timing. A worst case set of limits is established by selecting the minimum disposal limits (or maximum dose impacts of closure inventory) from these two cases.

4.7.2. Waste Zone Conceptual Model: Material and Hydraulic Properties

Hydraulic properties for the NRCDAAs are based on the waste zone representation for NRCDAAs developed by Hang and Hamm (2022).

4.7.2.1. Welded Casks

During the first 750 years following disposal, the welded casks (Figure 2-52 and Figure 2-81) remain hydraulically intact. Under these conditions, there is essentially no flow and no advective

release of contaminants; therefore, the characteristic curves are essentially irrelevant until a leak develops. The waste zone (NRcontainerNoLeak) shown in Figure 4-205(a) is assumed to exhibit essentially the same material properties as the ET containerized waste zone before dynamic compaction (ETboxesBefore; see Section 4.1.1.1.2); however, because the B-25 boxes are not hydraulically or chemically active, K_h , K_v , and D_e are set to extremely low values as listed in Table 4-68. At 750 years, the cask weld is assumed to corrode and develop a leak path for release of contaminants. The waste zone is expected to remain structurally intact during the entire 1,000-year period of performance. During this final period, no credit is taken for the container, and the waste zone (NRcontainerLeak) is assumed to exhibit the same blended material and hydraulic properties as the ET containerized waste zone before dynamic compaction (ETboxesBefore; see Section 4.1.1.1.2) as shown in Figure 4-205(b).

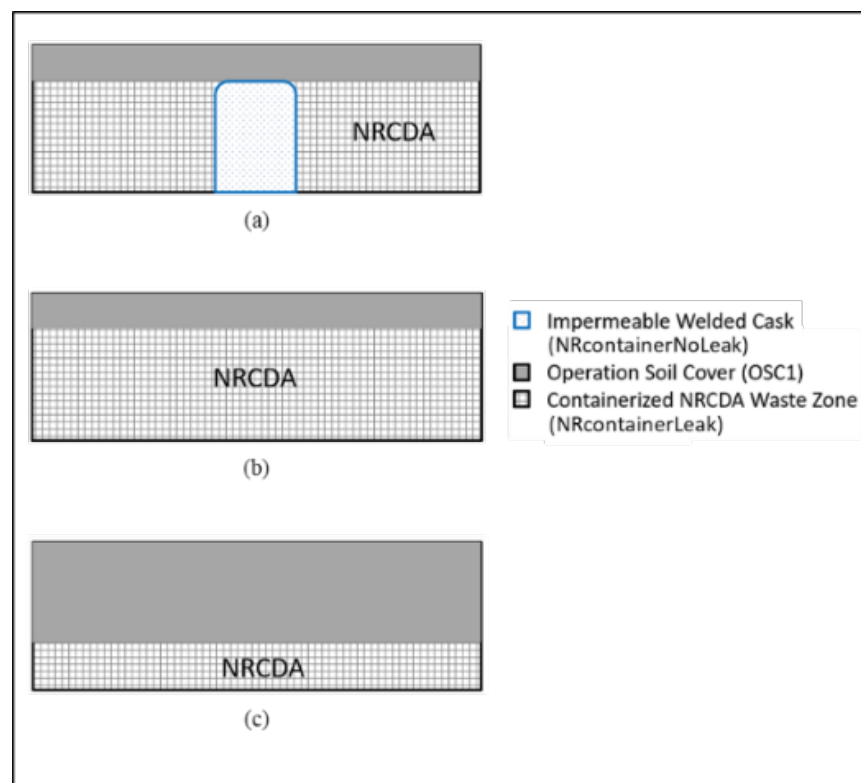


Figure 4-205. Naval Reactor Component Disposal Area Waste Zone Conceptual Model of Hydraulic Properties for (a) Intact Impermeable Welded Casks, (b) Hydraulically Failed Welded Casks, and (c) Generic NR Containerized Waste after Hydraulic Failure

4.7.2.2. Bolted Containers

As previously discussed, auxiliary equipment contaminated with ACP at low levels is stored within thinner-walled bolted containers. Because of the variety of bolted containers received from NR Programs, the large Shear Block disposal container (SBDC) is selected as the representative type of bolted container for the PORFLOW model (BMPC-KAPL, 2009a; 2009b). at final closure. Bounding Cases 1 and 2, as described above in Section 4.7.1.4, represent this generic waste form. In bounding Case 1, the waste zone (NRcontainerLeak) is assumed to instantaneously exhibit the same blended material and hydraulic properties as the ET containerized waste zone before dynamic

compaction (ETboxesBefore; see Section 4.1.1.1.2) as depicted in Figure 4-205(c). In bounding Case 2, during the first 750 years following waste placement, the waste zone (NRcontainerNoLeak) is assumed to exhibit essentially the same material properties as the ET containerized waste zone before dynamic compaction (ETboxesBefore; see Section 4.1.1.1.2); however, because the B-25 boxes are not hydraulically or chemically active, K_h , K_v , and D_e are set to extremely low values as listed in Table 4-68 (not depicted in Figure 4-205 but analogous to Figure 4-205(a) for welded casks). At 750 years the gasket underneath the bolted lid is assumed to fail, creating a leak path for release of contaminants. The waste zone is expected to remain structurally intact during the entire 1,000-year period of performance. After hydraulic failure, no credit is taken for the container, and the waste zone (NRcontainerLeak) takes on the properties of ETboxesBefore (see Section 4.1.1.1.2) as shown in Figure 4-205(c).

Table 4-68. Material and Hydraulic Properties Used in PORFLOW Naval Reactor Component Disposal Area Model Simulations

Material Type	Material Zones	Density (g mL ⁻¹)	Porosity	Diffusivity (cm ² yr ⁻¹)	K_h (cm yr ⁻¹)	K_v (cm yr ⁻¹)
UVZ	UVZ, TCCZ	2.69	0.385	167.26	1,956.57	274.55
LVZ	LVZ, LAZ	2.67	0.380	167.26	10,414.01	2,871.74
OSC1	BACKFILL	2.65	0.456	167.26	4,102.49	4,102.49
NRcontainerNoLeak	WASTE ¹	2.65	0.991	3.16E-06	1.58E-07	1.58E-07
NRcontainerLeak	WASTE ²	2.65	0.889	167.26	707.61	707.61

Notes:

¹ Before hydraulic failure

² After hydraulic failure

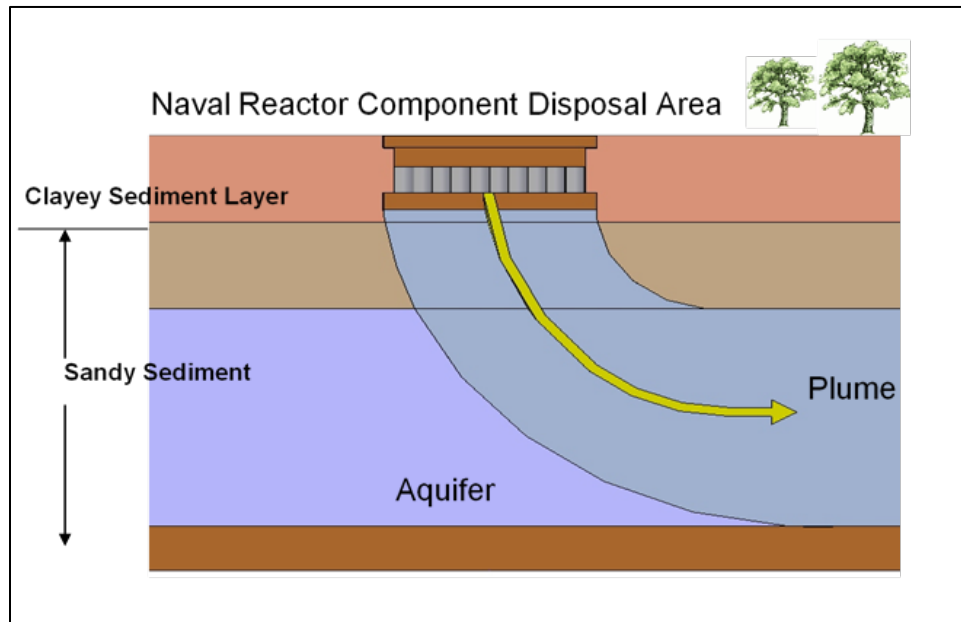
Table 3-64 summarizes NRCDA waste zone material properties for hydraulically intact and hydraulically degraded welded casks and bolted containers. Hydraulic properties employed in the PORFLOW models for each material type and corresponding material zone(s) are given in Table 4-68 (Nichols and Butcher, 2020). Due to PORFLOW convergence issues, only the NRcontainerLeak material property type is applied to the WASTE zone. This will not impact flux at the water table because no radionuclide is released from the WASTE zone before hydraulic failure.

4.7.3. Waste and Vadose Zone Conceptual Model: Geochemical Properties

Key features of the NRCDA that will impact the geochemical environments surrounding and beneath the NR casks are described in this section. More specifically, a geochemical conceptual model for NRCDA is presented that identifies the aqueous chemistry and associated solid phases comprising the waste zone, UVZ, LVZ, and aquifer. The conceptual model developed by Kaplan (2016b) also assigns geochemical parameters to each material zone. Kaplan (2016b) provides a detailed description of the development of the geochemical conceptual model, the definitions of the different geochemical environments and materials, and the assignment of appropriate geochemical parameters for each radionuclide of interest.

Figure 4-206 (Kaplan, 2016b) is a schematic of the geochemical conceptual model for the NRCDA. The cross-section does not show dimensionality and facility-specific details, which are

instead assigned in the numerical model (Section 4.7.8.2). The two relevant geochemical environments for the NRCDA are a clayey sediment and a sandy sediment. Section 3.8.2.5 provides a description of the four geochemical conceptual environments.



Note: Overlying final closure cap not shown.

Figure 4-206. Naval Reactor Component Disposal Area Geochemical Conceptual Model Schematic

Table 4-69 (Kaplan, 2016b) lists the relevant solid and aqueous phases for a NRCDA pad, together with the associated geochemical parameters (K_d and k_s values) necessary in the PA model to describe the chemical interactions of radionuclides with these geochemical materials (e.g., sandy sediment, clayey sediment, reducing cement). SRNL (2018) provides look-up tables containing the recommended K_d and k_s values for each radionuclide (table rows) as a function of the different geochemical materials or solid phases (table columns).

Table 4-69. Naval Reactor Component Disposal Areas: Conceptual Geochemical Model of Features and Parameters (see Figure 4-206)

Solid Phases	Aqueous Phase	Geochemical Parameter
Waste Zone: Active components are activated metal and corrosion products. It is assumed that the activated metal waste will rust to form Fe-oxides (crud) and that radionuclides will sorb to these Fe-oxides. ^a	Same as SRS GW: pH 5.5, ionic strength 0.01 molal, except for trace levels of radionuclides	Use Clayey Sediment K_d . Fe-oxide content will control the sorption chemistry of this zone. It is assumed that the geochemistry of the Clayey Sediment will approximate that of the rusted metal waste form. In reality, the rusted waste form will contain much greater Fe-oxide content than the typical clayey SRS sediment. Thus, use of a clayey sediment K_d is a bounding assumption. ^{b, c}
Clayey Sediment: Upper Vadose Zone	As above	Use Clayey Sediment K_d ^{b, c}
Sandy Sediment: Lower Vadose Zone		Use Sandy Sediment K_d ^{b, c}
Sandy Sediment: Aquifer Zone		Use Sandy Sediment K_d

^a NR wastes are highly radioactive components consisting of activated corrosion-resistant metal alloy (Inconel and Zircaloy) contained within thick steel-welded casks, and auxiliary equipment primarily contaminated with activated corrosion products (crud) at low levels and contained within thinner-walled bolted containers. The crud component is assumed to be instantaneously released when the container is breached (750 years after placement on the pad). The activation product component is released based on the corrosion rate of the steel and radioactive decay of the radionuclides. The waste zone consists of the welded casks and bolted containers placed on an above-grade gravel pad. The casks are assumed to be structurally stable well past the 1,000-year period of performance. Two separate areas within the ELLWF have been used for NR waste disposal.

^b As part of final closure, the casks will be surrounded with a structurally suitable material. This backfill may be emplaced sooner if radiation shielding is required for personnel protection during the operational or institutional-control period. The solid could be sand, aggregate, onsite soil, or a flowable cementitious material (Phifer et al., 2009). The assumption is that Fe-oxide content from the rusted waste form will control radionuclide sorption in the Waste Zone irrespective of whether clay, sand, or aggregate is used as the backfill. If a flowable cementitious fill is used, then cementitious-leachate-impacted K_d values should be used in the Waste Zone and the Upper and Lower Vadose Zones. In the Aquifer Zone, cementitious leachate pore water gets diluted with typical SRS GW and the aqueous phase takes on the properties of SRS GW (i.e., pH 5.8 and ionic strength 0.01), except for trace levels of radionuclides.

^c Unlike PA2008 when a simple GoldSim® model was used to represent the NRCDA, reactive transport simulations of the VZ for this PA are performed using a 3-D PORFLOW numerical model (Hang and Hamm, 2022).

4.7.4. 2008 E-Area Low-Level Waste Facility Performance Assessment Modeling Approach

GW pathway modeling of the NR26E pad in PA2008 assumed 100 component containers: 50 heavily shielded, welded KAPL casks and 50 thinner, bolted auxiliary equipment containers. The KAPL CB/TS was chosen to represent activated metal components while the KAPL Closure Head was selected to represent surface-contaminated ACP components. NR provided a representative isotopic content for each component type consisting of 65 radionuclides (Yu et al., 2002). A radionuclide screening was performed to reduce this list to seven radionuclides that were modeled in the PA. Greater than 99.9% of the inventory was contained in the heavily shielded, welded casks. Final inventories for the NR26E were obtained by multiplying the average isotopic curie content of each component type by 50 to represent a total closure inventory for the 100 component containers.

To simplify the analysis, the inventories of the activated metal components are conceptually combined with the ACP contaminated components in the KAPL cask. In this scenario, the release of activated metal inventories is corrosion limited (Inconel and Zircaloy), while the ACP inventories are assumed to be instantaneously released at the time of container breach (750 years after burial; Hsu and Roddy, 1997). In effect, this allows analyzation of the case where the component casks and equipment containers failed at the same time. In actuality, the bolted, thinner-

walled equipment containers will breach (and therefore peak) long before the welded casks. This is a bounding assumption because the contributions from the two sources will overlap to a greater degree in the GW pathway during the performance period.

A 1-D GoldSim[®] reactive transport model was employed where the source term was directly released into the aquifer (i.e., no VZ model). GW concentrations at the 100-meter GW POA were obtained by running the projected closure inventories from the Navy through the model, effectively representing a preliminary closure analysis. Plume interaction with other units was ignored because of the very low impact on the GW analysis. Dose impacts were obtained by running the maximum concentration for each radionuclide at the 100-meter POA through the SRNL dose and limits calculator. Dose impacts were significantly below DOE M 435.1-1, Chg. 3 (U.S. DOE, 2021b) POs (including EPA drinking water standards interpreted to meet U.S. DOE GW protection requirements) given the projected closure inventories from the Navy. To obtain limits, the source term was adjusted to match GW POs at the 100-meter well for each radionuclide during the period of performance. The results represent GW radionuclide disposal limits (in curies) for managing future NR waste receipts. Quantitative sensitivity and uncertainty analyses were also performed wherein the soil-water distribution (or partition) coefficients (K_d values), aquifer area, GW velocity, and time for weld breakthrough (assumed to be the time of contaminant release) were varied. The sensitivity analysis showed that the all-pathways dose is most sensitive to the failure time of the disposal cask welds and the aquifer cross-sectional area.

Modeling results for NR26E and corresponding radionuclide disposal limits for all the PA pathways were applied to NR07E based on comparable hydrology, disposal configuration, and waste forms.

4.7.5. Changes Since 2008 E-Area Low-Level Waste Facility Performance Assessment

In addition to PA modeling improvements, there have been notable changes in the types and projected inventories of NR waste as well as the NRCDA facility layout. Key NRCDA recommendations from the 2015 PA Strategic Plan (Butcher and Phifer, 2016a) are also implemented in the PA2022 revision.

The Navy has transitioned to a single lifetime fuel element load, reducing reactor maintenance requirements. This change eliminated the need for periodic removal and disposal of reactor components. As a result, the Navy no longer generates highly activated metal components such as the CB/TS, except at decommissioning, and these are currently sent to the Hanford site for disposal (Butcher, 2018f). A new shielding system of interlocking “shear blocks” is now used to reduce personnel exposures. As shear blocks are removed from service and replaced, they are packaged in standard boxes and sent to SRS for disposal. According to the Navy, shear block contamination consists almost entirely of surface ACP as opposed to activated metal. The typical activity level in each shear block container is orders of magnitude lower than the activated metal components (e.g., CB/TS) they replaced. Sixteen shear block boxes (12 large and 4 small) replace one KAPL CB/TS welded cask in the new reactor maintenance scheme (Butcher, 2018f).

The 2000 revision of the ELLWF PA (McDowell-Boyer et al., 2000) assumed the final conceptual facility layout of NR26E to be 100 KAPL CB/TS casks placed one meter apart in a rectangular arrangement. This results in an overall disposal area of approximately 140 feet x 140 feet, or approximately 20,000 square feet. The current, more realistic projected facility configuration in calendar year 2040 is 33 welded casks and 381 thinner-walled bolted containers of various dimensions with placement dictated by operational, dose rate reduction, and security considerations. In addition, should the NRCDA be needed beyond 2040, based on the projected end of EM site cleanup mission in 2065 (SRNS, 2015), additional NR waste will be received. Therefore, it is recommended that the entire area of the NR26E gravel pad be used as the waste footprint as delineated by the current coordinates (C-CV-E-00207, 2016). The corner coordinates of the NR26E disposal pad have changed since the 2008 E-Area PA to make room for adjacent Engineered Trenches ET03 and ET04 on two sides of the pad. Using the current coordinates, the total area of NR26E is 47,685 square feet, which is the area that should be used for calculating GW and non-GW disposal limits. Similarly, the area of the waste footprint for NR07E as calculated by the corner coordinates is 5,880 square feet.

Other changes and PA modeling improvements have occurred since 2008 as well. A new conceptual closure cap design has been developed (C-CT-E-00083, 2016; C-CT-E-00084, 2016) which will impact modeled infiltration rates and, therefore, radionuclide transport to the aquifer. The projected end of operations was initially changed from 2025 to 2040 by Sink (2016c), resulting in a higher projected inventory of NR waste (Sink, 2016a). Subsequent to this change, the ELLWF operational timeline has been extended further to 2065 based on the projected end of the EM site cleanup mission in 2065 (SRNS, 2015) and assuming the Navy's continued need for SRS disposal. Since PA2008, there have also been improvements in modeling techniques as well as a new General Separations Area (GSA) flow model (Flach, 2019). The radionuclide and dose (Smith et al., 2019), geochemical (Kaplan, 2016b), and hydraulic properties (Nichols and Butcher, 2020) data packages have also been updated and are utilized in the PA2022 models.

One key NRCDA GW pathway recommendation from the 2015 PA Strategic Plan (Butcher and Phifer, 2016a) is implemented in PA2022: Model NR26E in the same manner as the other DUs (i.e., unit curie inventories scaled up to disposal limits based on POs), rather than assuming a defined number of components and inventory.

The following two recommendations from the PA strategic plan are also evaluated by Wohlwend and Butcher (2018) resulting in a decision to not implement them in PA2022:

- Establish time to hydraulic failure of the new NR shear block containers if credit needs to be taken for container holdup.
- Evaluate one or more generic models that could bound NRCDA performance to simplify analysis.

4.7.6. Feasibility of a Simple Modeling Approach

4.7.6.1. Activated Corrosion Products Inventory

To determine if the NRCDA conceptual model for ACP waste (which is primarily new NR shear-block bolted containers) will need to credit container holdup to meet POs, the projected closure inventory provided by the Navy is compared to the PA2008 ST08 through ST11 GW limits to determine SOF impacts. The ST model assumes buried radionuclides are immediately available to the surrounding soil for transport (i.e., no holdup). Radionuclides contributing more than 0.01 (1%) to the Beta-Gamma (BG) SOF are shown in Table 4-70 for the three time periods established in PA2008. This comparison with PA2008 limits shows impacts ten times greater than the BG GW protection requirement in the first two time-intervals (orange-highlighted cells). Therefore, employing a generic waste model (i.e., ACP inventory immediately released to the surrounding soil upon disposal) results in unacceptable performance.

Table 4-70. Sum of Fractions: Naval Reactor Component Disposal Area Activated Corrosion Products Inventory versus 2008 E-Area Low-Level Waste Facility Performance Assessment ST08-ST11 Groundwater Limits

Radionuclide	Fraction of PO		
	BG1 (0-12 years)	BG2 (12-100 years)	BG2 (100-1,130 years)
C-14	9.7E+00	9.2E+00	2.2E-01
I-129	3.7E-02	3.7E-02	--
Nb-94	5.0E-01	4.8E-01	1.2E-02
Tc-99	1.5E-02	1.7E-02	--
Ni-59	--	--	2.0E-01
Total SOF	1.0E+01	9.7E+00	4.3E-01

Since 2008, numerous key input parameters and transport models used in the PA have been updated (e.g., from new U.S. DOE standards, International Committee publications, and ongoing SRNL research and development activities). An Unreviewed Disposal Question Evaluation (UDQE) in 2013 reevaluated trench performance using updated information available at the time in support of opening ET03, a third engineered trench (Hamm et al., 2013). One important update is to soil- water distribution coefficients for the key radionuclides present in the NRCDA ACP inventory.

Table 4-71 shows a comparison of these K_d values as they evolved from PA2008 to the 2013 ET03 UDQE, and most recently, to the 2016 geochemical data package (Kaplan, 2016b). A higher K_d value indicates that the radionuclide is more strongly sorbed to the soil phase, making it less mobile in the aqueous phase.

Table 4-71. K_d Changes Since 2008 E-Area Low-Level Waste Facility Performance Assessment

Isotope	Sediment	PA2008 K_d	2013 UDQE K_d	2016 DP K_d
C-14	Clay	0	30	30
	Sand	0	1	1
I-129	Clay	0.6	0.9	3
	Sand	0	0.3	1
Nb-94	Clay	0	0	1,000 ^a
	Sand	0	0	1,000 ^a
Tc-99	Clay	0.2	1.8	1.8
	Sand	0.1	0.6	0.6

Notes:

Changes shown in red.

^a There are few sediment sorption data for Nb. In an earlier version of the geochemical data package, Nb was assumed to behave like Cl⁻ or NO₃⁻. Recent studies show Nb sorbs strongly to soils.

New estimated limits for ET03 are calculated as part of the 2013 UDQE by Hamm et al. (2013), providing information for a more up-to-date comparison with NR ACP inventories. The total projected ACP inventories are compared with these estimated limits. Radionuclides contributing more than 0.01 to the SOF are shown in Table 4-72. Total closure inventories of ACP waste account for approximately 30% of the trench's radionuclide capacity based on BG limits, a significant improvement over the PA2008 comparison. Not shown are comparisons for other GW (all-pathways) and non-GW (air, radon, IHI) pathways. Dose impacts for these pathways are one to two orders of magnitude lower than their respective POs.

Table 4-72. Sum of Fractions: Naval Reactor Component Disposal Area Activated Corrosion Products Inventory versus Estimated 2013 Unreviewed Disposal Question Evaluation Limits for ET03

Radionuclide	Fraction of PO		
	BG1 (0-12 years)	BG2 (12-100 years)	BG2 (100-1,130 years)
C-14	--	--	2.2E-01
Nb-94	3.0E-01	2.9E-01	--
Ni-59	--	--	1.2E-01
Total SOF	3.0E-01	2.9E-01	3.4E-01

Over 90% of the projected closure inventory of ACP waste is contained in shear blocks. Assuming the Navy continues to use the new shielding system of interlocking “shear blocks” to reduce personnel exposures, shear blocks will continue to be removed from service and sent for disposal to SRS through E-Area closure in 2065. If trench limits in PA2022 provide adequate margin, disposal in trenches for all ACP waste is possible, especially considering shear block waste receipts and dose impacts will likely be distributed over multiple trench units throughout the remaining operational period. Alternatively, if NR26E disposal is selected, the simplest, bounding approach to the evaluation will be to superimpose peak GW impacts from ACP components with those from activated metal components as a sensitivity on the amount of plume interaction.

4.7.6.2. Activated Metal Inventory

Preliminary GW screening was performed by employing a methodology comparable to the NCRP Report 123 (NCRP, 1996) screening models to determine which radionuclides are important to GW performance. Considering uncertainty in the time to hydraulic failure of a representative NR cask (750 years), a range of holdup times (500, 750 and 1,000 years) was selected for the model to determine sensitivity to this parameter. The simple screening model accounts for radioactive decay, leaching from the waste zone, and dilution in the aquifer. It does not, however, credit the activated metal component for corrosion-controlled release nor transport and dispersion in the VZ and aquifer. The estimated inventory for each of the 128 radionuclides reported by NR for welded casks is evaluated by this simple model, and the concentration in the aquifer is converted to a dose impact and compared to the EPA BG drinking water limit (Smith et al., 2019). Results of this preliminary GW screening are shown in Table 4-73. Of the 128 radionuclides reported by NR, only 12 exceed 1% (0.01) of the PO after allowing the radionuclides to decay before cask breach at Year 500. Beyond a 750-year holdup period, only nine radionuclides exceed 1% of the PO. The three additional radionuclides not screened out at 500 years (Am-242m, Cs-137, and Sr-90) will be included in sensitivity cases.

Table 4-73. Groundwater Screening: Activated Metal Inventory

Radionuclide	Half-Life (years)	Fraction of PO at Container Breach		
		Year 500	Year 750 (baseline case)	Year 1,000
Am-242m	1.41E+02	1.46E-02	4.27E-03	1.25E-03
C-14	5.70E+03	2.01E+04	1.95E+04	1.90E+04
Cl-36	3.01E+05	8.70E+00	8.70E+00	8.69E+00
Cs-137	3.02E+01	2.02E-02	6.46E-05	2.07E-07
I-129	1.57E+07	5.47E+00	5.47E+00	5.47E+00
Mo-93	4.00E+03	8.15E-01	7.80E-01	7.47E-01
Nb-94	2.03E+04	5.01E+00	4.96E+00	4.92E+00
Ni-59	1.01E+05	4.51E+05	4.50E+05	4.50E+05
Ni-63	1.00E+02	9.85E+06	1.74E+06	3.09E+05
Sr-90	2.88E+01	2.68E-01	6.52E-04	1.59E-06
Tc-99	2.11E+05	1.56E+02	1.56E+02	1.56E+02
Zr-93	1.53E+06	3.72E+00	3.72E+00	3.72E+00

Note: Exceeds 1% (0.01) of the PO

Activated metal projected inventories for the nine radionuclides not screened out in the 750-year holdup case are then compared to the 2013 ET03 UDQE estimated limits to obtain a SOF result. Unlike the screening analysis, the 2013 estimated limits account for transport and dispersion in the VZ and aquifer out to the 100-meter well. Radionuclides contributing more than 0.01 to SOF (BG, All-Pathways, and IHI) are listed in Table 4-74 with SOFs greater than 1.0 highlighted in orange.

Table 4-74. Sum of Fractions: Naval Reactor Component Disposal Area Activated Metal Inventory¹ versus Estimated 2013 Unreviewed Disposal Question Evaluation Limits for ET03

Radionuclide	Fraction of PO							
	GW Protection Pathway ²			GW All-Pathways ³			IHI Pathway	
	BG1	BG2	BG3	AP1	AP2	AP3	Resident	Post Drilling ⁴
C-14	--	--	1.3E+01	--	1.3E+01	2.8E+00	--	3.5E-02
Cl-36	1.5E-01	1.4E-01		--	--	--	--	--
I-129	--	--	--	--	--	--	--	--
Mo-93	--	1.1E-01	4.7E-01	--	8.3E-02	1.0E-01	--	--
Nb-94	6.1E+01	5.9E+01	1.4E+00	2.7E+00	2.7E+00	2.7E+00	7.3E-01	--
Ni-59	--	--	4.8E+02	--	5.1E-01	2.7E+00	--	--
Ni-63	--	--	--	--	--	--	--	--
Tc-99	--	--	9.2E-02	--	1.4E-01	--	--	--
Zr-93	8.5E+00	1.7E+01	1.3E+01	--	2.5E+00	2.8E+00	--	--
Total SOF	7.0E+01	7.6E+01	5.1E+02	2.7E+00	1.9E+01	1.1E+01	7.3E-01	3.5E-02

Notes:

¹ NR projected inventories are allowed to decay for 750 years before release.² BG1 = 0 – 12 years, BG2 = 12 – 100 years, BG3 = 100 – 1,130 years³ AP1 = 130 – 200 years, AP2 = 200 – 1,000 years, AP3 = 1,000 – 1,130 years⁴ Post-drilling chronic exposure IHI scenario.

Compared to the results in Table 4-73, accounting for both transport and dispersion in the model results in a much smaller impact than the simpler screening analysis. However, all GW pathways still exceed a SOF of 1.0. The UDQE limits comparison accounted for container hold-up, but not corrosion-controlled release of radionuclides. Therefore, the NRCDA model for activated metal in welded casks will likely need to credit both container holdup and corrosion-controlled release from highly activated components.

4.7.7. Conceptual Modeling Approach

4.7.7.1. NR26E

The VZ model developed for PA2022 simulates both intact and degraded waste form conditions. Conceptually, all containers are placed on the NR26E pad on the first day of pad operations in 1997 (09/28/1997). Both ACP and activated metal inventory are placed vertically at-grade and uniformly distributed over the NR26E pad footprint. Highly activated metal components are represented by the heavily shielded, welded KAPL CB/TS cask in the model. Justification for this assumption is based on: (1) NR Programs estimates that KAPL CB/TS casks will contain 76% of the total inventory shipped to SRS (see Table 4-75); (2) the KAPL cask has a weld thickness of 1.25 inches which is representative of the minimum weld thickness in all other casks. Surface-contaminated ACP equipment is contained in thinner-walled bolted containers, predominately shear block boxes. Structural fill is placed around and over all the containers on the NR26E pad at the start of IC (09/28/2065).

Table 4-75. NR26E Existing and Projected Inventory through FY2040

Source and Type	Bolted			Welded			Total (curies)	Activity (%)
	Existing	Future	Total	Existing	Future	Total		
Bettis (total)¹	16	10	26	20	0	20	--	--
ICDC ²	N/A			20	0	20	8,270	1.8
Cover Plates ³	8	0	8	N/A			0.0027	5.9E-07
Adapter Flanges ³	8	0	8	N/A			3.5	0.00077
RCP ⁴	0	10	10	N/A			0.57	0.00013
KAPL (total)¹	33	322	355	11	2	13	--	--
CB/TS ⁵	N/A			9	0	9	347,000	76
Closure Heads	1	2	3	N/A			37.3	0.0082
CBDC	N/A			0	2	2	41,200	9.1
Unique	N/A			2	0	2	--	--
S3G	N/A			1	0	1	27,000	5.9
D1G PVA	N/A			1	0	1	30,200	6.6
Shear Blocks	32	320	352	N/A			--	--
Large ⁶	24	240	264	N/A			382	0.084
Small	8	80	88	N/A			113	0.025
TOTAL	49	332	381	31	2	33	454,206	100
Welded (activated metal) Curies							453,670	99.9
Bolted (ACP) Curies							536	0.1
Total Curies							454,206	100

Notes: Table from report by Wohlwend and Butcher (2018)

Abbreviations:

ICDC: Irradiated Component Disposal Container

CB/TS: Core Barrel/Thermal Shield

CBDC: Core Basket Disposal Container

RCP: Reactor Coolant Pumps

¹ From Sink 2016b and 01/21/2016 "Stored Package Age Report for NR1" printout from Kevin Tempel.² All 20 ICDC's onsite per K. Tempel 07/18/2017 personal communication.³ May be relocated to a trench (likely ET) in the future.⁴ Almost certain to place in a trench (either ST or ET).⁵ Assumed to be representative type of activated waste component.⁶ Assumed to be representative type of ACP waste component.

The CB/TS casks are assumed to undergo hydraulic failure at 750 years (estimated time to corrode through minimum 1.25-inch weld); no radionuclides are released from the welded casks until hydraulic failure. Dynamic compaction of the NRCDA before installation of the final closure cap is prohibited to preserve this assumption. Conversely, seals on the bolted containers are assumed to undergo hydraulic failure either immediately when the structural fill is placed (Case 1) or at the time of welded cask failure in 750 years (Case 2). Upon seal failure, ACP contamination is assumed to be instantaneously released into the surrounding soil (i.e., there is no holdup). Baseline generic disposal limits will be based on the minimum of the two seal-failure cases (immediate and at 750 years) for the bolted containers.

Welded casks containing activated metal components are treated as SWFs taking credit for both the welded vessel and activated metal components in calculating SWF limits. The model is executed assuming a unit curie or mole of each parent radionuclide with the resulting dose impacts/concentrations scaled to GW POs to obtain inventory limits. For activated metal components, the unit curie or mole is assumed to decay for 750 years before initiating the model to simulate container holdup. Corrosion-limited release of activated metal utilizes individual radionuclide release rates based on differences in activation product distribution and corrosion rates in Inconel and Zircaloy component parts of a KAPL CB/TS (Yu et al., 2002). Baseline SWF disposal limits are calculated assuming components are effectively either all Inconel or all Zircaloy, and final disposal limits will be selected based on the minimum of these two cases.

Bolted containers with ACP-contaminated equipment are treated as generic waste taking no credit for the container in calculating disposal limits. Again, the model is executed assuming a unit curie or mole of each parent radionuclide with the resulting dose impacts/concentrations scaled to GW POs to obtain inventory limits. Because of the difficulty in determining the impact of daughter ingrowth, ACP waste is modeled assuming decay starts at the beginning of the operational period (09/28/1997).

Contaminant fluxes to the water table serve as inputs to the latest GSA GW flow model using a cutout for the ELLWF (Flach, 2019). Peak GW concentrations at or beyond the 100-meter POA are used to obtain preliminary GW limits. Preliminary limits are initially calculated assuming no time windows. Limits are adjusted for plume overlap with neighboring DUs for final disposal limits. Final limits are assessed to determine if time windows are needed for acceptable performance.

In addition to disposal limits, a closure analysis is performed to demonstrate compliance with DOE 435.1 GW protection requirements and POs. Projected impacts are calculated based on currently disposed-plus-projected NR inventory. The following sensitivity cases are recommended:

- Assume a time for weld breakthrough of 500 years for the CB/TS casks.
- Assume an alternate aquifer model.
- To account for uncertainty in the time to hydraulic failure of bolted containers, superimpose peak GW impacts from ACP components with those from activated metal components (100% plume interaction) as a sensitivity on the amount of overlap between generic and SWF GW plumes.

4.7.7.2. NR07E

Because NR07E has been operationally closed since 1995 and is no longer accepting new inventory, only a closure analysis is performed. A total of 41 NR containers is modeled using the bounding inventory estimates supplied by SWM based on representative worst-case contaminated components (Tempel, 2002). As for NR26E, a heavily shielded, welded KAPL CB/TS cask is assumed to be the representative container for highly activated metal components, while a thinner-walled bolted SBDC is assumed to represent surface-contaminated ACP components. All

containers are placed on the NR07E pad on the first day of disposal operations in 1987 (assumed January 1, 1987). Loose fill was placed around and over all the containers on September 27, 2005.

The welded CB/TS casks are assumed to undergo hydraulic failure 750 years after initially being placed on the NR07E pad in 1987 (January 1, 2737). No corrosion of activated metal components inside the casks is assumed to occur during the 750-year period. Upon hydraulic failure, release of radionuclide contamination from the activated metal is corrosion-limited using individual radionuclide release rates based on differences in activation product distribution and corrosion rates in Inconel and Zircaloy component parts of a KAPL CB/TS. The performance evaluation assumes the components are effectively either all Inconel or all Zircaloy and final dose impacts will be based on the minimum of these two cases. Bolted containers on the NR07E pad, on the other hand, are assumed to have undergone hydraulic failure and instantaneously released contamination in 2005 when the soil fill was placed.

The conceptual model assumes all inventory is placed vertically at grade and is uniformly distributed over the NR07E pad footprint. The VZ and aquifer models are executed to obtain GW concentrations at or beyond the 100-meter boundary. Suggested sensitivity analyses include the impact of an alternate aquifer model, time-of-weld breakthrough, and ACP/activated metal GW plume peak super-positioning. Due to the location of NR07E relative to other ELLWF DUs, plume overlap is an unlikely concern based on GW flow direction and location of the 100-meter boundary for this unit (see Figure 2-78).

Table 4-76 provides a summary of the differences in the proposed modeling approach for the NRCDA in PA2022 versus PA2008.

Table 4-76. Comparison of Proposed Naval Reactor Component Disposal Area Modeling Approach for Current versus 2008 E-Area Low-Level Waste Facility Performance Assessment

Model Feature/ Aspect	PA2022 Approach	PA2008 Approach	Justification
Number of NR26E Containers	Open-ended	100 casks limit	Requested by SWM
Type of Analysis	Limits analysis: model unit curie of each rad for comparison with POs	Preliminary closure analysis: modeled dose impact of projected inventory supplied by NR; scaled results for limits	Requested by SWM
NR07E	Perform closure analysis on final inventory for 41 containers	Applied results of NR26E model to NR07E performance	Changes in flow paths due to new aquifer model
Limits	Separate limits: ACP and activated metal; bolted and welded casks	Single set of limits: combined all forms of inventory into a representative KAPL CB/TS cask	Limits improvement; more realistic plume overlap analysis
VZ Model	Model in same manner as other types of DUs: uniform distribution, placed at grade	No VZ model: projected inventory input directly into aquifer model	Requested by SWM
Modeling Software	PORFLOW for flow and contaminant transport	PORFLOW for flow field; 1-D GoldSim® model for contaminant transport	Use same modeling approach as for other DUs
Data	2016-2019 data packages: rad-dose, geochemical, hydraulic properties	2006 data packages: rad-dose, geochemical, hydraulic properties	Use latest data available
	2016 NR supplied: NR26E inventory projections		
	1990s NR supplied: NR07E inventories; cask and component descriptions		
Disposal Timing	NR07E: instantaneously placed when first container is received (1987)	All inventory for both pads placed on first day of ELLWF trench operations (1995)	More realistic plume overlap analysis
	NR26E: instantaneously placed when first container is received (1997)		

4.7.8. PORFLOW Implementation of Vadose Zone Conceptual Model

The above-grade NRCDA welded casks and bolted containers will be covered with soil or backfilled with CLSM before the installation of the final closure cap system. Release of radionuclides from the waste zone results from hydraulic failure of containers and casks followed by instantaneous release of activated corrosion products and corrosion-controlled release from activated metal components. Released radionuclides are transported by diffusion and convection processes through the VZ. The source term analysis described below focuses on the mechanisms of release of radionuclides in the VZ to ultimately predict the flux at the water table for specific radionuclides of interest.

The 3-D flow and transport models for the VZ have been developed using PORFLOW (ACRi, 2018) and are based on the NRCDA modeling approach proposed by Wohlwend and Butcher (2018) as described in Section 4.7.7. 3-D models are chosen to better accommodate the unique features of the infiltration barriers placed above these facilities.

4.7.8.1. Timelines

Table 2-21 provides a summary of the operational and closure lifecycles for the two NRCDAs that are used to help develop the more detailed modeling timelines for the PORFLOW flow and contaminant transport models.

NRCDA modeling timelines are established to correspond with key facility events for the two disposal pads (NR07E and NR26E). The time window for meeting GW protection requirements (i.e., U.S. EPA MCLs) begins with placement of the first container on each pad and runs until the end of the 1,000-year DOE M 435.1-1, Chg. 3 (U.S. DOE, 2021b) post-closure period. The all-pathways GW PO is evaluated from the end of the 100-year IC period through the end of the 1,000-year post-closure period. Model simulations will run for at least 10,000 years beyond the end of IC to capture GW peaks.

Modeling timelines for all E-Area DUs are calculated in relation to the start of ELLWF operations in 1994. Key modeling assumptions include:

- Each NRCDA pad receives its final inventory (i.e., the inventory at closure) on the date that the first container is placed on each pad. The first-container placement dates are estimated to be January 1, 1987, for NR07E and September 28, 1997, for NR26E; therefore, all subsequent events will involve the total ACP or activated-metal inventory on the pad.
- GW modeling starts at the assumed time for hydraulic failure of the container when initial radionuclide release occurs.
- Hydraulic failures of bolted containers and welded casks will in fact be distributed over time. However, to simplify the analysis, all casks and containers are assumed to fail simultaneously at the times introduced in Section 4.7.7 and summarized in Table 4-77 and Table 4-78 below. Likewise, release of radionuclides from hydraulically failed casks and containers is assumed to occur at the times discussed in these same report sections depending on whether activated metal or activated corrosion products are present.
- Radionuclide decay of waste and corrosion of the outer containers are assumed to begin on the date the NRCDA pads receive waste.

Table 4-77 and Table 4-78 summarize the timelines of facility events and the corresponding GW modeling assumptions for NR07E and NR26E, respectively. Facility and GW modeling events are given in calendar time that is then converted into absolute and relative modeling timelines.

Table 4-77. NR07E Timeline

Calendar Date	Absolute Date	Relative Time	Facility Event	Modeling Assumptions
01/01/1987	1987.003	-7.740	<ul style="list-style-type: none">First container placed in NR07E container storage area, which is subsequently repurposed as a disposal facility (NRCDA) on 06/29/2004 (Wilhite and Flach, 2004).Disposal of the 41 casks and containers is assumed to retroactively start on date of first waste placement.	<ul style="list-style-type: none">All containers placed on pad for disposal at this time.Start of decay for inventory in all 41 containers stored in the NR07E container storage area.Start of corrosion of outer cask or container assuming a soil cover.Start of 1,179-year GW protection compliance period.No corrosion of activated metal components inside welded casks until hydraulic failure in 750 years (Cases 3 and 4).No release of radionuclides from bolted containers until placement of soil cover in 2005 (Case 1) or at time of welded cask hydraulic failure in 750 years (Case 2).
09/28/1994	1994.742	0.000	Start of ELLWF Operations with first containers received in LAWV.	No modeling changes.
09/27/2005	2005.740	10.997	<ul style="list-style-type: none">Soil mounded over 41 containers in NR07E.Case 1: Early hydraulic failure of seals occurs on all bolted containers.	<ul style="list-style-type: none">Case 1: Start of GW flow and transport simulation for bolted containers in NR07E.Radionuclide inventory in bolted containers immediately released to surrounding soil.
09/28/2065	2065.742	71.000	<ul style="list-style-type: none">End of ELLWF Operations and start of IC.No further interim closure actions planned.	No modeling changes.
09/28/2165	2165.742	171.000	<ul style="list-style-type: none">End of IC.Installation of final closure cap.	Start of 1,000-year all-pathways compliance period.
01/01/2737	2737.003	742.260	<ul style="list-style-type: none">Case 2: Late hydraulic failure of seals occurs on all bolted containers.Cases 3 and 4: Hydraulic failure of welds occurs on KAPL CB/TS casks.	<ul style="list-style-type: none">Start of GW flow and transport simulation for casks (Cases 3 and 4) and bolted containers (Case 2).Case 2: Radionuclide inventory in bolted containers immediately released to the surrounding soil.Cases 3 and 4: Start of corrosion-controlled release of radionuclides from welded casks.
09/28/3165	3165.742	1,171.000	N/A	End of GW protection and all-pathways period of performance.
09/28/12165	12165.742	10,171.000	N/A	End of GW model simulation except as needed to capture peaks.

Notes:

Calendar Date = Past (certain or estimated) and future (predicted) dates of facility events relevant to the GW modeling timeline.

Absolute Date = Absolute time is calendar time converted to a numerical value.

Relative Time = Time based on years between event and start of ELLWF operations in 1994 (Year 0).

Facility Event = Past (certain) and future (predicted) facility events relevant to GW modeling timeline.

Time Windows:(1) GW protection limits based on peak release during single 1,179-year time window (relative Year -7.740 to 1,171) and (2) GW all-pathways limits based on peak release during single 1,000-year time window (relative Year 171 to 1,171).

Table 4-78. NR26E Timeline

Calendar Date	Absolute Date	Relative Time	Facility Event	Modeling Assumptions
09/28/1994	1994.742	0.000	– Start of ELLWF Operations with first containers received in LAWV.	N/A
09/28/1997	1997.742	3.000	– First container placed in NR26E.	– All containers placed on pad at this time. – Start of decay for all projected inventory to be disposed of in NR26E. – Start of corrosion of outer cask or container assuming a soil cover. – Start of 1,168-year GW protection compliance period. – No release of radionuclides from bolted containers until placement of soil cover in 2065 (Case 1) or at time of welded cask hydraulic failure 750 years post disposal (Case 2). – No corrosion of activated metal components inside welded casks and no release of radionuclides from welded casks until hydraulic failure in 750 years (Cases 3 and 4).
09/28/2065	2065.742	71.000	– End of ELLWF Operations with no more containers placed on pad. – Start of IC. – Soil mounded over all containers in NR26E. – Case 1: Early hydraulic failure of seals occurs on all bolted SBDCs.	– Case 1: Start of GW flow and transport simulation for bolted containers in NR26E. – Radionuclide inventory in bolted containers immediately released to surrounding soil.
09/28/2165	2165.742	171.000	– End of IC. – Installation of final closure cap.	Start of 1,000-year all-pathways compliance period.
09/28/2747	2747.742	753.000	– Case 2: Late hydraulic failure of seals occurs on all bolted containers. – Cases 3 and 4: Predicted hydraulic failure of welds on all KAPL CB/TS casks.	– Start of GW flow and transport simulation for casks (Cases 3 and 4) and bolted containers (Case 2) in NR26E. – Case 2: Radionuclide inventory in bolted containers immediately released to the surrounding soil. – Cases 3 and 4: Initial corrosion-controlled release of radionuclide inventory from activated metal components to the surrounding soil.
09/28/3165	3165.742	1,171.000	N/A	End of GW protection and all-pathways period of performance.
09/28/12165	12165.742	10,171.000	N/A	End of GW model simulation except as needed to capture peaks.

Notes:

Calendar Date = Past (certain or estimated) and future (predicted) dates of facility events relevant to the GW modeling timeline.

Absolute Date = Absolute time is calendar time converted to a numerical value.

Relative Time = Time based on years between event and start of ELLWF operations in 1994 (Year 0).

Facility Event = Past (certain) and future (predicted) facility events relevant to GW modeling timeline.

Time Windows:(1) GW protection limits based on peak release during single 1,168-year time window (relative Year 3 to 1,171) and (2) GW all-pathways limits based on peak release during single 1,000-year time window (relative Year 171 to 1,171).

4.7.8.2. Hydrostratigraphic Layers

Beneath E-Area, the relationship between the water table and various stratigraphic units is locally complex and is affected by sediment properties (hydraulic conductivity), seasonal and long-term precipitation (recharge), and proximity to Upper Three Runs Creek to the north of the model area. Figure 4-207 by Bagwell and Bennett (2017) illustrates this complexity by the multiple hydrostratigraphic units beneath E-Area. Bagwell and Bennett (2017) provide elevations for all identified subsurface units beneath the corner coordinates of each E-Area DU footprint, from which the average distance above the water table for each hydrostratigraphic surface is derived and shown in Table 4-79.

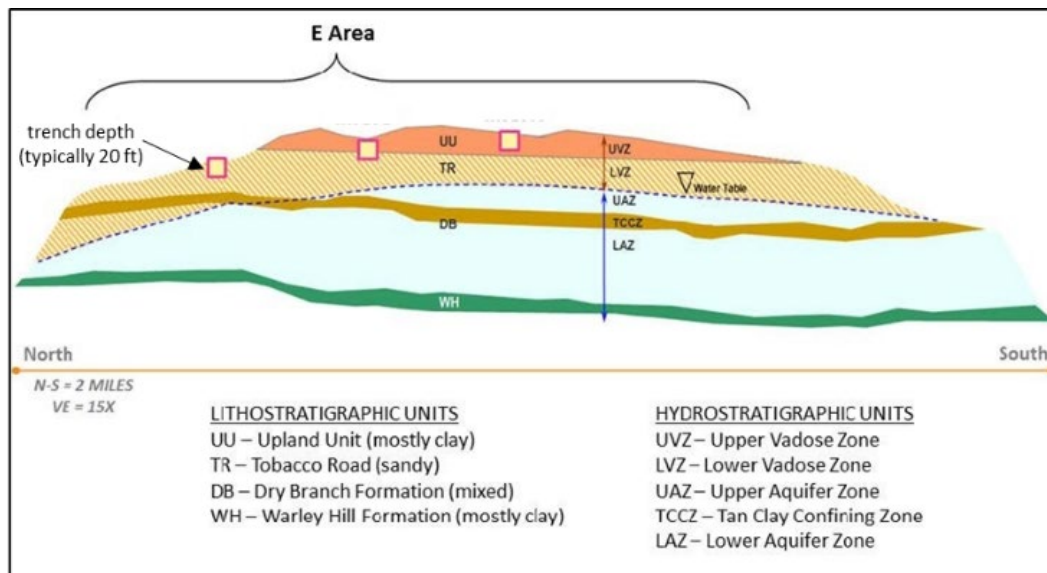


Figure 4-207. Schematic Cross-Section with Underlying Stratigraphic Units in E-Area

Table 4-79. Average Distances of Subsurface Layers to Water Table

Top of Subsurface Zones (Material Type for Model)	Height above Water Table	
	NR07E	NR26E
UVZ (UVZ)	63 feet	75 feet
LVZ (LVZ)	27 feet	57 feet
TCCZ (UVZ)	0	18 feet
LAZ (LVZ)	0	10 feet

Notes:

The average distance to the water table from the original ground surface is 63 feet and 75 feet for NR07E and NR26E, respectively.

Note in Table 4-79 that the water table is located above the TCCZ for NR07E (north side in Figure 4-207) but dips below the TCCZ for NR26E (south side in Figure 4-207), and therefore the distance is shown as zero.

4.7.8.3. Model Geometry

The footprint coordinates for both NRCDA pads are provided by Hamm (2019). Figure 4-208 and Figure 4-209 display the actual layouts (solid black outline) and equivalent footprints (red dashed

outline) modeled for NR07E and NR26E, respectively. For simplification, NRCDA footprints are modeled in the form of a square with an equivalent footprint area. Still, both the actual and equivalent footprints have the same center point (footprint centroid).

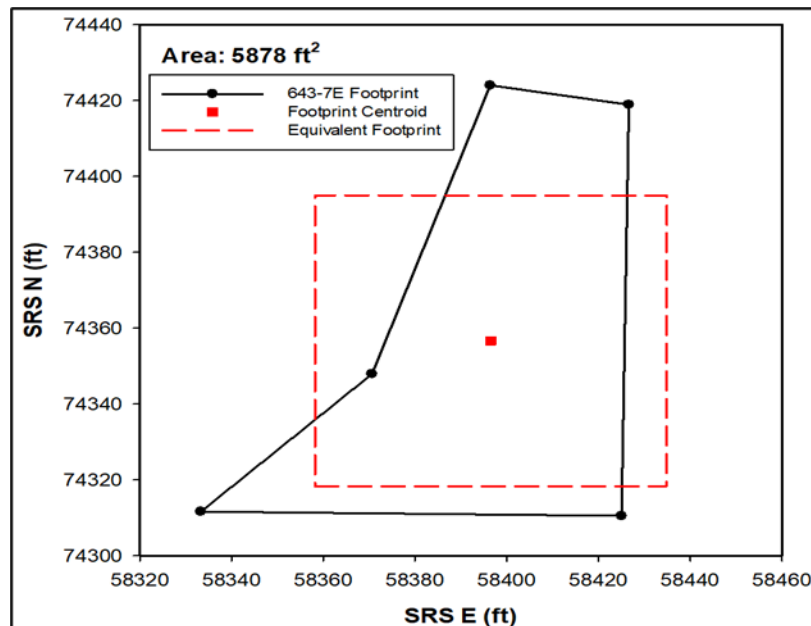


Figure 4-208. NR07E Actual versus Equivalent Model Footprint for PORFLOW Simulations

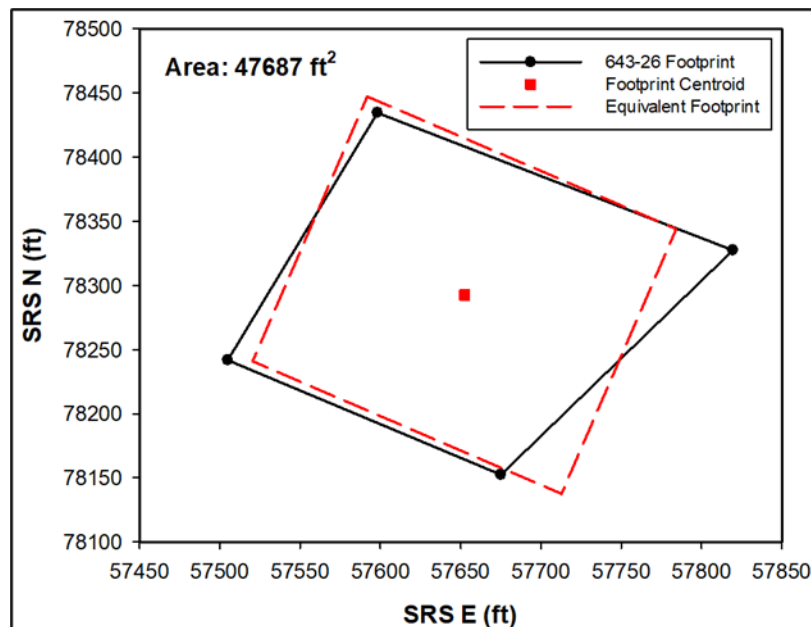


Figure 4-209. NR26E Actual versus Equivalent Model Footprint for PORFLOW Simulations

Because of the different subsurface features, elevations, and disposal pad sizes described here and in Section 4.7.8.2, NR07E and NR26E require separate PORFLOW VZ flow and transport models. Due to their locations in the ELLWF relative to other DUs, different final closure cap configurations are also required for the two NRCDA pads. The NR07E pad is somewhat isolated from the other ELLWF DUs (see Figure 2-78). At the end of the IC period, a final closure cap that

extends 40 feet beyond the edge of the disposal pad on all sides will be placed over NR07E. Beyond the reach of the closure cap is undisturbed soil that extends to the edge of the model domain. On the other hand, NR26E is surrounded by other DUs (i.e., ET03, ET04, and ST08) and can be represented in the PORFLOW model by an essentially infinite cap that extends to the edge of the model domain. Schematics of the NR07E and NR26E conceptual models are shown in Figure 4-210 and Figure 4-211, respectively. Note that the NRCDA VZ models are 3-D; therefore, the dimensions are the same in x- and y-directions.

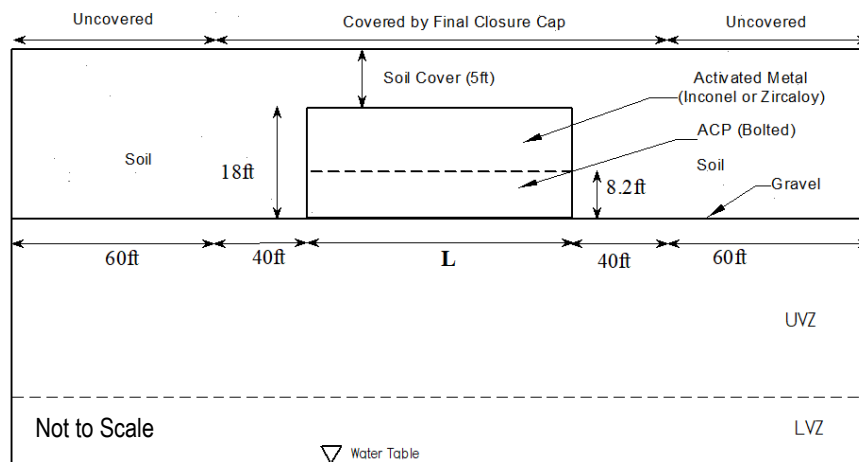


Figure 4-210. NR07E Vadose Zone Conceptual Model Schematic

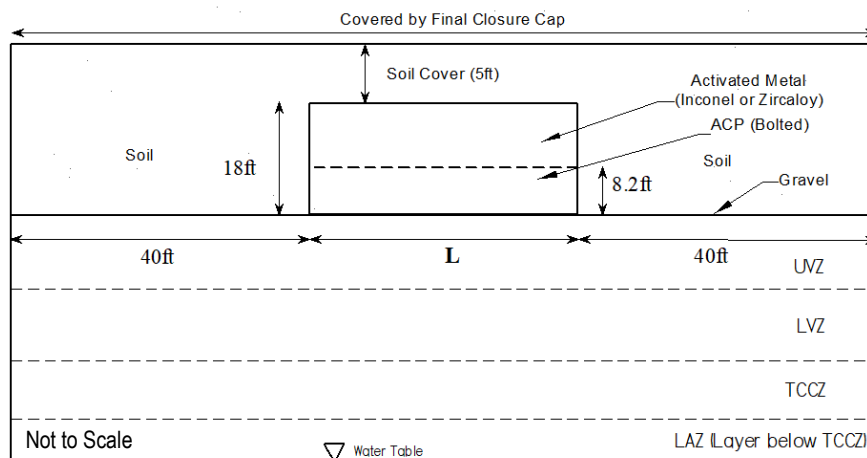


Figure 4-211. NR26E Vadose Zone Conceptual Model Schematic

The two figures, together with Table 4-80, summarize the relevant dimensions of the VZ conceptual models for both NRCDA. In both Figure 4-210 and Figure 4-211, the heights of the KAPL CB/TS welded cask (18 feet) and the double-stacked, large, SBDC bolted container (8.2 feet) are used to represent the waste zone thickness of the activated metal component waste fraction and ACP equipment waste fraction, respectively. Each waste form is modeled separately, and results are subsequently combined in the flux to the water table for aquifer PORFLOW

analyses. Other modeling geometries may be evaluated as potential sensitivity cases based on other stacking scenarios for SBDCs and partial filling of the disposal pad footprint.

Table 4-80. Naval Reactor Component Disposal Area Model Dimensions

Dimension	NR07E	NR26E
Footprint area ¹	546 m ² (5,878 ft ²)	4,430 m ² (47,687 ft ²)
Length (L)	23.37 m (76.67 ft)	66.6 m (218.375 ft)
Average Distance to Water Table ²	63 ft	75 ft

Notes:

¹ Hamm (2019)

² Bagwell and Bennett (2017)

4.7.8.4. Infiltration Boundary Conditions

The base of the final closure cap forms the top boundary of the PORFLOW VZ model. The infiltration rate through the intact closure cap is calculated separately using the HELP model and is provided as an input to the PORFLOW VZ model (Dyer, 2019b). Calculated infiltration rates for the nominal, intact case vary with time as the hydraulic performance of the closure cap degrades. The nominal, intact case is distinguished from closure cap subsidence cases where localized catastrophic failures are assumed to occur with the structural collapse of containers. However, because of the robust nature of NR container and cask designs, coupled with the high density of the internal components/equipment they contain, closure cap subsidence is not considered feasible for the NRCDA. Nominal, intact case infiltration rates for NR26E are listed in Table 4-81 (Dyer, 2019b). The infiltration rates in Table 4-81 apply to the top boundary of the PORFLOW VZ model domain and represent an upper-bound estimate for a closure cap with a minimum slope of 2% and a maximum slope length of 585 feet. Infiltration rates beyond the 10,100 years are set equal to the last value shown in Table 4-81.

The nominal, intact case infiltration rates listed in Table 4-81 are also assumed for the covered portion of the top model boundary for NR07E (i.e., final closure cap plus its 40-foot extension beyond the edge of the NR pad in all directions). Conversely, a nominal infiltration rate of 15.78 in yr⁻¹ applies to the uncovered portion of the model domain (i.e., beyond the 40-foot cap extension).

Table 4-81 also lists the calculated pessimistic case infiltration rates used in the NRCDA sensitivity analyses presented in Section 5.4.1.3. For the nominal, intact case, infiltration rates are based on SRS historical mean monthly rainfall data (49.14 in yr⁻¹ annual average). For the pessimistic, intact case, infiltration rates are based on an annual average rainfall of 61.68 in yr⁻¹ (+0.5 σ based on SRS historical mean monthly rainfall data or +1.6 σ on an annual average basis).

Table 4-81. Intact Case Infiltration Rates for Naval Reactor Component Disposal Area Simulations

Relative Year	Intact Infiltration Rate (in yr ⁻¹) ¹	
	Nominal Case	Pessimistic Case
0 ²	15.78	25.00
100 ³	0.0008	0.002
180	0.007	0.02
290	0.16	0.45
300	0.18	0.49
340	0.3	0.64
380	0.38	0.79
480	1.39	2.80
660	3.23	5.67
1,100	6.82	9.18
1,900	10.24	11.56
2,723	11.10	11.95
3,300	11.18	12.00
5,700	11.30	12.06
10,100 and later	11.35	12.08

Notes:

¹ Dyer (2019b)² Year 0: Beginning of IC period. Structural soil fill only.³ Year 100: End of IC period; installation of final closure cap.**4.7.8.5. PORFLOW Modeling Approach**

The following modeling approach is implemented for the NRCDA PA simulations based on the proposed conceptual model by Wohlwend and Butcher (2018):

1. Model each NRCDA in the same manner as other ELLWF DUs [i.e., 1.0 gram mole (gmole) inventories are scaled up to disposal limits based on POs].
2. Entire waste is placed within DUs at the time of first container disposal.
3. For bolted containers, a generic waste form is used. Calculations are performed for two cases from which minimum disposal limits will be selected:
 - Case 1: Immediate release of radionuclides from the containers at the start of IC (NR26E) or upon placement of the initial soil cover (NR07E).
 - Case 2: Release of radionuclides 750 years following waste placement corresponding with hydraulic failure of the welded casks.
4. For welded steel casks, an SWF is considered. Calculations are performed for two cases from which the minimum disposal limits will be selected:
 - Case 3: All radionuclides reside within Inconel with hydraulic failure at 750 years following waste placement.
 - Case 4: All radionuclides reside within Zircaloy with hydraulic failure at 750 years following waste placement.
5. Combined flux at the water table: The total flux for each radionuclide at the water table is a combination of the fluxes resulting from NR components in welded casks and

ACP-contaminated equipment in bolted containers based upon the corresponding inventory ratios.

Table 4-82 and Table 4-83 summarize the flow transport models for the four PORFLOW simulation cases for NR07E and NR26E, respectively. Table 4-84 summarizes the radionuclide transport models for both NR07E and NR26E.

Table 4-82. Cases Considered for NR07E Vadose Zone PORFLOW Flow Modeling

Vadose Zone Model	Description
Vadose7E_Container_Case1	Generic waste form for containers. All containers are placed on pad in 1987 (Year -8 in model time). Immediate release of radionuclides upon early hydraulic failure of bolted containers with placement of soil cover in 2005 (Year 11 in model time)
Vadose7E_Container_Case2	Generic waste form for containers. All containers are placed on pad in 1987 (Year -8 in model time). Immediate release of radionuclides upon late hydraulic failure of bolted containers in 2737 (Year 742 in model time)
Vadose7E_Cask_Case3	Special waste form for activated Inconel . All casks are placed on pad in 1987 (Year -8 in model time). Corrosion-limited release of radionuclides upon hydraulic failure of welded casks in 2737 (Year 742 in model time). No corrosion of activated metal before Year 742 due to insufficient levels of moisture inside the cask.
Vadose7E_Cask_Case4	Special waste form for activated Zircaloy . All casks are placed on pad in 1987 (Year -8 in model time). Corrosion-limited release of radionuclides upon hydraulic failure of welded casks in 2737 (Year 742 in model time). No corrosion of activated metal before Year 742 due to insufficient levels of moisture inside the cask.

Notes:

The end of the compliance period is calendar year 3165 or Year 1,171 in model time.

The flow model is the same in all cases.

Table 4-83. Cases Considered for NR26E Vadose Zone PORFLOW Flow Modeling

Vadose Zone Model	Description
Vadose26E_Container_Case1	Generic waste form for containers. All containers are placed on pad in 1997 (Year 3 in model time). No release of radionuclides until placement of soil cover in 2065 (Year 71 in model time).
Vadose26E_Container_Case2	Generic waste form for containers. All containers are placed on pad in 1997 (Year 3 in model time). Release of radionuclides upon hydraulic failure of bolted containers in 2747 (Year 753 in model time).
Vadose26E_Cask_Case3	Special waste form for activated Inconel . All casks are placed on pad in 1997 (Year 3 in model time). Release of radionuclides upon hydraulic failure of welded casks in 2747 (Year 753 in model time). No corrosion of activated metal before Year 753 due to insufficient levels of moisture inside the cask.
Vadose26E_Cask_Case4	Special waste form for activated Zircaloy . All casks are placed on pad in 1997 (Year 3 in model time). Release of radionuclides upon hydraulic failure of welded casks in 2747 (Year 753 in model time). No corrosion of activated metal before Year 753 due to insufficient levels of moisture inside the cask.

Notes:

The end of the compliance period is calendar year 3165 or Year 1,171 in model time.

The flow model is the same in all cases.

Table 4-84. Cases Considered for NR07E and NR26E Vadose Zone PORFLOW Transport Modeling

Disposal Unit	Waste Form	Waste Material	Release Time	Case ID
NR07E	Generic	Soil	Instantaneous at time of initial soil cover	Case 1
			Instantaneous at 750 years post disposal	Case 2
	Special	Inconel	Corrosion-limited starting 750 years post disposal	Case 3
		Zircaloy		Case 4
NR26E	Generic	Soil	Instantaneous at start of IC	Case 1
			Instantaneous at 750 years post disposal	Case 2
	Special	Inconel	Corrosion-limited starting at 750 years post disposal	Case 3
		Zircaloy		Case 4

4.7.8.5.1. Key Inputs and Assumptions

The following key inputs and assumption supplement all other key inputs and assumptions presented in PA2008 (WSRC, 2008):

- Entire waste is placed within DUs at the time of first burial.
- Immediate NR waste burial is under a soil cover (i.e., ignoring the open-air period). This assumption is conservative because carbon-steel corrosion rates in air are at or below the low end of corrosion rates in soil for atmospheric conditions representative of SRS (Wohlwend and Butcher, 2018).
- The casks are welded shut, while the bolted containers are hydraulically gasket-sealed and are assumed to potentially leak hydraulically much earlier than the casks.
- Corrosion from inside the cask to the outside is expected to be insignificant due to the negligible amount of water present in the casks before being welded shut. Taking these disposal conditions into consideration, corrosion is estimated to penetrate the welds after 750 years of disposal allowing water to enter the disposal casks via small holes in the welds (i.e., hydraulic failure).
- Considering soil instead of CLSM, a flowable soil-cement material used as backfill, as the interim cover material is conservative due to the impact of slightly acidic soil moisture on corrosion of carbon steel.
- Hydraulic failures of bolted containers and welded casks are, in fact, distributed over time. However, to simplify the analysis, all casks and containers are conservatively assumed to fail simultaneously at the times provided in the NRCDA timelines for NR07E and NR26E (Table 4-77 and Table 4-78, respectively). Likewise, release of radionuclides from hydraulically failed casks and containers is assumed to occur at these provided times.
- Radionuclide decay of waste and corrosion of the outer container are assumed to start from the date the pad receives waste.
- Due to the robust nature of NR container and cask designs, and the density of the internal component/equipment they contain, significant subsidence is not considered feasible for the NRCDA.

4.7.8.5.2. Rate of Generic Waste Release

For generic waste, radioactive material contained within the Waste Zone is assumed to be instantaneously available for transport (i.e., no rate-limiting mechanism is included in the PORFLOW model). Release can occur at any chosen point in time. For the cases listed in Table 4-84, the time of release for generic waste is:

- Case 1: Start of IC or application of a soil cover
- Case 2: 750 years after waste placement

At the time of release, the waste is assumed to be completely available for local interaction with the porous media and subsequent transport.

In PORFLOW transport simulations, a generic waste is handled by setting a specified inventory uniformly distributed throughout the Waste Zone. Generally, 1.0 gmole of the parent radionuclide of interest is placed within the Waste Zone. This inventory placement is made on the date each pad received the first container and the material is assumed to be available for transport once hydraulic failure occurs.

4.7.8.5.3. Rate of Special Waste Form Release

For SWFs, a rate-limiting mechanism and/or a delayed release (holdup) is considered. For the Inconel and Zircaloy reactor components, the radioactive constituents are embedded throughout the metal material. For actual physical release and transport to occur, the surface material must first corrode away. Therefore, for this SWF, a corrosion-based, rate-limited process that proceeds from the surface to the interior of the component is assumed. The distribution throughout the metal component is assumed to be uniform, where a constant peaking factor is applied to account for the spatially varying neutron flux field during reactor operations. The release rate from one of the metal components (either Inconel or Zircaloy) is the product of fractional corrosion rate (yr^{-1}), λ_I or λ_Z , and the inventory (Ci), $I_{\text{Inconel},i}(t)$ or $I_{\text{Zircaloy},i}(t)$.

The overall release rate for any radionuclide from activated metal stored in a welded steel cask is defined in Section 4.7.1.2. This SWF (a corrosion-limited release mechanism) is handled within PORFLOW by using source term tables entered through “INCLude” files for each species within the short chain. By combining the rate equation and the fractional corrosion rate parameters listed in Table 4-67, the individual release rates for activated waste Inconel and Zircaloy components are derived as follows.

For Inconel activated metal:

$$R_i(t) = (6.2194 \times 10^{-5} \text{ yr}^{-1}) I_{\text{Inconel},i}(t) \quad \text{Eq. (4-54)}$$

where:

$I_{\text{Inconel},i}(t)$ total inventory of the i^{th} radionuclide in activated Inconel (Ci)

For Zircaloy activated metal:

$$R_i(t) = (9.5832 \times 10^{-6} \text{ yr}^{-1}) I_{\text{Zircaloy},i}(t) \quad \text{Eq. (4-55)}$$

where:

$I_{\text{Zircaloy},i}(t)$ Total inventory of the i^{th} radionuclide in activated Zircaloy (Ci)

Note that Eq. (4-54) and Eq. (4-55) do include the radioactive decay of each member in the short chain [i.e., $I_i(t)$] that is computed externally to the PORFLOW analysis and then brought into the analysis by way of timetables through INCLude files. An example of these source-term files was extracted from the Am-241 input deck for NR07E/Inconel:

```
/Define source release
INCLude ".../.../Common/Sources/Am-241/Source_7E_Inconel_Am-241.dat"
INCLude ".../.../Common/Sources/Am-241/Source_7E_Inconel_Np-237.dat"
INCLude ".../.../Common/Sources/Am-241/Source_7E_Inconel_U-233.dat"
INCLude ".../.../Common/Sources/Am-241/Source_7E_Inconel_Th-229.dat"
```

The computed metal corrosion rates are in units of gmol yr^{-1} per gmole of parent buried. Radioactive decay (and ingrowth of progeny) begins at the time of disposal, while actual corrosion does not begin until hydraulic failure (i.e., leaking) of the casks occurs (i.e., assumed 750 years after disposal). The release of material continues until the entire mass of buried material has corroded away. Corrosion is assumed to be minimal while the casks are hydraulically isolated from the local environment because limited quantities of reactants exist within the casks upon their closure. Based on their corrosion rates and average component thicknesses, the following corrosion time periods are considered for complete corrosion: 16,079 years for Inconel and 104,349 years for Zircaloy.

An example of the source term from corrosion of Inconel is provided in Figure 4-212 which shows the release rate over time for Am-241 and its daughters Np-237, U-233, and Th-229 in NR07E welded casks. Note that a 1.0 gmole inventory of Am-241 is assumed at the time of burial (i.e., none of its decay daughter is present initially). The corrosion rate is assumed to be zero for the first 750 years after burial (or 742 years in model simulation time), the Inconel then corrodes at a constant material rate for 16,079 years (i.e., until 16,821 years in model simulation time), and finally the corrosion rate returns to zero beyond that time (i.e., no Inconel material is left). As Figure 4-212 illustrates, the source term for Am-241 continually declines during this period because of its decay, while its daughters are generated.

Similar source term files are created for every parent (and its progeny) for both Inconel and Zircaloy. Because the corrosion rates and release rates are independent of waste zone properties, the source term files are computed externally and then employed in subsequent PORFLOW transport simulations.

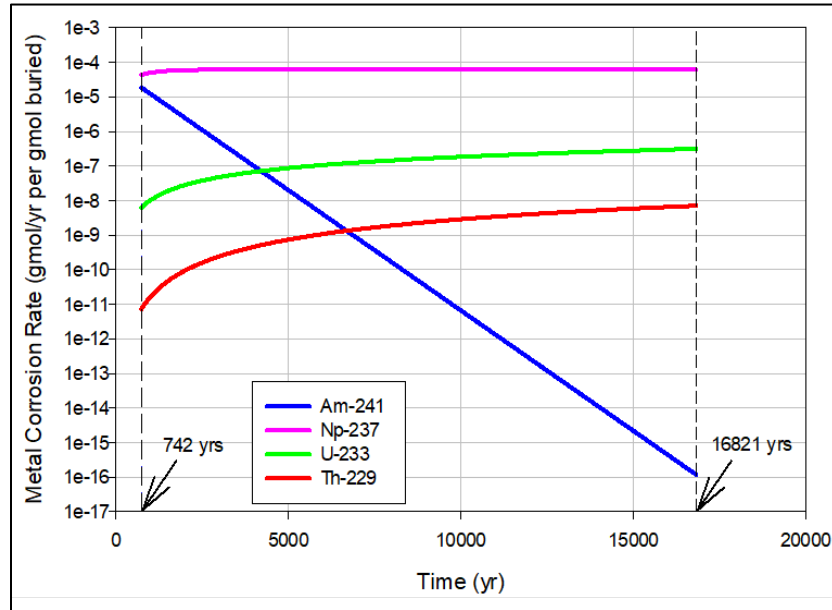


Figure 4-212. Metal Corrosion Rate Release from NR07E/Inconel for Am-241 and Daughters Np-237, U-233, and Th-229

4.7.8.5.4. Radioactive Decay and Growth

The relationship between a parent radionuclide and its daughter radionuclides is discussed here. The mass of each daughter radionuclide is determined by two processes: (1) radioactive decay and (2) radioactive growth by decay of the parent radionuclide, respectively. Consider a chain of decaying nuclei of arbitrary length:

$$(1) \rightarrow (2) \rightarrow (3) \rightarrow \dots \rightarrow (n) \rightarrow$$

Assuming no daughter nuclei are present at time $t = 0$, the mass (N_n) of radionuclide n at time t is calculated by Loveland et al. (2017):

$$N_n = C_1 e^{-\lambda_1 t} + C_2 e^{-\lambda_2 t} + C_3 e^{-\lambda_3 t} + \dots + C_n e^{-\lambda_n t} \quad \text{Eq. (4-56)}$$

where:

$$C_1 = \frac{\lambda_1 \lambda_2 \dots \lambda_{n-1}}{(\lambda_2 - \lambda_1)(\lambda_3 - \lambda_1) \dots (\lambda_n - \lambda_1)} N_1^o \quad \text{Eq. (4-57)}$$

$$C_2 = \frac{\lambda_1 \lambda_2 \dots \lambda_{n-1}}{(\lambda_1 - \lambda_2)(\lambda_3 - \lambda_2) \dots (\lambda_n - \lambda_2)} N_1^o \quad \text{Eq. (4-58)}$$

$$C_3 = \frac{\lambda_1 \lambda_2 \dots \lambda_{n-1}}{(\lambda_1 - \lambda_3)(\lambda_2 - \lambda_3) \dots (\lambda_n - \lambda_3)} N_1^o \quad \text{Eq. (4-59)}$$

$$C_n = \frac{\lambda_1 \lambda_2 \dots \lambda_{n-1}}{(\lambda_1 - \lambda_n)(\lambda_2 - \lambda_n) \dots (\lambda_{n-1} - \lambda_n)} N_1^o \quad \text{Eq. (4-60)}$$

and

N_i Mass of radionuclide i in the chain present at time t (g)

N_1^o Initial mass of the parent radionuclide ($i = 1$) (g)

λ_i Decay constant of radionuclide i (yr^{-1})

For illustration, consider a parent radionuclide with 4 daughters [e.g., Pu-241 (1), Am-241 (2), Np-237 (3), U-233 (4), and Th-229 (5)].

Parent radionuclide:

$$N_1 = N_1^o e^{-\lambda_1 t} \quad \text{Eq. (4-61)}$$

Daughter 1:

$$N_2 = \lambda_1 N_1^o \left(\frac{e^{-\lambda_1 t}}{(\lambda_2 - \lambda_1)} + \frac{e^{-\lambda_2 t}}{(\lambda_1 - \lambda_2)} \right) \quad \text{Eq. (4-62)}$$

Daughter 2:

$$N_3 = \lambda_1 \lambda_2 N_1^o \left(\frac{e^{-\lambda_1 t}}{(\lambda_2 - \lambda_1)(\lambda_3 - \lambda_1)} + \frac{e^{-\lambda_2 t}}{(\lambda_1 - \lambda_2)(\lambda_3 - \lambda_2)} + \frac{e^{-\lambda_3 t}}{(\lambda_1 - \lambda_3)(\lambda_2 - \lambda_3)} \right) \quad \text{Eq. (4-63)}$$

Daughter 3:

$$N_4 = \lambda_1 \lambda_2 \lambda_3 N_1^o \left(\frac{\frac{e^{-\lambda_1 t}}{(\lambda_2 - \lambda_1)(\lambda_3 - \lambda_1)(\lambda_4 - \lambda_1)} + \frac{e^{-\lambda_2 t}}{(\lambda_1 - \lambda_2)(\lambda_3 - \lambda_2)(\lambda_4 - \lambda_2)}}{\frac{e^{-\lambda_3 t}}{(\lambda_1 - \lambda_3)(\lambda_2 - \lambda_3)(\lambda_4 - \lambda_3)} + \frac{e^{-\lambda_4 t}}{(\lambda_1 - \lambda_4)(\lambda_2 - \lambda_4)(\lambda_3 - \lambda_4)}} \right) \quad \text{Eq. (4-64)}$$

Daughter 4:

$$N_5 = \lambda_1 \lambda_2 \lambda_3 \lambda_4 N_1^o \left(\frac{\frac{\frac{e^{-\lambda_1 t}}{(\lambda_2 - \lambda_1)(\lambda_3 - \lambda_1)(\lambda_4 - \lambda_1)(\lambda_5 - \lambda_1)} + \frac{e^{-\lambda_2 t}}{(\lambda_1 - \lambda_2)(\lambda_3 - \lambda_2)(\lambda_4 - \lambda_2)(\lambda_5 - \lambda_2)}}{\frac{e^{-\lambda_3 t}}{(\lambda_1 - \lambda_3)(\lambda_2 - \lambda_3)(\lambda_4 - \lambda_3)(\lambda_5 - \lambda_3)} + \frac{e^{-\lambda_4 t}}{(\lambda_1 - \lambda_4)(\lambda_2 - \lambda_4)(\lambda_3 - \lambda_4)(\lambda_5 - \lambda_4)}}}{\frac{e^{-\lambda_5 t}}{(\lambda_1 - \lambda_5)(\lambda_2 - \lambda_5)(\lambda_3 - \lambda_5)(\lambda_4 - \lambda_5)}} \right) \quad \text{Eq. (4-65)}$$

The mass decay and ingrowth for Pu-241 and its daughters in NR07E welded casks are shown in Table 4-85. From the calculated radionuclide mass inventory, the release rates for activated Inconel and Zircaloy are obtained by applying release rate equations Eq. (4-54) and Eq. (4-55), respectively, as presented in Section 4.7.8.5.3. The release rates are then used as source terms in PORFLOW radionuclide transport runs.

Table 4-85. Decay and Ingrowth for Pu-241 and its Daughters in NR07E Welded Casks

Time (year)	Pu-241 (gmol)	Am-241 (gmol)	Np-237 (gmol)	U-233 (gmole)	Th-229 (gmol)
-8.00	1	0	-2.8E-16	0	2.66E-19
0.00	0.679483	0.318339	0.002179	1.94E-09	1.72E-14
741.99	1.85E-16	0.310665	0.689239	9.67E-05	1.1E-07
742.00	1.85E-16	0.31066	0.689244	9.67E-05	1.1E-07
752.00	1.14E-16	0.305717	0.694184	9.89E-05	1.14E-07
762.00	7.03E-17	0.300853	0.699046	0.000101	1.18E-07
16,802	0	2.02E-12	0.994787	0.005033	0.000114
16,812	0	1.99E-12	0.994784	0.005036	0.000114
16,821	0	1.96E-12	0.994781	0.005039	0.000114
16,821.01	0	1.96E-12	0.994781	0.005039	0.000114
500,000	0	0	0.850916	0.059132	0.002717

4.7.8.5.5. Generic and Special Waste Form Modeling

The list of parent radionuclides consistent with GW screening criteria (Aleman and Hamm, 2021) considered in these transport cases is provided in Table 4-86 along with radionuclide decay and elemental chemical properties (Kaplan, 2016b). For simplification, the NRCDA waste zone composed of bolted containers (generic waste form) and welded casks (SWF) is assigned the same material properties (“NRcontainerLeak”) [see Table 4-68]. Because the release of inventory for both the generic and SWFs is zero before being available for transport, the transport properties for both waste forms (Waste Zones) can be established at the beginning of the PORFLOW transport run with K_d equal to $1\text{E}+20$ and D_e equal to 0.0 (zero diffusivity). Both K_d and D_e will be changed to their actual values at the time of inventory release as specified in Table 4-83 and Table 4-84.

Table 4-86. List of Parent Radionuclides Considered in PORFLOW Vadose Zone Transport Models

Parent Radionuclide	Waste Form	Half-Life (years)	Sand K_d (mL g ⁻¹)	Clay K_d (mL g ⁻¹)
Am-241	Generic, Special	4.322E+02	1,100	8,500
Be-10	Special	1.510E+06	5	17
C-14	Generic, Special	5.700E+03	1	30
Cl-36	Generic, Special	3.010E+05	1	8
Cs-135	Generic	2.300E+06	10	50
H-3	Generic	1.232E+01	0	0
I-129	Generic, Special	1.507E+07	1	3
Ni-59	Generic, Special	1.010E+05	7	30
Ni-63	Generic, Special	1.001E+02	7	30
Np-237	Generic, Special	2.144E+06	3	9
Pu-241	Generic, Special	1.435E+01	650	6,000
Sr-90	Generic	2.879E+01	5	17
Tc-99	Generic, Special	2.111E+05	0.6	1.8
U-235	Generic, Special	7.040E+08	300	400

4.8. REFERENCES

- ACRi (2018). "PORFLOW User's Manual, Keyword Commands Version 6.42.9, Revision 0." Analytical & Computational Research, Inc., Los Angeles, CA. April 23, 2018.
- Aleman, S. E. (2019). "Savannah River National Laboratory Dose Toolkit." SRNL-TR-2019-00337, Rev. 0. Savannah River National Laboratory, Aiken, SC.
- Aleman, S. E., and Hamm, L. L. (2021). "E-Area Low-Level Waste Facility Multitiered Groundwater and Intruder Radionuclide Screening." SRNL-STI-2020-00566, Rev. 0. Savannah River National Laboratory, Aiken, SC. January 2021.
- Bagwell, L. A., and Bennett, P. L. (2017). "Elevation of Water Table and Various Stratigraphic Surfaces Beneath E-Area Low Level Waste Disposal Facility." SRNL-STI-2017-00301, Rev. 1. Savannah River National Laboratory, Aiken, SC.
- Bagwell, L. A., Bennett, P. L., and Flach, G. P. (2017). "General Separations Area (GSA) Groundwater Flow Model Update: Hydrostratigraphic Data." SRNL-STI-2016-00516. Savannah River National Laboratory, Aiken, SC.
- BMPC-KAPL (2009a). "Container Approval Request (Large)." CAR-SWE-2009-00004, Rev. 0. Bechtel Marine Propulsion Corporation – Knolls Atomic Power Laboratory, Schenectady, NY. December 2009.
- BMPC-KAPL (2009b). "Container Approval Request (Small)." CAR-SWE-2009-00003, Rev. 0. Bechtel Marine Propulsion Corporation – Knolls Atomic Power Laboratory, Schenectady, NY. December 2009.
- Butcher, B. T. (2018f). "Summary of Meeting on Changes in Naval Reactor Component Waste and Container Types since 2008 E-Area Performance Assessment (B. T. Butcher to K. L. Tempel)." SRNL-L3200-2018-00129. Savannah River National Laboratory, Aiken, SC. October 30, 2018.
- Butcher, B. T., and Phifer, M. A. (2016a). "Strategic Plan for Next E-Area Low-Level Waste Facility Performance Assessment." SRNL-STI-2015-00620, Rev. 0. Savannah River National Laboratory, Aiken, SC. February 2016.
- C-CT-E-00083 (2016). Preliminary E-Area Low Level Waste Facility (ELLWF) Conceptual Closure Cap – Overall Site Plan (Sheets 1 of 5 through 5 of 5, Rev. A). Savannah River Nuclear Solutions, Aiken, SC. July 20, 2016.
- C-CT-E-00084 (2016). Preliminary E-Area Low Level Waste Facility (ELLWF) Conceptual Closure Cap – Details (Sheet 1 of 4 through 4 of 4, Rev. A). Savannah River Nuclear Solutions, Aiken, SC. July 20, 2016.
- C-CV-E-00207 (2016). West E-Area Slit Trenches & 643-26E Location Plan, Section & Details (Revision 7). Savannah River Nuclear Solutions, Aiken, SC. September 21, 2016.
- Carey, S. (2005). "Low Activity Waste (LAW) Vault Structural Degradation Prediction." T-CLC-E-00018, Rev. 1. Westinghouse Savannah River Company, Aiken, SC. October 27, 2005.

Chandler, G. T. (1998). "Corrosion Evaluation of Accelerator Production of Tritium and Tritium Extraction Facility Low-Level Waste Forms and Disposal Boxes in the E-Area Vaults." SRT-MTS-98-2028. Washington Savannah River Company, Aiken, SC. August 7, 1998.

Collard, L. B. (2000). "Special Analysis for Disposal of High-Concentration I-129 Waste in the Intermediate-Level Vaults at the E-Area Low-Level Waste Facility." WSRC-RP-99-01070, Rev. 1. Westinghouse Savannah River Company, Aiken, SC. July 31, 2000.

Collard, L. B. (2001). "Special Analysis for Disposal of High-Concentration I-129 Waste in Slit Trenches at the E-Area Low-Level Waste Facility." WSRC-TR-2001-00021, Rev. 0. Westinghouse Savannah River Company, Aiken, SC.

Collard, L. B. (2003). "Special Analysis: Disposal of ETF Activated Carbon Vessels in Slit Trenches at the E-Area Low-Level Waste Facility." WSRC-TR-2003-00255, Rev. 0. Westinghouse Savannah River Company, Aiken, SC.

Cook, J. R., McDowell-Boyer, L., Yu, A. D., Kocher, D. C., Wilhite, E. L., Holmes-Burns, H., and Young, K. E. (1999). "Special Analysis for Disposal of Cement-Stabilized Encapsulated Waste at the E-Area Low-Level Waste Facility." WSRC-RP-99-00596, Rev. 0. Westinghouse Savannah River Company, Aiken, SC. December 8, 1999.

Cook, J. R., and Yu, A. D. (2002). "Special Analysis: Disposal of M-Area Glass in Trenches." WSRC-TR-2002-00337, Rev. 1. Westinghouse Savannah River Company, Aiken, SC.

Danielson, T. L. (2019a). "A Limited-In-Scope Comparison of Subsidence Scenarios for 3D Vadose Zone PORFLOW Trench Models." SRNL-STI-2019-00636, Rev. 1. Savannah River National Laboratory, Aiken, SC.

Danielson, T. L. (2019b). "A Monte Carlo Rectangle Packing Algorithm for Identifying Likely Spatial Distributions of Final Closure Cap Subsidence in the E-Area Low-Level Waste Facility." SRNL-STI-2019-00440, Rev. 0. Savannah River National Laboratory, Aiken, SC.

Danielson, T. L. (2019c). "PORFLOW Implementation of Vadose Zone Conceptual Model for Slit and Engineered Trenches in the E-Area Low Level Waste Facility Performance Assessment." SRNL-STI-2019-00193. Savannah River National Laboratory, Aiken, SC.

Danielson, T. L. (2020a). "A Case Study Using ST06 for Slit and Engineered Trench Model Implementation in the E-Area Low-Level Waste Facility Performance Assessment." SRNL-STI-2019-00750, Rev. 0. Savannah River National Laboratory, Aiken, SC.

Danielson, T. L. (2020b). "Comparison of Slit Trench and Engineered Trench 3D Vadose Zone Conceptual Models." SRNL-STI-2019-00637, Rev. 0. Savannah River National Laboratory, Aiken, SC.

Danielson, T. L. (2020c). "Component-In-Grout Model Implementation for the E-Area Low-Level Waste Facility's Performance Assessment." SRNL-STI-2020-00365, Rev. 0. Savannah River National Laboratory, Aiken, SC. September, 2020.

Danielson, T. L. (2021). "PORFLOW Implementation of Special Waste Form Models for Slit and Engineered Trenches in the E-Area Low Level Waste Facility Performance Assessment (T. L. Danielson to D. A. Crowley)." SRNL-STI-2020-00162, Rev. 1. Savannah River National Laboratory, Aiken, SC.

Datovech, R. J. (1994). "Disposal Container Corrosion Issues (Attachment 2 to WAPD-SEA(RE)MD-23)." October 17, 1994.

Dunn, K. A. (2002). "B-25 Corrosion Evaluation Summary Report (U)." WSRC-TR-2001-00587. Westinghouse Savannah River Company, Aiken, SC.

Dyer, J. A. (2017b). "Conceptual Modeling Framework for E-Area PA HELP Infiltration Model Simulations." SRNL-STI-2017-00678. Savannah River National Laboratory, Aiken, SC.

Dyer, J. A. (2017d). "Recommended Henry's Law Constants for Non-Groundwater Pathways Models in GoldSim." SRNL-STI-2017-00331. Savannah River National Laboratory, Aiken, SC.

Dyer, J. A. (2018a). "Impact of Different Vegetative Cover Scenarios on Infiltration Rates for the E-Area PA Intact Case." SRNL-STI-2018-00141, Rev. 0. Savannah River National Laboratory, Aiken, SC.

Dyer, J. A. (2018b). "Method for Including Uncertainty in Infiltration Rates in the E-Area PA System Model." SRNL-STI-2018-00121, Rev. 0. Savannah River National Laboratory, Aiken, SC.

Dyer, J. A. (2019b). "Infiltration Data Package for the E-Area Low-Level Waste Facility Performance Assessment." SRNL-STI-2019-00363, Rev. 0. Savannah River National Laboratory, Aiken, SC. November 2019.

Dyer, J. A. (2019c). "Justification for Use of the HELP Model to Estimate Infiltration Rates for the E-Area Low-Level Waste Facility Performance Assessment." SRNL-STI-2019-00362, Rev. 0. Savannah River National Laboratory, Aiken, SC.

Dyer, J. A., and Flach, G. P. (2017). "E-Area LLWF Vadose Zone Model: Probabilistic Model for Estimating Subsided-Area Infiltration Rates." SRNL-STI-2017-00729, Rev. 0. Savannah River National Laboratory, Aiken, SC.

Dyer, J. A., and Flach, G. P. (2018). "Infiltration Time Profiles for E-Area LLWF Intact and Subsidence Scenarios." SRNL-STI-2018-00327, Rev. 0. Savannah River National Laboratory, Aiken, SC.

Flach, G. P. (2017c). "Method for Modeling the Gradual Physical Degradation of a Porous Material (Greg Flach to Tom Butcher)." SRNL-STI-2017-00525. Savannah River National Laboratory, Aiken, SC. September 20, 2017.

Flach, G. P. (2019). "Updated Groundwater Flow Simulations of the Savannah River Site General Separations Area." SRNL-STI-2018-00643, Rev. 0. Savannah River National Laboratory, Aiken, SC.

Flach, G. P., Collard, L. B., Phifer, M. A., Crapse, K. P., Dixon, K. L., Koffman, L. D., and Wilhite, E. L. (2005). "Preliminary Closure Analysis for Slit Trenches #1 and #2." WSRC-TR-2005-00093. Westinghouse Savannah River Company, Aiken, SC.

Flach, G. P., and Jones, W. E. (2010). "Unreviewed Disposal Question Evaluation: Disposal of Tall Used Equipment Storage Boxes in Slit Trench Numbers 8, 9 and 10." SRNL-STI-2010-00799, Rev. 0. Savannah River National Laboratory Aiken, SC.

Flach, G. P., Smith, F. G., Hamm, L. L., and Butcher, B. T. (2014). "Unreviewed Disposal Question Evaluation: Impact of New Information since 2008 PA on Current Low-Level Solid Waste Operations." SRNL-STI-2013-00011, Rev. 1. Savannah River National Laboratory, Aiken, SC.

Flach, G. P., and Whiteside, T. S. (2016). "Interpretation of Vadose Zone Monitoring System Data near Engineered Trench 1." SRNL-STI-2016-00546, Rev. 0. Savannah River National Laboratory, Aiken, SC.

Gorensek, M. B. (2021). "Updated Estimate of Tritium Permeation from TPBAR Disposal Containers in ILV (U)." SRNL-TR-2020-00298, Rev. 1. Savannah River National Laboratory, Aiken, SC. December 7, 2021.

Hamm, L. L. (2019). "Confirmation of Disposal Unit Footprints for Use in E-Area Performance Assessment Revision." SRNL-STI-2019-00205, Rev. 0. Savannah River National Laboratory, Aiken, SC.

Hamm, L. L., Aleman, S. E., Danielson, T. L., and Butcher, B. T. (2018). "Special Analysis: Impact of Updated GSA Flow Model on E-Area Low-Level Waste Facility Groundwater Performance." SRNL-STI-2018-00624, Rev. 0. Savannah River National Laboratory, Aiken, SC.

Hamm, L. L., Collard, L. B., Aleman, S. E., Gorensek, M. B., and Butcher, B. T. (2012). "Special Analysis for Slit Trench Disposal of the Reactor Process Heat Exchangers." SRNL-STI-2012-00321, Rev. 0. Savannah River National Laboratory, Aiken, SC.

Hamm, L. L., and Smith, F. G. (2010). "Special Analysis for Slit Trench Disposal of the Heavy Water Components Test Reactor." SRNL-STI-2010-00574, Rev. 0. Savannah River National Laboratory, Aiken, SC.

Hamm, L. L., Smith, F. G., Flach, G. P., Hiergesell, R. A., and Butcher, B. T. (2013). "Unreviewed Disposal Question Evaluation: Waste Disposal In Engineered Trench #3." SRNL-STI-2013-00393, Rev. 0. Savannah River National Laboratory, Aiken, SC.

Hang, T., and Hamm, L. L. (2022). "PORFLOW Implementation of Vadose Zone Conceptual Model for Naval Reactor Component Disposal Areas in the E-Area Low Level Waste Facility Performance Assessment." SRNL-STI-2019-00357, Rev. 1. Savannah River National Laboratory, Aiken, SC. January 2022.

Hiergesell, R. A. (2004). "Special Analysis: Re-Evaluation of the Slit Trench Uranium Disposal Limits with Implications for Disposal of the Paducah Demonstration Cask." WSRC-TR-2003-00521, Rev. 0. Westinghouse Savannah River Company, Aiken, SC.

Hiergesell, R. A. (2005). "Special Analysis: Production TPBAR Waste Container Disposal Within the Intermediate Level Vault." WSRC-TR-2005-00531. Westinghouse Savannah River Company, Aiken, SC.

Hsu, R. H., and Roddy, N. S. (1997). "Response to Naval Reactor Comments on WSRC-RP-94-218, Appendix L, 'NR Waste Disposal Performance Assessment'." SRT-WED-97-0159. Washington Savannah River Company, Aiken, SC. February 18, 1997.

Jenkins, J. F. (1993). "Corrosion Behavior of HY-80 Steel, Type 304 Stainless Steel, and Inconel Alloy 500 at 218-E-12B Burial Ground, Hanford, WA." TR-2001-SHR. Naval Facilities Engineering Service Center, Port Hueneme, CA.

Jones, W. E., and Phifer, M. A. (2007). "E-Area Low-Activity Waste Vault Subsidence Potential and Closure Cap Performance (U)." WSRC-TR-2005-00405. Washington Savannah River Company, Aiken, SC.

Jones, W. E., Phifer, M. A., and Kukreja, J. (2004). "Unreviewed Disposal Question Evaluation: Components-In-Grout Options for Structural Stability – Component Filling, Component Stability, or Concrete Mat Cover." WSRC-TR-2004-00039, Rev. 0. Westinghouse Savannah River Company, Aiken, SC.

Kaplan, D. I. (2006). "Geochemical Data Package for Performance Assessment Calculations Related to the Savannah River Site." WSRC-TR-2006-00004, Rev. 0. Washington Savannah River Company, Aiken, SC. February 28, 2006.

Kaplan, D. I. (2010). "Geochemical Data Package for Performance Assessment Calculations Related to the Savannah River Site." SRNL-STI-2009-00473, Rev. 0. Savannah River National Laboratory, Aiken, SC.

Kaplan, D. I. (2012). "Revised Guidelines for using Cellulose Degradation Product-Impacted Kd Values for Performance Assessments and Composite Analyses." SRNL-STI-2012-00138, Rev. 0. Savannah River National Laboratory, Aiken, SC.

Kaplan, D. I. (2016b). "Geochemical Data Package for Performance Assessment Calculations Related to the Savannah River Site." SRNL-STI-2009-00473, Rev. 1. Savannah River National Laboratory, Aiken, SC.

Kaplan, D. I., and Iversen, G. (2001). "Free-Moisture Content and ¹²⁹I-Kd Values of Filtercake Material Generated from the F-Area Groundwater Treatment Unit." WSRC-TR-2001-00253, Rev. 0. Westinghouse Savannah River Company, Aiken, SC. August 17, 2001.

Kaplan, D. I., and Serkiz, S. M. (2000). "¹²⁹Iodine Desorption from Resin, Activated Carbon, and Filtercake Waste Generated from the F- and H-Area Water Treatment Units." WSRC-TR-2000-00308, Rev. 0. Westinghouse Savannah River Company, Aiken, SC. October 26, 2000.

Kaplan, D. I., Serkiz, S. M., and Bell, N. C. (1999). "I-129 Desorption from SRS Water Treatment Media from the Effluent Treatment Facility and the F-Area Groundwater Treatment Facility." WSRC-TR-99-00270. Westinghouse Savannah River Company, Aiken, SC. August 24, 1999.

Lanning, D. D., and Gilbert, E. R. (2005). "Long-Term Release Estimate for TEF Disposal Containers (U)." PNN-TTP-5-683, Rev. 0, S/RD (Extracted information is unclassified). Pacific Northwest National Laboratory, Richland, WA. August 2005.

Logan, K. H. (1939). Engineering Significance of National Bureau of Standards Soil Corrosion Data, J. Research NBS 22, 109 (1939) RP1171. *Underground Corrosion* 273(274), 441-443.

Loveland, W. D., Morrissey, D. J., and Seaborg, G. T. (2017). "Modern Nuclear Chemistry," 2nd/Ed. John Wiley & Sons, Inc.

McDowell-Boyer, L., Yu, A. D., Cook, J. R., Kocher, D. C., Wilhite, E. L., Holmes-Burns, H., and Young, K. E. (2000). "Radiological Performance Assessment for the E-Area Low-Level Waste Facility." WSRC-RP-94-218, Rev. 1. Westinghouse Savannah River Company, Aiken, SC.

Morcillo, M., Chico, B., Díaz, I., Cano, H., and De la Fuente, D. (2013). Atmospheric Corrosion Data of Weathering Steels. A Review. *Corrosion Science* 77, 6-24.

NCRP (1996). "Screening Models for Releases of Radionuclides to Atmosphere, Surface Water and Ground." NCRP Report No. 123 I and II. National Council on Radiation Protection and Measurements, Bethesda, MD. Jan. 22, 1996.

Nichols, R. L., and Butcher, B. T. (2020). "Hydraulic Properties Data Package for the E-Area Soils, Cementitious Materials, and Waste Zones - Update." SRNL-STI-2019-00355, Rev. 1. Savannah River National Laboratory, Aiken, SC.

Peregoy, W. (2006a). "Structural Evaluation of Component-in-Grout Trenches." T-CLC-E-00026, Rev. 0. Washington Savannah River Company, Aiken, SC.

Peregoy, W. (2006b). "Structural Evaluation of Intermediate Level Waste Storage Vaults for Long-Term Behavior." T-CLC-E-00024, Rev. 0. Washington Savannah River Company, Aiken, SC. June 27, 2006.

Phifer, M. A. (2004b). "Unreviewed Disposal Question Evaluation: Low Strength Containers with Compressible Waste in Component-In-Grout Trenches." WSRC-TR-2004-00475, Rev. 0. Westinghouse Savannah River Company, Aiken, SC.

Phifer, M. A. (2010). "Slit Trench Waste Representation (M. A. Phifer to D. A. Crowley)." SRNL-L6200-2010-00018. Savannah River National Laboratory, Aiken, SC.

Phifer, M. A., Crapse, K. P., Millings, M. R., and Serrato, M. G. (2009). "Closure Plan for the E-Area Low-Level Waste Facility." SRNL-RP-2009-00075, Rev. 0. Savannah River National Laboratory, Aiken, SC.

Phifer, M. A., Millings, M. R., and Flach, G. P. (2006). "Hydraulic Property Data Package for the E-Area and Z-Area Vadose Zone Soils, Cementitious Materials, and Waste Zones." WSRC-STI-2006-00198, Rev. 0. Washington Savannah River Company, Aiken, SC.

Phifer, M. A., and Wilhite, E. L. (2001). "Waste Subsidence Potential versus Supercompaction." WSRC-RP-2001-00613. Westinghouse Savannah River Company, Aiken, SC.

Powell, K. R., Kaplan, D. I., and Fondeur, F. (2002). "Resin Longevity Studies." WSRC-TR-2002-00091. Westinghouse Savannah River Company, Aiken, SC.

Romanoff, M. (1957). "Underground Corrosion." Circular 579. National Bureau of Standards, US Government Printing Office, Washington, DC.

Sink, D. F. (2010). "Percentage Waste Volumes in Slit Trenches (e-mail message from D. F. Sink to B. T. Butcher)." Savannah River Nuclear Solutions, Savannah River Site, Aiken, SC. June 7, 2010.

Sink, D. F. (2016a). "643-26E Naval Reactor Component Disposal Area - Revised Radionuclide Inventories at Closure (D. F. Sink to J. L. Mooneyham and M. G. Looper)." SRNS-N4222-2016-00004. Savannah River Nuclear Solutions, Aiken, SC. May 2, 2016.

Sink, D. F. (2016c). "FY16 SWMF Low Level Waste Plan and Disposal Strategies." SRNS-RP-2016-00162, Rev. 0. Savannah River Nuclear Solutions, Aiken, SC. April 2016.

Smith, F. G., III (2021a). "PORFLOW Modeling of Vadose Zone Flow and Transport for the E-Area Intermediate Level Vault." SRNL-STI-2020-00410, Rev. 1. Savannah River National Laboratory, Aiken, SC. December 2021.

Smith, F. G., III (2021b). "PORFLOW Modeling of Vadose Zone Flow and Transport for the E-Area Low Activity Waste Vault." SRNL-STI-2021-00063, Rev. 0. Savannah River National Laboratory, Aiken, SC. February 2021.

Smith, F. G., III, Butcher, B. T., Hamm, L. L., and Kubilius, W. P. (2019). "Dose Calculation Methodology and Data for Solid Waste Performance Assessment and Composite Analysis at the Savannah River Site." SRNL-STI-2015-00056, Revision 1. Savannah River National Laboratory, Aiken, SC. August 2019.

Snider, B. T. (2007). "TEF Waste Containers (U)." M-SPP-H-00418, Rev. 2. Washington Savannah River Company, Aiken, SC. October 8, 2007.

SRNL (2017). "The Hydrostratigraphic Surfaces Data Package [Change Control Rev1 and Rev0 dataset (Appendix 5 to SRNL-STI-2017-00301).xlsx]." Rev. 1. Retrieved August, 2020 from \\godzilla-01\hpc_project\projwork50\QA\Data\ELLWF\SubsurfaceElevDepth. *Last Updated* November 3, 2017. SRNL High Performance Computing File Server Network, Savannah River National Laboratory, Aiken, SC.

SRNL (2018). "The Geochemical Data Package (GeochemPackage_Ver3.1_4-27-18_FINAL.xls)." Version 3.1. Retrieved December, 2018 from \\godzilla-01\hpc_project\projwork50\QA\Data\ELLWF\Rad-Dose. *Last Updated* April 27, 2018. SRNL High Performance Computing File Server Network, Savannah River National Laboratory, Aiken, SC.

SRNL (2019b). "RadDosePackage_Version-2.0_CLEAN_8-13-19_FINAL.xlsx." Version 2.0. Retrieved August, 2019 from \\godzilla-01\hpc_project\projwork50\QA\Data\ELLWF\Rad-Dose\Current\Rev1Report_Ver2.0-Database. SRNL High Performance Computing File Server Network, Savannah River National Laboratory, Aiken, SC.

SRNL (2020). "The Hydraulic Properties Data Package (HydraulicProperties_Rev3_12-01-2020.xlsm)." Rev. 3. Retrieved December, 2020 from \\godzilla-01\hpc_project\projwork50\QA\Data\ELLWF\Material\Current. *Last Updated* December 1, 2020. SRNL High Performance Computing File Server Network, Savannah River National Laboratory, Aiken, SC.

SRNS (2015). "Savannah River Site Ten Year Site Plan FY2016-2025." SRNS-RP-2015-00001. Savannah River Nuclear Solutions, Aiken, SC. June 2015.

SRS (2021c). "Requirements Specification for Software for the Consolidated Waste Tracking System (CWTS)." B-RS-G-00107, Rev. 2. Savannah River Nuclear Solutions, Savannah River Site, Aiken, SC.

Tempel, K. L. (2002). "Radionuclide Inventory Calculation for 643-7E Naval Reactor Component Storage Area." N-CLC-E-00085, Rev. 0. Solid Waste Engineering, Savannah River Site, Aiken, SC. October 16, 2002.

U.S. DOE (2021b). "Radioactive Waste Management Manual." DOE M 435.1-1, Chg 3: 1-11-2021. U. S. Department of Energy, Washington, DC. January 11, 2021.

U.S. NRC (2000). "A Performance Assessment Methodology for Low-Level Radioactive Waste Disposal Facilities." NUREG-1573. U.S. Nuclear Regulatory Commission, Washington, DC. October 2000.

Wilhite, E. L., and Flach, G. P. (2004). "Evaluation of Proposed New LLW Disposal Activity: In-Place Disposal of Naval Reactor Components at the 643-7E Naval Reactor Component Storage Area." WSRC-RP-2004-00443, Rev. 0. Westinghouse Savannah River Company, Aiken, SC. June 29, 2004.

Wohlwend, J. L. (2020). "E-Area Low-Level Waste Facility GoldSim System Model." SRNL-STI-2020-00079, Rev. 0. Savannah River National Laboratory, Aiken, SC. April 2020.

Wohlwend, J. L., and Aleman, S. E. (2020). "GoldSim E-Area Low-Level Waste Facility Vadose Zone Model Benchmarking." SRNL-STI-2020-00372, Rev. 0. Savannah River National Laboratory, Aiken, SC. October 2020.

Wohlwend, J. L., and Butcher, B. T. (2018). "Proposed NRCDA Groundwater Pathway Conceptual Model." SRNL-STI-2018-00633, Rev. 0. Savannah River National Laboratory, Aiken, SC.

Wohlwend, J. L., and Hamm, L. L. (2020). "GoldSim E-Area Low-Level Waste Facility Aquifer Zone Model Calibration Methodology." SRNL-STI-2020-00346, Rev. 0. Savannah River National Laboratory, Aiken, SC. October 2020.

WSRC (1997). "Composite Analysis, E-Area Vaults and Saltstone Disposal Facilities." WSRC-RP-97-311, Rev. 0. Westinghouse Savannah River Company, Aiken, SC.

WSRC (2008). "E-Area Low-Level Waste Facility DOE 435.1 Performance Assessment." WSRC-STI-2007-00306, Rev. 0. Washington Savannah River Company, Savannah River Site, Aiken, SC.

Yu, A. D., McDowell-Boyer, L. M., Cook, J. R., and Young, K. E. (2002). "Special Analysis: Naval Reactor Waste Disposal Pad (U)." WSRC-RP-2001-00948, Rev. 2. Westinghouse Savannah River Company, Aiken, SC. December 2002.